



I. R. IRAN

ISSN: 1728-1431

e-ISSN: 1735-9244



International Journal of Engineering

Journal Homepage: www.ije.ir



TRANSACTIONS A: BASICS

Volume 35, Number 04, April 2022

Materials and Energy Research Center

INTERNATIONAL JOURNAL OF ENGINEERING

Transactions A: Basics

DIRECTOR-IN-CHARGE

A. R. Khavandi

EDITOR-IN-CHIEF

G. D. Najafpour

ASSOCIATE EDITOR

A. Haerian

EDITORIAL BOARD

- | | | | |
|------|--|-------|---|
| S.B. | Adelaju, Charles Sturt University, Wagga, Australia | A. | Mahmoudi, Bu-Ali Sina University, Hamedan, Iran |
| K. | Badie, Iran Telecomm. Research Center, Tehran, Iran | O.P. | Malik, University of Calgary, Alberta, Canada |
| M. | Balaban, Massachusetts Ins. of Technology (MIT), USA | G.D. | Najafpour, Babol Noshirvani Univ. of Tech., Babol, Iran |
| M. | Bodaghi, Nottingham Trent University, Nottingham, UK | F. | Nateghi-A, Int. Ins. Earthquake Eng. Seis., Tehran, Iran |
| E. | Clausen, Univ. of Arkansas, North Carolina, USA | S. E. | Oh, Kangwon National University, Korea |
| W.R. | Daud, University Kebangsaan Malaysia, Selangor, Malaysia | M. | Osanloo, Amirkabir Univ. of Tech., Tehran, Iran |
| M. | Ehsan, Sharif University of Technology, Tehran, Iran | M. | Pazouki, Material and Energy Research Center, Meshkindasht, Karaj, Iran |
| J. | Faiz, Univ. of Tehran, Tehran, Iran | J. | Rashed-Mohassel, Univ. of Tehran, Tehran, Iran |
| H. | Farrahi, Sharif University of Technology, Tehran, Iran | S. K. | Sadrnezhaad, Sharif Univ. of Tech, Tehran, Iran |
| K. | Firoozbakhsh, Sharif Univ. of Technology, Tehran, Iran | R. | Sahraeian, Shahed University, Tehran, Iran |
| A. | Haerian, Sajad Univ., Mashhad, Iran | A. | Shokuhfar, K. N. Toosi Univ. of Tech., Tehran, Iran |
| H. | Hassanpour, Shahrood Univ. of Tech., Shahrood, Iran | R. | Tavakkoli-Moghaddam, Univ. of Tehran, Tehran, Iran |
| W. | Hogland, Linnaeus Univ, Kalmar Sweden | T. | Teng, Univ. Sains Malaysia, Gelugor, Malaysia |
| A.F. | Ismail, Univ. Tech. Malaysia, Skudai, Malaysia | L. J. | Thibodeaux, Louisiana State Univ, Baton Rouge, U.S.A |
| M. | Jain, University of Nebraska Medical Center, Omaha, USA | P. | Tiong, Nanyang Technological University, Singapore |
| M. | Keyanpour rad, Materials and Energy Research Center, Meshkindasht, Karaj, Iran | X. | Wang, Deakin University, Geelong VIC 3217, Australia |
| A. | Khavandi, Iran Univ. of Science and Tech., Tehran, Iran | | |

EDITORIAL ADVISORY BOARD

- | | | | |
|-------|--|-------|--|
| S. T. | Akhavan-Niaki, Sharif Univ. of Tech., Tehran, Iran | A. | Kheyroddin, Semnan Univ., Semnan, Iran |
| M. | Amidpour, K. N. Toosi Univ of Tech., Tehran, Iran | N. | Latifi, Mississippi State Univ., Mississippi State, USA |
| M. | Azadi, Semnan university, Semnan, Iran | H. | Oraee, Sharif Univ. of Tech., Tehran, Iran |
| M. | Azadi, Semnan University, Semnan, Iran | S. M. | Seyed-Hosseini, Iran Univ. of Sc. & Tech., Tehran, Iran |
| F. | Behnamfar, Isfahan University of Technology, Isfahan | M. T. | Shervani-Tabar, Tabriz Univ., Tabriz, Iran |
| R. | Dutta, Sharda University, India | E. | Shirani, Isfahan Univ. of Tech., Isfahan, Iran |
| M. | Eslami, Amirkabir Univ. of Technology, Tehran, Iran | A. | Siadat, Arts et Métiers, France |
| H. | Hamidi, K.N.Toosi Univ. of Technology, Tehran, Iran | C. | Triki, Hamad Bin Khalifa Univ., Doha, Qatar |
| S. | Jafarmadar, Urmia Univ., Urmia, Iran | S. | Hajati, Material and Energy Research Center, Meshkindasht, Karaj, Iran |
| S. | Hesaraki, Material and Energy Research Center, Meshkindasht, Karaj, Iran | | |

TECHNICAL STAFF

M. Khavarpour; M. Mohammadi; V. H. Bazzaz, R. Esfandiar; T. Ebadi

DISCLAIMER

The publication of papers in International Journal of Engineering does not imply that the editorial board, reviewers or publisher accept, approve or endorse the data and conclusions of authors.

CONTENTS

Transactions A: Basics

M. E. Ergin; H. O. Tezcan	Joint Logit Model Approach to Analyze Soccer Spectators' Arrival Time and Location Preferences for Interim Activities in Istanbul	613-625
A. Parnak; Y. Baleghi Damavandi; S. J. Kazemitabar	A Novel Image Splicing Detection Algorithm Based on Generalized and Traditional Benford's Law	626-634
N. Ebrahimi; A. Sedaghat Ahangari Hosseinzadeh; M. Vaezi; M. Mozafari	Evaluation of Corrosion Resistance of Bi-layered Plasma-sprayed Coating on Titanium Implants	635-643
H. Boodaghi; M. M. Etghani; K. Sedighi	Advanced Exergy Scrutiny of a Dual-loop Organic Rankine Cycle for Waste Heat Recovery of a Heavy-duty Stationary Diesel Engine	644-656
M. Behzadi; M. Amirahmadi; M. Tolou Askari; M. Babaeinik	Identification of Combined Power Quality Disturbances in the Presence of Distributed Generations using Variational Mode Decomposition and K-nearest Neighbors Classifier	657-674
A. Bennabi; A. Adjeloua; H. Ameer; N. Boualem; M. Younsi	Influence of Multiple Repairs on the Quality of Duplex Welded Joints	675-684
M. Vatani; D. Domiri-Ganji	Experimental Examination of Gas-liquid Two-phase Flow Patterns in an Inclined Rectangular Channel with 90° Bend for Various Vertical Lengths	685-691
F. Marchione	Analytical Investigation on the Stress Distribution in Structural Elements Reinforced with Laminates Subjected to Axial Loads	692-697
A. Kumar; A. Kumar; K. K. Sharma	Investigation of Dielectric Properties of Ni/n-TiO ₂ /p-Si/Al Heterojunction in Wide Range of Temperature and Voltage	698-705
A. S. A. Al-Gharbawi; M. Y. Fattah; M. R. Mahmood	Effect of Carbonation on the Collapse Potential of Magnesium Oxide Treated Gypseous Soil	706-714
A. Abaei Kashan; A. Maghsoudi; N. Shoeibi; M. Heidarzadeh; K. Mirnia	An Automatic Optic Disk Segmentation Approach from Retina of Neonates via Attention Based Deep Network	715-724
R. Manda; R. Gowri	Universal Filtered Multicarrier Receiver Complexity Reduction to Orthogonal Frequency Division Multiplexing Receiver	725-731

T. A. Mohammed; H. M. Kadhim	Static and Dynamic Behavior of High-strength Lightweight Reinforced Concrete One-way Ribbed Slabs	732-739
D. Shijing; C. Hongru; W. Xudong; W. Deshi; Z. Yongyong	Modal Optimization Design of Supporting Structure Based on the Improved Particle Swarm Algorithm	740-749
U. D. Dixit; M. S. Shirdhonkar	An Improved Fingerprint-based Document Image Retrieval using Multi-resolution Histogram of Oriented Gradient Features	750-759
P. Rashidi Rad; S. A. Haj Seiyed Taghia; H. R. Darvishvand; M. Ebrahimi	Technical and Economical Approaches in Application of Micro Silica Gel and Calcium Carbonate Powder in Self-compacting Concrete	760-773
A. M. Hashim; A. Y. Ali	Structural Behavior of Reinforced Concrete Horizontally Curved Box Beam with Opening	774-783
M. Rupesh; T. S. Vishwanath	Intelligent Controllers to Extract Maximum Power for 10 KW Photovoltaic System	784-793
D. Kumar; S. Angra; S. Singh	Mechanical Properties and Wear Behaviour of Stir Cast Aluminum Metal Matrix Composite: A Review	794-801
A. A. Fallah; A. Soleymani; H. Khosravi	A Method for Automatic Lane Detection using a Deep Network	802-809
S. Adebayo; F. O. Aweda; I. A. Ojedokun; O. T. Olapade	Refractive Index Perception and Prediction of Radio wave through Recursive Neural Networks using Meteorological Data Parameters	810-818
S. T. Nemati Aghamaleki; M. Naghipour; J. Vaseghi Amiri; M. Nematzadeh	Experimental Study on Compressive Behavior of Concrete-filled Double-skin Circular Tubes with Active Confinement	819-829
T. K. Biswas; S. Chaki	Applications of Modified Simple Additive Weighting Method in Manufacturing Environment	830-836
H. A. T. Nguyen	Probabilistic Assessment of Bending Strength of Statically Indeterminate Reinforced Concrete Beams	837-844



Joint Logit Model Approach to Analyze Soccer Spectators' Arrival Time and Location Preferences for Interim Activities in Istanbul

M. E. Ergin^{*a}, H. O. Tezcan^b

^a Istanbul Commerce University, Faculty of Business, Department of Logistics Management, Istanbul, Turkey

^b Istanbul Technical University, Faculty of Civil Engineering, Department of Transportation Engineering, Istanbul, Turkey

PAPER INFO

Paper history:

Received 16 September 2021

Received in revised form 27 November 2021

Accepted 02 December 2021

Keywords:

Planned Special Event

Interim Activity

Joint Modelling

Multinomial Logit Model

Choice Model

Arrival Time

ABSTRACT

Planned Special Event (PSE) is a public activity that has a defined location and time and has an influence on transportation system operations as a consequence of increases in travel demand or decreases in road capacity. Apart from the event itself, PSEs might generate additional activities based on location, time and duration of the event, and individual preferences. This paper focuses on the interim activities of soccer spectators in Istanbul. This paper is motivated by the mostly disregarded but significantly important demand for these activities by jointly analyzing the arrival time and location preferences for the interim activities carried out before the main activity. For this aim, a joint logit model capturing the factors influencing the arrival time and location choice collectively within the PSE circumstances is estimated. In this estimation, each trip and behavior of spectator groups are modeled separately. According to the results of the models, one significant and interesting finding is the behavioral differences of supporters of different teams which is mostly influenced by the activity opportunities present in the surrounding of the venues. Last motorized trips of the Besiktas and Fenerbahce's spectators end at the sub-centers in general, while the spectators of the Galatasaray prefer the stadium as their final destination. Moreover, league matches being on weekdays or weekends does not have a statistically significant effect on the choice of arrival time and location of the spectators. The findings provide useful information that might assist event organizers and decision-makers especially in planning special events.

doi: 10.5829/ije.2022.35.04a.01

NOMENCLATURE

U	Utility of an alternative	Greek Symbols	
C	Choice set	ϵ	Stochastic component of the utility function (error term)
V	Deterministic component of the utility function	\sum	Sum operator
P	Probability of a chosen alternative	Subscripts	
e	Exponential form of formula	i, j	Alternatives

1. INTRODUCTION

Planned special event (PSE) impacts on transportation network with its known location and scheduled time as a result of increases in travel demand or decreases in the capacity of road segments [1]. The effects of special events are mostly experienced on main arterials [2]. In addition, secondary roads and public transportation capacity are also affected to a lesser extent [3]. Skolnik

et al. [3] reported that the level of the effectiveness of traffic demand management for PSEs is related to the number of attendees, arrival and departure patterns, available modes of transportation to and from the event, location and time.

PSEs frequently attract people from anywhere with different backgrounds into the host society, and then there can be interaction between societies and cultures [4]. Moreover, people create this interaction voluntarily

*Corresponding Author Institutional Email: meergin@ticaret.edu.tr
(M. E. Ergin)

and obviously, the driven force of this sharing is PSE [5].

Events can be classified in different ways in terms of their size, form, content, location and impact area [5]. Even though PSEs are planned occurrences, they raise the travel demand, abnormally and temporarily [3]. For PSE, Day [6] expressed that trip makers decide their departure times under consideration of the possible travel times and arrival times for their activity.

In general, individuals who participate in PSEs as the main activity attend to other derived activities such as eating, shopping, drinking, hanging out with friends, etc. These derived activities can be named as interim activities and they took place before and until the start of the PSE. This study analyzes the interim activity behavior of spectators by focusing on the preferences for the arrival time of the interim activity and the location of it. This analysis is performed by considering arrival time and location jointly as alternative pairs. The reason why arrival time is considered is straightforward; spectators who already paid for the tickets will always want to be at the venue at a convenient time before the event starts. This behavior is also applicable for the interim activities because, even though these activities are not compulsory and flexible by nature, their schedule must be arranged to avoid missing the start of the PSE. However, in the literature, mostly departure time is considered and although the departure time seems to be what is chosen, it is the time to arrive what matters in the context of PSEs.

In the preferences for interim activities, location is also critical in a sense that in addition to (or combined with) the arrival time, the place where the interim activities are carried out is directly linked with the concerns for being at the PSE venue on time. The selection of the location mainly depends on the distance to the venue, the traffic situation of the roads leading to the venue, travel time between the location and the venue, and the characteristics of the participants. In this study, soccer games, a type of PSEs, are discussed. The aim of the study is to obtain an acceptable and applicable model by considering the arrival time and location choices as time and space dimensions. The paper concerns with the variables that affect the joint choice of arrival time and location of the spectators and model these variables by using the Joint Multinomial Logit Model (JMNL) approach. Only last motorized trips made for interim activities are considered, on the other hand, non-motorized trips are omitted because of the fact that these locations are fairly close to the venue.

The paper is structured as follows: The next section presents an overview of the literature, and then in the third section the modeling methodology is demonstrated. The fourth section explains details of the study area and data. The fifth section describes the modelling approach and variables of the model. The results of the model are

given in the sixth section and the final section presents the discussions and final thoughts.

2. LITERATURE REVIEW

In the literature, PSE models generally consider only the main activity and travel demand from other zones to the event venues is solely forecasted [7-10], except very rare studies [11]. Moreover, PSE is analyzed by traffic management in some studies [1, 12-15] and spectator (customer) satisfaction point of view in others [16]. Most of the time, the literature on PSE studies is dominated by large-scale events such as Olympic Games, World Cup Tournaments, Winter Games, etc. [10, 13, 15].

A study conducted by Shin and Lyu [16] who argue the impacts of mega-scale planned special events' on the environment in terms of city planning and indicate urban regeneration challenges from the local residents' point of view. In this study, the PSE was a mega-scale event, which is called Glasgow 2014 Commonwealth Games. In another study, Giampiccoli et al. [17] compared the FIFA World Cup Football championship which is organized every four years and Comrades Marathon that is held yearly. They presented the effects of these sports events on economic development, tourism, and city plans. An analysis of these studies shows that mega-scale events have an important influence in the local economy. As can be seen from the examples, this effect on the immediate surroundings of the main activity areas is due to the presence of derived activities. For example, its contribution to the local economy is the crowd that comes there for the main event.

Generally, in literature in the field of urban trips or freight transport, mode and destination choice [18, 19], destination and parking choice [20], mode and departure time choice [21-23], time-use expenditure and mode choice [24] are jointly modelled. In some cases, nested logit model approach can be used for destination choice, departure time and mode choice analysis [25]. However, studies in the field of PSE are very limited.

PSE travel demand models are also studied at various scales, including microscopic, mesoscopic and macroscopic. The study by Zhou and Tian [26] who investigated the link between incident clearing time and highway clearance time by using micro-simulation software in order to run multiple traffic incident scenarios. Another study focuses on the microscopic models by Florez et al. [27] who analyzed and highlight the most essential features related with the choice of walking as a mode of transportation, based on interviews done with spectators during three FIFA Confederations Cup matches performed in June 2013 at Maracan stadium in Rio de Janeiro. Furthermore, during special events such as festivals, Pratiwi et al. [28] looked into visitor

satisfaction with pedestrian accessibility. Zagidullin [14] investigated traffic management models during a major sporting event in a city and developed dynamic models to assess the influence of background traffic flow and public transportation that serves the sporting event. In another study, with various event scenarios, a mesoscopic traffic assignment tool is designed to examine participants' behavior during planned special events for mode and departure time choices [29]. Shakibaei et al. [9] tried to get to the bottom of estimation of mode choice preferences by conducting revealed preference surveys. Kuppam et al. [7] discussed from all aspects of the data gathering to the four-step trip-based model building of planned special event travel demand in the Phoenix metropolitan region. Chang and Lu [30] used the Multinomial Logit Model (MNL) to research concertgoers' behavior in terms of mode and arrival time choices. Consequently, as detailed above, even though in PSE field microscopic [26-28], mesoscopic [14, 29], or macroscopic [9, 30, 31] analyses were undertaken, jointly modelling of "mode and time", "mode and destination" or "time and destination" studies are very rare in the literature. Therefore, it can be argued that there is a gap in the literature about this aspect of PSEs that is needed to be explored by using various modelling approaches.

3. METHODOLOGY

To understand the arrival time and location choice decisions of the interim activities, a joint MNL is estimated. MNL, which is easy to use and comprehend, is a commonly used modeling technique for choice modeling.

The utility theory underpins MNL's approach. This theory posits that among a choice set, each individual chooses the alternative that maximizes his or her utility. The utility of an alternative i (U_i) is comprised of two components given in Equation (1). In the equation, V_i is the deterministic (non-random) component of the utility and ε_i is the stochastic term that represents the differences in tastes [31]:

$$U_i = V_i + \varepsilon_i \quad (1)$$

In the MNL model, the probability of choosing an alternative i (P_i) over the alternatives in a choice set C is computed by using Equation (2) [32]:

$$P_i = \frac{e^{V_i}}{\sum_j e^{V_j}} \quad i, j \in C \quad (2)$$

P_i takes a value between 0 and 1, and the sum of the probabilities of each alternative equals to 1. In the literature, some research employed the MNL to model PSEs [9, 11, 30, 31], while others used the activity based modeling method [33, 34], and still others attempted various techniques like the mesoscopic simulation model

[29], the category based modeling approach [35] and so on. The flowchart of the proposed model is given in Figure 1. After defining the overall choice set, the well-known MNL process is followed.

4. STUDY AREA and DATA

In this study, soccer games are considered as the main activities and 3 stadiums that belong to the 3 biggest football clubs, Besiktas, Fenerbahce and Galatasaray, with the most fans in Turkey and Istanbul are selected (Figure 2). Among these stadiums, Besiktas Vodafone Park and Fenerbahce Ulker Stadium are located in two of the central districts which are Besiktas and Kadikoy, with a capacity of 41,903 and 50,530, respectively. On the other hand, Galatasaray Turk Telekom Stadium is located at a peripheral region in the Sariyer district with a capacity of 52,280. As a result, the transportation connections of the Vodafone Park and Fenerbahce Ulker Stadium are better than the Turk Telekom Stadium. Except the game days, the travel demand of the metro line connects the Turk Telekom Stadium to the transport network is very low. The details of the stadium connections are presented in Figure 3.

Face-to-face surveys were employed to gather the data. 7 games were chosen in 2018 – 2019 Turkish Super League for each and a total 21 different game days are used. The surveys began roughly 3 hours before the game and ended just before the game. Only, randomly selected home team fans were surveyed. The questioners, on the other hand, were divided into groups by the stadium entrances in order to acquire non-biased statistics and fan information from diverse stadium stands. Furthermore, to eliminate prejudice, interviews with any of the observers were conducted attentively and in the absence of other people's attention.

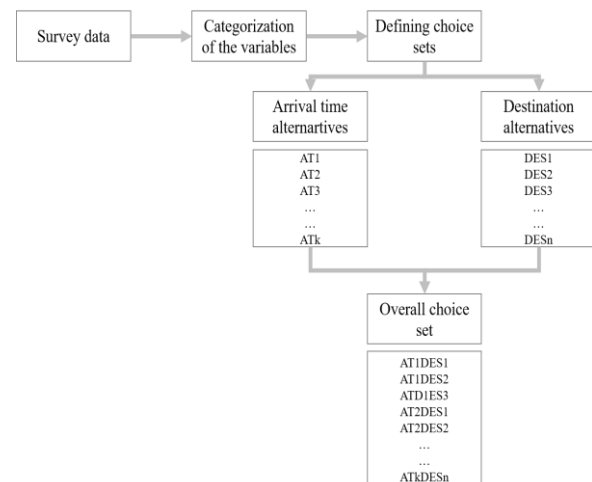


Figure 1. Flowchart of the proposed methodology



Figure 2. Selected stadiums and their location on the city



Figure 3. Selected stadiums and their connections to the transportation network

The survey is split into two parts. In the first section, fans' socioeconomic data were acquired, and their fandom levels were assessed using a series of structured questions. The second section of the survey inquired about the fans' travel and activity patterns. The survey consists of 17 questions and sub-questions that were provided to the participants.

The descriptive statistics of the data are provided in Table 1. The number of valid surveys at Besiktas Vodafone Park, Fenerbahce Ulker and Galatasaray Turk Telekom Stadium were 357, 386 and 378, respectively.

In accordance with Table 1, while Besiktas and Galatasaray's games were generally organized on weekends, Fenerbahce's games were mostly played on

TABLE 1. Descriptive statistics

Criteria	Groups	Besiktas (N=357)	Percentage	Fenerbahce (N=386)	Percentage	Galatasaray (N=378)	Percentage
Weekend	Weekend	82	23%	268	69%	56	15%
	Weekday	275	77%	118	31%	322	85%
Gender	Female	21	6%	16	4%	27	7%
	Male	336	94%	370	96%	351	93%
Private Car Ownership	No	188	53%	221	57%	213	56%
	Yes	169	47%	165	43%	165	44%
Who Does the Activity with?	Alone	81	23%	78	20%	84	22%
	Not Alone	276	77%	308	80%	294	78%
Seasonal Ticket	No	251	70%	235	61%	215	57%
	Yes	106	30%	151	39%	163	43%
Watching Outside Stadium	No	24	7%	24	6%	29	8%
	Yes	333	93%	362	94%	349	92%

Activity Types	Eating	64	18%	61	16%	67	18%
	Entertainment	89	25%	61	16%	112	30%
	Transfer	141	39%	232	60%	15	4%
	Waiting	41	11%	15	4%	182	48%
	Other	22	6%	17	4%	5	1%
Age Groups	15-24	82	23%	159	41%	109	29%
	25-34	141	39%	127	33%	159	42%
	35-44	94	26%	67	17%	91	24%
	45 +	40	11%	33	9%	19	5%
Income Groups (TRY)	0-3000	141	39%	216	56%	164	43%
	3001-5000	103	29%	79	20%	111	29%
	5001 +	113	32%	91	24%	103	27%
Ticket Groups	0-75	71	20%	200	52%	143	38%
	76 - 150	195	55%	112	29%	169	45%
	151 +	91	25%	74	19%	66	17%
Last Activity Cost (TRY)	0	187	52%	249	65%	186	49%
	1-50	101	28%	100	26%	144	38%
	51 +	69	19%	37	10%	48	13%
Last Activity Duration (min)	0	161	45%	236	61%	18	5%
	1-120	120	34%	87	23%	192	51%
	121 +	76	21%	63	16%	168	44%

weekdays. The rate of playing on weekdays is 23% and 15% for Besiktas and Galatasaray, respectively; it is 69% for Fenerbahce. The number of female fans at venues is quite small and the percentage of them is changing between 4 - 7%. The rate of having a private vehicle is slightly smaller than not having a private vehicle for each club. Commonly, people prefer to attend the PSE with someone else. As it is seen in Table 1, for each club, around 80% of spectators participate to the PSE with someone. Of course, attending with someone or alone is strongly related with the social network of the spectators; however, because of the purpose of the study, the external circumstances like these are neglected.

The team with the highest number of seasonal tickets is Galatasaray with 43%. It is followed by Fenerbahce with 39% and Besiktas with 30%. Moreover, more than 92% of spectators follow their teams' away games via different ways and 7, 6 and 8% of Besiktas, Fenerbahce and Galatasaray spectators, respectively; declared that they do not follow their team's away games. Activities are divided into groups that are Eating, Entertainment, Transfer, Waiting, and Other in accordance with the responses of the participants. Transfer is the mostly preferred activity type for spectators of Besiktas and Fenerbahce, with respect to 39% and 60%. The situation is not the same for Galatasaray fans, because of the land

use of vicinity of the stadium. As mentioned earlier, the Turk Telekom Stadium is located in the periphery of the urban area and because of the lack of beverage places, spectators cannot choose a close place to transfer. Therefore, the stadium is their last destination of their last motorized trips. Moreover, age and income of the spectators are also grouped in order to use categorical data. For each club, games are followed mostly by 25-34 age group, and 3,000 Turkish Lira (TRY per 1 EUR varies between 5.98 and 6.90 in 2018) monthly income group of people. Tickets are also grouped as cheap (0 – 75 TRY), moderate (76 – 150 TRY) and expensive (151 + TRY). Ticket price means a single game price. The spectators of Besiktas and Galatasaray prefer moderate price for the ticket, while Fenerbahce's spectators normally choose the cheap tickets, mostly. Last activity is the interim activity which is participated just before the PSE starts.

Mainly, spectators are not willing to spend money mostly for each club. While the duration of the interim activity is less for Besiktas and Fenerbahce (45% and 61%, respectively), the activity duration of Galatasaray fans is considerably longer than the others. The rate of those whose activity duration is more than 120 minutes is around 44%. The source of this difference is related with the spectators' behavior. In this study, the interim

activities at the destination with the last motorized trip is examined. Spectators of Besiktas and Fenerbahce get closer to the stadium by walking mode after motorized trips and spend more time here, as there are places where interim activities can be done. Galatasaray fans, on the other hand, participate in interim activities when they arrive by motorized vehicle and then come to the stadium only to enter the game.

The rate of those whose activity duration is more than 120 minutes is around 44%. The source of this difference is related with the spectators' behavior. In this study, the interim activities at the destination with the last motorized trip is examined. Spectators of Besiktas and Fenerbahce get closer to the stadium by walking mode after motorized trips and spend more time here, as there are places where interim activities can be done. Galatasaray fans, on the other hand, participate in interim activities when they arrive by motorized vehicle and then come to the stadium only to enter the game.

5. MODELLING ESTIMATION AND VARIABLES

In this study, the joint MNL method was utilized to determine the probability of arrival time and location choice decisions. Spectators choose various arrival times for interim activities. In order to examine spectators' behavior, the difference between arrival time and PSE starting time is used and called as Arrival Time Difference (ATD). The 3rd percentile of the ATD which means three categories will be created and the number of observations in each group should be equal very close to each other is taken into consideration for each club. The classification of ATD differs among the clubs as in Table 2. Spectators of Besiktas arrive to the destination almost 197 minutes on average before the PSE start. This duration is 204 minutes for Fenerbahce's fan and 163 minutes for Galatasaray's spectators.

According to the observations and survey analysis, spectators tend to choose stadium and other close areas to arrive in order to participate in an interim activity just before the games start as their final destination of their last motorized trips. In this study, official postal codes are used to distinguish interim activity locations. For

stadiums fictitious codes are assigned. These codes of the destinations are presented in Figure 4 and Table 3. As it was mentioned before, stadiums of Besiktas and Fenerbahce are located in central districts, so that people can find various places to attend any interim activity. For Besiktas district, Sinan Pasa neighborhood has several food and beverage places and main meeting point of Besiktas' spectators. Also it has strong transport connections with several central districts of the city. Omer Avni neighborhood is also has several commercial units but not as much as Sinan Pasa has, and it is also well connected to the transport network. Kadikoy district where Fenerbahce's stadium is located in is a central district and Caferaga neighborhood is one of the most visited area in the city and meeting point of the spectators. It is well connected area by sea line, metro, and other modes of transportation. Hasan Pasa neighborhood is also has several food and beverage places and strongly connected to the transportation infrastructure of the city, especially by metrobus. However, Turk Telekom Stadium is located at a peripheral district of Istanbul. Huzur neighborhood is newly developed area and the typical land use of the area is in the form of high-rise residences and offices. This neighborhood has a big shopping mall which is connected stadium by a monorail. Seyrantepe neighborhood is old developed but it is not a lively place like other important centers of the city. Seyrantepe and Huzur neighborhood is connected to the network by an additional metro line and several bus lines, only. As a result of the differences of the land use can be seen on the average cost and duration of the last activities, and average waiting time of the spectators. In order to test and compare the applicability of the model in the same city but in different land uses, a separate model should be estimated for each team spectator, including land use decisions. The land use and transportation network effect can be seen on the destination choice preferences. While approximately 16% of Besiktas and Fenerbahce's spectators prefer the stadiums as the destination of their last motorized trips, 70% of Galatasaray fans prefer the immediate vicinity of the stadium as their last motorized trips' destination.

TABLE 2. Various Arrival Time Difference groups according to 3rd percentile

ATD Groups	Besiktas (N=357)	Number	Percentage	Fenerbahce (N=386)	Number	Percentage	Galatasaray (N=378)	Number	Percentage
ATD1 (Short time)	0-120	109	31%	0-139	124	32%	0-119	122	32%
ATD2 (Medium time)	121-210	119	33%	140-239	134	35%	120-179	132	35%
ATD3 (Long time)	211 +	129	36%	240 +	128	33%	180 +	124	33%



Figure 4. Destinations and codes

TABLE 3. Last motorized trips destinations

Teams	Destination	Destination	Codes	Number of Obs.	Percentage
Besiktas	Vodafone Park Stadium	DES1	34001	58	16%
	Sinan Pasa Neigh.	DES2	34353	175	49%
	Omer Avni Neigh.	DES3	34427	124	35%
Fenerbahce	Ulker Stadium	DES1	34002	61	16%
	Caferaga Neigh.	DES2	34710	199	52%
	Hasanpasa Neigh	DES3	34722	126	33%
Galatasaray	Turk Telekom Stadium	DES1	34003	263	70%
	Seyrantepe Neigh.	DES2	34418	33	9%
	Huzur Neigh.	DES3	34396	82	22%

In order to avoid endogeneity issues, these two dimensions of activity participation are jointly modelled. Three ATD groups and three location alternatives account for a total of 9 alternatives for each stadium. In the study, three separate models having 9 alternatives for Beşiktaş, Galatasaray and Fenerbahçe are estimated.

Variables of the models

As in the ATD variable, some variables were grouped by using appropriate percentile. Income variable is divided into 3 groups and converted into a dummy variable by using 3rd percentile. This dummy variable is coded by using effects coding approach and the middle income group is taken as the base and coded as -1.

The same procedure is done for the Last Activity Duration. From the surveys it was seen that majority of Besiktas and Fenerbahce's spectators tend to get close to the stadium by walking. In other words, they prefer to spend their time within the walking distance of the stadiums. Therefore, for a large group of spectators of Besiktas and Fenerbahce games, the last activity duration is zero (because it is done with a non-motorized mode). Ticket cost is also classified according to the 3rd percentile as well. Here, the cost of single game ticket is used. For this reason, if the participant owns a seasonal ticket, the cost of the seasonal ticket is divided into the games in a season to obtain this cost. 3 group of ticket

cost are obtained which are cheap (base alternative and coded -1), moderate, and expensive. The variable "with whom" presents those who participate in the PSE with someone or alone. Participating the event with someone is coded as 1 while attending the event alone is coded -1. Surely, having a company with the activities is strongly related to his/her social network and other social issues. However, in this study these effects are neglected but this is another important perspective to study and analyze. The variable "weekend" represent the day of the games and "seasonal ticket" variables describes the spectators who has a seasonal ticket.

6. RESULTS

According to Leilei et al. [36], PSE participants typically come a short time before the start. However, from the sample it was observed that, the overall fans arrive at the vicinity of the stadium on average 188 minutes before the game begins, despite the fact that these games are held every two weeks.

Analyzing the relationship between the predicted model and the base model following results appear. For the estimated activity models, the value of -2LL for Besiktas, Fenerbahce, and Galatasaray are 822.950,

796.360, and 135.853, respectively (Equation (5)). These -2LL values are higher than the critical chi-square value of the degree of freedom of 72 for Besiktas and Fenerbahce which is 92.808 and 48 for Galatasaray which is 65.171 with significance at 5%. These results show that the estimated models are improved models. On the other hand, the Pseudo R2 (ρ^2) (Equation (6)) values

also show that the estimated models are strong ones with respect to goodness-of-fit. The Pseudo R2 value of Galatasaray is somewhat smaller than Besiktas and Fenerbahce's but it is still acceptable.

$$-2LL = -2(LL_{reference} - LL_{estimated}) \quad (5)$$

$$\rho^2 (Pseudo - R^2) = 1 - (LL_{estimated}/LL_{reference}) \quad (6)$$

TABLE 4. Model estimation results

Variables	Besiktas (N=357)		Fenerbahce (N=386)		Galatasaray (N=378)	
	Coefficient	t-stats	Coefficient	t-stats	Coefficient	t-stats
Constant 1	-0.22158	-0.36	1.25291**	2	1.88068***	3.64
Private Car Ownership 1	-0.12502	-0.32	0.3656	0.85	-0.81164**	-2.13
Income 1 1	-0.46741	-0.87	-0.3599	-0.56	-	-
Income 3 1	0.23644	0.5	0.0885	0.17	-	-
Waiting 1	-0.96077	-1.06	1.86609*	1.96	1.04974	1.49
Last Activity Duration 0 min 1	0.39843	0.9	1.99201***	2.86	-	-
Moderate Ticket Cost 1	0.1251	0.25	-1.04346*	-1.94	0.4076	0.8
Expensive Ticket Cost 1	-0.83745*	-1.74	0.33339	0.64	0.45306	1.05
Weekend 1	0.21233	0.52	-0.28128	-0.7	-	-
With Whom 1	.77193*	1.65	0.01084	0.02	-0.16808	-0.4
Seasonal Ticket 1	-	-	-	-	-0.37366	-1.02
Constant 2	-0.07052	-0.12	1.15617*	1.82	-0.51773	-0.7
Private Car Ownership 2	-0.71346**	-2.03	-0.11565	-0.28	0.10748	0.21
Income 1 2	-0.04938	-0.1	0.09329	0.16	-	-
Income 3 2	-0.57199	-1.25	0.34751	0.71	-	-
Waiting 2	-0.23862	-0.29	0.82767	0.82	0.76985	0.87
Last Activity Duration 0 min 2	1.16768**	2.53	3.49429***	4.89	-	-
Moderate Ticket Cost 2	-0.26673	-0.55	-0.44762	-0.93	0.67042	0.97
Expensive Ticket Cost 2	-0.4822	-1.07	0.61675	1.21	1.51243**	2.5
Weekend 2	0.19256	0.51	-0.01783	-0.05	-	-
With Whom 2	.77242*	1.84	0.6906	1.52	-0.20168	-0.38
Seasonal Ticket 2	-	-	-	-	-1.09176**	-2.26
Constant 3	0.53033	1.03	-1.27272	-1.1	0.57063	0.95
Private Car Ownership 3	-0.49172	-1.47	-0.44928	-1.03	-0.0628	-0.14
Income 1 3	0.5929	1.33	-0.156	-0.25	-	-
Income 3 3	-1.15370**	-2.53	0.68267	1.34	-	-
Waiting 3	-0.45935	-0.6	0.64567	0.38	0.20276	0.24
Last Activity Duration 0 3	1.61170***	3.6	5.95924***	4.91	-	-
Moderate Ticket Cost 3	-0.65051	-1.38	-0.5622	-1.1	0.64377	1.04
Expensive Ticket Cost 3	-0.55204	-1.28	0.41439	0.76	.88676*	1.7
Weekend 3	0.04702	0.14	0.00185	0	-	-
With Whom 3	-0.13142	-0.4	0.43473	0.93	-0.38452	-0.81
Seasonal Ticket 3	-	-	-	-	-0.4655	-1.08

Constant 4			-0.64341	-0.72	1.86623***	3.59
Private Car Ownership 4			0.41843	0.89	-1.05876***	-2.76
Income 1 4			-0.74077	-0.98	-	-
Income 3 4			0.37013	0.67	-	-
Waiting 4			2.01149**	2.02	0.75881	1.07
Last Activity Duration 0 4		Reference	0.22756	0.27	-	-
Moderate Ticket Cost 4			-0.70992	-1.19	0.3672	0.72
Expensive Ticket Cost 4			0.22337	0.4	0.44403	1.03
Weekend 4			-0.2116	-0.47	-	-
With Whom 4			0.83195	1.27	0.00059	0
Seasonal Ticket 4	-	-	-	-	-0.56056	-1.53
Constant 5	1.22770***	2.68	1.59782***	2.62	-1.06306	-1.16
Private Car Ownership 5	-.83776**	-2.56	-0.09704	-0.24	0.11075	0.2
Income 1 5	0.15351	0.35	0.06375	0.11	-	-
Income 3 5	-0.40941	-0.99	0.55153	1.16	-	-
Waiting 5	-1.43101**	-1.98	0.09203	0.1	0.5205	0.53
Last Activity Duration 0 5	0.2276	0.61	3.20792***	4.61	-	-
Moderate Ticket Cost 5	-.83354*	-1.79	-0.42093	-0.89	0.1434	0.2
Expensive Ticket Cost 5	-0.31951	-0.78	0.66143	1.32	0.25238	0.43
Weekend 5	0.23233	0.69	-0.12025	-0.32	-	-
With Whom 5	0.34328	1.03	0.44793	1.03	0.28869	0.43
Seasonal Ticket 5	-	-	-	-	0.7338	1.13
Constant 6	0.32271	0.61	0.54984	0.78	0.50004	0.83
Private Car Ownership 6	-.60624*	-1.78	-0.09001	-0.22	0.07851	0.18
Income 1 6	0.20985	0.46	0.20433	0.34	-	-
Income 3 6	-.77227*	-1.73	0.80916	1.63	-	-
Waiting 6	-0.42985	-0.53	1.39396	1.15	0.49766	0.63
Last Activity Duration 0 6	1.30850***	2.94	4.54810***	5.67	-	-
Moderate Ticket Cost 6	-0.73254	-1.5	-0.53355	-1.09	0.93183	1.59
Expensive Ticket Cost 6	-0.3749	-0.86	0.5706	1.09	0.58017	1.21
Weekend 6	0.3954	1.05	0.0314	0.08	-	-
With Whom 6	0.11974	0.35	0.0745	0.17	-0.08862	-0.19
Seasonal Ticket 6	-	-	-	-	-0.10622	-0.26
Constant 7	0.22174	0.4			1.60951***	3.05
Private Car Ownership 7	-.69394*	-1.75			-.83555**	-2.14
Income 1 7	0.28917	0.54			-	-
Income 3 7	-0.85132	-1.54			-	-
Waiting 7	-1.54227*	-1.89	Reference		0.93629	1.3
Last Activity Duration 0 7	-1.17656**	-2.34			-	-
Moderate Ticket Cost 7	-1.11858*	-1.72			-0.05013	-0.1
Expensive Ticket Cost 7	-0.00487	-0.01			0.61252	1.38
Weekend 7	-0.45788	-1.18			-	-

With Whom 7	0.01751	0.04			-0.37372	-0.87
Seasonal Ticket 7	-	-	-	-	-0.99732***	-2.62
Constant 8	1.70407***	3.88	2.12828***	3.6		
Private Car Ownership 8	-0.51117	-1.59	-0.21117	-0.55		
Income 1 8	0.03478	0.08	0.11445	0.21		
Income 3 8	-0.66786*	-1.66	0.33931	0.75		
Waiting 8	-1.88525***	-2.71	-0.77281	-0.99		
Last Activity Duration 0 8	-0.77805**	-2.14	2.26977***	3.4		Reference
Moderate Ticket Cost 8	-0.53645	-1.22	-0.31979	-0.72		
Expensive Ticket Cost 8	-0.40529	-1.03	0.43449	0.92		
Weekend 8	0.18437	0.57	-0.33152	-0.91		
With Whom 8	0.31064	0.97	0.40567	0.98		
Seasonal Ticket 8	-	-	-	-		
Constant 9	0.71653	1.47	0.15778	0.22	0.94310*	1.68
Private Car Ownership 9	-0.90463**	-2.49	-0.19307	-0.44	-0.27379	-0.68
Income 1 9	0.27043	0.56	0.36375	0.58	-	-
Income 3 9	-0.55238	-1.17	0.70111	1.34	-	-
Waiting 9	-2.40475***	-2.91	1.48767	1.21	0.82819	1.1
Last Activity Duration 0 9	0.27323	0.64	4.05461***	5.09	-	-
Moderate Ticket Cost 9	-0.53953	-1.08	-0.52154	-1.01	0.41473	0.76
Expensive Ticket Cost 9	-0.26747	-0.59	0.52172	0.95	0.53749	1.17
Weekend 9	-0.04309	-0.12	-0.25183	-0.6	-	-
With Whom 9	0.16158	0.44	0.40946	0.87	-0.06581	-0.15
Seasonal Ticket 9	-	-	-	-	-0.00302	-0.01
LL()	-628.49491		-666.17231		-497.52337	
LL(M)	-217.0219		-267.99219		-429.59698	
- 2LL	822.94602		796.36024		135.85278	
ρ^2	0.65		0.60		0.14	

***, **, * ==> Significance at 1%, 5%, 10% level.

According to the model results, the weekend variable is not statistically significant for any fan group. Similarly, a monthly income of less than 3,000 TRY do not have a significant effect on arrival time and location choice compared to an average monthly income group. Private car ownership variable took a positive value only in cases where people arrived in the immediate vicinity of the Turk Telekom an average of time before the start of the event. Others have negative values. As the private car ownership of spectators of Besiktas increases; the tendency to arrive in Sinanpasa at a short and medium time before the start of the event, at a medium and long time in Omer Avni, and at a long time in the immediate vicinity of the stadium decreases. As the private car ownership of Galatasaray fans increases, the tendency to

arrive at the stadium at a short or long time before the event decreases. Moreover, the tendency to arrive at the stadium at a medium time before the event increases, as well. However, the private car ownership variable is not significant for spectators of the Fenerbahce. According to the results, for Besiktas fans with a monthly income of more than 5,000 TRY arrive at the stadium on average of time before the start of the event, have a tendency to be in the immediate vicinity of the stadium at a short or average time before the event in Omer Avni, and at a long time before the event in Sinanpasa decreases. As the selection of the waiting activity increases, the tendency of Besiktas fans to arrive at the Sinanpasa with an average and long time before the start of the event, and at the Omer Avni Mahallesi and the stadium in a long time

decreases, while the tendency of Fenerbahce fans to arrive at the stadium with a short and average time before the event increases. As the duration of the activity at the last station of the motorized journey is 0 (zero), the probability of Besiktas fans to arrive at the stadium and Sinanpasa a long time before the start of the event decreases, while the probability of arriving at Omer Avni and Sinanpasa with a short and average time before the start of the event increases. Similarly, as the duration of the activity is 0, which means the spectators transfer from the motor vehicle to walking mode without waiting, the probability of arriving at the Caferaga and Hasanpasa on average or long time before the start of the event increases. As the ticket price is moderate, the tendency of Besiktas fans to be in Sinanpasa before the start of the games and in the Stadium with a long time before the start of the games decreases. Likewise, the possibility of Fenerbahce spectators being in the immediate vicinity of the stadium shortly before the games, moderate ticket price decreases. Moreover, as the ticket price increases, the tendency of Besiktas fans to be in immediate vicinity of the stadium shortly before the start of the event decreases, while the tendency of Galatasaray fans to come to the Seyrantepe and Huzur shortly before the event rises. As the number of Besiktas fans attending the event alone increases, the probability of being in the stadium or Sinanpasa climbs, as well. The tendency of Galatasaray fans with a seasonal ticket to prefer Seyrantepe shortly before the event, and the stadium for a long time before the event decreases according to their preference for being at Seyrantepe long time before the event. Having a seasonal ticket is insignificant for Besiktas and Fenerbahce's spectators as in the studies in the literature [9, 11].

Chang and Lu [30] developed a PSE model and variables such as age, gender, travel time, travel cost are significant. However, in this study, these variables were insignificant.

7. DISCUSSION

When the issue is a PSE that individuals pay for and expect happiness and pleasure, traffic management and understanding of the behavior of spectators become more important. The areas which face the travel demand more than the others are the destinations of the last motorized trips. In this study, the arrival time and location choice of the spectators for interim events are jointly analyzed to understand the behavioral differences of fans. As a result of this study, it is seen that whether the league matches are on weekdays or weekends does not have a statistically significant effect on the choice of arrival time and location. Spectators arrive at the immediate vicinity of the stadium approximately 4 hours before the game. As in the literature, cruise passengers expressed a high

degree of pleasure with their location and spent over 5 hours on land and they spent an average of about 36 € per capita at the destination [37]. According to the observations, it has been seen that the biggest reason for this situation is traffic congestion and insufficient parking space; a deduction not supported by the model findings due to lack of variables. The waiting activity is mostly done by the low-income supporter group. In addition, as the ticket price increases, the spectators do not reach the vicinity of the stadiums, but prefer to go to other sub-centers where there are more food and beverage venues, more than 4 hours before the event. Fenerbahce and Besiktas fans gather in the centers where they have met for years for almost every game, while Galatasaray fans gather in a shopping mall close to the stadium.

Evidently, interim activities should be considered for an effective traffic management for PSEs as they reflect a distinguishable behavioral pattern. As a result, travel demand prediction is a very crucial aspect that effects directly traffic management policies [35]. It is seen that sub-centers are the first place to encounter motorized travel demand derived by PSEs. Policies should be developed for everyone who participates or does not participate in these events which are organized regularly every week. The policies may be produced according to the results as follow:

- Arrangement and planning of parking areas according to the maximum walking distance, not immediate vicinity of the stadium,
- Planning safe walking spaces from parking lots to stadiums,
- Considering the destination of the derived travel demand originating from the PSE as sub-centered, not stadium-centered,
- Ensuring more effective traffic management by planning various and small centers (perhaps temporarily only on PSE days) rather than being a single and big center.

8. CONCLUSION

Finally, as a purpose of the study, establishing an acceptable and applicable model by considering the arrival time and location choices as time and space dimensions is needed to understand the behaviour of the spectators of the PSEs. The model and its variables may differ from the proposed model in this study, but as a result of the approach which is tried to be emphasized in this study is that time and space dimensions should not be separated for a better model structure. The findings show useful information that might assist special event planners and politicians with marketing and planning initiatives.

9. REFERENCES

1. Latoski, S.P., Dunn, W.M., Wagenblast, B., Randall, J. and Walker, M.D., *Managing travel for planned special events*. 2003, United States. Joint Program Office for Intelligent Transportation Systems.
2. Schrank, D., Eisele, B. and Lomax, T., "Urban mobility report powered by inrix traffic data. 2012", (2012), doi. <https://static.tti.tamu.edu/tti.tamu.edu/documents/umr/archive/mobility-report-2012.pdf>
3. Skolnik, J., Chami, R. and Walker, M., *Planned special events: Economic role and congestion effects*. 2008, United States. Federal Highway Administration.
4. Cook, R.A., Hsu, C.H. and Taylor, L.L., "Tourism: The business of hospitality and travel, Pearson New York, Vol. 6, (2018).
5. Getz, D.J.T.m., "Event tourism: Definition, evolution, and research", *Tourism Management*, Vol. 29, No. 3, (2008), 403-428, doi. <https://doi.org/10.1016/j.tourman.2007.07.017>
6. Day, N., "The joint modelling of trip timing and mode choice", (2008),
7. Kuppam, A., Copperman, R., Lemp, J., Rossi, T., Livshits, V., Vallabhaneni, L., Jeon, K. and Brown, E.J.T.L., "Special events travel surveys and model development", *Transportation Letters*, Vol. 5, No. 2, (2013), 67-82, doi. <https://doi.org/10.1179/1942786713Z.00000000007>
8. Li, Y., Wang, X., Sun, S., Ma, X. and Lu, G.J.T.R.P.C.E.T., "Forecasting short-term subway passenger flow under special events scenarios using multiscale radial basis function networks", *Transportation Research Part C*. Vol. 77, (2017), 306-328, doi. <https://doi.org/10.1016/j.trc.2017.02.005>
9. Shahin, S., Hüseyin, T.O., Kemal, Ö.S.J.P.-S. and Sciences, B., "Evaluating transportation preferences for special events: A case study for a megacity, istanbul", *Transportation. Procedia - Social and Behavioral Sciences*, Vol. 111, (2014), 98-106, doi. <https://doi.org/10.1016/j.sbspro.2014.01.042>
10. Frawley, S., Van den Hoven, P.J.S. and Society, "Football participation legacy and australia's qualification for the 2006 football world cup", *Soccer & Society*, Vol. 16, No. 4, (2015), 482-492, doi. <https://doi.org/10.1080/14660970.2014.882817>
11. E Ergin, M. and Tezcan, H.J.I.J.o.E., "Planned special event travel demand model development", *International Journal of Engineering, Transactions B: Applications*, Vol. 34, No. 2, (2021), 336-347, doi. <https://doi.org/10.5829/IJE.2021.34.02B.05>
12. Dunn, W., "Managing travel for planned special events handbook: Executive summary, US Department of Transportation, Federal Highway Administration, (2007).
13. Frantzeskakis, J.M. and Frantzeskakis, M.J.J.I.o.T.E.I.J., "Athens 2004 olympic games: Transportation planning, simulation and traffic management", *ITE Journal*, Vol. 76, No. 10, (2006), 26, doi. <https://trid.trb.org/view/795755>
14. Zagidullin, R.J.T.R.P., "Model of road traffic management in the city during major sporting events", *Transportation Research Procedia*, Vol. 20, (2017), 709-716, doi. <https://doi.org/10.1016/j.trpro.2017.01.115>
15. Yaun, F., Giese, K. and Lew, K., "A multiclass dynamic traffic assignment model for special events management", in 12th TRB National Transportation Planning Applications Conference, Citeseer. (2009).
16. Shin, J.-h. and Lyu, S.O.J.S.M.R., "Using a discrete choice experiment to estimate spectators' willingness to pay for professional baseball park sportscape", *Sport Management Review*, Vol. 22, No. 4, (2019), 502-512, doi. <https://doi.org/10.1016/j.smr.2018.06.009>
17. Giampiccoli, A., Lee, S.S. and Nauright, J.J.C.i.i.t., "Destination south africa: Comparing global sports mega-events and recurring localised sports events in south africa for tourism and economic development", *Current Issues in Tourism*, Vol. 18, No. 3, (2015), 229-248, doi. <https://doi.org/10.1080/13683500.2013.787050>
18. Keya, N., Anowar, S., Bhowmik, T., Eluru, N.J.T.R.P.E.L. and Review, T., "A joint framework for modeling freight mode and destination choice: Application to the us commodity flow survey data", *Transportation Research Part E: Logistics and Transportation Review*, Vol. 146, (2021), 102208, doi. <https://doi.org/10.1016/j.tre.2020.102208>
19. Ding, C., Xie, B., Wang, Y., Lin, Y.J.D.D.i.N. and Society, "Modeling the joint choice decisions on urban shopping destination and travel-to-shop mode: A comparative study of different structures", *Green Intelligent Transport System*, Vol. 2014, (2014), doi. <https://doi.org/10.1155/2014/492307>
20. Liu, W., Zhang, F. and Yang, H.J.T.R.P.C.E.T., "Modeling and managing the joint equilibrium of destination and parking choices under hybrid supply of curbside and shared parking", *Transportation Research Part C: Emerging Technologies*, Vol. 130, (2021), 103301, doi. <https://doi.org/10.1016/j.trc.2021.103301>
21. Seyedabrishami, S. and Izadi, A.R.J.T.R.P., "A copula-based joint model to capture the interaction between mode and departure time choices in urban trips", *Transportation Research Procedia*, Vol. 41, (2019), 722-730, doi. <https://doi.org/10.1016/j.trpro.2019.09.120>
22. Lizana, P., de Dios Ortúzar, J., Arellana, J., Rizzi, L.I.J.T.R.P.A.P. and Practice, "Forecasting with a joint mode/time-of-day choice model based on combined rp and sc data", *Transportation Research Part A: Policy and Practice*, Vol. 150, (2021), 302-316, doi. <https://doi.org/10.1016/j.tra.2021.06.006>
23. Tringides, C.A., Ye, X. and Pendyala, R.M.J.T.R.R., "Departure-time choice and mode choice for nonwork trips: Alternative formulations of joint model systems", *Transportation Research Record: Journal of the Transportation Research Board*, Vol. 1898, No. 1, (2004), 1-9, doi. <https://doi.org/10.3141/1898-01>
24. Jokubauskaitė, S., Hössinger, R., Aschauer, F., Gerike, R., Jara-Díaz, S., Peer, S., Schmid, B., Axhausen, K.W. and Leisch, F.J.T.R.P.B.M., "Advanced continuous-discrete model for joint time-use expenditure and mode choice estimation", *Transportation Research Part B: Methodological*, Vol. 129, (2019), 397-421, doi. <https://doi.org/10.1016/j.trb.2019.09.010>
25. Elmorssy, M. and Nur, T.J.I.J.o.E., "Modelling departure time, destination and travel mode choices by using generalized nested logit model: Discretionary trips", *International Journal of Engineering, Transactions B: Applications*, Vol. 33, No. 2, (2020), 186-197, doi. <https://doi.org/10.5829/IJE.2020.33.02B.02>
26. Zhou, H., Tian, Z.J.P.-s. and sciences, b., "Modeling analysis of incident and roadway clearance time", *Procedia - Social and Behavioral Sciences*, Vol. 43, (2012), 349-355, doi. <https://doi.org/10.1016/j.sbspro.2012.04.108>
27. Florez, J., Muniz, J., Portugal, L.J.P.-S. and Sciences, B., "Pedestrian quality of service: Lessons from maracanã stadium", *Procedia - Social and Behavioral Sciences*, Vol. 160, (2014), 130-139, doi. <https://doi.org/10.1016/j.sbspro.2014.12.124>
28. Pratiwi, A.R., Zhao, S. and Mi, X.J.F.o.A.R., "Quantifying the relationship between visitor satisfaction and perceived accessibility to pedestrian spaces on festival days", *Frontiers of Architectural Research*, Vol. 4, No. 4, (2015), 285-295, doi. <https://doi.org/10.1016/j.foar.2015.06.004>
29. Lin, Y.-Z. and Chen, W.-H.J.T.r.p., "A simulation-based multiclass, multimodal traffic assignment model with departure time for evaluating traffic control plans of planned special

- events", *Transportation Research Procedia*, Vol. 25, (2017), 1352-1379, doi. <https://doi.org/10.1016/j.trpro.2017.05.161>
30. Chang, M.-S. and Lu, P.-R.J.J.o.t.E.A.S.f.T.S., "A multinomial logit model of mode and arrival time choices for planned special events", *Journal of Eastern Asia Society for Transport Studies*, Vol. 10, (2013), 710-727, doi. <https://doi.org/10.11175/easts.10.710>
31. Koppelman, F.S. and Bhat, C., "A self instructing course in mode choice modeling: Multinomial and nested logit models", (2006), doi. <https://trid.trb.org/view/793000>
32. Kamboozia, N., Ameri, M., Hosseinian, S.M.J.I.j.o.i.c. and promotion, s., "Statistical analysis and accident prediction models leading to pedestrian injuries and deaths on rural roads in iran", *International Journal of Injury Control and Safety Promotion*, Vol. 27, No. 4, (2020), 493-509, doi. <https://doi:10.1080/17457300.2020.1812670>
33. Yan, L.C., Yang, S.S. and Fu, G.J.J.J.o.T.E., "Travel demand model for beijing 2008 olympic games", *Journal of Transportation Engineering*, Vol. 136, No. 6, (2010), 537-544, doi. [https://doi.org/10.1061/\(ASCE\)TE.1943-5436.0000105](https://doi.org/10.1061/(ASCE)TE.1943-5436.0000105)
34. Kwoczek, S., Di Martino, S., Nejd, W.J.J.o.V.L. and Computing, "Predicting and visualizing traffic congestion in the presence of planned special events", *Journal of Visual Languages and Computing*, Vol. 25, No. 6, (2014), 973-980, doi. <https://doi.org/10.1016/j.jvlc.2014.10.028>
35. Ghasemi, J. and Rasekhi, J.J.I.J.o.E., "Traffic signal prediction using elman neural network and particle swarm optimization", *International Journal of Engineering-Transactions B: Applications*, Vol. 29, No. 11, (2016), 1558-1564, doi. <https://doi:10.5829/idosi.ije.2016.29.11b.09>
36. Leilei, D., Zheng-liang, S., Jin-gang, G. and Hong-tong, Q., "Study on traffic organization and management strategies for large special events", in 2012 International Conference on System Science and Engineering (ICSSE), IEEE., (2012), 432-436.
37. Casado-Díaz, A.B., Navarro-Ruiz, S., Nicolau, J.L. and Ivars-Baidal, J.J.T.M., "Expanding our understanding of cruise visitors' expenditure at destinations: The role of spatial patterns, onshore visit choice and cruise category", *Tourism Management*, Vol. 83, (2021), 104199, doi. <https://doi.org/10.1016/j.tourman.2020.104199>

Persian Abstract

چکیده

رویداد ویژه برنامه ریزی شده (PSE) یک فعالیت عمومی است که مکان و زمان مشخصی دارد و در نتیجه افزایش تقاضای سفر یا کاهش ظرفیت جاده، بر عملیات سیستم حمل و نقل تأثیر می‌گذارد. جدا از خود رویداد، PSE ها ممکن است فعالیت‌های بیشتری را بر اساس مکان، زمان و مدت رویداد و ترجیحات فردی ایجاد کنند. این مقاله بر فعالیت‌های موقت تماشاگران فوتبال در استانبول تمرکز دارد. این مقاله با تحلیل مشترک زمان رسیدن و اولویت‌های مکان برای فعالیت‌های موقتی که قبل از فعالیت اصلی انجام شده است، انگیزه‌ی تقاضای عمدتاً نادیده گرفته شده اما بسیار مهم برای این فعالیت‌ها است. برای این هدف، یک مدل لاجیت مشترک که عوامل موثر بر زمان رسیدن و انتخاب مکان را به طور جمعی در شرایط PSE برآورد می‌کند. در این برآورد، هر سفر و رفتار گروه‌های تماشاگر به طور جداگانه مدل سازی شده است. با توجه به نتایج مدل‌ها، یکی از یافته‌های قابل توجه و جالب، تفاوت‌های رفتاری حامیان تیم‌های مختلف است که بیشتر متأثر از فرصت‌های فعالیت موجود در اطراف سالن‌ها است. آخرین سفرهای موتوری تماشاگران بشیکتاش و فنرباغچه به طور کلی در مراکز فرعی به پایان می‌رسد، در حالی که تماشاگران گالاتاسرای ورزشگاه را به عنوان مقصد نهایی خود ترجیح می‌دهند. علاوه بر این، برگزاری مسابقات لیگ در روزهای هفته یا آخر هفته از نظر آماری تأثیر معناداری بر انتخاب زمان ورود و مکان تماشاگران ندارد. این یافته‌ها اطلاعات مفیدی را ارائه می‌دهد که ممکن است به سازمان دهندگان رویداد و تصمیم‌گیرندگان به ویژه در برنامه ریزی رویدادهای خاص کمک کند.



A Novel Image Splicing Detection Algorithm Based on Generalized and Traditional Benford's Law

A. Parnak, Y. Baleghi*, J. Kazemitabar

Department of Electrical & Computer Engineering, Babol Noshirvani University of Technology, Babol, Iran

PAPER INFO

Paper history:

Received 13 September 2021

Received in revised form 08 December 2021

Accepted 23 December 2021

Keywords:

Image Forgery Detection

Image Splicing

Mantissa Distribution

Benford's Law

ABSTRACT

Due to the ease of access to platforms that can be used by forgers to tamper digital documents, providing automatic tools for identifying forged images is now a hot research field in image processing. This paper presents a novel forgery detection algorithm based on variants of Benford's law. In the proposed method, Mean Absolute Deviation (MAD) feature is extracted using traditional Benford's law. Also, generalized Benford's law is used for mantissa distribution feature vector. In addition to Benford's law-based features, other statistical features are used to construct the final feature vector. Finally, support vector machine (SVM) with three different kernel functions is used to classify original and forged images. The method has been tested on two common image datasets (CASIA V1.0 and V2.0). The experimental results show that 0.27% and 0.21% improvements on CASIA V1.0 and CASIA V2.0 datasets were achieved, respectively in detection accuracy by the proposed method in comparison to best state-of-the-art methods. The proposed efficient algorithm has a simple implementation. Moreover, on the basis of Benford's law rich features are extracted from images so that classification process is efficiently performed by a simple SVM classifier in a short time.

doi: 10.5829/ije.2022.35.04a.02

1. INTRODUCTION

Nowadays, with the development of digital image editing [1]. software and applications, it is possible to change the content of digital images and share them in a wide range of cyberspace more than before. Accordingly, a platform has been created for abusers to tamper digital documents and images according to their ominous aims. They try to do forgery in a way that is not recognizable through the human eye. Therefore, there is a need for automatic tools for detecting tampered images.

Generally, there are two common kinds of image forgeries: image cloning (or copy-move) and image splicing (or cut-paste). Image tampering is the process of replacing the content of an original image by one or some new content. If the content of original image is replaced by new content of the same image, it is named as copy-move, and if the content of original image is replaced by new content of another image, it is called image splicing. So far, many approaches have been suggested to detect

the two common forgeries, and are still being developed, which can be used to prevent possible further damages.

This paper presents a new method based on generalized and traditional Benford's law for detection of spliced images. To do this, the RGB image is converted into YCbCr image and after image blocking, two-dimensional discrete cosine transform (2D-DCT) is applied to each block. Then, features based on mantissa distribution, mean absolute deviation (MAD), standard deviation (STD) and entropy, are extracted and then combined to construct a final feature vector. Finally, support vector machine (SVM) [2]. is applied for classification. The proposed method is able to detect spliced images with the highest accuracy rate on CASIA V1.0 and CASIA V2.0 databases in compare to other recent methods. The method has a simple implementation and using the presented technique of applying Benford's law can extract the powerful features from images so that classification process is efficiently performed by an SVM in a short time.

*Corresponding Author Institutional Email: y.baleghi@nit.ac.ir
(Y. Baleghi)

Rest of the paper is organized as follows: Section 2 presents literature review. The proposed method for image splicing detection is described in section 3. The experimental results and performance evaluation are given in section 4. Finally, section 5 concludes the paper.

2. LITERATURE REVIEW

Despite the huge literature on image splicing detection [3], they can be categorized as handcrafted and deep features-based algorithms. In the category of deep features-based works, El-Latif et al. [4] applied an algorithm based on Convolutional Neural Network (CNN), that contains 6 convolutional layers and 3 pooling layers, to extract features from the spliced image. The results achieved 95.45% detection rate for CASIA V1.0 and 97.27% for CASIA V2.0 datasets.

On the other hand, several works are reported on handcrafted features. They are often based on coefficients of popular transforms like Discrete Wavelet Transform (DWT). In this category, Kasban and Nassar [5] applied Hilbert–Huang transform (HHT) features for copy-move and image splicing detection. The results showed that the suggested method achieved detection accuracies 98.95% and 99.13% for CASIA V1.0 and CASIA V2.0 databases, respectively.

Fusheng and Gao [6] suggested an approach based on Discrete Cosine Transform (DCT) Coefficient-Pair histogram. In this method, first, the image is transformed by DCT, and then the differential DCT coefficient matrix of two directions, such as horizontal and vertical direction are calculated. Then coefficient-pair histograms for each differential DCT coefficient matrix are computed within the given threshold. The experiments show 99.24% and 97.56% accuracy rates in CASIA V1.0 and CASIA V2.0 datasets, respectively. DWT and Local Binary Pattern (LBP) histogram have been suggested for detecting image splicing by Kaur and Gupta [7]. The results achieved detection accuracies 92.62% and 94.09% for CASIA V1.0 and CASIA V2.0 databases, respectively.

Application of the Markov features in Quaternion Discrete Cosine Transform (QDCT) was proposed by Li et al [8]. In this approach, 96.43% and 92.66% accuracies were achieved at the CASIA V1.0 and CASIA V2.0 datasets. Sheng et al. [9] proposed a method based on Discrete Octonion Cosine Transform (DOCT) and Markov features. Initially, the 8×8 block DOCT is applied to source image and then, the standard deviation is used to process the corresponding parts of all blocks of the image. Finally, the Markov feature vector of the DOCT coefficient is extracted. The method achieved 98.04% and 97.83% detection accuracies for CASIA V1.0 and CASIA V2.0 in databases their results.

Yildirim and Alutas [10] introduced an expert system that extracts features (statistical and textural) from high-level sub-bands of Stationary Wavelet Transform (SWT) domain to detect forgery. The results show that this approach has 99.29% and 99.58% detection rates on CASIA V1.0 and CASIA V2.0 datasets.

Muhammad et al. [11], used YCbCr colour space. A directional pyramid conversion is applied for the two Cb and Cr channels that will result in a number of sub-bands. From each sub-band, LBP features are calculated and finally the LBP histograms of each of these sub-bands are merged to construct the final feature vector. 94.89% and 97.33% accuracy rates were obtained on CASIA V1.0 and CASIA V2.0 databases, respectively. Agarwal and Chand [12] presented a technique that applies entropy filter and Local Phase Quantization (LPQ) texture operator. The entropy filter generally highlights the boundary of the forged regions. They achieved 95.41% and 98.33% accuracies for CASIA V1.0 and CASIA V2.0 datasets, respectively.

Alahmadi et al. [13] applied LBP and DCT for detecting forgery and obtained 97% and 97.5% detection rates on the CASIA V1.0 and CASIA V2.0 databases, respectively. Shen et al. [14] detected splicing through a model consisting of Textural Features based on the Gray Level Co-occurrence Matrices (TF-GLCM). In the TF-GLCM, the GLCM was computed based on the Difference Block Discrete Cosine Transform (DBDCT) arrays for capturing the textural information and the spatial relationship between image pixels. In addition, the mean and standard deviation of textural features were used instead as elements in feature vector. In this algorithm, 98.54% and 97.73% accuracy rates were obtained respectively on CASIA V1.0 and CASIA V2.0 datasets. Sharma and Ghanekar [15] presented a two-phase hybrid technique using some features and Extreme Learning Machine (ELM). In the first phase, Laplacian of Gaussian and autocorrelation were used to differentiate computer generated images and natural images. In the second phase, estimation of colour filter array pattern and sensor noise were used for splicing detection. A 98.51% precision rate under effect of simple splicing was obtained on Dresden Image database.

Habibi and Hassanpour [16] applied an algorithm based on color distribution of pixels in chroma space. First, edge pixels were extracted using contourlet transform and then, interquartile range (IQR) metric of the Cb and Cr histograms was utilized to distinguish the forged edges and authentic ones in YCbCr color space. The results achieved 97.08% accuracy Columbia Image Splicing Detection Evaluation Dataset.

Singh and Bansal [17] analyzed the use of Benford's law for detecting effects of single and double compression as a sign of image tampering. Their reported results showed that deviation from Benford's curve in the compressed images could be used to detect forgery.

Bonettini et al. [18], applied this law to detect Generative Adversarial Network (GAN)-generated images. Random forest classifier had been used for classification in their work.

3. PROPOSED METHOD

The framework of the proposed method is shown in Figure 1, which consists of four consecutive steps. In the first step, the RGB image is converted into YCbCr image. In the second step, the blocking operation is performed on the image and then a two-dimensional discrete cosine transform (2D-DCT) is applied to each block. In the third step, the proposed features are extracted and then combined to construct a final feature vector. Finally, support vector machine (SVM) is applied for classification. In the following, the proposed splicing forgery detection method is described in detail.

3. 1. Preprocessing The YCbCr color space, as a preprocessing operation, plays an important and effective role in detecting forged images. In most of the methods presented so far [5, 7, 10-14, 16, 19-25], this color space conversion has been used. YCbCr channels are given in the following equations:

$$Y = 0.299R + 0.587G + 0.114B \tag{1}$$

$$Cb = 0.168736R + 0.331264G + 0.5B \tag{2}$$

$$Cr = 0.5R + 0.418688G + 0.081312B \tag{3}$$

where Y , Cb , and Cr represent luminance, chrominance blue and chrominance red components, respectively. In this step, the input RGB image is converted into YCbCr image to obtain three images for the Y , Cb and Cr channels.

3. 2. Image Division and Applying 2D-DCT The image is divided into 8×8 non-overlapping blocks and a two-dimensional discrete cosine transform (2D-DCT) is applied to each block to obtain 64 DCT coefficients. The value located in the upper left corner of the block is called the direct current coefficient (DC) and the other 63 values are called the alternative current coefficients (AC). The 2D-DCT transformation is given in Equation (4).

$$F_{uv} = \alpha_u \alpha_v \sum_{x=0}^{M-1} \sum_{y=0}^{N-1} f_{xy} \cos \frac{\pi(2x+1)u}{2M} \cos \frac{\pi(2y+1)v}{2N}$$

$$\alpha_u = \begin{cases} \frac{1}{\sqrt{M}}, & x = 0 \\ \sqrt{\frac{2}{M}}, & 1 \leq x \leq M - 1 \end{cases} \tag{4}$$

$$\alpha_v = \begin{cases} \frac{1}{\sqrt{N}}, & y = 0 \\ \sqrt{\frac{2}{N}}, & 1 \leq y \leq N - 1 \end{cases}$$

where f_{xy} and F_{uv} denote the pixel values at coordinates (x, y) and the DCT coefficient at coordinates (u, v) , respectively. The values of M and N are equal to 8 here. Some studies [19-22], show that the low frequency AC components have effective role in performance of splicing detection system. In this paper, inspired by the studies and different tests, DCT coefficients are selected for extracting features.

3. 3. Feature Extraction In this step, four types of features are used, each of which can be identified separately with a very good percentage, and by combining them the recognition rate has increased. The most important proposed features are based on Benford's law including: mantissa distribution and mean absolute deviation (MAD). Their theoretical basis is given in the following subsections. Also, popular entropy and standard deviation (STD) are used as complementary features to discriminate the forged and authentic images.

3. 3. 1. Mean Absolute Deviation Benford's law [23], also called the first digit law, is an empirical law that states the probability distribution of the first digits in a set of natural numbers is logarithmic and is defined as:

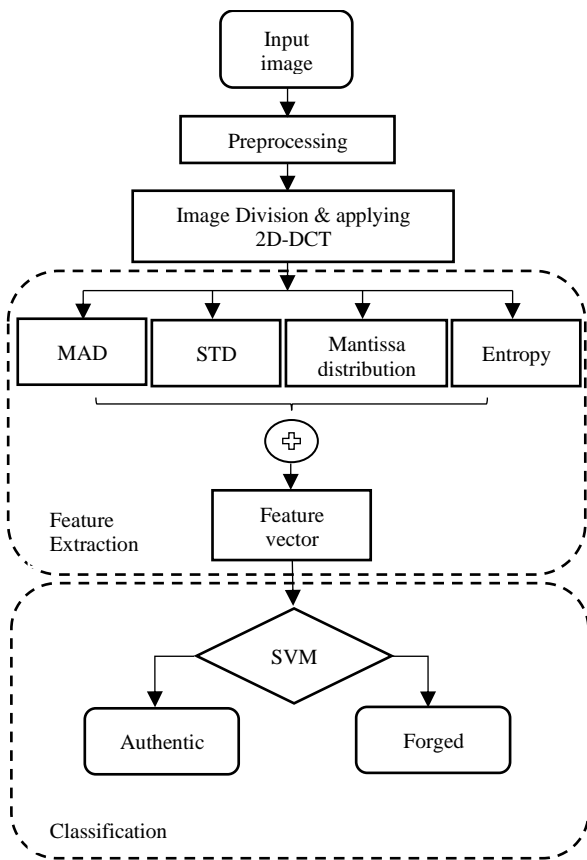


Figure 1. The framework of the proposed method

$$p(x) = \log_{10} \left(1 + \frac{1}{x} \right), \quad x = 1, 2, \dots, 9 \quad (5)$$

where x is the value of the first digits and $p(x)$ denotes the probability of the value x . The most significant digit or first digit (FD) [19] for a positive integer Y can be computed as Equation (6).

$$FD(Y) = \left\lfloor \frac{Y}{10^{\lfloor \log_{10} Y \rfloor}} \right\rfloor \quad (6)$$

where $\lfloor \cdot \rfloor$ is the operation of floor rounding. Mean absolute deviation (MAD) [24] in fraud detection systems is a measure of conformity to Benford's law and is calculated using Equation (7).

$$MAD = \frac{\sum_{i=1}^N |AP - EP|}{N} \quad (7)$$

where EP is the probability predicted by Benford's law, AP is the actual first digit probability, and N represents the number of bins (which equals 9 for the first digits). The data with the least MAD has the closest conformity to Benford's law. Here, the calculated MAD values are used as distinguishing features. All of the DCT coefficients located in the same position of the 8×8 blocks form a mode [21]. In order to achieve better performance in using these features, 25 first AC modes are selected from the DCT coefficients for each block. First, the proposed method obtains histogram of first digits with 10 bins for each of the 25 first AC modes and then, computes the MAD value for each of them. Therefore, a vector with 25 features is extracted. Lastly, the final feature vector contains 75 (3×25) features for three channels.

3. 3. 2. Mantissa Distribution The mantissa distribution in image forensics was first introduced by Parnak et al. [25], which is a generalized form of Benford's law. This distribution is mentioned centrally by Kazemitabar and Kazemitabar [26] The logarithmic property that was found by Newcomb and elaborated by Hill, states that if you take the logarithm of a set of practical numbers the fractional part of the log values will be uniformly distributed [25].

Mantissa distribution is defined as: if x is a positive random variable, then Φ is a function that maps x to a new random variable and is defined as follows:

$$\Phi(x) = \log_{10} x \quad \text{mod} 1 \quad (8)$$

$$\Phi(x) \sim \text{uniform} [0, 1) \quad (9)$$

where x is random variable, Φ is a function that maps x to a new variable, namely $\Phi(x)$ and mod denotes fractional part or mantissa of a number. If a dataset is presented to check whether it is valid or not, $\Phi(x)$ must be calculated for all information in the data set and compared to uniform $[0, 1)$. If it fits well, it obeys the law and vice versa. DCT coefficients play a key role in using this theorem in the field of image forensics, like

Benford's law. Experiments show that the mantissa distribution of DCT coefficients will have a uniform distribution from 0 to 1, while the mantissa distribution of other coefficients will have a non-uniform form. In order to achieve the features based on mantissa distribution, 25 first AC modes are selected from the DCT coefficients for each block. Then, histogram of the mantissa with 10 bins for each mode is calculated and finally, the 25 outputs obtained from these modes are arranged in a vector. The feature vector contains 750 ($3 \times 25 \times 10$) features for three channels.

3. 3. 3. Standard Deviation For a random variable vector x made up of N scalar observations, the standard deviation (STD) is the square root of the variance and is given in Equation (10).

$$s = \sqrt{\frac{1}{N-1} \sum_{i=1}^N |x_i - \bar{x}|^2} \quad (10)$$

where \bar{x} is the mean of x_i . The method computes the STD value for each of the 25 first AC coefficients obtained from the previous step. Therefore, a vector with 25 features is extracted. Finally, the final feature vector contains 75 (3×25) features for three channels.

3. 3. 4. Entropy Gonzalez [27] has mainly introduced Entropy's application in texture characterization in image processing. Entropy is a statistical measurement of variability and is defined as Equation (11).

$$e = - \sum_{i=0}^{L-1} p(z_i) \log_2 p(z_i) \quad (11)$$

where $p(z_i)$ is the probability of the gray-level z_i . In order to prepare the entropy features to detect forgery in the images, all 64 DCT coefficients are selected and entropy is applied for each block. So, the feature vector contains 192 (3×64) features according to three channels.

3. 3. 5. Final Feature Vector In this section, the output vectors obtained from previous step are combined to generate the final feature vector. This vector contains 1092 features.

3. 4. Classification Image tampering detection is a two-class classification problem (i.e., authentic and forged) and consequently, one of the most suitable classifiers for the problem is support vector machine (SVM). In the suggested approach, SVM with polynomial function with the first three degrees (i.e., linear, quadratic and cubic kernels) is employed for classification to detect authentic and tampered images based on the final feature vector.

4. EXPERIMENTAL RESULTS AND DISCUSSION

In this section, performance of the proposed method and

the results of the experiments are evaluated. The method is implemented in MATLAB R2017b, on the Laptop with Intel Core i7 CPU 2.40 GHZ and 8 GB RAM.

4.1. Datasets The method is tested with two different image datasets: CASIA V1.0 and CASIA V2.0 [28], which are publicly available. Table 1 summarized a description of the datasets. Some examples of the authentic and forged images from the datasets can be seen in Figure 2.

4.2. Evaluation and Results In this work, support vector machine (SVM) is applied and tested with three types of kernel functions (i.e. linear, quadratic, and cubic) for classification to detect authentic and forged images based on the feature vectors. The images were randomly split to 70:30%, 5/6:1/6 and 80:20% train/test sets before training and testing algorithm. In order to protect against overfitting, the performance is evaluated using 10-fold cross-validation in terms of the evaluation parameters and for reliability improvement the average of the parameters was calculated during 10 times of running the algorithm.

For evaluation of the system, accuracy, sensitivity, and specificity measures are considered which are defined as:

$$Accuracy = \frac{TP+TN}{TP+FP+FN+TN} \quad (12)$$

$$Sensitivity (TPR) = \frac{TP}{TP+FN} \quad (13)$$

$$Specificity (TNR) = \frac{TN}{TN+FP} \quad (14)$$

where TP (true positive) is the number of forged images classified as forged, FP (false positive) is the number of forged images classified as authentic, TN (true negative) is the number of authentic images classified as authentic and FN (false negative) is the number of authentic images classified as forged images. Table 2 shows the performance results of different channels for the proposed features separately on CASIA V1.0 dataset. In



Figure 2. Some samples of images in the two utilized datasets (top row = Authentic , bottom row = Forged)

TABLE 1. Characteristics of the datasets

Dataset	Authentic	Forged	Size	Format
CASIA V1.0	800	921	384×256, 256×384	JPEG
CASIA V2.0	7491	5123	240×160, 900×600	TIFF, JPEG, BMP

TABLE 2. Performance results of different channels for the proposed features separately on CASIA V1.0

Feature	Channel	Accuracy (%)	TPR(%)	TNR (%)	Size
MAD	Y	96.70	95.64	97.97	25
	Cb	84.76	84.49	85.11	25
	Cr	88.44	89.51	87.26	25
	CbCr	90.95	91.73	90.07	50
	YCbCr	98.15	98.12	98.18	75
	Y	85.27	80.15	91.43	25
	Cb	90.71	85.00	97.29	25
	Cr	90.09	81.99	99.26	25
	CbCr	91.22	84.68	98.43	50
	YCbCr	93.27	96.71	89.19	75
	Y	98.60	97.68	99.66	250
	Cb	98.54	99.67	97.31	250
Entropy	Cr	99.16	99.64	98.61	250
	CbCr	98.93	99.77	98.01	500
	YCbCr	99.76	99.67	99.87	750
	Y	95.58	95.16	96.05	64
	Cb	91.37	90.98	91.86	64
	Cr	93.37	93.43	93.28	64
	CbCr	95.33	94.18	96.64	128
	YCbCr	98.43	98.11	98.81	192

this experiment, SVM classifier with linear kernel function and the data dividing at rate of 70:30% were considered. As can be seen in this table, the highest detection accuracy is related to the features based on mantissa distribution with a value equal to 99.76%, which indicates the high performance of them compared with other features. In terms of feature dimensions, the features based on MAD and STD in three channels have lower feature size than others.

Table 3 indicates the performance results of the proposed method based on the kernel functions on

CASIA V1.0 database. 70% of the data is assigned to the training data and 30% of the data is assigned to the test data. The performance is evaluated using 10-fold cross-validation and 10 times of running the algorithm. As can be observed in the table, the highest mean accuracy, TPR and TNR are 99.94% (standard deviation, SD = 0.0918), 99.94% (SD = 0.1810) and 100% for SVM with quadratic kernel, respectively.

Tables 4 and 5 summarized the performance results of the proposed method based on data splitting and the kernel functions on two common image splicing evaluation datasets. As can be seen in Table 4, the highest detection accuracies for the three divisions 70:30%, 5/6:1/6, and 80:20% are 99.94%, 99.89% and 99.85% for SVM with quadratic kernel, respectively. According to Table 5, the highest detection accuracies for the three divisions 70:30%,

5/6:1/6, and 80:20% are 99.84% for SVM with quadratic kernel, 99.79% for SVM with cubic kernel and 99.78% for SVM with cubic kernel, respectively. So, it can be found that the proposed method has a high detection capability in CASIA V2.0, which is a challenging database.

TABLE 3. Performance results of the proposed method based on the kernel functions on CASIA V1.0

kernel	Accuracy (%) (mean ± SD)	TPR (%) (mean ± SD)	TNR (%) (mean ± SD)
Linear	99.71 ± 0.1391	99.71 ± 0.2434	99.67 ± 0.2590
Quadratic	99.94 ± 0.0918	99.94 ± 0.1810	100 ± 0.0000
Cubic	99.88 ± 0.0981	99.88 ± 0.1810	99.87 ± 0.2559

TABLE 4. Performance results of the proposed method based on data splitting and the kernel functions on CASIA V1.0

Kernel	70:30			5/6:1/6			80:20		
	Accuracy (%)	TPR (%)	TNR (%)	Accuracy (%)	TPR (%)	TNR (%)	Accuracy (%)	TPR (%)	TNR (%)
Linear	99.71	99.74	99.67	99.72	99.60	99.84	99.76	99.62	99.93
Quadratic	99.94	99.88	100	99.89	99.80	100	99.85	99.83	99.87
Cubic	99.88	99.88	99.87	99.75	99.75	99.78	99.79	99.83	99.75

TABLE 5. Performance results of the proposed method based on data splitting and the kernel functions on CASIA V2.0

Kernel	70:30			5/6:1/6			80:20		
	Accuracy (%)	TPR (%)	TNR (%)	Accuracy (%)	TPR (%)	TNR (%)	Accuracy (%)	TPR (%)	TNR (%)
Linear	99.56	99.55	99.56	99.56	99.54	99.58	99.56	99.66	99.50
Quadratic	99.84	99.90	99.79	99.76	99.82	99.71	99.77	99.80	99.75
Cubic	99.79	99.86	99.74	99.79	99.86	99.74	99.78	99.80	99.76

TABLE 6. Comparison between the detection performances of the proposed method and state-of-the-art techniques

Method	CASIA V1.0			CASIA V2.0			Size
	Accuracy (%)	TPR (%)	TNR (%)	Accuracy (%)	TPR (%)	TNR (%)	
El-Latif et al. [4]	95.45	-	-	97.27	-	-	2048
Kasban and Nassar [5]	98.95	98.91	99.00	99.13	99.70	98.30	32
Fusheng and Gao [6]	99.24	99.40	99.09	97.56	-	-	676
Kaur and Gupta [7]	99.62	89.25	95.55	94.09	91.87	97.35	1024
Li et al. [8]	96.43	95.73	97.13	92.66	89.42	95.91	1452
Sheng et al. [9]	99.06	-	-	97.59	-	-	1452
Yıldırım and Ulutas [10]	99.29	99.45	99.95	99.58	98.61	99.87	1002
Muhammad et al. [11]	94.89	95.15	93.91	97.33	98.50	96.53	475
Agarwal and Chand [12]	95.41	97.65	93.16	98.33	99.22	97.73	2048
Alahmadi et al. [13]	97.00	96.75	98.24	97.50	98.45	96.84	-
Shen et al. [14]	98.54	97.48	99.51	97.73	97.72	97.80	96
Proposed(linear)	99.72	99.60	99.84	99.56	99.54	99.58	1092
Proposed(quadratic)	99.89	99.80	100	99.76	99.82	99.71	1092
Proposed(cubic)	99.75	99.75	99.78	99.79	99.86	99.74	1092

4. 3. Comparison with Other Methods In this section, the suggested approach is compared with various state-of-the-art methods. The performance is evaluated in terms of accuracy, TPR, TNR, and feature vector size. Table 6 shows a comparison of detection results in previous studies and this work on CASIA V1.0 and CASIA V2.0 datasets. The classifier used in these studies is support vector machine (SVM) and since most of them had used a proportion of 5/6 training and 1/6 testing images, the same proportion for the proposed method is considered in this comparison. As it can be observed, the proposed method with the detection accuracies of 99.72% and 99.82% for quadratic SVM and cubic SVM, respectively on CASIA V1.0 and the detection accuracies of 99.76% and 99.79% for quadratic SVM and cubic SVM, respectively on CASIA V2.0 overperform other works. The highest sensitivity belongs to the proposed method with 99.80% and 99.86% on CASIA V1.0 and CASIA V2.0 datasets, respectively. In addition, the method has the highest value of 100% specificity on CASIA V1 dataset and only has 0.13% less specificity than the method introduced by Yıldırım and Ulutaş [10] on CASIA V2.0 dataset. In terms of feature dimension, the proposed approach has lower feature dimension in compare with the methods discussed in literature [4, 8, 9, 12]. Table 6 summarized comparative analysis of the proposed method with the others stated methods.

4. 4. Training Time In this section, training time of the proposed approach is compared with the method introduced by Niyishaka and Bhagvati [29] on CASIA V2.0 database. This method [29] is the only recent method that has been reported the training time on CASIA V2.0. using various classifiers such as LR, SVM, KNN, LDA, Dtree and NB with data dividing at rate of 60:40% for classification. The training time of their method was 210 seconds for all combined classifiers and the highest accuracy rate of their method was 93.79% on 12614 images from CASIA V2.0 dataset, when feature vector size was 768. In order to make a fair comparison in this experiment, the images are split to 60:40% train/test sets and the performance of the proposed method is evaluated using 10-fold cross-validation and the average of the parameters is calculated during 10 times of running the algorithm. The results show the detection accuracy of $99.54\% \pm 0.1243$ for linear SVM, $99.72\% \pm 0.0760$ for quadratic SVM and $99.69\% \pm 0.068$ for cubic SVM. Table 7 indicates a comparison of training time and feature vector size in method by Niyishaka and Bhagvati [29] and this work on CASIA V2.0 dataset. The reported training time of the proposed method is 36.35 ± 1.42 seconds for linear SVM, 34.07 ± 0.7326 seconds for quadratic SVM and 35.82 ± 0.9086 seconds for cubic SVM, which shows optimal performance of classification of the method compared to method by Niyishaka and Bhagvati [29]. Although as

mentioned earlier, the reported training time for the method by Niyishaka and Bhagvati [29] is for all combined classifiers and the time spent on 10-fold cross-validation for safe classification and the larger feature vector size of the proposed method should be considered in the relative comparison.

4. 5. Misclassification Cases In some images from the databases, the proposed algorithm failed and the images are misclassified (i.e. some forged images are classified as authentic and some authentic images are classified as forged). Figures 3 and 4 show examples of misclassified images from CASIA V2.0 database. The images shown in Figure 3 contain the following characteristics: JPG format, various sizes, small blurring regions, illumination variation, different texture pattern (such as regular and stochastic), same objects with scaling and rotation. The images shown in Figure 4 contain the following characteristics: TIFF format, various size, filtering small regions, blurred and smoothed edges, small forged regions same objects with scaling and rotation.

From the above characteristics, it can be seen that the proposed algorithm on the challenging dataset in some cases, is sensitive to very small forged regions,

TABLE.7. Comparison of training time and feature vector size in method by Niyishaka and Bhagvati [29] and this work on CASIA V2.0

Method	Training time (s) (mean \pm SD)	Feature vector size
Niyishaka et al. [29]	210	768
Proposed (linear)	36.35 ± 1.4200	1092
Proposed (quadratic)	34.07 ± 0.7326	1092
Proposed (cubic)	35.82 ± 0.9086	1092



Figure 3. Examples of authentic images misclassified as forged images



Figure 4. Examples of forged images misclassified as authentic images

blurred edges, regions containing copy-move forgery, compression and decompression of the images.

Our future works include the localization of the forgery in the image using segmentation fusion [30] and the variants of Benford's law and enriching the feature vector with other popular features like Zernike Moments [31]. In addition, other classifiers like Radial Basis Function (RBF) neural networks [32] can be applied to improve the classification accuracy.

5. CONCLUSION

This paper presents a novel forgery detection algorithm using combined features and SVM classifier. In the proposed method, features based on mantissa distribution (using generalized Benford's law), Mean Absolute Deviation (MAD) of traditional Benford's law, entropy and Standard Deviation (STD) are extracted and combined to construct the final feature vector. The method is evaluated on two common image datasets. The experimental results show the superiority of the suggested approach in comparison with previous works.

6. ACKNOWLEDGEMENT

The authors acknowledge the funding support provided by Babol Noshirvani University of Technology through Grant programs No. BNUT/370123/00. Authors also acknowledged the editor and anonymous reviewers for their constructive comments.

7. REFERENCES

1. Saadati, M., Vahidi, J., Seydi, V. and Sheikholharam Mashhadi, P.J.I.J.o.E., "Proposing a new image watermarking method using shearlet transform and whale optimization algorithm", *International Journal of Engineering, Transactions A: Basics*, Vol. 34, No. 4, (2021), 843-853, doi: 10.5829/ije.2021.34.04a.10.
2. Nasiri, J.A. and Shakibian, H., "Probabilistic twin support vector machine for solving unclassifiable region problem", *International Journal of Engineering, Transactions A: Basics*, Vol. 35, No. 1, (2022), 1-13, doi: 10.5829/ije.2022.35.01A.01.
3. da Costa, K.A., Papa, J.P., Passos, L.A., Colombo, D., Del Ser, J., Muhammad, K. and de Albuquerque, V.H.C.J.A.S.C., "A critical literature survey and prospects on tampering and anomaly detection in image data", *Applied Soft Computing*, (2020), 106727, doi: 10.1016/j.asoc.2020.106727.
4. El-Latif, A., Eman, I., Taha, A., Zayed, H.H.J.A.J.f.S. and Engineering, "A passive approach for detecting image splicing based on deep learning and wavelet transform", *Arabian Journal for Science & Engineering (Springer Science & Business Media BV)*, Vol. 45, No. 4, (2020), doi: 10.1007/s13369-020-04401-0.
5. Kasban, H. and Nassar, S.J.A.S.C., "An efficient approach for forgery detection in digital images using hilbert-huang transform", *Applied Soft Computing*, Vol. 97, (2020), 106728, doi: 10.1016/j.asoc.2020.106728.
6. Fusheng, Y. and Gao, T., "A novel image splicing forensic algorithm based on generalized dct coefficient-pair histogram", in Chinese Conference on Image and Graphics Technologies, Springer. (2015), 63-71.
7. Kaur, M. and Gupta, S., "A passive blind approach for image splicing detection based on dwt and lbp histograms", in International Symposium on Security in Computing and Communication, Springer. (2016), 318-327.
8. Li, Y., Wang, X., Sun, S., Ma, X. and Lu, G.J.T.R.P.C.E.T., "Forecasting short-term subway passenger flow under special events scenarios using multiscale radial basis function networks", Vol. 77, (2017), 306-328, doi: <https://doi.org/10.1016/j.trc.2017.02.005>
9. Sheng, H., Shen, X., Lyu, Y., Shi, Z. and Ma, S.J.I.I.P., "Image splicing detection based on markov features in discrete octonion cosine transform domain", *IET Image Processing*, Vol. 12, No. 10, (2018), 1815-1823, doi: 10.1049/iet-ipr.2017.1131.
10. Yildirim, E.O. and Ulutaş, G.J.E.S.w.A., "Augmented features to detect image splicing on swt domain", *Expert Systems with Applications*, Vol. 131, (2019), 81-93, doi: 10.1016/j.eswa.2019.04.036.
11. Bebis, G.J.M.V. and Applications, "Ghulam muhammad, munner h. Al-hammadi, muhammad hussain &", *Machine Vision and Applications*, Vol. 25, (2014), 985-995, doi: 10.1007/s00138-013-0547-4.
12. Agarwal, S., Chand, S.J.I.j.o.i., graphics and processing, s., "Image forgery detection using multi scale entropy filter and local phase quantization", *International Journal of Image, Graphics and Signal Processing*, Vol. 7, No. 10, (2015), 78, doi: 10.5815/ijjisp.2015.10.08.
13. Alahmadi, A., Hussain, M., Aboalsamh, H., Muhammad, G., Bebis, G. and Mathkour, H., "Passive detection of image forgery using dct and local binary pattern", *Signal, Image and Video Processing*, Vol. 11, No. 1, (2017), 81-88, doi: 10.1007/s11760-016-0899-0.
14. Shen, X., Shi, Z. and Chen, H.J.I.I.P., "Splicing image forgery detection using textural features based on the grey level co-occurrence matrices", *IET Image Processing*, Vol. 11, No. 1, (2017), 44-53, doi: 10.1049/iet-ipr.2016.0238.
15. Sharma, S. and Ghanekar, U.J.O., "A hybrid technique to discriminate natural images, computer generated graphics images, spliced, copy move tampered images and authentic images by using features and elm classifier", *Optik*, Vol. 172, (2018), 470-483, doi: 10.1016/j.ijleo.2018.07.021.
16. Habibi, M. and Hassanpour, H.J.I.J.o.E., "Splicing image forgery detection and localization based on color edge inconsistency using statistical dispersion measures", *International Journal of Engineering, Transactions B: Applications*, Vol. 34, No. 2, (2021), 443-451, doi: 10.5829/ije.2021.34.02b.16.
17. Singh, N. and Bansal, R., "Analysis of benford's law in digital image forensics", in 2015 International Conference on Signal Processing and Communication (ICSC), IEEE. (2015), 413-418.
18. Bonettini, N., Bestagini, P., Milani, S. and Tubaro, S., "On the use of benford's law to detect gan-generated images", in 2020 25th

- International Conference on Pattern Recognition (ICPR), IEEE. (2021), 5495-5502.
19. Milani, S., Tagliasacchi, M., Tubaro, S.J.A.T.o.S. and Processing, I., "Discriminating multiple jpeg compressions using first digit features", *APSIPA Transactions on Signal and Information Processing*, Vol. 3, (2014), doi: 10.1017/ATSIP.2014.19.
 20. Li, B., Shi, Y.Q. and Huang, J., "Detecting doubly compressed jpeg images by using mode based first digit features", in 2008 IEEE 10th Workshop on Multimedia Signal Processing, IEEE. (2008), 730-735.
 21. Li, X.H., Zhao, Y.Q., Liao, M., Shih, F.Y. and Shi, Y.Q.J.E.J.o.a.i.s.p., "Detection of tampered region for jpeg images by using mode-based first digit features", *EURASIP Journal on Advances in Signal Processing*, Vol. 2012, No. 1, (2012), 1-10, doi: 10.1186/1687-6180-2012-190.
 22. Alipour, N. and Behrad, A.J.T.J.o.E.E., "Forgery and double compression detection in digital images using combined features of quantization effects on dct coefficients", *Tabriz Journal of Engineering Electrical*, Vol. 47, No. 2, (2017), doi.
 23. Benford, F.J.P.o.t.A.p.s., "The law of anomalous numbers", *Proceedings of the American Philosophical Society*, (1938), 551-572, doi.
 24. Nigrini, M.J., "Benford's law: Applications for forensic accounting, auditing, and fraud detection, John Wiley & Sons, Vol. 586, (2012).
 25. Parnak, A., Baleghi, Y. and Kazemitabar, J., "A novel forgery detection algorithm based on mantissa distribution in digital images", in 2020 6th Iranian Conference on Signal Processing and Intelligent Systems (ICSPIS), IEEE. (2020), 1-4.
 26. Kazemitabar, J., Kazemitabar, J.J.C.i.S.-T. and Methods, "Measuring the conformity of distributions to benford's law", *Communications in Statistics-Theory and Methods*, Vol. 49, No. 14, (2020), 3530-3536, doi: 10.1080/03610926.2019.1590599.
 27. Gonzalez, R.C., Eddins, S.L. and Woods, R.E., "Digital image publishing using matlab, Prentice Hall, (2004).
 28. Dong, J. and Wang, W., *Casia tampered image detection evaluation database*. 2011.
 29. Niyishaka, P., Bhagvati, C.J.M.T. and Applications, "Image splicing detection technique based on illumination-reflectance model and lbp", *Multimedia Tools and Applications*, Vol. 80, No. 2, (2021), 2161-2175, doi: 10.1007/s11042-020-09707-7.
 30. Nikbakhsh, N., Baleghi Damavandi, Y. and Agahi, H.J.I.J.o.E., "Plant classification in images of natural scenes using segmentations fusion", *International Journal of Engineering, Transactions C: Aspects*, Vol. 33, No. 9, (2020), 1743-1750, doi: 10.5829/IJE.2020.33.09C.07.
 31. Dadgar, A., Baleghi, Y. and Ezoji, M.J.I.J.o.E., "Improved object matching in multi-objects tracking based on zernike moments and combination of multiple similarity metrics", *International Journal of Engineering, Transactions C: Aspects*, Vol. 34, No. 6, (2021), 1445-1454, doi: 10.5829/IJE.2021.34.06C.08.
 32. Asvadi, A., Karami-Mollaie, M., Baleghi, Y. and Seyyedi-Andi, H., "Improved object tracking using radial basis function neural networks", in 2011 7th Iranian Conference on Machine Vision and Image Processing, IEEE. (2011), 1-5.

Persian Abstract

چکیده

با توجه به سهولت دسترسی به بسترهایی که جاعلان می‌توانند اسناد دیجیتال را دستکاری نمایند، ارائه ی ابزارهای خودکار برای شناسایی تصاویر جعلی در حال حاضر یک زمینه تحقیقاتی داغ در پردازش تصویر است. این مقاله یک الگوریتم جدید تشخیص جعل بر اساس ماهیت قانون بنفورد ارائه می‌دهد. در روش پیشنهادی، ویژگی‌های میانگین قدرمطلق انحراف با استفاده از قانون بنفورد معمولی و ویژگی‌های توزیع مانیتیس با استفاده از قانون بنفورد تعمیم یافته استخراج می‌شوند. علاوه بر ویژگی‌های مبتنی بر قانون بنفورد، سایر ویژگی‌های آماری برای ساخت بردار ویژگی نهایی به کار گرفته شده است. در نهایت ماشین بردار پشتیبان با سه تابع هسته مختلف جهت طبقه‌بندی تصاویر اصلی و جعلی استفاده می‌شود. این روش روی دو پایگاه داده رایج CASIA V1.0 و CASIA V2.0 آزمایش شده است. نتایج تجربی نشان می‌دهد که به کمک روش پیشنهادی می‌توان به بهبود ۰/۲۷ درصدی روی پایگاه داده CASIA V1.0 و به بهبود ۰/۲۱ درصد روی پایگاه داده CASIA V2.0 در مقایسه با سایر روش‌های پیشرفته دست یافت. الگوریتم موثر پیشنهادی، پیاده‌سازی ساده‌ای دارد و با استفاده از تکنیک بکارگیری قانون بنفورد ارائه شده در این مقاله، می‌تواند ویژگی‌های غنی از تصاویر استخراج نماید تا فرآیند طبقه‌بندی به طور موثری توسط طبقه‌بند ساده‌ای مانند SVM در مدت زمان کوتاه انجام شود.



Evaluation of Corrosion Resistance of Bi-layered Plasma-sprayed Coating on Titanium Implants

N. Ebrahimi, A. Sedaghat Ahangari Hosseinzadeh*, M. Vaezi, M. Mozafari

Materials and Energy Research Center, Karaj, Iran

PAPER INFO

Paper history:

Received 16 November 2021

Received in revised form 15 December 2021

Accepted 23 December 2021

Keywords:

Coating

Plasma Spraying

Corrosion

Porosity

ABSTRACT

There are several attempts to improve surface characteristics of biomaterials with thick film coatings. In this research, a class of protective coating layers of bi-layered Hydroxyapatite (HA)/Al₂O₃-SiO₂ (with 10, 20, 30 %wt SiO₂) were deposited on titanium (Ti) surfaces by plasma spray technique. The surface features of the applied coating layers were evaluated in detail to confirm the effectiveness of the technique for further biomedical applications. The results demonstrated that uniform and bi-layered plasma sprayed coatings can be successfully prepared through the optimization of engineering parameters. Also, it was found that the roughness of the bi-layered coatings increases with increasing the number of coating layers. The corrosion behavior of the coated and uncoated samples was comparatively investigated using electrochemical tests. The measured current densities (i_{corr}) for HA, (HA)/Al₂O₃-SiO₂ (with 10, 20, 30 %wt SiO₂) were 0.27 $\mu\text{A}/\text{cm}^2$, 0.28 $\mu\text{A}/\text{cm}^2$, 0.23 $\mu\text{A}/\text{cm}^2$, 0.79 $\mu\text{A}/\text{cm}^2$, respectively. According to the results, corrosion resistance of samples with 20% SiO₂ is significantly improved compared to the single-layer HA and bare Ti. The outcomes of FESEM results revealed that porosity and cavities related to evaporation of adhesive PVA and it is confirmed by increasing the percentage of silica to more than 20%, porosity has increased. In conclusion, the proposed coating system showed promising abilities for future biomedical applications. It could be optimized and improved by changing the structural characteristics of the substrate, chemical composition and porosity of the coating layers.

doi: 10.5829/ije.2022.35.04a.03

NOMENCLATURE

FESEM	Field emission scanning electron microscopy	FTIR	Fourier-transform infrared spectroscopy
R _p	Polarization resistance	EDS	Energy-dispersion X-ray Spectroscopy
I _{corr}	Current density	SBF	Simulated body fluids
β _a	Anodic tafel slope	PE	Protection efficiency
β _c	Cathodic tafel slope	PVA	poly-vinyl alcohol
P	Total porosity of the coating	XRD	X-ray diffraction
R _p mm	Polarization resistance of the un-coated sample	TCP	Tricalcium phosphate
R _p	Polarization resistance of the coated sample	α-TCP	α-Ca ₃ (PO ₄) ₂
ΔE _{corr}	Different potential of the coated sample and the bare substrate	β-TCP	β-Ca ₃ (PO ₄) ₂
λ	Wavelength of X-ray beam	HA	Hydroxyapatite
β	Maximum intensity of the full width at half maximum	Ti	Titanium
Θ	Diffraction angle	AT	Al ₂ O ₃ -TiO ₂
K	Constant selected at 0.9	EPD	Electrophoretic deposition
l	Average crystallite size		

1. INTRODUCTION

Compared with other metallic biomaterials titanium (Ti) and its alloys have become the most pleasant metallic

materials used in orthopaedic implants because of the high corrosion resistance and favorable biocompatibility properties [1, 2]. Alloys used as implants should not show any unfavorable physiological responses in body

* Corresponding Author Institutional Email: a.sedaghat@merc.ac.ir
(A. Sedaghat Ahangari Hosseinzadeh)

environment and should be *chemically* stable.[3] The passive layer established on the surface of titanium alloys indicates the long-term stability after exposure in body which has a great influence on biocompatibility [4]. However, osseointegration and bone growth on implants are also influenced by the level of bioactivity of titanium alloys that could be varied by the type of the alloys and processing conditions. Modification of surfaces often improved the interactions between tissue and implant substrate [5, 6]. Calcium phosphate-based biomaterials have been shown a bone like chemical composition and porous structure. Although these biomaterials such as HA ($\text{Ca}_{10}(\text{PO}_4)_6(\text{OH})_2$) showed superior bioactive properties for orthopedic and clinical applications, they are restricted to nonload-bearing applications, because of their brittleness and low mechanical strength [7, 8]. Most of these implants failed after 15 years of implantations in the body due to weak resistance against wear and corrosion. One of the greatest effective surface modifications is applying a coating on the surface to enhance the corrosion resistance of metallic implants [9]. Previous researches showed that implants modified with nano ceramics such Al_2O_3 , SiO_2 and TiO_2 are generally improved in terms of corrosion behavior and biocompatibility [10-12]. A recent study by Bahraminasab et al. [13]. showed that the highest corrosion resistance of Al_2O_3 - 75vol.%Ti composite caused to apply for making the components of implants such as knee and hip prostheses. In addition, Farhadian et al. [14] showed that increasing SiO_2 content improved corrosion performance of ZrO_2 - SiO_2 coatings. Alumina (Al_2O_3) is a ceramic material that are used in artificial joints and hip prosthesis. This is related to superior wear resistance and excellent mechanical properties [15]. It should be noted that it is impossible to create an excellent bone grafting when Al_2O_3 is used in the body because of bioinertness and low osseointegration ability of alumina [16]. In this context, various Al_2O_3 - based composites were expanded to overcome these bugs, such as HA- Al_2O_3 and Al_2O_3 - ZrO_2 composites [17, 18]. In previous researches, this result has found that by adding the SiO_2 to the substrate can improve the protective properties because of high corrosion resistance of SiO_2 [19] There is not any study about the creation of alumina-silica nanocomposite as a bond coat. So, it was considered as the main point of the present research.

Various techniques were used for application of coatings on metallic substrates, for example electrophoretic deposition (EPD), sol-gel, sputtering and plasma spraying [20-23]. Among the techniques, plasma sprayed coatings exhibit high corrosion resistance. Some parameters, such as adhesive strength between substrate and coating, elements of precursors, porosity and composition of the coatings could potentially affect corrosion behavior [24]. Compared to different coating methods, plasma spray was a simple technique and

contains a wide deposition rate, widespread particle size range and exhibits high -quality coatings [25, 26].

Some studies have previously shown that during plasma spraying HA phase could be converted to α -TCP (α - $\text{Ca}_3(\text{PO}_4)_2$), β -TCP (β - $\text{Ca}_3(\text{PO}_4)_2$) or other calcium oxide phases [27]. It has been reported that rapid solidification can reduce the crystallinity degree of HA coatings [27, 28]. Also, most investigations were done to determine in vitro and in vivo properties of plasma-sprayed HA coating [29-36]. Vu et al. [29] presented that the superior bone information of ZnSiAg-HA coatings when they were implanted in 18 male Sprague-Dawley rats.

In this study, a bi-layer plasma sprayed coating consisting of HA as the top layer and Al_2O_3 - SiO_2 nanocomposite with 10, 20 and 30 %wt SiO_2 as the intermediate layer on the medical grade pure titanium was established (Figure 1(a)). Adding the SiO_2 to the substrate can improve the protective properties because of high corrosion resistance of SiO_2 . Afterward, microstructure, porosity and corrosion behavior of the coatings were compared with the single-layer HA coatings (Figure 1(b)) and the bare titanium substrate. The influence of the adding an intermediate layer on the electrochemical corrosion behavior of the pure titanium was evaluated by potentiodynamic polarization accompanied by Field emission scanning electron microscopy (FESEM).

2. MATERIALS AND METHODS

2.1. Materials Commercial pure Ti (grade #2, $1 \times 1 \text{ cm}^2$) was used as substrate. The chemical composition of N: 0.07, C:0.7, Fe: 0.02, O: 0.67 and others Ti, which is according to the reported data for ASTM grade #2 [24]. Prior to the plasma spraying, the substrate was degreased and grit blasted with $24 \mu\text{m}$ alumina mesh to achieve a

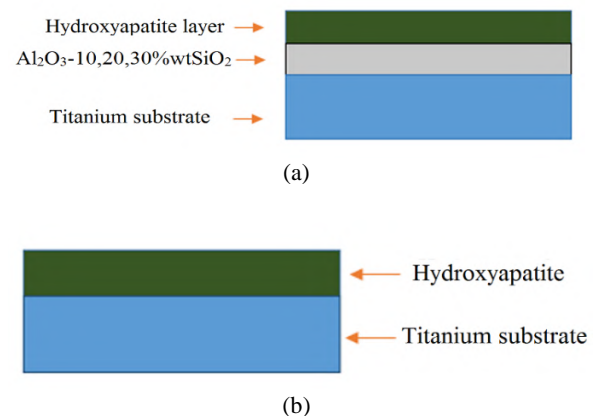


Figure 1. Schematic diagram of plasma-sprayed coatings a) bi-layered coating b) single-layered coating

rough surface (3.01-3.56 μm). Three types of powder were used in this study; $\alpha\text{-Al}_2\text{O}_3$ (99%, Merck, 40-50nm), amorphous SiO_2 (99%, Merck, 15-25nm), and synthesized hydroxyapatite nanopowder (20-40nm).

Hydroxyapatite nanoparticles were synthesized by a sonochemical technique. Starting materials used for the synthesis included high-purity calcium nitrate ($\text{Ca}(\text{NO}_3)_2 \cdot 4\text{H}_2\text{O}$) (99%, Merck), ammonium hydrogen phosphate ($(\text{NH}_4)_2\text{HPO}_4$) (99%, Merck), absolute ethanol and ammonium hydroxide. A high-intensity ultrasonic probe (Misonix S4000, Tihorn, 20 kHz, 500W/cm², USA) was used for the ultrasound irradiation reactor. Initially, 50 ml/mol of diammonium hydrogen phosphate was dissolved in distilled water and added drop wise to a solution of 84 mol/ml hydrated calcium nitrate in absolute ethanol at a temperature of 30 °C. The initial power of the sonicator was set at 40 W. The reaction was carried out for 1.5 h and pH of the solution was adjusted to 10 by using an adequate amount of NH_4OH solution. After formation of slurry, the sediment was centrifuged for 10 minutes and then washed three times. The precipitate was aged at 80°C for 5 h. Finally, the obtained powder was calcined at 700 °C with a rate of 10 K.min⁻¹.

2. 1. Plasma Spraying Process Al_2O_3 and 10, 20 and 30% wt SiO_2 powders were mixed with mechanically alloyed mixture for 3 h by using zirconia balls. In order to obtain desired flowability of nano powders and to optimize the deposition efficiency, primary nano powders were granulated with a 5%-wt poly-vinyl alcohol (PVA) solution as a binder. The powders were sieved by 140, 170, 200, 270 and 325 sieves. Size distribution of granular powders was 44-88 μm . In this work, plasma spraying was performed in air by a Plasma Metco 3MB gun (Sulzer- Metco; Switzerland). The coatings are shown schematically in Figure 1. The spraying parameters of both layers were listed in Table 1. The specimens of titanium substrates were preheated at 250 °C to increase the adhesion strength of coatings. The amount surface roughness of uncoated pure titanium and plasma sprayed coatings was measured by TR 100 Roughness of Surface tester. Ra (the average roughness of a surface) and Rz (the difference between the highest “peak” and the deepest “valley” in the surface) are different factors of roughness. These parameters were measured at four places on surface of specimens. The average amount of these parameters was presented.

2. 3. Characterizations of Feed Stokes X-ray diffraction (XRD) was used to analyze the phases obtained from the spraying experiments. This test was performed by a PW3710-based X-ray diffraction device manufactured by Philips Netherlands under a voltage of 40 kV and 30 mA (Cu $K\alpha$, 1.5405 Å, scan rate: 0.02 mv/s). The crystallite size of the samples was obtained from the X-ray diffraction pattern by the Debye–Scherrer

TABLE 1. Plasma spray parameters (Distance: 10 cm, Ar plasma gas flow rate: 85 SCFH, H_2 plasma gas flow rate: 15 SCFH)

Sample	Composition (%)	Current (A)	Plasma voltage (V)
H	100% HA	450	55
H-A-10S	HA / Al_2O_3 -10% SiO_2	450 / 500	55 / 58
H-A-20S	HA / Al_2O_3 -20% SiO_2	450 / 500	55 / 58
H-A-30S	HA / Al_2O_3 -30% SiO_2	450 / 500	55 / 58

equation [32]:

$$l = \frac{K \lambda}{\beta \cos \theta} \quad (1)$$

where λ is the wavelength of X-ray beam, β is the maximum intensity of the full width at half maximum, θ is the diffraction angle, K is constant selected at 0.9 and l is the average crystallite size.

Phase analysis was performed by Fourier-transform infrared spectroscopy (FTIR) studies of the synthesized HA nano particles. The powders and cross-section morphologies were assessed by field emission scanning electron microscope (FESEM, TESCAN MIRA3) and Energy-dispersion X-ray Spectroscopy (EDS; 15 kV). In order to investigate cross-sectional morphology, the coated samples were cut and embedded in epoxy. Then, the mounted samples were polished by SiC abrasive paper #600-#2000. A thin layer of gold was sputtered on the polished surface of samples to ensure adequate electrical conductivity during FESEM observation.

2. 4. Electrochemical Tests Polarization potentiodynamics test was performed by an Auto Lab device in simulated body fluids (SBF). Preparation of SBF solution was performed based on the protocol of Bansal et al. [26]. The electrochemical test of coating specimens was accomplished with three electrodes, the coated samples as working electrode, the saturated calomel electrode as reference electrode, and a platinum rod as counter electrode. The samples were kept in the solution for 90 min until the open circuit potential (OCP) was stabilized. All tests were measured at a potential of 0.25 -2 V with a scanning rate of 1 mV/s.

Polarization resistance was calculated from Stern Geary equation as indicated below [27]:

$$R_p = \frac{(\beta_a \times \beta_c)}{2.3 \times I_{corr} \times (\beta_a + \beta_c)} \quad (2)$$

In which R_p is polarization resistance, I_{corr} is current density, β_a and β_c are anodic and cathodic tafel slopes, respectively. The porosity of the plasma sprayed coatings was identified by electrochemical behavior of the coatings. The porosity was estimated by using the following relation [28]:

$$\%P = \frac{R_{pm}}{R_p} \times 10^{-\left| \frac{\Delta E_{corr}}{\beta_a} \right|} \quad (3)$$

where P is the total porosity of the coatings, R_{pm} the polarization resistance of the un-coated sample and R_p the polarization resistance of the coated sample. ΔE_{corr} is the different potential of the coated sample and the bare substrate.

The protection efficiency (PE) of the single layered and bi-layered coatings were obtained from the following relation [29]:

$$PE = \frac{(R_p - R_{pm})}{R_p} \times 100 \quad (4)$$

where R_p and R_{pm} are related to polarization resistance of the coated and uncoated samples respectively.

3. RESULTS and DISCUSSION

3. 1. FTIR and XRD Analysis

In this study a modified-sonochemical technique used to synthesize HA nanoparticles with increasing calcination temperature and decreasing reaction time compared to that of conventional sonochemical technique. FTIR analysis of the synthesized HA nanoparticles has been performed in the range of 400 cm^{-1} to 4000 cm^{-1} as shown in Figure 2. Vibrations of 3563 cm^{-1} , 3423 cm^{-1} bands and peaks around 632 cm^{-1} demonstrated the presence of hydroxyl groups. The presence of CO_3^{2-} groups was observed at 1458 cm^{-1} , 1418 cm^{-1} and 870 cm^{-1} . Bands located at 565 cm^{-1} and 603 cm^{-1} indicated the stretching vibrations of the phosphates group, and the tensile vibrations of the phosphate were measured at 1095 cm^{-1} , 1046 cm^{-1} and 962 cm^{-1} . The result of FTIR Spectra was in agreement with prior literature [37-39].

Figure 3 (a) shows XRD pattern of synthesized HA nanoparticles. The diffraction peaks are typical for the HA structure in accordance with the JCPDS standard card 00-009-0432. The XRD patterns indicate that the ultrasound waves are more impressive to achieve pure HA nanoparticles when calcination temperature was kept at $700 \text{ }^\circ\text{C}$. The XRD pattern (Figure 3 (a)) shows

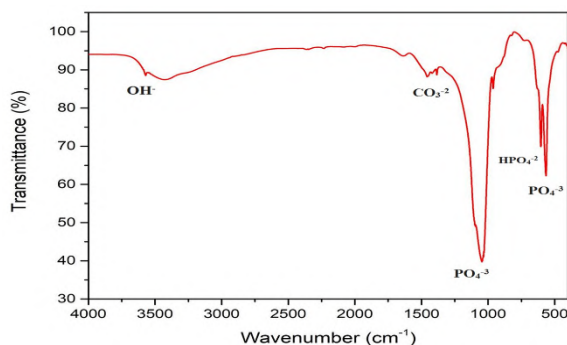


Figure 2. FTIR analysis of hydroxyapatite synthesized nanopowder

only HA crystallite phase. The crystallite size was assessed 15-25 nm.

Figure 4 indicates XRD pattern of Al_2O_3 -10% SiO_2 nanocomposite after 3 h ball milling. All the sharp peaks correspond to α - Al_2O_3 and the broadened peak at an angle of 15 to 25 degrees indicates the amorphous silica phase. According to previous research, the x-ray diffraction pattern of SiO_2 powder is made of one broadened peak that is identified Si-O-Si groups of amorphous SiO_2 [14]. By using the Scherrer equation as presented in Equation 1, the alumina crystallite size was calculated to be 45-65 nm.

The XRD pattern of HA/ Al_2O_3 -10% SiO_2 also is shown in Figure 3(b). By comparison the pattern of the HA before and after coating, it is observed that the tricalcium phosphate (TCP) and calcium oxide phases are formed during coating process. The dissolution degree of these phases as follows [32]:



TCP has been found to dissolve more in physiological solutions, as well as displaying a greater rate of dissolution or degradation than HA, when implanted in body environment [32]. Other researchers have also offered that the tricalcium phosphate and calcium oxide

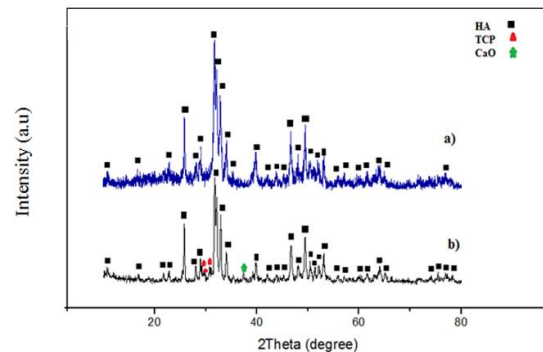


Figure 3. XRD pattern of (a) synthesized HA nanoparticles b) H-A-20S plasma-sprayed coating sample

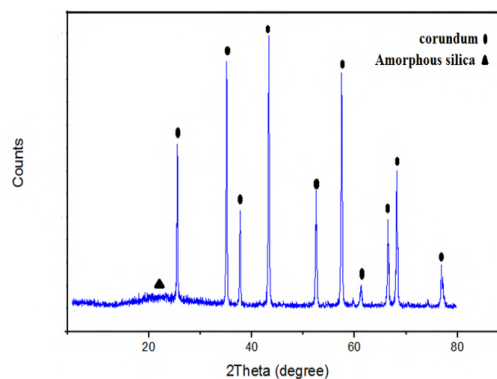


Figure 4. X-ray diffraction pattern of Al_2O_3 -10% SiO_2 nanocomposite

phases can be composed [33, 34]. The remarkable thing is the high mass absorption coefficient of the HA compared to corundum and silica phases and it causes the phases formed in the middle layer are not recognizable in this pattern. The mass absorption coefficient of the HA, corundum and silica was calculated and obtained 502.33, 101.96, and 60.08 cm^2/g , respectively. On the other hand, X-rays won't go through a thick coating. The X-ray diffraction pattern was taken from a coated sample without the HA layer for assessing the presence of corundum phase and other phases formed in the intermediate layer. The presence of the corundum ($\alpha\text{-Al}_2\text{O}_3$) and mullite can be observed in the XRD pattern of $\text{Al}_2\text{O}_3\text{-10\%SiO}_2$ coating without the top coat which is in accordance to cards 01-071-1123 and 00-015-0776 respectively, is revealed in Figure 5.

3. 2. Microstructure and Cross Sectional Analysis

Figure 6 shows morphology of the granulated HA and $\text{Al}_2\text{O}_3\text{-10\%SiO}_2$ nanocomposite powders. The granulated powders have spherical and semi-spherical morphology. The EDS spectra of the $\text{Al}_2\text{O}_3\text{-10\%SiO}_2$ nanocomposite also depicted 42.62% Al, 4.69% Si and 43.44% oxygen (Figure 6(c)). The nano powders do not have the ability to spray by plasma spraying due to the lack of adequate fluidity. Some portion of the nanoparticles should be melted because mechanical behavior of the coating is strongly related to melting degree of sprayed particles [35].

Scanning electron microscopy images of the plasma-sprayed samples are shown in Figure 7. Also, the thickness of the coatings is presented in Table 2. The cross-sectional images of the coatings indicated good adhesive bonding with substrate and no cracks are seen at the interface of coating and substrate. During the plasma spraying, the particles are exposed to a high temperature. Then, the powders are well sintered and they have fused together. HA layer and $\text{Al}_2\text{O}_3\text{-SiO}_2$ nanocomposite with 10, 20 and 30 percent of SiO_2

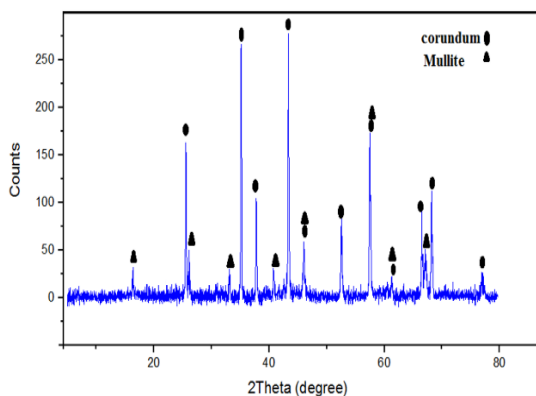


Figure 5. XRD pattern of plasma-sprayed $\text{Al}_2\text{O}_3\text{-20\%SiO}_2$ coating without top coat

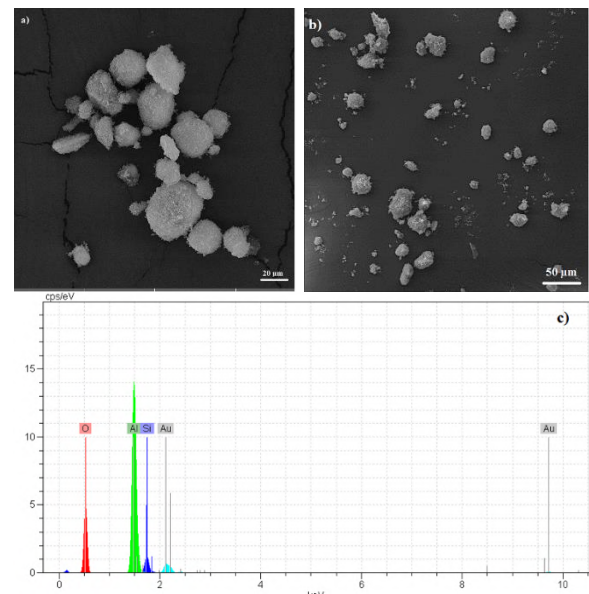


Figure 6. Scanning microscopic image of granulated powder of (a) HA (b) $\text{Al}_2\text{O}_3\text{-10\%SiO}_2$ nanocomposite (c) EDS of nanocomposite

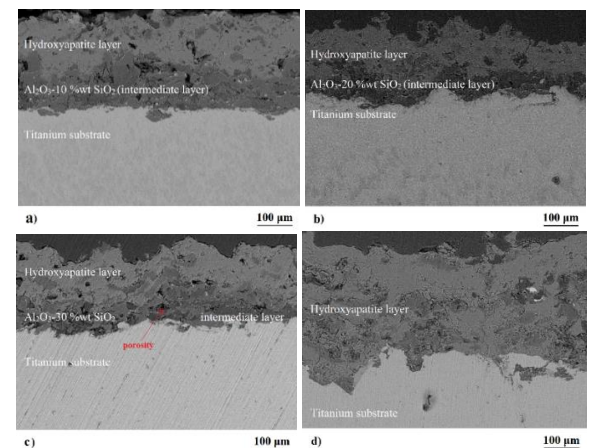


Figure 7. Cross-sectional images of plasma-sprayed coatings (a) H-A-10S (b) H-A-20S (c) H-A-30S (d) H

exhibited the lamellar structure. The porosity and cavities can be observed, which can be due to the evaporation of adhesive PVA. By image analysis of the high-resolution images, it can be concluded that H-A-30S coating displays more pores. The HA and H-A-20S coatings exhibit dense and low amount of the porosity. Also H-A-10S sample showed the distribution number of pores. It is clear that by increasing the percentage of silica to more than 20%, porosity has increased. Velocity of powder feeding, distance of the gun from the metal substrate and particle size are influencing melting of the particles during the plasma spraying [36]. The presence of the porosity, unmelted, semi-melted zones and cracks in the thermal sprayed coating also revealed in previous studies

[37, 38]. For example, Song et al. [39] showed increase in critical plasma spray parameter results in decrease in volume fractions of pores and partially melted regions, and consequently raises the overall hardness of the coatings. The overall hardness increase generally leads to decrease in wear rate.

It is observed that the nanostructured powders are porous and this inherent porosity will be maintained in the microstructure of the plasma-sprayed coatings. Lima et al. [40] discovered that the un-molten and nanostructured powders influence the elastic modulus, hardness, and thermal conductivity properties. Yilmaz [41] evaluated plasma-sprayed coatings on pure titanium substrate. It was observed that it is possible to coat Al_2O_3 and Al_2O_3 -13 wt.% TiO_2 on pure titanium substrate by using atmospheric plasma-spray process for determined conditions [42]. EDS Mapping of H-A-10S specimen is given in Figure 8. It shows the distribution of Al, Si, O, P, Ca and Ti in the sample. As expected, Ca and P are present in the upper layer. The mechanism of plasma-spray process can cause the presence of the titanium in the coating. But it is not noticeable.

3. 3. Polarization Studies The electrochemical behavior of the titanium substrate coated by HA and Al_2O_3 -10, 20, 30%wt SiO_2 was evaluated in simulated body fluids. The observed polarization plots of different plasma sprayed coatings are indicated in Figure 9. The corrosion parameters, such as current, potential corrosion, porosity and polarization resistance, which were calculated by the Stern Geary equation are presented in Table 3. It is clear that the corrosion currents of the coated samples decreased compared to the uncoated titanium. According to the polarization curves, it is considered that the current density of H-A-20S sample is lower than other samples. The corrosion potential and current density of H-A-20S are -468 mV and $0.23 \mu\text{A}/\text{cm}^2$, respectively, are shown in Figure 9. Also, amount of β_a and β_c were obtained 372.79 mV/dec and 182.73 mV/dec, respectively. Therefore, the polarization resistance was calculated $230498.6 \Omega/\text{cm}^2$.

The amount of porosity is very important for the corrosion resistance of coatings. The measured porosity of coated samples is listed in Table 3. The highest

TABLE 2. The measured thickness of the top coat and intermediate coat

Samples	Thickness top coat (μm)	Thickness intermediate coat (μm)
H	150-180	-
H-A-10S	100-130	90-100
H-A-20S	80-90	50-60
H-A-30S	80-100	50-60

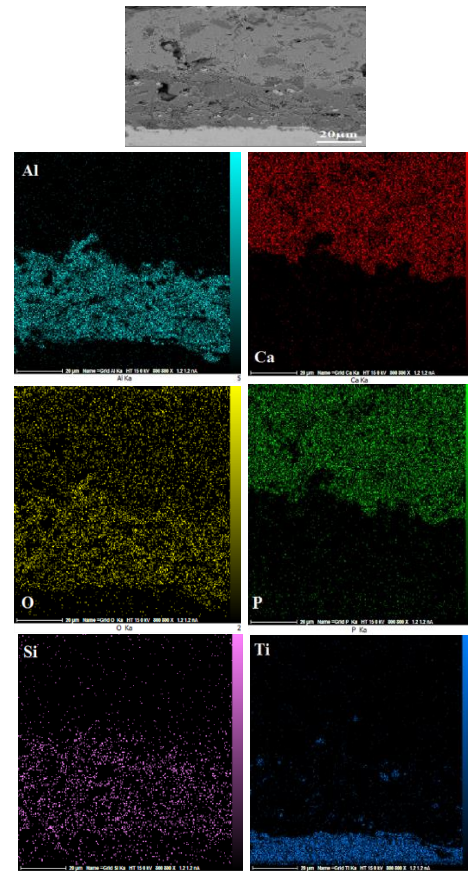


Figure 8. Cross-sectional images of plasma-sprayed coatings a) H-A-10S b) H-A-20S c) H-A-30S d) H

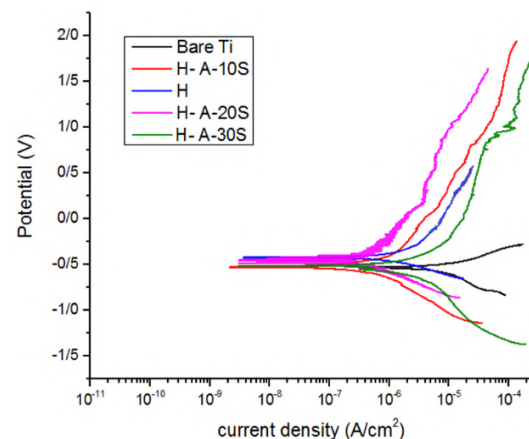


Figure 9. Potentiodynamic polarization curves of plasma-sprayed coating in SBF solution

porosity is related to H-A-30S. Also, H-A-20S coating contain low porosity compared to H-A-30S and H-A-10S. The current density of H-A-30S is more than other coatings.

TABLE 3. Corrosion parameters measured from polarization curves in SBF solution

Samples	Bare Ti	H	H-A-10S	H-A-20S	H-A-30S
β_a (mV/dec)	93.85	77.40	254.20	372.79	194.82
β_c (mV/dec)	145.71	67.23	209.40	182.73	221.02
i_{corr} ($\mu A/cm^2$)	3.25	0.27	0.28	0.23	0.79
E_{corr} (mV)	-529	-420	-510	-468	-496
R_p (Ω/cm^2)	7627.1	56402.5	177884.6	230498.6	56770.1
% Porosity	-	1.0	3.0	0.8	5.8
% PE	-	86.4	95.7	96.6	76.5

In fact, the high porosity increased corrosion current and reduced polarization resistance. The porosity, un-molten and semi-molten particles, pores and microstructural properties affected on the current density and corrosion resistance. Increased porosity goes along with increased corrosion rates. This is an effect of accessible surface area, which increases with increasing porosity [43]. The presence of pores and channels allow deeper penetration of the fluid, which, again, increases the corrosion rate. It is observed that addition of the intermediate coat with chemical composition of Al_2O_3 -20% wt SiO_2 increased corrosion resistance compared to the pure titanium and the single layer HA coating. Actually by increasing in the silica content of more than 20%, corrosion resistance has been reduced. The high presence of porosities in the microstructure of H-A-30S because of wide particle size distribution that cause to segregate during injection into the plasma jet. Smaller particles may not penetrate fully into the plasma jet, decreasing the deposition quality and increasing the porosity cause to low corrosion resistance [44, 45]. Usually, the intrinsic defects of plasma-sprayed coatings, for example pores (porosity), partially melted particles or un-molten and cracks have destructive on the mechanical, physical and chemical properties of the coatings [46-53]. The protection efficiency of H, H-A-10S, H-A-20S and H-A-30S coatings were obtained 86.47, 95.71, 96.69 and 76.56% respectively.

4. CONCLUSIONS

The present study revealed the use of an intermediate coat with the composition of Al_2O_3 -20% wt SiO_2 applied with the plasma spray technique on the surface of titanium implant. This led to considerable improvements in the corrosion resistance due to the presence of the

intermediate coat (corundum and mullite) with low porosity. The corundum, mullite, TCP and CaO phases without surplus phases were observed in the XRD patterns of the coatings. Electrochemical studies showed desirable corrosion resistance of the double-layer H-A-20S coating. Increased porosity (H-A-30S coating) goes along with increased corrosion rates. The presence of pores and channels allow deeper penetration of the fluid, which, again, increases the corrosion rate. In conclusion, the plasma-sprayed double-layer coatings can be used as protective coating systems for dental and orthopedic implants.

5. ACKNOWLEDGMENTS

The present study was supported by Materials and Energy Research Center (MERC) through grant No. 344596.

6. REFERENCES

- Bai, Y., Deng, Y., Zheng, Y., Li, Y., Zhang, R., Lv, Y., Zhao, Q., Wei, S.J.M.S. and C. E., "Characterization, corrosion behavior, cellular response and in vivo bone tissue compatibility of titanium-niobium alloy with low young's modulus", *Materials Science and Engineering: C*, Vol. 59, (2016), 565-576, doi: 10.1016/j.msec.2015.10.062
- Zhang, L.C. and Chen, L.Y.J.A.e.m., "A review on biomedical titanium alloys: Recent progress and prospect", *Advanced Engineering Materials*, Vol. 21, No. 4, (2019), 1801215, doi: 10.1002/adem.201801215
- Qosim, N., Supriadi, S., Puspitasari, P. and Kreshanti, P.J.I.I.o.E., "Mechanical surface treatments of Ti-6Al-4v miniplate implant manufactured by electrical discharge machining", *International Journal of Engineering, Transactions A: Basics*, Vol. 31, No. 7, (2018), 1103-1108. doi: 10.5829/ije.2018.31.07a.14
- Yu, S. and Scully, J.J.C., "Corrosion and passivity of ti-13% nb-13% zr in comparison to other biomedical implant alloys", *Corrosion*, Vol. 53, No. 12, (1997), doi: 10.5006/1.3290281
- Kokubo, T.J.B., "Hm kim and m. Kawashita", *Biomaterials*, Vol. 24, (2003), 2161, doi: 10.1016/S0142-9612(03)00044-9
- Ermis, M., Antmen, E. and Hasirci, V.J.B.m., "Micro and nanofabrication methods to control cell-substrate interactions and cell behavior: A review from the tissue engineering perspective", *Bioactive Materials*, Vol. 3, No. 3, (2018), 355-369, doi: 10.1016/j.bioactmat.2018.05.005
- Shirdar, M.R., Izman, S., Kheimehsari, H.M., Ahmad, N. and Ma'aram, A.J.S.I., "Evaluation of mechanical and electrochemical properties of fha-coated co-cr implant", *Surface Innovations*, Vol. 5, No. 2, (2017), 90-96, doi: 10.1680/jsuin.16.00028
- Singh, J., Chatha, S.S. and Singh, H., "Synthesis and characterization of plasma sprayed functional gradient bioceramic coating for medical implant applications", *Ceramics International*, Vol. 47, No. 7, (2021), 9143-9155, doi: 10.1016/j.ceramint.2020.12.039
- Bordbar-Khiabani, A., Yarmand, B. and Mozafari, M.J.S.I., "Functional peo layers on magnesium alloys: Innovative polymer-free drug-eluting stents", *Surface Innovations*, Vol. 6, No. 4-5, (2018), 237-243, doi: 10.1680/jsuin.18.00011

10. Çomaklı, O., Yazıcı, M., Yetim, T., Yetim, A. and Çelik, A.J.C.I., "Effect of ti amount on wear and corrosion properties of ti-doped Al₂O₃ nanocomposite ceramic coated cp titanium implant material", *Ceramics International*, Vol. 44, No. 7, (2018), 7421-7428, doi: 10.1016/j.ceramint.2018.01.046
11. Xu, J., Joguet, D., Cizek, J., Khor, K.A., Liao, H., Coddet, C., Chen, W.N.J.S. and Technology, C., "Synthesis and characterization on atomospheric plasma sprayed amorphous silica doped hydrxoyapatite coatings", *Surface and Coatings Technology*, Vol. 206, No. 22, (2012), 4659-4665, doi: 10.1016/j.surfcoat.2012.05.042
12. Ebrahimi, N., Zadeh, A.S.A.H., Vaezi, M., Mozafari, M.J.S. and Technology, C., "A new double-layer hydroxyapatite/alumina-silica coated titanium implants using plasma spray technique", *Surface and Coatings Technology*, Vol. 352, (2018), 474-482, doi: 10.1016/j.surfcoat.2018.08.022
13. Bahraminasab, M., Bozorg, M., Ghaffari, S., Kavakebian, F.J.M.S. and C, E., "Corrosion of Al₂O₃-ti composites under inflammatory condition in simulated physiological solution", *Materials Science and Engineering: C*, Vol. 102, (2019), 200-211, doi: 10.1016/j.msec.2019.04.047
14. Farhadian, M., Raeissi, K., Golozar, M., Labbaf, S., Hajilou, T. and Barnoush, A.J.A.S.S., "3d-focused ion beam tomography and quantitative porosity evaluation of ZrO₂-SiO₂ composite coating; amorphous SiO₂ as a porosity tailoring agent", *Applied Surface Science*, Vol. 511, (2020), 145567, doi: 10.1016/j.apsusc.2020.145567
15. Bahraminasab, M., Sahari, B.B., Edwards, K.L., Farahmand, F. and Arumugam, M., "Aseptic loosening of femoral components – materials engineering and design considerations", *Materials & Design*, Vol. 44, (2013), 155-163, doi: 10.1016/j.matdes.2012.07.066
16. Xie, H., Zhang, L., Xu, E., Yuan, H., Zhao, F. and Gao, J.J.C.I., "Sialon– Al₂O₃ ceramics as potential biomaterials", *Ceramics International*, Vol. 45, No. 14, (2019), 16809-16813, doi: 10.1016/j.ceramint.2019.05.22
17. Askari, N., Yousefpour, M. and Rajabi, M.J.I.J.o.A.C.T., "Determination of optimum al content in ha-al₂o₃ nanocomposites coatings prepared by electrophoretic deposition on titanium substrate", *International Journal of Applied Ceramic Technology*, Vol. 15, No. 4, (2018), 970-979, doi: 10.1111/ijac.12826
18. Jiao, C., Gu, J., Cao, Y., Xie, D., Liang, H., Chen, R., Shi, T., Shen, L., Wang, C. and Tian, Z.J.J.o.t.E.C.S., "Preparation of Al₂O₃-ZrO₂ scaffolds with controllable multi-level pores via digital light processing", *Journal of the European Ceramic Society*, Vol. 40, No. 15, (2020), 6087-6094, doi: 10.1016/j.jeurceramsoc.2020.06.024
19. Mazur, A., Szczurek, A., Chęćmanowski, J.G., Szczygieł, B.J.S. and Technology, C., "Corrosion resistance and bioactivity of SiO₂-Y₂O₃ coatings deposited on 316l steel", *Surface and Coatings Technology*, Vol. 350, (2018), 502-510, doi: 10.1016/j.surfcoat.2018.07.042
20. Farrokhi-Rad, M.J.J.o.A. and Compounds, "Effect of morphology on the electrophoretic deposition of hydroxyapatite nanoparticles", *Journal of Alloys and Compounds*, Vol. 741, (2018), 211-222, doi: 10.1016/j.jallcom.2018.01.101
21. Batebi, K., Khazaei, B.A., Afshar, A.J.S. and Technology, C., "Characterization of sol-gel derived silver/fluor-hydroxyapatite composite coatings on titanium substrate", *Surface and Coatings Technology*, Vol. 352, (2018), 522-528, doi: 10.1016/j.surfcoat.2018.08.021
22. Akbari, G., Nikravesh, M. and Poladi, A.J.I.J.o.E., "Mechanical properties and microstructural evolution of ta/tanx double layer thin films deposited by magnetron sputtering", *International Journal of Engineering, Transactions B: Applications*, Vol. 30, No. 2, (2017), 288-293, doi: 10.5829/idosi.ije.2017.30.02b.16
23. Ren, J., Zhao, D., Qi, F., Liu, W. and Chen, Y.J.J.o.t.m.b.o.b.m., "Heat and hydrothermal treatments on the microstructure evolution and mechanical properties of plasma sprayed hydroxyapatite coatings reinforced with graphene nanoplatelets", *Journal of the Mechanical Behavior of Biomedical Materials*, Vol. 101, (2020), 103418, doi: 10.1016/j.jmbbm.2019.103418
24. Celik, E., Ozdemir, I., Avci, E., Tsunekawa, Y.J.S. and Technology, C., "Corrosion behaviour of plasma sprayed coatings", *Surface and Coatings Technology*, Vol. 193, No. 1-3, (2005), 297-302, doi: 10.1016/j.surfcoat.2004.08.143
25. Gkomoza, P., Vardavoulias, M., Pantelis, D., Sarafoglou, C.J.S. and Technology, C., "Comparative study of structure and properties of thermal spray coatings using conventional and nanostructured hydroxyapatite powder, for applications in medical implants", *Surface and Coatings Technology*, Vol. 357, (2019), 748-758, doi: 10.1016/j.surfcoat.2018.10.044
26. Bansal, P., Singh, G., Sidhu, H.S.J.S. and Technology, C., "Investigation of surface properties and corrosion behavior of plasma sprayed ha/zno coatings prepared on az31 mg alloy", *Surface and Coatings Technology*, Vol. 401, (2020), 126241, doi: 10.1016/j.surfcoat.2020.126241
27. Bogya, E.S., Károly, Z. and Barabás, R.J.C.I., "Atmospheric plasma sprayed silica–hydroxyapatite coatings on magnesium alloy substrates", *Ceramics International*, Vol. 41, No. 4, (2015), 6005-6012, doi: 10.1016/j.ceramint.2015.01.041
28. Noorakma, A.C., Zuhailawati, H., Aishvarya, V. and Dhindaw, B.K., "Hydroxyapatite-coated magnesium-based biodegradable alloy: Cold spray deposition and simulated body fluid studies", *Journal of Materials Engineering and Performance*, Vol. 22, No. 10, (2013), 2997-3004, doi: 10.1007/s11665-013-0589-9
29. Vu, A.A., Robertson, S.F., Ke, D., Bandyopadhyay, A. and Bose, S.J.A.b., "Mechanical and biological properties of zno, SiO₂, and ag₂o doped plasma sprayed hydroxyapatite coating for orthopaedic and dental applications", *Acta Biomaterialia*, Vol. 92, (2019), 325-335, doi: 10.1016/j.actbio.2019.05.020
30. Girija, E., Kumar, G.S., Thamizhavel, A., Yokogawa, Y. and Kalkura, S.N.J.P.t., "Role of material processing on the thermal stability and sinterability of nanocrystalline hydroxyapatite", *Powder Technology*, Vol. 225, (2012), 190-195, doi: 10.1016/j.powtec.2012.04.007
31. Elias, C., Lima, J., Valiev, R. and Meyers, M.J.J., "Biomedical applications of titanium and its alloys", *JOM*, Vol. 60, No. 3, (2008), 46-49, doi: 10.1007/s11837-008-0031-1
32. Puspitasari, P. and Budi, L.J.I.J.o.E., "Physical and magnetic properties comparison of cobalt ferrite nanopowder using sol-gel and sonochemical methods", *International Journal of Engineering, Transactions B: Applications*, Vol. 33, No. 5, (2020), 877-884, doi: 10.5829/ije.2020.33.05b.20
33. Kokubo, T. and Takadama, H.J.H.u.i.S.i.p.i.v.b.b., Biomaterial, "Leading opinion", *Biomaterials*, Vol. 27, (2006), 2907-2915, doi: 10.1016/j.biomaterials.2006.01.017
34. Palanivelu, R., Kalainathan, S. and Kumar, A.R.J.C.I., "Characterization studies on plasma sprayed (at/ha) bi-layered nano ceramics coating on biomedical commercially pure titanium dental implant", *Ceramics International*, Vol. 40, No. 6, (2014), 7745-7751, doi: 10.1016/j.ceramint.2013.12.116
35. Jam, A., Derakhshandeh, S.M.R., Rajaei, H. and Pakseresh, A.H.J.C.I., "Evaluation of microstructure and electrochemical behavior of dual-layer nicaloy/mullite plasma sprayed coating on high silicon cast iron alloy", *Ceramics International*, Vol. 43, No. 16, (2017), 14146-14155, doi: 10.1016/j.ceramint.2017.07.155
36. Kumar, A.M., Rajendran, N.J.S. and Technology, C., "Influence of zirconia nanoparticles on the surface and electrochemical

- behaviour of polypyrrole nanocomposite coated 316l ss in simulated body fluid", *Surface and Coatings Technology*, Vol. 213, (2012), 155-166, doi: 10.1016/j.surfcoat.2012.10.039
37. Ch, A., Sagadevan, S. and Dakshnamoorthy, A.J.I.j.o.p.s., "Synthesis and characterization of nano-hydroxyapatite (n-hap) using the wet chemical technique", *International Journal of Physical Sciences*, Vol. 8, No. 32, (2013), 1639-1645, doi: 10.5897/IJPS2013.3990
 38. Poinern, G., Brundavanam, R., Le, X.T., Djordjevic, S., Prokic, M. and Fawcett, D.J.I.j.o.n., "Thermal and ultrasonic influence in the formation of nanometer scale hydroxyapatite bio-ceramic", *International Journal of Nanomedicine*, Vol. 6, (2011), 2083, doi: 10.2147/IJN.S24790
 39. Song, E.P., Ahn, J., Lee, S., Kim, N.J.J.S. and Technology, C., "Effects of critical plasma spray parameter and spray distance on wear resistance of Al₂O₃-8 wt.% TiO₂ coatings plasma-sprayed with nanopowders", *Surface and Coatings Technology*, Vol. 202, No. 15, (2008), 3625-3632, doi: 10.1016/j.surfcoat.2008.01.002
 40. Lima, R.S., Kucuk, A. and Berndt, C.C., "Bimodal distribution of mechanical properties on plasma sprayed nanostructured partially stabilized zirconia", *Materials Science and Engineering: A*, Vol. 327, No. 2, (2002), 224-232, doi: 10.1016/S0921-5093(01)01530-1
 41. Yılmaz, Ş.J.C.I., "An evaluation of plasma-sprayed coatings based on Al₂O₃ and Al₂O₃-13 wt.% TiO₂ with bond coat on pure titanium substrate", *Ceramics International*, Vol. 35, No. 5, (2009), 2017-2022, doi: 10.1016/j.ceramint.2008.11.017
 42. Zamani, S., Salahi, E. and Mobasherpour, I.J.C.C.T., "Removal of nickel from aqueous solution by nano hydroxyapatite originated from persian gulf corals", *Canadian Chemical Transactions*, Vol. 1, No. 3, (2013), 173-190, doi: 10.13179/canchemtrans.2013.01.03.0033
 43. Ben-Nissan, B.J.A.i.C.P.B., "Advances in calcium phosphate biomaterials preface", Vol. 2, (2014), Ix-Xi, doi: 10.1007/978-3-642-53980-0
 44. Singh, G., Singh, S. and Prakash, S., "Surface characterization of plasma sprayed pure and reinforced hydroxyapatite coating on Ti6Al4v alloy", *Surface and Coatings Technology*, Vol. 205, No. 20, (2011), 4814-4820, doi: 10.1016/j.surfcoat.2011.04.064
 45. Morks, M. and Kobayashi, A.J.A.S.S., "Effect of gun current on the microstructure and crystallinity of plasma sprayed hydroxyapatite coatings", *Applied Surface Science*, Vol. 253, No. 17, (2007), 7136-7142, doi: 10.1016/j.apsusc.2007.02.183
 46. Di Girolamo, G., Marra, F., Blasi, C., Serra, E., Valente, T. "Microstructure, mechanical properties and thermal shock resistance of plasma sprayed nanostructured zirconia coatings", *Ceramics International*, Vol. 37, No. 7, (2011), 2711-2717, doi: 10.1016/j.ceramint.2011.04.024
 47. Levingstone, T.J., Ardhaoui, M., Benyounis, K., Looney, L., Stokes, J.T.J.S. and Technology, C., "Plasma sprayed hydroxyapatite coatings: Understanding process relationships using design of experiment analysis", *Surface and Coatings Technology*, Vol. 283, (2015), 29-36, doi: 10.1016/j.surfcoat.2015.10.044
 48. Sun, L., Berndt, C.C., Grey, C.P.J.M.S. and A, E., "Phase, structural and microstructural investigations of plasma sprayed hydroxyapatite coatings", *Materials Science and Engineering: A*, Vol. 360, No. 1-2, (2003), 70-84, doi: 10.1016/S0921-5093(03)00439-8
 49. Abualigaledari, S., "Development of an anti-corrosion thermally sprayed coating system for oil and gas transmission pipeline", (2018).
 50. Salimijazi, H., Hosseini, M., Mostaghimi, J., Pershin, L., Coyle, T.W., Samadi, H. and Shafyei, A., "Plasma sprayed coating using mullite and mixed alumina/silica powders", *Journal of Thermal Spray Technology*, Vol. 21, No. 5, (2012), 825-830, doi: 10.1007/s11666-012-9766-x
 51. Pakseresht, A., Rahimpour, M., Vaezi, M., Salehi, M.J.M.C. and Physics, "Thermal plasma spheroidization and spray deposition of barium titanate powder and characterization of the plasma sprayable powder", *Materials Chemistry and Physics*, Vol. 173, (2016), 395-403, doi: 10.1016/j.matchemphys.2016.02.028
 52. Henao, J., Poblano-Salas, C., Monsalve, M., Corona-Castuera, J., Barceinas-Sanchez, O.J.J.o.M.R. and Technology, "Bio-active glass coatings manufactured by thermal spray: A status report", *Journal of Materials Research and Technology*, Vol. 8, No. 5, (2019), 4965-4984, doi: 10.1016/j.jmrt.2019.07.011
 53. Odhiambo, J.G., Li, W., Zhao, Y. and Li, C.J.C., "Porosity and its significance in plasma-sprayed coatings", *Coatings*, Vol. 9, No. 7, (2019), 460, doi: 10.3390/coatings9070460

Persian Abstract

چکیده

تلاش‌های زیادی برای بهبود ویژگی‌های سطحی مواد زیستی با پوشش‌های مختلف صورت گرفته است. در این پژوهش، یک نوع پوشش محافظ دولایه HA/Al₂O₃-SiO₂ (با ۱۰، ۲۰ و ۳۰ درصد وزنی SiO₂) به روش پلاسما اسپری بر روی سطح تیتانیوم اعمال شد. ویژگی‌های سطحی پوشش اعمال‌شده به تفصیل مورد ارزیابی قرار گرفت تا اثربخشی این کار برای کاربردهای زیست‌پزشکی بررسی شود. نتایج نشان داد که پوشش‌های یکنواخت و دولایه پلاسما اسپری شده را می‌توان با موفقیت از طریق بهینه‌سازی پارامترها تهیه کرد. همچنین مشخص شد که زبری پوشش‌های دولایه با افزایش تعداد لایه‌های پوشش افزایش می‌یابد. رفتار خوردگی نمونه‌های پوشش داده شده و بدون پوشش با استفاده از آزمون‌های الکتروشیمیایی مورد ارزیابی قرار گرفت. مقایسه مقاومت به خوردگی نمونه ۲۰ درصد SiO₂ با نمونه دارای پوشش تک لایه HA و نمونه تیتانیوم فاقد پوشش، بهبود قابل توجهی را نشان می‌دهد. پوشش پیشنهادی توانایی‌های امیدوارکننده‌ای را برای کاربردهای زیست‌پزشکی نشان داد.



Advanced Exergy Scrutiny of a Dual-loop Organic Rankine Cycle for Waste Heat Recovery of a Heavy-duty Stationary Diesel Engine

H. Boodaghi^a, M. M. Etghani^{*b}, K. Sedighi^a

^aDepartment of Mechanical Engineering, Babol Noshirvani University of Technology, Babol, Iran

^bDepartment of Mechanical Engineering, Payame Noor University, Tehran, Iran

PAPER INFO

Paper history:

Received 25 October 2021

Received in revised form 29 November 2021

Accepted 23 December 2021

Keywords:

Organic Rankine Cycle

Advanced Exergy Scrutiny

Heavy-duty Diesel Engine

Endogenous/Exogenous

(Un) Avoidable Exergy Destruction

ABSTRACT

In this paper, the normal exergy scrutiny (NES) and advanced exergy scrutiny (AES) of a waste heat recovery (WHR) system was performed. The proposed system contains a dual-loop organic Rankine cycle (DORC) which recovers the available waste heat of the intake air, exhaust gas, and coolant streams of a 12-cylinder heavy-duty stationary diesel engine. A well-known method of the AES called the thermodynamic cycle approach is utilized to determine each component exergy destruction parts namely exogenous/endogenous, unavoidable/avoidable, etc. Results showed that 59.04 kW from the 258.69 kW total exergy destruction rate of the system could be eliminated (22.82% of the total exergy destruction rate). The total avoidable exergy destruction part of the low-temperature loop accounts for 46.62 kW, which indicates that it requires more attention than that of the high-temperature loop by 12.42 kW. Furthermore, it is revealed that to enhance the overall productivity of the system, there is a relatively significant difference in priority order regarding the improvement of system components. The AES has proposed this ranking for improvement priority of components: condenser, expander 2, expander 1, respectively. While the NES has specified the priority as the evaporator 1, condenser, expander 2, respectively.

doi: 10.5829/ije.2022.35.04a.04

NOMENCLATURE

E	Exergy rate (kW)	HT	High-temperature
H	Enthalpy	ICE	Internal combustion engine
N	Engine Speed (RPM)	LT	Low-temperature
P	Pressure (kPa)	AES	Advanced exergy scrutiny
S	Entropy	MFR	Mass flow rate
W	Power (kW)	NES	Normal exergy scrutiny
Abbreviations		ORC	Organic Rankine cycle
AV	Avoidable	Subscripts	
UN	Unavoidable	D	Destruction
WHR	Waste heat recovery	ex	Exergy
EN	Endogenous	th	Thermal
EX	Exogenous		

1. INTRODUCTION

With the growing human population, dependence on energy and its applications is increasing dramatically. Nonetheless, the world's non-renewable main energy resources are restricted. As a result, it is crucial to develop energy conversion systems and technologies to

utilize the maximum capacity of existing resources optimally. In recent years, organic Rankine cycles (ORCs) have gained special attention due to their excellent reliability, low maintenance, and high productivity [1, 2]. Working fluid selection and developing the system configuration are two significant challenges in designing a well-productive ORC waste

*Corresponding Author Institutional Email: etghani@pnu.ac.ir
(M. M. Etghani)

heat recovery (WHR) system [3, 4]. Developing a hydrogen production solid oxide electrolysis (SOEC) by marine engine ORC-WHR system was evaluated by Wang et al. [5]. The results revealed that the rate of hydrogen production and power production in the proposed system were 0.43 kg/s and 32387 kW, respectively. Also, the ORC efficiency and the integrated system achieved at 12.12% and 53.56%, respectively. An innovative hybrid-reversible ORC, ejector refrigeration cycle (ERC), and mobile air conditioning (MAC) system was investigated numerically and experimentally by Di Cairano et al. [6] for series hybrid electric vehicles (SHEV). Results revealed that in the ORC mode, the proposed hybrid system indicates a maximum calculated net efficiency of 3.9%, and in the ERC mode, the estimated fuel economy was 1.4%. Wang et al. [7] studied a novel analysis technique for selecting of operating fluid pairs utilized in the dual-loop ORC-engine WHR system. According to the results, toluene/R124 was found a great fluid couple for the proposed system. Di Battista et al. [8] evaluated the WHR capability of Ireland Custom Exhaust (ICE) exhaust gases through a combined supercritical CO₂-ORC cycle. As a comparison between the combined system and a single-based system, they determined that the overall efficiency of the combined system was around 3-4% greater. For a solid oxide fuel cell (SOFC), Emadi et al. [9] investigated the selection of operating fluids plus optimization of a cogeneration DORC-WHR system. The Thermodynamic and economic performance of the DORC system by 20 organic fluids was examined, which the combination of R601 for the topping cycle and ethane for the bottoming cycle was selected as the optimum. Also, the exergy efficiency of 52% and the power production of 969 kW were determined. A high-efficiency WHR system comprising SOFC, HCCI engine, and ORC is developed and examined by Ouyang et al. [10]. The effects of input variables on HCCI engine performance were determined, and the optimal zeotropic working fluid of ORC was observed in terms of exhaust gas stream temperature. They found that the combined system's exergy and energy efficiencies are more than 61.3% and 63.6%, respectively. These are about 17.95% and 18.76% higher than that of a simple cell.

In recent years, researchers have performed the advanced exergy examination approach for multiple works. This approach is also called advanced exergy scrutiny (AES). The AES is defined as the division of the exergy destruction rate for a given stream into four-parts of avoidable-unavoidable and endogenous-exogenous. This analysis is applied to provide more information regarding the inefficiencies due to interconnection between system components that the normal exergy scrutiny (NES) could not indicate. In addition, this approach can be employed to find the real ability of the system in order to further improvements and

optimizations. Zhang et al. [11] investigated the performance of an integrated system containing an ORC and the transcritical CO₂ energy storage and using AES. R290 was selected as the organic operating fluid of ORC system. Results showed that the exergy efficiency of proposed system was determined around 35% under real conditions. For the unavoidable conditions it was near 42%. This exhibits the substantial improvement capacity of the system productivity. The AES of an ORC-based configuration for WHR of flue gases in processes of a coal-fired plant studied by Liao et al. [12]. Multiple configurations have been examined, and results showed that the exogenous exergy destruction part was fewer than the endogenous part in components. Also, results demonstrated that 25.65% part of the overall system exergy destruction is avoidable. Wang et al. [13] studied the AES and exergoeconomic analyzes of an integrated system containing CO₂ storage-capture plus WHR operations. The entire system exergy destruction rate was determined about 36 MW, of which the ORC process accounted for 32.35%, the CO₂ storage-capture process was 43.15%, and the absorption refrigeration cycle process determined near 25%. To achieve the actual potential of the system for improvement, the AES was performed for a recompression sCO₂-cycle by Mohammadi and co-workers [14]. The proposed system exergy efficiency was determined near 17.15% and 16.65% in terms of unavoidable and real conditions, respectively. The results revealed that the greatest potentiality for enhancement was calculated for 107 MW. Also, they found to enhance the system productivity, the priority ordering of system components obtained via the advanced exergy scrutiny differs from normal exergy scrutiny (NES). Moreover, many investigators studied this method for various new energy conversion systems and plants.

To the authors' knowledge, there are very few studies which investigated a waste heat recovery system consisting of a DORC and a stationary heavy-duty Diesel (HDD) engine by means of the advanced exergy scrutiny (AES) which could enhance the value of the conclusions obtained from a normal exergy scrutiny (NES) by demonstrating the real potential for performance improvement of system components. Hence, in this investigation, the DORC-HDD engine system is numerically modeled, and energy plus exergy characteristics of the system has been studied. In addition, the AES is utilized to reveal a detailed information regarding the components inefficiency on each other as well as the real potential of system for enhancement. The results achieved by both the exergy scrutiny approaches are compared, and the improvement priority of components in terms of each method has been provided. The structure of this study is as follows: the proposed system, HDD engine descriptions as well as exergy analysis are introduced in section 2. Section 3

contains the result and discussion. Eventually, the conclusion is provided in section 4.

2. SYSTEM DESCRIPTION

2. 1. Engine Modeling The engine exhaust gas, intake air, and coolant streams drive the bottoming DORC system. Thus, the 1-D numerical configuration of the 12-cylinder stationary HDD engine is simulated using the GT-Power [15] software. By employing the GT-Power, the heat transfer and flow processes through each component of the engine are modeled 1-dimensionally. The engine configuration model and the main technical specifications are provided in Figure 1 and Table 1. Moreover, it should be noted that the experimental validation of engine performance is provided in our previous work [16].

2. 2. Dual-loop Organic Rankine Cycle (DORC) The DORC system, the high-temperature (HT) loop comprises pump1, evaporator1, expander1, preheater, and reservoir1, recovering the HDD engine exhaust gases available waste heat. The low-temperature (LT) loop recovers the remaining unconsumed thermal energy of

the HT loop plus the dissipated energy of intake air and coolant streams. The LT loop has involved pump2, intercooler, evaporator2, expander2, condenser, and reservoir2. The proposed DORC system is illustrated in Figure 2.

Due to its appropriate thermodynamic properties, R245fa is one of the most common organic operating fluids applied in medium-high temperature ORC-WHR systems [17]. So, the fluid of R245fa is considered as the operating fluid of the HT loop. Because of the low temperature of the waste heats utilized, there is no matter regarding the de-composition of the LT loop working

TABLE 1. HDD engine specifications

Parameter	Value
Engine type	Turbocharged Heavy-duty Diesel, water-cooled
Rated speed	1500 RPM
Rated power	1000 kW
Displacement	38 L
Number of cylinders	12
Compression ratio	15:1
Bore × Stroke	150 mm × 180 mm
Exhaust gases temperature	530 °C
Exhaust gases mass flow rate	1.4 kg/s
Coolant temperature	84 °C

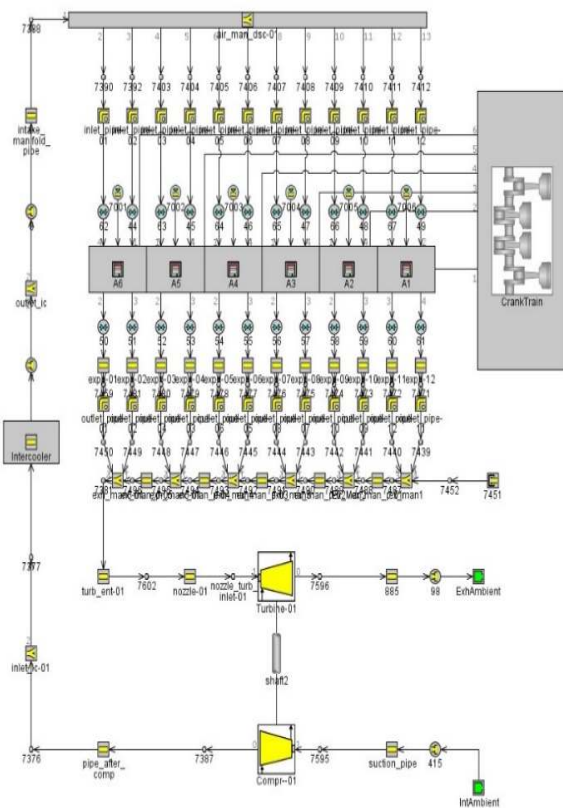


Figure 1. Configuration of the HDD engine model in GT-Power

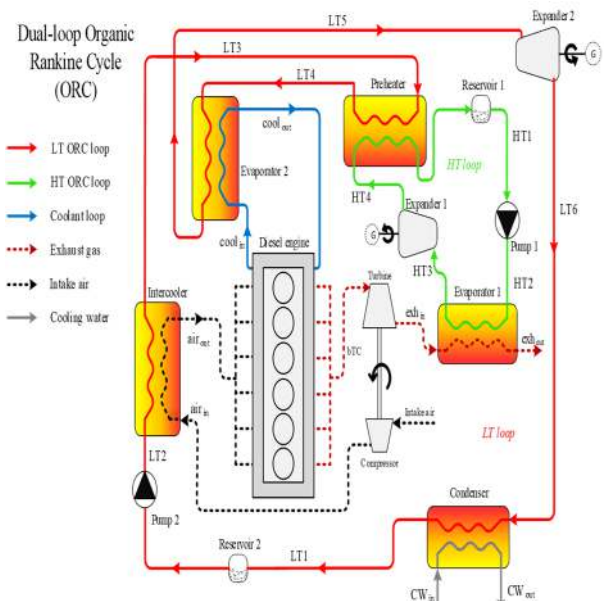


Figure 2. Construction of the proposed dual-loop ORC-WHR system

fluid. Therefore, because of its desirable thermal attributes, the R134a has been considered in the role of operating fluid for the LT loop. Thermo-environmental attributes of the organic fluids of loops are displayed in Table 2 [18-20].

The working process of the DORC system is as follows: the waste heat of the HDD engine exhaust gas stream is conveyed to the operating fluid of the HT loop, R245fa (process exh-in-exh-out). This makes the R245fa fluid evaporate and reach to the saturated vapor state (state HT3). Then, by operation HT3 to HT4, the expansion procedure occurs, and the useful power is produced. After that, the working fluid remains at the superheated vapor state. Then, the condensation operation proceeds by transferring the heat to the working fluid of the LT loop. Consequently, at HT1, the R245fa converts to the saturated liquid state. Eventually, the pumping happens and via the process HT1-HT2, R245fa is conveyed from reservoir 1 to pump 1. Meantime, by crossing into reservoir 2, the R134a is pumping over process LT1-LT2. Then, via passing into the intercooler, the working fluid is heated through the available dissipated energy of engine intake charge air (LT2-LT3). After that, over the LT3-LT4 process, the working fluid obtains some heat through the pre-heater and converts to the saturated two-phase of liquid-gas state. Then, to make sure there is no liquid that survives during the expansion process, the superheating is essential. Thus, via LT5 and through evaporator 2, the engine coolant stream is heating the R134a and converts it to the superheated state. Following the expansion process (LT5-LT6), the working fluid still experiences a superheated state. So, the condensation process is performed, and the R134a returns to the saturated liquid state (LT1).

2. 3. Exergy Scrutiny In order to facilitate the thermodynamic modeling process and simplifying the exergy scrutiny, some assumptions are required to make for the DORC system:

- 1) The changes in kinetic energy are neglected, and the entire system works at steady-state condition [21].
- 2) Pressure loss over the heat exchangers and pipes is ignored [22].

TABLE 2. Properties of the DORC working fluids

Loop	Working fluid	Critical pressure (kPa)	Critical temperature (K)	GWP (100 year)	ODP
HT loop	R245fa	3640	427.3	1030	0
LT loop	R134a	4060	374.2	1430	0

- 3) The pinch-point temperature difference is evaluated for each heat exchanger.
- 4) The ambient temperature and atmospheric pressure are defined as 20 °C and 101.325 kPa, respectively.
- 5) To avoid acid corrosion happening, the temperature of the exhaust gases after the recovery process should be over 100 °C [23].

2. 3. 1. Normal Exergy Scrutiny (NES) According to the presumptions of the last section, the thermodynamic balance equations for each DORC system component is defined as follows [24]:

$$E_Q + \sum m_i e_i = W + \sum m_e e_e + E_D \tag{1}$$

$$Q + \sum m_i h_i = W + \sum m_e h_e \tag{2}$$

$$\sum m_e - \sum m_i = 0 \tag{3}$$

$$E = m e \tag{4}$$

where, E_Q is considered as the exergy related to the heat transfer, $\sum m_i e_i$ is defined as the input exergy, $\sum m_e e_e$ is the rate of output work, denotes the rate of output exergy flow, E_D is the exergy destruction rate, represents the stream MFR, Q is the heat transfer rate, $\sum m_i h_i$ and $\sum m_e h_e$ indicate the rate of input enthalpy and output enthalpy, respectively. Also, the rate of exergy transferred by thermal energy at the given temperature of T can be examined by :

$$E_Q = Q \left(1 - \frac{T_0}{T}\right) \tag{5}$$

here, the ambient temperature is characterized by T_0 . To calculate the overall productivity of the DORC-WHR system, the exergy efficiency equation is required:

$$\eta = \left(\frac{\text{exergy of products}}{\text{total exergy inputs}} \right) \tag{6}$$

For the k th system component, the primary equations required for the NES are [25, 26]:

$$E_{F,k} = E_{P,k} + E_D \tag{7}$$

$$\varepsilon_k = \frac{E_{P,k}}{E_{F,k}} \times 100\% = \left(1 - \frac{E_D}{E_{F,k}} \right) \times 100\% \tag{8}$$

$$y_k^* = \frac{E_D}{E_{D,tot}} \times 100\% \tag{9}$$

$$y_k = \frac{E_{D,k}}{E_{F,k}} \times 100\% \tag{10}$$

here, $E_{F,k}$ is the fuel exergy rate, $E_{P,k}$ is the product exergy rate, ε_k denotes the exergy efficiency, y_k^* represents the relative exergy destruction, and y_k is the ratio of exergy destruction.

In Table 3, the balance equations of each component in terms of the energy and exergy analysis is provided [27].

2. 4. 1. Advanced Exergy Scrutiny (AES)

As mentioned before, the rate of exergy destruction for every component is split in four parts of avoidable-unavoidable as well as endogenous-exogenous. This dividing technique is called advanced exergy scrutiny (AES). It is implemented to exhibit the accurate information related to inefficiencies of interconnection within the system components, and in order to determine the system’s actual capability for extra enhancement.

In a system, the exergy destruction rate of each component is divided into two parts of the exogenous exergy destruction $E_{D,k}^{EX}$, and the endogenous exergy destruction $E_{D,k}^{EN}$ [28]:

$$E_{D,k} = E_{D,k}^{EX} + E_{D,k}^{EN} \tag{11}$$

Here, $E_{D,k}^{EX}$ presents the irreversible process within a component, and the irreversible process within other components is defined by $E_{D,k}^{EN}$. Defining the concept of dual exogenous-endogenous rate of exergy destruction helps to investigate various irreversibility in the proposed system. Applying this approach leads to identify whether the system modification must be assigned to the k th component or others [29, 30]. The exergy destruction rate can also be divided in unavoidable exergy destruction $E_{D,k}^{UN}$ part and avoidable exergy destruction $E_{D,k}^{AV}$ part [31, 32]:

$$E_{D,k} = E_{D,k}^{UN} + E_{D,k}^{AV} \tag{12}$$

here, $E_{D,k}^{UN}$ defines the certain exergy destruction part that could not be decreased because of engineering constraints. $E_{D,k}^{AV}$ is specified as other part of the exergy destruction that could be diminished through suitable modification techniques. In a certain system, the mentioned dividing approach can demonstrate the possible improvement of components.

TABLE 3. Balance equations of each component

Component	Energy balance equation	Exergy balance equation
Evap.1	$m_{HT2}(h_{HT3} - h_{HT2}) =$ $m_{exh,out}(h_{exh,in} - h_{exh,out})$	$E_{HT2} + E_{exh,in} =$ $E_{HT3} + E_{exh,out} + E_{D,eva1}$
Exp.1	$W_{exp1} = m_{HT3}(h_{HT3} - h_{HT4})$	$E_{HT3} = E_{HT4} + W_{exp1} + E_{D,exp1}$
Preh.	$m_{HT4}(h_{HT4} - h_{HT1}) =$ $m_{LT4}(h_{LT4} - h_{LT3})$	$E_{HT4} + E_{LT3} =$ $E_{HT1} + E_{LT4} + E_{D,pre}$
Pump1	$W_{pump1} = m_{HT1}(h_{HT2} - h_{HT1})$	$E_{HT1} + W_{pump1} = E_{HT2} + E_{D,pump1}$
Evap.2	$m_{cool,in}(h_{cool,in} - h_{cool,out}) =$ $m_{LT5}(h_{LT5} - h_{LT4})$	$E_{LT4} + E_{cool,in} =$ $E_{LT5} + E_{cool,out} + E_{D,eva2}$
Exp.2	$W_{exp2} = m_{LT5}(h_{LT5} - h_{LT6})$	$E_{LT5} = E_{LT6} + W_{exp2} + E_{D,exp2}$
Cond.	$m_{LT6}(h_{LT6} - h_{LT1}) =$ $m_{CW,out}(h_{CW,out} - h_{CW,in})$	$E_{LT6} + E_{CW,in} =$ $E_{LT1} + E_{CW,out} + E_{D,cond}$
Pump2	$W_{pump2} = m_{LT1}(h_{LT2} - h_{LT1})$	$E_{LT1} + W_{pump2} = E_{LT2} + E_{D,pump2}$
Interc.	$m_{air,in}(h_{air,in} - h_{air,out}) =$ $m_{LT3}(h_{LT3} - h_{LT3})$	$E_{LT2} + E_{air,in} =$ $E_{LT3} + E_{air,out} + E_{D,inter}$

Four parts of the exergy destruction rate are not influenced by each other. Hence, various equations for exogenous-endogenous and unavoidable-avoidable exergy destruction parts is provided as follows [33]:

$$E_{D,k}^{EX} = E_{D,k}^{EX,UN} + E_{D,k}^{EX,AV} \quad (13)$$

$$E_{D,k}^{EN} = E_{D,k}^{EN,UN} + E_{D,k}^{EN,AV} \quad (14)$$

$$E_{D,k}^{UN} = E_{D,k}^{EX,UN} + E_{D,k}^{EN,UN} \quad (15)$$

$$E_{D,k}^{AV} = E_{D,k}^{EN,AV} + E_{D,k}^{EX,AV} \quad (16)$$

in presented equations, $E_{D,k}^{EX,UN}$ is defined as the exogenous unavoidable part of exergy destruction rate, $E_{D,k}^{EX,AV}$ indicates the exogenous avoidable part, $E_{D,k}^{EN,UN}$ specifies the endogenous unavoidable exergy destruction rate, and $E_{D,k}^{EN,AV}$ denotes the endogenous avoidable part. The $E_{D,k}^{UN}$ is divided into exogenous and endogenous exergy destruction parts as represented by $E_{D,k}^{EX,UN}$ and $E_{D,k}^{EN,UN}$, respectively. Likewise, the $E_{D,k}^{AV}$ has an exact definition and is divided into $E_{D,k}^{EX,AV}$ and $E_{D,k}^{EN,AV}$ parts.

Equation (17) is an essential relationship that represents the combination of avoidable-unavoidable and endogenous-exogenous exergy destruction parts for the certain component of k :

$$E_{D,k} = E_{D,k}^{EN,AV} + E_{D,k}^{EN,UN} + E_{D,k}^{EX,AV} + E_{D,k}^{EX,UN} \quad (17)$$

Usually, through the engineering improvement of the k th component, the $E_{D,k}^{EN,AV}$ can be reduced. However, due to the technological restrictions of the component, the $E_{D,k}^{EN,UN}$ is irreducible. To reduce the $E_{D,k}^{EX,AV}$ of the k th component, increasing the k th component's efficiency as well as improving the efficiency of the related components is effective. Furthermore, due to the technical limitations related to the components of the system, the $E_{D,k}^{EX,UN}$ of the k th component cannot be modified.

In recent years, multiple approaches have been recommended for determining parts of the exergy destruction rate using the AES: 1. The structural theory approach, 2. Engineering approach, 3. Exergy balance approach, 4. Thermodynamic cycle approach, etc. [28, 34]. In this research, the thermodynamic cycle approach is implemented to estimate the components' exergy destruction in avoidable-unavoidable and exogenous-endogenous divisions. For relatively complex thermodynamic cycles, the high prediction accuracy is an

essential requirement. So, the thermodynamic cycle approach is considered the most suitable approach for these cycles [14].

Based on the thermodynamic cycle approach, to determine the exergy destruction parts it is required to identify the differences between the hybrid, real, and unavoidable cycles. The unavoidable cycle is defined in this way: the whole thermodynamic processes of the cycle are performed as ideal processes, while the technological limitations of the components are considered. The real cycle is: considering the whole thermodynamic processes of the system as irreversible processes under real conditions. The hybrid cycle is defined as: the thermodynamic process related to the k th component is examined as irreversible, while the other system components are operating as ideal process [35].

The unavoidable exergy destruction is calculated when the whole cycle operates under unavoidable conditions [36]:

$$E_{D,k}^{UN} = E_{P,k}^{real} \times \left(\frac{E_{D,k}}{E_{P,k}} \right)^{UN} \quad (18)$$

Via considering the hybrid cycle for the k th component, the endogenous part of the exergy destruction rate is computed:

$$E_{D,k}^{EN} = E_{P,k}^{real} \times \left(\frac{E_{D,k}}{E_{P,k}} \right)^{EN} \quad (19)$$

The endogenous unavoidable part of the exergy destruction rate can be determined as the given component runs under unavoidable conditions, while the other cycle components operate under reversible conditions:

$$E_{D,k}^{EN,UN} = E_{P,k}^{EN} \times \left(\frac{E_{D,k}}{E_{P,k}} \right)^{UN} \quad (20)$$

3. RESULTS AND DISCUSSIONS

The comprehensive examination of advanced exergy method for the DORC-HDD system is accomplished by solving the numerical model of the system under various conditions of hybrid, unavoidable, and real. The numerical model is developed in MATLAB [37] environment, and REFPROP [38] is utilized as the thermodynamic reference to specify the characteristics of the operating fluids. In Tables 4 and 5, the simulation presumptions as well as main designing variables for the ideal, unavoidable, and real conditions are outlined.

3. 1. Normal Exergy Scrutiny Results The DORC system is simulated numerically using the conservation equations of the energy, exergy, and mass balance for

TABLE 4. Main parameters applied in the simulation

Parameter	Unit	Value
Inlet pressure of pump1	kPa	690
Inlet pressure of expander1	kPa	3300
Inlet pressure of expander 2	kPa	2250
Inlet temperature of expander1	°C	148
Inlet temperature of pump2	°C	T_0+10
ΔT_{pp} for evaporator1	°C	28
ΔT_{pp} for other heat exchangers used in the cycle	°C	5-15
Isentropic pumps efficiency	-	85%
Isentropic expanders efficiency	-	80%

TABLE 5. Assumptions for components under ideal, real, and unavoidable conditions

Component	Parameter	Ideal	Real	Unavoidable
Evaporator 1	ΔT_{pp}	0	28	15
	ΔP	0	3%	1%
Preheater	ΔT_{pp}	0	5	3
	ΔP	0	3%	1%
Evaporator 2	ΔT_{pp}	0	5	3
	ΔP	0	3%	1%
Intercooler	ΔT_{pp}	0	18	10
	ΔP	0	3%	1%
Condenser	ΔT_{pp}	0	8	4
	ΔP	0	3%	1%
Expander 1	η_{Exp1}	1	0.85	0.95
Pump 1	η_{P1}	1	0.85	0.95
Expander 2	η_{Exp2}	1	0.85	0.95
Pump 2	η_{P2}	1	0.85	0.95

various components of the system working as an individual control volume under a steady-state conditions. The main thermodynamic characteristics of the system are computed in terms of ideal, real, and unavoidable conditions. The results are represented in Tables 6-8. Also, in Tables 9-11, the main results of exergy scrutiny for the components of the system in terms

of the ideal, real, and unavoidable conditions are specified.

Figures 3 and 4 demonstrate the exergy efficiency and exergy destruction rate of various components of the DORC system under real conditions, respectively. Also, Figure 5 indicates the relative exergy destruction of components in terms of the real conditions. As demonstrated in Figure 3, evaporator 2 plus turbomachines (pumps and expanders) have a relatively high exergy efficiency (>85%). In heat exchangers, higher temperature differences between the flowing streams within the components require higher energy consumption to perform the heat transfer process. This leads to increased exergy destruction as well as decreased exergy efficiency and vice versa. Hence, in evaporator 2, there is no phase change process which means the component requires little heat transfer. So, evaporator 2 has the maximum exergy efficiency between the heat exchangers and the whole system. In pumps and expanders, the greater the isentropic efficiency of the component, the greater value of exergy efficiency (Figure 3) as well as, the lower value of the exergy destruction (Figure 4) and vice versa.

Considering Figure 4, it is indicated that to perform the phase transition process in evaporator 1, the high-temperature difference between the exhaust gas and R245fa streams lead to the highest rate of the system exergy destruction (>95 kW). Considering Figure 5, it is demonstrated that 68.03% of the total exergy destruction rate of the system, is shared by evaporator 1 (36.69%) and condenser (28.34%). Also, pump 1 (0.38%) and pump 2 (0.76%) have the minimum relative exergy destructions of the system followed by evaporator 2 and expander 1.

TABLE 6. Thermodynamic properties and mass flow rates at different state points of the DORC system under real conditions at various state points

State	m (kg/s)	T (K)	P (kPa)	H (kJ/kg)	S (kJ/kg.K)	E (kW)
HT1	2.81	346.6	669.3	299.74	1.321	27.80
HT2	2.81	348.4	3300	302.32	1.322	34.15
HT3	2.81	419.9	3201	486.18	1.785	169.15
HT4	2.81	353.8	690	465.15	1.796	101.22
LT1	8.29	307.5	873	248.17	1.164	328.25
LT2	8.29	308.8	2550	249.85	1.165	340.20
LT3	8.29	316.6	2473.5	261.43	1.202	345.70
LT4	8.29	341.6	2399.2	317.60	1.372	398.25
LT5	8.29	358.1	2327.3	445.58	1.738	568.98
LT6	8.29	319.0	900	428.57	1.748	405.06

TABLE 7. Thermodynamic properties and mass flow rates of the DORC system under ideal conditions at various state points

State	<i>m</i> (kg/s)	T (K)	P (kPa)	H (kJ/kg)	S (kJ/kg.K)	<i>E</i> (kW)
HT1	2.85	347.86	690	301.45	1.325	29.02
HT2	2.85	349.36	3300	303.64	1.325	35.27
HT3	2.85	421.58	3300	484.76	1.781	171.19
HT4	2.85	349.35	690	459.95	1.781	100.28
LT1	7.81	308.67	900	249.78	1.169	310.15
LT2	7.81	309.73	2550	251.19	1.169	321.18
LT3	7.81	316.69	2550	261.42	1.202	326.30
LT4	7.81	342.86	2550	319.39	1.377	378.08
LT5	7.81	358.16	2550	440.22	1.718	540.15
LT6	7.81	310.39	900	419.32	1.720	376.82

TABLE 8. Thermodynamic properties and mass flow rates of the DORC system under unavoidable conditions at various state points

State	<i>m</i> (kg/s)	T (K)	P (kPa)	h (kJ/kg)	S (kJ/kg.K)	<i>E</i> (kW)
HT1	2.84	347.4	683.10	300.88	1.324	28.60
HT2	2.84	349.0	3300	303.19	1.324	34.88
HT3	2.84	421.0	3267	485.29	1.783	170.50
HT4	2.84	350.8	690	461.73	1.786	100.57
LT1	7.96	308.3	891	249.25	1.167	316.04
LT2	7.96	309.4	2550	250.74	1.168	327.36
LT3	7.96	316.6	2524.5	261.42	1.202	332.61
LT4	7.96	342.4	2499.3	318.80	1.375	384.66
LT5	7.96	358.1	2474.3	442.15	1.725	549.87
LT6	7.96	313.3	900	422.53	1.729	385.84

3. 2. Advanced Exergy Scrutiny Results As presented in Table 5, performing the AES needs more hypothesis for conditions of ideal, unavoidable, and real. The main result achieved by AES for the DORC is

TABLE 9. Results of exergy scrutiny for DORC system under real

Component	<i>E_F</i> (kW)	<i>E_P</i> (kW)	<i>E_D</i> (kW)	ε (%)	<i>y</i> [*] (%)	<i>y</i> (%)
Evaporator1	228.2	131.6	96.6	57.6	39.69	11.54
Expander1	67.9	58.9	9.0	86.7	3.70	1.08
Preheater	73.4	52.4	21.0	71.3	8.64	2.51
Pump 1	7.2	6.33	0.9	87.0	0.39	0.11
Evaporator2	187.5	178.8	8.6	95.3	3.56	1.03
Expander 2	163.9	140.5	23.3	85.7	9.60	2.79
Condenser	76.8	7.8	69.0	10.1	28.35	8.24
Pump 2	13.9	12.0	1.8	86.5	0.77	0.22
Intercooler	18.2	5.3	12.9	29.2	5.31	1.54
HT loop	376.8	249.2	127.5	22.7	-	-
LT loop	460.4	344.6	115.8	45.4	-	-
DORC syst.	837.3	593.9	243.4	41.2	100.0	29.07

TABLE 10. Results of exergy scrutiny for DORC system under ideal conditions

Component	<i>E_F</i> (kW)	<i>E_P</i> (kW)	<i>E_D</i> (kW)	ε (%)	<i>y</i> [*] (%)	<i>y</i> (%)
Evaporator1	229.9	137.9	91.9	60.0	57.90	11.37
Expander1	71.9	71.9	0.0	100	0.00	0.00
Preheater	72.3	52.5	19.7	72.6	12.45	2.44
Pump 1	6.3	6.3	0.0	100	0.00	0.00
Evaporator2	169.4	164.5	4.8	97.1	3.08	0.60
Expander2	165.7	165.7	0.0	100	0.00	0.00
Condenser	67.6	34.7	32.9	51.3	20.72	4.07
Pump2	11.1	11.1	0.0	100	0.00	0.00
Intercooler	14.4	5.2	9.29	35.8	5.85	1.15
HT loop	380.5	268.8	111.7	28.55	-	-
LT loop	428.5	381.4	47.0	60.34	-	-
DORC syst.	809.1	650.2	158.8	53.2	100	19.63

provided in Table A1 in Appendix. According to Table A1, it is inferred the endogenous part of the exergy destruction is larger than the exogenous part for each system component. Accordingly, the main portion of the components' exergy destruction rate originates through the internal irreversibility of each component itself.

Hence, it can be evolved that the interconnection between components is insignificant. It means the most essential consideration for system optimization should be given to improvement of system components. The greatest exogenous part of the exergy destruction rate is discovered in the condenser, intercooler, and evaporator 1. This indicate that modifications in other components' efficiency make a reduction in the value of exergy destruction for mentioned components, and consequently increment of the whole system productivity. The endogenous part of the exergy destruction for several components is greater than its exergy destruction. In the thermodynamic cycle, the interconnections among various components lead to the production of extra irreversibility. As an increase in entropy production of the system outweighs the reduction in the MFR. Thus, decreasing the rate of exergy destruction for these components can yield the increment in amount of this parameter in related components of the system. This demonstrates that the interconnection between the system components is not relatively simple.

Furthermore, by looking at the avoidable column of Table A1, it is inferred that 59.04 kW of the 258.69 kW total system exergy destruction could be eliminated. Thus, 22.82% of the DORC system exergy destruction rate can be decreased. Between the system components, the avoidable part of the exergy destruction rate for expander 2 is the most significant (16.43 kW), followed by expander 1, pump 2, and pump 1 (6.41 kW, 1.27 kW, 0.66 kW). Expander and pumps are holding 41.95% of the entire system avoidable part of the exergy destruction rate. This implies that these components possess an

TABLE 11. Results of exergy scrutiny for DORC system under unavoidable conditions

Component	E_f (kW)	E_p (kW)	E_d (kW)	ε (%)	y^* (%)	y (%)
Evaporator1	228.2	135.6	92.60	59.4	47.16	11.41
Expander 1	69.9	66.9	2.9	95.7	1.50	0.36
Preheater	71.9	52.0	19.9	72.3	10.14	2.45
Pump 1	6.5	6.2	0.2	95.8	0.14	0.03
Evaporator2	173.7	165.2	8.5	95.0	4.34	1.05
Expander 2	164.0	156.3	7.7	95.3	3.93	0.95
Condenser	69.8	16.2	53.5	23.2	27.29	6.60
Pump 2	11.8	11.3	0.5	95.2	0.29	0.07
Intercooler	15.4	5.2	10.2	33.9	5.21	1.26
HT loop	376.6	260.9	115.7	26.4	-	-
LT loop	434.9	354.3	80.6	55.3	-	-
DORC syst.	811.6	615.2	196.3	49.0	100.00	24.19

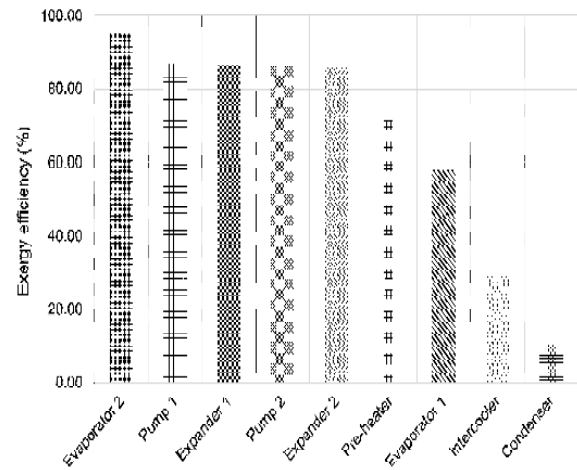


Figure 3. Exergy efficiency of each component in DORC-WHR system

excellent capacity for boosting by applying engineering modifications and modern technologies. Accordingly, decreasing the exergy destruction rate of pumps and expanders is possible, and this is directly relevant to enhancing the whole cycle performance. The LT loop avoidable part of the exergy destruction is calculated to be 46.62 kW (78.96%), which indicates that it requires more attention than that of the HT loop by near 12.42 kW (21.03%).

The avoidable-exogenous part as well as the avoidable-endogenous part of the exergy destruction rate can be decreased via enhancing the efficiency of components. Therefore, to boost the cycle productivity, improving performance of those components with larger avoidable endogenous part must be the prime concern. By a proper modification to the k th system component, the endogenous avoidable exergy destruction part which related to this component can be lessened. Moreover, the exogenous avoidable exergy destruction rate of the k th component can also be decreased by modifying the whole structure of the system, as well as improving the efficiency of each component including the k th component. According to Table A1, it represents that the avoidable endogenous parts of exergy destruction rate for all expanders and pumps are greater than the unavoidable endogenous part associated with these components. It means, through appropriate technological modifications, the performance of mentioned components as well as productivity of the entire cycle can be raised.

The exogenous avoidable part for almost any component of the system is calculated with a negative value. This shows decreasing the value of exergy destruction rate for most components can raise the exergy destruction rate of remaining components. However, the real value regarding the exogenous avoidable part of the condenser, evaporator 1, and intercooler is relatively

higher. This is denoting that the exergy destruction rate of the mentioned components had a more prominent effect on relevant components of the system. Applying improvements in productivity of the condenser, evaporator 1, and intercooler can directly add the rate of the exergy destruction for the entire cycle. Considering Table A1 once more, shows results regarding the entire cycle endogenous avoidable part as well as endogenous unavoidable part. As it is seen, the system overall endogenous unavoidable part is larger than the endogenous avoidable part, which denotes that the potential of the DORC system for improvement is not significant. In Figures 6-8, the relative exergy destruction rate of DORC system regarding endogenous avoidable, avoidable, and unavoidable parts is provided.

3. 3. Comparison Between Results of the AES and NES

Considering Figures 5 and 7, a comparison between results obtained by normal and advanced exergy scrutiny approaches is provided in Table 13. By observing at this table, it can be concluded that there is an important disparity amid the outcomes of these two

methods. For instance, based on the NES, evaporator 1 has the highest priority for improvement due to the irreversibility of high-temperature differences between the exhaust gas and R245fa streams. On the other hand, according to the AES, evaporator 1 ranked in sixth position. This indicates that there is a great proportion of exergy destruction rate which is not avoidable.

Possessing the greatest avoidable exergy destruction part associated with component *kth* demonstrates that this component has an excellent capability to increase the productivity of the whole cycle. Hence, referring to results of the AES in Table 13 reveals that the condenser has the highest priority for optimization, which it can make a significant advantage for the DORC system. Likewise, expander 1 is ranked in the sixth position in terms of NES, while it held in third place according to the AES results. The results also display that the AES does not recommend any improvement for the preheater, while according to the NES, a relatively significant amount of total exergy destruction rate is assigned to the preheater. The priority of each component for improvement based on the two approaches is plainly provided. This helps the designer to optimize the system with a clearer view.

Although the priority for improvement of system components based on two approaches is contrasting, but the optimizing techniques are identical. For instance, the primary exergy destruction rate produced by a pump/expander is because of the isentropic efficiency defined for the compression/expansion process. Therefore, to enhance the isentropic efficiency, it is recommended that effective design parameters of the pump/expander to be optimized. As stated before, a large part of the exergy destruction rate in heat exchangers is produced by relatively high temperature difference of heat transfer process. So, reduction of the temperature differences is essential to increase the efficiency of the heat exchanger as well as the power production of the system. Thus, various optimization algorithms such as GA, PSO, RSM, etc. were employed for optimization of the effective parameters at the inlet and outlet of the heat exchangers.

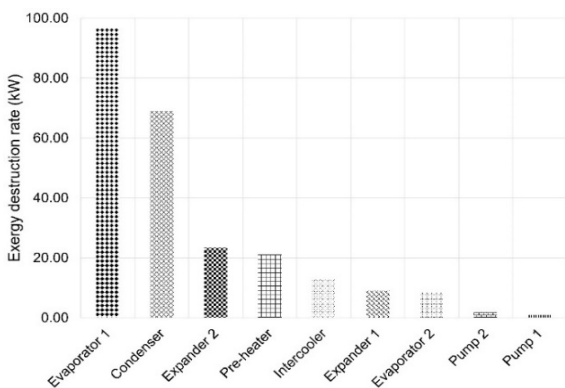


Figure 4. Exergy destruction rate of each component in DORC-WHR system

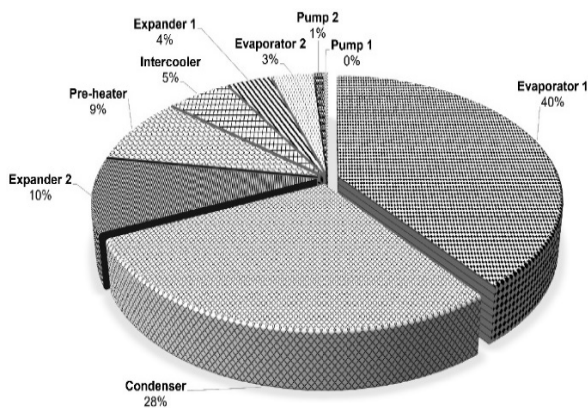


Figure 5. Relative exergy destruction of DORC system components under real condition

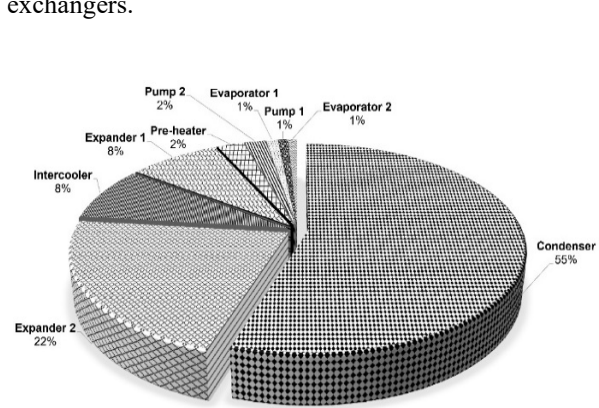


Figure 6. Relative endogenous avoidable exergy destruction rate of DORC system components

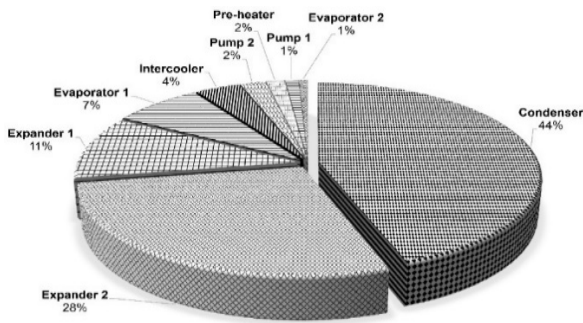


Figure 7. Relative avoidable exergy destruction rate of DORC system components

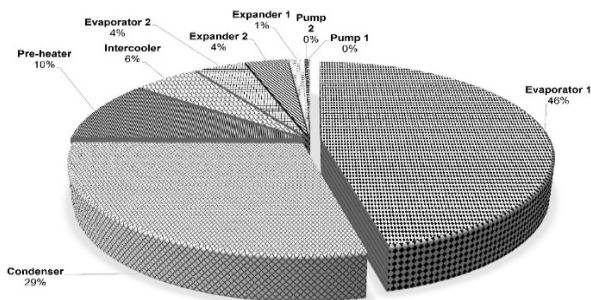


Figure 8. Relative unavoidable exergy destruction rate of DORC system components

TABLE 13. Improvement priority of the DORC system components in respect of two different approaches of exergy scrutiny

Priority	Advanced exergy scrutiny	Normal exergy scrutiny
1	Condenser	Evaporator 1
2	Expander 2	Condenser
3	Expander 1	Expander 2
4	Evaporator 1	Preheater
5	Intercooler	Intercooler
6	Pump 2	Expander 1
7	Preheater	Evaporator 2
8	Pump 1	Pump 2
9	Evaporator 2	Pump 1

4. CONCLUSIONS

In the present investigation, a WHR system containing a dual-loop ORC and an HDD engine was simulated and analyzed from viewpoints of two methods, normal and advanced exergy scrutiny. The exergy destruction rates of all system components based on these two approaches were achieved, and the significant differences between these methods were specified. The significant conclusions and the valuable outcomes of this study are presented below:

- According to the overall unavoidable and avoidable parts of the exergy destruction rate for the DORC system, the whole system exergy destruction rate can be decreased by around 23%. Pumps and expanders accounted for 41.95% of the total avoidable exergy destruction.
- For improving the entire system productivity, the advanced exergy scrutiny recommends the main consideration must assign to the condenser, expander 2, expander 1, and evaporator 1, respectively. However, the normal exergy scrutiny designates the arrangement of improvement priority as follows: evaporator 1, condenser, expander 2, and preheater, respectively.
- As a comparison between loops, the total avoidable exergy destruction part of the LT loop is 46.62 kW (78.96%), which indicates that it requires more attention than that of the HT loop by 12.42 kW (21.03%).
- The endogenous unavoidable exergy destruction rate in some components is calculated fewer than the endogenous avoidable parts of these components. This demonstrates that by proper technological modifications, the productivity of these components and eventually the whole cycle could be raised.
- The highest exogenous part of the exergy destruction rate is determined in the condenser, intercooler, and evaporator 1. This represents that modification in other components' efficiency can improve the performance of the mentioned components.

5. REFERENCES

1. Abdolalipouradi, M., Khalilarya, S. and Jafarmadar, S.J.I.J.o.E., "Energy and exergy analysis of a new power, heating, oxygen and hydrogen cogeneration cycle based on the sabalan geothermal wells", *International Journal of Engineering Transactions C: Aspects*, Vol. 32, No. 3, (2019), 445-450, doi: 10.5829/ije.2019.32.03c.13
2. Yağlı, H., Koç, Y., Kalay, H.J.S.E.T. and Assessments, "Optimisation and exergy analysis of an organic rankine cycle (ORC) used as a bottoming cycle in a cogeneration system producing steam and power", *Sustainable Energy Technologies and Assessments*, Vol. 44, (2021), 100985, doi: 0.1016/j.seta.2020.100985
3. Lu, P., Luo, X., Wang, J., Chen, J., Liang, Y., Yang, Z., Wang, C., Chen, Y.J.E.C. and Management, "Thermo-economic design, optimization, and evaluation of a novel zeotropic orc with mixture composition adjustment during operation", *Energy Conversion and Management*, Vol. 230, (2021), 113771, doi: 10.1016/j.enconman.2020.113771
4. Mohammadkhani, F. and Nami, H.J.I.J.o.E., "Thermodynamic analysis and optimization of a novel cogeneration system: Combination of a gas turbine with supercritical CO₂ and organic rankine cycles", *International Journal of Engineering Transactions C: Aspects*, Vol. 29, No. 12, (2016), 1765-1774, doi: 10.5829/idosi.ije.2016.29.12c.16
5. Wang, F., Wang, L., Zhang, H., Xia, L., Miao, H., Yuan, J.J.E.C. and Management, "Design and optimization of hydrogen

- production by solid oxide electrolyzer with marine engine waste heat recovery and orc cycle", *Energy Conversion and Management*, Vol. 229, (2021), 113775, doi: 10.1016/j.enconman.2020.113775
6. Di Cairano, L., Bou Nader, W. and Nemer, M., "A simulation and experimental study of an innovative mac/orc/erc system: Revercycle with an ejector for series hybrid vehicles", *Energy Conversion and Management*, Vol. 230, (2021), doi: 10.1016/j.energy.2021.120830
 7. Wang, Z., Hu, Y., Xia, X., Zuo, Q., Zhao, B. and Li, Z.J.E., "Thermo-economic selection criteria of working fluid used in dual-loop orc for engine waste heat recovery by multi-objective optimization", *Energy*, Vol. 197, (2020), 117053, doi: 10.1016/j.energy.2020.117053
 8. Di Battista, D., Fatigati, F., Carapellucci, R., Cipollone, R.J.E.C. and Management, "An improvement to waste heat recovery in internal combustion engines via combined technologies", *Energy Conversion and Management*, Vol. 232, (2021), 113880, doi: 10.1016/j.enconman.2021.113880
 9. Emadi, M.A., Chitgar, N., Oyewunmi, O.A. and Markides, C.N.J.A.E., "Working-fluid selection and thermoeconomic optimisation of a combined cycle cogeneration dual-loop organic rankine cycle (ORC) system for solid oxide fuel cell (SOFC) waste-heat recovery", *Applied Energy*, Vol. 261, (2020), 114384, doi: 10.1016/j.apenergy.2019.114384
 10. Ouyang, T., Zhao, Z., Wang, Z., Zhang, M. and Liu, B.J.E., "A high-efficiency scheme for waste heat harvesting of solid oxide fuel cell integrated homogeneous charge compression ignition engine", *Energy*, Vol. 229, (2021), 120720, doi: 10.1016/j.energy.2021.120720
 11. Zhang, Y., Liang, T., Yang, C., Zhang, X. and Yang, K., "Advanced exergy analysis of an integrated energy storage system based on transcritical CO₂ energy storage and organic rankine cycle", *Energy Conversion and Management*, Vol. 216, (2020), 112938, <https://doi.org/10.1016/j.enconman.2020.112938>, <https://www.sciencedirect.com/science/article/pii/S0196890420304763>
 12. Liao, G., E, J., Zhang, F., Chen, J. and Leng, E., "Advanced exergy analysis for organic rankine cycle-based layout to recover waste heat of flue gas", *Applied Energy*, Vol. 266, (2020), 114891, <https://doi.org/10.1016/j.apenergy.2020.114891>, <https://www.sciencedirect.com/science/article/pii/S0306261920304037>
 13. Wang, Y., Chen, Z., Shen, Y., Ma, Z., Li, H., Liu, X., Zhu, Z., Qi, J., Cui, P., Wang, L., Ma, Y. and Xu, D., "Advanced exergy and exergoeconomic analysis of an integrated system combining CO₂ capture-storage and waste heat utilization processes", *Energy*, Vol. 219, (2021), 119600, <https://doi.org/10.1016/j.energy.2020.119600>, <https://www.sciencedirect.com/science/article/pii/S0360544220327079>
 14. Mohammadi, Z., Fallah, M. and Mahmoudi, S.M.S., "Advanced exergy analysis of recompression supercritical CO₂ cycle", *Energy*, Vol. 178, (2019), 631-643, <https://doi.org/10.1016/j.energy.2019.04.134>, <https://www.sciencedirect.com/science/article/pii/S0360544219307674>
 15. Gamma Technologies. "GT-SUITE Engine Performance Tutorials." (2016).
 16. Boodaghi, H., Etghani, M.M., Sedighi, K.J.E.C. and Management, "Performance analysis of a dual-loop bottoming organic rankine cycle (ORC) for waste heat recovery of a heavy-duty diesel engine, part i: Thermodynamic analysis", *Energy Conversion and Management*, (2021), 113830, doi: 10.1016/j.enconman.2021.113830
 17. Abdolalipouradl, M., Mohammadkhani, F., Khalilarya, S. and Jafarmadar, S., "Thermodynamic analysis of new cogeneration cycle based on gaynarje hot spring", *International Journal of Engineering*, Vol. 33, No. 6, (2020), 1149-1155, <https://doi.org/10.5829/ije.2020.33.06c.13>, https://www.ije.ir/article_107819.html
 18. Wu, Z., Sha, L., Yang, X., Zhang, Y.J.E.C. and Management, "Performance evaluation and working fluid selection of combined heat pump and power generation system (HP-PGS) using multi-objective optimization", *Energy Conversion and Management*, Vol. 221, (2020), 113164, 10.1016/j.enconman.2020.113164
 19. Zhang, X., Zhang, C., He, M. and Wang, J.J.J.o.T.S., "Selection and evaluation of dry and isentropic organic working fluids used in organic rankine cycle based on the turning point on their saturated vapor curves", *Journal of Thermal Science*, Vol. 28, No. 4, (2019), 643-658, doi: 10.1007/s11630-019-1149-x
 20. Huster, W.R., Schweidtmann, A.M. and Mitsos, A., "Working fluid selection for organic rankine cycles via deterministic global optimization of design and operation", *Optimization and Engineering*, Vol. 21, No. 2, (2020), 517-536, <https://doi.org/10.1007/s11081-019-09454-1>.
 21. Pashapour, M., Jafarmadar, S. and Khalil Arya, S.J.I.J.o.E., "Exergy analysis of a novel combined system consisting of a gas turbine, an organic rankine cycle and an absorption chiller to produce power, heat and cold", *International Journal of Engineering Transactions C: Aspects*, Vol. 32, No. 9, (2019), 1320-1326, doi: 10.5829/ije.2019.32.09c.13
 22. Abdolalipouradl, M., Khalilarya, S. and Jafarmadar, S., "Energy and exergy analysis of a new power, heating, oxygen and hydrogen cogeneration cycle based on the sabalan geothermal wells", *International Journal of Engineering Transactions C: Aspects*, Vol. 32, No. 3, (2019), 445-450, https://www.ije.ir/article_85663.html
 23. Xiang, B., Zhang, M., Yang, H. and Lu, J., "Prediction of acid dew point in flue gas of boilers burning fossil fuels", *Energy & Fuels*, Vol. 30, No. 4, (2016), 3365-3373, <https://doi.org/10.1021/acs.energyfuels.6b00491>.
 24. Mansoury, M., Jafarmadar, S., Khalilarya, S.J.E.C. and Management, "Energetic and exergetic assessment of a two-stage organic rankine cycle with reactivity controlled compression ignition engine as a low temperature heat source", *Energy Conversion and Management*, Vol. 166, (2018), 215-232, doi: 10.1016/j.enconman.2018.04.019
 25. Khankari, G. and Karmakar, S., "Improvement of efficiency of coal-fired steam power plant by reducing heat rejection temperature at condenser using kalina cycle", *International Journal of Engineering Transactions A: Basics*, Vol. 31, No. 10, (2018), 1789-1795, https://www.ije.ir/article_82222_a3410a730addf0dd98fe1588becd2ee6.pdf
 26. Khalilarya, S., Mohammadkhani, F. and Seyyedvalilu, M.H., "A parametric study on exergy and exergoeconomic analysis of a diesel engine based combined heat and power system", *International Journal of Engineering Transactions A: Basics*, Vol. 28, No. 4, (2015), 608-617, https://www.ije.ir/article_72496_5f8c75773db456e5765ffedeb585e7032.pdf
 27. Mansoury, M., Jafarmadar, S. and Khalilarya, S.J.I.J.o.E., "Energy and exergy analyses of a combined cycle kalina and organic rankine cycles using waste heat", *International Journal of Exergy*, Vol. 27, No. 2, (2018), 251-286, 10.1504/IJEX.2018.094601
 28. Liu, Z., Liu, Z., Yang, X., Zhai, H. and Yang, X., "Advanced exergy and exergoeconomic analysis of a novel liquid carbon dioxide energy storage system", *Energy Conversion and Management*, Vol. 205, (2020), 112391, <https://doi.org/10.1016/j.enconman.2019.112391>, <https://www.sciencedirect.com/science/article/pii/S0196890419313986>
 29. Wang, Z., Xia, X., Pan, H., Zuo, Q., Zhou, N. and Xie, B.J.A.T.E., "Fluid selection and advanced exergy analysis of dual-loop orc using zeotropic mixture", *Applied Thermal Engineering*, Vol. 185, (2021), 116423, doi: 10.1016/j.applthermaleng.2020.116423

30. Wu, J. and Wang, N.J.E., "Exploring avoidable carbon emissions by reducing exergy destruction based on advanced exergy analysis: A case study", *Energy*, Vol. 206, (2020), 118246, doi: 10.1016/j.energy.2020.118246
31. Zhang, Y., Yao, E., Tian, Z., Gao, W. and Yang, K.J.A.T.E., "Exergy destruction analysis of a low-temperature compressed carbon dioxide energy storage system based on conventional and advanced exergy methods", *Applied Thermal Engineering*, Vol. 185, (2021), 116421, doi: 10.1016/j.applthermaleng.2020.116421
32. Gullo, P.J.E.C. and Management, "Impact and quantification of various individual thermodynamic improvements for transcritical r744 supermarket refrigeration systems based on advanced exergy analysis", *Energy Conversion and Management*, Vol. 229, (2021), 113684, doi: 10.1016/j.enconman.2020.113684
33. Caglayan, H., Caliskan, H.J.R. and Reviews, S.E., "Advanced exergy analyses and optimization of a cogeneration system for ceramic industry by considering endogenous, exogenous, avoidable and unavoidable exergies under different environmental conditions", *Renewable and Sustainable Energy Reviews*, Vol. 140, (2021), 110730, doi: 10.1016/j.rser.2021.110730
34. Zhang, S., Jing, J., Jiang, H., Qin, M., Chen, D. and Chen, C.J.J.o.C.P., "Advanced exergy analyses of modified ethane recovery processes with different refrigeration cycles", *Journal of Cleaner Production*, Vol. 253, (2020), 119982, doi: 10.1016/j.jclepro.2020.119982
35. Ustaoglu, A., "Parametric study of absorption refrigeration with vapor compression refrigeration cycle using wet, isentropic and azeotropic working fluids: Conventional and advanced exergy approach", *Energy*, Vol. 201, (2020), 117491, https://doi.org/10.1016/j.energy.2020.117491.
36. Chen, P., He, G., Gao, Y., Zhao, X., Cai, D.J.E.C. and Management, "Conventional and advanced exergy analysis of an air-cooled type of absorption-ejection refrigeration cycle with r290-mineral oil as the working pair", *Energy Conversion and Management*, Vol. 210, (2020), 112703, doi: 10.1016/j.enconman.2020.112703
37. Moler, C., Little, J., Bangert, S. and Kleiman, S.J.I., Sherborn, MA, "Pro-matlab, user's guide. The mathworks", (1987).
38. Lemmon, E., Huber, M. and McLinden, M.J.S.R.D.P., Gaithersburg, "Nist standard reference database 23: Reference fluid thermodynamic and transport properties-refprop, version 8.0. National institute of standards and technology, standard reference data program", (2007).

Appendix A

TABLE A1. Results of the advanced exergy scrutiny for the DORC system

Component	E_D (kW)	Splitting the exergy destruction				Combined two splitting approaches			
		$E_{D,k}^{EN}$ (kW)	$E_{D,k}^{EX}$ (kW)	$E_{D,k}^{AV}$ (kW)	$E_{D,k}^{UN}$ (kW)	$E_{D,k}^{EN,AV}$ (kW)	$E_{D,k}^{EN,UN}$ (kW)	$E_{D,k}^{EX,AV}$ (kW)	$E_{D,k}^{EX,UN}$ (kW)
Evaporator1	96.61	94.59	2.02	4.44	92.17	0.77	93.82	3.67	-1.65
Expander1	9.02	8.73	0.29	6.41	2.61	6.04	2.69	0.37	-0.09
Pre-heater	21.02	21.47	-0.45	0.91	20.11	1.78	19.69	-0.87	0.42
Pump1	0.94	0.91	0.03	0.66	0.28	0.63	0.29	0.03	-0.01
Evaporator2	8.66	9.04	-0.38	0.44	8.21	0.60	8.44	-0.15	-0.23
Expander2	23.37	23.38	-0.01	16.43	6.95	16.43	6.95	-0.01	0.00
Condenser	84.28	93.65	-9.37	26.27	58.01	41.45	52.20	-15.18	5.81
Pump2	1.87	1.98	-0.11	1.27	0.59	1.41	0.56	-0.14	0.03
Intercooler	12.91	15.41	-2.50	2.20	10.71	6.24	9.18	-4.04	1.54
HT loop	127.59	125.70	1.88	12.42	115.17	9.21	116.49	3.21	-1.33
LT loop	131.10	143.47	-12.3	46.62	84.48	66.14	77.33	-19.52	7.16
DORC	258.69	269.17	-10.4	59.04	199.65	75.35	193.82	-16.32	5.83

Persian Abstract

چکیده

در این مقاله، بررسی آگزرژی معمولی (NES) و بررسی آگزرژی پیشرفته (AES) یک سیستم بازیابی گرمای اتلافی (WHR) انجام شده است. سیستم پیشنهادی شامل یک چرخه دو حلقه‌ای رنگین آلی (DORC) است که گرمای اتلافی موجود در هوای ورودی، گازهای خروجی و جریان خنک کننده یک موتور دیزل سنگین ۱۲ سیلندر را بازیابی می‌کند. یک روش شناخته شده از AES به نام دیدگاه چرخه ترمودینامیکی برای تعیین هر یک از اجزای تخریب آگزرژی یعنی اجزای برون‌زا/درون‌زا و اجزای اجتناب-پذیر/اجتناب‌ناپذیر استفاده می‌شود. ۵۹/۰۴ کیلووات از ۲۵۸/۶۹ کیلووات مجموع تخریب آگزرژی کل سیستم را می‌توان از بین برد (۲۲/۸۲٪ از تخریب آگزرژی کل سیستم). کل تخریب آگزرژی اجتناب‌ناپذیر حلقه دما پایین برابر ۴۲/۶۲ کیلووات است، که نشان می‌دهد این حلقه نیاز به توجه بیشتری نسبت به حلقه دما بالا با مقدار ۱۲/۴۲ کیلووات دارد. علاوه بر این، مشخص شده است که برای افزایش بهره‌وری کلی سیستم، تفاوت نسبتا چشمگیری در ترتیب اولویت بهبود اجزای سیستم وجود دارد. بر همین اساس، AES این رتبه‌بندی را برای اولویت بهبود اجزاء ارائه داده است: کندانسور، منبسط‌کننده ۲ و منبسط‌کننده ۱. در حالی که NES اولویت بهبود را به ترتیب اواپراتور ۱، کندانسور و منبسط‌کننده ۲ تعیین کرده است.



Identification of Combined Power Quality Disturbances in the Presence of Distributed Generations using Variational Mode Decomposition and K-nearest Neighbors Classifier

M. Behzadi, M. Amirahmadi, M. Tolou Askari*, M. Babaeinik

Department of Electrical and Electronic Engineering, Semnan Branch, Islamic Azad University, Semnan, Iran

PAPER INFO

Paper history:

Received 27 October 2021

Received in revised form 19 December 2021

Accepted 23 December 2021

Keywords:

Power Quality

Distributed Generations

Identification

Variational Mode Decomposition

Wind Turbine

Photovoltaic

ABSTRACT

Identification of combined power quality disturbances in the modern power systems by considering the development of different types of loads and distribution generations has become increasingly important. The novelty of this paper comes from the accurate and fast identification of the combined power quality disturbances in the presence of different distributed generations and loads such as photovoltaic cell, wind turbine with doubly fed induction generators, diesel engines, electric arc furnace, DC machine, 6-pulse and 12-pulse rectifier loads. In this paper, the features are extracted using variational mode decomposition, just from voltage waveforms. To reduce the redundant data, dimension of features vector, and time, the Relief-F method and correlation feature selection method are applied on the extracted features and these two methods are compared together. In this paper, the K-nearest neighbors classifier is used to classify the multiple power quality disturbances. To verify the effectiveness of the proposed method, different scenarios such as misfiring, variation of sun radiation and wind speed, entrance and exit of loads, capacitors and distributed generators, different fault at the grid in half-load to full-load were simulated. This method can be used as an added algorithm for smart metering in modern and smart power systems.

doi: 10.5829/ije.2022.35.04a.05

NOMENCLATURE

$A_k(t)$	Envelope	\bar{l}_{ff}	Average feature-feature intercorrelation
α	Variance of noise	$M_j(c)$	Nearest misses in feature selection
C	Class	m	Repeat parameter in Relief-F
$class(\)$	Class function	$P(C)$	Prior probability of class in Relief-F method
D_i	Sample of features	$\varphi_k(t)$	Phase
$diff(\)$	Difference function	q	Number of components
F	Feature	R_s	Heuristic merit of a feature
$\hat{f}(\omega)$	Input signal	s	Counter of heuristic merit of feature
$G[F]$	Weight of feature	$value(\)$	Value function
H_j	Nearest hits in feature selection	ω_k	Central frequency of modes in VMD
i, j, k	Mode number or counter	$\hat{\lambda}$	Lagrangian coefficient
\bar{l}_{cf}	Mean feature-class correlation	$u_k(t)$	Various modes of variational mode decomposition (VMD)

*Corresponding Author Institutional Email: m.askari@semnaniau.ac.ir (M. Tolo Askari)

Please cite this article as: M. Behzadi, M. Amirahmadi, M. Tolou Askari, M. Babaeinik, Identification of Combined Power Quality Disturbances in the Presence of Distributed Generations using Variational Mode Decomposition and K-nearest Neighbors Classifier, *International Journal of Engineering, Transactions A: Basics* Vol. 35, No. 04, (2022) 657-674

1. INTRODUCTION

Nowadays, power quality has become a very important issue in modern power systems [1]. The reason for the importance of power quality is its effects on electrical equipment. Electrical equipment is designed to work with sinusoidal waveforms. The existence of different types of power quality disturbances (PQDs) such as voltage sag or swell, interruption, transient, harmonics, notch, spike, flicker, etc. leads to failure and reduction of life of electrical equipment [2]. Also, some PQDs lead to incorrect energy measurement and mal-operation of the protection relay. Power quality disturbances occur individually or in the combination of events. In traditional networks, the sources of production of power quality events have been usually known for power quality experts. Entrance and exit of large loads, power plants, or capacitor banks are the sources of production of power quality in these systems. Furthermore, the existence of 6-pulse and 12-pulse rectifiers and occurring short-circuit faults in these systems lead to product PQDs. In modern power systems by increasing the penetration level of distributed generations (DGs) the different combinations of PQDs also have increased [3, 4]. The modern power systems have been contained of different DGs such as photovoltaic (PV) generator [5], wind turbine generator [6], gas turbine generator, diesel generator, and energy storage unit. Prasad et al. [7] have introduced an approach to identify single as well as mixed PQDs in the power system connected to the grid in solar cells integrated DC micro-grid. The PQDs was analyzed by capturing the AC voltage signals from the PCC of the utility grid. Then, they proposed a developed combination morphological filter to increase the system robustness. A heuristic technique based on the deep learning method was proposed by Gonzalez-Abreu et al. [8]. This method has three stage from feature extraction of power networks and then carried out an adaptive pattern and finally using a neural network to detect disturbances. However, the DGs were neglected in this study. In addition, Shen et al. [9] have used a deep learning technique to monitor the power quality in electrical power systems by considering the DGs. Accordingly, signal processing based on VMD combined with deep learning to determine the times scales of multi-component signals and then to classify the disturbances, respectively. Furthermore, there are different loads such as electric arc furnaces (EAF), DC motors, and 6-pulse and 12-pulse rectifiers in these systems. Solar and wind energy have prominent characters of fluctuation, randomness, and intermittent. Entrance and exit of different DGs and fluctuation of their output power lead to different combined PQDs [6, 10]. Furthermore, inverter-based DGs such as PV generators generate different harmonic pollution. In a real modern power system, PQDs usually consists of a combination of the

power disturbances and most power disturbances are non-stationary [2]. Therefore, recognizing the different combinations of PQDs is a necessity in the modern power system.

Most PQDs identification studies are divided into three stages: signal analysis, feature extraction, and pattern recognition [11]. For signal analysis, several methods have been proposed including Fourier transform (FT) [12], discrete Fourier transform (DFT) , short-time Fourier transform (STFT) [13], wavelet transform (WT) [14], discrete wavelet transform (DWT) [15], wavelet packet transform (WPT) [16], Hilbert transform, S-transform (ST) [17], multiple time-window spectrum estimation (MTW) [18]. These methods often have some inherent disadvantages. Fourier transform only extract frequency information from the waveforms. Some of these methods only extract time information from the waveforms. Time-frequency information about PQDs can be extracted through DFT and STFT, but in the transforms, the transient feature cannot be clearly expressed in a fixed window size. A combined method based on the Hilbert–Huang Transform (HHT) and long short-term memory (LSTM) was proposed by Rodriguez et al. [19]. Also, recurrent artificial neural network was implemented to detect PQDs. Although this approach has effective outcomes, the combined PQDs in the presence of DGs was neglected. Therefore, studies have shifted to WT and ST [20, 21]. But, the WT [22] alone cannot generate high quality features. In other words, its overall performance depends on the feature extraction and classification types. The accuracy of ST is low in detecting non-stationary transient disturbances. Furthermore, most of the mentioned methods have a high computational burden.

Another method of spectral decomposition that, unlike WT, does not require pre-selective functions is empirical mode decomposition (EMD). This algorithm was first introduced by Huang to decompose non-stationary signals which is based on the extremities of a signal and the extraction of its intrinsic mode functions (IMFs). Since this algorithm is based on the use of extremity points, it is not a reliable solution because these points are strongly influenced by noise and sampling. The correct performance of the EMD algorithm and its improved methods requires the use of a noiseless signal that is rarely in practical conditions. On the other hand, another disadvantage of EMD is the lack of strong mathematical principles that make it difficult to predict the behavior of the algorithm on different signals. Recently, a method for decomposition of non-stationary signals has been proposed which, unlike EMD, has a higher resistance to noise and sampling. This method, called variational mode decomposition (VMD), has been able to overcome the decomposition defects of non-stationary signals that were available in EMD.

In many studies, the massive use of VMD can be observed. But, it is rarely used in PQDs identification. Some of its applications have been implemented in literature [23, 24]. A wind speed interval forecasting model based on VMD and multi-objective problem was proposed by Wang and Cheng [23]. This model included forecasting and noise reduction beside combination module to provide precise wind speed forecast for power model operation. Based on the VMD, a two stage method for eliminating the noise of Magnetic resonance imaging (MRI) was proposed by Pankaj et al. [24]. The VMD was introduced by Pankaj et al. [24] as an efficient technique to sequester the image into its components or modes based on frequency. An approach was proposed by Jalilian and Samadinasab [25] for measuring and finding short term PQ events in power systems by using micro-phasor measurement units. This measurement devise was used to monitor the PQ phenomena. Furthermore, variational mode extraction method was used by Jalilian and Samadinasab [25] to identify and analyze the non-stationary signals.

Previous studies have typically used expert knowledge or engineering experience in the feature extraction stage [6]. These feature extraction methods use only the static features of the main waveform. On the other hand, in these methods, the feature selection is highly desirable. A feature extraction technique based on fractional Fourier transform (FRFT) and extreme learning machine (ELM) was proposed by Samanta et al. [26]. Although this technique was useful, it can be still improved by using the developed version of these methods in order to provide accurate model. Motlagh, and Foroud [27] have given a method to recognize PQDs based on adaptive chirp mode pursuit in order to extract the features. Also, the grasshopper algorithm was applied to optimize the parameters of support vector machine (SVM) as the classifier.

This paper presents a novel PQDs identification method in the presence of different DGs and loads in a modern power system. To cope with the above mentioned problems, a high accuracy and high speed classification approach based on the VMD and k-nearest neighbors network (KNN) has been presented in this paper. In this paper, the VMD method is used to decompose the voltage signals. This method is a robust method to noise and sampling due to its strong relationship with Wiener filter. The results of different experiments on combined PQDs show that this method has better performance in extraction of PQD features than similar methods. Contrary to previous researches, different combination of PQDs and different scenarios of DGs and loads are considered in this paper. Often, in previous researches, mathematical equations have been used to create PQDs, but in this paper, real PQDs are created simultaneously in PSCAD software environment.

The presence of different DGs such as PV, wind turbine with doubly fed induction generator (DFIG), diesel engine (DE) was investigated in this paper. Furthermore, different loads such as EAF, DC motors, and 6-pulse and 12-pulse rectifiers from half-load to full-load are investigated in this paper. In this paper, only the voltage signals are used to identify the combined PQDs. This issue will decrease the measurement equipment and increase the speed of the method. The novelties of this article can be briefed as follows:

1. This paper presents a new method for identifying combined PQDs based on VMD, Relief-F, and KNN in a modern power system.
2. This paper uses VMD as a noise-resistant decomposition method and its performance is compared with EMD.
3. Different combinations of PQDs in the presence of different loads and DGs such as EAF, DC motors, and 6-pulse and 12-pulse rectifiers, PV, wind turbine with DFIG, and DE from half-load to full-load have been considered in this paper.
4. In this paper, the variation of sun radiation and wind speed are considered in generating PQDs in modern power systems.

To evaluate the proposed method, different comparative results have been presented in this paper. Results of VMD have been compared with EMD method. The proposed method is evaluated by comparing the different distance functions of the neural networks and other feature selectors such as correlation based feature selection (CFS). The comparative results confirm that the proposed method has a high accuracy in identifying the combined PQDs.

2. PROBLEM DEFINITION

To clarify the problem, we define the problem in both traditional power systems and modern power systems.

2.1. Power Quality Disturbances in the Traditional Power Systems

In traditional power systems, the issue of power quality disturbances is related to the classic linear load, classic nonlinear loads, different faults occurrence, entrance and exit of large loads, power plants, or capacitor banks [28]. Impulse transient PQDs are usually produced by switching loads, capacitor banks, or reactors in the traditional power systems. Voltage sag events are often produced by starting heavy engine loads or other heavy loads in the traditional power systems. Voltage swell event is often produced by single-phase faults. Under or over voltage events are often caused by load changes. Non-uniform distribution of single-phase loads or different transmission line specifications caused unbalanced voltage event in the traditional power

systems. Harmonics are generated by nonlinear load such as EAF, DC motors, 6-pulse, and 12-pulse rectifiers, etc. in the traditional power systems. Flicker events are often produced by starting heavy engine loads in the traditional power systems [29]. By increasing the penetration level of DGs, identification of PQDs has become more complex and traditional power systems have changed to the modern power systems.

2. 2. Power Quality Disturbances in the Modern Power Systems

In a modern power system, different DGs with different operations are added to the traditional power system. Adding different DGs leads to generate different combined PQDs in the modern power systems [28]. Identification of different combined PQDs is a big challenge in the modern power systems. In these systems, entrance and exit of different DGs lead to generate voltage swell and sag events, respectively [6, 10]. On the other hand, environmental changes such as variation in solar insolation and change in wind greatly change voltage profile in these systems [30, 31]. Furthermore, increasing penetration level of DGs with inverter such as wind turbine and PV lead to increase harmonics in the modern power system [32]. In the modern power systems, some events in diesel-engine driven generators such as misfiring in cylinders, and gearbox tooth crashing lead to generate flicker [33]. Also, some events in wind turbines such as tower shadow, wind shear, turbine blade break down, and blade pitching errors lead to generate flicker in the modern power systems [34]. To identify different combined PQDs in the modern power systems, a new method is presented in this paper.

3. PROPOSED ALGORITHM

The proposed method generally has the following four main steps (Figure 1):

1. Data generation using different loads and DGs simulations in PSCAD/EMTDC simulation program (version 4.5) in different scenarios.
2. Feature extraction using VMD.
3. Feature selection using Relief-F.
4. Classification of PQDs using KNN.

3. 1. Data Generation Using PSCAD

Data generation is an important challenge in the issue of identification of PQDs. These data must be close to the real data in the power system. Therefore, in this step, PQDs are really generated in different scenarios in PSCAD software environment such as connecting different linear, non-linear loads, capacitive banks, and DGs. Different loads are simulated in PSCAD, including EAF, DC motors, and 6-pulse and 12-pulse rectifiers. Different DGs are simulated, including PV, wind turbine

with DFIG, and DE. Loads are altered from half-load to full-loads. Also, the rate of active and reactive power of DGs is altered from half-load to full-load.

3. 2. Feature Extraction using VMD

Another challenge in the issue of identification of PQDs is a complete feature extraction. This feature extraction must be extract time and frequency information together. VMD is a time-frequency decomposition approach for robust analyzing adaptive, stationary and non-stationary signals [35]. Variational mode decomposition uses a new definition of IMFs and, unlike EMD, which considers IMFs as signal oscillating components, introduces them as amplitude-frequency modulation (AM-FM) signals in Equation (1) [36]:

$$u_k(t) = A_k(t) \cos(\varphi_k(t)) \quad (1)$$

where k is the mode number, $\varphi_k(t)$ is the phase, $A_k(t)$ is the envelope and non-negative ($A_k(t) \geq 0$). It is notable that, envelope $A_k(t)$ and instantaneous

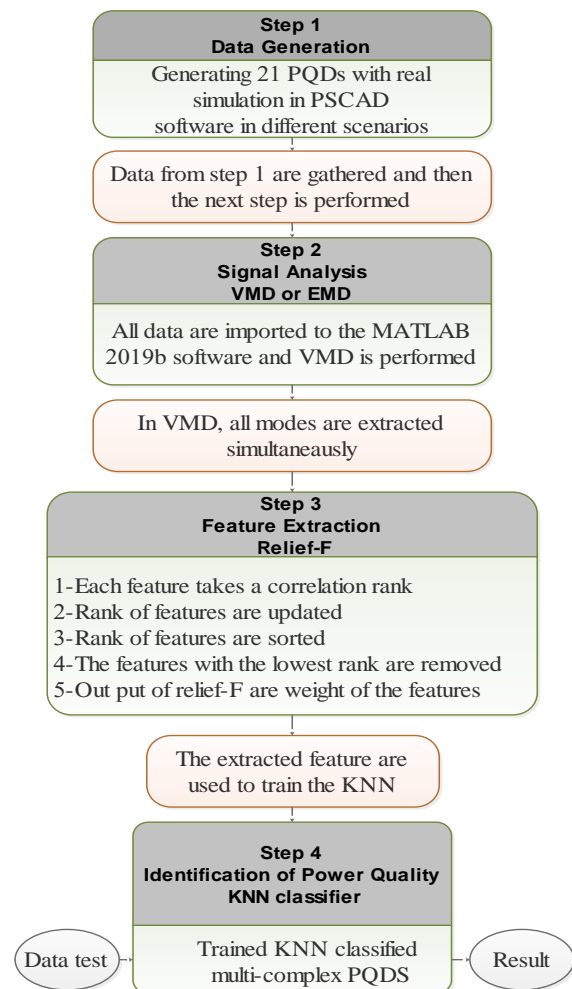


Figure 1. Flowchart of the methodology

frequency (equal to the phase derivative i.e. $\omega_k(t) = \varphi'_k(t)$) much slower than phase $\varphi_k(t)$ changes. Therefore, $u_k(t)$ mode can be introduced as a pure harmonic of signal with amplitude $A_k(t)$ and instantaneous frequency $\varphi'_k(t)$ in a suitable time frame. This new definition of the IMF leads to the creation of a narrow band signal, which is the main assumption of this method in the separation of modes.

In this method, each IMF is a finite band signal around a central frequency, which the value of the central frequency is estimated at any given moment as real-time. In fact, due to the strong relationship between VMD and Wiener filter, this method is more resistant to noise. In VMD, all modes are extracted simultaneously, while this is done in EMD through recursive operations. Variational mode decomposition includes Weiner filter for noise, Hilbert transform to reconstruct signal side-band, and shift the signal frequency by multiplying a mixed exponential function [35]. All modes in the frequency domain are directly updated. By using the Hermitian symmetry, the frequency spectrum of different mode signals is easily obtained. The real component of the reverse Fourier transformation of this filtered signal transmits the mode to the time domain. In this method, k mode in the frequency domain in the n replication can be computed by the Equation (2) [35]:

$$u_k^{n+1}(\omega) = \frac{\hat{f}(\omega) - \left(\sum_{i < k} \hat{u}_i(\omega) + \sum_{i > k} \hat{u}_i(\omega) - \frac{\hat{\lambda}(\omega)}{2} \right)}{1 + 2\alpha(\omega - \omega_k)^2} \quad (2)$$

where $\hat{f}(\omega)$ is the input signal in the frequency domain, α is the variance of noise and $\hat{\lambda}$ is the Lagrange coefficient for minimization. This equation is exactly like filtering current residual by Wiener filter. The central frequency of each mode is updated as Equation (3) [35]:

$$\omega_k^{n+1} = \frac{\int_0^\infty \omega |\hat{u}_k(\omega)|^2 d\omega}{\int_0^\infty |\hat{u}_k(\omega)|^2 d\omega} \quad (3)$$

The center of gravity of the power spectrum modes is this new ω_k . By repeating the above process in case of convergence, the decomposed modes are calculated.

Variational mode decomposition provides different modes to extract features. In this paper, to decrease the features, time, and the redundant data, Relief-F and CFS methods is applied as a filter tool.

3. 3. Feature Selection using Relief-F and CFS
Appropriate feature selection among a large number of features is an important challenge in classification problems. The reasons of feature selection are the reduction of the redundant data, number of features and,

time. In this paper, we use Relief-F and CFS methods as two tools for feature selection. Furthermore, in this paper, these two methods are compared together.

3. 3. 1. Relief-F Relief-F is a feature selection algorithm that is used to reduce the size of the problem. The Relief-F method is a robustness method and appropriate method for multiclass problems. The steps of the Relief algorithm, as an algorithm to reduce the dimensions of input data, are as follows: in the first step, each feature takes a correlation rank based on their relationship with the final goal. In the second step, the ranks are updated using randomly selected samples. Then these ranks are sorted and features with the lowest rank are removed, (a threshold is used for features ranking). The remaining features are saved as superior features and are introduced as inputs of a classifier algorithm. In other words, in Relief-F method, each feature initially takes a weight, and then the weight is updated by using the value of the feature for each sample. The outputs of Relief-F method are the values of the weight of features. The output of Relief-F method is calculated as Equation (4) which contains several loops [37]:

$$G[F] = G[F] - \sum_{j=1}^k \frac{diff(F, D_i, H_j)}{m.k} + \sum_{C \in class(D_i)} \left[\frac{P(c)}{1 - P(class(D_i))} \sum_{j=1}^k \frac{diff(F, D_i, M_j(C))}{m.k} \right] \quad (4)$$

The used parameters have been introduced in nomenclature. The difference between the values of the feature F for two samples D and H is computed by function $diff(F, D, H)$ as expressed by Equations (5) and (6) [37]:

- if one sample has been determined:

$$diff(F, D, H) = 1 - P(\text{value}(F, H) | \text{class}(D)) \quad (5)$$

- if both samples have not been determined:

$$diff(F, D, H) = 1 - \sum_v^{values(F)} (P(V | \text{class}(D)) \times P(V | \text{class}(H))) \quad (1)$$

3. 3. 2. Correlation Feature Selection (CFS)
Feature selection based on correlation is a powerful method for filtering that ranks feature subsets according to a correlation based heuristic evaluation function. The correlation method points to subsets that have properties with the highest correlation coefficient with the desired sample class [37]. Subsets that have the most points are considered as the main variable. The objective is to decrease feature-to-feature correlation and increase

feature-to-class correlation. The evaluation function of the CFS algorithm is presented in Equation (7) [37]:

$$R_s = \frac{\overline{q l_{qf}}}{\sqrt{q + q(q-1)l_{qf}}} \quad (7)$$

The used parameters have been introduced in nomenclature. The algorithm has a high ability to quickly detect unrelated and additional data.

3. 4. Identification of Combined PQDs using KNN

In this section, the extracted and selected features are used to train the classifier. In these years researchers are eager to use KNN as a power quality disturbance classifier because of high speed and accuracy, less-parametric, user- friendly frame, being compatible with oscillatory trends of electrical measurements.

K-nearest neighbors performs classification based on the data similarity. In fact, for each new test data, it calculates the near neighbor k distances and tags a ticket similar to the train data. In other words, in the KNN classifier, an unknown sample (test data) is classified based on the similarity with a known sample (train data) based on calculating the distance between them. For this reason, the KNN classification algorithm is dependent on the selected distance function. In the previous researches, different distance functions such as Cosine distance, Correlation distance, Cityblock distance, Euclidian distance have been used [38]. Selecting the appropriate distance function for the data set is an important issue. In this paper, the performance of four distance functions for PQDs data is compared together and the appropriate distance function is introduced. Each distance functions has advantages and disadvantages, for example, in Euclidean distance, the data amplitude has a great impact on the accuracy of classification. In the Cityblock distance, the computing volume is lower and the speed is higher. In the Cosine distance, the amplitude difference between the samples is not known. In this paper, KNN performance is investigated using different distance functions on the combined PQDs. Other hands, it is compared with PNN [39] network to introduce the best distance function.

4. SIMULATION AND RESULTS ANALYSIS

To verify the proposed method, different types of loads and DGs have been simulated in PSCAD/EMTDC simulation program (Version 4.5). Table 1 presents the sources of PQDs and grid conditions.

Figure 2 shows the simulated network. This network consists of four nonlinear loads, three DGs, one set capacitive bank, and one linear load. Nonlinear loads include EAF, DC motors, and 6-pulse and 12-pulse rectifiers. Distributed generations include PV, wind turbine, and DE.

Table 2 presents 21 classes of PQDs that were considered in this paper. Class 1 was dedicated to flicker sources. Wind turbine (aerodynamic), electric arc furnace, and diesel engine were considered as flicker sources. Classes 2 to 5 were dedicated to double combinations of flicker and other PQDs. For example, in the presence of wind turbine, EAF or DE, switch on or switch off a large load are lead to Flicker+Sag or Flicker+swell PQDs. Other scenarios in the presence of wind turbine, EAF, or DE are double line to ground (LLG) fault or switching a large capacitor that leads to Flicker+Interrupt or Flicker+Impulse PQDs. Class 6 was dedicated to harmonic sources include: wind turbine (power electronic), PV, 6-pulse, 12-pulse, and DC machine. Classes 7 to 10 were dedicated to double combinations of harmonic and other PQDs. For example, in the presence of wind turbine, PV, 6-pulse, 12-pulse, or DC machine switch on or switch off a large load are lead to Harmonic+Sag or Harmonic+Swell PQDs. Other scenarios such as LLG fault and switching a large capacitor are added to the mentioned harmonic sources. It is notable that wind turbines alone can be the cause of generating flicker and harmonic [34, 40]. Combined PQDs were introduced in classes 11 to 15. Finally, single PQDs were introduced in classes 16 to 21.

To generate data, different scenarios are implemented in this network (Table 2). Different scenarios such as misfiring, variation of sun radiation and wind speed, entrance and exit of loads, capacitors and DGs, different fault at the grid in half-load to full-load.

The capacity of PV is considered 1.6 MW which is modelled using 10 equal units in parallel mode. The output converter is 500 V DC. This DC voltage is converted into 480 V 3-phase AC power with an inverter. The variations in solar insolation are simulated in the variation of output power from half capacity to full capacity.

The capacity of wind turbine is considered 1.5 MW which is modelled as DFIG in 3-phase. The rated of wind speed is considered equal to 14 m/s.

TABLE 1. Details of simulated network

#	Load or DGs	Element	Conditions
1	6 pulse rectifier	PCC Voltage	20 kV
2	12 pulse rectifier		
3	DC machine (DM)		
4	EAF	Z Line	0.007+0.004231j
5	Photovoltaic (PV)	Z Grid	2.5+15j
6	Wind turbine		
7	Diesel engine (DE)	Grid Voltage	20kV
8	Capacitor bank	Short Circuit Power	20MVA

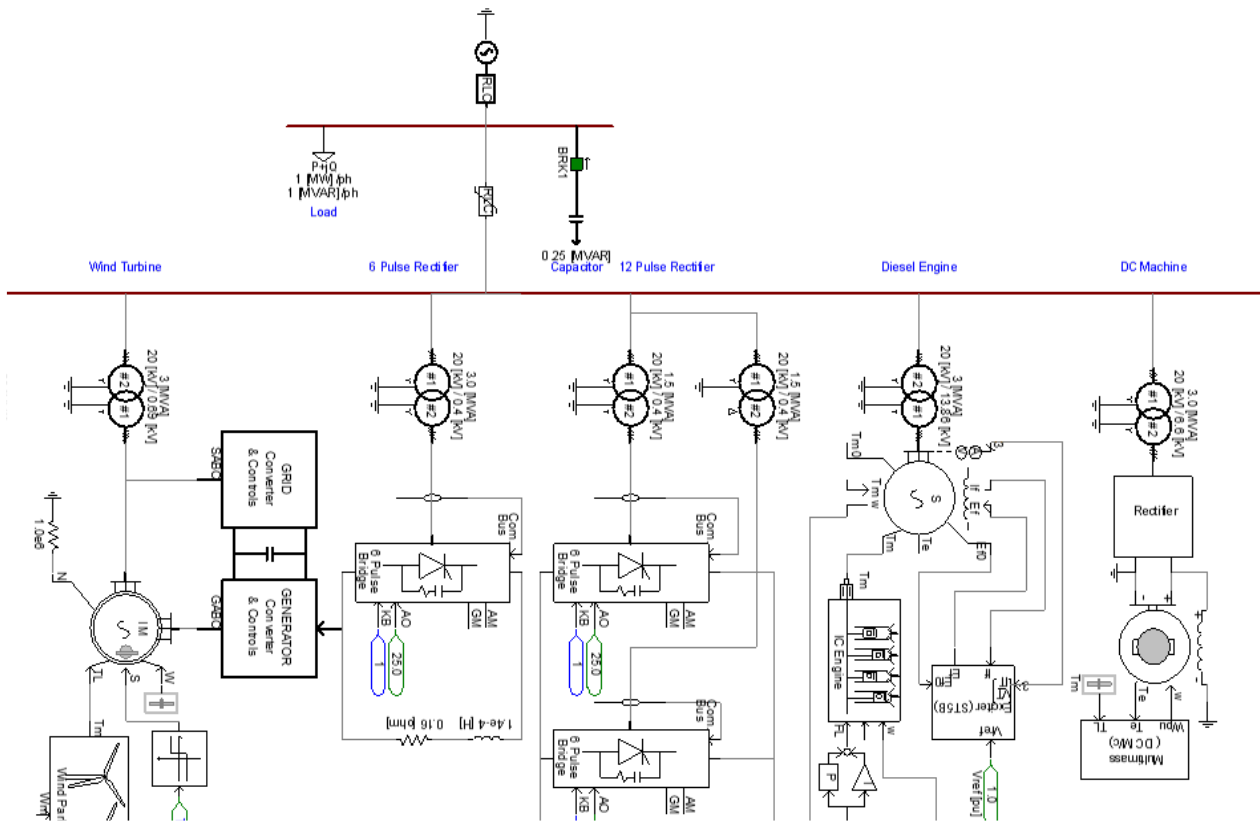


Figure 2. Schematic of the simulated network in PSCAD software

TABLE 2. Classes of combined power quality disturbances and their sources

Class	PQDs	Sources				
PQ1	Flicker	Wind turbine (aerodynamic)	EAF (coherence of Load)	DE (misfiring)		
PQ2	Flicker+Sag	Switch On a Large Load	Switch On a Large Load	Switch On a Large Load		
PQ3	Flicker+Swell	Switch Off a Large Load	Switch Off a Large Load	Switch Off a Large Load		
PQ4	Flicker+Interrupt	LLG	LLG	LLG		
PQ5	Flicker+Impulse	Switching a Large Capacitor	Switching a Large Capacitor	Switching a Large Capacitor		
PQ6	Harmonic	Wind turbine (power electronic)	PV	6 pulse rectifier	12 pulse rectifier	DC machine
PQ7	Harmonic+Sag	Switch On a Large Load	Switch On a Large Load	Switch On a Large Load	Switch On a Large Load	Switch On a Large Load
PQ8	Harmonic+Swell	Switch Off a Large Load	Switch Off a Large Load	Switch Off a Large Load	Switch Off a Large Load	Switch Off a Large Load
PQ9	Harmonic+Interrupt	LLG	LLG	LLG	LLG	LLG
PQ10	Harmonic+Impulse	Switching a Large Capacitor	Switching a Large Capacitor	Switching a Large Capacitor	Switching a Large Capacitor	Switching a Large Capacitor
PQ11	Harmonic+Flicker	Wind turbine (power electronic + aerodynamic)				
PQ12	Harmonic+Flicker+Sag	Switch On a Large Load				
PQ13	Harmonic+Flicker+Swell	Switch Off a Large Load				

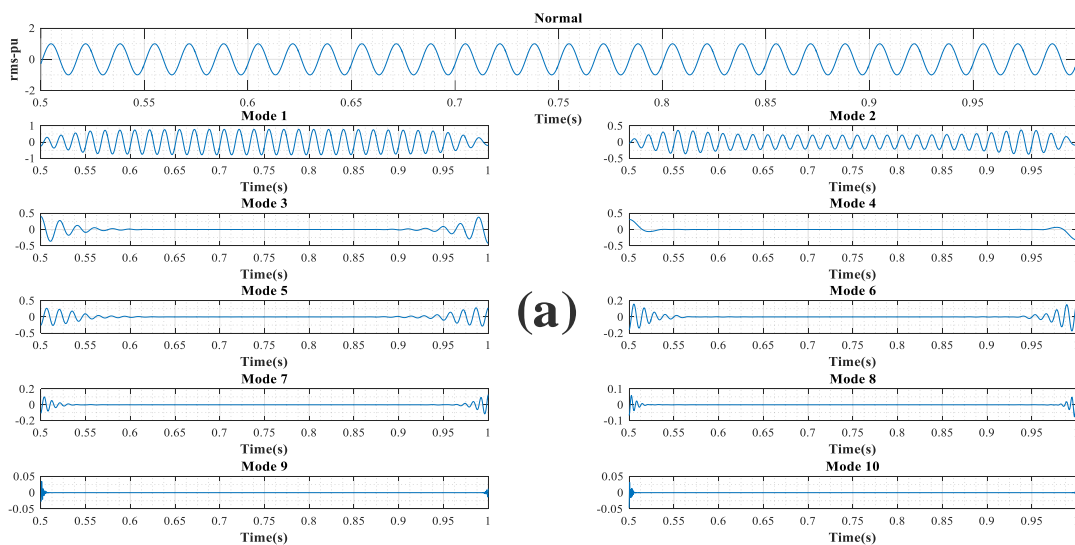
PQ14	Harmonic+Flicker+Interrupt	LLG
PQ15	Harmonic+Flicker+Impulse	Switching a Large Capacitor
PQ16	Normal	Normal Linear Load
PQ17	Sag	Switch On a Large Load
PQ18	Swell	Switch Off a Large Load
PQ19	Interrupt	LLG
PQ20	Impulse	Switching a Large Capacitor
PQ21	Notch	Normal Linear Load+Capacitor

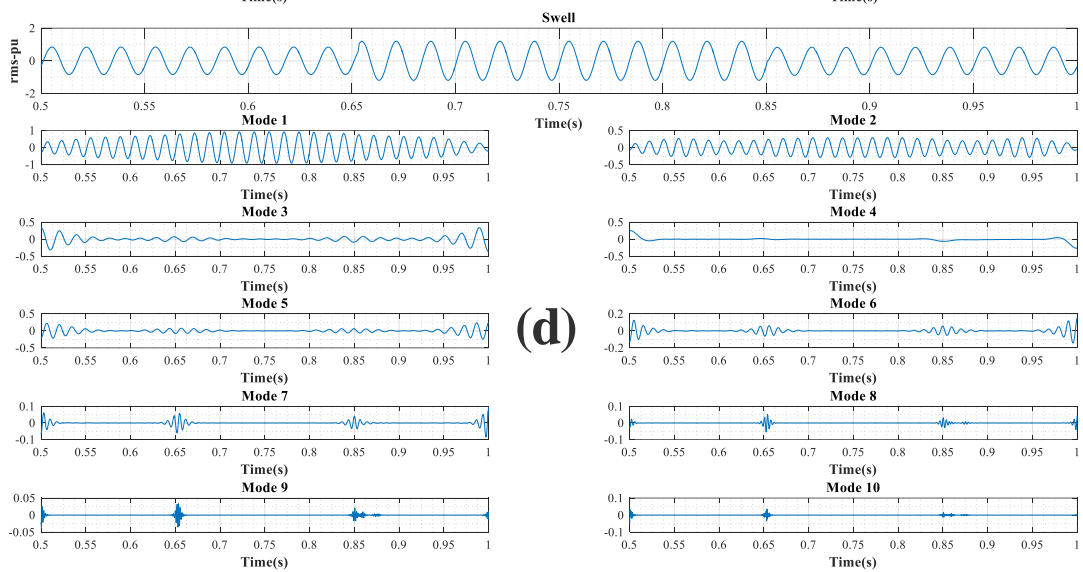
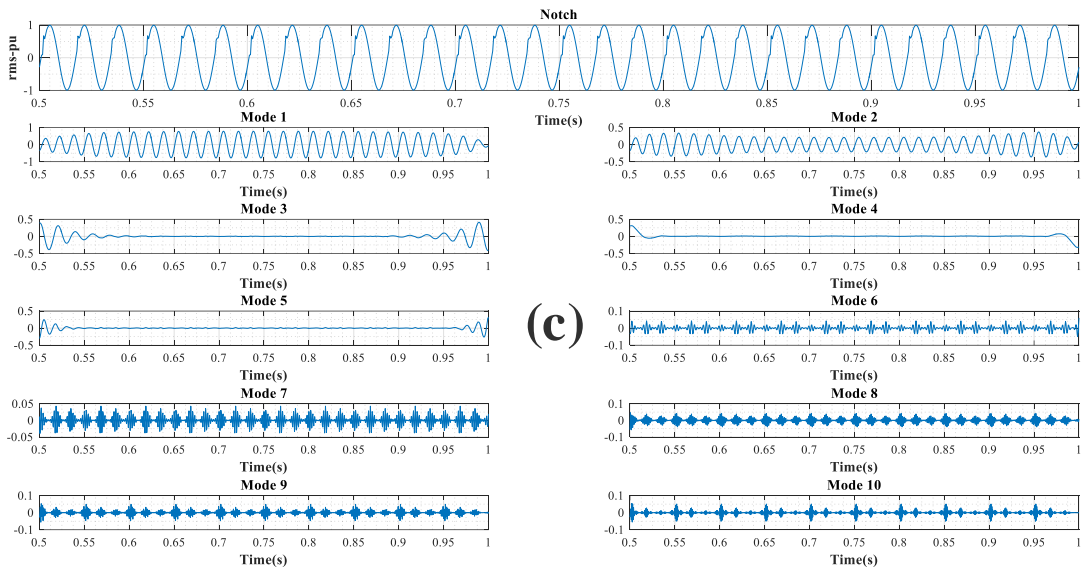
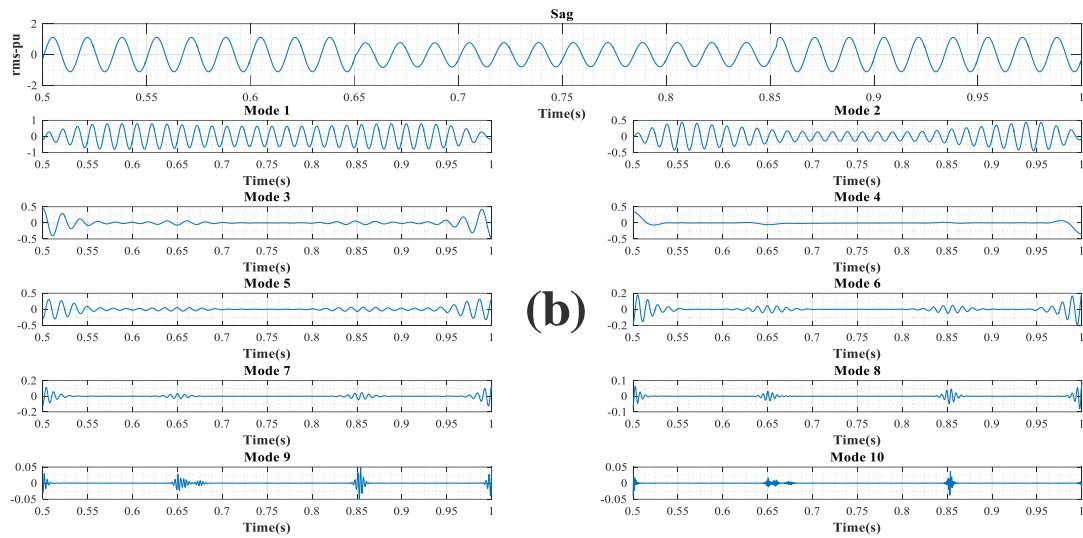
100 samples for train and 100 samples for the test are considered for any classes. The proposed methods were developed under the MATLAB environment version 9.7 on a Windows 10 with an Intel CORE i7 Pro processor and 12-GB RAM.

According to subsection 3.1, the first stage is data generation using accurate simulation in PSCAD software. All scenarios in Table 2 were implemented to generate the different combinations of power quality events. A complete database from different voltage waveforms was generated in different scenarios in PSCAD software. Some of the voltage waveforms of PQDs with their modes are shown in Figure 3. According to subsection 3.2, main voltages were decomposed to 10 modes using VMD. In Figure 3, the vertical and horizontal axes show the voltage amplitude and time, respectively. The voltage amplitude was normalized to the PCC voltage

To have powerful features, mathematical features such as mean value, the area under, kurtosis, second moment, third moment, fourth moment, skewness, and standard deviation (STD) were extracted from obtained

modes (Table 3). The first ten features are assigned to the mean value of modes 1-10. The second ten features are assigned to the area under the modes 1-10. The third ten features are assigned to the kurtosis of modes of 1-10. The fourth ten features are assigned to the second moment of modes of 1-10. The fifth ten features are assigned to the third moment of modes of 1-10. The sixth ten features are assigned to the fourth moment of modes of 1-10. The seventh ten features are assigned to the skewness of modes of 1-10. The eighth ten features are assigned to the STD of modes of 1-10. In the next stage, these 80 extracted features are filtered. The reason and method of filtering were described in subsection 3.3. The results of filtering by Relief-F method are presented in Table 4. The features with greater discriminating power located in the higher rank. In Table 4, features 24, 26 and 29 are the three features with the highest rank, . Features 33, 80 and 52 also have the lowest rank among the selected features. In other words, features 24, 26, and 29 have the most weight to separate PQD signals. Features 33, 80 and 52 also have the least weight in separating PQDs signals.





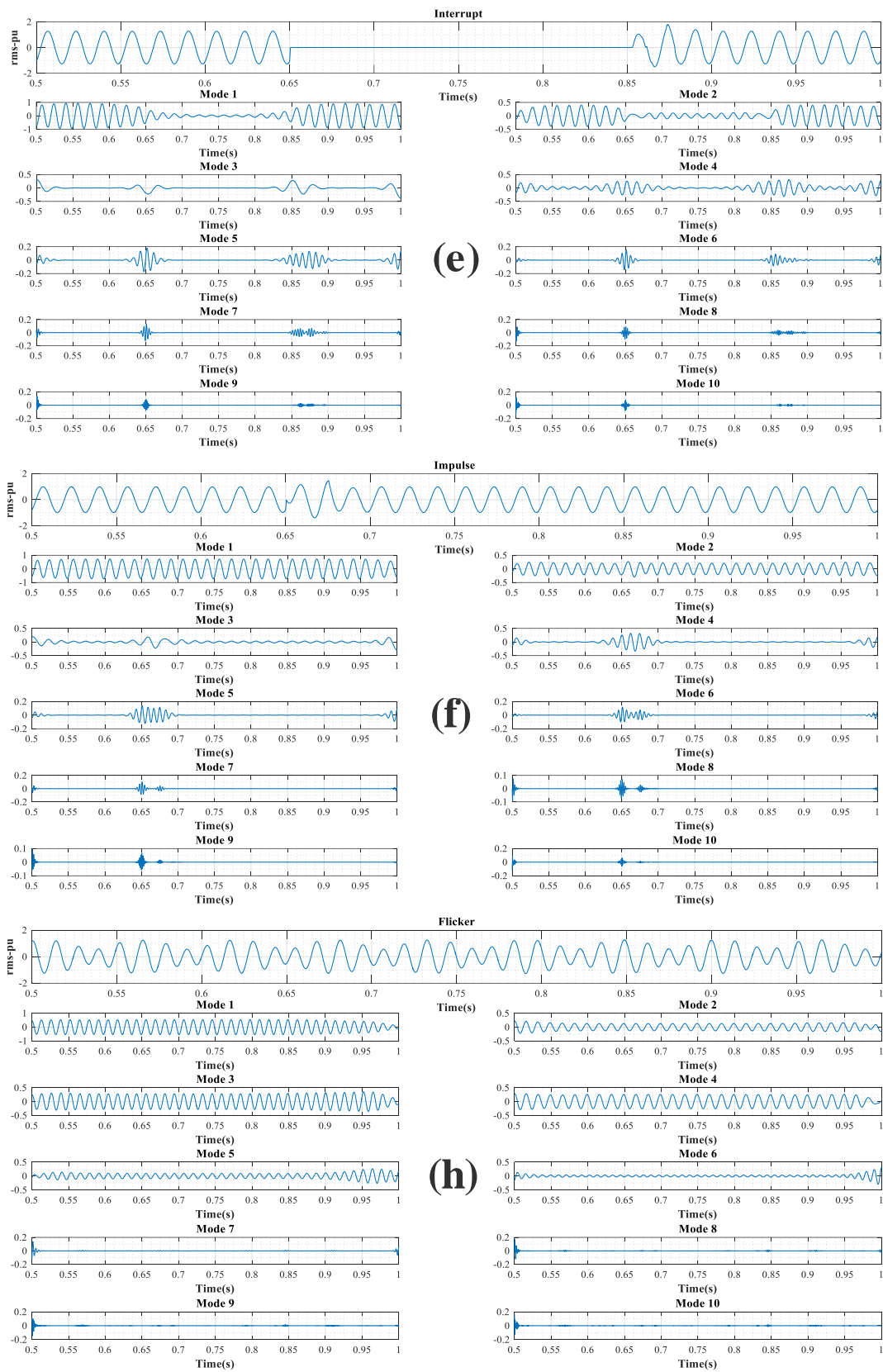


Figure 3. Power quality disturbances with their extracted modes using VMD: (a) normal; (b) sag; (c) notch; (d) swell; (e) interrupt; (f) impulse; (g) harmonic; (h) flicker

TABLE 3. Extracted features from VMD

Number	Feature
1-10	Mean value of modes 1-10
11-20	Area under the modes 1-10
21-30	Kurtosis of modes of 1-10
31-40	Second moment of modes of 1-10
41-50	Third moment of modes of 1-10
51-60	Forth moment of modes of 1-10
61-70	Skewness of modes of 1-10
71-80	STD of modes of 1-10

Table 5 provides a comparison between neural networks, distance functions, and feature selectors. Furthermore, the impact of features dimensions summarized in Table 5. Even in the PNN classifier, the relief-F feature selector performance is better than the CFS. Using relief-F and PNN the time and accuracy of classification were obtained 2.09 seconds and 96.80%, respectively, whereas using CFS and PNN the time and accuracy of classification were obtained 2.356 seconds

and 96.00%. The result show that the performance of relief-F is better than CFS in this problem. In other hand, the performance of the KNN classifier is better than the PNN classifier in all distance functions. The highest classification accuracy was obtained using KNN classifier with Cityblock distance function (99.74%). The performance of Relief-F and CFS methods were compared in Table 6. The results show that the performance of the Relief-F method is better than the CFS method in this problem.

To the best of the authors' knowledge, the different combinations of three PQDs in the presence of DGs have rarely been presented in previous studies. In this paper, different and complex combinations of PQ events have been considered in 21 classes. The performance of the Cityblock distance function of KNN is better in terms of accuracy and consumed time. Details of accuracy in each class and total accuracy are presented in Table 6. The lowest classification accuracy is 99.02% in the identification of combination of Harmonic+Flicker+Interrupt. The highest accuracy of classification with 100% belongs to individual class, such as sag, swell, interrupt, and etc. It is notable that total accuracy is 99.74%.

TABLE 4. Rank of features using Relief-F

Rank	Feature	Weight									
1	24	0.044817	21	16	0.010226	41	41	0.001009	61	5	0.001007
2	26	0.040434	22	65	0.009717	42	10	0.001008	62	42	0.001005
3	29	0.039383	23	64	0.009466	43	9	0.001008	63	4	0.001004
4	30	0.033054	24	17	0.007994	44	7	0.001008	64	36	0.001003
5	69	0.030889	25	18	0.007615	45	49	0.001008	65	37	0.001003
6	28	0.027448	26	22	0.006496	46	8	0.001008	66	39	0.001003
7	25	0.026843	27	20	0.005340	47	47	0.001008	67	2	0.001003
8	67	0.024697	28	19	0.004910	48	46	0.001008	68	40	0.001002
9	27	0.024424	29	63	0.004186	49	48	0.001008	69	38	0.001001
10	11	0.023712	30	71	0.003423	50	59	0.001008	70	76	0.000999
11	66	0.021257	31	62	0.003188	51	57	0.001008	71	3	0.000998
12	68	0.020584	32	1	0.002554	52	50	0.001008	72	53	0.000997
13	23	0.020296	33	31	0.002152	53	45	0.001008	73	35	0.000995
14	13	0.018209	34	72	0.001613	54	56	0.001008	74	32	0.000988
15	15	0.013704	35	73	0.001482	55	60	0.001008	75	77	0.000952
16	70	0.013252	36	51	0.001460	56	58	0.001008	76	78	0.000945
17	14	0.012604	37	74	0.001378	57	6	0.001008	77	79	0.000939
18	61	0.012226	38	75	0.001129	58	55	0.001008	78	33	0.000934
19	12	0.010971	39	34	0.001038	59	44	0.001008	79	80	0.000931
20	21	0.010867	40	54	0.001012	60	43	0.001007	80	52	0.000919

TABLE 5. Comparative results between classifiers, feature selectors, and feature dimensions

Classifier	distance function	Feature selector	Sets of features	Time assumed(s)	Classifier accuracy (%)
PNN	Gaussians	Relief-F	First 19 Features	2.085081	96.80
		CFS	First 22 Features	2.359369	96.00
KNN	Cityblock	Relief-F	First 20 Features	0.268652	99.74
		CFS	First 21 Features	0.275225	99.39
	Correlation	Relief-F	First 21 Features	0.280029	98.93
		CFS	First 21 Features	0.299565	98.46
	Euclidian	Relief-F	First 20 Features	0.319245	98.76
		CFS	First 20 Features	0.345749	98.46
		Relief-F	First 19 Features	0.312949	98.83
		CFS	First 22 Features	0.3144207	98.46

TABLE 6. Performance of the KNN-Cityblock classifier

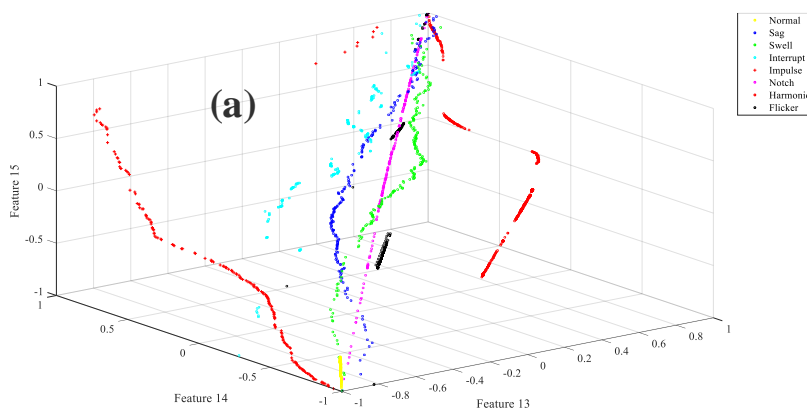
Class	Accuracy	Class	Accuracy	Class	Accuracy	Class	Accuracy
Normal	100 %	Harmonic	100 %	Flicker	100 %	Harmonic+Flicker	99.74 %
Sag	100 %	Harmonic+Sag	99.87 %	Flicker+Sag	99.83 %	Harmonic+Flicker+Sag	99.16 %
Swell	100 %	Harmonic+Swell	99.76 %	Flicker+Swell	99.85 %	Harmonic+Flicker+Swell	99.05 %
Interrupt	100 %	Harmonic+Interrupt	99.75 %	Flicker+Interrupt	99.72 %	Harmonic+Flicker+Interrupt	99.02 %
Impulse	100 %	Harmonic+Impulse	99.85 %	Flicker+Transient	99.82 %	Harmonic+Flicker+Impulse	99.12 %
Notch	100 %						
Total Accuracy				99.74 %			

To validate the proposed method, some 3D figures of separation results are shown in Figure 4. In these figures, different PQ events were compared together. The first figure shows the individual PQ events. Other figures show different combinations of PQ events. The results show that the proposed method identifies the combined PQDs with high accuracy and speed in the presence of different types of DGs.

To investigate the performance of the proposed method in noisy conditions, a new scenario have been added to this paper. Three SNR levels of Gaussian noise

include 20 dB, 30 dB, and 50 dB have been considered. Table 7 shows the comparative results between EMD and VMD in noisy conditions. Variational mode decomposition, unlike EMD, is robust against noise. The proposed method classifies the PQDs and their sources simultaneously with high accuracy even in noisy conditions.

In Table 8 the assumptions and results of this paper have been compared with other papers in this issue. Unlike other papers, this paper has the highest number of classes. Twenty- one multi-complex PQDs have been



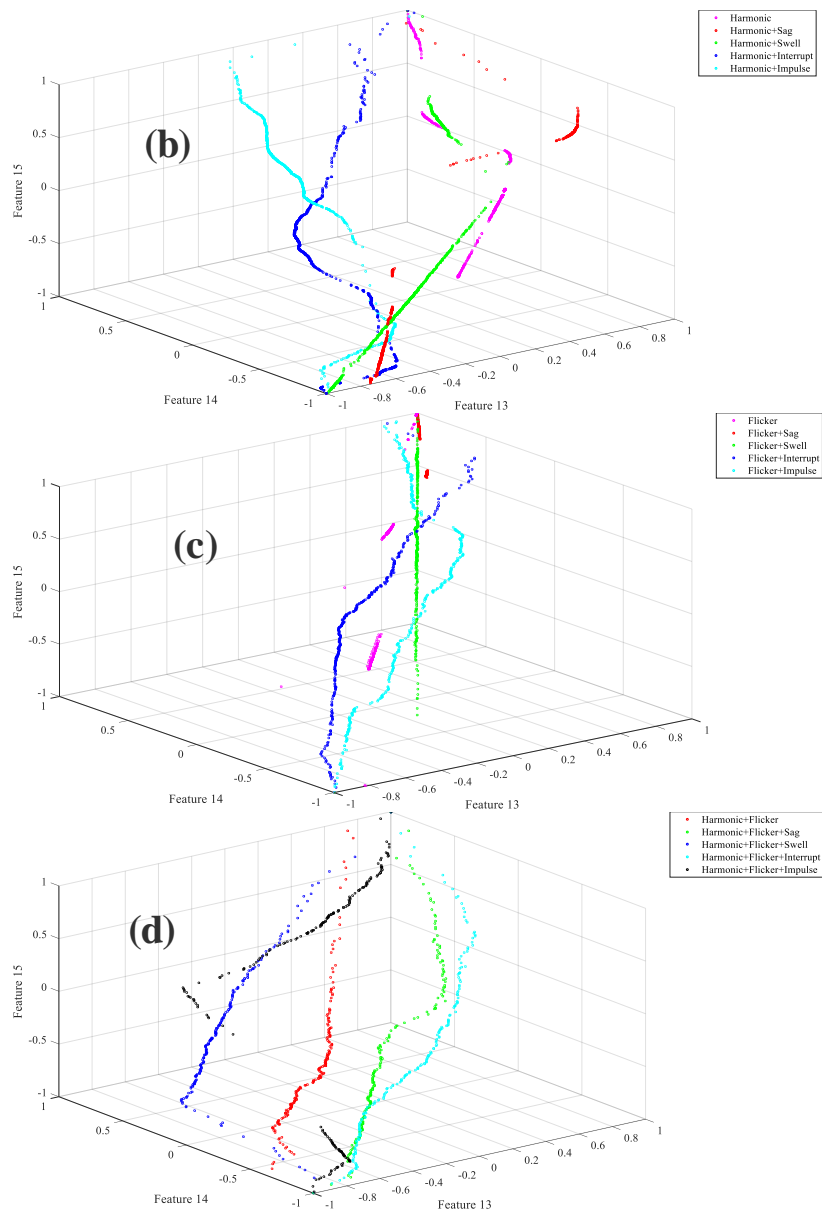


Figure 4. 3D figures of separation results: (a) individual PQDs; (b) double combination of harmonic disturbances; (c) double combination of flicker disturbances; (d) triple combination of PQDs

TABLE 7. Comparative results between EMD and VMD in noisy conditions

	Accuracy							
	PQDs classification				Source identification			
	Noiseless	20 dB	30 dB	50 dB	Noiseless	20 dB	30 dB	50 dB
EMD-KNN	97.65	91.55	93.22	96.57	98.48	95.63	96.87	98.15
VMD-KNN	99.74	99.05	99.21	99.34	99.87	99.58	99.69	99.79

considered in this paper. For this reason, it is not fair to compare the accuracy of classification regardless of the number of classes. However, the accuracy of the

classification of the proposed method in this paper is very desirable in noiseless and noisy mode. The listed papers have not considered the issue of penetration of DGs in

HMP systems [15, 20, 21, 41-45]. But in this paper, three types of DGs including wind turbine, PV, and DE have been considered. Shen et al. [10], Saini and Beniwal [31] only considered wind turbine as DGs. Contrary to other papers, we have considered different scenarios such as misfiring, variation of sun radiation and wind speed, entrance and exit of loads, capacitors and distributed generators, different faults at the grid in half-load to full-load in this paper. The listed papers in Table 8 have not addressed the issue of identifying the source type of PQDs, whereas in our paper, in addition to categorizing the multi-complex PQDs, the source type of PQDs is simultaneously identified. We believe the proposed approach can be used as an added algorithm for smart metering in modern and smart power systems.

For the purpose of verifying method, mentioned loads and DGs have connected to 34 bus radial distribution system in PSCAD. Table 9 presents the sources of PQDs and grid conditions [46]. Figure 5 shows the simulated network. This network consists of four nonlinear loads, three DGs, one set capacitive bank, and one linear load. Nonlinear loads include EAF, DC motors, and 6-pulse

and 12-pulse rectifiers. Distributed generations include PV, wind turbine, and DE.

For second test system, details of accuracy in each class and total accuracy are presented in Table 10. The lowest classification accuracy is 98% in the identification of combination of Harmonic+Interrupt AND Harmonic+Flicker+Impulse. The highest accuracy of classification with 100% belongs to individual classes, such as normal load, impulse, notch, and etc. It is notable that total accuracy is 99.55%.

The future direction of this research is to use this method in smart meters as an additional tool. So that new power quality meters can be produced with the ability to identify and classify power quality events. On the other hand, this proposed method can be added to existing power quality meters as a tool. It is noteworthy that the proposed method can be added in PMUs in transmission networks and in micro PMUs in distribution networks and lead to accurate identification and classification of power quality events. The limitations of this proposed method are related to its technology and industrialization. On the other hand, all power quality event classes must be trained to the classifier.

TABLE 8. Comparison of this paper with other papers

Method	Sources identification	# classes	# Features	# DGs types	accuracy			
					normal	20 dB	30 dB	50 dB
IPCA+ 1-D-CNN [10]	No	12	72	1	99.92	99.76	-	99.85
WT+ST [15]	No	8	20	0	99.81	97.69	99.31	-
DWT+HST [43]	No	9	26	0	99.77	99.22	99.77	-
DWT+PNN [44]	No	16	9	0	99.875	93.6	95.5	-
ST [42]	No	14	5	0	99.43	97.96	99.29	-
OMFST + CA [21]	No	12	67	0	-	91.50	98.58	98.92
VMD+SVM [47]	No	17	3	1	99.03	-	-	-
VMD+ELM [45]	No	14	4	0	99.71	99.3	99.7	-
WT+LSSVM [20]	No	4	21	0	99.71	-	-	-
NSGA III+DAG-SVM [41]	No	8	2	0	99.85	99.15	99.35	-
FTT+SR-ELM [31]	No	12	107	1	99.59	-	95.29	97.93
This paper	Yes	21	20	3	99.74	99.05	99.21	99.34

TABLE 9. Details of simulated network

Element	Conditions
PCC Voltage	24.9 kV
Z Grid	0.16038+j0.64151ohm
Grid Voltage	24.9kV
Short Circuit Power	12MVA

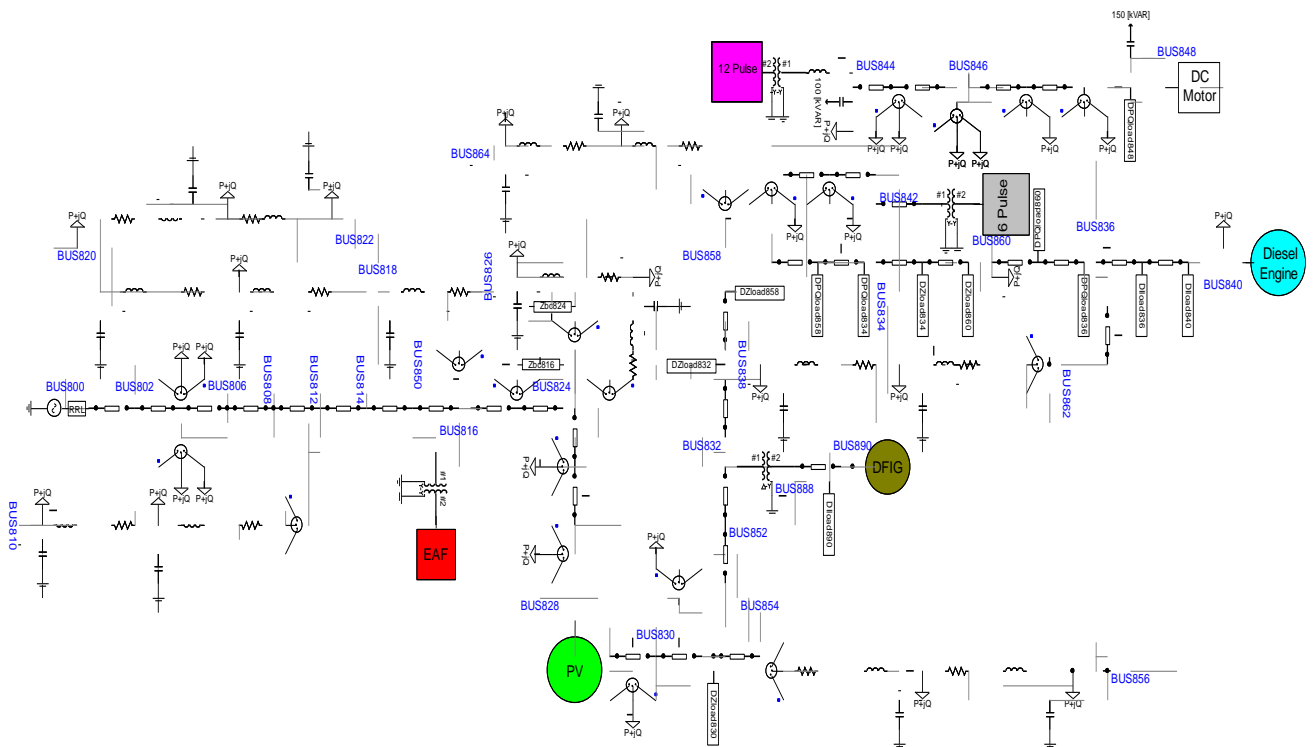
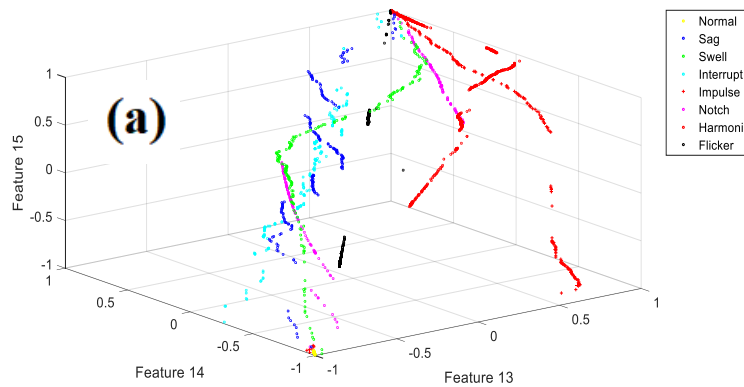


Figure 4. Schematic of 34 bus distribution grid [46]

TABLE 10. Performance of the KNN-Cityblock classifier in second test system

Class	Accuracy	Class	Accuracy	Class	Accuracy	Class	Accuracy
Normal	100	Harmonic	99.95	Flicker	99.76	Harmonic+Flicker	99.00
Sag	99.95	Harmonic+Sag	99.64	Flicker+Sag	99.94	Harmonic+Flicker+Sag	99.15
Swell	99.81	Harmonic+Swell	99.65	Flicker+Swell	99.50	Harmonic+Flicker+Swell	99.36
Interrupt	99.96	Harmonic+Interrupt	98.00	Flicker+Interrupt	99.48	Harmonic+Flicker+Interrupt	99.68
Impulse	100.00	Harmonic+Impulse	99.91	Flicker+Transient	99.86	Harmonic+Flicker+Impulse	98.00
Notch	100.00						
Total Accuracy				99.55%			



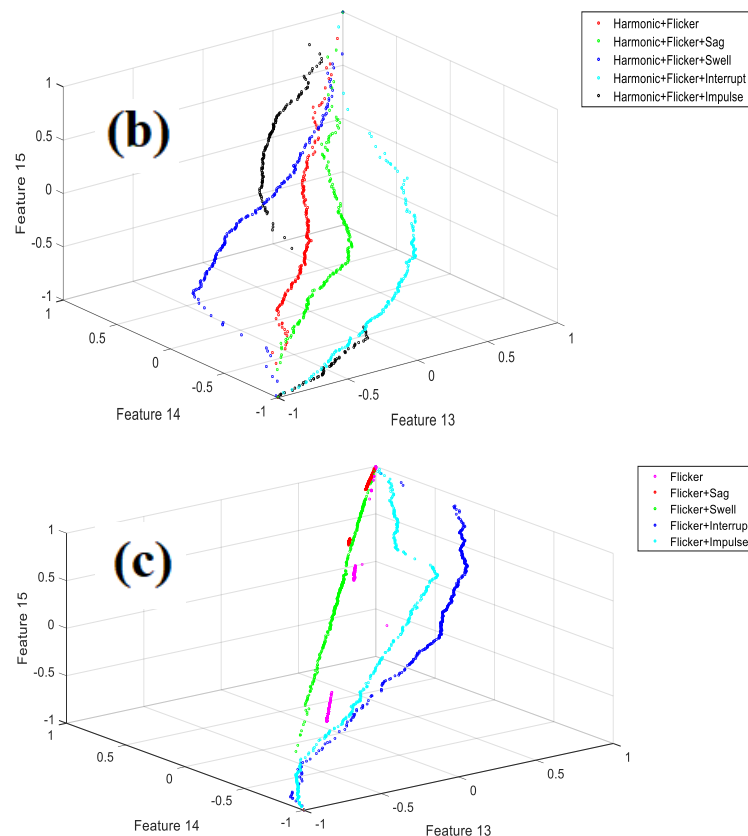


Figure 11. 3D figures of separation results: (a) individual PQDs; (b) double combination of harmonic disturbances; (c) triple combination of PQDs

5. CONCLUSION

This paper presents a novel approach with high accuracy based on the VMD and KNN for identification of complex combination of PQDs in hybrid modern power systems. In this paper, the VMD method was used to decompose the voltage signals. This method is a robust method to noise and sampling. The results of different experiments on combined PQDs show that this method has better performance in extraction of PQD features than similar methods. In this paper, in addition to classifying the PQDs, identifying their sources is also performed. In this paper, in order to evaluate the proposed method in noisy conditions, three signal-to-noise ratios of 20 dB, 30 dB, and 50 dB were investigated. The obtained results confirm that the proposed method is robust to noise and has a high accuracy in identifying the combined PQDs and their sources even in noisy conditions. To classify the PQDs only waveforms of voltages were used. To verify the proposed method, different scenarios such as half-load to full-load, variation of sun radiation and wind speed, misfiring of DE, etc. were considered. Furthermore, to verify the proposed method, our method was compared with PNN and different distance functions

of KNN. Also, two feature selectors Relief-F and CFS were compared together. Results show that the accuracy and speed of the Cityblock of KNN are better than other distance functions and PNN. Also, the performance of Relief-F is better than CFS in this problem. The obtained results verify that the proposed method has a high accuracy even for combined PQDs. This approach can be used as an added tool for smart metering in modern power systems and smart power systems.

6. REFERENCES

1. Yahyazadeh, M., Johari, M.S. and HosseinNia, S.H., "Novel particle swarm optimization algorithm based on president election: Applied to a renewable hybrid power system controller", *International Journal of Engineering, Transactions A: Basics*, Vol. 34, No. 1, (2021), 97-109, doi: 10.5829/ije.2021.34.01a.12.
2. Chandra, A. and Geng, H., "Power quality in microgrids based on distributed generators", MDPI AG, (2019), doi: 10.3390/books978-3-03928-007-0.
3. Ahmadi, M., Sharafi, P., Mousavi, M.H. and Veysi, F., "Power quality improvement in microgrids using statcom under unbalanced voltage conditions", *International Journal of Engineering, Transactions C: Aspects*, Vol. 34, No. 6, (2021), 1455-1467, doi: 10.5829/ije.2021.34.06c.09.

4. Abdolrahimi, H. and Arab Khaburi, D., "A novel model predictive voltage control of brushless cascade doubly-fed induction generator in stand-alone power generation system", *International Journal of Engineering, Transactions B: Applications*, Vol. 34, No. 5, (2021), 1239-1249, doi: 10.5829/ije.2021.34.05b.17.
5. Heidari, H. and Tarafdar Hagh, M., "Optimal reconfiguration of solar photovoltaic arrays using a fast parallelized particle swarm optimization in confront of partial shading", *International Journal of Engineering, Transactions B: Applications*, Vol. 32, No. 8, (2019), 1177-1185, doi: 10.5829/ije.2019.32.08b.14.
6. Mahela, O.P., Khan, B., Alhelou, H.H. and Siano, P., "Power quality assessment and event detection in distribution network with wind energy penetration using stockwell transform and fuzzy clustering", *IEEE Transactions on Industrial Informatics*, Vol. 16, No. 11, (2020), 6922-6932, doi: 10.1109/TII.2020.2971709.
7. Prasad, E.N., Dash, P. and Sahani, M., "Diagnosing utility grid disturbances in photovoltaic integrated dc microgrid using adaptive multiscale morphology with dfa analysis", *Sustainable Energy, Grids and Networks*, Vol. 1, No. 1, (2021), 100574, doi: 10.1016/j.segan.2021.100574.
8. Gonzalez-Abreu, A.-D., Delgado-Prieto, M., Osornio-Rios, R.-A., Saucedo-Dorantes, J.-J. and Romero-Troncoso, R.-d.-J., "A novel deep learning-based diagnosis method applied to power quality disturbances", *Energies*, Vol. 14, No. 10, (2021), 2839, doi: 10.3390/en14102839.
9. Cortes-Robles, O., Barocio, E., Obushevs, A., Korba, P. and Sevilla, F.R.S., "Fast-training feedforward neural network for multi-scale power quality monitoring in power systems with distributed generation sources", *Measurement*, Vol. 170, No. 1, (2021), 108690, doi: 10.1016/j.measurement.2019.107453.
10. Shen, Y., Abubakar, M., Liu, H. and Hussain, F., "Power quality disturbance monitoring and classification based on improved pca and convolution neural network for wind-grid distribution systems", *Energies*, Vol. 12, No. 7, (2019), 1280, doi: 10.3390/en12071280.
11. Igual, R. and Medrano, C., "Research challenges in real-time classification of power quality disturbances applicable to microgrids: A systematic review", *Renewable and Sustainable Energy Reviews*, Vol. 132, No. 1, (2020), 110050, doi: 10.1016/j.rser.2020.110050.
12. Pinto, L.S., Assunção, M.V., Ribeiro, D.A., Ferreira, D.D., Huallpa, B.N., Silva, L.R. and Duque, C.A., "Compression method of power quality disturbances based on independent component analysis and fast fourier transform", *Electric Power Systems Research*, Vol. 187, No. 1, (2020), 106428, doi: 10.1016/j.epsr.2020.106428.
13. Ukil, A., Yeap, Y.M. and Satpathi, K., *Frequency-domain based fault detection: Application of short-time fourier transform, in Fault analysis and protection system design for dc grids*, 2020, Springer, 195-221, doi: 10.1007/978-981-15-2977-1_6.
14. Rahmani, A. and Deihimi, A., "Reduction of harmonic monitors and estimation of voltage harmonics in distribution networks using wavelet analysis and NARX", *Electric Power Systems Research*, Vol. 178, No. 1, (2020), 106046, doi: 10.1016/j.epsr.2019.106046.
15. Erişti, H., Uçar, A. and Demir, Y., "Wavelet-based feature extraction and selection for classification of power system disturbances using support vector machines", *Electric Power Systems Research*, Vol. 80, No. 7, (2010), 743-752, doi: 10.1016/j.epsr.2009.09.021.
16. Khokhar, S., Zin, A.M., Mokhtar, A., Bhayo, M. and Naderipour, A., "Automatic classification of single and hybrid power quality disturbances using wavelet transform and modular probabilistic neural network", in 2015 IEEE Conference on Energy Conversion (CENCON), IEEE, Vol. 1, No. 1, (2015), 457-462, doi: 10.1109/CENCON.2015.7409588.
17. Qiu, W., Tang, Q., Liu, J., Teng, Z. and Yao, W., "Power quality disturbances recognition using modified s transform and parallel stack sparse auto-encoder", *Electric Power Systems Research*, Vol. 174, No. 1, (2019), 105876, doi: 10.1016/j.epsr.2019.105876.
18. Senroy, N., Suryanarayanan, S. and Ribeiro, P.F., "An improved hilbert-huang method for analysis of time-varying waveforms in power quality", *IEEE Transactions on Power Systems*, Vol. 22, No. 4, (2007), 1843-1850, doi: 10.1109/TPWRS.2007.907542.
19. Rodríguez, M.A., Sotomonte, J.F., Cifuentes, J. and Bueno-López, M., "A classification method for power-quality disturbances using hilbert-huang transform and lstm recurrent neural networks", *Journal of Electrical Engineering & Technology*, Vol. 16, No. 1, (2021), 249-266, doi: 10.1007/s42835-020-00612-5.
20. Eristi, B., Yildirim, O., Eristi, H. and Demir, Y., "A new embedded power quality event classification system based on the wavelet transform", *International Transactions on Electrical Energy Systems*, Vol. 28, No. 9, (2018), e2597, doi: 10.1002/etep.2597.
21. Huang, N., Peng, H., Cai, G. and Chen, J., "Power quality disturbances feature selection and recognition using optimal multi-resolution fast s-transform and cart algorithm", *Energies*, Vol. 9, No. 11, (2016), 927, doi: 10.3390/en9110927.
22. Gholami, M., "Islanding detection method of distributed generation based on wavenet", *International Journal of Engineering, Transactions B: Applications*, Vol. 32, No. 2, (2019), 242-248, doi: 10.5829/ije.2019.32.02b.09.
23. Wang, J. and Cheng, Z., "Wind speed interval prediction model based on variational mode decomposition and multi-objective optimization", *Applied Soft Computing*, Vol. 113, No. 1, (2021), 107848, doi: doi.org/10.1016/j.asoc.2021.107848.
24. Pankaj, D., Govind, D. and Narayanankutty, K., "A novel method for removing rician noise from mri based on variational mode decomposition", *Biomedical Signal Processing and Control*, Vol. 69, No. 1, (2021), 102737, doi: 10.1016/j.bspc.2021.102737.
25. Jalilian, A. and Samadinab, S., "Detection of short-term voltage disturbances and harmonics using ppmu-based variational mode extraction method", *IEEE Transactions on Instrumentation and Measurement*, Vol. 70, No. 1, (2021), 1-17, doi: 10.1109/TIM.2021.3075744.
26. Samanta, I.S., Rout, P.K. and Mishra, S., "An optimal extreme learning-based classification method for power quality events using fractional fourier transform", *Neural Computing and Applications*, Vol. 33, No. 10, (2021), 4979-4995, doi: 10.1007/s00521-020-05282-y.
27. Motlagh, S.Z. and Foroud, A.A., "Power quality disturbances recognition using adaptive chirp mode pursuit and grasshopper optimized support vector machines", *Measurement*, Vol. 168, No. 1, (2021), 108461, doi: 10.1016/j.measurement.2020.108461.
28. Sanjeevikumar, P., Sharmeela, C., Holm-Nielsen, J.B. and Sivaraman, P., "Power quality in modern power systems, Elsevier Science, (2020), doi: 10.1016/C2019-0-05409-X.
29. Sankaran, C., "Power quality, CRC Press, (2017).
30. Kharrazi, A., Sreeram, V. and Mishra, Y., "Assessment techniques of the impact of grid-tied rooftop photovoltaic generation on the power quality of low voltage distribution network-a review", *Renewable and Sustainable Energy Reviews*, Vol. 120, No. 1, (2020), doi: 109643, 10.1016/j.rser.2019.109643.
31. Saini, M.K. and Beniwal, R.K., "Detection and classification of power quality disturbances in wind-grid integrated system using fast time-time transform and small residual-extreme learning machine", *International Transactions on Electrical Energy Systems*, Vol. 28, No. 4, (2018), e2519, doi: 10.1002/etep.2519.
32. Kazeminejad, M., Banejad, M., Annakkage, U.D. and Hosseinzadeh, N., "Load pattern-based voltage stability analysis

- in unbalanced distribution networks considering maximum penetration level of distributed generation", *IET Renewable Power Generation*, Vol. 14, No. 13, (2020), 2517-2525, doi: 10.1049/iet-rpg.2019.1196.
33. Fooladi, M., Foroud, A.A. and Abdoos, A.A., "Detection and evaluation of effective factors on flicker phenomenon in diesel-engine driven generators", *Applied Thermal Engineering*, Vol. 113, No. 1, (2017), 1194-1207, doi: 10.1016/j.applthermaleng.2016.11.113.
34. Doustmohammadi, H. and Akbari Foroud, A., "A novel flicker detection method for vertical axis wind turbine using two-dimensional discrete wavelet transform", *International Transactions on Electrical Energy Systems*, Vol. 30, No. 11, (2020), e12584, doi: 10.1002/2050-7038.12584.
35. Dragomiretskiy, K. and Zosso, D., "Variational mode decomposition", *IEEE Transactions on Signal Processing*, Vol. 62, No. 3, (2013), 531-544, doi: 10.1109/TSP.2013.2288675.
36. Ali, M., Prasad, R., Xiang, Y., Khan, M., Farooque, A.A., Zong, T. and Yaseen, Z.M., "Variational mode decomposition based random forest model for solar radiation forecasting: New emerging machine learning technology", *Energy Reports*, Vol. 7, No. 1, (2021), 6700-6717, doi: 10.1016/j.egy.2021.09.113.
37. Hafiz, F., Swain, A., Naik, C. and Patel, N., "Feature selection for power quality event identification", in TENCON 2017-2017 IEEE Region 10 Conference, IEEE. Vol. 1, No. 1, (2017), 2984-2989, doi: 10.1109/TENCON.2017.8228373.
38. Kumar, V., Chhabra, J.K. and Kumar, D., Impact of distance measures on the performance of clustering algorithms, in Intelligent computing, networking, and informatics. 2014, Springer.183-190, doi: 10.1007/978-81-322-1665-0_17.
39. Akbari Foroud, A. and Hajian, M., "Discrimination of power quality distorted signals based on time-frequency analysis and probabilistic neural network", *International Journal of Engineering, Transactions C: Aspects*, Vol. 27, No. 6, (2014), 881-888, doi:10.5829/idosi.ije.2014.27.06c.06.
40. Bhadane, K.V., Ballal, M.S., Nayyar, A., Patil, D.P., Jaware, T.H. and Shukla, H.P., "A comprehensive study of harmonic pollution in large penetrated grid-connected wind farm", *MAPAN*, Vol. 1, No. 1, (2020), 1, doi: 10.1007/s12647-020-00407-z.
41. Choudhary, B., "An advanced genetic algorithm with improved support vector machine for multi-class classification of real power quality events", *Electric Power Systems Research*, Vol. 191, No. 1, (2021), 106879, doi: 10.1016/j.epr.2020.106879.
42. Enshae, A. and Enshae, P., "A new s-transform-based method for identification of power quality disturbances", *Arabian Journal for Science and Engineering*, Vol. 43, No. 6, (2018), 2817-2832, doi: 10.1007/s13369-017-2895-2.
43. Hajian, M. and Foroud, A.A., "A new hybrid pattern recognition scheme for automatic discrimination of power quality disturbances", *Measurement*, Vol. 51, No. 1, (2014), 265-280, doi:10.1016/j.measurement.2014.02.017.
44. Khokhar, S., Zin, A.A.M., Memon, A.P. and Mokhtar, A.S., "A new optimal feature selection algorithm for classification of power quality disturbances using discrete wavelet transform and probabilistic neural network", *Measurement*, Vol. 95, (2017), 246-259, doi: 10.1016/j.measurement.2016.10.013.
45. Sahani, M., Dash, P. and Samal, D., "A real-time power quality events recognition using variational mode decomposition and online-sequential extreme learning machine", *Measurement*, Vol. 157, No. 1, (2020), 107597, doi: 10.1016/j.measurement.2020.107597.
46. Satish, R., Vaisakh, K., Abdelaziz, A.Y. and El-Shahat, A., "A novel three-phase power flow algorithm for the evaluation of the impact of renewable energy sources and d-statcom devices on unbalanced radial distribution networks", *Energies*, Vol. 14, No. 19, (2021), 6152, doi: 10.3390/en14196152.
47. Cortes-Robles, O., Barocio, E., Segundo, J., Guillen, D. and Olivares-Galvan, J., "A qualitative-quantitative hybrid approach for power quality disturbance monitoring on microgrid systems", *Measurement*, Vol.1 154, No. 1, (2020), 107453, doi: 10.1016/j.measurement.2019.107453

Persian Abstract

چکیده

شناسایی وقایع ترکیبی کیفیت توان در سیستم های قدرت مدرن با در نظر گرفتن توسعه انواع مختلف بارها و تولیدات پراکنده، اهمیت روزافزونی یافته است. نوآوری این مقاله از شناسایی دقیق و سریع وقایع ترکیبی کیفیت توان در حضور انواع مختلف بارها و تولیدات پراکنده مانند سلول فتوولتائیک، توربین بادی با ژنراتور القایی دو سو تغذیه شونده، موتور دیزلی، کوره قوس الکتریکی، ماشین های DC، بارهای دارای یکسوساز ۶ پالسه و ۱۲ پالسه منشأ می گیرد. در این مقاله، ویژگی ها با استفاده از تجزیه حالت متغیر، فقط از شکل موج های ولتاژ استخراج می شوند. روش Relief-F و روش انتخاب ویژگی همبستگی به منظور کاهش داده های اضافی، کاهش ابعاد بردار ویژگی ها و زمان، بر روی ویژگی های استخراج شده اعمال شده و این دو روش با هم مقایسه می شوند. در این مقاله، طبقه بندی کننده K نزدیک ترین همسایه ها برای طبقه بندی وقایع چندگانه کیفیت توان استفاده می شود. به منظور بررسی اثربخشی روش پیشنهادی، سناریوهای مختلفی مانند احتراق ناقص، تغییر تابش خورشید و تغییر سرعت باد، ورود و خروج بارها، خازن ها و تولیدات پراکنده و خطاهای مختلف در شبکه از میان باری تا بار کامل شبیه سازی شده اند. این روش می تواند به عنوان یک الگوریتم برای دستگاه های اندازه گیری هوشمند در سیستم های برق مدرن و هوشمند مورد استفاده قرار گیرد.



Influence of Multiple Repairs on the Quality of Duplex Welded Joints

A. Bennabi^{*a}, A. Adjeloua^a, H. Ameur^b, N. Boualem^a, M. Younsi^{c,d}

^a *Laboratory of Composites Structures and Innovative Materials (LCSIM), Mechanical Engineering Faculty, USTO-MB Oran, El- M'Naouar, Oran, Algeria*

^b *Department of Technology, University Centre of Naama, Naama, Algeria*

^c *Mining and Metallurgy Department, Mechanical Engineering Faculty, USTO-MB Oran, El M'naouar, Oran, Algeria*

^d *Piping and Welding Engineer, Sonatrach Division of Production (SH-DP) Ohanet, El M'naouar, Oran, Algeria*

PAPER INFO

Paper history:

Received 17 September 2021

Received in revised form 28 November 2021

Accepted 16 December 2021

Keywords:

Duplex Stainless Steel

Pipelines

Successive Repair

Welding Defect

ABSTRACT

Duplex stainless steels (DSSs) find increasing use as a substitution to austenitic stainless steels in oil, gas and petrochemical industries, particularly in aggressive environments. Duplex stainless steels with appropriate controlled ferrite-austenite balance combine the attractive properties of excellent strength, general corrosion performance and adequate weldability. All the welding joints subjected to the regulation must be controlled before commissioning the pipeline and even before hydrostatic tests; all not acceptable defects detected with non-destructive testing (NDT) control methods must be eliminated. In some cases, several successive repairs are often preferred to part replacement in the pipeline due to lack of experience of the welder performing the repairs or lack of expertise of the controller ensuring the application of the welding procedure. The purpose of this work is to study the influence of repairs on the same welding joint on the microstructure and the mechanical properties of the heat-affected zone in duplex stainless steel with 22% chromium welding joints. For this purpose, a cylindrical specimen is prepared, on which the various repairs are carried out. Then, an NDT control and the main mechanical and micrographic tests are conducted. The results obtained after four repairs revealed that the multiple repairs made to the same joint did not affect the quality of the welding joints.

doi: 10.5829/ije.2022.35.04a.06

1. INTRODUCTION

Duplex stainless steels (DSSs) become commonly used for pipelines construction, particularly for some engineering applications in strongly corrosive environments and where high mechanical strength is required. These steels exhibit excellent characteristics particularly both corrosion and strength resistance when the ferrite-austenite balance is well controlled during welding process.

The effect of nitrogen content and cooling rate on austenite reformation on microstructure and stress corrosion cracking in heat affected zones of welded duplex stainless steels was investigated. It is noted that crack onset is induced by pitting corrosion and selective dissolution of ferrite phases, whereas crack propagation mode is affected by the types and amounts of reformed austenite in the heat affected zone (HAZ) [1, 2].

Various welded sections performed by gas tungsten arc welding (GTAW) process on a duplex stainless steel (DSS) pipeline were carried out according to heat input and weld type in order to study their effect on the weld structure and weld metallurgy in terms of precipitation phases [3], composition and mechanical properties to assess the susceptibility to intergranular corrosion [4]. The effect of weld metal chemical composition and heat input on the structure and properties of duplex stainless steel welds were also the subject of several studies [5–7].

Failure analyzes of 2205 duplex stainless steel welding joints have been presented [8–10], cracks detected in the HAZ are probably initiated due to poor welding process and unbalanced distribution of ferrite/austenite.

To achieve a high quality welded joint and to ensure long-term corrosion resistance of large structures by

*Corresponding Author Email: ambennabi@gmail.com (A. Bennabi)

using duplex stainless steels, it is recommended to allow a special attention to the welding and the welded joint surface treatment [11–13]. It was established that the mechanical properties vary depending upon the various heat treatment processes. Suitable heat treatment on duplex stainless steel is to improve ductility, toughness, strength, hardness and to relieve internal stress developed in the material [14]. The high service temperatures of the duplex stainless steels often source of secondary phase precipitations (mainly σ phase) should be avoided since they strongly deteriorate the mechanical properties of steels but small quantities of these phases could be acceptable in the microstructure according to the application of this steel [15]. The effect of heat treatments and strain hardening on microstructure and properties of super duplex stainless steels were highlighted. It is noted that quite homogeneous and good mechanical properties can be obtained controlling the composition, the treatment and strain hardening parameters [16, 17].

Multiple welding repairs on pipelines were carried out to evaluate the residual stresses and their effect on the macrostructure, microstructure and mechanical properties [18, 19].

Since the welding of the pipe is not done completely on the straight line (the nature of the pipe) and the test tube under the machine is moving. Pourasad and Afkar [20] designed an algorithm to reduce the environmental conditions and unstable industrial situations in order to track the weld seam with an acceptable speed. One advantage of this method is to reduce the measurement error and the elimination of mechanical and electrical sensors in non-destructive tests.

By using the Tungsten inert gas (TIG) welding process, Salehpour et al. [21] conducted an experimental investigation to determine the mechanical characteristics of the pieces through variation of three main welding parameters including advance speed, welding amperage and preheating temperature. In samples with low advance speed, in addition to increase the solidification time, the coarseness of the structure and the burning of the edges of the welded parts due to the low speed and high amps, reduce the tensile strength. Their results showed also that by increasing the amperage, the strength of welding parts decreases due to the burn defect of the plate edges, which can be minimized by increasing the welding speed and reducing the effect of extreme heat on the edges. Other interesting works may be found in literature [22–24].

In general, most manufacturers do not accept more than two repairs on the same welding joint, and they proceed directly to cutting the joint. The purpose of this work is to study the influence of welding defects of successive repairs on the microstructure and the mechanical properties of the welding joint. The technique adopted in the present work for carrying out the repairs is presented in Figure 1. The advantage of this original technique lies in the fact that the obtained test pieces

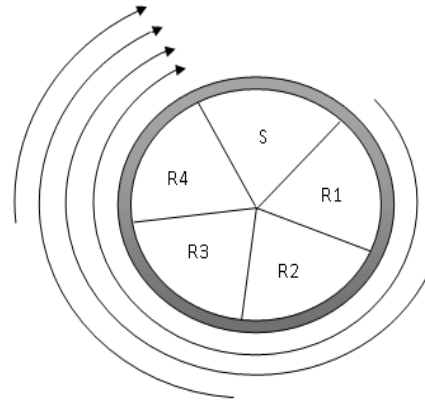


Figure 1. Repair technique on the same welding joint (Repair sequences)

belong to the same coupon, in which the metal used is duplex stainless steel with 22% of chromium intended for the hydrocarbons transmission in particular gases and aggressive products. This study requires the realization of the welded specimens, a visual and radiographic control, an in-depth examination of the micrographic structure, and mechanical tests.

Duplex stainless steels (commonly called DSS) are a class of stainless steels with a microstructure formed by two main phases: ferrite (alpha) and austenite (gamma). They are widely used in the transport of liquid and gaseous hydrocarbons at high pressure, due to their mechanical properties and corrosion resistance.

The steel used for this study is an austeno-ferritic steel called "duplex" because it contains two metallurgical phases, an austenitic phase and a ferritic phase hence the name austeno-ferritic.

This paper is divided into three main sections after the state-of-the art. Section 2 contains the experimental tests, where the details of steps for the preparation of test specimens are provided. Then, the experimental conditions are given in section 3, where the chemical composition and mechanical properties of metals under investigation are highlighted. In section 4, the parameters and process welding are summarized. The main results are plotted and analyzed in section 4.

2. EXPERIMENTAL TESTS

For the preparation of the test specimens used in the present work, a portion of 300 mm length was cut from a pipe of 12 m length, intended for the connection of gas wells to gas center production facilities (CPF), the section was divided into five identical portions and subsequently welded by mixed processes GTAW and shielded metal arc welding (SMAW), while leaving a healthy part and creating defects in the first pass over the rest of the section.

In order to get closer to reality, and for more authenticity and accuracy, the repairs were carried out on the same section and on which a visual and radiographic inspection was carried out before and after the repairs, the first control to locate the defects, the second to ensure that the defects have been completely eliminated.

The details of steps for the preparation of test specimens are as follows:

1. Preparation of samples of Ø8" and wall thickness 8.18 mm, of A928 UNS S31803 material.
2. The partition of the samples in five identical portions.
3. Complete welding of the part first once, while creating defects on the first pass, and leaving the first healthy portion (without any defect).
4. Repair of the four defective portions, for a first time.
5. Repair of the three last portions, for a second time.
6. Repair of the two last portions, for a third time.
7. Repair of the last portions, for a fourth time.
8. Finally we obtain: the first portion only welded once with neither defect nor repair which will be used as a reference part while the other portions will be successively re-paired once, twice, three times and four times at last.
9. A radiographic control carried out before and after repairs.
10. The five portions were cut out longitudinally to carry out the mechanical and micrographic tests.

Samples preparation and images of welded pipeline pieces are presented in Figure 2.

3. EXPERIMENTAL CONDITIONS

The chemical composition and mechanical properties of base metal: ASTM A928 CL1 Ø 8" SCH 40S 219 x 8.18 mm UNS S31803, stainless steel 22 Cr Duplex and two

filler metals welding rod GTAW ER2209 and E2209 coated electrode are given in Tables 1-4 [25].

4. WELDING PROCESS

The welding of the coupons was carried out by a certified welder using GTAW process for first passes with direct polarity and SMAW process for fill and cap passes with positive polarity, uphill position "5G" and direct current. Gas tungsten arc welding is performed with refractory electrode under gas protection with filler metal ER2209 for the first two passes and E2209 for the fill and cap passes (See Tables 5 and 6). The welding processes for the second, third and fourth repairs are summarized in Tables 7-9.

According to hardness values, it can be seen that, the hardness evolution is relatively variable; this can be attributed to the diffusion of Mn and Si from the base metal to the heat-affected zone (HAZ) and the fusion zone (FZ), as well as the concentration of the heat input.

The growth of the grains in the second and third repair is probably due to the repetitive thermal cycles of the welding process, causes a decrease in the hardness in the HAZ. The high hardness of the fusion zone may be related to the formation of acicular ferrite. The hardness values are higher in this region compared to those

TABLE 1. Chemical composition of base metal (BM) (wt%)

C	Si	Mn	Cr	Ni	Mo
0.03	1.0	2.0	22.00	5.5	3.0

TABLE 2. Mechanical properties of base metal (BM)

Yield stress [MPa]	Tensile strength [Mpa]	Elongation [A %]
450	620	25

TABLE 3. Chemical composition of filler metals E2209 and ER 2209 (wt%)

Filler metal	C	Si	Mn	Cr	Ni	Mo	N
E2209	<0.04	0.5	0.9	22.5	9.3	3.0	0.15
ER2209	<0.03	0.5	1.7	22.5	8.5	3.3	<0.3

TABLE 4. Mechanical properties of E2209 and ER2209

Filler metal	Yield stress [MPa]	Tensile strength [MPa]	Elongation [A %]
E2209	650	800	28
ER2209	600	765	28

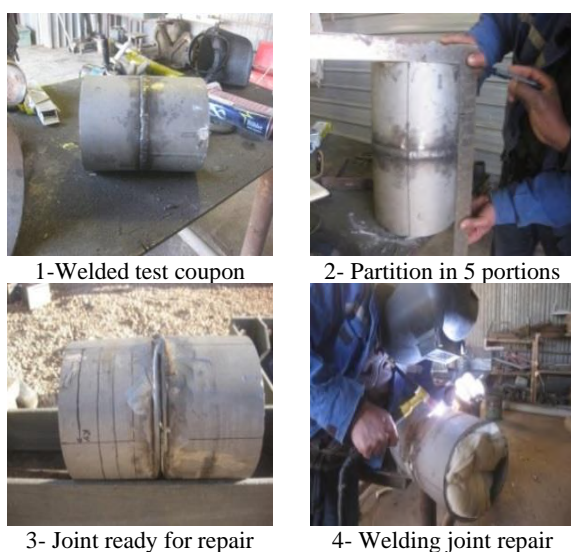


Figure 2. Samples preparation

TABLE 5. Part without repairs

Layers	1 st pass	2 nd pass	3 rd pass	4 th pass
Welding process	GTAW	GTAW	SMAW	SMAW
Welding position	↗ 5 G	↗ 5 G	↗ 5 G	↗ 5 G
Current & polarity	CC (-)	CC (-)	CC (+)	CC (+)
Filler metal	ER 2209	ER 2209	E2209	E2209
ΦElectrode (mm)	-	-	2.5-3,25	2.5-3,25
ΦRod (mm)	2.4	2.4	-	-
Amp. range (A)	100	140	140	100
Volt. range (V)	16	16	16	22
Travel speed (mm/mn)	9.85	19.71	15.33	15.33
Gas	Argon	Argon	-	-
Heat Input (kJ/mm)	36.548	6.818	101.052	8.610

TABLE 6. First repair (R1)

Layers	1 st pass	2 nd pass	3 rd pass	4 th pass
Welding process	GTAW	GTAW	SMAW	SMAW
Welding position	↗ 5 G	↗ 5 G	↗ 5 G	↗ 5 G
Current & polarity	CC (-)	CC (-)	CC (+)	CC (+)
Filler métal	ER 2209	ER 2209	E2209	E2209
Φ Electrode (mm)	-	-	2.5-3,25	2.5-3,25
ΦRod (mm)	2.4	2.4	-	-
Amp. range (A)	75	70	70	70
Volt. range (V)	10	30	30	30
Travel speed (mm/mn)	11.5	34.5	23	34.5
Gas	Argon	Argon	-	-
Heat input (kJ/mm)	3.913	3.652	5.478	3.652

TABLE 7. Second repair (R2)

Layers	1 st pass	2 nd pass	3 rd pass	4 th pass
Welding process	GTAW	GTAW	SMAW	SMAW
Welding position	↗ 5 G	↗ 5 G	↗ 5 G	↗ 5 G
Current & polarity	CC (-)	CC (-)	CC (+)	CC (+)
Filler métal	ER 2209	ER 2209	E2209	E2209
F Electrode (mm)	-	-	2.5-3,25	2.5-3,25
F Rod (mm)	2.4	2.4	-	-
Amp. range (A)	80	60	60	70
Volt. range (V)	30	25	25	25
Travel speed (mm/mn)	19.71	34.5	34.5	19.71
Gas	Argon	Argon	-	-
Heat input (kJ/mm)	7.305	0.260	2.608	5.327

TABLE 8. Third repair (R3)

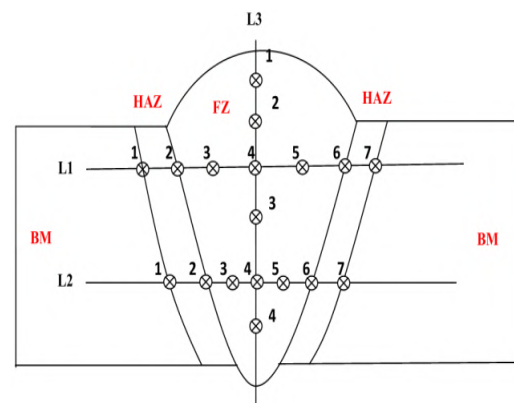
Layers	1 st pass	2 nd pass	3 rd pass	4 th pass
Welding process	GTAW	GTAW	SMAW	SMAW
Welding position	↖5 G	↖5 G	↖5 G	↖5 G
Current & polarity	CC (-)	CC (-)	CC (+)	CC (+)
Filler métal	ER 2209	ER 2209	E2209	E2209
ΦElectrode (mm)	2.4	2.4	2.5-3,25	2.5-3,25
ΦRod (mm)	-	-	-	-
Amp. range (A)	70	70	70	70
Volt. range (V)	21	20	19	25
Travel speed (mm/mn)	27.6	46	46	34.5
Gas	Argon	Argon	-	-
Heat input (kJ/mm)	3.195	1.826	1.734	3.043

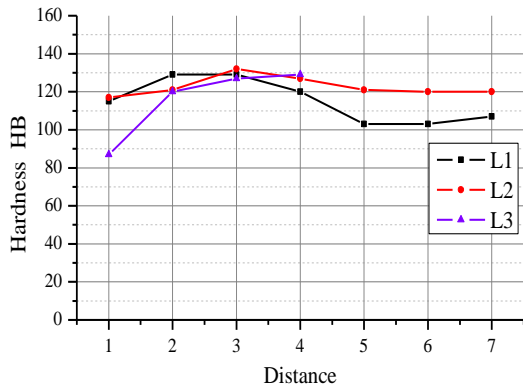
TABLE 9. Fourth repair (R4)

Layers	1 st pass	2 nd pass	3 rd pass	4 th pass
Welding process	GTAW	GTAW	SMAW	SMAW
Welding position	↖5 G	↖5 G	↖5 G	↖5 G
Current & polarity	CC (-)	CC (-)	CC (+)	CC (+)
Filler métal	ER 2209	ER 2209	E2209	E2209
ΦElectrode (mm)	-	-	2.5-3,25	2.5-3,25
ΦRod (mm)	2.4	2.4	-	-
Amp. range (A)	80	60	60	70
Volt. range (V)	30	25	25	25
Travel speed (mm/mn)	19.71	34.5	34.5	19.71
Gas	Argon	Argon	-	-
Heat input (kJ/mm)	7.305	0.260	2.608	5.327

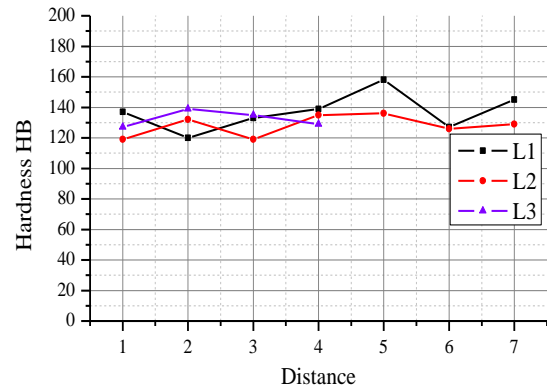
observed in the lower part (root pass). The refining of grains and the increase in the density of dislocations in the HAZ of the first repair increases the hardness. However, the molten metal of the weld is not homogeneous, which is the case for all multi-pass welds (Figure 4). The internal pass has higher hardness than the external pass, which can be explained by a slower cooling when welding the external pass.

The values of hardness are homogeneous and acceptable according to ASTM specification, whether in the longitudinal or transverse direction, since the succession of passes give a similar effect to heat treatments as noted in Figure 4.

**Figure 3.** Hardness points measurements

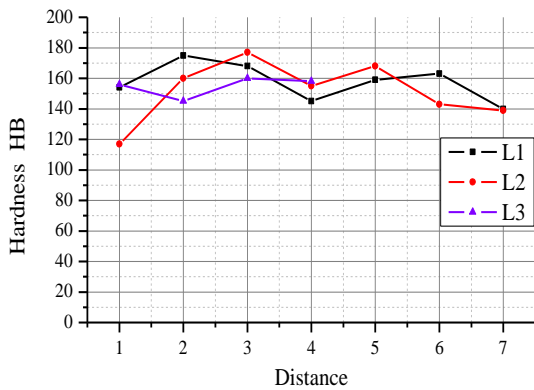


a) Hardness without repair

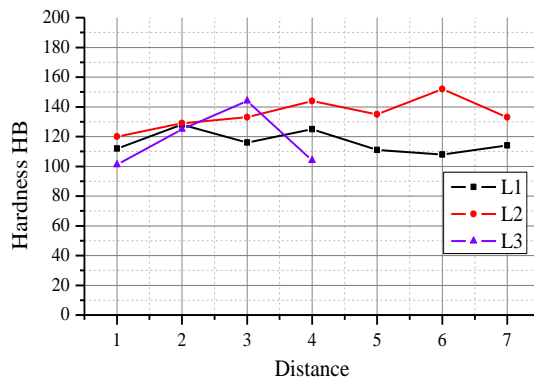


e) Hardness after fourth repair R4

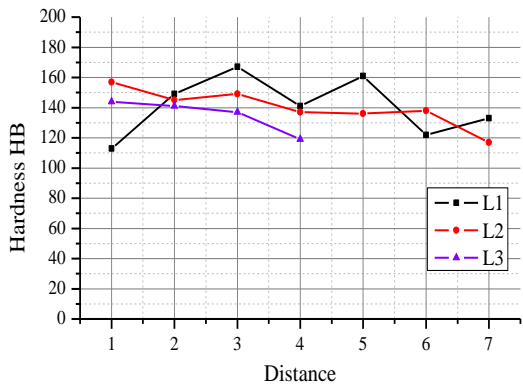
Figure 4. Hardness values a) before repair, b-e) after successive repairs



b) Hardness after first repair R1



c) Hardness after second repair R2



d) Hardness after third repair R3

5. 1. Mechanical Tests

Mechanical bending and tensile tests were carried out on a conventional machine; for the resilience tests, V shape specimens were used. Notched specimens results are gathered in Table 10.

This table illustrates the values corresponding to the tensile strength (Rm). An increase in the tensile strength for the specimens test R1 and R3 is observed, while the tensile strength values remain close to that of the base metal for the test specimens R2 and R4. Nevertheless, the values of the resilience display a minimum for specimen R1 and a maximum for R4. The values of the resilience remain substantially constant for S, R2 and R3 specimens.

Tensile tests reveal that rupture is located out of joint for the four repairs. The bending tests for both face and root test reveal nothing to report close to the joint.

The fourth repair R4 has absorbed a high energy compared to that of the initial weld; this can be attributed to both the grain refinement and the high dislocation density recorded in the HAZ. In addition, a slight decrease in energy in R2 and R4 was observed (126 and 166 J/cm², respectively). This may be related to the grain growth observed in the area near the melting line in accordance with a significant decrease in dislocation density. The toughness loss is due to the presence of hard and brittle constituents known by their low resistance to cracking distributed along the grain boundaries which generates a stress concentration zone, which allows the formation of micro-cracks in the constituents and thus a drop of the toughness.

5. 2. Radiographic Inspection

Radiographic inspections were carried out by means of the gamma rays Ir192, D7 films gave the following stereotypes before repair (Figure 5) and after repairs (Figure 6).

TABLE 10. Mechanical tests results

Tensile strength		Bending test		Impact test KCV [J/cm ²]	Elongation [A%]
Rm [MPa]	Rupture	Face bend	Root bend		
Sample without repair (Healthy part) S					
690	Out of joint	NTR	NTR	167	3.12
Sample with only one repair R1					
987	Out of joint	NTR	NTR	126	6.25
Sample with two repairs R2					
670	Out of joint	NTR	NTR	161	4.51
Sample with three repairs R3					
860	Out of joint	NTR	NTR	166	7.26
Sample with four repairs R4					
690	Out of joint	NTR	NTR	186	6.66

NTR: Nothing to report

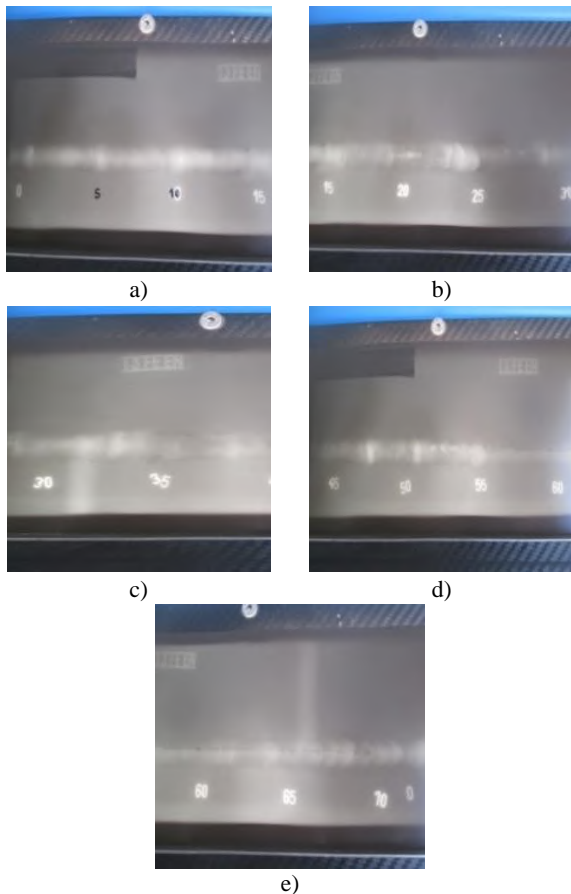


Figure 5. Radiographic stereotypes before repairs

Radiographic films present concavity defects from 25 to 30 (Figure 5b), lack of matter and excess of penetration from 20 to 25 (Figures 5b and 5d), an undercut defect from 35 to 40 (Figure 5c), a concavity and lack of fusion

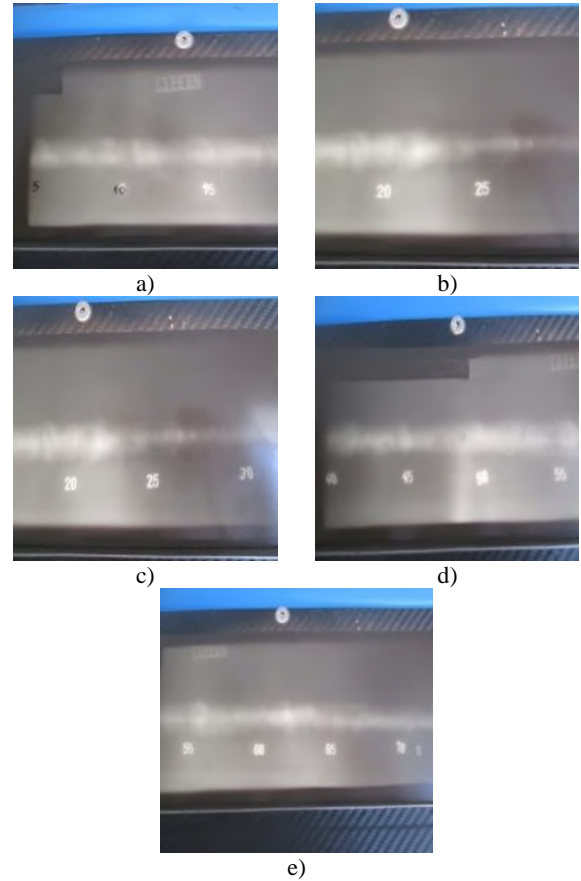


Figure 6. Radiographic stereotypes after repairs

from 55 to 60 (Figure 5d), and a film presenting a lack of penetration from 60 to 70 (Figure 5e).

This film (Figure 6c) shows the grinding traces from 22 to 32. All the rest of stereotypes reveal joints with acceptable defects.

5. 3. Metallography A semi-automatic polishing was carried out with abrasive papers (120, 150, 180 400, 500, 600, 1000, and 1200, respectively) followed by chemical etching in HCl solution with concentration ranging from 35% to 38. This steps are highly recommended for preparation of specimen surface which allows highlighting the metallographic structures for microscopic analysis.

The semi-automatic polishing allows a fast polishing; the holding of the sample is manual but the polishing action is automatic. It is effective in the case of samples taken from pipes whose shape is not flat.

The metallographic control for healthy(S) and repaired (R1 to R4) samples gave the micrographs represented in Figures 7-11.

The visual aspect of all the parts has an homogeneous structure without apparent defects, the succession of the passes is not visible (fillers of even similar close nuances).

Metallographic samples were prepared in welding joint cross-section. The micrographs using light microscopy up to 400X illustrate an austenitic-ferritic

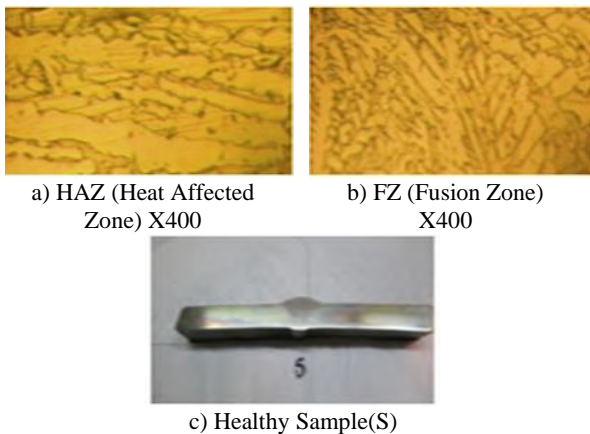


Figure 7. Micrographs before repair

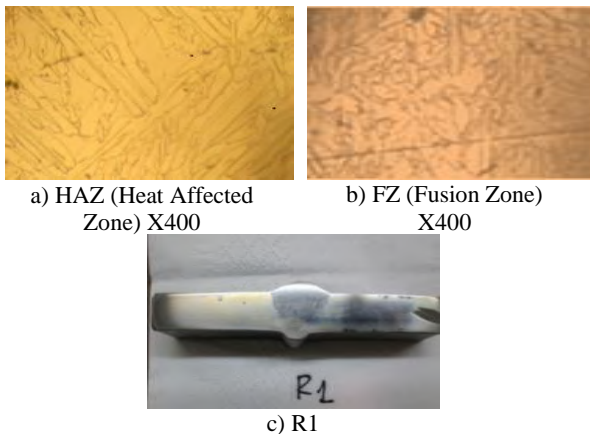


Figure 8. Micrographs after the first repair

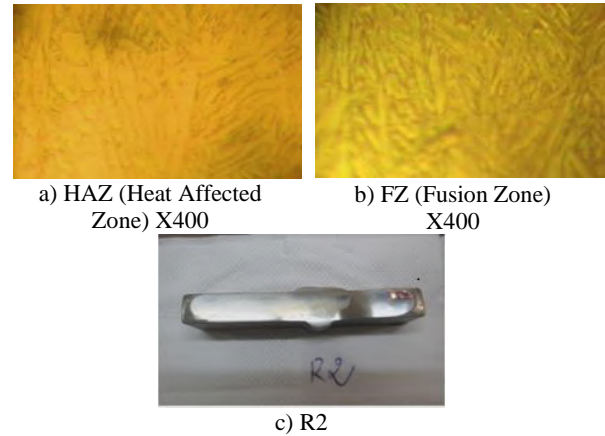


Figure 9. Micrographs after the second repair

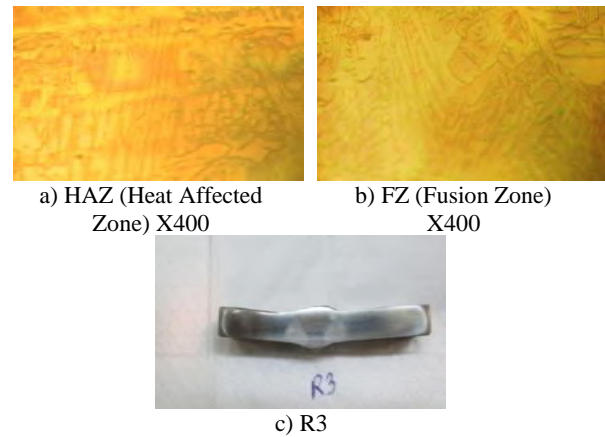


Figure 10. Micrographs after the third repair

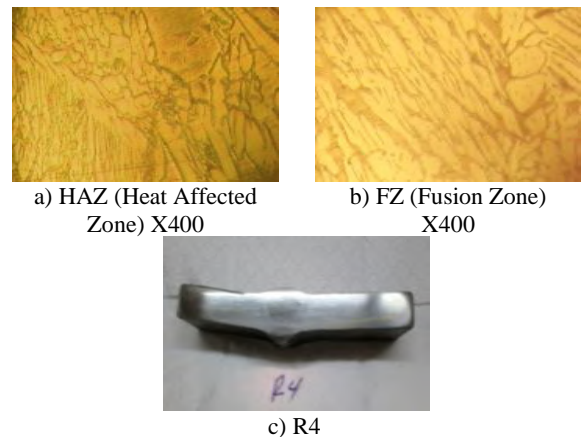


Figure 11. Micrographs after fourth repairs

two-phase structure, the dark color is ferrite while the light color is austenite, we also notice the absence of the sigma phase as shown in Figure 12. The heat affected area width is from 2 to 4 mm and it is similar from R1 to R4.

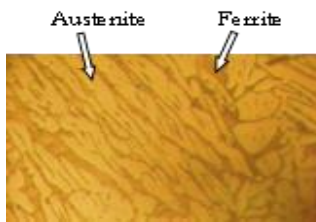


Figure 12. Ferrite dark and austenite light 400X

The heat affected zone presents a microstructure with fine grains, we notice that the number of repairs does not have any influence on morphologies of the HAZ microstructure, since the thermal cycles repeated during each repair lead to the same transformations.

6. CONCLUSIONS

The effect of multiple repairs on the quality of duplex welded joints has been investigated by experiments. The visual aspect of the healthy part had an intact surface quality and unaltered by the operation of grinding. The latter decreased the thickness of the base metal on the two edges of the groove. This reduction was about 0.2 mm for the first repair and 0.8 mm for the fourth repair. The reduced thickness does not have an impact on the mechanical properties of the welding joint and it can be easily avoided by a careful grinding.

All welding joint showed higher strength than the parent metal since tensile tests revealed that the tensile coupon failure was localized outside the welding joint for all of the four repairs.

The obtained results showed that the succession of repairs in the same place of the welding does not have any harmful effect on the mechanical properties of the welding joint. The successive repairs allow performing several repairs without a problem, saving thus a valuable time and effort for the production instead of cutting the entire joint and welding it again.

7. REFERENCES

- Liou, H.-Y., Hsieh, R.-I., and Tsai, W.-T. "Microstructure and stress corrosion cracking in simulated heat-affected zones of duplex stainless steels." *Corrosion Science*, Vol. 44, No. 12, (2002), 2841–2856. [https://doi.org/10.1016/S0010-938X\(02\)00068-9](https://doi.org/10.1016/S0010-938X(02)00068-9)
- Wang, H.-S. "Effect of Welding Variables on Cooling Rate and Pitting Corrosion Resistance in Super Duplex Stainless Weldments." *Materials Transactions*, Vol. 46, No. 3, (2005), 593–601. <https://doi.org/10.2320/matertrans.46.593>
- Ravindranath, K., and Malhotra, S. N. "The influence of aging on the intergranular corrosion of 22 chromium-5 nickel duplex stainless steel." *Corrosion Science*, Vol. 37, No. 1, (1995), 121–132. [https://doi.org/10.1016/0010-938X\(94\)00120-U](https://doi.org/10.1016/0010-938X(94)00120-U)
- Gideon, B., Ward, L., and Biddle, G. "Duplex Stainless Steel Welds and their Susceptibility to Intergranular Corrosion." *Journal of Minerals and Materials Characterization and Engineering*, Vol. 07, No. 03, (2008), 247–263. <https://doi.org/10.4236/jmmce.2008.73019>
- Muthupandi, V., Bala Srinivasan, P., Seshadri, S. K., and Sundaresan, S. "Effect of weld metal chemistry and heat input on the structure and properties of duplex stainless steel welds." *Materials Science and Engineering: A*, Vol. 358, No. 1–2, (2003), 9–16. [https://doi.org/10.1016/S0921-5093\(03\)00077-7](https://doi.org/10.1016/S0921-5093(03)00077-7)
- Paulraj, P., and Garg, R. "Effect of intermetallic phases on corrosion behavior and mechanical properties of duplex stainless steel and super-duplex stainless steel." *Advances in Science and Technology Research Journal*, Vol. 9, (2015), 87–105. <https://doi.org/10.12913/22998624/59090>
- Chan, K., and Tjong, S. "Effect of Secondary Phase Precipitation on the Corrosion Behavior of Duplex Stainless Steels." *Materials*, Vol. 7, No. 7, (2014), 5268–5304. <https://doi.org/10.3390/ma7075268>
- Yang, J., Wang, Q., Wei, Z., and Guan, K. "Weld failure analysis of 2205 duplex stainless steel nozzle." *Case Studies in Engineering Failure Analysis*, Vol. 2, No. 2, (2014), 69–75. <https://doi.org/10.1016/j.csefa.2014.05.001>
- Ibrahim, O. H., Ibrahim, I. S., and Khalifa, T. A. F. "Effect of Aging on the Toughness of Austenitic and Duplex Stainless Steel Weldments." *Journal of Materials Science & Technology*, Vol. 26, No. 9, (2010), 810–816. [https://doi.org/10.1016/S1005-0302\(10\)60129-6](https://doi.org/10.1016/S1005-0302(10)60129-6)
- Ibrahim, O. H., Ibrahim, I. S., and Khalifa, T. A. F. "Impact behavior of different stainless steel weldments at low temperatures." *Engineering Failure Analysis*, Vol. 17, No. 5, (2010), 1069–1076. <https://doi.org/10.1016/j.engfailanal.2009.12.006>
- Pankaj, P., Tiwari, A., Biswas, P., Rao, A. G., and Pal, S. "Experimental studies on controlling of process parameters in dissimilar friction stir welding of DH36 shipbuilding steel–AISI 1008 steel." *Welding in the World*, Vol. 64, No. 6, (2020), 963–986. <https://doi.org/10.1007/s40194-020-00886-3>
- Prater, T. "Friction Stir Welding of Metal Matrix Composites for use in aerospace structures." *Acta Astronautica*, Vol. 93, (2014), 366–373. <https://doi.org/10.1016/j.actaastro.2013.07.023>
- Nowacki, J., and Zajac, P. "Mechanical properties of duplex steel welded joints in large-size constructions." *Welding International*, Vol. 26, No. 6, (2012), 424–435. <https://doi.org/10.1080/09507116.2011.581345>
- Tahchieva, A., Llorca-Isern, N., and Cabrera, J.-M. "Duplex and Superduplex Stainless Steels: Microstructure and Property Evolution by Surface Modification Processes." *Metals*, Vol. 9, No. 3, (2019), 347. <https://doi.org/10.3390/met9030347>
- Santos, T. F. de A., López, E. A. T., Fonseca, E. B. da, and Ramirez, A. J. "Friction stir welding of duplex and superduplex stainless steels and some aspects of microstructural characterization and mechanical performance." *Materials Research*, Vol. 19, No. 1, (2016), 117–131. <https://doi.org/10.1590/1980-5373-MR-2015-0319>
- Miodownik, A. P., and Saunders, N. "Modelling of materials properties in duplex stainless steels." *Materials Science and Technology*, Vol. 18, No. 8, (2002), 861–868. <https://doi.org/10.1179/026708302225004694>
- Paulraj, P., and Garg, R. "Effect of welding parameters on mechanical properties of GTAW of UNS S31803 and UNS S32750 weldments." *Manufacturing Review*, Vol. 2, (2015), 29. <https://doi.org/10.1051/mfreview/2015032>
- Contreras, A., Hernández, S., Galvan, R., and Vega, O. "The Influence of Multiple Welding Repairs of Pipelines in Residual Stress Assessment Related to Stress Corrosion Cracking." *British Journal of Applied Science & Technology*, Vol. 6, No. 6, (2015),

- 621–634. <https://doi.org/10.9734/BJAST/2015/14931>
19. Mauliddin, D. S., and Ginta, T. L. "The effect of repeated welding cycles on the properties of 25Cr super duplex stainless steel by automatic orbital TIG welding." *ARPN Journal of Engineering and Applied Sciences*, Vol. 11, No. 14, (2016), 8754–8758.
 20. Pourasad, Y., and Afkar, A. "A study on the modified algorithm for image processing in Tracking Seam Welding." *International Journal of Engineering, TransactionB: Applications*, Vol. 34, No. 8, (2021), 1913–1922. <https://doi.org/10.5829/ije.2021.34.08b.13>
 21. Salehpour, F., Nematifard, V., Maram, G., and Afkar, A. "Experimental Investigation of TIG Welding Input Parameters Effects on Mechanical Characteristics." *International Journal of Engineering, TransactionB: Applications*, Vol. 34, No. 2, (2021), 564–571. <https://doi.org/10.5829/ije.2021.34.02b.30>
 22. Hoseinzadeh, S., and Heyns, P. S. "Thermo-structural fatigue and lifetime analysis of a heat exchanger as a feedwater heater in power plant." *Engineering Failure Analysis*, Vol. 113, (2020), 104548. <https://doi.org/10.1016/j.engfailanal.2020.104548>
 23. Ahmadpar, M., Hoseinzadeh, S., Nakhacai, F., and Memon, S. "Experimental Modal Analysis of Distinguishing Microstructural Variations in Carbon Steel SA516 by Applied Heat Treatments, Natural Frequencies, and Damping Coefficients." *Journal of Materials Engineering and Performance*, Vol. 30, No. 12, (2021), 9256–9261. <https://doi.org/10.1007/s11665-021-06125-0>
 24. Ramezani, A. H., Hoseinzadeh, S., Ebrahiminejad, Z., Hantehzadeh, M. R., and Shafiee, M. "The study of mechanical and statistical properties of nitrogen ion-implanted Tantalum bulk." *Optik*, Vol. 225, (2021), 165628. <https://doi.org/10.1016/j.ijleo.2020.165628>
 25. Wang, S., Ma, Q., and Li, Y. "Characterization of microstructure, mechanical properties and corrosion resistance of dissimilar welded joint between 2205 duplex stainless steel and 16MnR." *Materials & Design*, Vol. 32, No. 2, (2011), 831–837. <https://doi.org/10.1016/j.matdes.2010.07.012>

Persian Abstract

چکیده

فولادهای زنگ نزن دوبلکس (DSS) به عنوان جایگزینی برای فولادهای زنگ نزن آستیل در صنایع نفت، گاز و پتروشیمی، به ویژه در محیط‌های تهاجمی، کاربرد روزافزونی پیدا می‌کنند. فولادهای ضد زنگ دوبلکس با تعادل فریت-آستنیت کنترل شده مناسب، خواص جذاب استحکام عالی، عملکرد خوردگی عمومی و جوش‌پذیری کافی را ترکیب می‌کنند. قبل از راه‌اندازی خط لوله و حتی قبل از آزمایشات هیدرواستاتیک، کلیه اتصالات جوشکاری که تحت مقررات تنظیم می‌شوند باید کنترل شوند. تمام عیوب غیرقابل قبول شناسایی شده با روش‌های کنترل NDT باید حذف شوند. در برخی موارد، به دلیل عدم تجربه جوشکار در انجام تعمیرات یا عدم تخصص کنترل‌کننده که اجرای روش جوشکاری را تضمین می‌کند، معمولاً چندین تعمیر متوالی به تعویض قطعه در خط لوله ترجیح داده می‌شود. هدف از این کار بررسی تأثیر تعمیرات روی همان اتصال جوشی بر روی ریزساختار و خواص مکانیکی ناحیه متأثر از حرارت در فولاد ضد زنگ دوبلکس با اتصالات جوشکاری کروم ۲۲ درصد است. برای این منظور یک نمونه استوانه‌ای تهیه می‌شود که تعمیرات مختلف روی آن انجام می‌گیرد. سپس یک کنترل NDT و آزمایشات مکانیکی و میکروگرافیک اصلی انجام گرفت. نتایج به‌دست‌آمده پس از چهار تعمیر نشان داد که تعمیرات متعدد انجام‌شده در یک اتصال بر کیفیت اتصالات جوش تأثیری ندارد.



Experimental Examination of Gas-liquid Two-phase Flow Patterns in an Inclined Rectangular Channel with 90° Bend for Various Vertical Lengths

M. Vatani, D. Domiri Ganji*

Department of Mechanical Engineering, Babol University of Technology, Babol, Iran

PAPER INFO

Paper history:

Received 17 Octobr 2021

Received in revised form 02 December 2021

Accepted 23 December 2021

Keywords:

Flow Pattern Map

Churn Flow

Vertical Length

Rectangular Channel

90° Bend

Froude Number

A B S T R A C T

In order to realize the behavior of two-phase flow in an inclined rectangular channel with 90° bend for various vertical lengths, an experimental investigation has performed. The test section (a channel with 30 m length) contains two horizontal parts and a middle vertical section. Three vertical lengths of 50, 100 and 150 cm were utilized along the test section. The cross section of the rectangular channel is 10 cm × 15 cm. Air and water were the fluids used in this work. Various flow patterns are created by varying the volumetric flow-rates of gas and liquid; the air and water flow rates were in the range of 2 to 10 m³/h and 34 to 235m³/h, respectively. The high speed video system was utilized to achieve image subsequence of the flow under various conditions. The effects of vertical length on flow regimes and pattern transition borders are examined. According to the flow visualization, no vortex was observed in the vertical section. The significant flow regime in the vertical section is churn flow regime. It is concluded that the flow pattern structures are not greatly affected by changing the vertical length.

doi: 10.5829/ije.2022.35.04a.07

1. INTRODUCTION

Two-phase flows are of considerable interest to many industries such as power generation, thermal hydraulic reactor system, chemical plants and food production. The two-phase flow in a rectangular channel has attracted special research interest in recent decades owing to its numerous applications such as in plate type nuclear fuels [1–3], high performance micro-electronics [4, 5] and polymer melt filling process [6–8].

In the previous decades, many researchers have concentrated on comprehensive two-phase flow treatment utilizing experimental system and modeling numerical methods. However, most of these studies are focused on two phase flow in horizontal and vertical systems with little consideration given to this phenomenon in different pipe inclinations between horizontal and vertical. Regarding to the great utilization of pipe lines transferring two-phase flow in chemical and petroleum equipments, it is necessary to investigate the effect of channel inclination on the two-phase flow cases.

When two-phase flows move along a pipe or channel, various flow patterns can be created, affected by different variables. Many flow patterns have been investigated by number of researchers in horizontal, vertical and inclined pipes or channels. Wilmarth and Ishii [9, 10] perceived the flow patterns and measured the void fraction and the interfacial area concentration of adiabatic co-current vertical and horizontal air-water flow in narrow rectangular channels with gaps of 1 and 2 mm. Nguyen [11] and Beggs [12] examined two-phase flow pattern, pressure drop and hold-up of the flow in a pipe with different inclinations. Hasan and Kabir [13] investigated a model for approximating void fraction of two-phase flow through vertical and inclined annuli. Four flow regimes of bubbly, slug, churn and annular flow are identified in the study. Ghiaasiaan et al. [14] experimentally investigated the counter-current two-phase flow in vertical and inclined channels. They explored the influences of liquid properties on void fraction and two-phase flow patterns. Barnea et al. [15] accomplished two-phase flow experiments in inclined

*Corresponding Author Institutional Email: mirgang@nit.ac.ir
(D. D. Ganji)

tubes. It is concluded that bubbly and churn flow are formed for the inclination higher than 50° and 70° , respectively. Oddie et al. [16] carried out two-phase examinations on an inclined pipe. They investigated flow pattern map for various inclination angles. Wongwises and Pipathattakul [17] investigated void fraction, pressure drop and flow patterns of two-phase flow in a narrow annular channel with horizontal and inclined orientation. The plug, slug, annular, bubbly-plug, bubbly-slug, churn, and distributed bubbly flow patterns were perceived in the research. The results demonstrated that the inclination angle affect greatly on the transition of the flow pattern, void fraction and pressure drop. Ali et al. [18] examined two-phase flow in a capillary channel between two plates with various directions consisting horizontal, vertically downward and upward and inclined. They evaluated the flow pattern and average and local void fraction for all direction. Bhagwat and Ghajar [19, 20] experimentally studied the gas-liquid two-phase flow in upward and downward inclined pipes. The results display a great influence of the pipe inclination on two-phase flow structure and the two-phase flow variables at small amounts of gas and liquid flow-rates. Kim et al. [21] studied the flow regimes of two-phase flow through a downward rectangular channel. The results show some different flow patterns such as falling film flow pattern and large-bubbly flow which identified in the low liquid superficial velocity wherever buoyancy force has a great influence. Resemblance and differences between vertically downward and upward churn flow are perused by Bouyahiaoui et al. [22]. It is concluded that the structure velocity through vertical downward flow is greater than vertical upward flow.

Compared with vertical and horizontal two-phase flow, a little data is accessible about two-phase flow in inclined channel. To investigate the present extent of knowledge, the significant purpose of this study is experimentally examine the influence of upward channel inclination (horizontal to vertical) on two-phase flow. To achieve this purpose, examinations of concentrated on flow visualization in gas-liquid two-phase flow were performed in 30 m channel utilizing air and water as fluid for the two phase flow system.

2. EXPERIMENTAL APPARATUS

The experimental setup displayed in Figure 1 is utilized for two-phase flow system that contains two horizontal sections and variable vertical sections. The test section made of transparent Plexiglas plates is utilized for flow visualization. The air supplied by compressor first moved through an air filter and pressure regulator. An air cooling system was utilized to decrease the high pressure and temperature of the compressed air. Next, the air is

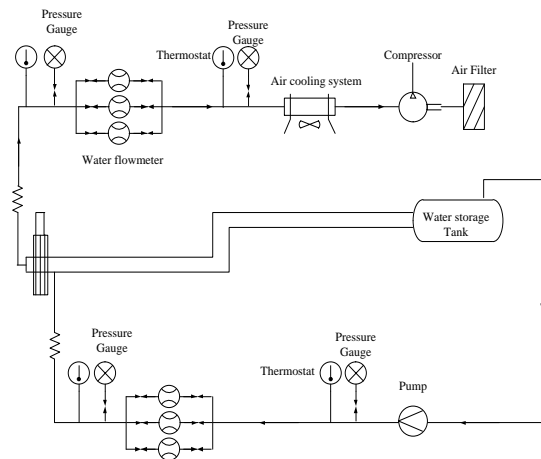


Figure 1. Deposition efficiency on a single square in channel

transported to gas mass flow-meters where the mass flow rate of air is adjusted accurately. The compressed air is then transmitted through a mixer to enter the test section. The liquid phase contains pure water supplied in a water tank is circulated in the setup utilizing a centrifugal pump. The pure water is then moved through a mass flow-meter where the flow-rate of the liquid phase is controlled. Afterwards, the water is permitted to mix with air at T-type mixer. The gas and liquid volumetric flow-rates were modified in an area of 2 to 10 m^3/h and 34 to 235 m^3/h , respectively. The system pressure is at atmospheric pressure and the system temperature is maintained at 25°C . The uncertainty related to measurements of mass flow-rates of air and water is approximated to be between $\pm 4\%$ and $\pm 10\%$, respectively. The thermocouples were utilized to evaluate temperatures at some positions in the experimental setup and the pressure gauges are used to measure pressure at some locations of the setup. The uncertainty of temperature measurements is $\pm 1^\circ\text{C}$.

Experiments were performed at several gas and liquid mass flow-rates, different vertical lengths of the channel. The bend of 90° was joined to the horizontal and vertical sections utilizing flanges. The bend is made of laser cutting Plexi-glass plates. Different length of channels including 50, 100 and 150 cm were utilized in the vertical section of the experimental setup to survey the effect of vertical section on the flow patterns.

3. RESULTS AND DISCUSSIONS

This section exhibits the result of flow visualization of two-phase flow in an inclined rectangular channel with 90° bend for various vertical lengths. The various flow patterns were created by systematically modified volumetric flow-rates of gas and liquid in the range of 2 to 10 m^3/h and 34 to 235 m^3/h , respectively. Based on the

observations, slug, churn and annular-mist flow are the significant flow regimes perceived in the vertical section of the channel. The physical appearance of these flow regimes in vertical section is demonstrated in Figures 2-4.

Flow pattern maps are depicted for different cases with the superficial air velocity varying between 1 and 20 m/s and superficial water velocity varying between 0.08 and 0.6 m/s . Three distinguished flow regimes are seen in vertical section concluding slug, churn and annular-mist flow regimes described as follows:

- Slug flow

An alternative mass of liquid comes into the vertical section and at the time the major mass of the liquid proceed the middle section, a little part of liquid comes downward. Also, another liquid mass goes upward and when these counter-current flows contact each other, some vortices are formed on the interface of the two phases of air and water. As a result, the liquid hold-up gets larger and consequently the gas phase appears as bubbles with a bullet shape in the liquid phase. The velocity of liquid phase is reduced due to this contrary flow.

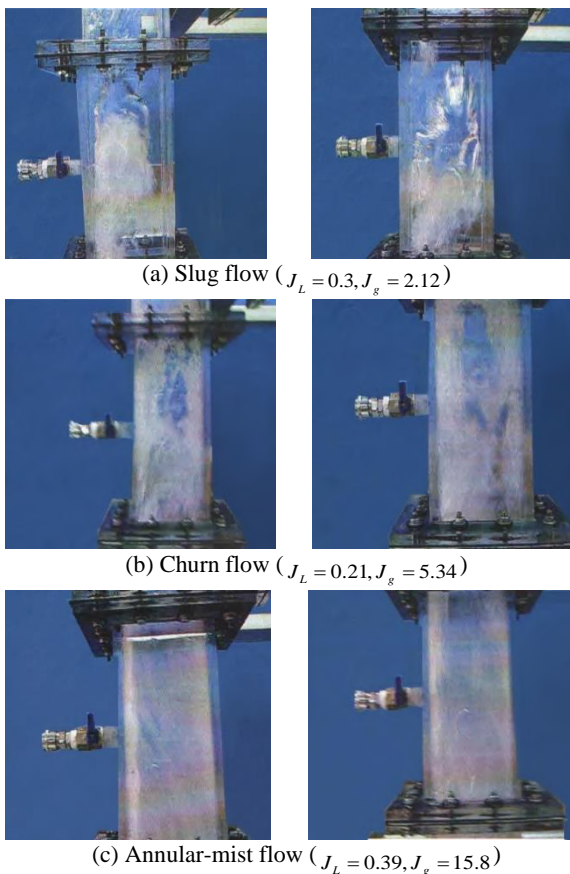


Figure 2. Flow regimes in horizontal-vertical-horizontal rectangular channel with vertical length of 0.5 m (a) Slug flow, (b) Churn flow, and (c) Annular-mist flow

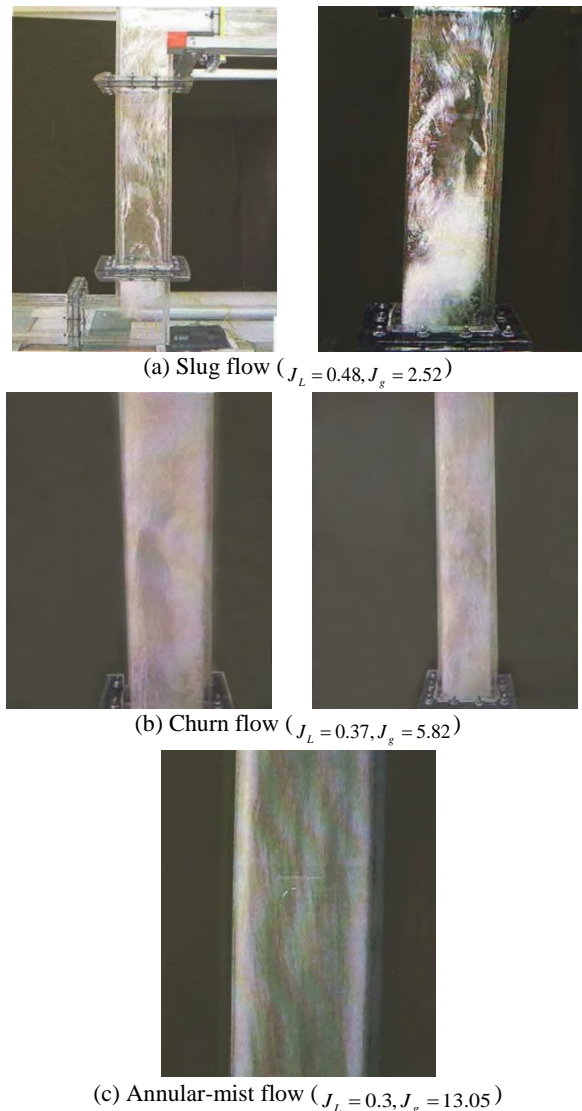


Figure 3. Flow regimes in horizontal-vertical-horizontal rectangular channel with vertical length of 1 m (a) Slug flow, (b) Churn flow, and (c) Annular-mist flow

- Churn flow

This pattern treat like the slug pattern, but the characteristic of disturbance and turbulence is distinct from that of slug flow. At greater liquid and gas superficial velocities, the flow became disordered and frothy. Churn flow is appeared by a failure of the slug flow bubbles. This causes an oscillatory movement, like the liquid down-ward and up-ward flow in the vertical section.

- Annular-mist flow

As mentioned in the previous studies, the main characteristic of annular flow is the conjunction of gas phase along the channel length. Also, the liquid phase reveals as an oscillating liquid film on the channel wall. With a greater increment in the gas flow-rate, the liquid

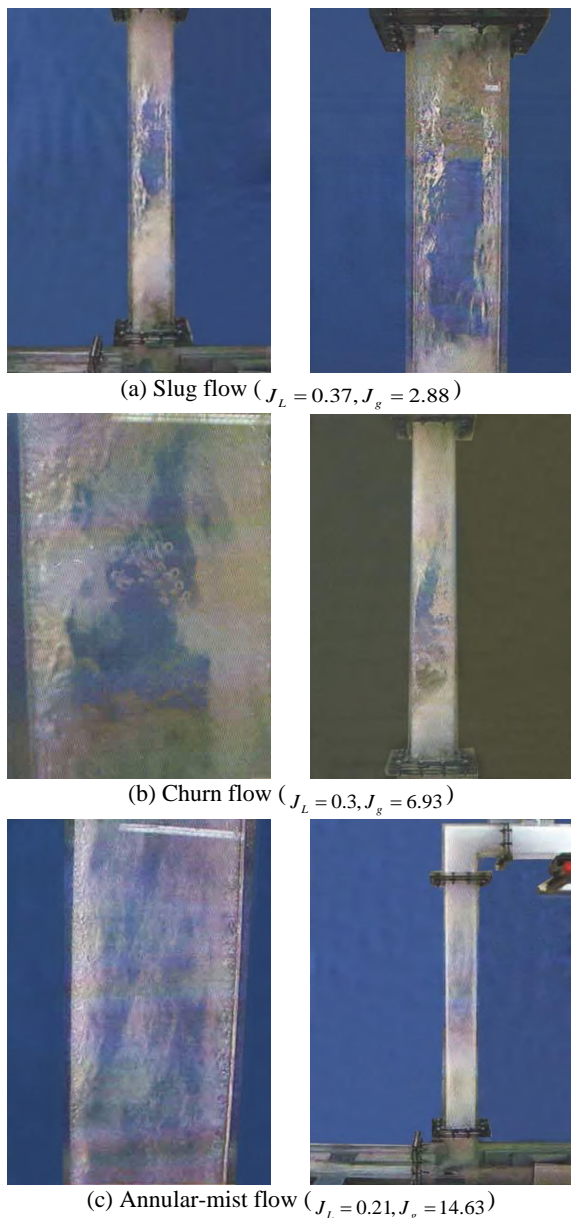


Figure 4. Flow regimes in horizontal-vertical-horizontal rectangular channel with vertical length of 1.50 m (a) Slug flow, (b) Churn flow, and (c) Annular-mist flow

slug is broke down and a consecutive gas core is created. In an annular-mist flow, the liquid current is not enough to sustain bridging liquid slug. A considerable volume of air bubbles is distributed in water which is now moving as layers nearby the walls. The water layer surface shows a great size of wavy flow. With a greater increment of the gas flow-rate, this wave size was observed to be withdrawing.

The observed flow regimes for the vertical length of 0.5 m are shown in Figure 2. Three different flow regimes, namely slug flow, churn flow and annular-mist flow are observed. Compared with the previous

researches for inclined and vertical pipe, bubbly flow was not seen for the present study at lower liquid and gas flow-rates. The reason is that air and water go into the vertical part of channel in a distinguished pattern at upstream of the channel. It causes the liquid phase obstructed air flow in the inclined bend and the gas flow is fastened, totally. Enhancing the mass flow-rate of the gas phase causes the pressure of air increased and the slug flow is formed instead of bubbly flow. At small amount of liquid mass flow-rate, pressure drop according to the vertical line is more than two-phase momentum, so water condensed at 90° bend and therefore the significant flow pattern at low liquid flow-rate is slug flow. With enhancing gas flow-rate, the formed bubble in the slug flow is disfigured and the flow regime disorganized and therefore the churn flow is formed. For higher gas flow-rat, gas shear force conducted liquid phase into the walls of the channel, thus the annular flow is formed.

Further pictures taken at close range by high speed camera for the vertical length of 1 m are presented in Figure 3. In this case, by increasing the vertical length, the size of Taylor bubbles is enhanced. As the length of the vertical section increased, the gravity force dominates the kinetic energy of the two-phase mixture, thus the droplets of liquid phase return into the Taylor-bubbles. Thus, the interface of two-phase became disordered. The closer it got to the end of the middle section, the more deformation caused for the Taylor bubble.

Figure 4 shows two-phase flow regimes for e rectangular channel with vertical length of 1.5 m. It can be seen that the area of the churn flow extended for higher vertical section. According to that the transition from the churn flow and annular-mist occurred gradually, the distinctive characteristic between these two flows is forward and backward flow in the churn flow pattern. Thus, for the vertical length of 150 cm, by increasing the riser length, the observed flow became more distorted, frothy and bubbly. It can be concluded that the outstanding flow regime in the present examination is churn flow. The main influence of enhancing the vertical length is greater back-ward flow. Enlarging the vertical section causes the momentum of liquid to disintegrate due to the effect of gravitational force and greater pressure drop.

Flow visualizations at various vertical lengths display that the flow pattern structures are not greatly varied by changing the vertical length. The change in upward middle section has an influence on the transition boundaries between various flow patterns. The flow pattern maps with transition boundaries between various flow patterns for different vertical lengths are exhibited in Figures 5-7.

These flow pattern maps are introduced by utilizing gas and liquid superficial velocities (U_{sg} and U_{sl}) as frame of references. As a result, these flow pattern maps are introduced to be utilized for affiliating the evaluated

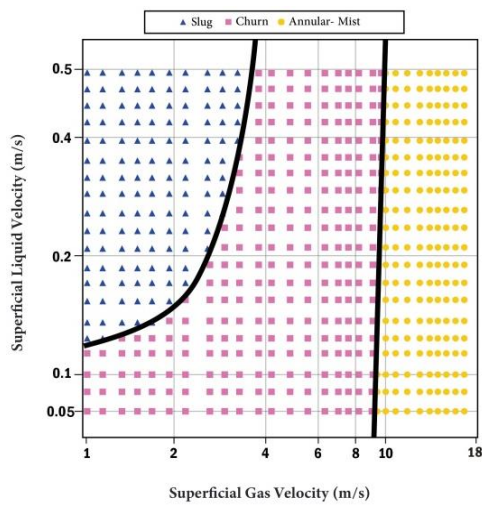


Figure 5. The flow pattern map for the vertical length of 0.5m

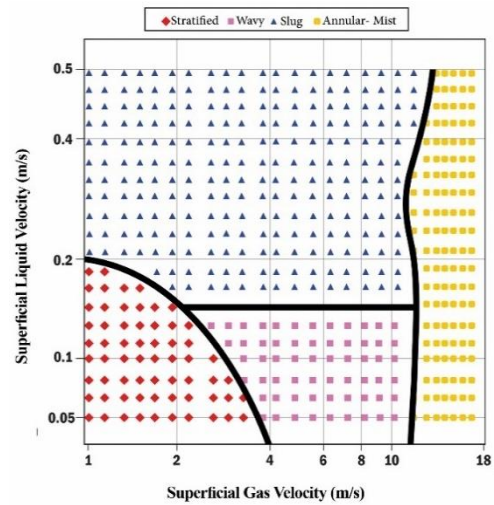


Figure 8. The flow pattern map in the fully developed section of horizontal line

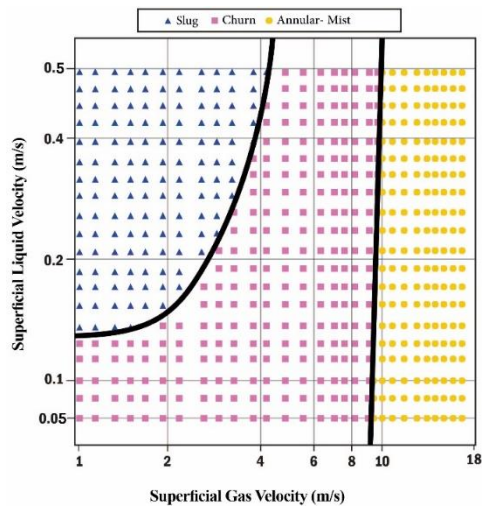


Figure 6. The flow pattern map for the vertical length of 1m

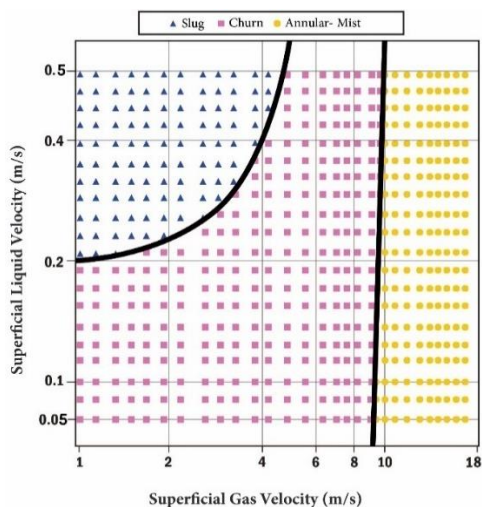


Figure 7. The flow pattern map for the vertical length of 1.5m

data in this study with corresponding flow patterns. The liquid and gas superficial velocity is acquired from the mass flow-rates using Equations. (1) and (2).

$$U_{sl} = \frac{Q_l}{A} \tag{1}$$

$$U_{sg} = \frac{Q_g}{A} \tag{2}$$

where Q_l and Q_g are the volumetric flow-rates of liquid and gas phase, respectively and A is the area of the cross section of the channel.

The two-phase flow regimes through horizontal line of channel are under the effect of disturbance persuaded by vertical section and mixer. The vertical length between two horizontal lines influences the upstream flow regimes, greatly. The considerable influence of back-ward flow of vertical part on the horizontal line is greater hold-up of water. Increasing the vertical interval between the horizontal lines creates greater momentum loss across the channel. Also, it is observed that enhancing the height between entry and exit parts leads the beginning of annular flow to greater air superficial velocities. This happening is because of that increasing the liquid amount at 90° bend inlet part needs greater gas shear force for passing to annular flow regime.

The flow regimes in the present study are characterized by gas shear force and gravity force. The gravity force results in forming of vortexes and back-ward flow. This event is connected to the length of vertical part of the test section. The dimensionless parameter linked to the present study is Froude number. The Froude number is the ratio of the flow inertia to the external field (the gravity force). This dimensionless number is determined as follow:

$$Fr = \sqrt{\frac{\rho_G}{\rho_L - \rho_G}} \frac{U_G}{\sqrt{D_h g}} \quad (3)$$

The variation of Froude number for the transitions of available flow patterns are explained according to the dimensionless vertical length in Table 1. The transition between slug and churn flow happens whereas the mass flow-rate of gas phase was enhanced and, accordingly, the liquid phase did not amass at 90° bend inlet. It can be observed that by increasing vertical length of channel, the Froude number became greater. It is due to that the liquid hold-up in 90° bend inlet is higher, therefore slug became greater. The transition to the annular-mist flow pattern takes place when the gas shear force is increased. Increasing the vertical section does not affect the gas shear force, greatly. So, the influence of various middle sections on this transition is not distinguished by vertical lengths.

Two-phase flow regimes through inlet and outlet horizontal sections of the channel are affected by disturbances caused by inclined section. For both horizontal lines, the flow patterns are categorized into two parts: fully developed part and inclined section. The flow pattern map in the fully developed section is shown in Figure 8 which contains stratified, wavy, slug and annular flow. The result of this figure is in a great agreement with the result of the study of Mandhane et al. [23] for horizontal pipes. The flow treatment at inclined

inlet section is specified by gas-liquid interaction among the inlet and inclined section. Three flow regimes of wavy, slug and annular were seen at 90° bend inlet section as shown in Table 2. As seen, the prominent flow pattern is slug flow. The significant effect of backward flow of vertical section on the 90° bend inlet part is larger hold-up of water. When the flow moves along the vertical section, the hold-up of water flourish slowly and this treatment resulted the slug flow creation. By enhancing the vertical length between the inlet and outlet horizontal sections, the greater upstream flow regimes are affected. It can also be observed that, enhancing the vertical section shifts the beginning of annular flow to greater gas superficial velocities. This behavior can also be illustrated by increased liquid level at inlet bend section which needs greater gas shear force for transition to annular flow pattern.

TABLE 1. Froude number variation for various middle lengths

Length of middle section, cm	Froude number variations	
	Slug to churn flow	Churn to annular-mist flow
50	0.041-0.170	0.401-0.446
100	0.041-0.191	0.408-0.457
150	0.041-0.213	0.419-0.462

TABLE 2. Two-phase flow regimes types according to the gas and liquid superficial velocities at the inclined inlet section of the channel

	H=50 cm		H=100 cm		H=150cm	
	U_{sl} (m/s)	U_{sg} (m/s)	U_{sl} (m/s)	U_{sg} (m/s)	U_{sl} (m/s)	U_{sg} (m/s)
Slug flow	0.11-0.5	0.6-3.8	0.14-0.5	0.6-4.5	0.2-0.5	0.6-5
Churn flow	0.05-0.5	0.6-9	0.05-0.5	0.6-9	0.05-0.5	0.5-9.5
Annular-mist flow	0.05-0.5	9-18	0.05-0.5	9-18	0.05-0.5	9.5-18
Transition line of slug to churn	0.11-0.5	0.6-3.8	0.14-0.5	0.6-4.5	0.2-0.5	0.6-5
Transition line of churn to annular-mist flow	0.05-0.5	Constant value of 9	0.05-0.5	Constant value of 9	0.05-0.5	Constant value of 9.5

4. CONCLUSION

In the present study, two-phase flow experiments for the rectangular channel with 90° bends have been accomplished and flow pattern maps for vertical section have been depicted according to the measured data. A high speed video camera was utilized to evaluate flows. Three various flow patterns, namely slug flow, churn flow and annular flow were recognized for the middle vertical section.

The following conclusions are resulted from the present work:

- The prominent flow regime in the vertical section is churn flow regime. Two other flow regimes namely slug and annular-mist flow regime are also identified.
- The transition between slug and churn flow happens whereas the mass flow-rate of gas phase was enhanced.
- The flow pattern structures are not greatly varied by changing the vertical length.
- Increasing the vertical length leads the beginning of annular flow to greater air superficial velocities.

5. REFERENCES

- Park, C., Kim, Y. K., Lee, B. C., Ryu, J. S., & Kwon, Y. S., 'Overview of KJRR design features,' 2015.
- Gong, D., Huang, S., Wang, G., and Wang, K. "Heat Transfer Calculation on Plate-Type Fuel Assembly of High Flux Research Reactor." *Science and Technology of Nuclear Installations*, Vol. 2015, (2015), 1–13. <https://doi.org/10.1155/2015/198654>
- Abbasalizadeh, M., Jafarmadar, S., and Shirvani, H. "The Effects of Pressure Difference in Nozzle's two Phase Flow on the Quality of Exhaust Mixture." *International Journal of Engineering, TransactionB: Applications*, Vol. 26, No. 5, (2013), 553–562. <https://doi.org/10.5829/idosi.ije.2013.26.05b.12>
- Cerriotti, L., Weible, K., de Rooij, N. F., and Verpoorte, E. "Rectangular channels for lab-on-a-chip applications." *Microelectronic Engineering*, Vol. 67–68, (2003), 865–871. [https://doi.org/10.1016/S0167-9317\(03\)00148-5](https://doi.org/10.1016/S0167-9317(03)00148-5)
- Gong, L., Zhao, J., and Huang, S. "Numerical study on layout of micro-channel heat sink for thermal management of electronic devices." *Applied Thermal Engineering*, Vol. 88, (2015), 480–490. <https://doi.org/10.1016/j.applthermaleng.2014.09.048>
- Li, X., and He, J.-H. "Variational multi-scale finite element method for the two-phase flow of polymer melt filling process." *International Journal of Numerical Methods for Heat & Fluid Flow*, Vol. 30, No. 3, (2019), 1407–1426. <https://doi.org/10.1108/HFF-07-2019-0599>
- Li, X., and Wang, D. "Effects of a cavity's fractal boundary on the free front interface of the polymer filling stage." *Fractals*, Vol. 29, No. 07, (2021), 2150225. <https://doi.org/10.1142/S0218348X2150225X>
- Trimulyono, A., Chrismianto, D., Samuel, S., and Aslami, M. "Single-phase and Two-phase Smoothed Particle Hydrodynamics for Sloshing in the Low Filling Ratio of the Prismatic Tank." *International Journal of Engineering, Transaction B: Applications*, Vol. 34, No. 5, (2021), 1345–1351. <https://doi.org/10.5829/ije.2021.34.05b.30>
- Wilmarth, T., and Ishii, M. "Two-phase flow regimes in narrow rectangular vertical and horizontal channels." *International Journal of Heat and Mass Transfer*, Vol. 37, No. 12, (1994), 1749–1758. [https://doi.org/10.1016/0017-9310\(94\)90064-7](https://doi.org/10.1016/0017-9310(94)90064-7)
- Wilmarth, T., and Ishii, M. "Interfacial Area Concentration and Void Fraction of Two-Phase Flow in Narrow Rectangular Vertical Channels." *Journal of Fluids Engineering*, Vol. 119, No. 4, (1997), 916–922. <https://doi.org/10.1115/1.2819517>
- Nguyen, V. T. Two-phase, gas-liquid concurrent flow: an investigation of holdup, pressure drop and flow pattern in a pipe at various inclinations. Doctoral dissertation, ResearchSpace@ Auckland.
- Beggs, H. D. An experimental study of two-phase flow in inclined pipes. The University of Tulsa.
- Hasan, A. R., and Kabir, C. S. "Two-phase flow in vertical and inclined annuli." *International Journal of Multiphase Flow*, Vol. 18, No. 2, (1992), 279–293. [https://doi.org/10.1016/0301-9322\(92\)90089-Y](https://doi.org/10.1016/0301-9322(92)90089-Y)
- Ghiaasiaan, S. M., Wu, X., Sadowski, D. L., and Abdel-Khalik, S. I. "Hydrodynamic characteristics of counter-current two-phase flow in vertical and inclined channels: effects of liquid properties." *International Journal of Multiphase Flow*, Vol. 23, No. 6, (1997), 1063–1083. [https://doi.org/10.1016/S0301-9322\(97\)00027-X](https://doi.org/10.1016/S0301-9322(97)00027-X)
- Barnea, D., Shoham, O., Taitel, Y., and Dukler, A. E. "Gas-liquid flow in inclined tubes: Flow pattern transitions for upward flow." *Chemical Engineering Science*, Vol. 40, No. 1, (1985), 131–136. [https://doi.org/10.1016/0009-2509\(85\)85053-3](https://doi.org/10.1016/0009-2509(85)85053-3)
- Oddie, G., Shi, H., Durllofsky, L. J., Aziz, K., Pfeiffer, B., and Holmes, J. A. "Experimental study of two and three phase flows in large diameter inclined pipes." *International Journal of Multiphase Flow*, Vol. 29, No. 4, (2003), 527–558. [https://doi.org/10.1016/S0301-9322\(03\)00015-6](https://doi.org/10.1016/S0301-9322(03)00015-6)
- Wongwises, S., and Pipathattakul, M. "Flow pattern, pressure drop and void fraction of two-phase gas-liquid flow in an inclined narrow annular channel." *Experimental Thermal and Fluid Science*, Vol. 30, No. 4, (2006), 345–354. <https://doi.org/10.1016/j.expthermflusci.2005.08.002>
- Ali, M. I., Sadatomi, M., and Kawaji, M. "Adiabatic two-phase flow in narrow channels between two flat plates." *The Canadian Journal of Chemical Engineering*, Vol. 71, No. 5, (1993), 657–666. <https://doi.org/10.1002/cjce.5450710502>
- Bhagwat, S. M., and Ghajar, A. J. "Experimental investigation of non-boiling gas-liquid two phase flow in upward inclined pipes." *Experimental Thermal and Fluid Science*, Vol. 79, (2016), 301–318. <https://doi.org/10.1016/j.expthermflusci.2016.08.004>
- Bhagwat, S. M., and Ghajar, A. J. "Experimental investigation of non-boiling gas-liquid two phase flow in downward inclined pipes." *Experimental Thermal and Fluid Science*, Vol. 89, (2017), 219–237. <https://doi.org/10.1016/j.expthermflusci.2017.08.020>
- Kim, T. H., Chalgeri, V. S., Yoon, W., Yun, B. J., and Jeong, J. H. "Visual observations of flow patterns in downward air-water two-phase flows in a vertical narrow rectangular channel." *Annals of Nuclear Energy*, Vol. 114, (2018), 384–394. <https://doi.org/10.1016/j.anucene.2017.12.053>
- Bouyahiaoui, H., Azzi, A., Zeghloul, A., Hasan, A. H., Al-Sarkhi, A., and Parsi, M. "Vertical upward and downward churn flow: Similarities and differences." *Journal of Natural Gas Science and Engineering*, Vol. 73, (2020), 103080. <https://doi.org/10.1016/j.jngse.2019.103080>
- Mandhane, J. M., Gregory, G. A., and Aziz, K. "A flow pattern map for gas-liquid flow in horizontal pipes." *International Journal of Multiphase Flow*, Vol. 1, No. 4, (1974), 537–553. [https://doi.org/10.1016/0301-9322\(74\)90006-8](https://doi.org/10.1016/0301-9322(74)90006-8)

Persian Abstract

چکیده

در این مقاله به منظور تحلیل رفتار جریان دو فازی در یک کانال مستطیلی شیبدار با زاویه ۹۰ درجه برای طول‌های مختلف عمودی، یک بررسی آزمایشگاهی انجام شده است. بخش اصلی آزمایش (با طول ۳۰ متر) شامل دو بخش افقی و یک بخش عمودی میانی است. سه طول عمودی ۵۰، ۱۰۰ و ۱۵۰ سانتی‌متری در طول بخش آزمایش استفاده شده است. سطح مقطع کانال مستطیلی ۱۰ سانتی‌متر × ۱۵ سانتی‌متر می‌باشد. سیال‌های مورد استفاده در این تحقیق هوا و آب بوده است. الگوهای جریان مختلفی با تغییر دبی حجمی گاز و مایع به ترتیب در محدوده ۲ تا ۱۰ و ۳۴ تا ۲۳۵ m³/h ایجاد می‌شود. سیستم ویدئویی با سرعت بالا برای دستیابی به دنباله تصویر جریان تحت شرایط مختلف مورد استفاده قرار گرفت. اثرات طول عمودی بر رژیم‌های جریان و مرزهای انتقال الگو مورد بررسی قرار گرفته است. با توجه به تجسم جریان، هیچ گردابی در بخش عمودی مشاهده نگردید. نتایج نشان داد که رژیم جریان در بخش عمودی بصورت ریزشی است. در نهایت می‌توان دریافت که ساختارهای الگوی جریان تحت تأثیر تغییر طول عمودی قرار نمی‌گیرند.



Analytical Investigation on the Stress Distribution in Structural Elements Reinforced with Laminates Subjected to Axial Loads

F. Marchione*

Dipartimento di Ingegneria Civile, Edile e Architettura (DICEA), Università Politecnica delle Marche, via B. Bianche, Ancona, Italy

PAPER INFO

Paper history:

Received 22 November 2021

Received in revised form 24 December 2021

Accepted 31 December 2021

Keywords:

Stress Distribution

Buckling Behavior

Delamination Growth

FRP Composites

Layered Materials

ABSTRACT

The present paper investigates the stress distribution in structural elements reinforced with laminates and subjected to axial loads. The proposed analysis provides an analytical solution for the shear stress distribution between the substrate and the reinforcement, and for the normal stresses in the cross-section of the reinforcement. The stress analysis assumes a linear elastic mechanical behaviour of the adherents. The solutions obtained are applied to the problem of the elastic stability of a beam/column supported at its ends. The manifestation of the buckling phenomena leads to the failure of the structural element for loads lower than the characteristic strengths of the materials. In particular, the critical load represents the watershed value between the purely compressive and flexural behaviour of the element considered. In the case of stiff substrate, the buckling phenomenon leads to delamination of the reinforcement in the compressed area. Since buckling is an elastic problem, the stress distribution in the elastic range is used here to determine the value of the delamination length of the reinforcement at the critical load. In this way an analytical analysis which may be useful in the design phase of the reinforcement is proposed.

doi: 10.5829/ije.2022.35.04a.08

1. INTRODUCTION

Structural composite materials have recently seen increasing use in a number of industrial fields, such as aeronautical, civil and automotive applications [1-3]. This is due to many advantages of composite technology, which is characterised by high mechanical properties and the possibility of increasing the strength of structural elements without adding weight to the structure [4, 5].

Composite laminates are widely used for reinforcement or repair works of cracked structural elements or characterised by mechanical performance lower to those prescribed by the standards [6, 7]. The reinforcement applications through the use of laminates have the objective of reducing the concentration of stresses in the structural element of the substrate, transferring the stresses to the reinforcement layer, to avoid the propagation of the fracture [8].

Unlike traditional mechanical reinforcement technologies (e.g. reinforced injections, tying, etc.), reinforcement by adhesive application of laminates involves less preventive work and no removal of the substrate material, resulting in a more uniform distribution of stresses.

Xiong and Sheno [9] developed an experimental procedure based on static and fatigue strength concepts for an alloyed composite repair scheme for cracked aluminium alloy panels. The results showed that due to the reduction of the stress concentration caused by the repair, there is an improvement of the residual strength of the repaired specimens; thus, the residual tensile strengths of the repaired specimens are higher than those of the unrepaired specimens.

Jones and Chiu [10] carried out a series of experimental and numerical studies on crack repair in thick structural components. For this purpose, various problems were considered, such as semi-elliptical surface defects, integer surface defects, cracked fixing holes and cracked fins.

*Corresponding Author Institutional Email:
f.marchione@pm.univpm.it (F. Marchione)

The use of patches for reinforcing substrate materials also has applications in microelectronics and the medical field, where thin films are made mechanically cooperating in the substrate. The most frequent failure mechanism in this type of application is buckling of the patch.

Two buckling failure modes of the reinforcement could be observed: delamination and wrinkling. The first type consists in the detachment of the reinforcement from the substrate; the second occurs when the deformation of the patch exceeds that of the substrate. The occurrence of either type depends on the stiffness ratio between the substrate and the reinforcement; in particular, delamination occurs for stiff substrates and wrinkling for elastic substrates, as stated by Mei et al. [11].

The study of the reinforcement system of existing structures is an important issue [12]. Ozturk et al. [13] studied the effect of applying FRP reinforcements on historic buildings in Nigde, Turkey. Further work by Ozturk and Yilmaz [14] also provided an analytical solution for the modelling of FRP structural reinforcement by analysing a case study of historic buildings in Cappadocia.

In the present paper, the special case of a longitudinally developed structural element reinforced on both major faces is studied. In particular, the load transfer mechanism between the substrate and the reinforcement is analysed by means of a shear-lag model, through a parametric study on the influence of the elastic moduli of the materials and their geometries. Then, through the energy formulation for the critical delamination stress, a method of determining the delamination length at the critical axial load is proposed.

2. THEORY AND MODELING

In this section the theoretical analysis of the mechanical model is presented. By means of a shear-lag model the governing equations related to the interfacial shear stresses between patch and substrate and those related to the normal stresses in the reinforcement layer are exposed and analyzed through a parametrical study.

2.1. Analytical Model Figure 1 illustrates the shear-lag model analyzed. In particular, this model considers the case of a composite beam reinforced by two laminates on the external faces and subjected to uniform tensile stresses σ_0 . These stresses are applied directly to the structural substrate element and are transferred to the reinforcing laminates through shear stresses.

The assumptions underlying the calculation are:

- i. all structural elements are homogeneous, elastic, linear and isotropic;
- ii. normal (peel) stresses between patch and substrate are neglected;
- iii. laminates are made of the same material;
- iv. the tensile load is applied uniformly at the ends of the substrate.

Figure 2 shows the free body diagram of the overlap region between the patch and the substrate. The equilibrium of the longitudinal loads yields:

$$d\sigma_f \cdot t_f \cdot b + \tau \cdot b \cdot dx = 0 \tag{1.1}$$

$$\frac{d\sigma_f}{dx} = -\frac{\tau}{t_s} \tag{1.2}$$

The shear strain is equal to:

$$\gamma = \frac{u_s - u_f}{t_s} \tag{2}$$

Given the relationship:

$$\gamma = \frac{\tau}{G_s} \tag{3}$$

Replacing Equations (2) and (3) in (1.2) the following could be obtained:

$$\frac{d^2\sigma_f}{dx^2} = -\frac{G_s}{t_f t_s} \left(\frac{du_s}{dx} - \frac{du_f}{dx} \right) = -\frac{G_s}{t_f t_s} \left(\frac{\sigma_s}{E_s} - \frac{\sigma_f}{E_f} \right) \tag{4}$$

Considering the symmetry of the applied reinforcements, the following could be obtained:

$$\sigma_0 \cdot t_s = \sigma_s \cdot t_s + 2 \cdot \sigma_f \cdot t_f \tag{5}$$

$$\sigma_s = \sigma_0 - \frac{2 \cdot \sigma_f \cdot t_f}{t_s} \tag{6}$$

Combining Equations (4) and (6) the following is obtained:

$$\frac{d^2\sigma_f}{dx^2} = -\frac{G_s}{t_f t_s} \left(\frac{\sigma_0}{E_s} - 2 \frac{\sigma_f t_f}{E_f t_s} - \frac{\sigma_f}{E_f} \right) \tag{7}$$

The result of the differential Equation (7) is given as follows:

$$\sigma_f(x) = K_1 \cdot \sinh(\lambda x) + K_2 \cdot \cosh(\lambda x) + \frac{E_f t_s}{E_s t_s + E_f t_f} \sigma_0 \tag{8}$$

where:

$$\lambda = \sqrt{\frac{G_s}{t_f t_s} \left(\frac{1}{E_f} + 2 \frac{t_f}{E_s t_s} \right)} \tag{9}$$

The boundary conditions relative to Equation (7), are:

$$x = \pm L; \sigma_f = 0 \tag{10}$$

From Equation (8) the following could be obtained:

$$\sigma_f(x) = \frac{E_f t_s}{E_s t_s + E_f t_f} \sigma_0 \left[1 - \frac{\cosh(\lambda x)}{\cosh(\lambda L)} \right] \tag{11}$$

Shear stresses are given by the following:

$$\tau(x) = \frac{E_f t_s t_f}{E_s t_s + E_f t_f} \sigma_0 \frac{\lambda \sinh(\lambda x)}{\cosh(\lambda L)} \tag{12}$$

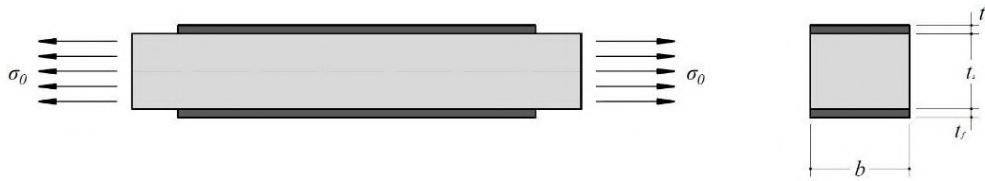


Figure 1. Reinforced structural element, longitudinal and cross-section

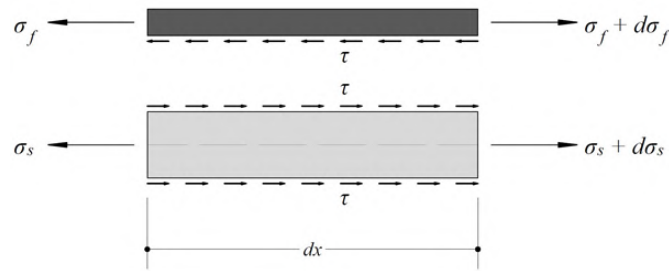


Figure 2. Free body diagram

2. 2 A Parametric Study on the Stress Distribution

The following section deals with a parametric study on the distribution of normal stresses in the reinforcement layer and of the interfacial shear stresses between the reinforcement and the substrate. In particular, the effects of the elastic modulus of the adherents, the length and thickness of the reinforcement are investigated.

2. 2. 1. Elastic Modulus

The elastic modulus of the adherents is a crucial element in the design phase for the correct choice of reinforcement elements. It is necessary to choose reinforcement elements with stiffness values compatible with those of the substrate to avoid the occurrence of unwanted stress peaks. The result of the calculation for different values of elastic modulus is graphically illustrated in Figure 3(a-b).

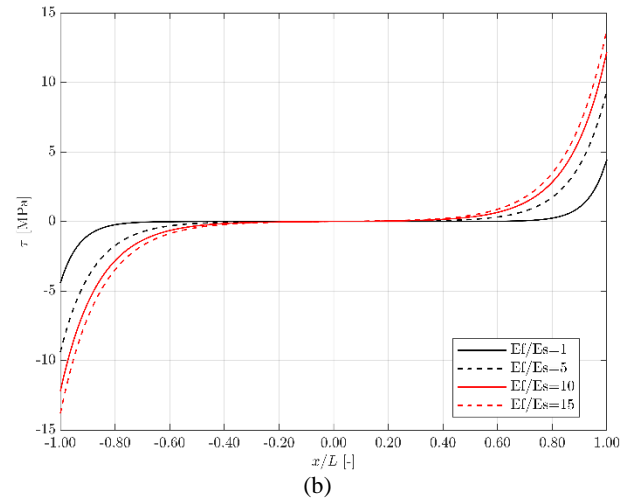
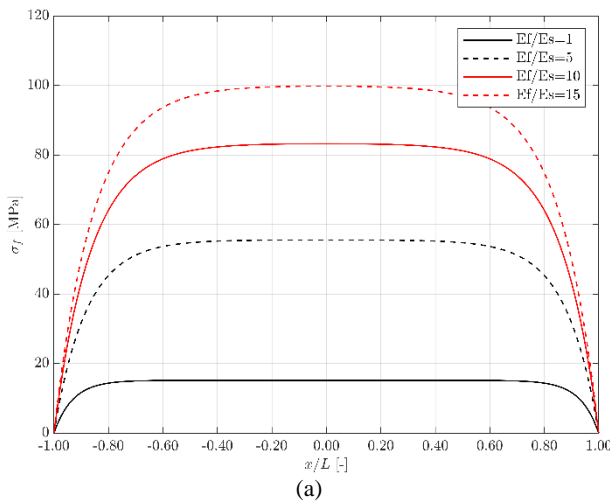


Figure 3. Effect of the Young moduli ratio of the adherents on the normal stress distribution in the reinforcement (a) and on the interfacial shear stress distribution (b)



It could be observed that for each configuration the normal and shear stresses show the same qualitative trend. For the normal stresses, it can be observed that an increase in the ratio between the elastic moduli of the reinforcement and the substrate leads to an evident increase of the normal stresses near the central zone of the reinforcement. On the other hand, for the shear stresses, it is noted that the concentration of the stresses tends to flatten towards zero values for lower elastic moduli ratios. As the ratio of elastic moduli increases, it tends towards the extreme of the reinforcement.

2. 2. 3. Reinforcement Thickness

In the present work, a further geometrical factor influencing the stress

distribution, the thickness of the adherents was investigated. In fact, the stress distribution can be considered as constant through the width of the adherents. The effect of the anchorage thickness of the reinforcement to the substrate is shown in Figure 4(a-b).

It could be observed that in the case of normal stresses, an increase in the thickness of the reinforcement layer leads to a reduction in the stress peak; on the contrary, an increase in thickness leads to a reduction in normal stresses. On the contrary, in the case of shear stresses, there is an increase in the stress peaks as the thickness of the reinforcement increases.

2. 3. Buckling Delamination The mechanical contribution to the stability of a beam given by the reinforcement in the stretched zone could be investigated by means of the Winkler elastic model of the beam on elastic soil. The value of the critical load was determined by Timoshenko and Gere [15]:

$$P_{cr, RB} = \frac{\pi^2 EI}{l^2} + \frac{kl^2}{\pi^2} = P_{cr, E} + \frac{kl^2}{\pi^2} \tag{13}$$

where k is the flexural stiffness constant of the reinforcement and can be determined experimentally. The value of the critical load of the reinforced beam is greater than the classical Eulerian critical load by an amount proportional to the length of the beam and the stiffness of the reinforcement [15].

Considering the energy criterion, as reported by Mei et al. [11], the delamination stress for reinforcement could be expressed by the following expression:

$$\sigma_{cr} = \frac{\pi^2 E_f}{3(1-\nu_s^2)} \left(\frac{t_f}{2x} \right)^2 \tag{14}$$

where E is the Young modulus and ν is the Poisson's modulus, h is the reinforcement thickness and x is the half delamination length.

Since the occurrence of elastic buckling is an elastic phenomenon, it is possible to derive the delamination length by equating the critical elastic stress to the elastic stress distribution shown in the previous section. Equalizing Equations (14) and (11), the following could be obtained:

$$x^2 \left(1 - \frac{\cosh(\lambda x)}{\cosh(\lambda L)} \right) = \frac{\pi^2 (E_s t_s + E_f t_f) t_f^2}{12 (1-\nu_s^2) \sigma_0 t_s} \tag{15}$$

By solving Equation (15) by iteration, the delamination length of the reinforcement at the critical load is obtained.

3. NUMERICAL APPLICATION

The following is a numerical application carried out by solving Equation (15), considering different values of flexural stiffness k . The application herein reported provides an analytical analysis in alternative to the one presented in literature [16]. Figure 5 shows, when varying the ratio of the elastic moduli of the support and of the reinforcement (E_f/E_s), the trend of the percentage of the delamination semi-length in correspondence of the critical load with respect to the total length of the reinforcement (x/L).

Fixed values – obtained from experimental campaign conducted by Capozucca et al. [16] – are considered for the elastic moduli of the reinforcement (also characterised by a constant k) and as the stiffness of the substrate varies, the percentages of the delamination length are obtained.

It is observed that as the E_f/E_s ratio increases, the behaviour of the curve is creepy. In particular, increasing the stiffness of the reinforcement with respect to that of the substrate, the laminate absorbs an increasing amount of strain and this determines an increase in the delamination length in correspondence with the critical load.

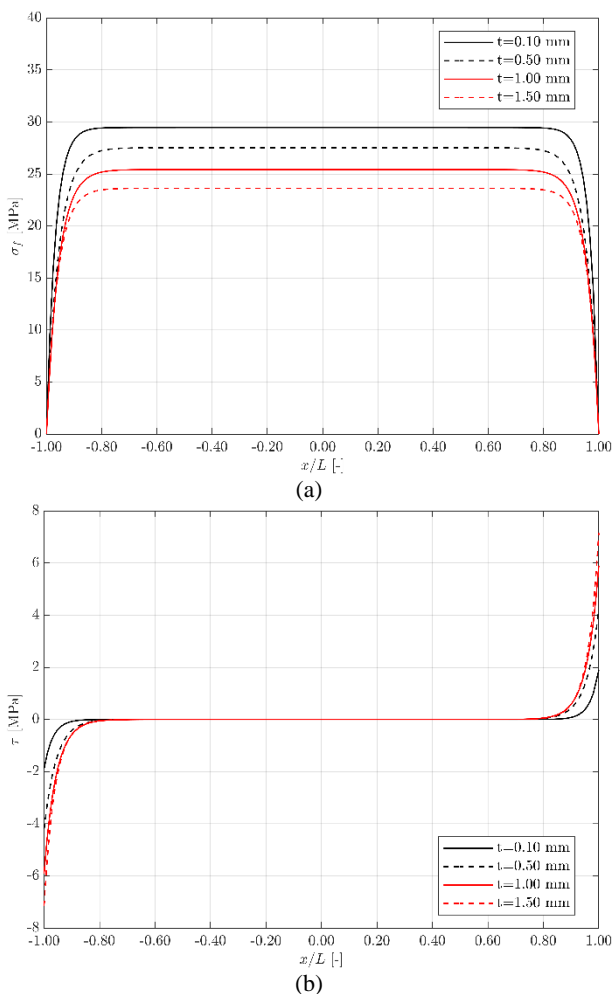


Figure 4. Effect of the reinforcement's thickness on the normal stress distribution in the reinforcement (a) and on the interfacial shear stress distribution (b)

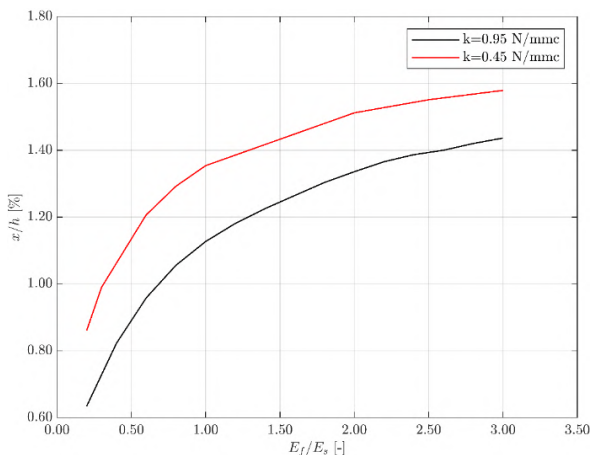


Figure 5. Delamination length percentage vs stiffness ratio (adimensional graph)

4. CONCLUSIONS

In the present paper the elastic stress distribution in a structural element subjected to axial loads is treated. By means of a shear-lag model, the distribution of both the interfacial shear stresses between the reinforcement and the substrate and the normal stresses inside the reinforcement layer are analysed. The study of the stresses is deepened through a parametric study, highlighting the influence of material and geometric factors on the distribution of the stresses. The results show that the greatest influence is exerted by varying the ratio between the elastic moduli of the reinforcement and the substrate.

The proposed analysis is then extended to the application case of a reinforced structural element subjected to axial buckling loads. Since buckling is an elastic phenomenon, the stress analysis previously exposed is extended - through the energetic formulation - to the determination of the initial delamination length of the reinforcement layer. These considerations are deepened through a parametric study that correlates the stiffness ratio to the initial delamination length.

The main objective of this paper is to provide an accurate analysis of the stress distribution, which allows the designer to assess the possible damage caused by delamination under compressive axial loads. An experimental campaign is under process, in order to validate the theoretical analysis here presented.

5. REFERENCES

1. A.A. Baker, R.J. Callinan, M.J. Davis, R. Jones, J.G. Williams, Repair of mirage III aircraft using the BFRP crack-patching technique, *Theoretical and Applied Fracture Mechanics*, Vol. 2, No. 1, (1984) 1-15. [https://doi.org/10.1016/0167-8442\(84\)90035-1](https://doi.org/10.1016/0167-8442(84)90035-1).
2. L. Molent, R.J. Callinan, R. Jones, Design of an all boron/epoxy doubler reinforcement for the F-111C wing pivot fitting: Structural aspects, *Composite Structures*, Vol. 11, No. 1, (1989) 57-83. [https://doi.org/10.1016/0263-8223\(89\)90030-5](https://doi.org/10.1016/0263-8223(89)90030-5).
3. A. Rarthlomeusz, R. J.J. Paul, J.D. Roberts, Application of Bonded Composite Repair Technology to Civil Aircraft — B747 Demonstration Programme, *Aircraft Engineering and Aerospace Technology*, Vol. 65, (1993), 4-7. <https://doi.org/10.1108/eb037363>.
4. F. Marchione, Stress distribution in double-lap adhesive joints: Effect of adherend reinforcement layer, *International Journal of Adhesion and Adhesives*, Vol. 105, (2021). <https://doi.org/10.1016/j.ijadhadh.2020.102780>.
5. F. Marchione, Investigation of Vibration Modes of Double-lap Adhesive Joints: Effect of Slot, *International Journal of Engineering, Transactions A: Basics*, Vol. 33, No. 10, (2020), 1917-1923. <https://doi.org/10.5829/ije.2020.33.10a.10>.
6. A.H. Makwana, N. Vyas, R.S. Barot, Numerical investigation of composite patch repair of inclined cracked panel using XFEM, *Mater. Today Proceedings*, Vol. 45, (2021). <https://doi.org/10.1016/j.matpr.2021.01.643>.
7. N. Constantin, M. Sandu, Ş. Sorohan, Restoration of the mechanical performance of damaged Al panels using bonded composite repair patches, *International Journal of Adhesion and Adhesives*, Vol. 42, (2013), 69-76. <https://doi.org/10.1016/j.ijadhadh.2013.01.003>.
8. X. Zhang, J. Wu, Z. Fan, S. Yang, F. Huang, A. Wang, Cohesive shear stress and strength prediction of composite patch bonded to metal reinforcement, *International Journal of Adhesion and Adhesives*, Vol. 90, (2019), 144-153. <https://doi.org/10.1016/j.ijadhadh.2019.02.008>.
9. J.J. Xiong, R.A. Sheno, Integrated experimental screening of bonded composites patch repair schemes to notched aluminum-alloy panels based on static and fatigue strength concepts, *Composite Structures*, Vol. 83, (2008), 266-272. <https://doi.org/10.1016/j.compstruct.2007.04.019>.
10. R. Jones, W.K. Chiu, Composite repairs to cracks in thick metallic components, *Composite Structures*, Vol. 44, (1999), 17-29. [https://doi.org/10.1016/S0263-8223\(98\)00108-1](https://doi.org/10.1016/S0263-8223(98)00108-1).
11. H. Mei, R. Huang, J.Y. Chung, C.M. Stafford, H.-H. Yu, Buckling modes of elastic thin films on elastic substrates, *Applied Physics Letters*, Vol. 90, (2007), 151902. <https://doi.org/10.1063/1.2720759>.
12. Strengthening of RC Beams using Steel Plate-Fiber Concrete Composite Jackets (Finite Element Simulation and Experimental Investigation), *International Journal of Engineering, Transactions A: Basics*, Vol. 35, No. 1 (2022), 73-92. <https://doi.org/10.5829/ije.2022.35.01A.07>.
13. B. Ozturk, C. Yilmaz, T. Senturk, Effect of FRP retrofitting application on seismic behavior of a historical building at Nigde, Turkey, in: 14th European Conference on Earthquake Engineering 2010: Ohrid, Republic of Macedonia, (2010), Macedonia.
14. B. Ozturk, C. Yilmaz, "Analytical Investigation of Effect of Retrofit Application using FRP on Seismic Behavior of a Monumental Building at Historical Cappadocia Region of Turkey", 9th U.S. National and 10th Canadian Conference on Earthquake Engineering, Toronto, Canada, (2010), 25-29.
15. S.P. Timoshenko, J.M. Gere, *Theory of Elastic Stability*, Dover Publications, 2009. https://books.google.it/books?id=rAk_AwAAQBAJ.
16. Capozucca, R., Magagnini, E. and Vecchiotti, M.V., "Delamination Buckling of FRP: Experimental Tests and Theoretical Model", In Proceedings of the 13th International Conference on Damage Assessment of Structures, (2020), 753-766. Springer, Singapore. https://doi.org/10.1007/978-981-13-8331-1_59.

Persian Abstract

چکیده

مقاله حاضر به بررسی توزیع تنش در عناصر سازه‌ای تقویت‌شده با لایه‌های لایه‌ای و تحت بارهای محوری می‌پردازد. تحلیل پیشنهادی یک راه حل تحلیلی برای توزیع تنش برشی بین زیرلایه و تقویت‌کننده و برای تنش‌های نرمال در مقطع آرماتور ارائه می‌کند. تحلیل تنش رفتار مکانیکی الاستیک خطی چسبنده ها را فرض می‌کند. راه‌حل‌های به‌دست‌آمده برای مسئله پایداری الاستیک تیر/ستون که در انتهای آن پشتیبانی می‌شود، اعمال می‌شود. تجلی پدیده کمانش منجر به شکست عنصر ساختاری برای بارهای کمتر از مقاومت مشخصه مواد می‌شود. به طور خاص، بار بحرانی نشان دهنده مقدار حوضه بین رفتار صرفاً فشاری و خمشی عنصر در نظر گرفته شده است. در مورد بستر سفت، پدیده کمانش منجر به جدا شدن آرماتور در ناحیه فشرده می‌شود. از آنجایی که کمانش یک مشکل الاستیک است، در اینجا از توزیع تنش در محدوده الاستیک برای تعیین مقدار طول لایه لایه شدن آرماتور در بار بحرانی استفاده می‌شود. به این ترتیب یک تحلیل تحلیلی - که ممکن است در مرحله طراحی تقویت‌کننده مفید باشد - پیشنهاد می‌شود.



Investigation of Dielectric Properties of Ni/n-TiO₂/p-Si/Al Heterojunction in Wide Range of Temperature and Voltage

A. Kumar^{*a}, A. Kumar^b, K. K. Sharma^a

^a Department of Physics and Photonics Science, National Institute of Technology, Hamirpur, India

^b Department of Physics, Government College Sujapur Tihra, India

PAPER INFO

Paper history:

Received 23 August 2021

Received in revised form 31 December 2021

Accepted 11 January 2022

Keywords:

Dielectric Constant

Electric Moduli

Conductivity

Interface States

ABSTRACT

In the present study we have investigated the dielectric properties such as dielectric constant (ϵ'), dielectric loss (ϵ''), real part of electrical modulus (M'), imaginary part of electric modulus (M'') and AC electrical conductivity, (σ_{ac}) in wide range of applied voltage, temperature and frequency for Ni/n-TiO₂/p-Si/Al heterojunction. A nanocrystalline TiO₂ layer was grown on p-type boron doped silicon in oxygen-controlled environment using optimized KrF excimer laser. Ohmic contact of pure nickel and aluminum metals was made on TiO₂ and silicon respectively, with thermal coating system. The characteristics obtained with the help of conductance-voltage and capacitance-voltage measurements also known as impedance/admittance spectroscopy. The studied parameters are found to be very sensitive to frequency, temperature and voltage. The restructuring and reordering of interface state density due to temperature variations and interfacial polarizations due to frequency variations collectively result the observed changes in the ϵ' and ϵ'' . With an increase in frequency AC conductivity and electrical modulus also increases. The relaxation mechanism can be observed in the complex electrical modulus analysis. The thermally activated conduction process was indicated by the frequency dependent AC conductivity at different temperatures. Using power law, the AC conductivity was analyzed and found to increase with temperature, applied voltage.

doi: 10.5829/ije.2022.35.04a.09

1. INTRODUCTION

In semiconductor technology the metal semiconductor heterojunctions are well known basic devices which are used in various electronic circuits. These devices are very significant for the electronic industry [1-3] because of their technological applications as rectifiers, inverters, polarity protection solar cells, photodetectors etc. The stability, reliability and performance of these devices are dominantly influenced by the characteristics prevailing at the interface [4]. The density of interface states at the interface of heterojunction and also the interfacial layer thickness dominantly impacts the dielectric and electrical parameters of these devices [5-7]. The interface capacitance also known as excess capacitance is strongly dependent on frequency and voltage which in turn strongly affect the admittance spectroscopy of the

devices [5-8]. The frequency response of ϵ' and ϵ'' shows strong dispersion at low frequencies [9-10]. The presence of metal oxide thin films significantly changes the dielectric and electric behavior of the heterojunction devices [11-15]. Moreover, there is formation of large number of defects and impurities at the semiconductor surface as a result of periodic interruption of lattice structure. These physical processes result the large number of energy levels associated with interface states well within the energy band gap of the semiconductor which are strongly influenced by applied frequency, temperature and voltage. So, it is obvious that the existence of the localized interface states greatly alters the functioning and characteristics of the device from the ideal case by modifying the electric and dielectric parameters of the heterojunction devices [16-21]. These dependencies occur because the temperature variations of

*Corresponding Author Email: puri_nir@yahoo.com (A. Kumar)

the device lead to the interface states readjustments and sharing of applied bias between depletion layer, interfacial layer and series resistance [20-21]. The $C-V$ and $G/\omega-V$ analysis in the forward as well as in reverse direction only at small frequency range cannot supply the comprehensive information about the electrical and dielectric properties of the device. Whereas, wide range frequency measurements can supply complete information about the dielectric properties along with the transport mechanism of the devices [22-25]. The electrode polarization due to the accumulation of charges hides the relaxation processes and the complete analysis of the device parameters becomes difficult. In these cases, the complex electrical modulus is a powerful tool for understanding bulk relaxation processes because it minimizes conductivity and permittivity variations in the low frequency regions [26-27].

The modified behavior observed in electrical and dielectric characteristics of the heterojunction diodes is generally due to the effect of interfacial layer properties [28-30]. In general, the $C-V$ and $G/\omega-V$ characteristics of these devices in an ideal situation are independent of frequency [31-32]. But the idealized situations are often disturbed by the interfacial layer separating the metal semiconductor junction and also by interface states at the interface of thin oxide layer and the semiconductor [31-33]. The characteristics of the heterojunction diodes can be deliberately modified when a suitable thin layer separate the metal from semiconductor component [34-36].

Since the electronic device applications are significantly influenced by the dielectric properties of the heterojunction, so in the present study we have made the detailed analysis of the dielectric properties namely, dielectric constant (ϵ'), dielectric loss (ϵ''), real and imaginary electric modulus (M', M'') and AC electrical conductivity (σ_{ac}) of the heterojunction Ni/n-TiO₂/p-Si/Al through admittance/impedance spectroscopic techniques which require the $C-V$ and $G/\omega-V$ measurements in wide temperature and voltage ranges at different frequencies.

2. EXPERIMENTAL PROCEDURE

First, aluminum metal was deposited on the back side of p-type silicon wafer with (100) surface orientation under 3×10^{-6} mbar vacuum to form the ohmic contacts followed by annealing for 1 h at 300 °C to achieve best ohmic performance. Then TiO₂ thin films were grown on using pulsed laser ablation technique to fabricate Ni/n-TiO₂/p-Si/Al heterojunction diode. The sintered pallets of TiO₂ at 1000 °C for 12 h were used for deposition of thin films. To ablate the TiO₂ target KrF (248 nm) COHERENT COMPLEX PRO 205 F laser was used with

repetition rate of 10 Hz at energy of 300 mJ. Eventually, nickel metal was thermally evaporated through masks with circular holes of 1 mm diameter from the tungsten filament into the TiO₂ film to form metal contacts. Ni/TiO₂ and p-Si/Al interfaces are ohmic in nature. Wayne Kerr 6520A, precision impedance analyzer was employed to study the $C-V$ and $G/\omega-V$ measurements.

3. RESULTS AND DISCUSSIONS

3.1. Dielectric Studies at Different Voltages The complex permittivity can be expressed through the following relation [37]:

$$\epsilon^* = \epsilon' - i\epsilon'' = \frac{C}{C_0} - i \frac{G}{\omega C_0} \quad (1)$$

The values of ϵ' and ϵ'' can be expressed using Equation (1) as:

$$\epsilon' = \frac{C}{C_0} \quad (2)$$

$$\epsilon'' = \frac{G}{\omega C_0} \quad (3)$$

ϵ^* is the complex dielectric constant, $C_0 = \frac{\epsilon_0 A}{d}$, is the capacitance of capacitor without any dielectric, A is the diode area, ϵ_0 is the permittivity of free space and d is the thickness of interlayer, i is the imaginary root of $\sqrt{-1}$, ω is the angular frequency.

The variations of ϵ' and ϵ'' with logarithmic frequency $\ln(\omega)$ for the Ni/n-TiO₂/p-Si/Al heterojunction have been evaluated by using equations (2) and (3) at different applied voltages. The charge reordering and restructuring due to the external bias at n-TiO₂/p-Si interface and interface polarization usually produce the change in conductivity of the device. The dielectric characteristics as well as interface properties dominantly affect the electric parameters of the device since the interface states respond differently in the high and low frequency regimes. So the quantities, ϵ' and ϵ'' are plotted with frequency in Figures 1 and 2, respectively, for various forward bias voltages and then comprehensively analyzed in the following.

The experimental values of ϵ' and ϵ'' as a function of frequency at selected applied voltages from 0.2 V to 2.0 V, as shown in Figs. 1 and 2 are found to be strongly dependent on frequency as well as applied voltage. Moreover, at low and intermediate frequency range the variations become considerably high while they become almost frequency independent in the high frequency regimes. The swingeing decrease in the values of ϵ' and

ϵ'' with increase in frequency shows the shortage of time available for interfacial dipoles to align themselves with the direction of external alternating electric field [38-39]. Due to the insufficient time available, the dipoles are unable to orient themselves with the field at very high frequency and this results the decrease in the dielectric constant values [40]. The displacement of charges from the traps or equilibrium states occur as a result of the polarization of dielectric or polymeric material at low and intermediate frequencies under the effect of external field. So, it is obvious that the relaxation time plays a dominant role in changing of dielectric properties with the frequency of applied field. In this study it is revealed that the interfacial as well as dipole polarization can easily take place at low and intermediate frequencies. Moreover, the charges in the traps follow the field at low frequencies thereby increasing the dielectric constant. However, the inability of interface states in following the high frequency signal leads to the saturation of dielectric constant. At this stage interface states do not contribute towards admittance spectroscopy hence ϵ' and ϵ'' values become independent of the frequency of the field since there is the absence of any mechanism which can produce interface polarization. The charges located at the surface states or interface traps which are between the semiconductor and the interfacial layer greatly impact the dielectric and electric properties of the devices because the release of this charge on the application of appropriate external AC voltage produce a charge effect in these devices [4, 41]. The frequency dependent dispersion observed in dielectric constant as well as in the dielectric loss is mainly due to the Maxwell–Wagner process [34] and space charge polarization [35]. The Maxwell–Wagner process is associated with the relaxation time that deals with the surface charges that remain uncompensated at interface inside the capacitors [36].

3. 2. Dielectric Studies at Different Temperatures

Figure 3 depicts the changes in dielectric constant with the logarithmic angular frequency of the applied AC signal applied at different temperatures. Here it was

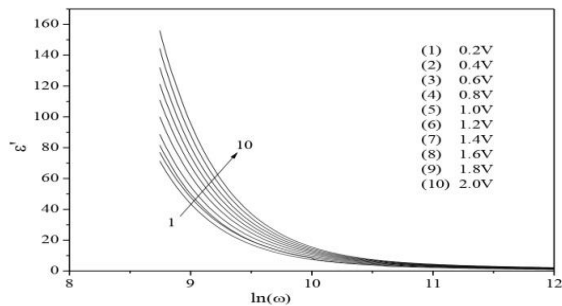


Figure 1. Frequency dependence of ϵ' for the heterojunction, Ni/n-TiO₂/p-Si/Al at different voltages

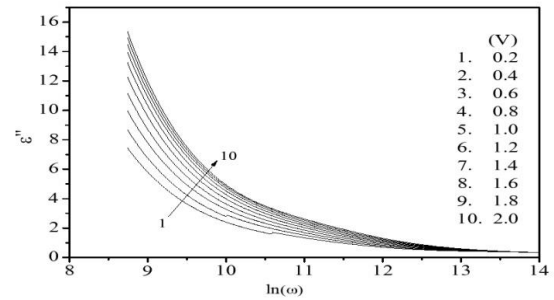


Figure 2. Frequency dependence of ϵ'' for the heterojunction, Ni/n-TiO₂/p-Si/Al at different voltages

noticed that at low frequency, the dielectric constant decreases as the frequency increases, hence showing strong dependence on the signal frequency, which is popularly known as dielectric dispersion. However, the dielectric constant increases as the temperature increases (step size 20 K). Such variations were shown by the heterojunction because the dipoles are not able to orient themselves in low temperatures regimes. However, with rise in temperature, the alignment of dipoles becomes easier (following thermal movements) which results in the increase of dielectric constant values.

Figure 4 depicts the variations of measured imaginary dielectric constant, ϵ'' of the heterojunction with respect to the frequency of the ac signal at different temperatures. With the increase in temperature the dielectric loss increases showing similar behavior as noticed for the dielectric constant in Figure 3. At high temperatures the large values of the dielectric loss, ϵ'' and sharp decrease with frequency shows the contributions of space charge polarizations and conductivity of the device. Moreover, this also clearly predicts thermally activated behavior of the dielectric relaxation process of the device. The rapid increasing behavior of ϵ'' with temperature at small frequencies may be attributed to the polarization phenomenon taking place due to the thermally activated transport mechanism of mobile charges and the defects. Large values of dielectric constants are found only either

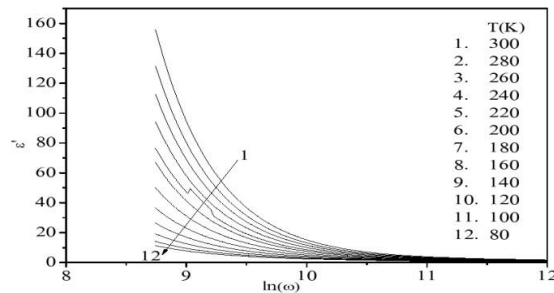


Figure 3. Frequency dependence of ϵ' for the heterojunction, Ni/n-TiO₂/p-Si/Al at different temperatures

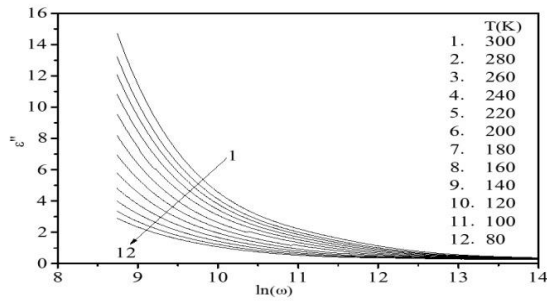


Figure 4. Frequency dependence of ϵ'' for the heterojunction, Ni/n-TiO₂/p-Si/Al at different temperatures

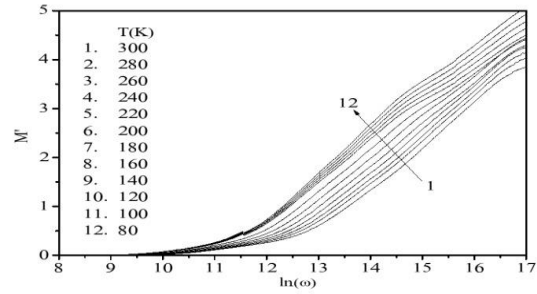


Figure 5. Frequency dependence of M' for the heterojunction, Ni/n-TiO₂/p-Si/Al at different temperatures

at low frequencies or high temperature because of the buildup of free charges at the interfaces between the sample and the electrodes called space-charge polarization process [7].

3. 3. Complex Modulus Analysis

More information can be obtained from the admittance spectroscopy data in the form of electric modulus formalisms. Variations of electric modulus with AC signal frequency allow us to confirm the existence of relaxation mechanisms in Ni/n-TiO₂/p-Si/Al heterojunction. The electric modulus analysis, real as well as the imaginary part provides significant information about electrode polarization and electrical conductivity [37]. For the considered heterostructure real and imaginary electric modulus are calculated from ϵ' and ϵ'' data as:

$$M^* = \frac{\epsilon'}{\epsilon'^2 + \epsilon''^2} + i \frac{\epsilon''}{\epsilon'^2 + \epsilon''^2} = M' + iM'' \quad (4)$$

Figure 5 depicts the variations in the real part of electric modulus with angular frequency at selected values of device temperature. The variations clearly show that M' approaches to zero at low frequencies. Moreover M' has a dispersing behavior at each temperature and at higher frequencies it tends towards M'_∞ . Monotonous increasing behavior of M' with the increasing frequency at each temperature is due to the presence of transport mechanism and very limited charge mobility under the influence of an induced electric field. These results imply the lack of restoring force which governs the mobility of the carriers. Figure 6 reports the frequency dependent variations of imaginary part of electric modulus (M'') at different selected temperatures. The M'' versus frequency plot evidently illustrates the strong thermally activated relaxation peaks whose positions i.e. M''_{max} get shifted towards high frequency region as the device temperature increases. The charge carriers being mobile at short distances are confined to potential wells at frequency above the peak maximum, whereas they are mobile at long distances in the frequency region below peak maximum. So, the frequency corresponding to the

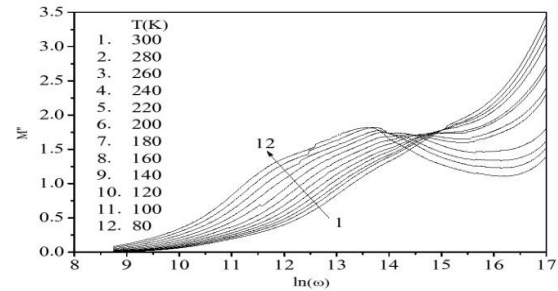


Figure 6. Frequency dependence of M'' for the heterojunction, Ni/n-TiO₂/p-Si/Al at different temperatures

peak is indicative of transition from short range to long range charge mobility. From the behavior of M'' the hopping mechanism get confirmed which intrinsically dominates in the material.

Figures 7 and 8 illustrate frequency dependent variations of logarithmic M' and M'' for the Ni/n-TiO₂/p-Si/Al heterojunction at different selected voltages. With an increase in the frequency both the parameters show increasing trends because of the polarization [42]. Corresponding to $M_\infty = 1/\epsilon'_\infty$, these parameters attain certain maximum values for each voltage at high frequencies due to relaxation processes [42-43]. At low frequencies M' and M'' almost approach to zero value. It is obvious that charge effect appears in these devices because of the release of charge from the surface states or interface traps on the application of appropriate external ac voltage [40]. Hence, the peak behavior in electric modulus indicates the existence of relaxation phenomena [44]. Due to short range charge mobility M' increases rapidly with increasing frequency and it is due to the lack of restoring force which govern the mobility of the carriers under the influence of electric field [45-47]. Correlation between the charge motions is exhibited by the imaginary part of the electric modulus [45-47]. Moreover, the conduction mechanism is dominated by the hopping of carriers between surface states i.e. the conductivity may be treated as electric field activated hopping from traps to traps.

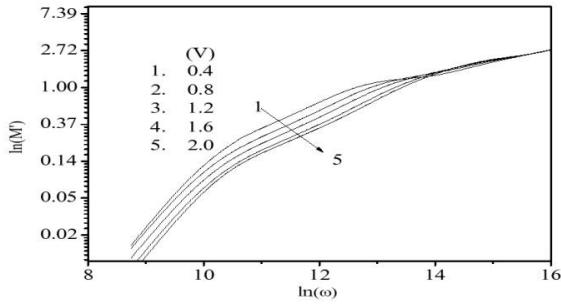


Figure 7. Frequency dependence of M' for the heterojunction, Ni/n-TiO₂/p-Si/Al at different voltages

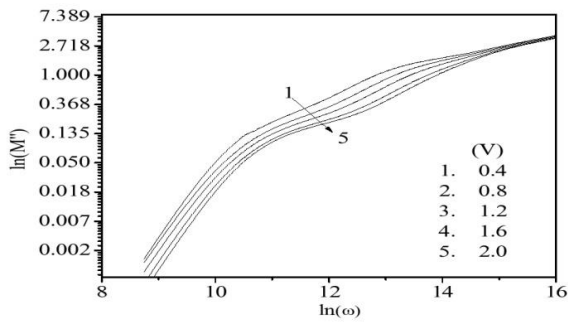


Figure 8. Frequency dependence of M'' for the heterojunction, Ni/n-TiO₂/p-Si/Al at different voltages

3. 4. Electrical Conductivity Analysis The complex conductivity σ^* obtained from the dielectric loss values can be expressed by the following relation:

$$\sigma^* = i\epsilon_0\omega\epsilon^* = i\epsilon_0\omega(\epsilon' - i\epsilon'') = \epsilon_0\omega\epsilon'' + i\epsilon_0\omega\epsilon' \quad (5)$$

The real part of σ^* is called ac conductivity (σ_{ac}) given by:

$$\sigma_{ac} = \epsilon_0\omega\epsilon'' \quad (6)$$

Figure 9 shows the dependence of the electric conductivity on the frequency at various selected temperatures. The graph reveals the conductivity dispersion which occurs due to the polarization effects in low frequency region [48]. Drop of conductivity at low frequency region occurs due the accumulation of charge. The frequency dependence of electrical conductivity is explained by Jonscher's power law given by:

$$\sigma_{ac} = \sigma_{dc} + A\omega^n \quad (7)$$

where, DC conductivity is denoted by σ_{dc} at frequency limiting to zero value, $\omega = 2\pi f$ denotes the angular frequency, A is called pre-exponential constant, and n represents the power law exponent whose value lies

between zero and one i.e. $0 < n < 1$ [49]. From the plot it is found that the conductivity of the device also increases with temperature. The dependence of AC conductivity on frequency for the heterojunction, Ni/n-TiO₂/p-Si/Al, has been obtained using the following equation [49]:

$$\sigma_{ac} = \epsilon''\omega\epsilon_0 \quad (8)$$

at different selected external applied voltages applied at room temperature and shown in Figure 10. The polarization decreases with increase in frequency which results in an increase in AC conductivity of the considered heterojunction. The higher values of AC conductivity increase the eddy currents as well as energy losses. The observed trends are found to be compatible with those quoted in literature, wherein it was recommended that the gradual decrease in series resistance (R_s) with increasing frequency increases the AC conductivity [39-40]. σ_{ac} increases with an increase in voltage as well as frequency. This is attributed to the fact that the dipoles in the heterostructure have better polarization as the increase of voltage and frequency.

The overall variations in the ϵ' , ϵ'' , M' , M'' and ac electric conductivity (σ_{ac}) are the result of reordering and restructuring of charges at the interface of Ni/n-TiO₂/p-Si/Al heterojunction under the effect of external electric field or voltage and interface polarization.

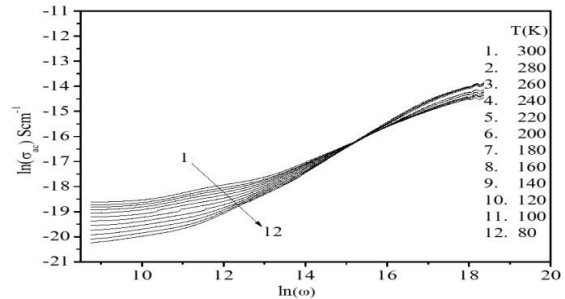


Figure 9. Frequency dependence of σ_{ac} for the heterojunction, Ni/n-TiO₂/p-Si/Al at different temperatures

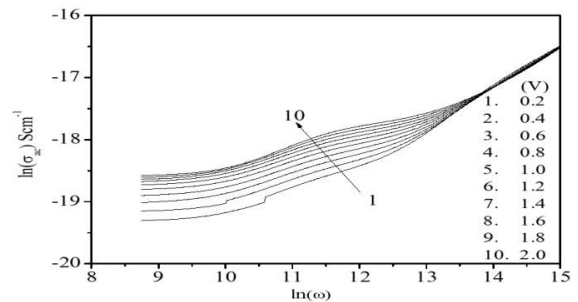


Figure 10. Frequency dependence of σ_{ac} for the heterojunction, Ni/n-TiO₂/p-Si/Al at different voltages

4. CONCLUSION

The paper reports the analysis of the dielectric properties at the interface of n-TiO₂/p-Si heterojunction obtained through pulsed laser deposition process in wide range of applied bias and temperature with frequency. The parameters ϵ' , ϵ'' , M' , M'' and AC electric conductivity (σ_{ac}) have been obtained through admittance spectroscopy ($C-V$ and $G/\omega-V$) measurements. These parameters are sensitive to applied voltage and temperature at wide range of frequency. The parameters ϵ' and ϵ'' decrease while electric moduli as well as AC conductivity increase with the frequency. The values of ϵ' , ϵ'' , σ_{ac} increase while the values of M' and M'' decrease with increase in temperature. The value of σ_{ac} increases with the increasing frequency and temperature. The increase in the σ_{ac} with the increasing temperature can be attributed to the rise in thermally generated free charge carriers. The observed behavior is due to the mobility of charge carriers in TiO₂ thin film, which are responsible for electronic polarization and hopping across the surface states. The frequency and temperature dependence of $C-V$ and $G/\omega-V$ characteristics confirmed that both the frequency and the temperature variations strongly affect the dielectric permittivity, AC conductivity and electric moduli. The findings can be inferred to suggest that interfacial polarization can occur more easily at low frequencies, thus leading to the Ni/n-TiO₂/p-Si/Al heterostructure variance of dielectric properties and electrical conductivity.

5. REFERENCES

1. Cho, M., Seo, JH., Park, DW., Zhou, W., Ma, Z., "Capacitance-voltage characteristics of Si and Ge nanomembrane based flexible metal-oxide-semiconductor devices under bending conditions", *Applied Physics Letters*, Vol. 108, (2016), 233505, <https://doi.org/10.1063/1.4953458>.
2. Pudasaini, PR., Noh, JH., Wong, AT., Ovchinnikova, OS., Haglund, AV., Dai, S., Ward, TZ., Mandrus, D., Rack, PD., "Ionic liquid activation of amorphous metal-oxide semiconductors for flexible transparent electronic devices", *Advanced Functional Materials*, Vol. 26, (2016), 2820-2825, <https://doi.org/10.1002/adfm.201505274>.
3. Kocyigit, A., Orak, I., Turut, A., "Temperature dependent dielectric properties of Au/ZnO/n-Si heterojunction", *Materials Research Express*, Vol. 5, (2018), 035906, <https://doi.org/10.1088/2053-1591/aab2e3>.
4. Sze, SM., "Physics of Semiconductor Devices, 2nd Edition, Wiley, New York", (1981).
5. Deuling, H., Klausmann, E., Goetzberger, A., "Interface states in Si/SiO₂ interfaces", *Solid State Electronics*, Vol. 15, (1972), 559-571, [https://doi.org/10.1016/0038-1101\(72\)90157-8](https://doi.org/10.1016/0038-1101(72)90157-8).
6. Kar, S., Narasimhan, RI., "Characteristics of the Si/SiO₂ interface states in thin (70-230 Å) oxide structures", *Journal of Applied Physics*, Vol. 61, (1987), 353-359, <https://doi.org/10.1063/1.338273>.
7. Dokme, I., Altindal, S., "The $C-V$ and $G/\omega-V$ characteristics of Au/SiO₂/n-Si capacitors", *Physica B*, Vol. 391, (2007), 59-64, <https://doi.org/10.1016/j.physb.2006.08.049>.
8. Yucedag, I., Altindal, S., Tataroglu, A., "On the profile of frequency dependent series resistance and dielectric constant in MIS structure", *Microelectronic Engineering*, Vol. 84, (2007), 180-186, <https://doi.org/10.1016/j.mee.2006.10.071>.
9. Kar, S., Varma, S., "Determination of silicon-silicon dioxide interface state properties from admittance measurements under illumination", *Journal of Applied Physics*, Vol. 58, (1985), 4256-4266, <https://doi.org/10.1063/1.335561>.
10. Yuksel, OF., Ocak, SB., Selcuk, AB., "High frequency characteristics of tin oxide thin films on Si", *Vacuum*, Vol. 82, (2008), 1183-1186, <https://doi.org/10.1016/j.vacuum.2008.02.002>.
11. Demirezen, S., "Frequency and voltage dependent dielectric properties and electrical conductivity of Au/PVA (Bi-doped)/n-Si Schottky barrier diodes at room temperature", *Applied Physics A*, Vol. 112, (2013), 827-833, DOI 10.1007/s00339-013-7605-7.
12. Padma, R., Lakshmi, BP., Reddy, VR., "Capacitance frequency ($C-f$) and conductance frequency ($G-f$) characteristics of Ir/n-InGaN Schottky diode as a function of temperature", *Superlattices and Microstructures*, Vol. 60, (2013), 358-369, <https://doi.org/10.1016/j.spmi.2013.05.014>.
13. Tekeli, Z., Gokcen, M., Altindal, S., Ozelcik, S., Ozbay, E., "On the profile of frequency dependent dielectric properties of (Ni/Au)/GaN/Al_{0.3}Ga_{0.7}N heterostructures", *Microelectronics Reliability*, Vol. 51, (2011), 581-586, <https://doi.org/10.1016/j.microrel.2010.09.018>.
14. Hill, W.A., Coleman, CC., "A single-frequency approximation for interface-state density determination", *Solid State Electronics*, Vol. 23, (1980), 987-993, [https://doi.org/10.1016/0038-1101\(80\)90064-7](https://doi.org/10.1016/0038-1101(80)90064-7).
15. Orak, I., Kocyigit, A., Karatas, S., "The analysis of the electrical and photovoltaic properties of Cr/p-Si structures using current-voltage measurements", *Silicon*, Vol. 10, (2018), 2109-2116, <https://doi.org/10.1007/s12633-017-9731-x>.
16. Rayssi, C., Rhouma, FIH., Dhahri, J., Khirouni, K., Zaidi, MA. Belmabrouk, H., "Structural, electric and dielectric properties of Ca_{0.85}Er_{0.1}Ti_{1-x}Co_{4x/3}O₃ (0 ≤ x ≤ 0.1)", *Applied Physics A: Materials Science and Processing*, Vol. 123, (2017), 1-13, <https://doi.org/10.1007/s00339-017-1365-8>.
17. Tataroglu, A., "Electrical and dielectric properties of MIS Schottky diodes at low temperatures", *Microelectronics Engineering*, Vol. 83, (2006), 2551-2557, <https://doi.org/10.1016/j.mee.2006.06.007>.
18. Baris, B., "Frequency dependent dielectric properties in Schottky diodes based on rubrene organic semiconductor", *Physica E*, Vol. 54, (2013), 171-176, DOI:10.1016/j.physe.2013.06.018.
19. Shiwakoti, N., Bobby, A., Asokan, K., Antony B., "Temperature dependent dielectric studies of Ni/n-GaP Schottky diodes by capacitance and conductance measurements", *Materials Science in Semiconductor Processing*, Vol. 42, (2016), 378-382, <https://doi.org/10.1016/j.mssp.2015.11.010>.
20. Schroder, DK., "Semiconductor material, device characterization, Wiley, Hoboken, NJ", (2006).
21. Symth, CP., "Dielectric behaviour and structure, McGraw-Hill, New York", (1955).
22. Fandiyeva, A., Demirezen, IM., Altindal, S., "Temperature dependence of forward and reverse bias current voltage characteristics in Al-TiW-PtSi/n-Si Schottky barrier diodes with the amorphous diffusion barrier", *Journal of Alloys and*

- Compounds*, Vol. 552, (2013), 423-429, <https://doi.org/10.1016/j.jallcom.2012.11.093>.
23. Pakma, O., Serin, N., Serin, T., Altindal, S., "Influence of frequency and bias voltage on dielectric properties and electrical conductivity of Al/TiO₂/p-Si/p+ (MOS) structures", *Journal of Physics D: Applied Physics*, Vol. 41, (2018), 215103, DOI: 10.1088/0022-3727/41/21/215103.
 24. Afandiyeva, IM., Bulbul, MM., Altindal, S., Bengi, S., "Frequency dependent dielectric properties and electrical conductivity of platinum silicide/Si contact structures with diffusion barrier", *Microelectronics Engineering*, Vol. 93, (2012), 50-55, <https://doi.org/10.1016/j.mee.2011.05.041>.
 25. Sattar, AA., Rahman SA., "Dielectric Properties of Rare Earth Substituted Cu-Zn Ferrites", *Physica Status Solidi*, Vol. 200, (2003), 415-422, DOI: 10.1002/pssa.200306663.
 26. Popescu, M., Bunget, I., "Physics solid dielectrics, Amsterdam: Elsevier", 1984.
 27. Tugluoglu, N., Karadeniz, S., Sahin, M., Safak, H., "Temperature-dependent barrier characteristics of Ag/p-SnSe Schottky diodes based on I-V-T measurements", *Semiconductor Science and Technology*, Vol. 19, (2004), 1092-1097, DOI: 10.1088/0268-1242/19/9/004.
 28. Coskun, C., Biber, M., Efeoglu, H., "Temperature dependence of current-voltage characteristics of Sn/p-GaTe Schottky diodes", *Applied Surface Science*, Vol. 211, (2003), 360-366, [https://doi.org/10.1016/S0169-4332\(03\)00267-8](https://doi.org/10.1016/S0169-4332(03)00267-8).
 29. Yakuphanoglu, F., Tugluoglu, N., Karadeniz, S., "Space charge-limited conduction in Ag/p-Si Schottky diode", *Physica B*, Vol. 392, (2007), 188-191, <https://doi.org/10.1016/j.physb.2006.11.018>.
 30. Tugluoglu, N., Karadeniz, S., "Analysis of current-voltage and capacitance-voltage characteristics of perylene-monoimide/n-Si Schottky contacts", *Current Applied Physics*, Vol. 12, (2012), 1529-1535, <https://doi.org/10.1016/j.cap.2012.04.027>.
 31. Nicollian, EH., Goetzberger, A., "The Si-SiO₂ interface-electrical properties as determined by the metal-insulator-silicon conductance technique", *Bell System Technical Journal*, Vol. 46, (1967), 1055-1133, DOI: 10.1002/j.1538-7305.1967.tb01727.x.
 32. Castagne, R., Vapaille, A., "Description of the SiO₂-Si interface properties by means of very low frequency MOS capacitance measurements", *Surface Science*, Vol. 28, (1971), 157-193, [https://doi.org/10.1016/0039-6028\(71\)90092-6](https://doi.org/10.1016/0039-6028(71)90092-6).
 33. Kumar, N., Chand, S., "Effects of temperature, bias and frequency on the dielectric properties and electrical conductivity of Ni/SiO₂/p-Si MIS Schottky diodes", *Journal of Alloys and Compounds*, Vol. 817, (2019), 153294, <https://doi.org/10.1016/j.jallcom.2019.153294>.
 34. Wagner, KW., "Zur Theorie der unvollkommenen Dielektrika", *Annals of Physics*, Vol. 40, (1913), 817-855, <https://doi.org/10.1002/andp.19133450502>.
 35. Bidault, O., Goux, P., Kchikech, M., Belkaoumi, M., Maglione, M., "Space-charge relaxation in perovskites", *Physical Review B*, Vol. 49, (1994), 7868-7873, <https://doi.org/10.1103/PhysRevB.49.7868>.
 36. Gorodea, I., Goanta, M., Toma, M., "Impact of A cation size of double perovskite A₂AlTaO₆ (A = Ca, Sr, Ba) on dielectric and catalytic properties", *Journal of Alloys Compounds*, Vol. 632, (2015), 805-809, <https://doi.org/10.1016/j.jallcom.2015.01.310>.
 37. Sutar, BC., Choudhary, RNP., Das, PR., "Dielectric and impedance spectroscopy of Sr(Bi_{0.5}Nb_{0.5})O₃ ceramics", *Ceramic International*, Vol. 40, (2014), 7791-7798, <https://doi.org/10.1016/j.ceramint.2013.12.122>.
 38. Ho, J., Jow, TC, Boggs, S., "Historical introduction to capacitor technology", *IEEE Electrical Insulation Magazine*, Vol. 26, (2010), 20-25, DOI: 10.1109/MEI.2010.5383924.
 39. Lin, JH., Zeng, JJ., Lin, YJ., "Electronic transport for graphene/n-type Si Schottky diodes with and without H₂O₂ treatment", *Thin Solid Films*, Vol. 550, (2014), 582-586, <https://doi.org/10.1016/j.tsf.2013.11.079>.
 40. Chandrakala, HN., Bommulu, R., Shivakumaraiah, Madhu, G.M., Hatna, S., "The influence of zinc oxide-cerium oxide nanoparticles on the structural characteristics and electrical properties of polyvinyl alcohol films", *Journal of Materials Science*, Vol. 47, (2012), 8076-8084, DOI: 10.1007/s10853-012-6701-y.
 41. Tataroglu, A., Altindal, S., "Study on the frequency dependence of electrical and dielectric characteristics of Au/SnO₂/n-Si (MIS) structures", *Microelectronics Engineering*, Vol. 85, (2008), 1866-1871, DOI: 10.1016/j.mee.2008.05.025.
 42. Tripathi SK., Sharma, M., "Analysis of the forward and reverse bias I-V and C-V characteristics on Al/PVA:n-PbSe polymer nanocomposites Schottky diode", *Journal of Applied Physics*, Vol. 111, (2012), 074513, <https://doi.org/10.1063/1.3698773>.
 43. Yeriskin, SA., Unal, HI., Sari, B., "Electrical and dielectric characteristics of Al/polyindole Schottky barrier diodes. II. frequency dependence", *Journal of Applied Polymer Science*, Vol. 120, (2011), 390-396, DOI: 10.1002/app.33148.
 44. Ishai, PB., Sader, E., Feldman, Y., Felner, Y., Weger, M., "Dielectric properties of Na_{0.7}CoO₂ and of the superconducting Na_{0.3}CoO₂·13H₂O", *Journal of Superconductivity*, Vol. 18, (2005), 455-459, DOI: 10.1007/s10948-005-0024-z.
 45. Pissis, P., Kyritsis, A., "Electrical conductivity studies in hydrogels", *Solid State Ionics*, 97, (1997), 105-113.
 46. Champness, CH., Clark, WR., "Anomalous inductive effect in selenium Schottky diodes", *Applied Physics Letters*, Vol. 56, (1990), 1104-1106, <https://doi.org/10.1063/1.102581>.
 47. Prabakar, K., Narayandass, SK., Mangalaraj, D., "Dielectric properties of Cd_{0.6}Zn_{0.4}Te thin films", *Physica Status Solidi*, Vol. 199, (2003), 507-514, doi.org/10.1002/pssa.200306628
 48. Du, H., Li, Y., Li, H., Shi, X., Liu, C., "Relaxor behavior of bismuth layer-structured ferroelectric ceramic with m=2", *Solid State Communications*, Vol. 148, (2008), 357-360, [10.1016/j.ssc.2008.05.017](https://doi.org/10.1016/j.ssc.2008.05.017).
 49. Dutta, P., Biswas, S., De, SK., "Dielectric Relaxation in Polyaniline-polyvinyl alcohol composites", *Materials Research Bulletin*, Vol. 37, (2002), 193-200, [https://doi.org/10.1016/S0025-5408\(01\)00813-3](https://doi.org/10.1016/S0025-5408(01)00813-3).

Persian Abstract

چکیده

در مطالعه حاضر خواص دی الکتریک مانند ثابت دی الکتریک (ϵ')، تلفات دی الکتریک (ϵ'')، بخش واقعی مدول الکتریکی (M')، قسمت خیالی مدول الکتریکی (M'') و رسانایی الکتریکی AC، (σ_{ac}) در طیف وسیعی از ولتاژ اعمالی بررسی شده است. دما و فرکانس برای اتصال ناهمگون Ni/n-TiO₂/p-Si/Al یک لایه نانوکریستالی TiO₂ بر روی سیلیکون دوپ شده با بور نوع p در محیط کنترل شده با اکسیژن با استفاده از لیزر آگزایمر بهینه شده Krf رشد داده شد. تماس اهمی فلزات نیکل خالص و آلومینیوم به ترتیب روی TiO₂ و سیلیکون با سیستم پوشش حرارتی ایجاد شد. ویژگی هایی که با کمک اندازه گیری های رسانایی-ولتاژ و ظرفیت-ولتاژ به دست می آیند که به عنوان طیف سنتزی امپدانس/ادمیتانس نیز شناخته می شوند. پارامترهای مورد مطالعه به فرکانس، دما و ولتاژ بسیار حساس هستند. بازسازی و ترتیب مجدد چگالی حالت رابط به دلیل تغییرات دما و قطبش های سطحی به دلیل تغییرات فرکانس در مجموع منجر به تغییرات مشاهده شده در و . با افزایش فرکانس هدایت AC و مدول الکتریکی نیز افزایش می یابد. مکانیسم آرامش را می توان در تحلیل مدول الکتریکی پیچیده مشاهده کرد. فرآیند هدایت حرارتی فعال شده با هدایت AC وابسته به فرکانس در دماهای مختلف نشان داده شد. با استفاده از قانون توان، هدایت AC مورد تجزیه و تحلیل قرار گرفت و مشخص شد که با دما و ولتاژ اعمالی افزایش می یابد.



Effect of Carbonation on the Collapse Potential of Magnesium Oxide Treated Gypseous Soil

A. S. A. Al-Gharbawi*, M. Y. Fattah, M. R. Mahmood

Civil Engineering Department, University of Technology, Baghdad, Iraq

PAPER INFO

Paper history:

Received 28 October 2021

Received in revised form 06 January 2022

Accepted 13 January 2022

Keywords:

Collapsible Soil

Gypseous Soil

Magnesium Oxide

Carbonation

ABSTRACT

Collapsible soils are soils susceptible to large volumetric strains when they become saturated. Numerous soil types fall in the general category of collapsible soils, including gypseous soil which is characterized by relatively low density, appreciable strength and stiffness in the dry state, but is susceptible to significant deformations as a result of wetting. The aim of this study is to investigate the effectiveness of curing period time of carbonation on magnesium oxide stabilization of gypseous soil. In this research, magnesium oxide is used to improve a collapsible gypseous soil by using (0, 5, 10 and 15%) with two relative densities (35 and 75%) and carbonation at different carbonation periods (0, 1, 3 and 24 hours). Conventional collapse tests, single oedometer and double oedometer and modified collapse test are used in this research to investigate the effect of carbonation periods on the improvement of the soil. The modified collapse test apparatus is used. The results illustrated that the collapse potential decreased more than 65% and 55% for the carbonated soil without treatment for conventional tests and modified collapse test, respectively. A decreased about 55% for treated soil with 10% magnesium oxide and carbonated for 3 hours for both of conventional tests and modified collapse test. The carbonation period time is used to accelerate the improvement of the soil as well as decreased the collapse potential and the results showed that no clear change in collapse potential for the period time more than 3 hours.

doi: 10.5829/ije.2022.35.04a.10

1. INTRODUCTION

Gypseous soil is one of the most problematic soils which is subjected to collapse under both of saturation and loading. It covers about 27 - 36% of Iraq area [1].

Collapsible soils are characterized by very distinct geotechnical properties that include high void ratio, low initial bulk density and water content, great dry strength and stiffness, high percentage of fine grained particles and zero or slight plasticity. The main geotechnical problem associated with these soils is the significant loss of shear strength and volume reduction occurring when they are subjected to additional water from rainfall, irrigation, broken water or sewer lines, moisture increase due to capillarity or "pumping" as a result of loading, ground water rise, etc. Generally, collapsible soils are under unsaturated conditions in the dry state, with negative pore pressure resulting in higher effective

stresses and greater shear strength. Cases of wetting induced collapse in gypseous type soils have been documented in natural deposits and in man-made fills. In the latter case they can often cause large differential settlements that reduce the serviceability of the structure, and raise the frequency and cost of rehabilitation.

Many researches dealt with improving the collapsible gypseous soil with different materials to reduce the collapsibility of the soil such as lime, cement, silica fume etc. Currently, various types of recyclable materials are used in civil engineering applications. One of the future challenges in civil engineering field facing sustainability and the bulk utilization of waste materials without affecting the performance of the product related to civil engineering field [2].

The work conducted by Hayal et al. [3] was using nano silica and nano clay with different percentages to improve the gypseous soil brought from Bahr Al-Najaf.

*Corresponding Author Institutional Email:
ahmed.s.algharbawi@uotechnology.edu.iq (A. S. A. Al-Gharbawi)

The results showed that using nano clay reduced the collapse potential about 73.75%.

Abdulrahman et al. [4] used different percentages of fiber plastic to improve the collapsibility of the gypseous soil and they have concluded that 1% of fiber plastic reduce the collapse potential from 12.5% to 0.96%.

Large scale reinforcement of the collapsible soil by using encased stone column was performed by Bahrami and Marandi [5] with aspect ratio (diameter to length) 10 to 25%. They have concluded that the optimum aspect ratio is about 15% which reduces the collapse potential about 82%.

One of the recent developments in additive materials is the reactive magnesia or reactive magnesium oxide (MgO). Magnesium oxide is a white solid material that occurs naturally as periclase, it is a source of Magnesium. The magnesium oxide is not virulent but it is one of the materials friendly with environment [6, 7].

Some researches used magnesium oxide and carbonated magnesium oxide for stabilizing soil and compared results with lime, cement etc. Carbonated magnesium oxide is adequate with sand and porous blocks, there were laboratory studies by treating sandy soil with 5 and 10% magnesium oxide; then, the mixture is subjected to carbon dioxide gas for about 3 hours to accelerate the treating and the results were compared with Portland cement. When the carbon dioxide increased, the pressure that caused increasing in carbonation till reaching improvement percent about 20% then increasing the carbonation did not reveal a clear increasing in strength. The strength will be at the same range when the carbonation period was about 2 days [8].

Yi et al. [9] studied the treatment of silty soil with two percentages of magnesium oxide and carbonated at different period times 0.5 hour, 6 hours and 7 days with three pressures of carbonation 50, 100 and 200 kPa. The results showed that the pressure of carbonation increased the strength of the soil but no clear increasing in strength with increasing pressure. The work confirmed that the carbon dioxide is rapiding the magnesium oxide treatment, as well as this method is adequate to soil improvement (stabilization and solidation).

Liu et al. [10] used the unconfined compressive strength to investigate the improvement of the clayey silt soil with different percentages of 12 hours carbonation magnesium oxide. The results showed that the unconfined compressive strength increased and the structure of the soil after treatment changed from elastic-plastic to brittleness.

Hwang et al. [11] studied the improvement of the silty sand sediment in South Korea by using unconfined compressive strength of soil treated with 30% of carbonated magnesium oxide. The results illustrated that the strength after 1 year was 4.78 MPa which is higher than Portland cement about 1.3 times.

Cai et al. [12] depended on cycles of drying and wetting to mixing of silty soil with 15 % of carbonated Magnesium Oxide for curing periods 3 and 6 hours then compared this 15% Portland cement. The results showed that the strength of carbonated magnesium oxide higher than on cement as well as at carbonated magnesium oxide, the durability of the soil increased with the cycles of drying and wetting and curing period for 3 hours gave results similar to 6 hours.

Wang et al. [13] depended on mixing a clayey soil with different percentages of magnesium oxide, calcium oxide and fly-ash then carbonated the mixture. The results showed that the strength after carbonating period time 0.5 hour was about 75% as compared with the strength in the soil stabilized with 10% Portland cement after 28 days. The optimum time of carbonation was 6 hours.

The main purpose of this study is to investigate the effectiveness of curing period time of carbonation on magnesium oxide stabilization of gypseous soil by using different percentages of magnesium oxide prepared at two relative densities. This study was done by conducting conventional tests (single oedometer test and double oedometer test) and modified collapse test.

2. MATERIALS

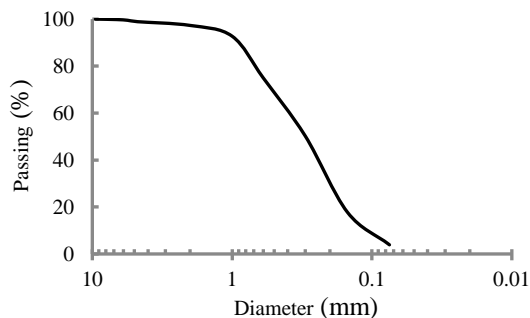
2. 1. Soil The granular soil utilized in this study was supplied from Tikrit, north of Baghdad, and had a gypsum level of 49%. Table 1 shows the physical parameters, whereas Figure 1 shows the grain size distribution. The specifications of the American Society or Testing and Materials were adopted. The Unified Soil Classification System classifies the soil as poorly graded sand (SP).

2. 2. Magnesium Oxide The magnesium oxide used in this research has a light weight with a unit weight of 1 kN/m³. Magnesium oxide, with the chemical formula MgO, is a common alkaline earth metal oxide. White powder with a melting point of 2852°C and a boiling temperature of 3600°C, as well as a relative density of 3.58 (at 25°C). It can be dissolved in acid or ammonium salt solutions. It produces magnesium hydroxide when it reacts slowly with water, having a solubility of 0.01 g/l. It can be made into magnesium bicarbonate by dissolving it in a carbon dioxide aqueous solution.

2. 3. Carbonation The carbonation is the carbon dioxide pressure made by using carbonation apparatus. The apparatus was manufactured from several parts as illustrated in Figure 2. The main purpose of carbonation is to stabilize the improvement of magnesium oxide in the soil.

TABLE 1. Physical properties of soil

Physical properties	Value
Gypsum content (%)	49
Specific gravity (Gs)	2.41
Liquid limit (L.L) (%)	26
Plastic limit (P.L) (%)	N.P
Gravel (%)	0
Sand (%)	96
Fines (%)	4
D ₆₀ (mm)	0.4
D ₃₀ (mm)	0.2
D ₁₀ (mm)	0.11
Uniformity coefficient (Cu)	3.64
Curvature coefficient (Cc)	0.91
(O.M.C) (%)	12
γ _{dry max.} (kN/m ³)	17.45
γ _{dry min.} (kN/m ³)	12.12
Classification	SP

**Figure 1.** Grain size distribution

The carbonation curing apparatus was used to apply a low pressure of pure carbon dioxide gas on soil samples. The major components of the set-up include compressed gas tanks, pressure vessel, thermocouple, data acquisition, vacuum and pressure transducer. A gas injection-releasing carbonation process was used for all carbonation tests.

The soil carbonation procedure is made as follows:

1. Mixing the soil with using a percentage of magnesium oxide carefully.
2. Placing the mix in the carbonation container if the test needs a carbonation process.
3. The valve of vacuum is turned on and the electric power of vacuum is on to extract the air from the soil and container.
4. The valve of vacuum is closed and opens the valve of carbon dioxide till reaching the same pervious pressure.

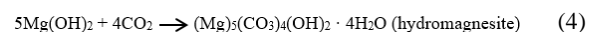
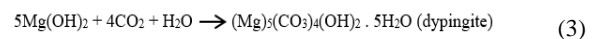
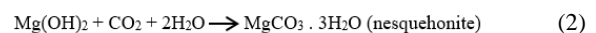
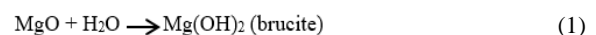
**Figure 2.** Carbonation apparatus

5. The carbon dioxide valve is turned off and the curing continues for a period of time.

The carbonation curing apparatus was used to subject samples to a low pressure of pure carbon dioxide gas and oxygen gas. A gas injection-releasing carbonation process was used for all carbonation tests [14].

3. CHEMICAL REACTIONS

The carbonation of any structure is provided enough of carbon dioxide to penetrate through its porous, reactive magnesium oxide hydrates by this equation as described by Al-Tabbaa [8] and Yi et al. [9]:



4. TESTING PROGRAM

The testing program of the gypseous soil treated with magnesium oxide and carbonated magnesium oxide is presented in Figure 3.

4. 1. Single Oedometer Test (SOT) This type of test depends on loaded the sample at initial water content till reached the vertical stress to 200 kPa then the sample soaked with water for 24 hours. The difference between

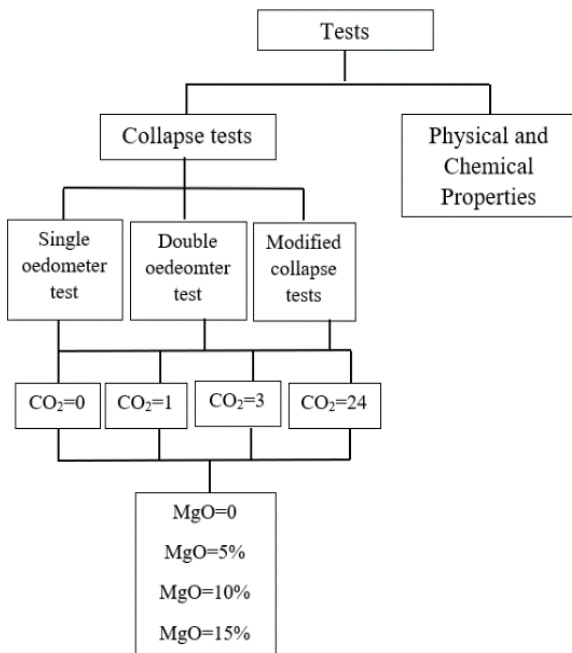


Figure 3. Testing program flow chart

the soaked and unsoaked settlement results represents the collapse potential. After that, the test is continued the same as consolidation test from loading and unloading.

4. 2. Double Oedometer Test DOT This test can be performed with two identical samples: the first is tested at its natural water content until the end of the test, while the second sample is soaked at the start. The testing procedure is the same as the consolidation test procedure. At any given pressure, the difference between the two curves of the void ratio - pressure ($e - \log P'$) denotes soil collapse. Collapse potential is evaluated using a typical oedometer instrument in a constant temperature and humidity condition, according to ASTM D5333 [15].

4. 3. Modified Collapse Test MCT There are some weaknesses in the traditional methods (single oedometer test and double oedometer test) such as the size of sample is too small to measure the collapse and saturation method from up by downward flow that may not making saturation for all the soil particles and do not show the right collapse potential; therefore, a new type of tests that is proposed in this study and used to calculate the collapse potential and compare the results with the single and double oedometer results.

The dimensions of a modified Rowe cell are employed in the test. An electric motor with a load cell and indication is used to load a load with a diameter of 150 mm and a height of 50 mm. The sample is loaded in the same way as a single oedometer test until it reaches a vertical stress of (200 kPa), after which it is soaked with water from the bottom up using a scaling tank filled with

water with a hydraulic gradient of 3.667 by a hydraulic height of 170 mm above the soil sample and monitoring the saturation point with SMCS sensors [16].

The frame of loading consists of a motor with piston to shed a required load with a gear box to control the rate of velocity. Load cell of 5 ton capacity is used with its indicator to record the load with a dial gauge to record the settlement. The load is applied gradually over a short period of time every 24 hours, and the settlement is recorded every 15 minutes with the time the loading is calibrated.

The test employs two filter sheets to prevent gypsum salt that has not dissolved in water from entering the porous stone holes. The sample is soaked for 24 hours after saturation to document any additional settlement. The test then continues with more loading and unloading, as in a traditional consolidation test. Figure 4 illustrates the all the parts of modified collapse test (MCT).

5. RESULTS AND DISCUSSION

The effect of carbonation time on the collapse potential for the conventional tests (SOT and DOT) for different percentages of magnesium oxide and relative densities are described in Figures 5 to 8. A summary of all collapse test results is illustrates in Table 2.

The effect of carbonation time on collapse potential for the modified collapse test (MCT) for different

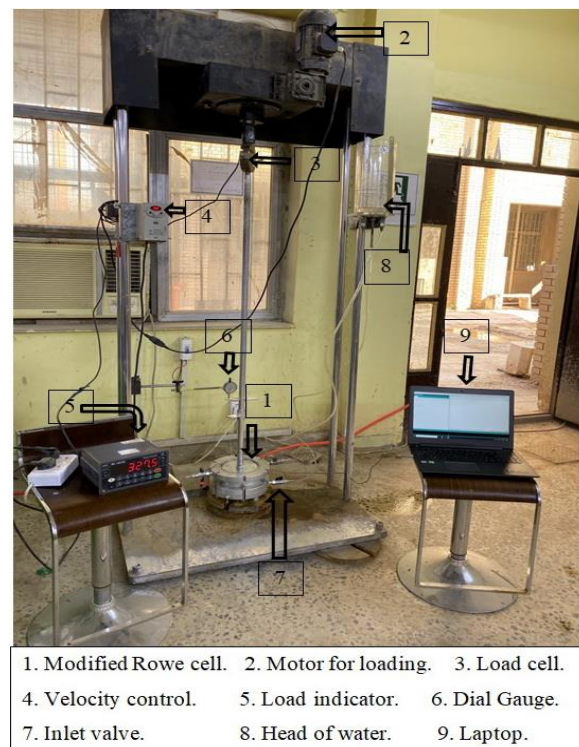


Figure 4. Modified apparatus for collapse test

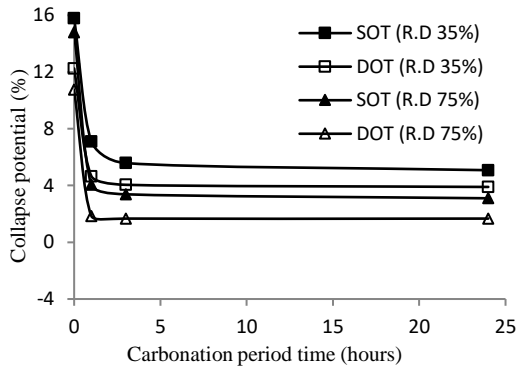


Figure 5. Change in collapse potential with increase of carbonation period time for 0% magnesium oxide

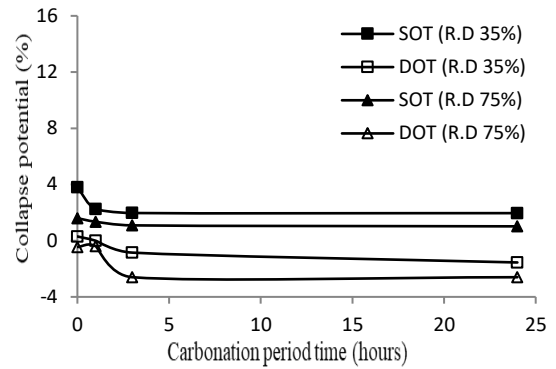


Figure 7. Change in collapse potential with increase of carbonation period time for 10% magnesium oxide

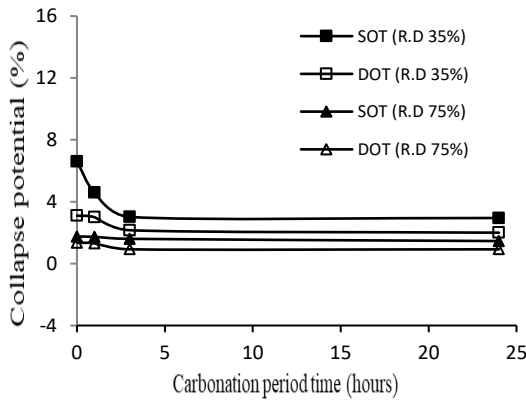


Figure 6. Change in collapse potential with increase of carbonation period time for 5% magnesium oxide

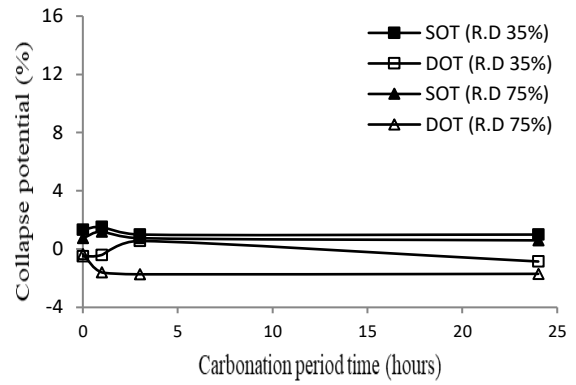


Figure 8. Change in collapse potential with increase of carbonation period time for 15% magnesium oxide

TABLE 2. Summary of the collapse potential of all tests

Collapse Potential															
R.D 35(%)															
CO ₂ =0 hr				CO ₂ =1 hr				CO ₂ =3 hrs				CO ₂ =24 hrs			
MgO (%)	MCT (%)	SOT (%)	DOT (%)	MgO (%)	MCT (%)	SOT (%)	DOT (%)	MgO (%)	MCT (%)	SOT (%)	DOT (%)	MgO (%)	MCT (%)	SOT (%)	DOT (%)
0	22.3	15.8	12.25	0	11.11	7.1	4.65	0	10.28	5.58	4.05	0	9.97	5.08	3.9
5	9.07	6.6	3.1	5	6.17	4.6	3	5	3.88	3.02	2.	5	3.75	2.95	2
10	4.78	3.8	0.3	10	3.85	2.25	0.005	10	2.32	1.97	-0.85	10	2.24	1.96	-1.55
15	2.39	1.33	-0.85	15	2.36	1.52	0.56	15	1.78	1	-0.4	15	1.67	1	-0.5
R.D 75(%)															
CO ₂ =0 hr				CO ₂ =1 hr				CO ₂ =3 hrs				CO ₂ =24 hrs			
MgO (%)	MCT (%)	SOT (%)	DOT (%)	MgO %	MCT (%)	SOT (%)	DOT (%)	MgO (%)	MCT (%)	SOT (%)	DOT (%)	MgO (%)	MCT (%)	SOT (%)	DOT (%)
0	19.93	14.8	10.75	0	8.95	4.05	1.85	0	5.8	3.38	1.67	0	5.22	3.1	1.67
5	3.02	1.75	1.35	5	2.65	1.73	1.31	5	1.99	1.6	0.925	5	1.73	1.46	0.925
10	2.67	1.6	-0.45	10	2.12	1.35	-0.4	10	1.5	1.09	-2.6	10	1.22	1.02	-1
15	1.92	0.75	-0.35	15	1.93	1.2	-1.6	15	1	0.75	-1.73	15	0.96	0.6	-1.5

percentages of magnesium oxide is described in Figures 9 and 10 for soils prepared at relative density 35 and 75%, respectively. A summary of all collapse test results illustrates in Table 2. This result agrees with the finding of Cai et al. [12], who found that magnesium oxide with 3 hours carbonated period time in silty soil was better than 6 hours.

Figures 11 and 12 illustrate the volume of water that is needed in the sample till 100% saturation with increasing the period time of carbonation for relative density 35% and 75%, respectively. Figures 13 and 14 illustrate the time of saturation with an increasing the period time of carbonation for relative density 35% and 75%, respectively. A summary of time and volume of water that needed to saturate are illustrated in Table 3.

When the soil is soaked and subjected to constant stress σ_v , large volume changes and sudden collapses occur. Soil settlement happened when the results of the dissolving of cementing bonds of gypsum, that is resulting the significant increasing in the soil compressibility. According to the movement of the

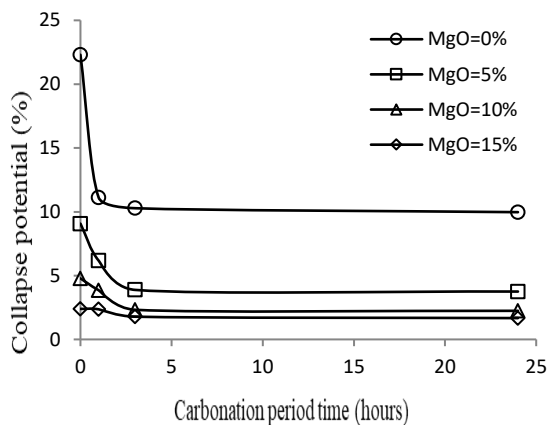


Figure 9. Change in collapse potential with increase of carbonation period time for relative density 35%

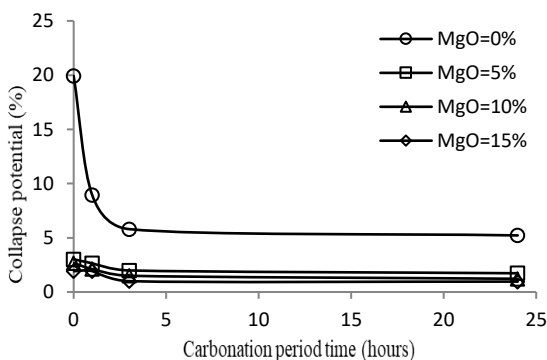


Figure 10. Change in collapse potential with increase of carbonation period time for relative density 75%

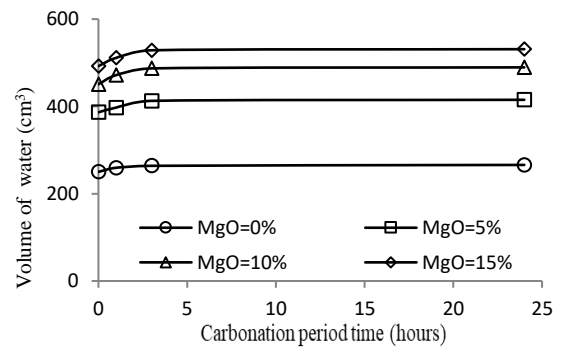


Figure 11. Volume of water to saturate the sample versus carbonation period time for relative density 35%

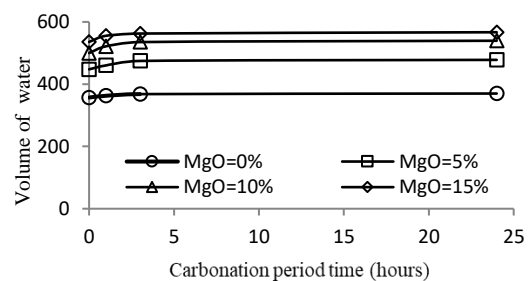


Figure 12. Volume of water to saturate the sample versus carbonation period time for relative density 75%

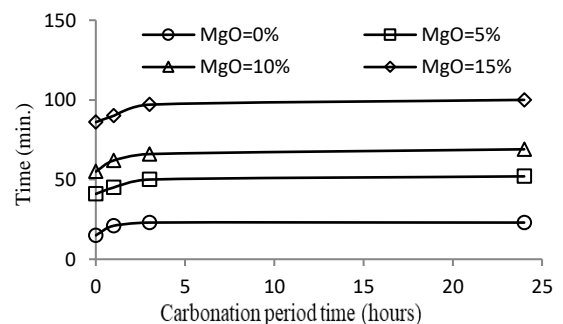


Figure 13. Time of saturation with increase of carbonation period time for relative density 35%

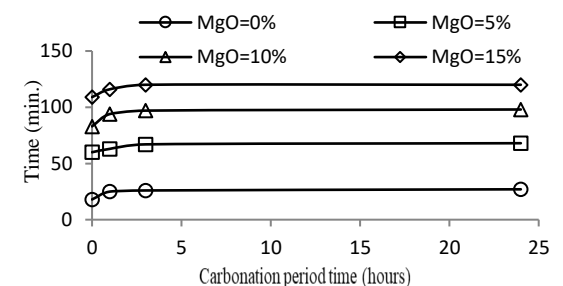


Figure 14. Time of saturation with increase of carbonation period time for relative density 35%

TABLE 3. Summary of time and volume of water needed to saturate the samples

R.D 35(%)											
CO ₂ =0 hr			CO ₂ =1 hr			CO ₂ =3 hrs			CO ₂ =24 hrs		
MgO (%)	Time for saturation (min.)	Volume of water (cm ³)	MgO (%)	Time for saturation (min.)	Volume of water (cm ³)	MgO (%)	Time for saturation (min.)	Volume of water (cm ³)	MgO (%)	Time for saturation (min.)	Volume of water (cm ³)
0	15	250	0	21	259.4	0	23	263.9	0	23	365.9
5	41	386.5	5	45	397.3	5	50	412.7	5	52	415.1
10	55	450.8	10	62	471.7	10	66	487.1	10	69	489.4
15	86	492.3	15	90	511.2	15	97	528.6	15	100	531.1

R.D 75(%)											
CO ₂ =0 hr			CO ₂ =1 hr			CO ₂ =3 hrs			CO ₂ =24 hrs		
MgO (%)	Time for saturation (min.)	Volume of water (cm ³)	MgO (%)	Time for saturation (min.)	Volume of water (cm ³)	MgO (%)	Time for saturation (min.)	Volume of water (cm ³)	MgO (%)	Time for saturation (min.)	Volume of water (cm ³)
0	18	357.1	0	25	362.8	0	26	368.1	0	27	369.9
5	60	447.7	5	63	460.3	5	67	474.6	5	68	478.1
10	83	500	10	94	521.7	10	97	535.2	10	98	539.5
15	109	535.7	15	116	555.5	15	120	562.6	15	120	566.8

Papadopoulos et al. [17] reported on his soaked samples to check their dissolution that in the first hour of saturation early increase of mass was obtained and then with logarithm of time almost regular solubility rate can be noticed.

The main points of collapse potential in this research can be summarized as follows:

All test results showed increasing in collapse

1. potential as compared with conventional tests for both of single oedometer test and double oedometer test.
2. Carbonation of collapsible gypseous soil without using magnesium oxide for the natural soil showed a noticeable decrease in collapsibility in the order of 200-250%.
3. For the carbonation period time, for all percentage of magnesium oxide, when increasing the carbonation time from 0 hour to 3 hours, there is a good reduction in collapse potential (about 1.5 to 2%), but there is no noticeable reduction in collapse potential when increasing the carbonation time from 3 hours to 24 hours.
4. At relative density 35%, the collapse potential for magnesium oxide 10% and 15% gave nearest value at the same time of carbonation period. At relative density 75%, the collapse potential for all magnesium oxide percentages gave nearest value at the same time of carbonation period.
5. The time and the volume of water that are needed for saturation were increasing with increasing both of

magnesium oxide percentages and time of carbonation periods till reached carbonation 3 hours then became about steady line.

6. For conventional tests, the results of the collapse potential decreased when adding magnesium oxide which agreed with Shakir's [18] reported data when adding cutback asphalt to gypseous soil the using of magnesium oxide in this study decreased the collapse potential about 5 times as compared with cutback asphalt reported by Al-Hadidi and Al-Maamori [19] using cement to gypseous soil the using of magnesium oxide in this study decreased the collapse potential about 1.5 times as compared with cement.

Because the density of the soil reduces with an increase in volume, the time required for saturation increases faster than the time required for saturation of the same model under the initial load [20, 21].

6. CONCLUSIONS

From the results of collapse tests carried out on gypseous soil treated with magniseoum oxide and subjected to different periods of carbonation, it can be concluded that:

- The carbonation of the soil treated with magnesium oxide accelerated the improvement of the gypseous soil and decreased collapse.
- Carbonation of collapsible gypseous soil without using magnesium oxide for the natural soil showed a

noticeable decrease in collapsibility in the order of 200 – 250%. The carbonation on untreated gypseous soil decreased the collapse potential more than 50% for modified collapse test and for the two relative densities, and more than 55% for conventional tests.

- The carbonation periods 3 and 24 hours revealed closely equal results for all tests; therefore, the optimum carbonation period time is 3 hours.
- Using the modified collapse test, the time needed to saturate the sample and volume of water required for sample saturation increased with increasing the carbonation period time. The increase is about 50% and 5% for time and volume of water, respectively for untreated soil.
- When the soil is treated with 10% magnesium oxide and carbonated for 3 hours, the increase in time and volume of water is around 20% and 4%, respectively.
- Carbonation of the collapsible gypseous soil treated with magnesium oxide for a period of 3 hours resulted in a good reduction in collapse potential (about 1.5 to 2%),

7. REFERENCES

1. Al-Kaaby, F., "Distribution of the gypsiferous soil in Iraq", State Company of Geological Survey and Mining, (2007).
2. Al-Hasan, S.J.A., Balamuralikrishnan, R., Altarawneh, M.J.J.o.H., Earth, and Future, "Eco-friendly asphalt approach for the development of sustainable roads", *Journal of Human, Earth, and Future*, Vol. 1, No. 3, (2020), 97-111, doi: 10.28991/HEF-2020-01-03-01
3. Hayal, A., Al-Gharrawi, A. and Fattah, M.J.I.J.o.E., "Collapse problem treatment of gypseous soil by nanomaterials", *International Journal of Engineering, Transaction C: Aspects*, Vol. 33, No. 9, (2020), 1737-1742, doi: 10.5829/ije.2020.33.09c.06
4. AbdulRahman, S., Fattah, M. and Ihsan, E.J.I.J.o.E., "Influence of plastic fiber on the geotechnical properties of gypseous soil", *International Journal of Engineering, Transactions B: Applications*, Vol. 34, No. 2, (2021), 367-374, doi: 10.5829/ije.2021.34.02b.08
5. Bahrami, M. and Marandi, S.J.I.J.o.E., "Large-scale experimental study on collapsible soil improvement using encased stone columns", *International Journal of Engineering, Transactions B: Applications*, Vol. 34, No. 5, (2021), 1145-1155, doi: 10.5829/ije.2021.34.05b.08
6. Crittenden, J.C., Trussell, R.R., Hand, D.W., Howe, K.J. and Tchobanoglous, G., "Mwh's water treatment: Principles and design, John Wiley & Sons, (2012).
7. Sampson, A., Weli, V., Nwagbara, M., Eludoyin, O.J.J.o.H., Earth, and Future, "Sensations of air temperature variability and mitigation strategies in urban environments", *Journal of Human, Earth, and Future*, Vol. 2, No. 2, (2021), 100-113, doi: 10.28991/HEF-2021-02-02-02
8. Concrete, E.-E., "19-reactive magnesia cement", (2013), doi: 10.1533/9780857098993.4.523
9. Yi, Y., Liska, M., Unluer, C. and Al-Tabbaa, A.J.C.G.J., "Carbonating magnesia for soil stabilization", *Canadian Geotechnical Journal*, Vol. 50, No. 8, (2013), 899-905, doi: 10.1139/cgj-2012-0364
10. Liu, S.-Y., Cai, G.-H., Cao, J.-J., Wang, F.J.E.J.o.E. and Engineering, C., "Influence of soil type on strength and microstructure of carbonated reactive magnesia-treated soil", *European Journal of Environmental and Civil Engineering*, Vol. 24, No. 2, (2020), 248-266, doi: 10.1080/19648189.2017.1378925
11. Hwang, K.-Y., Kim, J.Y., Phan, H.Q.H., Ahn, J.-Y., Kim, T.Y., Hwang, I.J.E.S. and Research, P., "Effect of CO₂ concentration on strength development and carbonation of a mgo-based binder for treating fine sediment", *Environmental Science and Pollution Research*, Vol. 25, No. 23, (2018), 22552-22560, doi: 10.1007/s11356-018-2338-y
12. Cai, G.-H., Liu, S.-Y., Zheng, X.J.C. and Materials, B., "Influence of drying-wetting cycles on engineering properties of carbonated silt admixed with reactive mgo", *Construction and Building Materials Journal*, Vol. 204, (2019), 84-93, doi: 10.1016/j.conbuildmat.2019.01.125
13. Wang, D., Zhu, J., He, F.J.C. and Materials, B., "CO₂ carbonation-induced improvement in strength and microstructure of reactive mgo-cao-fly ash-solidified soils", *Construction and Building Materials Journal*, Vol. 229, (2019), 116914, doi: 10.1016/j.conbuildmat.2019.116914
14. A li, I. M. "Sustainable Processing to Produce Different Types of Wood-Based Cementitious Boards", (2015).
15. ASTM, "Standard test method for measurement of collapse potential of soils.", Annual Book of ASTM Standards, (2003).
16. Al-Gharbawi, A.S., Mahmood, M.R.J.E. and Journal, T., "New trend to measure the saturation point and suction in granular soil", *Engineering and Technology Journal*, Vol. 38, No. 11, (2020), 1570-1579, doi: 10.30684/etj.v38i11A.746
17. Papadopoulos, Z., Kolaiti, E., Mourtzas, N.J.Q.J.o.E.G. and Hydrogeology, "The effect of crystal size on geotechnical properties of neogene gypsum in crete", *Quarterly Journal of Engineering Geology and Hydrogeology*, Vol. 27, No. 3, (1994), 267-273.
18. Shakir, Z.H.J.J.o.E., "Improvement of gypseous soil using cutback asphalt", *Journal of Engineering*, Vol. 23, No. 10, (2017), 44-61.
19. Al-Hadidi, M.T. and AL-Maamori, Z.H.N.J.J.o.E., "Improvement of earth canals constructed on gypseous soil by soil cement mixture", *Journal of Engineering (Chemical, Petroleum and Environmental Engineering)*, Vol. 25, No. 3, (2019), 23-37, doi: 10.31026/j.eng.2019.03.03
20. Fattah, M.Y. and Dawood, B., "Effect of load history on time-dependent collapse behavior of unsaturated collapsible gypseous soils", in Proc of the 16th Asian regional conference on soil mechanics and geotechnical engineering. (2019).
21. Fazelabdolabadi, B., Golestan, M.H.J.H. and Journal, I., "Towards bayesian quantification of permeability in micro-scale porous structures—the database of micro networks", *High Tech and Innovation Journal*, Vol. 1, No. 4, (2020), 148-160, doi: 10.28991/HIJ-2020-01-04-02

Persian Abstract

چکیده

خاک های جمع شونده خاک هایی هستند که در صورت اشباع شدن به کرنش های حجمی زیاد حساس هستند. انواع مختلفی از خاکها در دسته کلی خاکهای جمع شونده قرار می گیرند، از جمله خاک گچی که در حالت خشک با چگالی نسبتاً کم، استحکام و سفتی قابل توجه مشخص می شود، اما در نتیجه خیس شدن مستعد تغییر شکل های قابل توجه است. در این تحقیق از اکسید منیزیم برای اصلاح خاک گچی تاشو با استفاده از (۰، ۵، ۱۰ و ۱۵ درصد) با دو تراکم نسبی (۳۵ و ۷۵ درصد) و کرناته شدن در دوره های مختلف کرناته سازی (۰، ۱، ۳ و ۲۴) استفاده شده است. ساعت ها). در این تحقیق از آزمون های فروپاشی متداول (تک بادسنج و دو کیلومتر شمار و آزمون فروپاشی اصلاح شده برای بررسی تأثیر دوره های کرناته شدن بر بهبود خاک استفاده شده است. از دستگاه آزمایش فروپاشی اصلاح شده استفاده شده است. نتایج نشان می دهد که پتانسیل ریزش بیش از حد کاهش یافته است. به ترتیب ۶۵ و ۵۵ درصد برای خاک گازدار بدون تیمار برای آزمایش های معمولی و آزمون فروپاشی اصلاح شده، و حدود ۵۵ درصد برای خاک تیمار شده با ۱۰ درصد اکسید منیزیم و کرناته به مدت ۳ ساعت برای هر دو آزمایش معمولی و آزمون فروپاشی اصلاح شده کاهش یافت. برای تسریع بهبود خاک و همچنین کاهش پتانسیل ریزش از زمان دوره کرناته استفاده می شود و نتایج نشان داد که برای دوره بیش از ۳ ساعت هیچ تغییری واضحی در پتانسیل ریزش وجود ندارد.



An Automatic Optic Disk Segmentation Approach from Retina of Neonates via Attention Based Deep Network

A. Abaei Kashan^a, A. Maghsoudi^b, N. Shoeibi^c, M. Heidarzadeh^d, K. Mirnia^{*e}

^a Department of Mechanical Engineering, Iran University of Science and Technology, Tehran, Iran

^b Department of Mechanical Engineering, Tehran University of Medical Science, Tehran, Iran

^c Department of Ophthalmology, Mashhad University of Medical Sciences, Mashhad, Iran

^d Department of Pediatrics, Tabriz University of Medical Science, Tabriz, Iran

^e Department of Pediatrics, Tehran University of Medical Science, Tehran, Iran

PAPER INFO

Paper history:

Received 30 October 2021

Received in revised form 09 December 2021

Accepted 23 December 2021

Keywords:

Image Segmentation
Convolutional Neural Network
Attention Mechanism
Retinopathy of Premature
Optic Disk

ABSTRACT

Every year, many newborns lose their sight to retinopathy of prematurity (ROP) worldwide. Despite its high prevalence and adverse consequences, periodic examinations can effectively prevent it. The use of an intelligent system enables physicians to avoid medical mistakes while examining newborns. The optic disk (OD) is an integral part of the retina for grading the severity and progression of ROP. Due to the uneven brightness and lack of a defined OD border, the use of retinal images of infants is very challenging for OD diagnosis. This paper provides an innovative model of OD segmentation based on attention gate. Initially, the images were collected and preprocessed and inputted into a novel deep convolutional neural network consisting of attention in skip connections. The architecture is comprised of a two-stage convolutional network. Different outputs are obtained from two individual branches of the original image and image features in the first stage. The outputs were concatenated to transfer into the post-processing stage to identify the area related to the OD. The final results based on the Dice coefficient (Dice) and the Intersection-Over-Union (IoU) were 94.22% and 86.1%, respectively.

doi: 10.5829/ije.2022.35.04a.11

1. INTRODUCTION

Retinopathy of prematurity (ROP) is the major leading cause of neonatal blindness worldwide [1], affecting approximately 10% of neonates each year [2]. ROP is caused by abnormal growth of retinal arteries in neonates [1], leading to various visual impairments varying from minor vision defects to retinal detachment and blindness [3]. Since the disease is preventable, early diagnosis makes it treatable and retards its progression [4]. Periodic examinations are crucial because neonates are not able to express their vision problems. Treatment in the early stages of ROP decreases disease consequences and treatment expenses. Due to the development of neonatal intensive care units, the probability of preterm infants' survival increases [5]; hence, a significant

amount of neonates are at risk of ROP. Therefore, it has heightened the need for intelligent systems in their inspection. Over the past year, due to the coronavirus pandemic, there has been a dramatic increase in artificial intelligence implementation to reduce hospital visitation. An intelligent examination of ROP is based on detecting the anatomic structures in retinal images. The optic disk (OD) is one of the specific structures, and identification of it plays a notable role in determining ROP's zone and stage as a criterion for severity [6]. Accordingly, in this study, we have introduced a method for detecting and segmenting OD in neonatal images. Furthermore, OD detection in adults is used to diagnose glaucoma [7] and papilloma [8]. An optic disk is a bright, circular area (Figure 1) where blood vessels converge. This definition

*Corresponding Author Institutional Email: kmimia@sina.tums.ac.ir
(K. Mirnia)

is the base of OD detection algorithms, which are discussed subsequently.

Walter et al. [9] segmented OD as a bright area of the retina using a watershed transform. Welfer et al. [10] used a similar procedure, in that they applied adaptive morphology instead of a watershed transform. In a study, Tjandrasa et al. [11] proposed another morphological approach, where the OD area is cropped following image enhancement, and the vessels are removed using thresholding in the cropped area. Then, the OD region is recognized by the Hough transform with a predefined radius. Finally, the Selective Binary-and-Gaussian Filtering Regularized Level Set (SBGFRLS) method is used for segmentation. This method was evaluated on Drive Database and achieved 75.56% accuracy. The mentioned algorithm's performance depends highly on the quality of vessel removal, the assumed OD radius for OD, and the SBGFRLS parameters [11]. Abdullah et al. [12] used a morphological procedure to remove the vessels in a separate investigation. Next, since the algorithm's inputs are acquired from different databases, they should resize the images to obtain a circle with a certain radius through the Hough transform as the OD center. Then, it is used as the initial point for expanding the OD region via search. Although the algorithm is robust to noise and illumination artifacts, some errors occur in pathological structure [12].

Contrary to retinal images, there are scant studies on neonates' retinas. According to Thongnuch and Uyyanonvara's [13] neonatal retina analysis, the contrast histogram equalization could be improved by an average filter in the red channel. Then, closing morphology and the Canny are used to remove vessels and edge detection, respectively. OD edges were segmented through a sequence of morphology operations: filling, erosion, connected component selection, and noise reduction.

Pathan et al. [14] proposed a two-step algorithm to determine OD. First, the authors segmented the vessels by applying the green channel because of its high contrast. Then they extracted the vessels by using a linear directional filter (eight main directions), dilation,

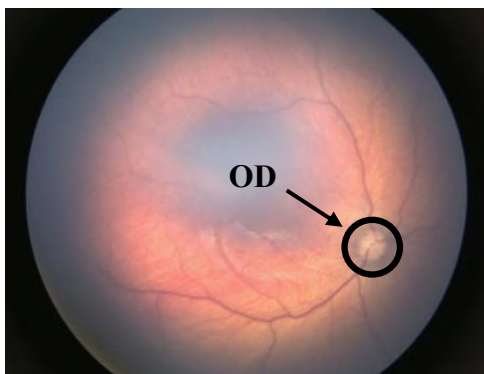


Figure 1. Optic disk

erosion, and thresholding. To improve OD detection, the extracted vessels were removed. Unlike previous stages, the red channel was subtracted from its average. The process was repeated three times to find the existing circles, using the Hough Transform. Eventually, the light intensity threshold between OD and non-OD was obtained from annotated images and used as a threshold in a decision tree [14]. Mookiah et al. [15] found that proper preprocessing is through applying the Limited Adaptive Histogram Equalization to enhance contrast. Later, they separated the vessels through Gabor's two-dimensional Matched filter and closing morphology. Then, the authors determined the location of OD and segmented it by a fuzzy histogram [15]. The Hough transform is an extensively used technique in retinal imaging to detect microaneurysms [16] and OD. Thongnuch and Uyyanonvara [17] indicated that the Canny edge detection method, followed by the Hough transform, has an accuracy of 81.7% in neonatal images. The scientists found that using a deformable contour model with gradient vector flow as an external force enhanced segmentation accuracy by 85.34% [13]. Similarly, Zahoor et al. [18] segmented the OD by utilizing the following steps: morphology to remove vessels, Hough transform and polar transformation to find OD location, and adaptive thresholding to find edges.

There are several studies in the literature on OD segmentation via Thresholding. This method is beneficial in combination with others. For example, Ghadiri et al. [19] initially found the OD kernel, then segmented the OD region using adaptive thresholding, light intensity, and vessel width. Likewise, Septiaria et al. [20] determined OD through thresholding after the removal of vessels.

To solve this issue, many researchers have proposed various segmentation methods, including Superpixel [21, 22], principal component analysis (PCA) [23], and Dolph-Chebyshev matched filter [24].

The past decade was accompanied by the rapid development of deep learning in various fields, such as machine vision [25], object tracking [26], and segmentation [27]. OD segmentation is one of its applications. Sevastopolsky [28] used the U-Net network to segment OD and Optic Cup (OC). Unlike the current U-Net type, the number of filters remained constant after Max Pooling and Up Sampling. As a result, the network training speed increased. Sevastopolsky [28] initially segmented the OD by using the mentioned network and cropped it. The OC was segmented based on this patch [28]. In the same vein, Kim et al. [29] used a pre-trained convolutional neural network (CNN) to classify OD and NOD patches of images. A U-Net model was used to segment OD [29].

Yu et al. [30] initially segmented OD by pre-trained ResNet-34 encoder in the U-Net network and then

separated the optic cup region. To improve the results, they performed morphology [30]. This view is supported by Juneja et al. [31], who utilized red channels in the first CNN and RGB channels to segment OC. In another similar study, Bhatkalkal et al. [32] used Deeplabv3 + and U-Net with Novel Attention Gate inputs in their architecture. Lastly, Conditional Random Fields (CRF) were used for post-processing [32]. A broader perspective has been adopted by Jiang et al. [33] who extracted vessels through a CNN. Then, they cropped 800×800 area around the brightest point, as a region of interest (ROI), to reduce the input size of images. OD and OC were segmented in the desired ROI using Faster R-CNN [33]. As a prediction model, Zheng et al. [34] proposed a multi-scale convolutional neural network to provide level set initial contour and evolution parameters. According to the evolution criteria, the existing shape will be modified subsequently. The model was enhanced with previous data and controlled by active contour loss, resulting in more precise contour and edge features in the level set evolution [34]. In a recent literature review on this subject, joint segmentation of OD and OC was defined by Tabassum et al. [35] as a semantic pixel-wise labeling issue.

The retina images of neonates are mostly low contrast. Due to the lack of clarity in the eye media and the difficulties of capturing a moving preterm child, they are often noisy and blurry. Furthermore, the OD's diameter, shape, and color vary significantly across images, making automated identification of OD a difficult process. Due to the high rates of recording artifacts (blurring, reflections), inter-image color fluctuations, and intra-image changes in illumination, the techniques that typically succeed on mature retina images fail on infant fundus images. Therefore, few researchers have addressed neonatal OD segmentation. Nisha et al. [36] proposed assigning an OD score to each pixel of neonates' retina, showing the probable OD localities. The OD area is then segmented employing a region growth approach. The seed growth method begins with the OD center as the first seed. The intensity of the seed pixel is compared to the intensity of adjacent pixels. The zone is then expanded by repeatedly adding nearby pixels, which are comparable to the seed pixel until the stopping threshold is achieved [37]. Since the majority of previous studies did not consider neonate images, a new technique that improves OD segmentation is suggested in this study. Local properties of OD are considered to be the model input to increase the precision of segmentation, contributing to existing knowledge of OD segmentation by providing (1) a novel model architecture with pre-trained VGG-16 model as encoder layer, (2) local image features as input, and (3) significant emphasis on edges property.

The remaining parts of the paper are as follows:

- Collecting data

- Pre-processing
- Data augmentation
- Extracting the OD edge properties
- Designing a CNN architecture
- Illustrating results and discussion

2. METHODOLOGY

Various OD segmentation methods have been developed and proposed; however, most recent studies have used the CNN models for OD because of their capability in extracting features. Therefore, the present study carried out this goal by implementing a novel CNN architecture stated in the following sections.

2. 1. Database In reviewing the literature, no public databases were found on neonate retinal images. Hence, our colleagues spend much time and effort gathering RetCam imaging data from Khatam-al- Anbya Hospital between 2019 to 2020. Out of the 420 images considered, ROP was recognized on 132 images. The remaining images indicated healthy eyes. The resolution of images was 640×480 and has a 130° field of view (FOV). In contrast to the adult retinal images, the infants' OD's dimensions, direction, and location in each image varied because of imaging conditions.

Data are divided into three sets:

- Training (tuning model parameters)
- Validating (evaluating model performance during the learning process)
- Testing (evaluation of the final model)

Each image is accompanied by an OD ground truth, which an ophthalmologist manually annotated twice with an interval and then averaged.

2. 2. Pre-processing A preprocessing step was taken to improve the image quality. It is used to reduce noise or brightness variations during image acquisition without missing essential information. In this paper, preprocessing step included zero-padding and cropping operations to acquire a 512×512 resized resolution. Zero-padding is a method often used to ensure that the size of the image input is a power of two. In contrast to the reported cases [38, 39], which reduced the image size to be less costly to run, reducing the image size of neonatal retinal is not possible for two reasons:

- i. Neonatal retinal images have a wider FOV, so retinal structures are displayed in a small size. Hence, they may be removed during the resizing process
- ii. The neonatal retina is not matured. It contains fewer veins and anatomic structures than adult retina images; therefore, removing or changing some of them during resizing influences processing procedures significantly.

The output of the main processing procedures was affected by these brightness differences. Contrast improvements can be made via image normalization, sometimes defined as Histogram equalization, to ensure that the image's pixel value contains the whole intensity range. Therefore, we normalized the images to improve training time. The technique, used to conduct linear normalizing on a grayscale image, was formulated as:

$$I_N = \frac{I_{raw} - I_{raw,min}}{I_{raw,max} - I_{raw,min}} \quad (1)$$

where I_{raw} is the input image; $I_{raw,max}$ and $I_{raw,min}$ are the maximum and minimum pixel values, respectively; I_N is the normalized image.

2. 3. Data Augmentation Overfitting is the major practical issue that jeopardizes the learning procedure. Many researchers have proposed various methods to solve this problem. In the present study, data augmentation was used to solve this issue. Augmented data are generated based on problem constraints. The following is the list of procedures applied to augment retinal images: brightness variations, horizontal flips, vertical flips, blur, Gaussian noise, motion blur, and random brightness contrast.

2. 4. Feature Extraction Despite the vital role of contour borders in the segmentation, few studies have evaluated the impact of the extracted feature on CNN performance [40, 41]. This paper investigated the strengths of two descriptors, namely local binary pattern (LBP) and Histogram of Oriented Gradient (HOG), to extract local characteristics. The considered descriptors are widely used in computer vision applications [42] to identify edges more accurately. LBP, also known as a texture descriptor, reflects the relation among pixels intensity within a given area. For a point (x, y) surrounded by n pixels in radius r, the value of LBP can be computed by the following equations:

$$LBP(n, r) = \sum_1^n g(x) \times 2^{n-1} \quad (2)$$

$$g(x) = \begin{cases} 1 & I_c < I_i \\ 0 & I_c \geq I_i \end{cases} \quad i \in \{1, 2, \dots, n\} \quad (3)$$

In the above relations, I_c and I_i demonstrate the center point (x, y) and its adjacents light intensity, respectively.

HOG descriptor calculates occurrences of gradient orientation in local divisions of an image to recognize specific objects. As shown in Figure 2, the image is initially partitioned into equal areas, known as blocks. Each block is a set of cells made up of pixels that Gradient intensities are calculated within them and used to organize the histograms. Eventually, the histogram of the cells in each block is located consecutively to obtain an image description.

To concentrate on edge features during training, only boundaries' LBP and HOG values are inputted into the model. For this purpose, mathematical morphological operations are applied. Mathematical morphological operation is an image processing technique that deals with an image's form and shape. Morphological methods are commonly utilized in preprocessing or post-processing steps to filter, narrow, or clean up images. The two fundamental morphological operators are dilation and erosion, where dilation detects the highest value in a region and erosion finds the lowest element in a neighborhood. Various techniques, including morphological gradients, are developed from these functions. It would be utilized for edge detection and segmentation. The morphological gradient is obtained by subtracting erosion from dilation with adjusted kernel size parameters. In the below equations, f presents the input image, k relates to the desired kernel in morphological gradient $G(f, k)$, \otimes demonstrates elementwise multiplication, and \oplus and \ominus illustrate erosion and dilation, respectively. Figure 3 exhibits a preprocessed image, its extracted features, and ground truth.

$$G(f, k) = f \oplus k - f \ominus k \quad (4)$$

$$LBP_{OD} = LBP_{image} \otimes G(f, k)_{OD \text{ ground truth}} \quad (5)$$

$$HOG_{OD} = HOG_{image} \otimes G(f, k)_{OD \text{ ground truth}} \quad (6)$$

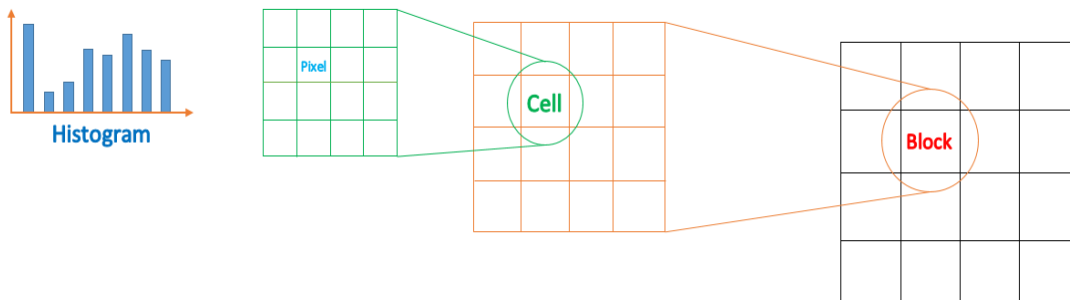


Figure 2. Subdividing procedure in HOG calculation

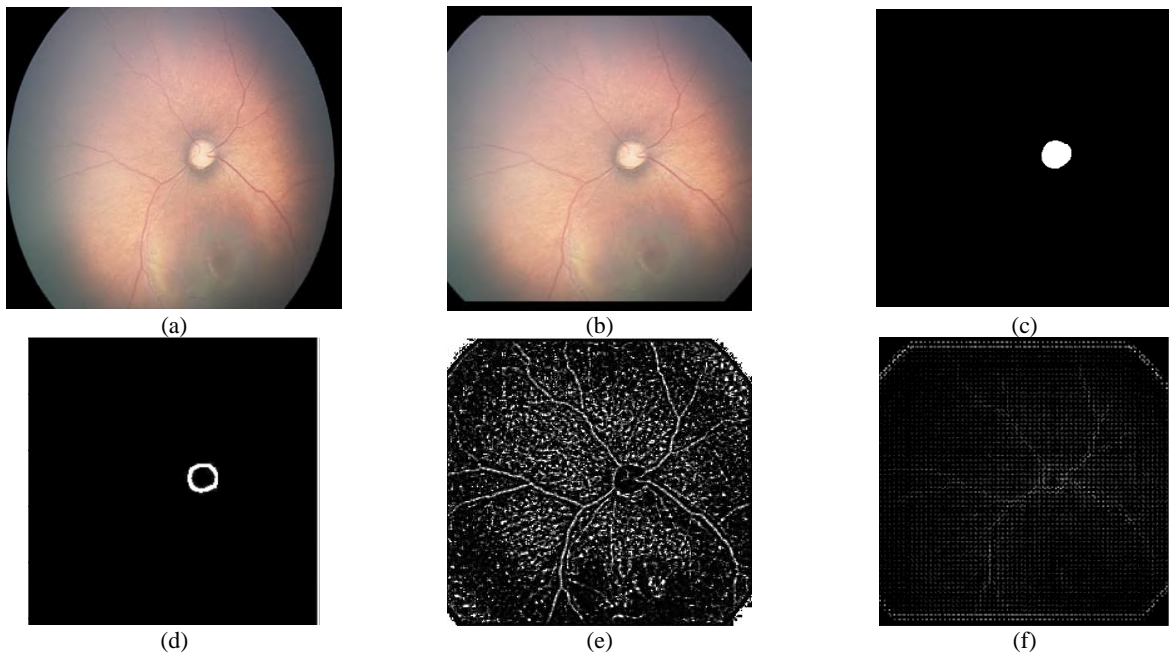


Figure 3. (a) Input image (b) Preprocessed image (c) Ground truth (d) Morphological gradient of OD ground truth (e) Local binary pattern (f) Histogram of oriented gradient

2. 5. Model Architecture

In this step, the model’s architecture is designed, which greatly affects the final outcome of the model. In recent years, there has been increasing literature on biomedical segmentation by using the U-Net architecture; a U-shape convolutional network consists of a contracting path (encoder) expanding path (decoder), presented in Figure 4. The contracting steps include a successive bunch of two convolutional layers, followed by a downsampling operation. Each expanding stage concatenates the up-sampled feature maps from the previous stage with corresponding feature maps from the contracting layers. Due to the capability of the U-Net architecture to train on

small samples in segmentation tasks, various derivations of it have been proposed in recent studies.

As illustrated in Figure 5, the concept of our model architecture is based on the U-Net. To import extracted features, a mini U-Net is parallelized to the main U-Net. In addition, pre-trained VGG-16 weights are substituted in the primary encoder, so only the decoder section is trained. Main model inputs are preprocessed RGB channels that acquire an initial segmentation output. The mini U-Net outcomes are another raw output obtained from the green channel besides LBP and HOG feature maps. In the recommended model, before concatenating the skip connection and upsampling, an attention gate

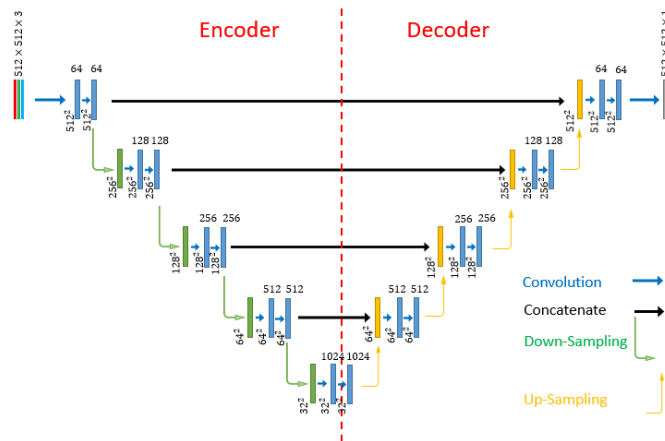


Figure 4. U-Net architecture

(Figure 6) was implemented to suppress irrelevant regions' activations and reduce the excessive characteristics brought across. Ultimately, these results are inputted into the post-processing model to amend each other. Another advantage of the attention gate is that it does not require crop ROI to be inputted into the model, and the entire image is used as the input.

3. RESULTS

Since our segmentation problem has unbalanced foreground and background pixels, a linear combination of dice coefficient and binary cross-entropy loss function was preferred. Let define them by L_{dice} and L_{bce} as below:

$$L_{dice} = \frac{1}{N} \left(1 - \frac{2 \sum_{i=1}^h \sum_{j=1}^w w_{ij}^2 y_{ij} \hat{y}_{ij} + \epsilon}{\sum_{i=1}^h \sum_{j=1}^w w_{ij}^2 y_{ij} + \sum_{i=1}^h \sum_{j=1}^w w_{ij}^2 \hat{y}_{ij} + \epsilon} \right) \quad (7)$$

$$L_{bce} = \frac{1}{N} \left(\sum_{i=1}^h \sum_{j=1}^w \hat{y}_{ij} \log(y_{ij}) + (1 - \hat{y}_{ij}) \log(1 - y_{ij}) \right) \quad (8)$$

$$L_{total} = L_{dice} + L_{bce} \quad (9)$$

where N is the number of training images, w_{ij}^2 is the gained weight from ground truth, ϵ is minimum amount prevent from zero division, and \hat{y}_{ij} and y_{ij} are the target and predicted value, respectively.

Nadam was selected, as an optimizer, to train the proposed model. The momentum in Nadam is the opting motivation since the momentum prevents from getting stuck in local minimums.

IoU and dice coefficient are selected criteria to measure segmentation accuracy. The equations that describe them are stated as follows:

$$Dice = \frac{2 \times TP}{TP + TN + FP + FN} \quad (10)$$

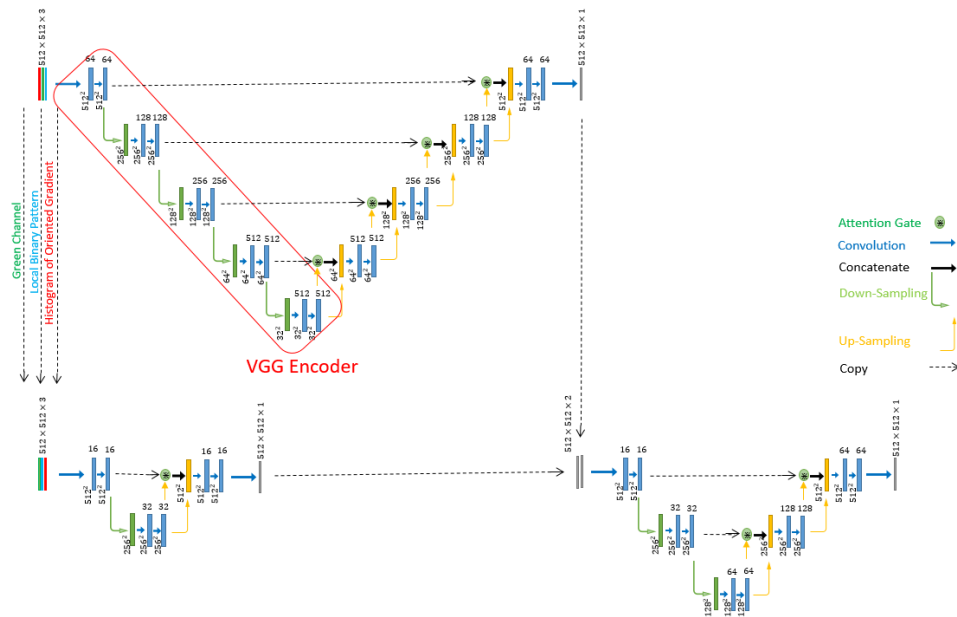


Figure 5. Proposed model

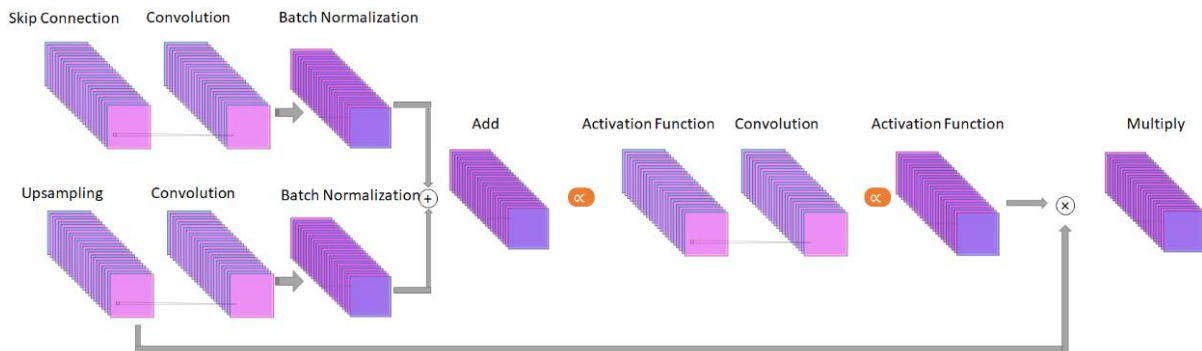


Figure 6. Attention block

$$IoU = \frac{TP}{TN+FP+FN} \tag{11}$$

Parameters used in Equations (9) and (10) are presented in Table 1.

The previous sections have revealed that the suggested model consists of modified U-Net models and a VGG-16 encoder. Hence, the authors have also considered the original U-Net, pre-trained U-Net encoder, and proposed model without attention. These comparisons can highlight model advantages. It appears from Figure 7 that the U-Net model and pre-trained U-Net performance individuality are not very accurate for OD segmentation on the database; by contrast, the recommended model without attention gate has performed admissible. Moreover, it is apparent from Figure 7 that accentuating on edge features and model architecture could improve the results significantly.

A more detailed comparison is presented in Figure 8. As shown in this figure, our method functions the same as the absence of attention gate on typical images, and they beat the original U-Net and pre-trained U-Net. As illustrated in Figure 9, the suggested method performs significantly superior to the architecture without attention to challenging images. In these images, OD boundaries have low contrast and cause problems due to the illumination and retina structure. The recommended technique could dominate this issue by emphasizing on edge features throughout the training time. The most striking result from the comparison was the lack of contour recognition on the image by the original U-Net.

TABLE 1. Parameters definition

Expected Output \ Model output	Non Optic Disk	Optic Disk
	Optic Disk	False Negative (FN)
Non Optic Disk	True Negative (TN)	False Positive (FP)

4. DISCUSSION

Due to the growing rate of premature infants' birth and their inability to express vision problems, researchers' consideration has been drawn to intelligent diagnosis. Hence, the objective of the paper is to contribute to ROP computer-aided systems through segmenting OD. In this study, a novel adaptation of U-Net attention architecture was designed. In addition to the main image channels (RGB), the model inputs contain extracted local features (LBP and HOG) focused on OD boundaries. Pre-trained weights are employed in the primary U-Net encoder to lessen training time cost and enhance the operation. The findings obtained in this research are consistent with previous studies [40, 41], which have evaluated the effect of local features as model inputs. Figure 8 indicates extreme improvements within modifications initiated from the original U-Net toward the proposed model.

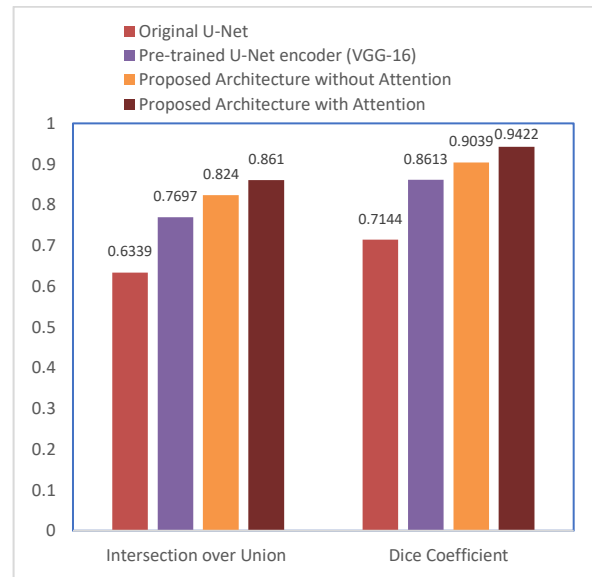


Figure 7. Comparison of segmentation accuracy in different models

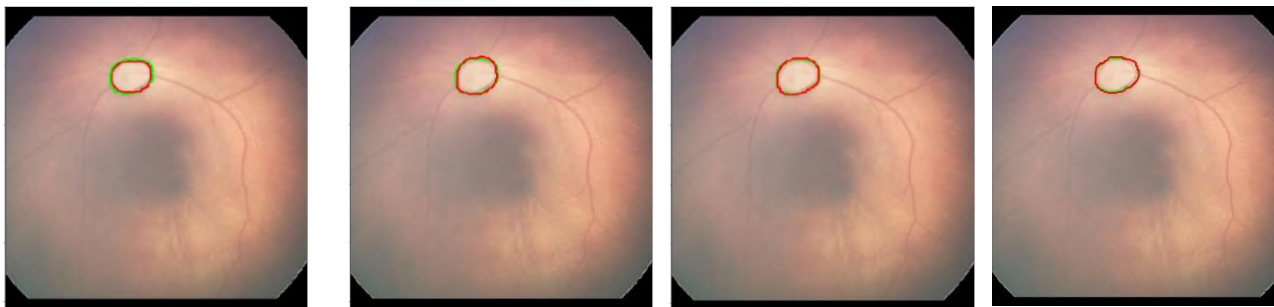


Figure 8. Segmentation results (Ground truth and segmented object are plotted in green and red respectively)

Original U-Net Pre-trained U-Net encoder (VGG-16) Proposed architecture without attention gate Proposed Model

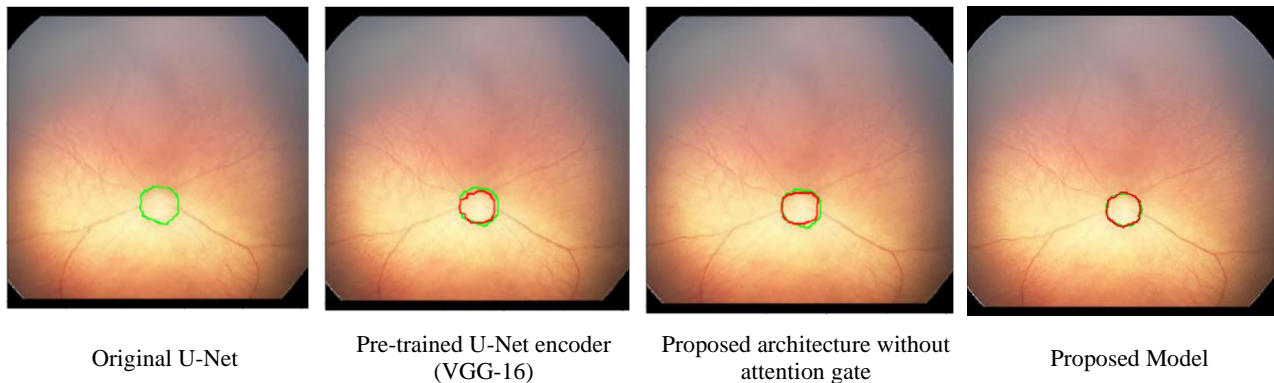


Figure 9. Various segmentation methods comparison on challenging image (Ground truth and segmented object are plotted in green and red respectively)

As a consequence of the shortage of infants' retina imaging equipment, there is no publicly available database. To the best of the authors' knowledge, this study is the first research on dealing with neonatal OD segmentation; hence, the paper's main study limitation was the lack of similar studies to compare the results and make a proper assessment. It enables readers to review the advantages and disadvantages of different techniques.

Since the peripapillary choroid pigmentation is usually different in adults than infants, OD borders detection is more complex in neonates [43]. Moreover, the OD color is mostly pink or reddish because some premature infants have primary vitreous vessels covering the OD's surface. Furthermore, the OD boundaries of infants are blurred compared to adults and relatively irregular. In neonatal retinal imaging, numerous captured images are slightly blurred due to infants' lack of cooperation (crying and intense shaking) during imaging. Besides, the eyes' blood vessels of infants are forming and growing more rapidly than adults; consequently, OD characteristics are in a broader range that adds to recognition challenges. Consequently, fundus data acquire from adults are not proper diagnostic criteria for neonatal fundus screening.

To provide a valid database, semi-blurred images are also collected, which reduces accuracy. Considerably more work will be required to be done to automatically detect anatomical structures of the retina. These attempts can push forward the study to determine the ROP zone and stage. Moreover, it could be regulated and modified regarding adult retina and utilized in glaucoma diagnosis. Further, it is recommended to perform more general studies on other local features.

5. CONCLUSION

The progression of neonatal intensive care units has led to pay heed to ROP as a serious, worldwide public health concern. This study set out to determine the infants' OD

boundary by CNN. The novel architecture results show a reliable response to OD segmentation. The illumination robustness of the method is achieved from importing the extracted features and executing the attention gate. On the other hand, the significant limitation of this study is the deficiency of similar investigation, the current outcomes append to a growing body of literature on segmenting, and ROP automated examination. It is recommended to conduct more studies on adding further properties to the models and determining ROP severity.

6. ETHICAL ISSUES

The ethical code for this research is IR.TUMS.CHMC.REC.1398.038.

7. ACKNOWLEDGEMENT

This study was funded and supported by Tehran University of Medical Sciences (Grant no: 98-01-30-41662).

8. REFERENCES

1. Chen, J. and Smith, L.E., "Retinopathy of prematurity", *Angiogenesis*, Vol. 10, No. 2, (2007), 133-140, [https://doi.org/10.1016/S0140-6736\(13\)60178-6](https://doi.org/10.1016/S0140-6736(13)60178-6)
2. Lumley, J., "1 the epidemiology of preterm birth", *Bailliere's Clinical Obstetrics Gynaecology*, Vol. 7, No. 3, (1993), 477-498, [https://doi.org/10.1016/S0950-3552\(05\)80445-6](https://doi.org/10.1016/S0950-3552(05)80445-6)
3. Hartnett, M.E., "Pathophysiology and mechanisms of severe retinopathy of prematurity", *Ophthalmology*, Vol. 122, No. 1, (2015), 200-210, <https://doi.org/10.1016/j.ophtha.2014.07.050>
4. Tasman, W.S., "Revised indications for the treatment of retinopathy of prematurity: Results of the early treatment for retinopathy of prematurity randomized trial", *Arch Ophthalmol*, Vol. 121, (2003), 1684-1695, <https://doi.org/10.1001/archophth.121.12.1684>

5. Stensvold, H.J., Klingenberg, C., Stoen, R., Moster, D., Braekke, K., Guthe, H.J., Astrup, H., Rettedal, S., Gronn, M. and Ronnestad, A.E., "Neonatal morbidity and 1-year survival of extremely preterm infants", *Pediatrics*, Vol. 139, No. 3, (2017), <https://doi.org/10.1542/peds.2016-1821>
6. Aslam, T., Fleck, B., Patton, N., Trucco, M. and Azegrouz, H., "Digital image analysis of plus disease in retinopathy of prematurity", *Acta Ophthalmologica*, Vol. 87, No. 4, (2009), 368-377, <https://doi.org/10.1111/j.1755-3768.2008.01448.x>
7. Naqvi, S.S., Fatima, N., Khan, T.M., Rehman, Z.U. and Khan, M.A., "Automatic optic disk detection and segmentation by variational active contour estimation in retinal fundus images", *Signal, Image Video Processing*, Vol. 13, No. 6, (2019), 1191-1198, <https://doi.org/10.1007/s11760-019-01463-y>
8. Fatima, K.N., Akram, M.U. and Bazaz, S.A., "Papilledema detection in fundus images using hybrid feature set", in 2015 5th International Conference on IT Convergence and Security (ICITCS), IEEE. (2015), 1-4.
9. Walter, T., Klein, J.-C., Massin, P. and Erginay, A., "A contribution of image processing to the diagnosis of diabetic retinopathy-detection of exudates in color fundus images of the human retina", *IEEE Transactions on Medical Imaging*, Vol. 21, No. 10, (2002), 1236-1243, <https://doi.org/10.1109/TMI.2002.806290>
10. Welfer, D., Scharcanski, J., Kitamura, C.M., Dal Pizzol, M.M., Ludwig, L.W. and Marinho, D.R., "Segmentation of the optic disk in color eye fundus images using an adaptive morphological approach", *Computers in Biology Medicine*, Vol. 40, No. 2, (2010), 124-137, <https://doi.org/10.1016/j.compbiomed.2009.11.009>
11. Tjandrasa, H., Wijayanti, A. and Suciati, N., "Optic nerve head segmentation using hough transform and active contours", *Telkomnika*, Vol. 10, No. 3, (2012), 531, <https://doi.org/10.12928/telkomnika.v10i3.833>
12. Abdullah, M., Fraz, M.M. and Barman, S.A., "Localization and segmentation of optic disc in retinal images using circular hough transform and grow-cut algorithm", *PeerJ*, Vol. 4, (2016), e2003, <https://doi.org/10.7717/peerj.2003>
13. Thongnuch, V. and Uyyanonvara, B., "Automatic optic disk detection from low contrast retinal images of rop infant using gvf snake", *Suranaree J Sci Technol*, Vol. 14, No. 3, (2007), 223-234, doi.
14. Pathan, S., Kumar, P., Pai, R. and Bhandary, S.V., "Automated detection of optic disc contours in fundus images using decision tree classifier", *Biocybernetics Biomedical Engineering*, Vol. 40, No. 1, (2020), 52-64, <https://doi.org/10.1016/j.bbe.2019.11.003>
15. Mookiah, M.R.K., Acharya, U.R., Chua, C.K., Min, L.C., Ng, E., Mushrif, M.M. and Laude, A., "Automated detection of optic disk in retinal fundus images using intuitionistic fuzzy histon segmentation", *Proceedings of the Institution of Mechanical Engineers, Part H: Journal of Engineering in Medicine*, Vol. 227, No. 1, (2013), 37-49, <https://doi.org/10.1177/0954411912458740>
16. ASADI, A.S., Hassanpour, H., Shahiri, M. and Ghaderi, R., "Detection of microaneurysms in retinal angiography images using the circular hough transform", (2012).
17. Thongnuch, V. and Uyyanonvara, B., "Automatic detection of optic disc from fundus images of rop infant using 2d circular hough transform", *Sirindhorn International Institute of Technology, Thammasat University, Thailand*, Vol., (2006).
18. Zahoor, M.N. and Fraz, M.M., "Fast optic disc segmentation in retina using polar transform", *IEEE Access*, Vol. 5, (2017), 12293-12300, <https://doi.org/10.1109/ACCESS.2017.2723320>
19. Ghadiri, F., Bergevin, R. and Shafiee, M., "An adaptive thresholding approach for automatic optic disk segmentation", arXiv preprint arXiv:05104, (2017).
20. Septirini, A., Harjoko, A., Pulungan, R. and Ekantini, R., "Optic disc and cup segmentation by automatic thresholding with morphological operation for glaucoma evaluation", *Signal, Image Video Processing*, Vol. 11, No. 5, (2017), 945-952, doi. <https://doi.org/10.1007/s11760-016-1043-x>
21. Rehman, Z.U., Naqvi, S.S., Khan, T.M., Arsalan, M., Khan, M.A. and Khalil, M., "Multi-parametric optic disc segmentation using superpixel based feature classification", *Expert Systems with Applications*, Vol. 120, (2019), 461-473, <https://doi.org/10.1016/j.eswa.2018.12.008>
22. Dutta, M.K., Mourya, A.K., Singh, A., Parthasarathi, M., Burget, R. and Riha, K., "Glaucoma detection by segmenting the super pixels from fundus colour retinal images", in 2014 international conference on medical imaging, m-health and emerging communication systems (MedCom), IEEE. (2014), 86-90.
23. Morales, S., Naranjo, V., Angulo, J. and Alcañiz, M., "Automatic detection of optic disc based on pca and mathematical morphology", *IEEE Transactions on Medical Imaging*, Vol. 32, No. 4, (2013), 786-796, doi. <https://doi.org/10.1109/tmi.2013.2238244>
24. Dharmawan, D.A., Ng, B.P. and Rahardja, S., "A new optic disc segmentation method using a modified dolph-chebyshev matched filter", *Biomedical Signal Processing Control*, Vol. 59, (2020), 101932, <https://doi.org/10.1016/j.bspc.2020.101932>
25. Sezavar, A., Farsi, H. and Mohamadzadeh, S., "A modified grasshopper optimization algorithm combined with cnn for content based image retrieval", *International Journal of Engineering, Transactions A: Basics*, Vol. 32, No. 7, (2019), 924-930, <https://doi.org/10.5829/ije.2019.32.07a.04>
26. Feizi, A., "Convolutional gating network for object tracking", *International Journal of Engineering, Transactions A: Basics*, Vol. 32, No. 7, (2019), 931-939, <https://doi.org/10.5829/ije.2019.32.07a.05>
27. Bagheria, F., Tarokh, M. and Ziaratbanb, M., "Semantic segmentation of lesions from dermoscopic images using yolo-deeplab networks", *International Journal of Engineering, Transactions B: Applications*, Vol. 34, No. 2, (2021), 458-469, doi. <https://doi.org/10.5829/ije.2021.34.02b.18>
28. Sevastopolsky, A., "Optic disc and cup segmentation methods for glaucoma detection with modification of u-net convolutional neural network", *Pattern Recognition Image Analysis*, Vol. 27, No. 3, (2017), 618-624, <https://doi.org/10.1134/s1054661817030269>
29. Kim, J., Tran, L., Chew, E.Y., Antani, S. and Thoma, G.R., "Optic disc segmentation in fundus images using deep learning", in Medical Imaging 2019: Imaging Informatics for Healthcare, Research, and Applications, International Society for Optics and Photonics. Vol. 10954, (2019), 109540H.
30. Yu, S., Xiao, D., Frost, S. and Kanagasigam, Y., "Robust optic disc and cup segmentation with deep learning for glaucoma detection", *Computerized Medical Imaging Graphics*, Vol. 74, (2019), 61-71, doi. <https://doi.org/10.1016/j.compmedimag.2019.02.005>
31. Juneja, M., Singh, S., Agarwal, N., Bali, S., Gupta, S., Thakur, N. and Jindal, P., "Automated detection of glaucoma using deep learning convolution network (g-net)", *Multimedia Tools Applications*, Vol. 79, (2020), <https://doi.org/10.1007/s11042-019-7460-4>
32. Bhatkalkar, B.J., Reddy, D.R., Prabhu, S. and Bhandary, S.V., "Improving the performance of convolutional neural network for the segmentation of optic disc in fundus images using attention gates and conditional random fields", *IEEE Access*, Vol. 8,

- (2020), 29299-29310, <https://doi.org/10.1109/access.2020.2972318>
33. Jiang, Y., Xia, H., Xu, Y., Cheng, J., Fu, H., Duan, L., Meng, Z. and Liu, J., "Optic disc and cup segmentation with blood vessel removal from fundus images for glaucoma detection", in 2018 40th annual international conference of the IEEE engineering in medicine and biology society (EMBC), IEEE. (2018), 862-865.
 34. Zheng, Y., Zhang, X., Xu, X., Tian, Z. and Du, S., "Deep level set method for optic disc and cup segmentation on fundus images", *Biomedical Optics Express*, Vol. 12, No. 11, (2021), 6969-6983, <https://doi.org/10.1364/boe.439713>
 35. Tabassum, M., Khan, T.M., Arsalan, M., Naqvi, S.S., Ahmed, M., Madni, H.A. and Mirza, J., "Cded-net: Joint segmentation of optic disc and optic cup for glaucoma screening", *IEEE Access*, Vol. 8, (2020), 102733-102747, <https://doi.org/10.1109/access.2020.2998635>
 36. Nisha, K., Sreelekha, G., Sathidevi, P., Mohanachandran, P. and Vinekar, A., "A robust algorithm for automated detection of optic disc in retina of premature infants", in TENCON 2019-2019 IEEE Region 10 Conference (TENCON), IEEE. (2019), 684-689.
 37. Alais, R., Dokládal, P., Erginay, A., Figliuzzi, B. and Decencièrè, E., "Fast macula detection and application to retinal image quality assessment", *Biomedical Signal Processing Control*, Vol. 55, (2020), 101567, <https://doi.org/10.1016/j.bspc.2019.101567>
 38. Wang, L., Liu, H., Lu, Y., Chen, H., Zhang, J. and Pu, J., "A coarse-to-fine deep learning framework for optic disc segmentation in fundus images", *Biomedical Signal Processing Control*, Vol. 51, (2019), 82-89, <https://doi.org/10.1016/j.bspc.2019.01.022>
 39. Ke, P., Cai, M., Wang, H. and Chen, J., "A novel face recognition algorithm based on the combination of lbp and cnn", in 2018 14th IEEE International Conference on Signal Processing (ICSP), IEEE. (2018), 539-543.
 40. Touahri, R., AzizI, N., Hammami, N.E., Aldwairi, M. and Benaïda, F., "Automated breast tumor diagnosis using local binary patterns (lbp) based on deep learning classification", in 2019 International Conference on Computer and Information Sciences (ICCIS), IEEE. (2019), 1-5.
 41. Badaghei, R., Hassanpour, H. and Askari, T., "Detection of bikers without helmet using image texture and shape analysis", *International Journal of Engineering, Transactions C: Aspects*, Vol. 34, No. 3, (2021), 650-655, <https://doi.org/10.5829/ije.2021.34.03c.09>
 42. Hellström, A., Hård, A., Chen, Y., Niklasson, A. and Albertsson-Wikland, K., "Ocular fundus morphology in preterm children. Influence of gestational age, birth size, perinatal morbidity, and postnatal growth", *Investigative Ophthalmology Visual Science*, Vol. 38, No. 6, (1997), 1184-1192.
 43. Feng, X., Nan, Y., Pan, J., Zou, R. and Shen, L., "Comparative study on optic disc features of premature infants and term infants", (2020), <https://doi.org/10.21203/rs.3.rs-30626/v1>

Persian Abstract

چکیده

بیماری رتینوپاتی نارسی مهمترین علت نابینایی در نوزادان بوده که هر سال تعداد بسیار زیادی از نوزادان به آن مبتلا می‌شوند. با توجه به گسترش زیاد بیماری و عوارض نامطلوب آن تشخیص صحیح و به موقع رتینوپاتی نارسی بسیار ارزشمند است. تشخیص به موقع بیماری نیازمند افزایش معاینات نوزادان بوده که موجب افزایش نیاز به پزشک متخصص شده که اجرای آن دشوار است. به همین علت لزوم وجود سیستم‌های هوشمند برای کمک به پزشکان بیش از پیش احساس می‌گردد. در طراحی سیستم‌های هوشمند تشخیص رتینوپاتی نارسی یکی از مهمترین قسمت‌های شبکه برای تعیین میزان شدت و پیشروی این بیماری سر عصب بینایی که در این پژوهش به آن پرداخته شده است. در این مقاله یک مدل نوآورانه یادگیری عمیق بر مبنای مکانیزم توجه برای شناسایی محل و ناحیه سر عصب بینایی معرفی شده است. در روش ارائه شده، ابتدا تصاویر را پیش پردازش کرده و سپس تعداد آنها افزایش داده می‌شود. پس از آن برای تعیین محل دقیق ناحیه مربوط به سر عصب بینایی با بهبود شبکه U-Net به یک معماری بهینه دست می‌یابیم. معماری به کار رفته یک شبکه کانولوشنی دو مرحله‌ای است. در مرحله اول با استفاده از تصویر و ویژگی‌های تصویر به دو خروجی متفاوت دست پیدا کرده که ورودی مرحله دوم شبکه می‌باشد. مرحله دوم به عنوان پس پردازش، با بررسی خروجی‌ها و استفاده از مکانیزم توجه یک نتیجه نهایی فراهم نموده که براساس معیار ضرب تشابه سورنسون و معیار ژاکارد به ترتیب دارای دقت ۹۴/۲۲ درصد و ۸۶/۱ درصد می‌باشد.



Universal Filtered Multicarrier Receiver Complexity Reduction to Orthogonal Frequency Division Multiplexing Receiver

R. Manda*, R. Gowri

Department of Electrical and Electronics, School of Engineering, UPES, Dehradun, India

PAPER INFO

Paper history:

Received 12 November 2021

Received in revised form 08 January 2022

Accepted 09 January 2022

Keywords:

Fifth Generation

Bit Error Rate

Complexity Reduction Ratio

Fast Fourier Transform

Finite Impulse Response

Signal to Noise Ratio

Universal Filtered Multicarrier

ABSTRACT

The Universal Filtered Multicarrier (UFMC) waveform technology is one of the promising waveforms for 5G and beyond 5G networks. Owing 2N-point Fast Fourier Transform (FFT) processor at the UFMC receiver, the computational and implementation complexity is two times more than the conventional Orthogonal Frequency Division Multiplexing (OFDM) receiver system. In this paper, we proposed a simplified UFMC receiver structure to reduce computational complexity as well as hardware requirements. The received UFMC symbol simplified exactly to its equivalent after performing 2N-point FFT and decimation operations. In which, the mathematical model of the frequency-domain UFMC signal is rederived after processing through 2N-point FFT and decimator, and the simplified signal is generated with an N-point FFT. Accordingly, the 2N-point FFT processor and decimator are replaced with a single N-point FFT processor. This approach reduces the 50% computational complexity at the FFT processor level hence the hardware and processing time. The computational complexity of the proposed receiver model is approximately equivalent to the OFDM receiver. Additionally, analyzed the mathematical model for the simplified UFMC receiver and the comparative performance of the UFMC system with the conventional model.

doi: 10.5829/ije.2022.35.04a.12

NOMENCLATURE

$f_p[l]$	The impulse response of p^{th} sub-band filter	$Y_{2N}[k]$	2N-point DFT of $y_{i,zp}[n]$
$f[l]$	Desired/ideal filter impulse response	W_N	The twiddle factor of N-point DFT $W_N = e^{-\frac{j2\pi}{N}}$
$h[n]$	The impulse response of the wireless channel	L_f	Length of the sub-band filter
$S_{ip}[k]$	p^{th} sub-band input constellation mapped data sequence of i^{th} UFMC symbol	L_h	Length of the wireless channel
$s_{ip}[n]$	The output of N-point IFFT block of p^{th} sub-band	N	Size of the IFFT block
$x_i[n]$	The final i^{th} UFMC symbol	N_b	Number of sub-bands
$x_{ip}[n]$	p^{th} sub-band filter output of i^{th} UFMC symbol	Q	Number of data subcarriers per sub-band
$y_i[n]$	The received i^{th} UFMC symbol	V_{sc}	Half of the virtual sub-carriers
$y_{i,zp}[n]$	The received i^{th} UFMC symbol after zeros padded to $y_i[n]$		

1. INTRODUCTION

The ongoing fifth-generation (5G) systems continue to reveal the inherent limitations due to the rise of intelligent communication environments, and some 5G application use cases like massive machine-type communications

(mMTC), and ultra-reliable low latency communications (URLLC) [1]. These limitations are motivation to define the technical requirements and targets of the next-generation (6G) cellular networks that can transfer beyond personalized communication toward the full realization of the Internet of Things (IoT) standard, that

*Corresponding Author Institutional Email: rmanda@ddn.upes.ac.in
(R. Manda)

connects everything, not just people, but also sensors, vehicles, wearables, computing resources, and even robotic agents [2–4]. Therefore, 5G and beyond 5G network use cases complicate the required specifications in many aspects such as data rate, delay or latency, reliability, energy consumption, multicast connectivity, and the type of protocols that provides diverse ways to exchange information between the devices [5]. These systems are impacted by the modulation format used at the physical layer [6–8].

In the last few years, several physical layer waveforms have been proposed like Filter bank multicarrier (FBMC) [9], generalized frequency division multiplexing (GFDM) [10], filtered orthogonal frequency division multiplexing (F-OFDM) [11], and universal filtered multicarrier (UFMC) [12]. Out of these, the UFMC waveform technique is one of the competitive modulation schemes for future generation wireless systems to provide flexible packet transmission services, low interference due to OBE, and relaxed synchronization [13, 14]. However, the transmitter and receiver complexity of UFMC is higher compared to the conventional (CP-OFDM) due to its filtering operation at the transmitter and 2N-point FFT processor at the receiver. To reduce the system complexity and to improve the energy efficiency, the baseband signal processing time and hardware requirement for the new modulation waveform can be reduced by simplifying the structure of the transceiver architecture in terms of computations. In recent years, some methods have been proposed to reduce the computational complexity of the UFMC transmitter [15–18]. The transmitter complexity was reduced by approximating the frequency domain UFMC signal [15], by introducing the FIR filter structure and the poly-phase filter structure based on the lightweight method into the UFMC transmitter structure [17]. A reduced hardware complexity solution [16] was proposed for the implementation of IFFT and filtering operation by avoiding redundant computations. Recently, a reconfigurable baseband UFMC transmitter architecture was proposed by Kumar et al. [18], which has the flexibility to choose the number of subcarriers per sub-band and the pulse-shaping filter. Wu et al. [19] have proposed an advanced receiver for UFMC, which uses the odd number samples of 2N-point FFT along with even number samples to improve the performance at high computations, and here the computational complexity burden of 2N-point FFT has not been reduced. The FFT pruning approach [20], in which removing the operations related to the zero inputs reduces the computational complexity of the UFMC transmitter and receiver. In this paper, the method mainly focused on the system complexity, baseband signal processing latency, and power consumption at the receiver. The proposed approach simplifies the UFMC receiver model, which uses a single N-point FFT to generate the frequency-

domain baseband signal for data detection like the conventional OFDM. This approach avoids the zero-padding operation and decimation part at the UFMC receiver baseband signal processing. Therefore, UFMC reduces the hardware requirement, computational complexity, and hence latency and power consumption. The FFT pruning approach at the UFMC receiver gives fewer computations compared to the conventional model but requires high-level reprogramming since the non-zero inputs vary over time. However, the proposed model requires a smaller number of computations compared to the conventional and the FFT pruning algorithm [20] which is clearly explained in the result analysis session. One of the minor drawbacks of the proposed model is that the hardware implementation needs to use L_f+L_b-2 number of adders before the N-point FFT, which may cause the rise of connectivity complexity and word length effect when it processes through the FFT processor. Otherwise, the proposed model is superior to the conventional model.

The rest of the paper is organized as follows; section 2 described the conventional UFMC transceiver model, section 3 explained the proposed UFMC receiver model that how it is derived from the traditional UFMC receiver model, and section 4 discusses the computational complexity. Section 5, described the performance analysis in terms of complexity and SNR versus BER, and finally, concluded in section 6.

2. CONVENTIONAL UFMC SYSTEM MODEL

2.1. The UFMC Transmitter Model The UFMC waveform technique is a generalized form of OFDM and FBMC, in which a group of subcarriers is individually filtered with a bandpass filter [12]. The schematic block diagram of the traditional UFMC transceiver model is depicted in Figure 1. Whereat the UFMC transmitter, the entire frequency band (total subcarrier) is divided into several blocks (a group of sub-carriers) called sub-band and filtered individually. The final i^{th} UFMC time-domain symbol is the sum of the outputs of all sub-band filters, which can be expressed as

$$x_i[n] = \sum_{p=0}^{N_b-1} x_{ip}[n] \quad (1)$$

The p^{th} sub-band filter output of i^{th} UFMC symbol

$$x_{ip}[n] = \sum_{l=0}^{L_f-1} f_p[l] s_{ip}[n-l]; \quad n = 0, 1, 2, \dots, N + L_f - 2 \quad (2)$$

where $f_p[l]$; $l = 0, 1, \dots, L_f - 1$ is p^{th} sub-band filter impulse response, which is the frequency-shifted version of prototype filter $f[l]$ to the center of p^{th} sub-band.

$$f_p[l] = f[l] e^{j\frac{2\pi}{N}(v_{sc} + (p-\frac{1}{2})Q + \frac{N}{2})l} \quad (3)$$

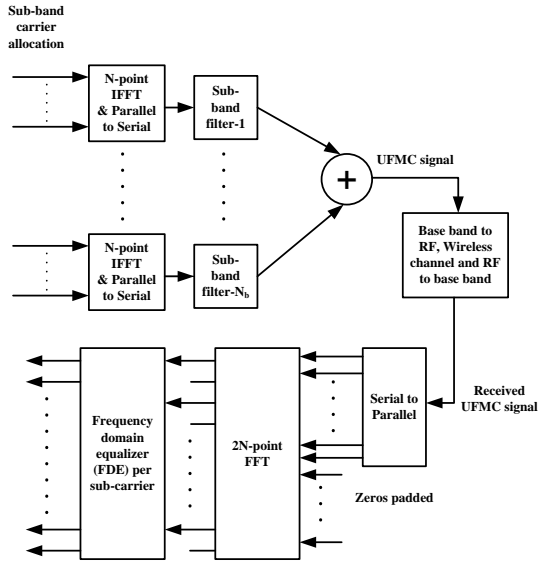


Figure 1. Traditional UFMC transceiver model

The output of the N-point IFFT $s_{ip}[n]$ can be written as

$$s_{ip}[n] = \frac{1}{N} \sum_{k=0}^{N-1} S_{ip}[k] e^{j\frac{2\pi}{N}kn}; n = 0, 1, \dots, N-1 \quad (4)$$

The final UFMC symbol $x_i[n]$ with the length of $N + L_f - 1$ transmitted through the wireless channel, which is

$$y_i[n] = x_i[n] * h[n] + z[n]; n = 0, 1, \dots, N_T - 1 \quad (5)$$

where $z[n]$ is a complex-valued Additive White Gaussian noise (AWGN) with zero mean and variance of σ_z^2 , $N_T = N + L - 2$ and $L = L_f + L_h$.

2.2. The UFMC Receiver Model At the receiver, the zeroes padded to the received symbol to perform the 2N-point FFT to consider the sub-band filter tails. The received signal after zeros padded

$$y_{i,zp}[n] = \begin{cases} y_i[n]; & 0 \leq n \leq N_T - 1 \\ 0; & N_T \leq n \leq 2N - 1 \end{cases} \quad (6)$$

The frequency-domain of the received UFMC signal after processing through the 2N-point FFT is mathematically formulated as

$$Y_{2N}[k] = \sum_{n=0}^{2N-1} y_{i,zp}[n] W_{2N}^{kn}; k = 0, 1, \dots, 2N-1 \quad (7)$$

The receiver only needs to extract the even-numbered samples after the 2N-point FFT transformation to estimate the data symbols because the odd-numbered samples consist of an interference component (proof can see in the appendix). In conventional UFMC receiver, this is implemented with 2N-point FFT and decimator with factor 2 shown in Figure 1, which is twice the size of FFT that is used in conventional OFDM receiver and increases the UFMC receiver complexity compared to the OFDM receiver.

2.3. Data Detection The final UFMC transmitted symbol $x(n)$ having the length $N + L_f - 1$, can be expressed in matrix form as

$$X = \sum_{p=1}^B [F_p]_{(N+L_f-1) \times N} [V_p]_{N \times Q} [S_p]_{Q \times 1} \quad (8)$$

where $[F_p]_{(N+L_f-1) \times N}$ is a Toeplitz matrix of p^{th} sub-band FIR filter impulse response with the first column $[f_p(0), f_p(1), \dots, f_p(L_f - 1), [0]_{1 \times N-1}]^T$ and first row $[f_p(0), [0]_{1 \times N-1}]$, $[V_p]_{N \times Q}$ is the IFFT matrix that relevant to p^{th} sub-band carriers and S_p is the column matrix of the p^{th} sub-band data sequence.

$$X = \mathcal{F}\mathcal{V}\mathcal{S} \quad (9)$$

$$\begin{aligned} \mathcal{F} &= [F_0, F_1, \dots, F_{B-1}] \\ \mathcal{V} &= \text{blockdiag}([V_0, V_1, \dots, V_{B-1}]) \\ \mathcal{S} &= [S_0^T, S_1^T, \dots, S_{B-1}^T]^T \end{aligned}$$

This UFMC symbol is transmitted through the wireless channel, which can be defined as

$$y = HX + z = \mathcal{H}\mathcal{F}\mathcal{V}\mathcal{S} + z \quad (10)$$

where \mathcal{H} is the Toeplitz matrix of the channel coefficients $h(n)$ with the first column $[h(0), h(1), \dots, h(L_h - 1), [0]_{1 \times N+L_f-2}]^T$ and first row $[h(0), [0]_{1 \times N+L_f-2}]$ and z is the zero mean Additive White Gaussian Noise (AWGN) vector having length $N + L - 2$. After performing the 2N-point FFT, the even-numbered frequency domain samples are

$$Y_e = \mathcal{P}_e \mathcal{W} \mathcal{H} \mathcal{F} \mathcal{V} \mathcal{S} + \mathcal{P}_e^T \mathcal{W} z \quad (11)$$

where the matrix $[\mathcal{P}_e]_{N \times 2N}$ with elements

$$\mathcal{P}_e(m, k) = \begin{cases} 1; & \text{for } k = 2m \\ 0; & \text{for } k \neq 2m \end{cases} \quad (12)$$

where $m = 0, 1, \dots, N-1$ and $k = 0, 1, \dots, 2N-1$. Where $[\mathcal{W}]_{2N \times (N+L-2)}$ are the 2N-point FFT twiddle factor matrix and its elements are $\mathcal{W}(k, r) = W_{2N}^{kr}$; where $k = 0, 1, \dots, 2N-1$; and $r = 0, 1, \dots, N+L-3$. These even-numbered samples are used for data detection. By Least squares algorithm, the estimated data sequence is defined as

$$\hat{S} = (A^H A)^{-1} A^H Y_e; A = \mathcal{P}_e^T \mathcal{W} \mathcal{H} \mathcal{F} \mathcal{V} \quad (13)$$

3. THE PROPOSED UFMC RECEIVER MODEL

The even-numbered samples/sub-carriers of 2N-point FFT are defined as

$$Y_e[k] = Y_{2N}[2k] = \sum_{n=0}^{2N-1} y_{i,zp}[n] W_{2N}^{2kn}; k = 0, 1, \dots, N-1 \quad (14)$$

We know that

$$W_{2N}^{2kn} = e^{-\frac{j2\pi}{2N}2kn} = e^{-\frac{j2\pi}{N}kn} = W_N^{kn} \quad (15)$$

We rewrite Equation (8) as

$$Y_e[k] = \sum_{n=0}^{2N-1} y_{i,zp}[n] W_N^{kn} = \sum_{n=0}^{N-1} y_{i,zp}[n] W_N^{kn} + \sum_{n=N}^{2N-1} y_{i,zp}[n] W_N^{kn} \quad (16)$$

Let assume that $m = n - N$, then, Equation (16) can be rewritten as

$$Y_e[k] = \sum_{n=0}^{N-1} y_{i,zp}[n] W_N^{kn} + \sum_{m=0}^{N-1} y_{i,zp}[m+N] W_N^{k(m+N)} \quad (17)$$

where $W_N^{kN} = e^{-\frac{j2\pi}{N}kN} = e^{-j2\pi k} = 1$

$$Y_e[k] = \sum_{n=0}^{N-1} y_i[n] W_N^{kn} + \sum_{m=0}^{L-3} y_i[m+N] W_N^{km} \quad (18)$$

Finally, Equation (18) can be written as

$$Y_e[k] = \sum_{n=0}^{N-1} y'[n] W_N^{kn} \quad (19)$$

where

$$y'[n] = \begin{cases} y_i[n] + y_i[n+N]; & 0 \leq n \leq L-3 \\ y_i[n]; & L-2 \leq n \leq N-1 \end{cases} \quad (20)$$

Now, according to Equation (20) the even-numbered subcarriers can be generated with a single N-point FFT having $y'[n]$ as input, which is shown in Figure 2. Here, both the 2N-point DFT and decimator operations can be implemented with the single N-point DFT. The computational complexity can be reduced twice compared to the conventional UFMC receiver.

4. COMPLEXITY ANALYSIS OF THE PROPOSED MODEL

The major computational complexity in the UFMC receiver system includes the 2N-point FFT processor, the channel estimation, and equalization algorithms. The UFMC baseband signal model at the receiver is like the OFDM signal except for the filter equalization, so, the same algorithms can be applied in the UFMC system for channel estimation and equalization. Therefore, the

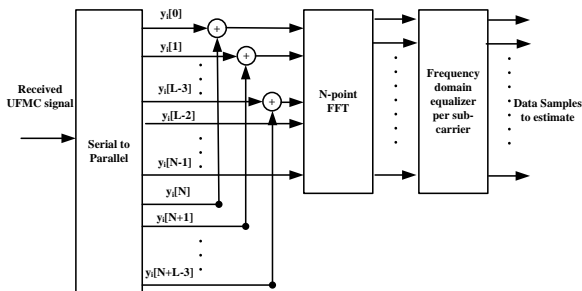


Figure 2. Block diagram of the proposed UFMC receiver model

UFMC receiver complexity is two times higher compared to the OFDM receiver. Furthermore, the additional memory or control overhead is one of the main disadvantages of the implementation.

The N-point DFT is efficiently computed by the FFT algorithm [21], which requires the total number of arithmetic operations (real multiplications and additions) using radix-2 FFT algorithm is $5N \log_2 N$. The split-radix FFT algorithm [22] has a lower number of arithmetic operations compared to the radix-2 FFT algorithm, which requires the total number of arithmetic operations to be $4N \log_2 N - 6N + 8$. With the FFT pruning algorithm, the number of real operations (additions and multiplications) required to process the UFMC baseband received signal [20] is $5N \log_2 N - 2N + 4(L - 2)$. Table 1 describes the computational complexity comparison between the conventional, FFT pruning approach and the proposed receiver model. Which states that the proposed UFMC receiver model has a smaller number of arithmetic operations, it is simple and effective compared to conventional CP-OFDM and UFMC receivers. The complexity efficiency of the system can be measured by complexity reduction ratio (CRR), which is defined as the ratio of the total number of computations required for the conventional model (CM_{ufmc}^{conv}) to the total number of computations required for the conventional model (CM_{ufmc}^{prop}).

$$CRR = \frac{CM_{ufmc}^{conv}}{CM_{ufmc}^{prop}} \approx 2 \left(1 + \frac{1}{\log_2 N} \right) \quad (21)$$

From Equation (21), the proposed model reduces the computational complexity more than two times as compared to the conventional UFMC receiver model. Also, in the proposed model, there are no zeros padding operations to process through 2N-point FFT. Therefore, the number of read/ write memory locations was reduced by two times approximately. However, the required storage space for read/ write operations is the same as the conventional OFDM receiver model. In the proposed

TABLE 1. Computational complexity comparison

Receiver model type	Number arithmetic operations (CM)	Required hardware blocks for the baseband signal processing at the receiver
CP-OFDM receiver	$4N \log_2 N - 6N + 8$	CP remover, N-point FFT, FDE
Conventional UFMC receiver	$8N \log_2 N - 4N + 8$	Zeros padder, 2N-point FFT, Decimator, FDE
UFMC receiver with FFT pruning	$5N \log_2 N - 2N + 4(L - 2)$	Zeros padder, 2N-point FFT, FDE
Proposed UFMC receiver	$4N \log_2 N - 6N + 8 + 2(L-2)$	N-point FFT, FDE

model, the adder blocks are used before N-point FFT which may increase the connectivity complexity compared to the traditional model.

The power carried by odd-numbered frequency samples of 2N-point FFT is not utilized in the conventional UFMC receiver, hence the power efficiency is 50%. But in the proposed model, there is no 2N-point FFT and which uses all the samples processed by FFT. Therefore, the power efficiency can be improved to 100%. Finally, we can say that the proposed UFMC receiver model is more suitable for ultra-low latency and low energy consumption IoT uses cases as well as for next-generation cellular networks.

5. SIMULATION RESULTS

The computational complexity of the receiver depends only on the size of the FFT. In this session, some computer simulation results are presented. The numerical analysis of computational complexity and its comparison is shown in Figure 3 for different bandwidth (BW) configurations mentioned in Table 2 under the NR-TDL vehicular-A channel model with a length of 24. These comparisons conclude that the proposed receiver model has a lesser number of arithmetic operations (i.e., two times lesser) at the baseband FFT signal processing level compared conventional model and almost achieved the same computational complexity of the CP-OFDM receiver. Furthermore, the complexity ratio (CR) of the UFMC receiver to the OFDM receiver $\left(\frac{CM_{ufmc}}{CM_{ofdm}}\right)$ for different methods are shown in Figure 4. Consider the bandwidth of 20 MHz and $N = 1024$ for numerical comparison between the proposed and conventional models, in this case, the CR values are 2.1904, 1.3881, and 1.0036 for the conventional, conventional with FFT pruning algorithm and the proposed UFMC receiver model respectively. From these numerical analyses, the proposed model has less complexity ratio and is more

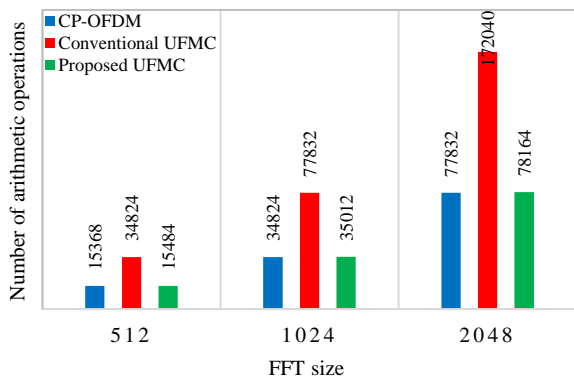


Figure 3. Comparison of computational complexity (with split-radix FFT algorithm)

TABLE 2. Bandwidth configuration for NR frequency band range (FR)-1 for SCS = 15 kHz [23]

Bandwidth/specifications	5 MHz	10 MHz	20 MHz
Number of subcarriers	333	666	1333
Data subcarrier	300	624	1272
FFT/IFFT size	512	1024	2048
CP length = $L_f - 1$	36	72	144

efficient in terms of computational complexity. Also, the FFT's per energy [24] can be improved, which is defined as

$$FFT's/Energy = \frac{Technology}{Power \times Execution\ time \times 10^{-6}} \quad (22)$$

where Technology is the CMOS process in micrometers, the power consumption is proportional to supply voltage, clock frequency, and load capacitance. The execution time depends on the number of operations/computations required to complete a particular task. From Equation (22), the FFT's per energy is inversely proportional to the execution time, which means for the proposed model the FFT processor requires lesser execution time compared to the conventional one. Finally, we can say that the proposed UFMC receiver model is more suitable for ultra-low latency and low energy consumption uses cases of the next-generation cellular networks.

The proposed model is a simplified model of the conventional model. Therefore, it gives almost the same performance in terms of SNR versus BER at lower computational cost, which is shown in Figure 5 for the simulation parameters mentioned in Table 3.

In practical cases due to the additional adders on the receiver side, the proposed model may increase the connectivity complexity and occurs small losses; hence small performance degradation (shown in Figure 5).

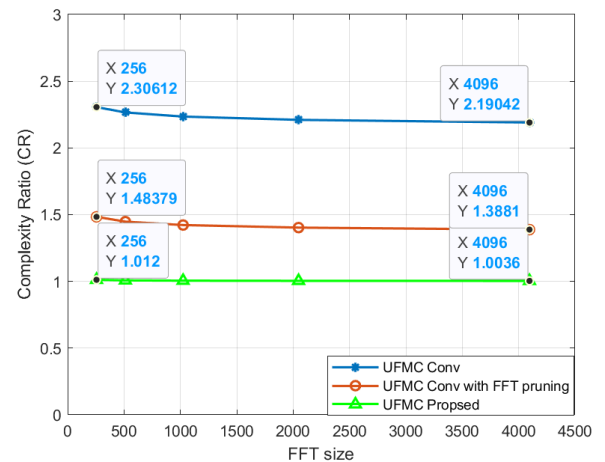


Figure 4. Complexity ratio (CR) of the UFMC receiver to the OFDM receiver

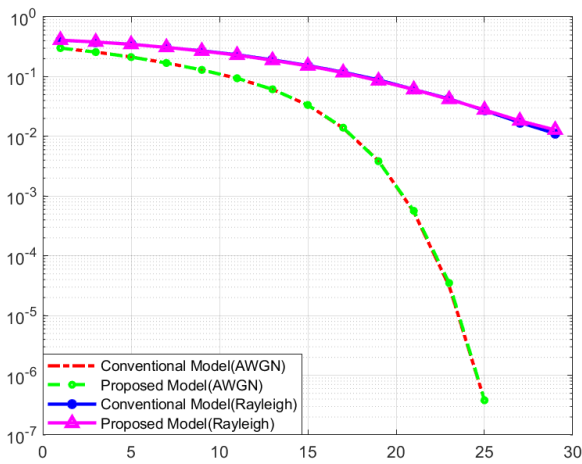


Figure 5. SNR versus BER for UPMC transceiver system

TABLE 3. Simulation parameters

Parameter name	Value
Channel bandwidth	10 MHz
Modulation type	16-QAM
FFT size	1024
CP length	72
Number of UPMC symbols	7
Sub-band size	12
Stopband attenuation (A_s)	40 dB
Channel type	AWGN/ Rayleigh fading

6. CONCLUSION

The UPMC was one of the candidate waveforms for 5G, but the computational and hardware complexity of the UPMC transceiver system has more than the CP-OFDM system due to filtering operation at the transmitter and $2N$ -point FFT processing at the receiver. In this point of view, here we proposed the simplified UPMC receiver model, in which the exact frequency domain UPMC received symbol after FFT processor and decimator is derived and simplified to implement with a single N -point FFT and that reduced the computational complexity more than two times (i.e., 50%) compared to the traditional receiver model without degrading the system performance. At the receiver, the zero-padding for processing $2N$ -point FFT and decimation part is simply replaced by one N -point FFT, which reduced the number of hardware components at baseband signal processing and the storage requirement for read/write operation to process the data and the number of computations or operations. This model reduced the hardware requirement and hence the power consumption. The real-time hardware implementation of this model is the future scope of this work.

7. REFERENCES

- Saad, W., Bennis, M., and Chen, M. "A Vision of 6G Wireless Systems: Applications, Trends, Technologies, and Open Research Problems." *IEEE Network*, Vol. 34, No. 3, (2020), 134–142. <https://doi.org/10.1109/MNET.001.1900287>
- Yang, P., Xiao, Y., Xiao, M., and Li, S. "6G Wireless Communications: Vision and Potential Techniques." *IEEE Network*, Vol. 33, No. 4, (2019), 70–75. <https://doi.org/10.1109/MNET.2019.1800418>
- Zhang, Z., Xiao, Y., Ma, Z., Xiao, M., Ding, Z., Lei, X., Karagiannis, G. K., and Fan, P. "6G Wireless Networks: Vision, Requirements, Architecture, and Key Technologies." *IEEE Vehicular Technology Magazine*, Vol. 14, No. 3, (2019), 28–41. <https://doi.org/10.1109/MVT.2019.2921208>
- Giordani, M., Polese, M., Mezzavilla, M., Rangan, S., and Zorzi, M. "Toward 6G Networks: Use Cases and Technologies." *IEEE Communications Magazine*, Vol. 58, No. 3, (2020), 55–61. <https://doi.org/10.1109/MCOM.001.1900411>
- Raza, R., and Al-Ani, M. "Routing Protocols for IOT Applications based on Distributed Learning." *International Journal of Engineering, Transaction A: Basics*, Vol. 34, No. 4, (2021), 825–831. <https://doi.org/10.5829/ije.2021.34.04a.08>
- Banelli, P., Buzzi, S., Colavolpe, G., Modenini, A., Rusek, F., and Ugolini, A. "Modulation Formats and Waveforms for 5G Networks: Who Will Be the Heir of OFDM?: An overview of alternative modulation schemes for improved spectral efficiency." *IEEE Signal Processing Magazine*, Vol. 31, No. 6, (2014), 80–93. <https://doi.org/10.1109/MSP.2014.2337391>
- Schulz, P., Matthe, M., Klessig, H., Simsek, M., Fettweis, G., Ansari, J., Ashraf, S. A., Almeroth, B., Voigt, J., Riedel, I., ... Windisch, M. "Latency Critical IoT Applications in 5G: Perspective on the Design of Radio Interface and Network Architecture." *IEEE Communications Magazine*, Vol. 55, No. 2, (2017), 70–78. <https://doi.org/10.1109/MCOM.2017.1600435CM>
- Mukherjee, A. "Energy Efficiency and Delay in 5G Ultra-Reliable Low-Latency Communications System Architectures." *IEEE Network*, Vol. 32, No. 2, (2018), 55–61. <https://doi.org/10.1109/MNET.2018.1700260>
- Farhang-Boroujeny, B. "OFDM Versus Filter Bank Multicarrier." *IEEE Signal Processing Magazine*, Vol. 28, No. 3, (2011), 92–112. <https://doi.org/10.1109/MSP.2011.940267>
- Michailow, N., Matthe, M., Gaspar, I. S., Caldevilla, A. N., Mendes, L. L., Festag, A., and Fettweis, G. "Generalized Frequency Division Multiplexing for 5th Generation Cellular Networks." *IEEE Transactions on Communications*, Vol. 62, No. 9, (2014), 3045–3061. <https://doi.org/10.1109/TCOMM.2014.2345566>
- Zhang, L., Ijaz, A., Xiao, P., Mulu, M. M., and Tafazolli, R. "Filtered OFDM Systems, Algorithms, and Performance Analysis for 5G and Beyond." *IEEE Transactions on Communications*, Vol. 66, No. 3, (2018), 1205–1218. <https://doi.org/10.1109/TCOMM.2017.2771242>
- Vakilian, V., Wild, T., Schaich, F., ten Brink, S., and Frigon, J.-F. "Universal-filtered multi-carrier technique for wireless systems beyond LTE." In 2013 IEEE Globecom Workshops (GC Wkshps) (pp. 223–228). IEEE. <https://doi.org/10.1109/GLOCOMW.2013.6824990>
- Schaich, F., and Wild, T. "Waveform contenders for 5G - OFDM vs. FBMC vs. UPMC." In 2014 6th International Symposium on Communications, Control and Signal Processing (ISCCSP) (pp. 457–460). IEEE. <https://doi.org/10.1109/ISCCSP.2014.6877912>
- Schaich, F., Wild, T., and Chen, Y. "Waveform Contenders for 5G - Suitability for Short Packet and Low Latency

- Transmissions.” In 2014 IEEE 79th Vehicular Technology Conference (VTC Spring) (pp. 1–5). IEEE. <https://doi.org/10.1109/VTCSpring.2014.7023145>
15. Wild, T., and Schaich, F. “A Reduced Complexity Transmitter for UF-OFDM.” In 2015 IEEE 81st Vehicular Technology Conference (VTC Spring) (pp. 1–6). IEEE. <https://doi.org/10.1109/VTCSpring.2015.7145643>
 16. Jafri, A. R., Majid, J., Shami, M. A., Imran, M. A., and Najam-Ul-Islam, M. “Hardware Complexity Reduction in Universal Filtered Multicarrier Transmitter Implementation.” *IEEE Access*, Vol. 5, (2017), 13401–13408. <https://doi.org/10.1109/ACCESS.2017.2728605>
 17. Guo, Z., Liu, Q., Zhang, W., and Wang, S. “Low Complexity Implementation of Universal Filtered Multi-Carrier Transmitter.” *IEEE Access*, Vol. 8, (2020), 24799–24807. <https://doi.org/10.1109/ACCESS.2020.2970727>
 18. Kumar, V., Mukherjee, M., and Lloret, J. “Reconfigurable Architecture of UFMC Transmitter for 5G and Its FPGA Prototype.” *IEEE Systems Journal*, Vol. 14, No. 1, (2020), 28–38. <https://doi.org/10.1109/JSYST.2019.2923549>
 19. Wu, M., Dang, J., Zhang, Z., and Wu, L. “An Advanced Receiver for Universal Filtered Multicarrier.” *IEEE Transactions on Vehicular Technology*, Vol. 67, No. 8, (2018), 7779–7783. <https://doi.org/10.1109/TVT.2018.2831245>
 20. Saad, M., Al-Ghouwayel, A., and Hijazi, H. “UFMC Transceiver Complexity Reduction.” In 2018 25th International Conference on Telecommunications (ICT) (pp. 295–301). IEEE. <https://doi.org/10.1109/ICT.2018.8464863>
 21. Cooley, J. W., and Tukey, J. W. “An Algorithm for the Machine Calculation of Complex Fourier Series.” *Mathematics of Computation*, Vol. 19, No. 90, (1965), 297. <https://doi.org/10.2307/2003354>
 22. Duhamel, P., and Hollmann, H. “ ‘Split radix’ FFT algorithm.” *Electronics Letters*, Vol. 20, No. 1, (1984), 14. <https://doi.org/10.1049/el:19840012>
 23. 3GPP TS 38.101-1 v15.1.0, ‘NR: User Equipment (UE) radio transmission and reception part1., 2011.
 24. Yang, C.-H., Yu, T.-H., and Markovic, D. “Power and Area Minimization of Reconfigurable FFT Processors: A 3GPP-LTE Example.” *IEEE Journal of Solid-State Circuits*, Vol. 47, No. 3, (2012), 757–768. <https://doi.org/10.1109/JSSC.2011.2176163>

APPENDIX

The frequency-domain received UFMC signal after processing through the 2N-point FFT

$$Y_{2N}(k) = \sum_{n=0}^{2N-1} y_{zp}(n) e^{-\frac{j2\pi}{2N}kn} \quad (23)$$

To detect the data from this received signal like in the OFDM system, we require to collect N- samples from 2N- samples and these samples do not contain any interference components. For this purpose, the 2N-samples are divided into even and add number samples.

For even-numbered samples, $k = 0, 2, 2N - 2$ and $k = 2k'$; $k' = 0, 1, \dots, N - 1$ therefore, the even-numbered subcarriers of 2N-point FFT are

$$Y_e(k') = Y_{2N}(2k') = \sum_{n=0}^{2N-1} y_{zp}(n) e^{-\frac{j2\pi}{N}k'n} \quad (24)$$

Similarly, the odd-numbered subcarriers are

$$Y_o(k') = Y_{2N}(2k' + 1) = \sum_{n=0}^{2N-1} y_{zp}(n) e^{-\frac{j2\pi}{2N}(2k'+1)n} = \sum_{n=0}^{2N-1} y_{zp}(n) e^{-\frac{j2\pi}{N}k'n} e^{-\frac{j\pi}{N}n} \quad (25)$$

From Equations (23) and (24), it was observed that the data can be directly retrieved from the even-numbered subcarriers, but it cannot be retrieved from odd-numbered subcarriers due to the presence of interference component. That is why the odd-numbered subcarriers are discarded and even-numbered subcarriers are extracted for data detection at the receiver using a single-tap frequency domain equalizer (FDE).

Persian Abstract

چکیده

فناوری شکل موج چند حامل فیلتر شده جهانی (UFMC) یکی از شکل‌های موج امیدوارکننده برای شبکه‌های 5G و فراتر از آن است. با توجه به پردازشگر تبدیل فوریه سریع (FFT) 2N در گیرنده UFMC، پیچیدگی محاسباتی و پیاده‌سازی دو برابر بیشتر از سیستم گیرنده متعارف تقسیم فرکانس متعامد (OFDM) است. در این مقاله، ما یک ساختار گیرنده UFMC ساده شده را برای کاهش پیچیدگی محاسباتی و همچنین نیازهای سخت‌افزاری پیشنهاد کردیم. نماد دریافتی UFMC دقیقاً پس از انجام عملیات FFT نقطه 2N و حذف دقیقاً به معادل خود ساده شد که در آن، مدل ریاضی سیگنال UFMC حوزه فرکانس پس از پردازش از طریق FFT نقطه 2N و دسیماتور دوباره استخراج می‌شود و سیگنال ساده شده با یک FFT نقطه N تولید می‌شود. بر این اساس، پردازنده FFT 2N و Decimator با یک پردازنده FFT نقطه N جایگزین می‌شود. این رویکرد پیچیدگی محاسباتی را 50٪ در سطح پردازنده FFT کاهش می‌دهد و در نتیجه زمان سخت‌افزار و پردازش را کاهش می‌دهد. پیچیدگی محاسباتی مدل گیرنده پیشنهادی تقریباً معادل گیرنده OFDM است. علاوه بر این، مدل ریاضی برای گیرنده UFMC ساده شده و عملکرد مقایسه‌ای سیستم UFMC با مدل معمولی مورد تجزیه و تحلیل قرار گرفت.



Static and Dynamic Behavior of High-strength Lightweight Reinforced Concrete One-way Ribbed Slabs

T. A. Mohammed*, H. M. Kadhim

Civil Engineering Department, Collage of Engineering, University of Babylon, Babylon, Iraq

PAPER INFO

Paper history:

Received 23 November 2021

Received in revised form 29 December 2021

Accepted 31 December 2021

Keywords:

Steel Fiber

Ribbed Slab

Sugar Molasses

Serviceability

Harmonic Loading

ABSTRACT

Nowadays, reducing the self-weight of structures and vibration problems is the primary goal for design requirements in most civil constructions. Two-point loading and harmonic loading tests were conducted to examine the strength and serviceability of high-strength reinforced concrete one-way ribbed slabs. Six slabs were cast and tested. The behavior of cracking, deflection, and vibration was investigated. The experimental results showed that using high strength-lightweight concrete (HSLWC) instead of high strength-normal weight concrete (HSNWC) in constructed one-way ribbed slab led to a decrease in the density by 19.31%, the strength by 17.70%, and ultimate deflection by 17.33%. Although the addition of steel fibers to HSLWC led to an increase in the density of concrete its addition enhances the load-deflection relationship and ultimate load for slab specimen which reduced the reduction in strength by 14.49%. Furthermore, ductility index, stiffness, and toughness index for ribbed slab specimens with steel fibers showed better behavior than those without steel fibers. The HSNWC gave a negative impact on the vibration of the one-way ribbed slab at both operation frequencies (25 and 50) Hz, while using HSLWC with and without steel fibers, led to reducing the vibration effect by (30.11 and 30.68) % and (15.26 and 20.25) % at 25Hz and 50Hz, respectively.

doi: 10.5829/ije.2022.35.04a.13

NOMENCLATURE

e	Eccentric distance (m)	Greek Symbols	
f_c'	Cylinder compressive strength (MPa)	μ_d	Displacement ductility index
f_{cu}	Cubic compressive strength (MPa)	ω_o	Operating frequency (rad/sec)
f_r	Flexural strength (MPa)	Subscripts	
f_t	Splitting tensile strength (MPa)	ACI	American concrete institute
m	Eccentric rotating mass (kg)	ASTM	American society for testing and materials
P_{cr}	Cracking (kN)	HSLWC	High strength-lightweight concrete
P_d	Dynamic load (N)	HSNWC	High strength – normal weight concrete
P_s	Service load (kN)	LVDT	Linear variable differential transducer
P_u	Ultimate load (kN)	LWA	Lightweight aggregate
t	Dynamic time (sec)	LWC	Lightweight concrete
V_f	Volume fraction of fiber	NSLWC	Normal strength lightweight concrete
w_c	Unit weight of concrete (kg/m^3)	SE	Structural efficiency
		SLWC	Structural lightweight concrete

1. INTRODUCTION

The serviceability behavior of slabs is crucial because it deals with concepts such as cracking, excessive

deflection, and vibration. Even if the structure may remain stable, poor performance under service load will affect the comfort of those who use it. Slabs are slender elements with a much smaller dimension in the direction

*Corresponding Author Email: eng.tamaraamer@gmail.com
(T. A. Mohammed)

of the action than spans. Because of this, they are susceptible to deflection. The requirement for reduced deflection governs the design criteria in a large number of cases [1].

Structural construction in the world forwards towards using sustainability structure throughout decrease in weight of building which is leading to decrease in usage of the concrete material. The introduction of high strength-normal weight concrete (HSNWC) may result in the reduction of the slab thickness. This means you'll be more sensitive to deflection [1]. Also, other approaches to reduce the weight of slabs by using lightweight concrete (LWC). One of the most common methods of producing LWC is to use lightweight aggregate (LWA). During the last few decades, a variety of lightweight aggregates, such as (Leca, pumice, perlite, scoria, etc.) [2].

Solid slabs consider as one of the most structural elements in multi-story buildings consuming concrete, so many researchers investigated the possibility of using different types of concrete and slabs to overcome this problem [3-7].

The application of ribbed slabs contributes to the reduction of the floor weight; this is achieved by removing the part of concrete volume underneath the neutral axis of the normal solid slab [8]. The addition of steel fiber to reinforced concrete structures appears to be a good combination for strength. It has good ductile behavior and energy absorption that can help brittle concrete. The steel fiber incorporation in ribbed slabs may aid in the reduction of reinforcement in structures while also improving slab flexural strength [9].

Ahmad et al. [10] studied the performance of reinforced normal strength normal weight concrete ribbed slab with fiber inclusion with different top slab thickness. The results indicated that the addition of steel fibers helped in reducing the sudden brittle failure, thus proving its ability to increase energy absorption capacity and improve cracking behavior.

The behavior of reinforced ribbed slabs of normal strength lightweight concrete (NSLWC) was investigated by authors [11]. The ratio of rib depth to overall beam depth was the variable in this study. The findings revealed that increasing the rib depth to overall beam depth in ratio improved structural behavior by increasing ultimate load carrying capacity and lowering deflection.

The vibration of floor systems in buildings can be caused by a variety of sources, including the sources that occur inside of a building such as (walking, aerobics, elevator, conveyance systems, HVAC equipment, and rotating mechanical equipment on an elevated floor or roof), also, the external sources outside or attached to a building such as nearby roadways, construction activities, and industrial activities.

Vibration is an important factor to consider when designing a building. Vibrations can be simply annoying

or cause significant problems, especially when occupants' daily activities, sensitive equipment performance, or important functions are routinely disrupted [12].

The main aim of this study is to investigate structural and serviceability behavior for (high strength-lightweight, high strength-normal weight, and fiber high strength-lightweight) reinforced concrete one-way ribbed slabs under static load and dynamic load (harmonic load) to choose the best slab which gives an improvement in the structural efficiency and lead to mitigate and control the dynamic effect of vibrating sources like generators.

2. EXPERIMENTAL PROGRAM

The experimental program includes studying the effect of replacing normal weight aggregate (gravel) with lightweight aggregate (pumice stone) with and without steel fiber (volume fraction ($V_f = 0.25\%$)) on the strength and serviceability behavior of HSNWC reinforced one-way ribbed slabs under static and dynamic (harmonic) loading. As shown in Table 1.

The experimental program consisted of casting and testing six reinforced concrete one-way ribbed slabs with dimensions 2000 mm length, 900 mm width, and 150 mm depth. The slabs were designed by the ultimate method to fail by flexure under the applied static load according to ACI 318-19 [13]. The main reinforcement in each rib was 2 \emptyset 8mm. Square mesh sheet reinforcement of ($\emptyset 6 @ 150$) mm was used in the slab flange to achieve the requirements of shrinkage and temperature reinforcement. To ensure that the shear failure occurring is prevented, (2 $\emptyset 6$) mm diameter stirrups were provided in each rib. The reinforcement and geometry details of the one-way slab sections are shown in Figure 1.

2. 1. Materials Table 2 shows the materials that were used to casting the specimens with their properties. In this study, The HSLWC mix proportion was obtained by conducting several trial mixes by ACI 363.2R [14] to select a suitable mix that meets the workability, strength,

TABLE 1. Designation and study variables of the specimens

S/N	Slab symbol	Variables to study the effect of			
1	S1	Loading type	Static loading	Concrete type	HSNWC
2	S2				HSLWC
3	S3				F0.25 HSLWC
4	HS1	Loading type	Dynamic loading	Concrete type	HSNWC
5	HS2				HSLWC
6	HS3				F0.25 HSLWC

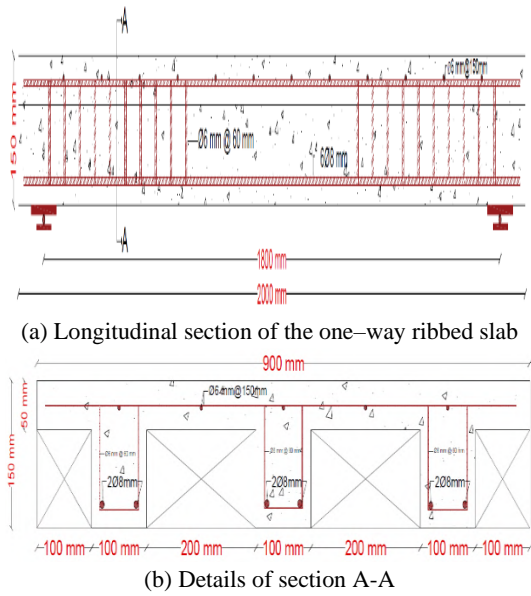


Figure 1. Steel reinforcement details of all tested one-way ribbed slabs

TABLE 2. The materials of the one-way ribbed slabs with their properties

Materials	Properties
Cement	Iraqi manufactured Portland limestone cement (KARASTA) was used in this study. These properties are confirmed with EN 197-1[15].
Fine aggregate	Al-Ukhidher natural fine aggregate was used in this study. The grading of this sand within zone 2 and conformed to the IQS limits No.45/1984 [16].
Coarse aggregate	10 mm maximum size natural normal weight aggregate (gravel) from Al-Nebai quarry, with a dry density of 1573 kg/m ³ which conforms to Iraqi specification No.45, 1984 [16]. 9.5mm maximum size natural lightweight aggregate (Pumice Stone) with dry density 708 kg/m ³ , which conforms to ASTM C330 [17].
Silica fume	Micro Silica Fume, commercially known as MegaAdd MS(D), was used in this study. It is complying with ASTM C 1240-20 [18].
Superplasticizer	Sika ViscoCrete® 5930-L was used in this study. It meets the requirement for a superplasticizer according to ASTM C494/C494 – 19[19].
Water	Ordinary tap water was used for mixing, pouring, and curing all concrete mixes in this study.
Sugar molasses	byproduct liquid material was supplied from a sugar factory in Babylon city of Iraq.
Steel fiber	Macro hooked ends steel fiber with a length of 35 mm, and an aspect ratio of 70 was used in this study.
Steel reinforcement	Deformed steel bars of diameters (6 mm and 8 mm) and square mesh sheet of 6 mm were used in this study and yield stress of (495,509, and 495) MPa, respectively. It meets the requirement of ASTM A 615/615M-20 [20].

and density requirements of most codes of structural lightweight concrete (SLWC).

The other mixes have the same mix proportion detail of HSLWC except to replace pumice stone with gravel at the same volumetric ratio, for (HSNWC) mix and add steel fibers for (F0.25HSLWC) mix, Due to the high specific gravity of steel fibers (0.25%) of the volumetric ratio was used in this study, as shown in Table 3.

2. 2. Testing Setup

In the static testing, a hydraulic testing machine was used to test the ribbed slab specimens at the laboratory of civil Engineering/ Babylon University. The ribbed slabs were tested as a simply supported slab with a 1700mm clear span under two-point loads. Steel plates were placed under the two-point loads and on the supports to prevent stress concentration and local crushing of concrete. The static load was applied monolithically with a loading rate of 0.05kN/sec until the failure.

The vertical deflection was measured using one LVDT (KTR-100mm) type with a maximum capacity of 100mm with an accuracy of 0.01, that was placed at the bottom face of the mid-span of the slab, and the data was collected by using a data logger, which was connected to the computer, as shown in Figure 2.

On the other hand, the dynamic testing was conducted by using an electric motor (ZW-5) with a capacity of 1100 Watt, which can run up to the maximum speed

TABLE 3. Concrete mixes

Material	Concrete mixes quantity (kg/m ³)		
	HSNWC	HSLWC	F0.25HSLWC
Cement	525	525	525
Silica fume	75	75	75
Sand	590	590	590
Gravel	1100	----	----
Pumice stone	----	495	495
Water	142	142	142
Superplasticizer	7.85	7.85	7.85
Sugar molasses	1.05	1.05	1.05
Steel fiber	----	----	19.5

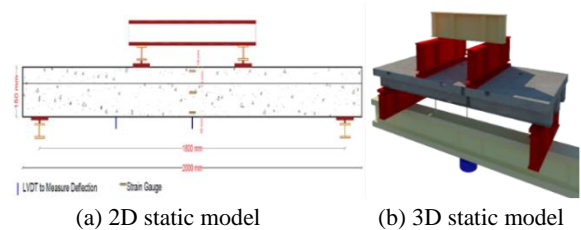


Figure 2. Test details of the one-way ribbed slabs tested under static load

50Hz; the rotary speed of the motor was controlled through using a control speed unit (AC Driver), the weight of the motor and its unbalance mass was about of (22 and 2.1) kg, respectively. The dynamic load applied to the slabs was sinusoidal load (harmonic load) induced by an unbalanced rotating motor mass. The value of this load depends on the characteristics of an unbalance mass and operating frequency of the motor, as shown in Equation (1).

The vibration amplitude was measured by using laser sensor type (LK-081). The data was collected by using data acquisition for sound and vibration type NI PXIe - 1062QP [21]. Over the steel plate, the motor was suitably positioned with the help of bolts, then was mounted at the top surface of the slab, as shown in Figure 3. In this study, the results of applying two frequencies (maximum and a half) motor capacity (i.e., 25Hz and 50Hz) were chosen to be discussed. At each of these frequencies, the amplitude of displacement was found to stabilize approximately after 20 sec.; once it was stabilized, the readings were taken.

3. RESULTS AND DISCUSSION

3. 1. Mechanical Properties Results of Concrete Mixes

From Table 4, It can be seen that using HSLWC mix without steel fiber instead of HSNWC decreased the compressive strength of cube (150) mm and cylinder (150×300) mm specimens by 23.61% and 27.24%, respectively. The tensile strength also decreased by 34.04% and 37.5 % for f_t and f_r , respectively. On the other hand, the density was improved by 19.31%. Moreover, the addition of 0.25 % as volume fraction in the HSLWC mix led to enhancement in its compressive and tensile strength properties only. The enhancement was (3.9, 4.7, 0.7, 0.6) MPa for f_{cu} , f_c^* , f_t , and f_r , respectively, while the density increased by 19 kg/m³.

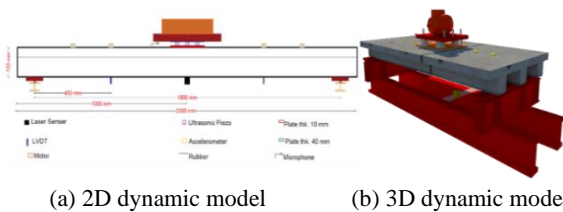


Figure 3. Test details of the one-way ribbed slabs tested under harmonic load

TABLE 4. Mechanical properties of concrete mixes

Conc. Mix	f_{cu} (MPa)	f_c^* (MPa)	f_t (MPa)	f_r (MPa)	w_c (kg/m ³)
HSNWC	68.2	58.0	4.7	5.6	2408
HSLWC	52.1	42.2	3.1	3.5	1943
F0.25HSLWC	56.0	46.9	3.8	4.1	1962

3. 2. Slab Specimens under Static Loading

3. 2. 1. Cracking Behavior The cracking behavior results of ribbed slabs, which are shown in Table 5, revealed that:

- Using HSLWC in slab S2 instead of HSNWC reduced the cracking and ultimate loads by 44.4 % and 17.70 %, respectively.
- Using steel fiber in HSLWC slab S3 instead of HSNWC led to reducing the cracking and ultimate loads by 33.24 % and 3.21%, respectively.
- The addition of steel fiber in slab S3 increased first crack and ultimate strength capacity by 20.06 % and 17.60 %, respectively, concerning a slab without fibers.
- The initial crack had a width not exceeding 0.02mm, while the maximum crack width at service load was 0.11mm, 0.22 mm, and 0.2 mm for S1, S2, and S3, respectively. These values meet the limitation requirement of ACI 318-19 [13], which is 0.4 mm.

Figure 4 shows the cracking patterns for specimens tested under static load.

3. 2. 2. Deflection Behavior From the load-deflection curve for all specimens tested under static load, as shown in Figure 5, it was found the following characteristics:

- **Deflection at Service Stage** The deflection at the service load stage was 6.02 mm, 7.20 mm, and 7.84 for slabs S1, S2, and S3, respectively. These values are compared with limitations of ACI 318-

TABLE 5. Results of cracking behavior under static load

S/N	Slab Symbol	P_{cr} (kN)	% Diff. in P_{cr}	P_s (kN)	W_{cr}^* (mm)	P_u (kN)	% Diff. in P_u
1	S1	22.50	---	60.93	0.11	93.74	---
2	S2	12.51	-44.4	50.15	0.22	77.15	-17.7
3	S3	15.02	-33.24	58.97	0.20	90.73	-3.21

*Crack width at service load ($P_s = 0.65 P_u$) [22]



Figure 4. Cracking patterns for specimens tested under static load

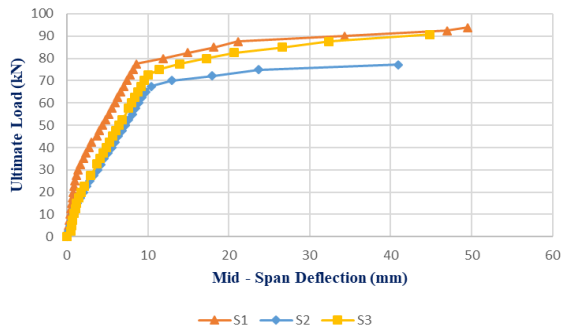


Figure 5. Load–deflection curves for specimens tested under static load

19 for immediate deflection for roofs due to maximum live load (effective span /180 = 10 mm) [13]. It was found that using three types of concrete (HSNWC, HSLWC, F0.25HSLWC) in ribbed slabs meets the ACI serviceability requirement.

• **Ductility Index**

The term ductility is defined as “the ability of the material/ member to sustain deformation beyond the elastic limit while maintaining a reasonable load carrying capacity until total failure” [23]. In the present study, the displacement ductility index (μ_d) is calculated according to the deflection at ultimate load divided by the deflection at the yield load. The yield load is indicated by a change in curve slope between the first crack appearing and the curve achieving its peak value [24].

It can be seen in Figure 6 that using HSLWC in slab S2 instead of HSNWC led to a decrease in the μ_d by 28.52%, while the addition of steel fiber in slab S3 led to reducing the μ_d only 23.77%.

• **Stiffness**

From the load-deflection curves, the value of stiffness of the tested slabs was obtained. The stiffness at the service load level [22] is indicated by the slope of the line at about 65% of the ultimate load. The value of slabs stiffness is shown in Figure 7. From the load-deflection curves in Figure 5, it can be seen that the slope becomes steeper when using HSNWC slab S1 more than using HSLWC slab S2 and F0.25HSLWC slab S3. The stiffness of slabs S2 and S3 reduced by about 31.13 %

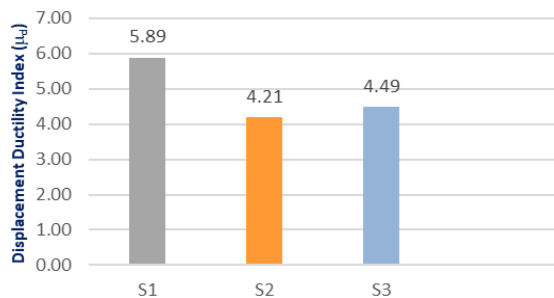


Figure 6. Ductility index for specimens tested under static load

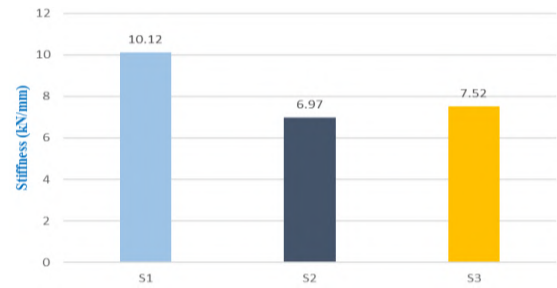


Figure 7. Stiffness for specimens tested under static load

and 25.69%, respectively, compared to slab S1. This indicates that the stiffness depends on the strength, types of aggregate, and strength of concrete. The addition of steel fiber in S3 recovered about 5.44% of stiffness reduction due to replacing gravel with a pumice stone.

• **Toughness Index**

Toughness index values were calculated by using the ASTM C1018 method [25]. The areas under the load-deflection curve up to the deflection of the first crack and at selected multiples deflection (3, 5.5, and 10.5) of the first crack of reinforced concrete ribbed slab specimens were calculated by Microsoft Excel software computer program. The values of toughness index and residual strength factors for all tested slab specimens under static load have been presented in Table 6.

From Table 6 can be seen that toughness index I_5 , I_{10} , and I_{20} improved in slabs S2 and S3 by (5.11 % and 34.53 %), (16.47 % and 55.83%), and (42.48 % and 79.43 %) over slab S1, respectively. The residual strength factors $R_{5,10}$ and $R_{10,20}$ also improved in slabs S2 and S3 by (24.03 % and 70.07%), and (57.45% and 93.03%), respectively.

From the results above, it was found that the addition of steel fiber plays a significant role in enhancement the toughness index and residual strength of the HSLWC slab due to its ability to absorb energy.

3.2.3. Structural Efficiency The ratio of strength to density is used to define structural efficiency (SE) [26]. In this study, the SE is calculated by dividing the ultimate

TABLE 6. Toughness index and residual strength factor

Slab Symbol	S1	S2	S3
Toughness Index			
I_5	6.66	7.00	8.96
I_{10}	16.64	19.38	25.93
I_{20}	45.55	64.90	81.73
Residual Strength factor*			
$R_{5,10}$	199.60	247.56	339.46
$R_{10,20}$	289.10	455.18	558.05

* $R_{5,10} = 20 (I_{10} - I_5)$, $R_{10,20} = 10 (I_{20} - I_{10})$

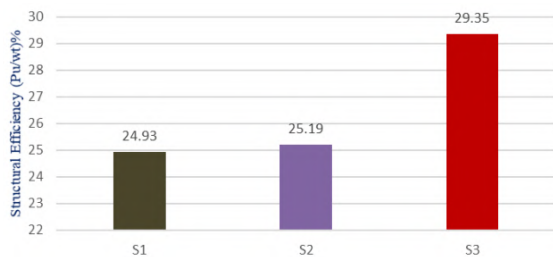


Figure 8. Structural efficiency for specimens tested under static load

strength of the slab by its weight. SE in slabs S2 and S3 increased by 1.04% and 17.73%, respectively, as depicted schematically in Figure 8. This behavior was due to decreasing the weight of slab S2 and increasing the strength of slab S3, respectively.

3. 3. Slab Specimens under Harmonic Loading

3. 3. 1. Cracking Behavior Here, the vibration serviceability of slab specimens was assessed by finding the response of specimens under the effect of harmonic loading induced by an electric motor. The applied harmonic load on slabs (HS1, HS2, and HS3) induced by applied 25 Hz and 50 Hz can be calculated mathematically by using the formula below [27]. Figure 9 shows the details of considered cases of harmonic load.

$$P_d = 2 * m * e * \omega_o^2 * \sin \omega_o * t \tag{1}$$

where: P_d is the induced harmonic dynamic load (N), m is the eccentric rotating mass (kg), e is the eccentric distance (m), and ω_o is the operating frequency (rad/sec).

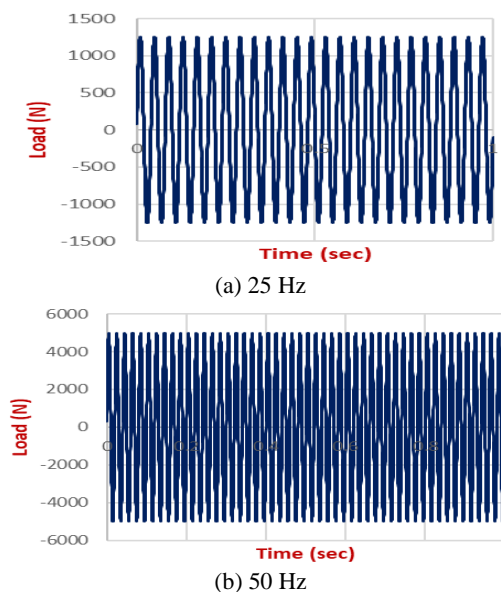


Figure 9. Load-time history for specimens tested under harmonic load

After applied 50 Hz, the hairline cracks have appeared in the slab HS2 while not noticed any hairline cracks in slabs HS1 and HS3. As shown in Figure 10. From this outcome can be concluded the addition of steel fiber in the slab HS3 improves the cracking behavior of slab HS2.

3. 3. 2. Vibration Behavior The peak amplitude of vibration for time one – the second was drawn as displacement- time history for slabs tested under harmonic load for 25 Hz and 50 Hz, respectively. As shown in Figure 11.

The displacement amplitude outcomes in Figure 12 implied that the vibration of slabs has induced by the harmonic load is affected by characteristics of a slab (stiffness, natural frequency, and damping) and applied of an operating frequency. It was found that in both



Figure 10. Cracking patterns for specimens tested under harmonic load

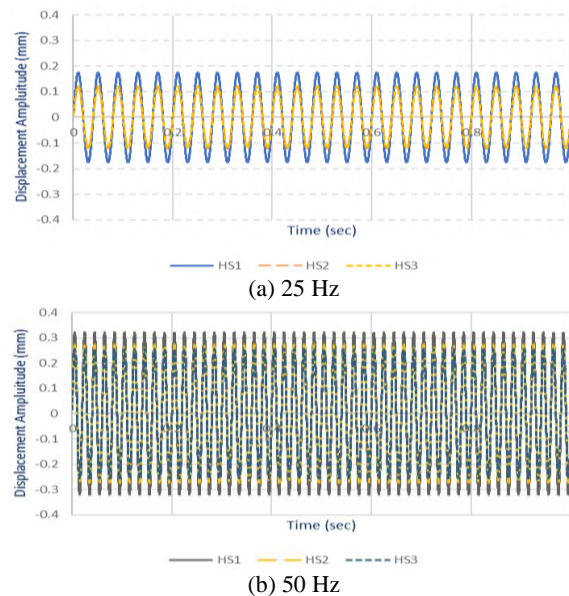


Figure 11. Displacement – time history for all specimens tested under harmonic load

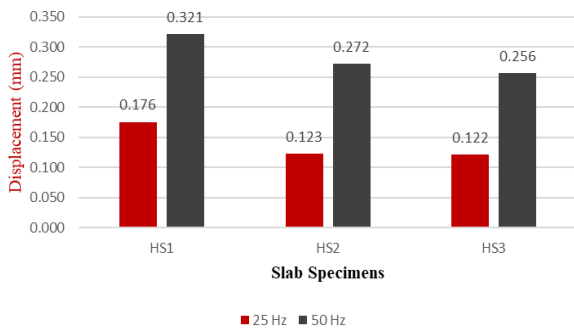


Figure 12. Displacement amplitude for specimens tested under harmonic load

operation frequencies (25 and 50) Hz, the HSNWC in slab HS1 gave the highest displacement value followed by HSLWC in slab HS2 and F0.25HSLWC in slab HS3. This behavior may belong to the nature of HSNWC which was a denser composition and a larger bonding strength between the aggregate and mortar, which results in a reduction of energy dissipation and damping ratio of the slab.

The displacement in slabs HS2 and HS3 decreased by (30.11 and 30.68) % for 25 Hz and (15.26 and 20.25) % for 50 Hz in comparison to slab HS1, respectively.

4. CONCLUSION

The behavior of one-way ribbed slabs that were produced from three types of concrete (HSNWC, HSLWC, and F0.25HSLWC) under the effect of static and dynamic loads was tested. Based on the experimental test results, the following main conclusions can be drawn.

- Using HSLWC mix without steel fiber instead of HSNWC mix led to a decrease in the density of concrete by 19.31%, while the inclusion of steel fiber in HSLWC mix with $V_f = 0.25\%$ led to the increasing density of concrete from (1943 to 1962) kg/m^3 , but remain with limitation of lightweight concrete.
- The mechanical properties of the HSLWC mix (f_{cu} , f'_c , f_t , and f_r) improved by using steel fiber (0.25%) by (7.49, 11.37, 22.58, and 17.14) %, respectively.
- Using HSLWC in slab S2 instead of HSNWC led to a decrease in the first crack and ultimate load capacity by 44.4% and 17.70%, respectively.
- The addition of steel fiber in the HSLWC slab led to a recovery of 11.16 % and 14.49 % of lack in a first crack and ultimate load capacity, respectively.
- Using three different types of concrete (HSNWC, HSLWC, F0.25HSLWC) in construction one-way ribbed slab gave crack width and deflection that meet with ACI-code serviceability requirement.
- the addition of steel fiber in the ribbed slab led to overcoming almost 4.75% of ductility reduction.

- The toughness indices I5 and I10 for all ribbed slab specimens are higher than the standard values 5, 10, and 20, respectively. The values of the toughness index indicated that all the behavioral pattern of the slabs approaches perfectly – plastic condition.
- The highest improvement in structural efficiency was in the F0.25HSLWC ribbed slab.
- Using HSLWC in ribbed slab instead of HSNWC under dynamic load effect led to a significant reduction in the amplitude displacement by 30.11% and 15.26% at 25 Hz and 50 Hz, respectively.
- The addition of steel fibers in the ribbed slab led to reducing the negative effect of vibration by 0.81% and 5.88% at 25 Hz and 50 Hz, respectively.

5. REFERENCES

1. Bliuc, R. Particularities of the structural behaviour of reinforced high strength concrete slabs. University of New South Wales, Australian Defence Force Academy, School of Aerospace, Civil and Mechanical Engineering, (2004). Retrieved from <https://unsworks.unsw.edu.au/fapi/datastream/unsworks:3247/SOURCE01?view=true>.
2. Ghanbari, M., Kohnehpooshi, O., and Tohidi, M. "Experimental Study of the Combined Use of Fiber and Nano Silica Particles on the Properties of Lightweight Self Compacting Concrete." *International Journal of Engineering*, Vol. 33, No. 8, (2020), 1499–1511. <https://doi.org/10.5829/ije.2020.33.08b.08>
3. Eom, T.-S., Hwang, I.-H., Lee, S.-J., and Park, T.-W. "Failure Mode and Shear Strength of Nonprestressed Hollow-Core Slabs in One-Way Shear." *ACI Structural Journal*, Vol. 115, No. 4, (2018), 1131–1141. <https://doi.org/10.14359/51702064>
4. Al-Gasham, T. S., Hilo, A. N., and Alawsy, M. A. "Structural behavior of reinforced concrete one-way slabs voided by polystyrene balls." *Case Studies in Construction Materials*, Vol. 11, No. October, (2019), e00292. <https://doi.org/10.1016/j.cscm.2019.e00292>
5. Sirimontree, S., Thongchom, C., Keawsawavong, S., Nuaklong, P., Jongvivatsakul, P., Dokdua, W., Bui, L. V. H., and Farsangi, E. N. "Experimental Study on the Behavior of Steel-Concrete Composite Decks with Different Shear Span-to-Depth Ratios." *Buildings*, Vol. 11, No. 12, (2021), 624. <https://doi.org/10.3390/buildings11120624>
6. Mahdi, A. A., and Ismael, M. A. "Structural Behavior of Hollow-core One Way Slabs of High Strength Self-compacting Concrete." *International Journal of Engineering*, Vol. 34, No. 1, (2021), 39–45. <https://doi.org/10.5829/ije.2021.34.01a.05>
7. M. Kadhum, M., M. Harbi, S., S. Khamees, S., Abdulraheem, M. S., and Farsangi, E. N. "Punching Shear Behavior of Flat Slabs Utilizing Reactive Powder Concrete with and without Flexural Reinforcement." *Practice Periodical on Structural Design and Construction*, Vol. 26, No. 1, (2021), 04020060. [https://doi.org/10.1061/\(ASCE\)SC.1943-5576.0000551](https://doi.org/10.1061/(ASCE)SC.1943-5576.0000551)
8. Fodzi, N. H. M., and Hisbany, M. H. M. "Structural Effect of Using Steel Fiber Reinforcement on the Punching Shear of Self-Compacting Fiber Reinforced Concrete (SCFRC) Ribbed Slabs." *Materials Science Forum*, Vol. 972, (2019), 99–104. <https://doi.org/10.4028/www.scientific.net/MSF.972.99>
9. Rahman, F. A., Bakar, A. A., Hashim, M. H. M., and Ahmad, H. "Flexural performance of steel fiber reinforced concrete (SFRC) ribbed slab with various topping thicknesses." In Proceedings of

- the 3rd International Conference on Construction and Building Engineering (ICONBUILD) (Vol. 020013, p. 020013). <https://doi.org/10.1063/1.5011493>
10. Ahmad, H., Hashim, M. H. M., Bakar, A. A., Hamzah, S. H., and Rahman, F. A. "Flexural strength and behaviour of SFRSCC ribbed slab under four point bending." In AIP Conference Proceedings (Vol. 1903, p. 020014). <https://doi.org/10.1063/1.5011494>
 11. S. Abdulhussein, S., and A. Alfeehan, A. "Experimental study of depth variation in flanged ribbed lightweight concrete slabs." *Journal of Engineering and Sustainable Development*, Vol. 24, No. Special, (2020), 359–364. <https://doi.org/10.31272/jeasd.conf.1.38>
 12. Fanella, D. A., Mahamid, M., and Mota, M. "Flat Plate-Voided Concrete Slab Systems: Design, Serviceability, Fire Resistance, and Construction." *Practice Periodical on Structural Design and Construction*, Vol. 22, No. 3, (2017), 04017004. [https://doi.org/10.1061/\(ASCE\)SC.1943-5576.0000322](https://doi.org/10.1061/(ASCE)SC.1943-5576.0000322)
 13. ACI Commentary 318. "Building Code Requirements for Structural Concrete (ACI 318-19)." American Concrete Institute, 2019.
 14. ACI Committee 363. "ACI 363.2R-11: Guide to Quality Control and Assurance of High-Strength Concrete." American Concrete Institute, 2011.
 15. EN 197-1. "Cement - Part 1: Composition, specifications and conformity criteria for common cements." British Standard Institution BSI, 2011.
 16. Iraqi Specification No.45. Aggregate from natural sources for concrete and building construction Central Agency for Standardization and Quality Control, Planning Council, Baghdad, Iraq, 1984.
 17. ASTM C330/C330M-17a. "Standard Specification for Lightweight Aggregates for Structural Concrete." American Society for Testing and Materials, 2017.
 18. ASTM C1240-20. "C1240 Standard Specification for Silica Fume Used in Cementitious Mixtures." *Annual Book of ASTM Standards*. (2020), 1–7. <https://doi.org/10.1520/C1240-15.2>
 19. ASTM C494/C494M-19, Specification for Chemical Admixtures for Concrete, American Society for Testing and Materials, 2019.
 20. A 615/A 615M – 20. "Standard Specification for Deformed and Plain Carbon-Steel Bars for Concrete Reinforcement." American Society for Testing and Material, 2020, 1–8.
 21. Data Acquisition and Control/ Sound and Vibration. Retrieved from <https://www.ni.com/en-lb/shop/hardware/products/pxi-sound-and-vibration-module.html>
 22. Jeffrey, S. R. Prestrextives in Civil Engineering. ASCE Publications, 2003.
 23. Kwan, A. K. H., Ho, J. C. M., and Pam, H. J. "Flexural strength and ductility of reinforced concrete beams." *Proceedings of the Institution of Civil Engineers - Structures and Buildings*, Vol. 152, No. 4, (2002), 361–369. <https://doi.org/10.1680/stbu.2002.152.4.361>
 24. Akmaluddin, Pathurahman, Suparjo, and Galalza, Z. "Flexural Behavior of Steel Reinforced Lightweight Concrete Slab with Bamboo Permanent Formworks." *Procedia Engineering*, Vol. 125, (2015), 865–872. <https://doi.org/10.1016/j.proeng.2015.11.054>
 25. ASTM C1018 -97. "Standard Test Method for Flexural Toughness and First-Crack Strength of Fiber-Reinforced Concrete (Using Beam With Third-Point Loading)." *Annual Book of ASTM Standards*, Vol. 04, No. October, (1998), 1–8.
 26. ACI 213R-14. "Guide for structural lightweight concrete." American Concrete Institute, 2014.
 27. Das, B. M., and Ramana, G. V. Principles of Soil Dynamics (Second Edi.). USA: Stamford, CT 06902, 2011.

Persian Abstract

چکیده

امروزه کاهش وزن سازه‌ها و مشکلات ارتعاشی هدف اولیه برای الزامات طراحی در اکثر سازه‌های عمرانی است. آزمایش‌های بارگذاری دو نقطه‌ای و بارگذاری هارمونیک برای بررسی استحکام و قابلیت سرویس دهی دال های آجدار یک طرفه بتن مسلح با مقاومت بالا انجام شد. شش نمونه اسلب ریخته‌گری و آزمایش شدند. رفتار ترک خوردگی، انحراف و ارتعاش مورد بررسی قرار گرفت. نتایج تجربی نشان داد که استفاده از بتن سبک با مقاومت بالا (HSLWC) به جای بتن با وزن معمولی با مقاومت بالا (HSNWC) در دال آجدار یک طرفه ساخته شده منجر به کاهش دانسیته تا ۱۹/۳۱ درصد، مقاومت به میزان ۱۷/۷۰ درصد و ۱۷/۳۳ درصد انحراف نهایی شد. اگرچه افزودن الیاف فولادی به HSLWC منجر به افزایش چگالی بتن شد، اما افزودن آن رابطه بار-انحراف و بار نهایی را برای نمونه دال افزایش می‌دهد که کاهش مقاومت را تا ۱۴/۴۹ درصد کاهش داد. علاوه بر این، شاخص شکل پذیری، سفتی و چقرمگی برای نمونه‌های دال آجدار با الیاف فولادی رفتار بهتری نسبت به نمونه‌های بدون الیاف فولادی نشان دادند. HSNWC تأثیر منفی بر ارتعاش دال آجدار یک طرفه در هر دو فرکانس عملیاتی (۲۵ و ۵۰) هرگز گذاشت، در حالی که استفاده از HSLWC با و بدون الیاف فولادی، منجر به کاهش اثر ارتعاش به میزان (۳۰/۱۱ و ۳۰/۶۸) درصد و (۱۵/۲۶ و ۲۰/۲۵) درصد به ترتیب در ۲۵ هرتز و ۵۰ هرتز شد.



Modal Optimization Design of Supporting Structure Based on the Improved Particle Swarm Algorithm

D. Shijing^{*a}, C. Hongru^b, W. Xudong^c, W. Deshi^a, Z. Yongyong^a

^a Naval University of Engineering, Wuhan, China

^b 92199 Unit of the Chinese People's Liberation Army Navy, Qingdao, Chin

^c 92064 Unit of the Chinese People's Liberation Army Navy, Dongguan, China

PAPER INFO

Paper history:

Received 16 December 2021

Received in revised form 11 January 2022

Accepted 14 January 2022

Keywords:

Supporting Structure

Modal Analysis

Finite Element

Improved Particle Swarm Algorithm

Gun Mount

Modal Modification

ABSTRACT

To cope with the strong vibration of a supporting structure excited by external loads under operating conditions, and in order to achieve the purpose of vibration reduction by structural optimization through modal modification, a modal modification method was proposed, through structural vibration theory. Subsequently, the search performance of an improved particle swarm optimization method was analyzed before conducting a case study on the structural optimization. Finally, aiming at the problem of strong vibration of gun mount at the time of firing, a finite element model of the gun mount was constructed and the type and natural frequency of the gun vibration in a free state was analyzed. Meanwhile, taking the thickness, height and width of the stiffening structure of the bracket as the design variables, combined with the improved particle swarm algorithm, an optimized mathematical model was developed with the first-order natural frequency of the gun mount as the objective function. The secondary development of Abaqus finite element software by using Python is used as a tool to calculate the optimization model. By virtue of optimization, thickness, width and height of the stiffening structure are 156.4mm, 453.7mm and 238.9mm at the range of [100,600]mm, [100,700]mm, [100,700]mm, respectively, and the base frequency of the gun mount has been increased by 11.3%. The effect is remarkable.

doi: 10.5829/ije.2022.35.04a.14

1. INTRODUCTION

Vibration is a phenomenon that occurs when a structure or system repeats a reciprocating motion at a balanced position under the input excitation of dynamic loads. The vibration of a structure or system is known as a dynamic response output [1-3]. In the vibration of a system, the dynamic loads will cause resonance when the excitation frequency falls near the natural frequency of the system. Resonance is harmful to most mechanical systems because it may generate a strong vibration and noise while causing severe structural damage. Under actual operating conditions, a structure which supports a whole system is the position that has the strongest vibration in the entire system and is most vulnerable to resonance. Usually, the excitation of external loads is normally certain. Therefore, in the mechanical industry, many researchers have presently focused on how to make a

modal modification to such a supporting structure, which can keep its natural frequency away from the excitation frequency of loads with the goal of preventing resonance.

Liu et al. [4] conducted a research on the horizontal vibration problem of a building that noticeably exceeded the limit. The natural frequency of the building structure was solved by considering its mechanical characteristics, and then the natural frequency was employed to identify the source of excitation. By adding an inverter on the source of excitation, the frequency of excitation is kept away from the natural frequency of the building, so as to achieve the purpose of vibration reduction. This method is applicable to a system with known but mutable source of vibration. However, most mechanical vibration systems has vibration source with complex structure and composition, which make it very difficult to change the frequency of external loads on them.

*Corresponding Author Email: diaoshijing@163.com (D. Shijing)

Ma et al. [5] attached some ultralight locally resonant plate-type units onto the vibration structure as dampers. The structural vibration in the pre-defined band gap range is localized and consumed by the dampers, which realized the purpose of a vibration damping. In this method, much additional structure is added, and the application other structures has limitations practically. Shi and Li [6] adopted the anti-resonance method to reduce the vibration of a girder structure excited by the engine of a warship. By taking the first-order excitation frequency of the engine as the anti-resonance frequency, the mass and stiffness of the hull girder structure were modified, respectively; which changed the natural frequency of the hull, which achieved remarkable vibration optimization. This method is applicable when excitation frequency, excitation points, and response points are known. It is mainly used in the initial structural design of a system. However, the application in the structural improvement of a complex system should be further explored.

Modal modification means to modify the dynamic properties of the structure for a vibration system based on the modal data after the modal analysis of the vibration system provides its modal parameters. To some extent, modal modification may achieve this type of natural frequency as desired by a designer, so as to avoid the excitation frequency of the external load and reduce vibration and noise. Therefore, it is presently a commonly used method for structural optimization in the engineering field [7-15].

In the low-frequency structural vibration optimization of steering wheel of a passenger vehicle, Ye et al. [16] measured the vibration response of the steering wheel using the experimental apparatus and analysis procedures in performing the TPA. According to the results of the modal analysis, the mounting structure of the exhaust system was modified by the finite element method to reduce the vibration of the steering wheel. Li et al. [17] adopted modal prediction and sensitive parameter identification in the dynamic performance optimization of machine tools, and employed Simcenter Test.lab software to implement modal modification, which enhanced the natural frequency of machine tools and reduced the amplitude of vibration.

In order to solve the problem that the mechanical properties of CFRP structures are difficult to grasp comprehensively and accurately, Zhang et al. [18] proposed a finite element model correction method of CFRP laminated structures based on correlation analysis and established an approximate model. The approximate model was updated based on the multi-island genetic algorithm (MIGA) to modify the finite element model of the CFRP laminated structure model. Although Zhang paid attention to building a dynamic model for a system, but the proposed method for modifying modal parameters is also applicable to the modal modification of any known structure.

The present study focused on the vibration of a supporting structure impacted by heavy loads under practical operating conditions, and presented a case study on the modal modification for a naval gun mount. First, in section 2, according to the structural vibration theory, a method to modify the mode shape and natural frequency of the structure by modifying the parameters of the boundary conditions of the supporting structure was proposed. In the third section, for the parameter optimization method, the improved particle swarm algorithm is determined and its performance is analyzed. In the fourth section, the optimization of a certain type of naval gun mount was taken as an example. First, a finite element model was built using the actual structure of the gun mount. Secondly, a structural optimization method was put forward, and design parameters were selected. Lastly, an improved particle swarm optimization algorithm was adopted to conduct the modal modification of the gun mount, which takes the maximum natural frequency of the specified order as the optimization goal. In conclusion, the research results and managerial insight are summarized, and the next research direction is proposed.

The comparison between related research and the research in this paper is shown in Table 1.

Aiming at the problem that the support structure will produce strong vibration under external excitation, a modal modification method is proposed to improve the natural frequency of the structure in order to avoid the excitation frequency. Taking the naval gun mount as an optimization case, taking the maximum fundamental frequency as the optimization objective, and combining

TABLE 1. Comparison between related research and this paper

Research content	This paper	Related research
Method of vibration reduction	Change the structure of the forced system	Change the excitation frequency of the source
Method of structural modification	Increase the stiffening structure under the condition that the main structure remains unchanged	Change the main structure
Engineering application stage	After the main structure is determined or the main structure cannot be greatly changed	Structural initial design
Scope of application	A type of structure	A specific structure

with the PSO algorithm, the shape parameters of the optimal reinforcement structure are obtained. The optimization method in this paper is aimed at a class of structures, rather than a single structure. In addition, the optimization method proposed in this paper can be used not only in the initial design of the structure, but also in the improvement of the existing structure under working conditions, so as to achieve the purpose of completing the structure optimization without disassembling the structure, which is more suitable for actual engineering needs.

2. STRUCTURAL VIBRATION THEORY

When the structure is subject to an external excitation, the frequency domain form of its response can be obtained by performing Fourier transform on the differential equation of motion, as shown in Equation (1):

$$[K] - \omega^2[M] + j\omega[C] = \{f\} \quad (1)$$

Damping is normally low for engineering structure, and may be regarded as proportional damping to solve the natural frequency ω_i of the structural system as well as the corresponding mode of vibration ϕ_i . Equation (1) can be used to obtain the displacement response of the system as follows:

$$[X(\omega)] = \sum_{i=1}^n \frac{\{\phi_i\}\{\phi_i\}^T \{f\}}{k_i - m_i\omega^2 + jc_i\omega} \quad (2)$$

In Equation (2), $k_i = \{\phi_i\}^T [K] \{\phi_i\}$, $m_i = \{\phi_i\}^T [M] \{\phi_i\}$, $c_i = \{\phi_i\}^T [C] \{\phi_i\}$.

Displacement response is one of the quantity characterizing the vibration of structure [19]. In most cases, the motion response of structure can be characterized by displacement response. From Equation (2), it is learned that, under the same external load, the mode of vibration and natural frequency should be identical so that the designed boundary condition domain and the original domain has the same displacement response when their finite element models are similar.

In the modal modification, it is very difficult to ensure the consistence of the required frequencies at several orders and the similar mode of vibration at these orders. It is also unnecessary in engineering. In the practical engineering, the response of structure is highly affected by the mode at low orders, but slightly affected by the mode at high orders. While modifying the dynamic boundary conditions of structure, the natural frequency at the front orders is taken as the design index and the low-order modes is similar in the process of optimization. With this strategy, the dynamic response of the modified

structure is nearly consistent with that of the original structure [20].

Following the strategy of modifying lower-order modes by modifying boundary conditions, the modification method is established as follow. The characteristic equation of structural system is state as follows:

$$[K][\phi] = [M][\phi][\Lambda] \quad (3)$$

In Equation (3), $[\phi]$ is the mode of vibration matrix after orthonormalization; $[\Lambda]$ is the natural frequency matrix.

Considering only the dynamic characteristics at low orders, the following relationship is obtained by the dynamic substructure method as follows:

$$([K_A^0] + [K_B^0])[\phi^0] = ([M_A^0] + [M_B^0])[\phi^0][\Lambda^0] \quad (4)$$

$$\begin{cases} [\phi_r^0]^T ([K_A^0] + [K_B^0])[\phi_r^0] = [\Lambda_r^0] \\ [\phi_r^0]^T ([M_A^0] + [M_B^0])[\phi_r^0] = [I_r] \end{cases} \quad (5)$$

In Equations (4) and (5), $[M_B^0]$ and $[K_B^0]$ are the mass and stiffness matrices of boundary conditions; $[M_A^0]$ and $[K_A^0]$ are the mass and stiffness matrices in structure excluding boundary conditions; $[\phi^0]$ and $[\Lambda^0]$ are the natural frequency matrix and mode of vibration matrix of the designed structure.

The mass matrix and stiffness matrix of boundary conditions consist of the structural boundary condition parameters. In other words, the mass matrix and stiffness matrix of boundary conditions are the function of boundary structural parameters, and represented by $[M_B^0](b)$ and $[K_B^0](b)$ respectively. In the process of modal modification, $[M_B^0](b)$ and $[K_B^0](b)$ can be changed by modifying the parameters of the boundary conditions, so that the mode shape and natural frequency of the system after the modification of the boundary conditions can meet the requirements of the measured data.

3. BASIC PRINCIPLES OF IMPROVED PARTICLE SWARM ALGORITHM

Particle swarm algorithm is an intelligence algorithm to simulate the bird flock foraging. Each particle is characterized as a possible solution vector [21-24]. The quality of particles is judged by the value of fitness function. Moreover, the position and velocity of particles are constantly updated by learning from the global and individual optimal solutions to eventually fulfill the

purpose of global optimization [25] **Error! Reference source not found.** The position and velocity of particles are denoted by $X_i = (x_{i1}, x_{i2}, x_{i3}, \dots, x_{in})$ and $V_i = (v_{i1}, v_{i2}, v_{i3}, \dots, v_{in})$, respectively; and updated by Equations (6) and (7):

$$V_{id}^{t+1} = V_i^t + c_1 r_1 (p_i^t - X_i^t) + c_2 r_2 (p_g^t - X_i^t) \quad (6)$$

$$X_i^{t+1} = X_i^t + V_i^{t+1} \quad (7)$$

In Equations (6) and (7), p_i^t and p_g^t stand for the individual optimal solution and global optimal solution of particles when the iterations equal t ; r_1 and r_2 are the random numbers in the range (0,1); c_1 and c_2 are learning factors.

In the particle swarm algorithm, parameters exert a very high effect on the search capability of the algorithm. The role of parameters and the criteria for selecting them are briefly described in the following sections.

(1) Swarm size p_s

Undoubtedly, the larger swarm, the more particles under mutual effect, and more easily the advantage of the particle swarm algorithm in is demonstrated. If the swarm size is too small, the calculation result will easily fail into local convergence, failing to achieve the goal of global optimum. If the swarm is too large, the efficiency of calculation will decrease dramatically, which increases the time cost. In the meanwhile, an increase in swarm size will make little contribution to the improvement of search capability after a certain level. For this reason, it is very important to choose a proper swarm size according to the complexity of the problem

(2) Learning factors c_1 、 c_2

In the particle swarm algorithm, learning factors c_1 and c_2 are two factors that regulate the degree of individual and group experience learning. In the iterative process, the learning factor is used to control the particle to seek a balance between the local search and the global search. That is, when the particle approaches the optimal solution, the learning factor plays the role of inertial weight. The smaller the value is, the better the global search performance of the algorithm is. Normally, the value of c_1 and c_2 is between 0 and 4.

(3) Maximum velocity V_{max}

The maximum distance of particles in iterations depends on the maximum velocity V_{max} . Its increase can improve the capability of global search, but makes it easy to overlook a better solution. When it goes down, the capability of local search is enhanced, but easily leading to local convergence. In this paper, the maximum speed is set as the value range of the initial variable, which remains unchanged during the search process.

In the original particle swarm algorithm, if the velocity of particles V_i^t is low, particles are very easy to converge on the same position, and trapped in the local search. Therefore, the solution depends too much on the setting of initial swarm. Increasing the particle velocity V_i^t can effectively improve the global search performance, but when solving optimization problems, both global search and local search need to be considered. How to seek a balance between them is therefore crucial to improving the performance of particle swarm algorithm. Reference [25] introduced inertia weight w into Equation (6) in particle swarm algorithm. Equation (6) that introduces the inner weight is shown in Equation (8):

$$V_{id}^{t+1} = wV_i^t + c_1 r_1 (p_i^t - X_i^t) + c_2 r_2 (p_{gd}^t - X_i^t) \quad (8)$$

Inertia weight w plays a role in coordinating global search and local search. When the inertia weight is (0.9, 1.2), the performance of algorithm is better. The decreasing strategy of inertia weight points out that as the iteration progresses, the value of inertia weight needs to be decreased linearly. This strategy can not only update the search area in a wide range, so that ensure the global search performance of the algorithm in the early stage of iteration, but also has strong local search ability in the later stage of iteration, which can speed up the convergence speed and ensure that the algorithm searches finely near the possible optimal solution. Equation (2) is combined with Equation (3) to generate the most widely recognized standard particle swarm algorithm. The particle swarm algorithm mentioned in the subsequent sections of this paper refers to this standard particle swarm algorithm. The linear decreasing strategy of inertia weight is shown in Equation (9). Shi [26], Shi and Eberhart [27] pointed out that the optimization tends to be better when the weight varies linearly between 0.4 and 1.4.

$$w = w_{max} - \frac{t}{T}(w_{max} - w_{min}) \quad (9)$$

The basic procedure of particle swarm algorithm is as follows:

1. Initialize: Initialize the particle swarm including random velocity and position;
2. Evaluate particles: Calculate the fitness of each particle in the problem space;
3. Update the optimal position: Compare the current position and optimal experienced position p_i for all particles:

If the former is better, the optimal experienced position is replaced by the current position of the particle. In the comparison of the optimal experienced position p_i and the global optimal position p_g , if the former is

better, the global optimal position is replaced by the optimal experienced position;

4. Update particles: Update the particles based on their velocity and position using Equations (6) and (7);

5. If stop conditions are met, the search is stopped. If not, move back to step 2 for iteration.

4. EXAMPLE: MODAL OPTIMIZATION DESIGN OF GUN MOUNT BASED ON MODIFICATION OF STRUCTURAL PARAMETERS

Gun vibration is a movement phenomenon accompanying the process of firing. As an inherent property of gun, it is a major factor affecting the firing accuracy and reliability of the gun [28]. The mount bears the recoil impact and the transmission torque of the following rotation during the firing process of the naval gun. Moreover, the inertia moment caused by the naval gun when the warship rocks, absorbed by the mount. The mount enables the gun to keep a certain direction at the time of firing. Therefore, the performance of the mount directly determines the operational stability and firing accuracy of the gun.

In the structural optimization design of the naval gun mount, static optimization design is often employed to improve the existing structure [29]. In the modal analysis and structural optimization of the gun mount, the dynamic design of structure is studied with the swarm intelligence algorithm, i.e. determining the modification of physical parameters under the constraints of modal parameters. For this reason, efforts should be further made to explore the measures against the low-frequency vibration of the mount under the impact, and find the general method for the dynamic design of the naval gun structure [30, 31].

4. 1. Finite Element Model for Mount Structure

A model for the structure of a naval gun mount is presented in Figure 1.

The gun mount is made of around 100 parts by virtue of welding, including many solid structures such as shell, stiffening beam, and so on. In the finite element model, it must be properly simplified to lower the complexity of modeling, reduce the number and improve mass of grid elements, etc. The simplification ignores the holes, protrusions, chamfers, cambers, and other matters that have little influence on the response of structure. The mount structure is mostly made of plates and stiffeners. So the plates are meshed using shell elements, and shell or solid elements are chosen for stiffeners based on the ratio of length and thickness.

The finite element model is consistent with the actual model in the experiment. During the modal test, the state of structure may not be completely consistent with the given three-dimensional model. Thus, the finite element

model should be adjusted to the actual state of structure at the test site. During the modal test in this paper, some structures are installed inside the bracket including sensor mount and stop. Additionally, the base of the gun mount rests on the mounting seat, which is made of steel structure and cement, and the seat ring is suspended as shown in Figure 2.

In the modal test, the bracket and other components have not been installed on the gun mount, and the mount is placed on the steel plate and cement seat on the ground. There is a good test environment. In this case, the gun mount can be regarded as a constrained structure with specific boundary conditions.

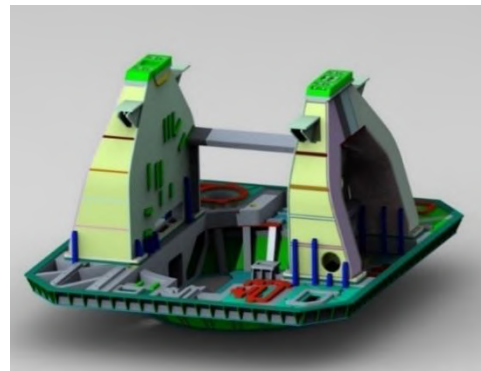


Figure 1. Model for a naval gun mount



(a) Mass in bracket



(b) Bottom connection

Figure 2. Test state of a naval gun mount

Structure domain in this paper is described by the equilibrium equation of continuum motion, which takes into account small deformation but ignores the volume force and damping of the structure. The equilibrium equation of the structure is given below:

$$\nabla \cdot \boldsymbol{\sigma} + \nabla \cdot \boldsymbol{\tau} - \rho_s \ddot{\mathbf{u}}_s = \mathbf{0} \tag{10}$$

In Equation (10), $\boldsymbol{\sigma}$ is the stress of the structure; \mathbf{u}_s is the displacement of the structure; ρ_s is the density of the structure. The boundary conditions are fixed supporting and force boundary conditions. The mathematical model for such two boundaries is stated as follows:

1) Fixed supporting wall

$$\mathbf{u} = \mathbf{0} \tag{11}$$

2) Force boundary conditions

$$\nabla \cdot \boldsymbol{\sigma}_s + \nabla \cdot \boldsymbol{\tau}_s = \mathbf{f}_s \tag{12}$$

In Equation (12), \mathbf{n}_s is the vertical vector of the coupling plane in the structure domain. Equations (10)-(12) are the classical fundamental equations for the vibration of structure. Following the principles of virtual work, it is very easy to solve the vibration of structure in the form of finite element,

$$\mathbf{M}_s \ddot{\mathbf{u}}_s + \mathbf{K}_s \mathbf{u}_s = \mathbf{f}_s \tag{13}$$

In Equation (13), the mass matrix \mathbf{M}_s , stiffness matrix \mathbf{K}_s , and coupling force matrix \mathbf{f}_s are

$$\begin{cases} \mathbf{M}_s = \rho_s \int_{S_s} \mathbf{N}_s^T \mathbf{N}_s ds \\ \mathbf{K}_s = \int_{S_s} (\nabla \cdot \mathbf{N}_s)^T \mathbf{D}_s \nabla \cdot \mathbf{N}_s ds \end{cases} \tag{14}$$

Equation (14), is the shape function of structure element; \mathbf{D}_s is the elastic coefficient matrix. When the structure has the free vibration without damping, the solution of the equation is obtained in the following form

$$\mathbf{u}_t = \hat{\mathbf{u}} e^{i\omega t} \tag{15}$$

Equation (15) is the form of harmonic vibration, which is a constant, and substituted into Equation (13). The term of external load is overlooked to obtain

$$(\mathbf{K}_s - \omega^2 \mathbf{M}_s) \hat{\mathbf{u}}_s = \mathbf{0} \tag{16}$$

This is the characteristic equation of structure.

Based on Equations (15) and (16), boundary conditions have a great impact on the dynamics of the system. Comparing Equations (10) and (13), it can be seen that the change of boundary conditions can directly change the mode shape of the structure. So, compared with the internal parameters of the structure, the structural dynamics of the system is more sensitive to the

changes of boundary condition parameters. Therefore, the dynamic characteristics of the structure can be modified to a certain extent by modifying the boundary conditions [32]. The number of boundary condition parameters is generally less than that of the internal parameters of the system structure. And in actual projects, due to working conditions and performance limitations, the internal structure cannot be changed significantly. Therefore, dynamic modification of boundary conditions to meet the overall dynamic characteristics of the system structure is an effective method. In addition, the main structural parameters of the gun mount should not be modified too much during the modal modification, so as to avoid the subsequent optimization design of the gun mount structure being difficult to apply to the actual structure.

In the modal test, the mount is placed on the steel plate and cement seat on the ground, but not connected, so that it is deemed to be in the free state. A finite element model is built in the commercial finite element software ABAQUS [33]. The trunnion seat and bracket are simplified into a whole. The trunnion seat is solid in the model. The finite element model is presented in Figure 3. The mount is made of gun steel and aluminum alloy by welding. The material parameters are shown in Table 2.

Based on the design of a naval gun, the stiffeners at both sides of the bracket have a great influence on the mode of the gun mount. Therefore, this paper focuses on how the gun mount is affected by the arrangement and geometry of stiffeners.

4. 2. Modal Modification of Gun Mount

The natural frequency and mode of vibration in a free state before optimization are shown in Figure 4. The indices are compared on this basis after optimization.

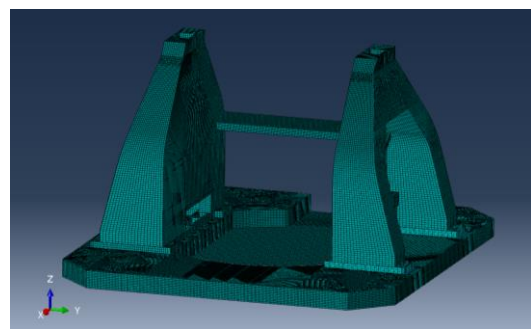


Figure 3. A finite element model for a naval gun mount

TABLE 2. Material parameters of gun mount

Material parameters	Density (kg/m ³)	Elastic modulus (Gpa)	Poisson's ratio
Gun steel	7.8×10 ³	210	0.3
Aluminum alloy	3.8×10 ³	68	0.35

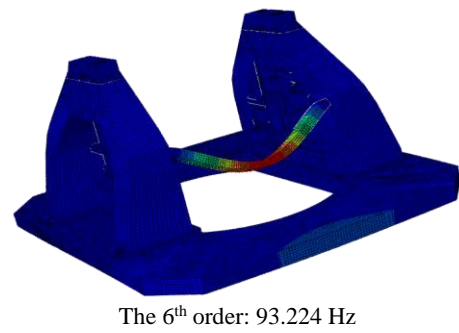
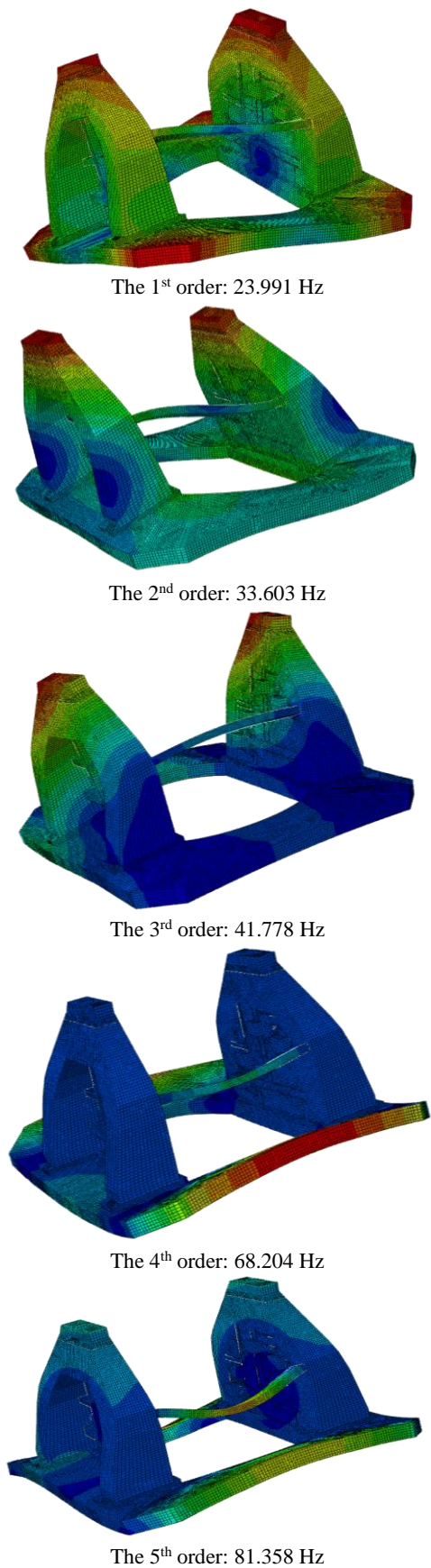


Figure 4. Parameters at the initial free mode of structure for a gun mount

In the modal modification design process of the gun mount structure, the design level should first be determined according to the design variables, and the finite element model should be established according to the relevant structural domain. The constructed finite element model is then utilized to carry out numerical calculation, and obtain the response variables. At the end, the analysis model and objective function are employed in the parameters optimization of gun mount with the particle swarm algorithm. The optimization result is input into the finite element model for verification.

As shown in Figure 5, the stretched thickness, height and width of the stiffening structure at both sides of the bracket are taken as the design variables in the optimization calculation. To guarantee the symmetry of the gun mount, the stiffening structure of the left and right brackets has exactly the same structural size and material properties. Therefore, there are only three design variables regardless of two stiffening structures. The mount assembly model and finite element grid of the stiffening structure domain are presented in Figure 6.

Table 3. presents the setting of parameters for particle swarm algorithm, and the range of design variables. Among them, the maximum iterations are 400 times; the range of stretched thickness is [100,600]mm; the range of stiffening structure height is [100,700]mm; and the range of structure width is [100,700]mm. The fundamental frequency of structure has a great influence on the

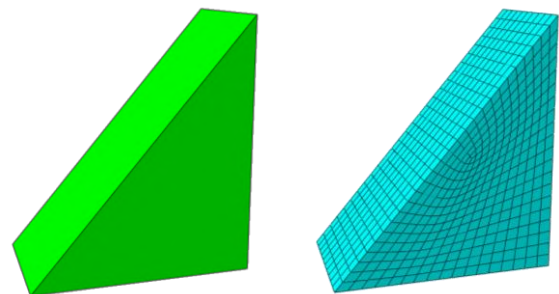


Figure 5. Structure model and finite element grid of stiffeners at both sides of the bracket

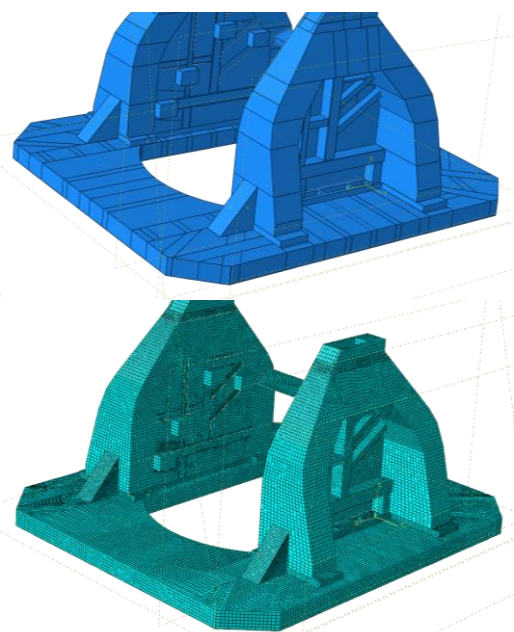


Figure 6. Assembly model and finite element grid of a gun mount

TABLE 3. Parameters of particle swarm optimization algorithm

Parameter	Value
Number of particles	3
Initial velocity	0
Stretched thickness W_{\min}	100mm
Stretched thickness W_{\max}	600mm
Height W_{\min}	100mm
Height W_{\max}	700mm
Width W_{\min}	100mm
Width W_{\max}	700mm
Acceleration constant	2.05
Maximum iterations	400

response to vibration. Especially under the heavy impact load, the high impact energy may trigger the fluctuation of fundamental frequency, and significantly affect the firing stability and mechanical reliability. Therefore, this paper takes the maximization of the fundamental frequency, that is, the first-order natural frequency, as the objective function, and performs iterative calculation within a given range to obtain the optimized iterative curve and the optimized stiffening structure size as shown in Figure 7 and Table 4.

Through building a mathematical model with the improved particle swarm optimization algorithm and using such design variables as the stretched thickness,

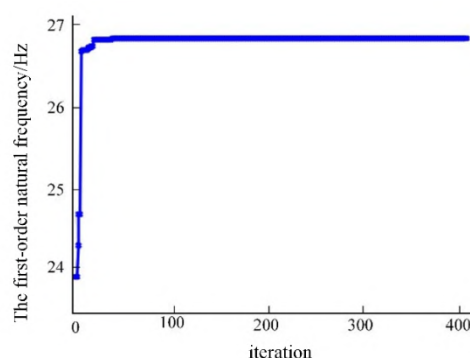


Figure 7. Optimization by iteration with PSO algorithm

TABLE 4. Optimal results after particle swarm optimization

Parameter	Value
Stretched thickness	156.4mm
Width	453.7mm
Height	238.9mm
Frequency after optimization	26.7Hz

width and height of the stiffening structure, after iterations, the optimal solution of the stiffening structure under the constraints is obtained. As shown in Table 4, the optimal solutions for stretched thickness, width, and height are 156.4mm, 453.7mm, and 238.9mm, respectively. It is found that the optimization algorithm increases the first-order natural frequency to 26.7Hz. The natural frequency at the designated order is improved by 11.3%. Therefore, the optimization is significantly effective.

5. CONCLUSION

In the present study, structural vibration equations were deduced under the effect of external excitation. A strategy was proposed to modify the low-order modes, and used together with the mathematical model based on the improved particle swarm optimization algorithm, so as to present an optimized design scheme for the supporting structure based on structural parameters. In a case study on the optimization of the gun mount, a solid finite element model was constructed for the gun mount. Taking the optimization of the gun mount as an example, by establishing the solid finite element model of the gun mount and combining with the finite element calculation, the mode shape and natural frequency of the gun mount in the free state are obtained. The stretch thickness, width and height of the stiffening structure on both sides of the gun mount were taken as the design variables to obtain the optimal solutions of the stiffening structure under

constraints by virtue of iteration. The results revealed that:

(1) Modal modification was proposed in this paper to increase the natural frequency of a supporting structure to avoid the excitation frequency of external loads for the purpose of reducing the vibration of the structure;

(2) Taking the modal modification of a naval gun mount as an example, an improved particle swarm optimization algorithm was used to optimize the gun mount, which increased the natural frequency of the designated order by 11.3%. Therefore, optimization was remarkably effective.

(3) As revealed in a case study on computing, the proposed modal optimization method based on structural parameters in this paper could effectively optimize the supporting structure to avoid the external excitation frequency in a way that lowered vibration. The proposed method can be extended to a large number of supporting structures with different shapes and working conditions in engineering practice.

(4) In engineering practice, there are many structures whose main structure should not be changed too much due to material and manufacturing process limitations. The research results of this article showed that an appropriate stiffening structure might be added, e.g. adding a supporting structure in the supporting structure, to effectively improve the dynamic performance of the supporting structure. The method proposed in this paper solves the problem of small-scale structural optimization in engineering practice to a certain extent, and can achieve the purpose of improving the required optimized structure without disassembling the main structure by welding the external structure to save costs.

(5) This article is aimed at the optimization of supporting structure, and the application of the proposed optimization method to other structures needs further study. In addition, the type of stiffening structure used in structural optimization is also an issue that needs to be considered in the future study.

6. REFERENCES

- Hussey, M., "Fundamentals of mechanical vibrations, Macmillan International Higher Education, (1983).
- Zare, H.G., Maleki, A., Rahaghi, M.I. and Lashgari, M., "Vibration modelling and structural modification of combine harvester thresher using operational modal analysis and finite element method", *Structural Monitoring Maintenance*, Vol. 6, No. 1, (2019), 33-46, doi.
- Sung, S.-H., Koo, K.-Y. and Jung, H.-J., "Modal flexibility-based damage detection of cantilever beam-type structures using baseline modification", *Journal of Sound Vibration*, Vol. 333, No. 18, (2014), 4123-4138, doi: 10.1016/j.jsv.2014.04.056.
- Liu, P., Zhu, H.-X., Yang, W.-G. And Huangfu, N.-q., "Tests on resonance and vibration mitigation responses of high-rise building under machine excitations", *Journal of ZheJiang University*, Vol. 54, No. 1, (2019), 102-109, doi: 10.3785/j.issn.1008-973X.2020.01.012.
- Ma, F., Cai, Y. and Wu, J.H., "Ultralight plat-type vibration damper with designable working bandwidth and strong multi-peak suppression performance", *Journal of Physics D: Applied Physics*, Vol. 54, No. 5, (2020), 055303, doi.
- Shi, Y. and Li, S., "An inverse modification method for assigning antiresonant frequencies", *Applied Acoustics*, Vol. 170, (2020), 107524, doi: 10.13465/j.cnki.jsv.2021.03.018.
- Braun, S. and Ram, Y., "Modal modification of vibrating systems: Some problems and their solutions", *Mechanical Systems Signal Processing*, Vol. 15, No. 1, (2001), 101-119, doi: 10.1006/mssp.2000.1354.
- Zhou, Y., Zhang, Y., Zeng, W. and Sun, Y., "Fast modification-aimed stress modal analysis of thin plates with holes/notches", *Engineering Structures*, Vol. 238, (2021), 112248, doi: 10.1016/j.engstruct.2021.112248.
- Mohamed, M.F.B.F. and Azmir, N.A.B., "Study on behavior of water treatment pump before and after modification using finite element modal analysis", in IOP Conference Series: Materials Science and Engineering, IOP Publishing. Vol. 824, No. 1, (2020), 012004.
- Pourzangbar, A., Vaezi, M., Mousavi, S. and Saber, A., "Effects of brace-viscous damper system on the dynamic response of steel frames", *International Journal of Engineering, Transactions B: Applications*, Vol. 33, No. 5, (2020), 720-731, doi: 10.5829/ije.2020.33.05b.02.
- Richardson, M. and Formenti, D., "Structural dynamics modification and modal modeling", Handbook of Experimental Structural Dynamics, Vol., No., (2020), 1-61, doi: 10.1007/978-1-4939-6503-8_25-1.
- Marinone, T., Avitabile, P., Foley, J. and Wolfson, J., "Efficient computational nonlinear dynamic analysis using modal modification response technique", *Mechanical Systems Signal Processing*, Vol. 31, No., (2012), 67-93, doi: 10.1016/j.ymsp.2012.02.011.
- Luk, Y.W., "System modeling and modification via modal analysis", Virginia Polytechnic Institute and State University, (1981),
- MA, B.-j., FENG, H.-h., LIAO, R.-d. and YAO, L.-m., "Modal analysis of engine structure based on the modal correlation and model modification [j]", *Vehicle Power Technology*, Vol. 2, No., (2006), doi: 10.16599/j.cnki.1009-4687.2006.02.010.
- Cury, A., Cremona, C. and Dumoulin, J., "Long-term monitoring of a psc box girder bridge: Operational modal analysis, data normalization and structural modification assessment", *Mechanical Systems Signal Processing*, Vol. 33, No., (2012), 13-37, doi: 10.1016/j.ymsp.2012.07.005.
- Ye, S., Hou, L., Zhang, P., Bu, X., Xiang, J., Tang, H. and Lin, J., "Transfer path analysis and its application in low-frequency vibration reduction of steering wheel of a passenger vehicle", *Applied Acoustics*, Vol. 157, No., (2020), 107021, doi.
- Li, T., Wu, C., Shen, L., Kong, X. and Ding, X., "Improving machine tool dynamic performance using modal prediction and sensitivity analysis method", *J Mech Eng*, Vol. 55, No. 7, (2019), 178-186, doi.
- Zhang, Y., Yang, Y.e., Du, W. and Han, Q., "Research on finite element model modification of carbon fiber reinforced plastic (CFRP) laminated structures based on correlation analysis and an approximate model", *Materials*, Vol. 12, No. 16, (2019), 2623, doi.
- Khan, A., Ko, D.-K., Lim, S.C. and Kim, H.S., "Structural vibration-based classification and prediction of delamination in smart composite laminates using deep learning neural network",

- Composites Part B: Engineering**, Vol. 161, (2019), 586-594, doi: 10.1016/j.compositesb.2018.12.118.
20. Azim, M.R., Zhang, H. and Gül, M., "Damage detection of railway bridges using operational vibration data: Theory and experimental verifications", **Structural Monitoring Maintenance**, Vol. 7, No. 2, (2020), 149-166, doi: 10.12989/smm.2020.7.2.149.
 21. Fadaei, S. and Rashno, A., "Content-based image retrieval speedup based on optimized combination of wavelet and zernike features using particle swarm optimization algorithm", **International Journal of Engineering, Transactions B: Applications**, Vol. 33, No. 5, (2020), 1000-1009, doi: 10.5829/ije.2020.33.05b.34.
 22. Yousefipour, A., Rahmani, A. and Jahanshahi, M., "Improving the load balancing and dynamic placement of virtual machines in cloud computing using particle swarm optimization algorithm", **International Journal of Engineering, Transactions C: Aspects**, Vol. 34, No. 6, (2021), 1419-1429, doi: 10.5829/ije.2021.34.06c.05.
 23. Hasibi, H., Mahmoudian, A. and Khayati, G., "Modified particle swarm optimization-artificial neural network and gene expression programming for predicting high temperature oxidation behavior of ni-cr-w-mo alloys", **International Journal of Engineering, Transactions B: Applications**, Vol. 33, No. 11, (2020), 2327-2338, doi: 10.5829/IJE.2020.33.11B.23.
 24. Yektaniroumand, T., Niaz Azari, M. and Gholami, M., "Optimal rotor fault detection in induction motor using particle-swarm optimization optimized neural network", **International Journal of Engineering, Transactions B: Applications**, Vol. 31, No. 11, (2018), 1876-1882, doi: 10.5829/ije.2018.31.11b.11.
 25. Ji-feng, L., "Traffic flow prediction based on improved particle swarm optimization".
 26. Shi, Y., "Particle swarm optimization: Developments, applications and resources", in Proceedings of the 2001 congress on evolutionary computation (IEEE Cat. No. 01TH8546), IEEE. Vol. 1, (2001), 81-86.
 27. Shi, Y. and Eberhart, R.C., "Parameter selection in particle swarm optimization", in International conference on evolutionary programming, Springer. (1998), 591-600.
 28. Wu, Y., Cheng, Q., Yang, G. and Dai, J., "Research on vibration characteristics of a multi-barrel artillery", **Journal of Vibroengineering**, Vol. 21, No. 5, (2019), 1241-1250.
 29. Zinando, G., "Structural modification approaches to modal design optimisation of vibrating systems", (2011).
 30. Pal, S., Roy, B. and Choudhury, S., "Comparative performance study of tuned liquid column ball damper for excessive liquid displacement on response reduction of structure", **International Journal of Engineering**, Vol. 33, No. 5, (2020), 753-759, doi: 10.5829/IJE.2020.33.05B.06.
 31. Zhang, R., Liu, J., He, C., Zhao, H. and Wang, Q., "Test and simulation study of the effect of transverse impact stress on the rosette 19-hole gun propellant under low temperature", **FirePhysChem**, (2021).
 32. Chuan-jian, L., Guo-lai, Y. and Xiao-feng, W., "Structural dynamics optimization of gun based on neural networks and genetic algorithms", **Acta Armamentarii**, Vol. 36, No. 5, (2015), 789, doi.
 33. Yuan, W.-H., Wang, H.-C., Zhang, W., Dai, B.-B., Liu, K. and Wang, Y., "Particle finite element method implementation for large deformation analysis using abaqus", **Acta Geotechnica**, (2021), 1-14.

Persian Abstract

چکیده

با توجه به مشکل ارتعاش قوی سازه نگهدارنده تحت تحریک بار خارجی، به منظور دستیابی به هدف بهینه سازی سازه از طریق اصلاح مودال برای دستیابی به هدف کاهش ارتعاش، ابتدا روشی برای اصلاح مودال از طریق تئوری ارتعاش سازه پیشنهاد شده است. ثانیاً، عملکرد جستجوی الگوریتم ازدحام ذرات بهبودیافته تحلیل می شود؛ در نهایت، با در نظر گرفتن بهینه سازی ساختاری پایه تفنگ به عنوان مورد، ساختار پایه تفنگ دریایی برای مشکل نوع خاصی از پایه تفنگ دریایی که ارتعاش می کند بهینه سازی شده است. در حین شلیک یک مدل فیزیکی اجزای محدود پایه تفنگ برای تجزیه و تحلیل شکل ارتعاش و فرکانس طبیعی پایه تفنگ در حالت آزاد ایجاد شد؛ در همان زمان، با توجه به الگوریتم ازدحام ذرات بهبود یافته، پارامترهای اندازه ساختار تقویت کننده در هر دو مورد از کناره های براکت به عنوان متغیرهای طراحی استفاده شد و فرکانس ذاتی مرتبه اول پایه تفنگ فرکانس تابع هدف برای ایجاد یک مدل ریاضی بهینه است و نرم افزار اجزای محدود **Abaqus** برای توسعه ثانویه استفاده می شود. پس از بهینه سازی و تکرار، فرکانس اساسی افزایش یافته است و اثر قابل توجه است.



An Improved Fingerprint-based Document Image Retrieval using Multi-resolution Histogram of Oriented Gradient Features

U. D. Dixit^{*a}, M. S. Shirdhonkar^b

^a Department of Electronics and Communication Engineering, BLDEA's V. P. Dr .P. G. Halakatti College of Engineering & Technology, Vijayapura, India

^b Department of Computer Science and Engineering, BLDEA's V. P. Dr .P. G. Halakatti College of Engineering & Technology, Vijayapura, India

PAPER INFO

Paper history:

Received 04 November 2021

Received in revised form 28 December 2021

Accepted 02 January 2022

Keywords:

Document Image Retrieval

Top-hat Filter

Bottom-hat Filter

Histogram of Oriented Gradients

Discrete Wavelet Transform

ABSTRACT

Recently most of the documents are authenticated by using a latent fingerprint impression. Examples of such documents are property registration, banking transactions, insurance documents, etc. The fingerprint-based document retrieval (FPDIR) has emerged to provide an easier way of accessing, browsing, or searching such document images. This paper proposes efficient fingerprint-based document image retrieval by employing multi-resolution Histogram of Oriented Gradient (HOG) features. The preprocessing technique presented in this paper employs a combination of top-hat and bottom-hat filtering operations to enhance the detected fingerprint image. Multi-resolution HOG features are constructed from horizontal, vertical and diagonal directional components of the enhanced fingerprint image. Finally, a standardized Euclidean distance metric is used as a tool for matching, ranking and retrieval of the document images. The proposed system is assessed by experimenting with a dataset of 1200 images. The precision and recall results obtained using the proposed research work have given an improvement of 8% to 14% in retrieval performance compared to earlier methods.

doi: 10.5829/ije.2022.35.04a.15

1. INTRODUCTION

To provide high security and authentication, recently the documents are embedded with fingerprint impressions instead of a signature. Property registration, banking transactions, insurance documents, etc. are some of the examples. Figure 1 shows a sample document image with fingerprint impressions

Fingerprint represents “a unique pattern of ridges and valleys of the surface of the fingers” [1]. The traditional method uses paper-ink whereas; a group of sensors has been employed for producing a finger-print impression in an electronic form. In general, a three-level hierarchy is employed for the representation of the fingerprint friction ridge information. “These include a pattern of fingerprints, minute points and ridge contours. Generally, level 1 features are employed for matching latent fingerprints whereas levels 2 and 3 features are used in fingerprint identification systems” [2].

The major challenges in FPDIR are poor retrieval performance due to the high similarity between the fingerprints and the presence of noise introduced during the digitization process. The preprocessing techniques, feature extraction schemes and application of relevant distance metrics are solutions to overcome the above-

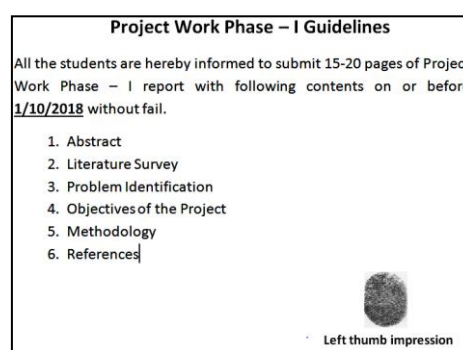


Figure 1. Sample Image

*Corresponding Author Institutional Email: uddixit@rediffmail.com
(U. D. Dixit)

mentioned challenges. This work was carried out to provide an efficient finger-print-based document retrieval. This is achieved by the application of suitable preprocessing techniques and the proposal of multi-resolution HOG features. The contribution of this work is as follows:

- Developed a pre-processing method for enhancing the quality of detected fingerprint impressions.
- Proposing of multi-resolution HOG features to obtain distinguished properties of the finger-print.
- Experimentation of standardized Euclidean similarity metric to match and retrieve the relevant documents.

The rest of this article is structured as follows: Section 2 describes the literature of the work, section 3 briefs about the proposed FPDIR, section 4 explain the results obtained, section 5 highlight the limitations and finally, in section 6 we conclude the work and provide future direction to the proposed research work.

2. LITERATURE REVIEW

This section describes the algorithms and techniques proposed by researchers to match the fingerprints for recognition, verification and retrieval.

Jiang et al. [3] presented the fingerprint retrieval technique by employing the features that are extracted from the orientation field and the dominant ridge distance. They proposed a new similarity measure that finds the average of the unit vector with phase doubled the orientation for matching the features of fingerprints. Fuzzy Feature Match (FFM) based technique for matching the deformed fingerprints was discussed by Chen et al. [4]. To estimate the similarity, the feature vectors are normalized before applying the distance metric. He et al. [5] described a three-stage technique for global comprehensive similarity. In the first stage, they developed a “minutia-simplex comprising of a pair of minutiae with their textures that include a transformation-variant and invariant set of features”. In the second stage, ridge-based relative features associated with minutiae are used for grouping the minutia depending on their affinity with the ridge. In the third stage, they presented the relationship between transformation and the comprehensive similarity of two fingerprint images in the form of a histogram.

A database clustering model-based fingerprint search technique for narrowing the search space was presented by Liu et al. [6]. It employs multi-scale orientation field-based features as the primary set of features and the average ridge distance as secondary features. A modified K-means clustering algorithm was used to divide the orientation feature space into clustering. The fingerprint friction ridge details consist of 3 levels of features. They

are level 1 comprising of pattern, level 2 that include minutia points and level 3 consisting of pores and ridge contours. Jain et al. [7] proposed the use of level 3 features to match high-resolution fingerprints. Zegarra et al. [8] proposed a wavelet feature-based fingerprint retrieval method with 3 important tasks: feature extraction, similarity measurement and indexing of the features. They used different types of wavelets namely Discrete Wavelet Transform (DWT), tree-structured DWT and the Gabor wavelets for the decomposition of the given image. The features are extracted using the energy and standard deviation of decomposed fingerprint images.

Jain and Feng [9] presented a method to match latent fingerprints with rolled fingerprints. The proposed system employs the use of a quality map in addition to minutiae. Nanni and Lumini [10] presented the hybrid fingerprint matching technique using Local Binary Pattern (LBP) based features. Initially, the 2 fingerprints are matched and allied using their corresponding minutiae and then separated into non-overlapping blocks. These non-overlapping blocks are convolved with the Gabor filters to construct LBP histograms. Jung and Lee [11] proposed a method for the classification of fingerprints employing the probabilistic approach using features of ridges. Bharkad and Kokare [12] suggested the use of discrete wavelet packet transform by neglecting horizontal coefficients to obtain redundant features for matching the fingerprint images.

A method for detection of the convex core points of different category of fingerprints was presented by Le and Van [13]. A modified complex filter also known as the semi-radial filter is employed in their method for the detection. The vertical variation feature is used for removing spurious core points. Cappelli and Ferrara [14] developed a method for fingerprint retrieval using the combination of a levels1 and 2 set of features. A hybrid fusion-based technique is used for the evaluation of various scores and ranking of the fingerprints. Shalaby and Ahmed [15] proposed the use of a multi-level structural approach to recognize the fingerprints, by decomposing them into regions using multi-level features. Paulino et al. [16] proposed a technique to match the latent fingerprints. They used descriptor-based Hough transforms to align the fingerprints. The orientation field is used to measure the similarity of fingerprints in the proposed method. Arun et al. [17] proposed a texture-based finger knuckle print recognition method with the help of features formed using LBP variants. They used Local Directional Pattern (LDP), Local Derivative Ternary Pattern (LDTP), Local Texture Description Framework (LTDF) and Modified Local Directional Pattern (MLDN) based feature extraction in their proposed method. Nearest neighbor and Extreme

Learning Machine (ELM) classifiers are used for the classification task. Rodrigues et al. [18] presented a technique to recognize the finger knuckle prints. The Sobel gradient operator was used for detecting the edges. Different similarity metrics are used for the recognition of binarized images. Gray Level Co-occurrence Matrix (GLCM) [19], as well as Singular Value Decomposition (SVD) [20] features were employed for face-based document image retrieval by Dixit and Shirdhonkar. Tzalavra et al. [21] provided the comparative analysis of 3 multi-resolution transform-based features namely DWT, Stationary Wavelet Transform (SWT) and Fast Discrete Curvelet Transform (FDCT) for assessing breast tumors. FDCT based features provided better performance in comparison with the other two. Qayyum et al. [22] employed SWT for feature extraction for the identification of facial expressions. Particularly, the combinations of vertical and horizontal coefficients have been used for obtaining information about muscle movement. Dixit and Shirdhonkar [23] presented two sets of features DWT-based LBP and SWT-based LBP. They used Euclidean distance for similarity matching and also to retrieve the documents.

Cao and Jain [24] presented fingerprint recognition for latent fingerprints using Convolution Neural Network (CNN). Hindi et al. [25] investigated the performance of fingerprint recognition using 3 sets of image features extracted from minutiae, reduced center symmetric local binary pattern (RCSLBP) and C-mean clustering methods. Xu et al. [26] developed a rotation-invariant edge descriptor for fingerprint identification. The descriptor was built by combining the length of the edge, angles between the edges and the orientation of pores. Zohrevand and Imani [27] Presented CNN-based approach for Persian handwritten word images, which were segmented at the character level. A three-stage filtering approach to improve the performance of face recognition was proposed by Ghasemi and Hassanpour [28].

From the literature, it is learned that the major issues in implementing FPDIR were; the development of a suitable enhancement technique, a set of features to extract more accurate attributes and the use of a proper distance metric for matching and retrieval. This paper aims to provide solutions to the above challenges by proposing efficient preprocessing techniques and multi-resolution HOG features to improve the overall retrieval performance.

3. PROPOSED METHODOLOGY

The architecture of the proposed fingerprint-based document retrieval is depicted in Figure 2. The major

blocks of the architecture include fingerprint detection, preprocessing, feature extraction, matching and retrieval of documents from the database. The discussion about these blocks is provided in the subsequent sections.

3. 1. Fingerprint Detection System

We are motivated by the simpler and high detection rate of the fingerprint detection method employed by Dixit and Shirdhonkar [23]. A modified version of the fingerprint detection is presented in this paper. It includes a two-phase approach: a training phase and the testing phase. The first phase employs 140 patches comprising of a variety of text, logos, fingerprints and different symbols are used. These patches are generated from the first 100 document images of the database. Initially, the patches from the submitted query document are obtained using connected component analysis, their DWT [29] based features are extracted and then these patches are classified as fingerprint and non-fingerprint patches using Support Vector Machine (SVM) [30] classifier. The steps used in the process of fingerprint detection are given in Algorithm 1.

Algorithm 1: Fingerprint Detection

1. Begin

Input: Document Image (D), 140 patches generated from 100 document images

Output: Detected fingerprint (DFP)

2. Divide the document (D) into four sub-bands S1, S2, S3 and S4 by applying DWT. Where S1, S2, S3, S4 are approximate, horizontal, vertical and diagonal sub-bands respectively.
3. Compute energy and standard deviation of S2, S3, S4 using Equations (1) and (2).

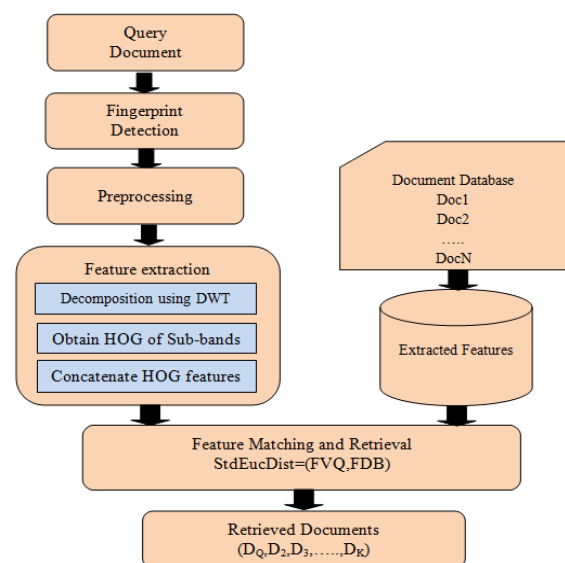


Figure 2. Architecture of the proposed system

$$E_i = \frac{1}{M \times N} \sum_{m=1}^N \sum_{n=1}^N |S_i| \quad \text{for } i = 2, 3, 4 \quad (1)$$

$$SD_i = \sqrt{\frac{1}{M \times N} \sum_{x=1}^N \sum_{y=1}^N (S_i - \mu_i)^2} \quad \text{for } i = 2, 3, 4 \quad (2)$$

where E_i is Energy, SD_i is standard deviation and μ_i is the mean of i^{th} sub-band. M and N represent the row and column dimensions of the sub-bands

4. Form the feature vector FV using Equation (3)

$$FV = \{E_1, E_2, E_3, SD_1, SD_2, SD_3\} \quad (3)$$

5. Compute FV for 140 patches and train the SVM.
6. Compute FV for patches of the input document image and detect the patch containing fingerprint using trained SVM.
7. DFP = Patch classified as fingerprint
8. **End**

In the proposed fingerprint detection system instead of four, only the three sub-bands providing directional information are used to compute the features. This has reduced the number of computations required. The detection rate is used for estimating the performance of the fingerprint detection system and is computed using Equation (4).

$$\text{etection rate} = \frac{\text{Successfully detected fingerprints}}{\text{Total number of document imaes}} \quad (4)$$

The image results containing at least 80% of fingerprint impressions are considered as successfully detected fingerprints. The proposed method yielded a detection rate of 99%. Figure 3 shows the sample result. It shows an input query document and the detected fingerprint impression. A marked rectangle indicates the detected fingerprint.

The detected fingerprint images of the document are preprocessed by employing the combination of top-hat and bottom-hat filtering techniques [31]. This step has helped in improving the contrast of the image and also removed the un-even illumination background from the fingerprint impression. Figure 4 shows the steps used during preprocessing.

Algorithm 2 provides the preprocessing operations used in the proposed method.

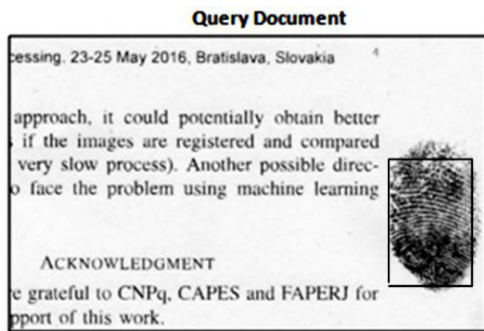


Figure 3. Sample result of fingerprint detection

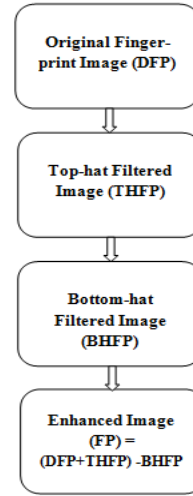


Figure 4. Preprocessing Step

Algorithm 2: Preprocessing steps

1. **Begin**
Input: Detected Fingerprint Image (DFP)
Output: Enhanced Fingerprint Image (FP)
2. Obtain Top-Hat Filtering (THFP) of detected fingerprint image (DFP) using Equation (5)
$$THFP = (DFP \circ SE) - DFP \quad (5)$$
 where SE is the structuring element
3. Obtain bottom-hat filtering (BHFP) of detected fingerprint image (DFP) using Equation (6)
$$BHFP = (DFP \circ SE) - DFP \quad (6)$$
4. Compute the enhanced fingerprint image (FP) using Equation (7)
$$FP = \{DFP + THFP\} - BHFP \quad (7)$$
5. Return FP
6. **End**

The top-hat filtering is used to extract small elements and details of the image. It is achieved by subtracting the morphological opening of an image from its original version. Mathematically the top hat filtering is computed by using Equation (1). However, the bottom-hat filtering is the difference between the original image and its morphological closing. Equation (2) is used for obtaining bottom-hat filtering of the input image. Finally, Equation (3) is used to get an enhanced version of the detected fingerprint image (FP). Empirically, by conducting the experiments, it is observed that a better version of the enhanced fingerprint image is possible with the usage of a disk-shaped structuring element having the size of 12 pixels. Figure 5 depicts the stepwise results of the preprocessed image.

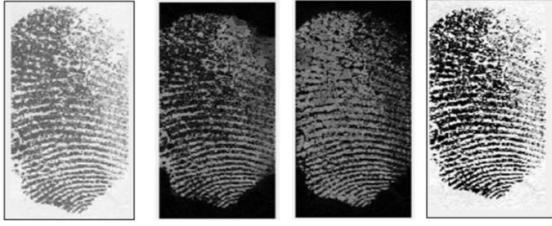


Figure 5. Preprocessing Steps (a) Original image (b) Top-hat filtered image (c) Bottom-hat filtered image (d) Enhanced image

3. 2. Feature Extraction HOG features are found to provide better results in the classification, recognition and retrieval of images [32]. This paper proposes multi-resolution HOG features to improve performance. Algorithm 3 shows the procedure employed in the proposed feature extraction scheme.

Algorithm 3: Proposed Feature Extraction Method

1. Begin

Input: Detected fingerprint image FP

Output: Multi-resolution features FV

2. Convert the detected fingerprint image into grayscale.
3. Resize the fingerprint image FP to 256×256 pixels.
4. Decompose fingerprint image FP into approximate, horizontal, vertical and diagonal sub-bands by using Equation (8)

$$(A, H, V, D) = DWT\{FP\} \quad (8)$$

where, A, H, V and D are approximate, horizontal, vertical and diagonal sub-bands of size 128×128 .

5. Divide H, V and D sub-bands into cells of size 32×32 pixels. This results in (4×4) 16 cells per sub-band.
6. Chose block size as (2×2) 4 cells resulting in 9 non-overlapping blocks per sub-band.
7. Compute the HOG of H, V and D sub-bands with 9 bins, resulting in a total of 324 features per sub-band. Let F_1 , F_2 and F_3 be the HOG features of horizontal, vertical and diagonal sub-bands obtained using Equations (9), (10) and (11).

$$F_1 = HOG\{H\} \quad (9)$$

$$F_2 = HOG\{V\} \quad (10)$$

$$F_3 = HOG\{D\} \quad (11)$$

8. Concatenate the features F_1 , F_2 and F_3 using Equation (12)

$$FV = \{F_1\} \cup \{F_2\} \cup \{F_3\} \quad (12)$$

9. Return FV

10. End

Algorithm 3 has three important steps: Image decomposition by applying DWT, computing multi-

resolution HOG features of sub-bands and concatenation of the features.

3. 2. 1. Image Decomposition by Applying DWT

DWT is widely used in almost all applications of digital image processing. It employs a series of low-pass and high-pass filters and provides a multi-resolution version of an image. Let FP is the detected fingerprint from the document. The image FP is initially resized to 256×256 pixels. Then the resized image is divided into approximate, horizontal, vertical and diagonal sub-bands with the help of DWT using the Equation (1). These sub-bands will have a size of 128×128 pixels. The horizontal (H), vertical (V) and diagonal (D) sub-bands represent the directional components of the input image. As approximate sub-band (A) is similar to the original image with reduced size, it won't provide any directional information and hence it is ignored during the feature extraction. Omission of approximate sub-band for feature extraction also helped in reducing the number of features.

3. 2. 2. Computing Multi-resolution HOG Features

The three sub-bands H, V and D are treated as separate images containing multi-resolution information of the fingerprint and used for feature extraction. Each sub-band is divided into cells of size 32×32 . This resulted in a total of (4×4) 16 cells per sub-band. These cells are arranged to form 9 overlapping blocks of size (2×2) 4 cells to extract HOG features. The numbers of resulting HOG features for an image are provided by Equation (13).

$$\text{Number of HOG features} = \text{BlkSz} \times \text{NOB} \times \text{NHB} \quad (13)$$

where 'BlkSz' is the size of a block, 'NOB' indicates the number of overlapping blocks per image and the 'NHB' is the number of histogram bins used. As in the proposed algorithm, the block size is 4, the number of overlapping blocks is 9 and the histogram bins are chosen 9, which leads to a total of $(4 \times 4 \times 9)$ 324 HOG features per sub-band. The gradients values in this scheme are computed using the Equations (14) and (15) are used to compute the gradients.

$$\text{GRADIENT}_H(X, Y) = FP(X + 1, Y) - FP(X - 1, Y) \quad (14)$$

$$\text{GRADIENT}_V(X, Y) = FP(X, Y + 1) - FP(X, Y - 1) \quad (15)$$

where GRADIENT_H and GRADIENT_V are horizontal and vertical gradients. The GRADIENT_H and GRADIENT_V are computed as the difference of consecutive pixels in the horizontal and vertical directions. The magnitude and orientation of gradients are then computed using Equations (16) and (17).

$$\text{Mag}(X, Y) = \quad (16)$$

$$\sqrt{\text{GRADIENT}_H(X, Y)^2 + \text{GRADIENT}_V(X, Y)^2}$$

$$\Theta(X, Y) = \tan^{-1} \frac{\text{GRADIENT}_H(X, Y)}{\text{GRADIENT}_V(X, Y)} \quad (17)$$

where $\text{Mag}(X, Y)$ and $\Theta(X, Y)$ are the magnitude and orientation of the gradients.

3. 2. 3. Concatenation of the Features The HOG features resulting from the sub-bands of DWT are combined to form the final feature set FV using Equation (12). Feature vector consisting of 324 directional HOG values per sub-band results in a total of 972 features due to the concatenation process. Figure 6 shows the flow diagram proposed feature extraction scheme.

3. 2. 4. Fingerprint Matching and Retrieval A similarity metric is employed to match the features of query fingerprint with fingerprint present in the document images. To speed up the retrieval process a database of fingerprint features extracted from the documents is stored in the repository. Most of the retrieval schemes in the literature employ Euclidean distance for matching the features. However, in the normal Euclidean distance; classification is influenced by features with larger values and the features with lower values contribute very little. This drawback has been removed by normalizing the features in standardized Euclidean distance. Hence a standardized Euclidean distance given by Equation (18) is used for fingerprint matching and retrieval of the documents.

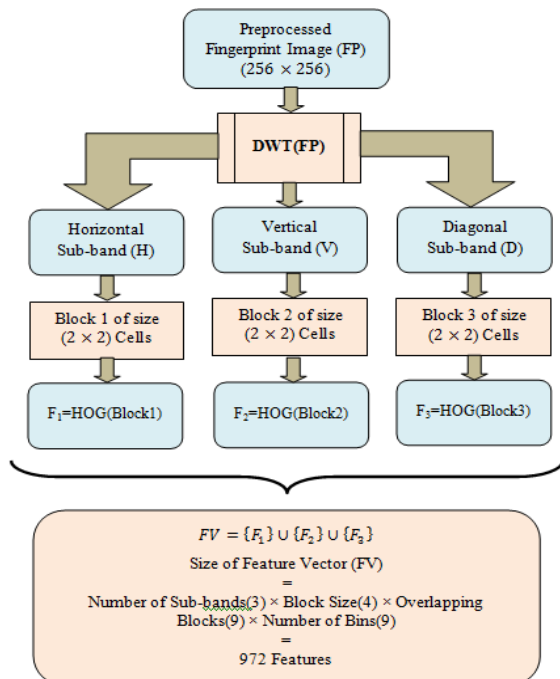


Figure 6. Proposed Feature Extraction Scheme

$$\text{StdEucDist} = \frac{1}{\sqrt{(FVQ - FDB) \times V^{-1} \times (FVQ - FDB)}} \quad (18)$$

where,

- StdEucDist is a vector to hold computed similarity values for ‘N’ documents.
- FVQ is the features of the query image.
- FDB is pre-extracted fingerprint features of documents stored in the database.
- ‘V’ is the n -by- n diagonal matrix whose j^{th} diagonal element is $S(j)^2$ and ‘S’ being the vector of standard deviations.

After computing the distance values, the documents present in the database are indexed based on their distance values concerning the query document. The lowest distance corresponds to the closest match and vice-versa. Now based on the user request top ‘K’ number of documents are accessed from the database and displayed on the user console.

4. EXPERIMENTAL RESULTS AND DISCUSSION

Core-i5/4GB RAM/windows8 machine with MATLAB is used for the implementation of the proposed method. To avoid legal issues and conflict of interest, we created a database consisting of 1200 documents. The details about the database used for experimentation are provided below.

About the database: Right thumb impression of 50 persons is taken on documents for the creation of the database. Each person was asked to provide a thumb impression on 24 printed documents using a black ink pad. Thus, it leads to a dataset of (50×24) 1200 documents. These documents are then scanned by using HP M1005 scanner to get an image database.

The precision, recall and F-measure parameters are employed to evaluate the performance of the proposed system. Precision is the ratio of number of relevant documents retrieved out of the total number of documents retrieved. It is similar to the accuracy parameter used in the classification of images. The recall is the ratio of number of relevant documents retrieved to the total number of relevant documents present in the dataset. However, the F-measure is a performance parameter summarizing both precision and recall. The Equations (19), (20) and (21) are used to compute the evaluation parameters.

$$\text{Precision} = \frac{\text{Number of relevant document retrieved}}{\text{Total number of documents retrieved}} \quad (19)$$

$$\text{Recall} = \frac{\text{Number of relevant document retrieved}}{\text{Number of relevant documents in the database}} \quad (20)$$

$$F - measure = 2 \times \frac{Precision \times Recall}{Precision + Recall} \quad (21)$$

The performance of the system is assessed by conducting an exhaustive set of experiments. In each experiment, the user was asked to choose a query document randomly from each of the 50 classes. The precision and recall values are computed for retrieval of top 1, top 5, top 8, top 10, top 15 and top 20 documents. A total of 300 queries are executed to test the developed algorithm. Figure 7 shows the sample result of FPDIR. The sample result is obtained by giving a query document and the number of documents to be retrieved as 4. Table 1 shows average precision, average recall computed using the proposed method and the state of art techniques.

Figure 8 shows the comparison of average precision values computed using the proposed method and other state-of-art techniques. The comparison of precision values reveals that an improvement of 8 to 14% performance is obtained with the proposed system.

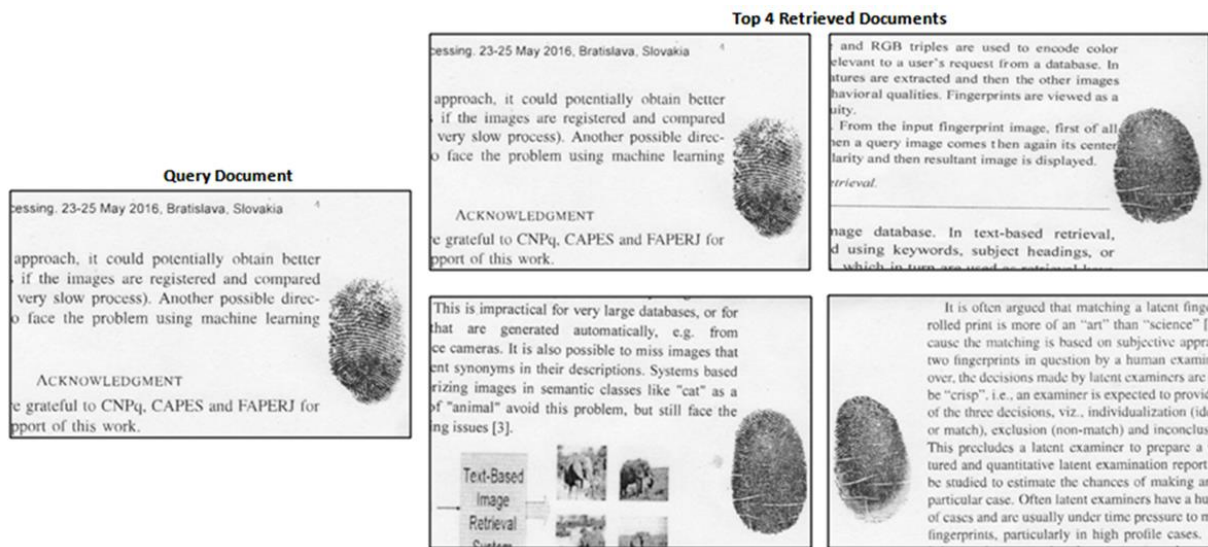


Figure 7. Sample result of FPDIR

Figure 9 shows a graphical comparison of average recall values. The proposed system outperforms by providing better recall results in comparison with earlier methods.

Table 2 shows the F-measure values computed by using different methods and the proposed system. Graphical comparison of F-measure performance for top 1, top 5, top 8, top 10, top 15 and top 20 values are depicted in Figure 10. The graphical comparison ensures that the proposed system provides encouraging results in terms of recall measures.

5. LIMITATIONS OF THE PROPOSED WORK

The limitations of the work are listed below.

- The proposed work in this paper experiments on a database of 1200 documents. We were unable to experiment on a huge dataset due to the non-availability of public database of document images with fingerprint impressions publicly.

TABLE 1. Average Precision and Average Recall Values

Number of Top Matches	LBP Features [33]		RLBP Features [25] (Rotation Invariant LBP Features)		HOG Features [32]		DWT based LBP Features [23]		Proposed Method	
	Average Precision (AP)	Average Recall (AR)	Average Precision (AP)	Average Recall (AR)	Average Precision (AP)	Average Recall (AR)	Average Precision (AP)	Average Recall (AR)	Average Precision (AP)	Average Recall (AR)
TOP 1	100	4.16	100	4.16	100	4.16	100	4.16	100	4.16
TOP 5	75.66	15.85	76.01	15.88	76.34	15.97	86.96	18.16	94.78	19.75
TOP 8	66.85	22.28	67.28	22.36	68.11	22.56	72.83	24.28	86.41	28.8
TOP 10	62.6	26.09	64.26	26.56	65.60	27.37	68.7	28.62	82.61	34.42
TOP 15	53.33	33.33	54.13	33.55	54.38	33.67	58.26	36.41	71.01	44.38
TOP 20	46.52	38.77	46.93	38.91	47.19	39.14	51.74	43.11	60.65	50.54

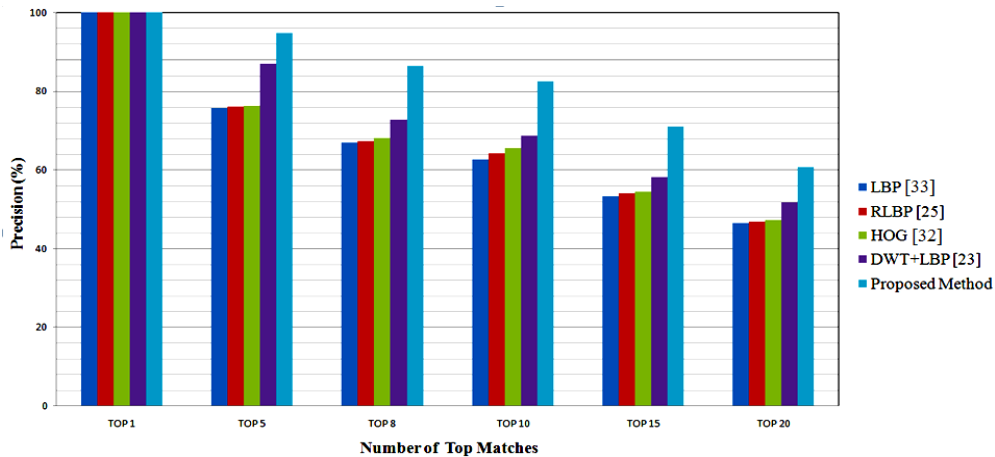


Figure 8. Graphical Comparison of Precision Values

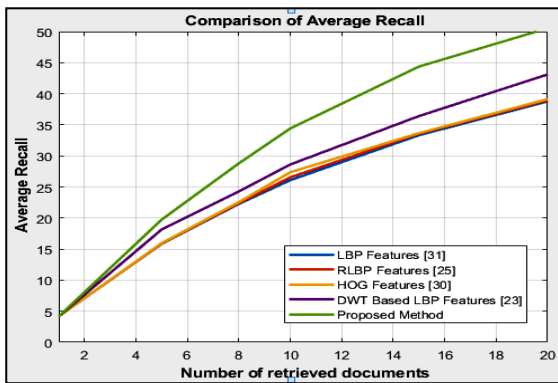


Figure 9. Comparison of Average Recall

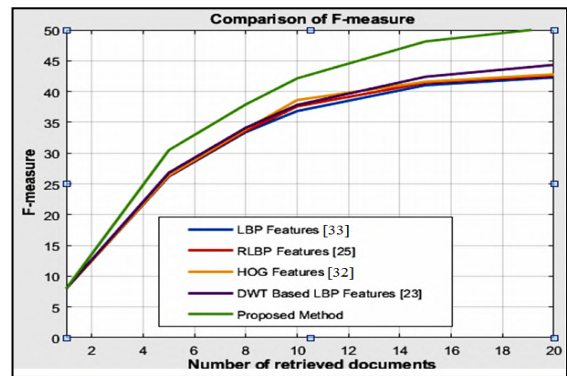


Figure 10. Graphical Comparison of F-measure

TABLE 2. Comparison of F-measure

Number of top matches	LBP Feature [33]	RLBP Feature [25]	HOG Feature [32]	DWT based LBP [23]	Proposed Method
TOP 1	7.99	7.99	7.99	7.99	7.99
TOP 5	26.21	26.27	26.41	26.81	30.48
TOP 8	33.42	33.56	33.89	34.12	37.91
TOP 10	36.83	37.59	38.62	37.82	42.14
TOP 15	41.02	41.42	41.59	42.40	48.14
TOP 20	42.29	42.55	42.79	44.33	50.4

The database used has documents with only left thumb impression. The retrieval performance may vary if a document includes multiple fingerprints.

6. CONCLUSION AND FUTURE SCOPE

This work presented an improved method for FPDIR. The improved performance is due to the use of preprocessing techniques that enhanced the quality of

detected fingerprint images and multi-resolution HOG features proposed in the system. The selection of only the directional components has provided more distinguished HOG features. It also helped in reducing the features as approximate sub-band is not considered for feature extraction. The proposed system is evaluated by testing a database of 1200 document images. It is observed from the results that, there is an increase of 8 to 14% precision with different retrieval results with the proposed algorithms. Both recall and F-measure results also demonstrate the outperformance of the proposed algorithms.

Future Scope: The results show that the performance parameters of the system decrease with an increase in the number of retrieved documents. This is found to be a major challenge in most document retrieval systems. The future design may consider the following to achieve better results.

- Suitable distance metrics
- Experimentation with new feature extraction schemes
- Feature reduction techniques to reduce retrieval time of the documents.

7. REFERENCES

- Ross, A. and Jain, A., "Biometric sensor interoperability: A case study in fingerprints", in International Workshop on Biometric Authentication, Springer. (2004), 134-145.
- Jain, A.K., Chen, Y. and Demirkus, M., "Pores and ridges: High-resolution fingerprint matching using level 3 features", *IEEE Transactions on Pattern Analysis Machine Intelligence*, Vol. 29, No. 1, (2006), 15-27, doi: 10.1109/TPAMI.2007.250596.
- Jiang, X., Liu, M., Kot, A.C. and Security, "Fingerprint retrieval for identification", *IEEE Transactions on Information Forensics*, Vol. 1, No. 4, (2006), 532-542, doi: 10.1109/TIFS.2006.885021.
- Chen, X., Tian, J., Yang, X., Zhang, Y. and security, "An algorithm for distorted fingerprint matching based on local triangle feature set", *IEEE Transactions on Information Forensics*, Vol. 1, No. 2, (2006), 169-177, doi: 10.1109/TIFS.2006.873605.
- He, Y., Tian, J., Li, L., Chen, H. and Yang, X., "Fingerprint matching based on global comprehensive similarity", *IEEE Transactions on Pattern Analysis Machine Intelligence*, Vol. 28, No. 6, (2006), 850-862, doi: 10.1109/TPAMI.2006.119.
- Liu, M., Jiang, X. and Kot, A.C., "Efficient fingerprint search based on database clustering", *Pattern Recognition*, Vol. 40, No. 6, (2007), 1793-1803, <https://doi.org/10.1016/j.patcog.2006.11.007>
- Jain, A.K., Feng, J., Nagar, A. and Nandakumar, K., "On matching latent fingerprints", in 2008 IEEE Computer Society Conference on Computer Vision and Pattern Recognition Workshops, IEEE. (2008), 1-8.
- Zegarra, J.A.M., Leite, N.J. and da Silva Torres, R., "Wavelet-based fingerprint image retrieval", *Journal of Computational Applied Mathematics*, Vol. 227, No. 2, (2009), 294-307, <https://doi.org/10.1016/j.cam.2008.03.017>
- Jain, A.K. and Feng, J., "Latent fingerprint matching", *IEEE Transactions on Pattern Analysis Machine Intelligence*, Vol. 33, No. 1, (2010), 88-100, doi: 10.1109/TPAMI.2010.59.
- Nanni, L. and Lumini, A., "Local binary patterns for a hybrid fingerprint matcher", *Pattern Recognition*, Vol. 41, No. 11, (2008), 3461-3466, <https://doi.org/10.1016/j.patcog.2008.05.013>
- Jung, H.-W. and Lee, J.-H., "Fingerprint classification using the stochastic approach of ridge direction information", in 2009 IEEE International Conference on Fuzzy Systems, IEEE. (2009), 169-174.
- Bharkad, S. and Kokare, M., "Fingerprint matching using discreet wavelet packet transform", in 2013 3rd IEEE International Advance Computing Conference (IACC), IEEE. (2013), 1183-1188.
- Le, T.H. and Van, H.T., "Fingerprint reference point detection for image retrieval based on symmetry and variation", *Pattern Recognition*, Vol. 45, No. 9, (2012), 3360-3372, <https://doi.org/10.1016/j.patcog.2012.02.017>
- Cappelli, R. and Ferrara, M., "A fingerprint retrieval system based on level-1 and level-2 features", *Expert Systems with Applications*, Vol. 39, No. 12, (2012), 10465-10478, <https://doi.org/10.1016/j.eswa.2012.02.064>
- Shalaby, M.W. and Ahmad, M.O., "A multilevel structural technique for fingerprint representation and matching", *Signal Processing*, Vol. 93, No. 1, (2013), 56-69, <https://doi.org/10.1016/j.sigpro.2012.06.02>
- Paulino, A.A., Feng, J., Jain, A.K. and Security, "Latent fingerprint matching using descriptor-based hough transform", *IEEE Transactions on Information Forensics*, Vol. 8, No. 1, (2012), 31-45, doi: 10.1109/TIFS.2012.2223678.
- Arun, D., Columbus, C.C. and Meena, K., "Local binary patterns and its variants for finger knuckle print recognition in multi-resolution domain", *Circuits Systems*, Vol. 7, No. 10, (2016), 3142-3149, doi: 10.4236/cs.2016.710267.
- Rodrigues, E., Porcino, T.M., Conci, A. and Silvah, A.C., "A simple approach for biometrics: Finger-knuckle prints recognition based on a sobel filter and similarity measures", in 2016 International Conference on Systems, Signals and Image Processing (IWSSIP), IEEE. (2016), 1-4.
- Dixit, U.D. and Shirdhonkar, M., "Face-based document image retrieval system", *Procedia Computer* Vol. 132, (2018), 659-668, <https://doi.org/10.1016/j.procs.2018.05.065>
- Dixit, U.D. and Shirdhonkar, M., Face biometric-based document image retrieval using svd features, in Computational intelligence in data mining. 2017, Springer.481-488.
- Tzalavra, A., Dalakleidi, K., Zacharakis, E.I., Tsiaparas, N., Constantinidis, F., Paragios, N. and Nikita, K.S., "Comparison of multi-resolution analysis patterns for texture classification of breast tumors based on dce-mri", in International Workshop on Machine Learning in Medical Imaging, Springer. (2016), 296-304.
- Qayyum, H., Majid, M., Anwar, S.M. and Khan, B., "Facial expression recognition using stationary wavelet transform features", *Mathematical Problems in Engineering*, Vol. 2017, (2017), <https://doi.org/10.1155/2017/9854050>
- Dixit, U.D. and Shirdhonkar, M., "Fingerprint-based document image retrieval", *International Journal of Image Graphics*, Vol. 19, No. 02, (2019), 1950008, <https://doi.org/10.1142/S0219467819500086>
- Cao, K. and Jain, A.K., "Automated latent fingerprint recognition", *IEEE transactions on pattern analysis machine intelligence*, Vol. 41, No. 4, (2018), 788-800, doi: 10.1109/TPAMI.2018.2818162.
- Hindi, A., Dwairi, M.O. and Alqadi, Z., "Analysis of procedures used to build an optimal fingerprint recognition system", Vol., No., (2020), doi.
- Xu, Y., Lu, G., Lu, Y. and Zhang, D., "High resolution fingerprint recognition using pore and edge descriptors", *Pattern Recognition Letters*, Vol. 125, (2019), 773-779, <https://doi.org/10.1016/j.patrec.2019.08.006>
- Zohrevand, A. and Imani, Z., "Holistic persian handwritten word recognition using convolutional neural network", *International Journal of Engineering, Transactions B: Applications*, Vol. 34, No. 8, (2021), 2028-2037, doi: 10.5829/ije.2021.34.08b.24.
- Hassanpour, H. and Ghasemi, M., "A three-stage filtering approach for face recognition", *International Journal of Engineering, Transactions B: Applications*, Vol. 34, No. 8, (2021), doi: 10.5829/ije.2021.34.08b.06.
- Arivazhagan, S. and Ganesan, L., "Texture classification using wavelet transform", *Pattern Recognition Letters*, Vol. 24, No. 9-10, (2003), 1513-1521, [https://doi.org/10.1016/S0167-8655\(02\)00390-2](https://doi.org/10.1016/S0167-8655(02)00390-2)
- Cote, M. and Albu, A.B., "Texture sparseness for pixel classification of business document images", *International Journal on Document Analysis Recognition*, Vol. 17, No. 3, (2014), 257-273, <https://doi.org/10.1007/s10032-014-0217-8>
- Bright, D.S. and Steel, E.B., "Two-dimensional top hat filter for extracting spots and spheres from digital images", *Journal of Microscopy*, Vol. 146, No. 2, (1987), 191-200, <https://doi.org/10.1111/j.1365-2818.1987.tb01340.x>
- Dalal, N. and Triggs, B., "Histograms of oriented gradients for human detection", in 2005 IEEE computer society conference on computer vision and pattern recognition (CVPR'05), IEEE. Vol. 1, (2005), 886-893.
- Hassan, T. and Khan, H.A., "Handwritten bangla numeral recognition using local binary pattern", in 2015 international conference on electrical engineering and information communication technology (ICEEICT), IEEE. (2015), 1-4.

Persian Abstract

چکیده

اخیراً اکثر اسناد با استفاده از اثر انگشت نهفته احراز هویت می شوند. نمونه‌هایی از این اسناد عبارتند از: ثبت ملک، تراکنش‌های بانکی، اسناد بیمه، و غیره. بازیابی اسناد مبتنی بر اثر انگشت (FPDIR) برای ارائه راه آسان‌تری برای دسترسی، مرور یا جستجوی چنین تصاویر اسنادی پدید آمده است. این مقاله بازیابی تصویر سند مبتنی بر اثر انگشت کارآمد را با استفاده از ویژگی‌های هیستوگرام گرادین جهت‌دار (HOG) با وضوح چندگانه پیشنهاد می‌کند. تکنیک پیش پردازش ارائه شده در این مقاله از ترکیبی از عملیات فیلتر کردن کلاه بالا و پایین برای بهبود تصویر اثر انگشت شناسایی شده استفاده می‌کند. ویژگی‌های HOG با وضوح چندگانه از اجزای جهت‌دار افقی، عمودی و مورب تصویر اثر انگشت بهبودیافته ساخته شده‌اند. در نهایت، یک متریک فاصله اقلیدسی استاندارد شده به عنوان ابزاری برای تطبیق، رتبه‌بندی و بازیابی تصاویر سند استفاده می‌شود. سیستم پیشنهادی با آزمایش با مجموعه داده ای از ۱۲۰۰ تصویر ارزیابی می‌شود. نتایج دقت و یادآوری به‌دست‌آمده با استفاده از کار تحقیقاتی پیشنهادی باعث بهبود عملکرد بازیابی ۸ تا ۱۴ درصد نسبت به روش‌های قبلی شده است.



Technical and Economical Approaches in Application of Micro Silica Gel and Calcium Carbonate Powder in Self-compacting Concrete

P. Rashidi Rad^a, S. A. Haj Seiyed Taghia^{*a}, H. R. Darvishvand^a, M. Ebrahimi^b

^a Department of civil Engineering, Qazvin Branch, Islamic Azad University, Qazvin, Iran

^b Engineering Technology Department, South Carolina State University, SC, USA

P A P E R I N F O

Paper history:

Received 10 December 2021

Received in revised form 08 January 2022

Accepted 13 January 2022

Keywords:

Calcium Carbonate Powder

Concrete Properties

Economic Analysis

Micro Silica Gel

Self-compacting Concrete

A B S T R A C T

Effects of two admixtures, calcium carbonate powder (CCP) and micro silica gel (MSG) on self-compacting concrete (SCC) properties, such as workability, compressive strength, and durability are investigated. Results, show that, in some cases, concrete with MSG is unable to provide a stable condition, although flowability is higher. Experimental results indicate that the effect of CCP on sustainability, strength and durability of mixture is remarkable. Combo mix design is introduced to benefit from the positive characteristics of two admixtures. Results of decision making method show that this mix can be considered as a proper sample along with the sample containing the optimal dosage of CCP. Moreover, this method indicates the optimal dosage of CCP is 31.25%, which leads to the best improvement in characteristics of fresh and hardened concrete. In practical engineering, economic analysis demonstrates that using CCP is more cost effective, because is accessible and inexpensive in Iranian market.

doi: 10.5829/ije.2022.35.04a.16

1. INTRODUCTION

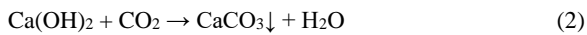
Concrete vibrating is essential for consolidation and reducing the voids in normal concrete pouring process. But there are some problems using this process such as congested reinforcement, complex geometrical shapes and forms, and the cost. To overcome these problems, self-compacting concrete (SCC) was proposed by Okamura [1] for the first time and extended gradually from Japan to Europe and other parts of the world [2]. In this type of concrete, the higher dosage of superplasticizer is used in the mixture in order to gain more workability in comparison to use normal concrete; but, addition of superplasticizer has a risk of segregation and losing the integrity of SCC and as a result, the role of admixtures [3–5] and the grading of aggregates in SCC is more crucial in comparison to the normal concrete. It should also stress that, the extra fine aggregates are used in SCC because of filler role too. Moreover, in order to

provide the required viscosity, it is necessary to use viscosity modifying admixture (VMA). VMAs increase the density of the mixture and capability of the cement paste in maintaining the floating ingredients which further lead to improvement of sustainability, viscosity, cohesion and internal friction of fresh concrete in microscopic scale. However, excessive dosage of VMA increases cohesion and duration of pouring in concrete, but normally, this effect can be compensated by adding more superplasticizer to the mixture [6–8]. Calcium carbonate powder (CCP) and micro silica (MS) are two VMAs which have all feature mentioned above and also, have positive effects on improving the mechanical properties and concrete durability. For further information, see sections 1.1 and 1.2.

1.1. Calcium Carbonate Powder The most part of CCP used in industry is obtained through mining. CCP is produced from calcium oxide. The chemical reactions for

*Corresponding Author Institutional Email: ali.taghia@qiau.ac.ir
(S. A. Haj Seiyed Taghia)

obtaining calcium hydroxide and precipitated CCP are given by Equations (1) and (2), respectively [9].



CCP as a cement substitute, has been used in concrete production for many years. CCP has many characteristics such as reduction in cement production, decrease in environmental pollution, and improving the workability and sustainability of fresh mixture. In addition, CCP increases the volume of cement paste, and this causes the better interlocking of aggregates and enhances the concrete durability [10].

Sua-iam and Makul [11] assessed the possibility of using CCP in SCC as a substitution for sand. The results showed that CCP with the amount of 30% by cement weight has the capability to improve the characteristics of SCC.

Justnes et al. [12] indicated that 20% of CaCO_3 as a replacement with Portland cement, considerably increases the compressive and flexural strengths of mortar. In other research, Okeyinka and Oladejo [13] showed that the application of CCP equal to 20% replacement, rises the compressive strength up to 43.9% at 28 days curing time.

Silva and Brito [14] conducted the durability tests of SCC's made with different dosages of CCP with respect to percentages of cement. They used Scanning electron microscopy (SEM) instrument for analyzing chloride penetration, electrical resistance, and carbonation. They revealed that, using CCP, improves the workability, sustainability, and durability.

Makul and Sua-Iam [15] studied the effect of rice husk ash and CCP on properties of SCC. Their investigation indicated that the workability of SCC containing CCP fall within an allowable range in accordance with EFNARC standard [16].

Lertwattanaruk et al. [17] investigated the impact of CCP on the characteristics of SCC. CCP was used as a cement substitute at percentage replacements of 20% and 40% by weight. They observed that the maximum compressive strength could be reached with 20% of CCP in the mix design.

Daoud and Mahgoub [18] evaluated the effect of CCP on fresh and hardened specifications of SCC. Mix designs with different replacement levels of 0%, 10%, 20%, and 30% by cement weight were prepared. The addition of CCP up to 30% by cement weight, decreased cost and improved the performance of SCC.

In the current study, CCP is used with the diverse weight percentages of cement 12.5, 25, 31.25, 37.5, 43.75, and 50.

1. 2. Micro Silica (MS) MS is a pozzolanic material. It was first used in Norway and then in the U.S,

Canada, and Europe. Today, MS is considered as one of the most practical and beneficial admixtures for concrete production. Fundamentally, it is made of amorphous siliceous with a spherical shape. The application of superplasticizer is necessary for increasing workability and decreasing the water-to-cement ratio especially in concrete with pozzolanic materials such as MS. MS is becoming more popular in application. There are several advantages of using MS, one is filling and binding the gaps among cement particles, and simultaneously, increasing the adhesion between the cement paste and coarse aggregate; by that, when voids are reduced, MS considerably decreases permeability and increases lifetime of concrete. The other advantages are, replacing cement by MS, influences the viscosity of mixture and furthermore, this material improves mechanical properties of concrete [19–22].

Vikan et al. [23] indicated that replacement of cement with silica fume (up to 10 vol.%) enhances the yield stresses of all mix designs.

Park et al. [24] understood that application of MS to substitute 5, 10 and 15% of the cement may lead to increase in compressive strength and plastic viscosity whereas decreases the segregation of mixture [25].

Bouzoubaa et al. [26], Gesoğlu et al. [27], Valipour et al. [28], Shaikh et al. [29], Zhang et al. [30, 31], Gupta et al. [32] and Barati et al. [33] investigated the effect of MS on improvement of mechanical properties and durability characteristics of concrete.

Micro silica gel (MSG) is actually the composition of Silica fume and a superplasticizer in a pasty form and ready-to-use which has not only the ability to enhance the chemical resistance and mechanical strength of concrete, but also does not have any breathing problems (the tiny particles of the silica fume are harmful).

Laboratory results of the Building and Housing Research Center (BHRC) [34] in compliance with ASTM C1202 [35], showed that using 7% to 10% MSG in the mix design, lead to the reduction of water consumption as well as enhancing the mechanical strength of concrete up to 30%. In addition, the properties and workability of concrete indicated, an increase of 10%, comparing to the mixture using of MS and superplasticizer. In other words, with high certainly, for improving the properties and workability, the system of silica fume and superplasticizer could be replaced by only MSG in the mix design.

Nandhini and Ponmalar [36] found that SCC with dosage of 10% MS, leads to the best performance regarding workability and compressive strength. Shashi [37] proposed that the adequate dosage of MS in SCC, is 7.5% to reach maximum compressive strength. In the similar research, Mohanraj et al. [38] obtained the dosage of 10% for MS. In this case, the compressive strength increased by 12% at 28 days of curing period.

Kumar et al. [39] investigated the effect of MS application in improving of normal concrete properties. They concluded that the optimal dosage of MS is 8% for reaching maximum compressive strength.

In the current work, the dosage of MSG, limited to 7% of the cement weight, was taken from conclusion of the study of BHRC [34].

1. 3. Innovative Significance of Research

Overhauling literature review and perusing previous works, are shown that, they have studied the effects of using VMAs on characteristics of fresh and hardened SCC, separately. They have paid less attention on comparing the concrete properties containing CCP and MSG. It is expected MSG containing superplasticizer and MS, has positive effect on concrete flowability. Meanwhile, the prior researches (section 1.1) confirm that CCP is more effective on concrete characteristics such as sustainability of mixtures, improving of mechanical property, and durability in comparison to MSG. The aim of current study is therefore to simultaneously benefit from the advantages of two admixtures in practical engineering.

In the most cases, prior investigations were focused on the effect of two admixtures on three significant concrete characteristics, namely, workability, strength, and durability, separately. But, current study in a comprehensive approach, is considering these characteristics, simultaneously so as to provide a ground for practical application.

Besides, CCP is accessible and more inexpensive than cement in the local market of Iran. On the other hand, CCP as a substitution for portions of cement dosage, is very important regarding impact of cement production in environment. Therefore, the design of concrete mixing compatible with Iran environment is crucial.

Above all, an economic analysis is considered to avoid concerning the practical approach of the current research.

2. METHODOLOGY

2. 1. Materials The following ingredients were used:

2. 1. 1. Cement Ordinary Portland cement based on ASTM C150 [40] with the cement content of 400 kg/m³ was used. The chemical and physical properties of cement are given in Table 1.

2. 1. 2. Aggregates Sand and gravel aggregates were river type in accordance with ASTM C33 [41]. The sand sizes were ranged from 0 to 4.75 mm with density of 1270 kg/m³ apparent weight in Saturated Surface Dry (SSD) state, and the 24-hour water absorption is 2.63%. The gravel sizes were ranged from 4.75 to 12 mm with

TABLE 1. Chemical and physical properties of cement

Blaine cm ² /g	Physical properties					Density (kg/m ³)
	Setting time (min)		Compressive strength (kg/cm ²)			
	Initial	Final	3 days	7 days	28 days	
2910	154	195	205	288	411	3130

Chemical properties							
Property	SiO ₂	Al ₂ O ₃	Fe ₂ O ₃	CaO	MgO	SO ₃	K ₂ O
Content (%)	20.82	4.98	3.57	62.84	2.79	2.27	0.63

450 kg/m³ apparent weight in SSD state and the 24-hour water absorption is 2.65%.

Darvishvand et al. [42] stated that the maximum gravel size should be limited to 12.5 mm to reach the highest compressive strength and ductility of concrete. Therefore, in this research, this limit was chosen as the highest range of gravel size.

Figure 1 shows the gradation curves for sand and gravel aggregates.

2. 1. 3. Water Water to cement ratio of 0.45 was used through the entire experiment.

2. 1. 4. Calcium Carbonate Powder (CCP) CCP is a substitute for the part of cement content used in the mix design. Chemical and physical properties of CCP are given in Table 2. Variety of percentages of this material, 12.5%, 25%, 31.25%, 37.5%, 43.75%, and 50% by

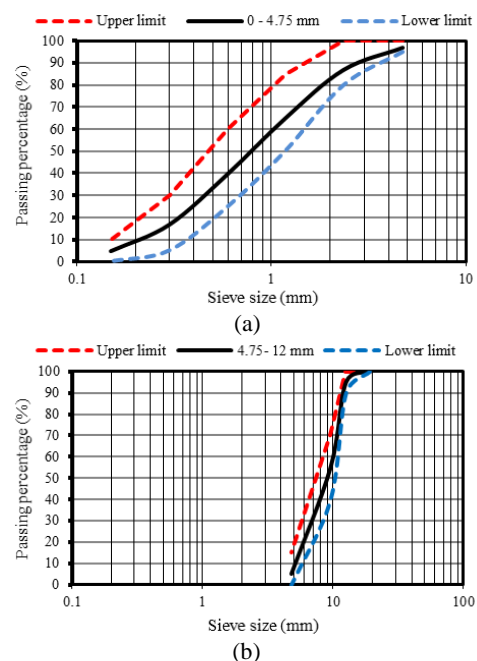


Figure 1. Gradation curves for aggregates: (a): sand aggregate, (b): gravel aggregate

TABLE 2. Chemical and physical properties of CaCO₃

Physical properties													
Form	Particle size			Color	Humidity (%)			Specific surface area (m ² /kg)			Density (g/mL)		
powder	≤150 μm			Light brown	0.08			1540			2.93		
Chemical properties													
Property	SiO ₂	Al ₂ O ₃	Fe ₂ O ₃	CaO	Na ₂ O	K ₂ O	MgO	TiO ₂	Mno	P ₂ O ₅	S	L.O.I	CaCO ₃
Content (%)	0.9	0.06	0.03	54.69	0.03	0.02	0.86	0.019	0.002	0.142	0.011	43.89	98.5

weight of cement, were used which are equivalent to 50, 100, 125, 150, 175 and 200 kg in one cubic meter of the concrete, respectively. The particle size of CCP utilized, was less than 150 microns in this experiment (see Figure 2).

2. 1. 5. Micro Silica Gel (MSG) The image of MSG is shown in Figure 3 and according to the technical specification of MSG product [43], this material was used to 7% of cement weight (28 kg/m³) in the mixture. Table 3 presents physical and chemical data of the MSG.



Figure 2. Image of calcium carbonate powder used in mix design



Figure 3. Image of micro silica gel used in mix design

TABLE 3. Chemical and physical properties of MSG

Physical properties								
Color	Physical state				Density (g/cm ³)			
Gray	Gel				1.45			
Chemical properties								
Property	SiO ₂	Al ₂ O ₃	Fe ₂ O ₃	CaO	MgO	SO ₃	K ₂ O	Na ₂ O
Content (%)	93	0.4	0.2	1.2	1.2	0.3	1.1	0.1

2. 1. 6. Superplasticizer The trade name for superplasticizer (SP) was Powor plast W/A. The archetypal of SP is given in Table 4. In this research, the amount of SP was 1% of cement weight (according to manufacturer 2018 [44]) which is 4 kg/m³ of entire mix designs with the except for the control sample 1 (see section 2.2).

2. 1. 7. Air Entrainment Air entrainment (AE) materials were used in samples containing MSG as an adherent agent to bond the cement particles and aggregates. This ensures the enhancement of concrete sustainability. According to the technical specification of product [45], 0.08% of the cement weight of this material was used. Technical data of the material is reported in Table 5.

2. 2. Mix Design Table 6 is designated with 10 mix designs which are labeled with specific abbreviation codes.

The following is the description for the codes. Characters C and M followed by the numbers represent samples containing CCP, MSG, and the weight dosage of materials per cubic meter of the mix design.

TABLE 4. The archetypal of superplasticizer at 20°C

Description	Specification
Name	Power plast W/A
Ingredient	Modified poly carboxylate
Color	Light brown
State	Liquid
Density (g/mL)	0.02 ±1.06
pH	1±6

TABLE 5. Air entrainment specifications at 20°C

Specification	Description
Type	Surface active agent
Color	Brown
State	Liquid
Density, g/mL	0.01± 1.01
Ion chlorine	None (based on standard BS 5075)

TABLE 6. Mix designs used for different ingredients

Mixture code	Cement (kg/m ³)	Water (kg/m ³)	Gravel (kg/m ³)	Sand (kg/m ³)	CCP (kg/m ³)	MSG (kg/m ³)	SP (kg/m ³)	AE (kg/m ³)
Control1	400	180	450	1270	-	-	-	-
Control2	400	180	450	1270	-	-	4	-
C50	350	180	450	1270	50	-	4	-
C100	300	180	450	1270	100	-	4	-
C125	275	180	450	1270	125	-	4	-
C150	250	180	450	1270	150	-	4	-
C175	225	180	450	1270	175	-	4	-
C200	200	180	450	1270	200	-	4	-
M28	400	180	450	1270	-	28	4	0.32
Combo	275	180	450	1270	125	28	4	0.32

In this research, control samples were made as the reference samples for comparison of experimental data to ensure the reliability of the results. Control sample 1 does not contain any admixture to find out the role of SP and VMAs on SCC properties. Control sample 2 was planned to evaluate the effect of SP on the workability of mixture. The mix designs from C50 through C200 were selected to determine the optimal percentage of the consumed CCP. M28 mix design was utilized to evaluate the effect of the MSG on concrete behavior. The combo mix design was considered for the purpose of estimating the effect of simultaneous use of two admixtures, CCP and MSG.

The experimental data showed that the dosage of CCP corresponding the sample that leads to the maximum compressive strength, was 125 kg/m³. This amount was used in the mix design with both admixtures.

2.3. Mix Preparation The design of mixture was performed according to ACI-211-89 [46] and concrete was made according to ASTM C 192 [47]. Each component of the mixture was determined using the

weighing balance. The mixing sequence of concrete was accomplished by adding aggregates, cement and 70% of water. The SP dissolved in the remainder of water and added to the mixture. Then, the VMA was added to the admixture and it was stirred for 10 minutes. Finally, the fresh characteristics of concrete were measured.

2.4. List of Performed Tests along with Acceptance Criteria

2.4.1. On Fresh Concrete Several methods were used based on EFNARC standard [16] and European Guidelines for SCC [8] to determine the workability of concrete. List of methods and images of the process are shown in Table 7 and Figure 4 (a-e), respectively.

2.4.2. On Hardened Concrete According to BS 1881: Part 111 standard [48], cubic samples with dimensions of 15 × 15 × 15 cm were made and kept inside the molds for 24 hours and then were cured inside a water reservoir at the temperature of 20±2 °C. Figure 5 shows the final blocks of concrete samples.

TABLE 7. List of experiments for determination of SCC workability and acceptance limits in EFNARC standard

Test	Property	Unit	Typical range of values	
			Minimum	Maximum
Slump flow	Filling ability	mm	650	800
T _{50cm} Slump	Filling ability	s	2	5
J-ring	Passing ability	mm	0	10
V-funnel	Filling ability	s	6	12
V-funnel at T5 minutes	Segregation resistance	s	6	15
L-box	Passing ability	h ₂ /h ₁	0.8	1.0
U-box	Passing ability	h ₂ -h ₁ (mm)	0	30



Figure 4. Different methods of SCC tests on fresh concrete: a. Slump-flow; b. J-ring; c. V-funnel and V-funnel at T_{5minutes}; d. L-box; e. U-box

2. 4. 2. 1. Compressive Strength Three samples were prepared for each mix design for this test. The experiment performed at the ages of 7, 28 and 90 days based on British Standard 1881: Part 108 [49].

2. 4. 2. 2. Water Absorption The amount of percentage of water absorption in a cement matrix composite, is an indication of volume and distribution of the capillary voids, and the porosity in material [50]. The test is a criterion to evaluate the durability of concrete for the long life. Two samples were prepared for each mix design. Samples were tested in compliance with ASTM C642 [51] for the age of 42 days. The test results were evaluated based on CEB-FIP reference [52]. The reference categorizes the quality and acceptance limit of water absorption. This is illustrated in Table 8.



Figure 5. Preparation of concrete blocks

TABLE 8. Categories of water absorption according to CEB-FIP reference [52]

Category	Acceptance limit (%)
Good	<3
Average	3-5
Poor	>5

2. 4. 2. 3. Electrical Resistivity This is to evaluate the durability of concrete for the long life. The test was performed on three samples at the age of 42 days. The experimental set up is shown in Figure 6. AC voltage was measured during the process and resistance was estimated using Ohm's law for each run [53]. Test evaluation was done according to ACI 222R-01 standard [54].

3. EXPERIMENTAL RESULTS AND DISCUSSION

In this section, the results of each test from fresh and hardened concrete containing CCP and MSG, are presented and discussed.

3. 1. Fresh Concrete The followings are presentation of results and discussion based on explanation of methods in Table 5.

3. 1. 1. Slump Flow Test and T_{50cm} Test Figure 7 illustrates the slump flow measurement from diameter of each mix design. The results from this figure indicate that SP significantly improves the flowability of concrete. This can be seen by comparing control samples 1 and 2 in such a way that sample 1, doesn't extend to diameter of 500 mm and that's because of lack of SP in this mix design. Slump flow is slowed down in samples containing CCP in comparison to control sample 2 because of formation of higher viscosity in the sample, meanwhile the flowability is further declined for weight percentage of CCP over 37.5%, and this is passed beyond the limit of EFNARK standard [16]. Mixture containing MSG (i.e. M28), is shown improvement in concrete flowability which is higher than CCP mix designs and control sample 2. The dashed lines on Figures 7 and 8 are shown to stress the acceptance limits.

Similar results can also be deduced from Figure 8. The data in Figure 8 show that more dosage of CCP increases time for the mix designs to reach diameter of 500 mm, but if the percentage of dosage reaches 50%, the mix design C200, will not be within the acceptance limit of the EFNARK standard [16] due to formation of higher viscosity in the mixture. Data in Figure 8 reveal a shorter



Figure 6. Electrical resistivity apparatus

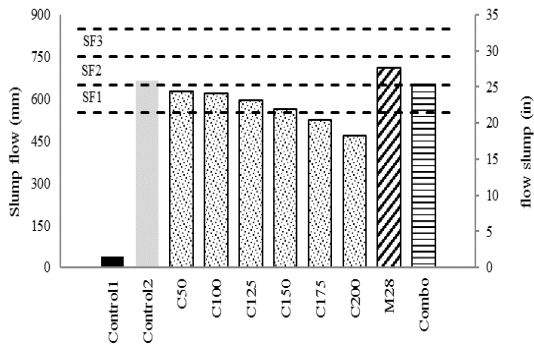


Figure 7. Results of slump flow test

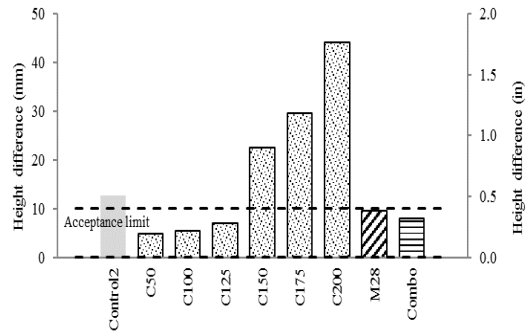


Figure 10. Height difference between the slump flow inside and outside of the J-ring

time for the mix designs to reach diameter of 500 mm. This indicates that mix design containing MSG, offers higher flowability of concrete in comparison to the mix designs with CCP. The word “infinity” in Figure 8, indicates the impossibility of mixture, reaching to diameter of 500 mm in practice. Although, study of mix design containing mixture of CCP and MSG, indicates that appearance of CCP causes relatively low reduction in the concrete flowability, but in general, the role of presence of MSG is dominant in the mixture.

3. 1. 2. J-ring Test and Height Difference between the Slump Flow Inside and Outside of the J-ring

Figures 9 and 10 present the test results for slump flow and height difference between slump inside and outside of the J-ring, respectively. The dashed lines in the figures illustrate the range of acceptance limit complying with the requirements of EFNARK standard [16]. It is impossible to illustrate the result of slump flow test for control sample 1 with the J-ring in which no SP is involved. Additional amount of CCP, leads to reduce the flowability of slump due to the higher viscosity in the samples and increases the height difference of slump of the ring. These are clearly demonstrated in Figures 9 and 10, respectively. Mixture shows more flowability when is containing MSG in comparison to samples with CCP. Similar results are drawn as in the previous section, the effect of using CCP and MSG, simultaneously, lead to a

relatively low reduction in flowability, although the effect of CCP is not as tangible as the effect of MSG.

3. 1. 3. V-funnel Test and V-funnel Test at T_{5minutes}

The results of V-funnel test and increase of flow time in V-funnel test (T_{5minutes}), are presented in Figures 11 and 12, respectively. The dashed lines in the figures, exhibit the acceptance range of EFNARK standard [16]. Data in Figure 11 indicate that CCP increases the flow time with satisfaction whereas, it is shorter in control sample 2 in comparison to the acceptance limit of the standard and this can be attributed to the unsustainability of mixture. The figure also, reveals by adding MSG, there would be excessive flowability in the mixture, but doesn't meet the requirements of acceptance criteria based on EFNARK standard [16]. The data in Figure 12 clearly show that increasing of flow time in V-funnel test (5 min. waiting period) verifies that control sample 2 cannot be freely discharged due to the segregation of components of mixture which causes blocking the flow. The word “infinity in Figure 12, points out unlimited flow time. Figure also, provides that the mix design C125 has the minimum increase in flow time. This shows consistency and continuity of mix designs containing CCP, is much better in comparison to the mixture with MSG sample, M28. Data in Figures 11 and 12 illustrate that the addition of CCP, develops mixture sustainability when both admixtures are used simultaneously in comparison to use of only MSG.

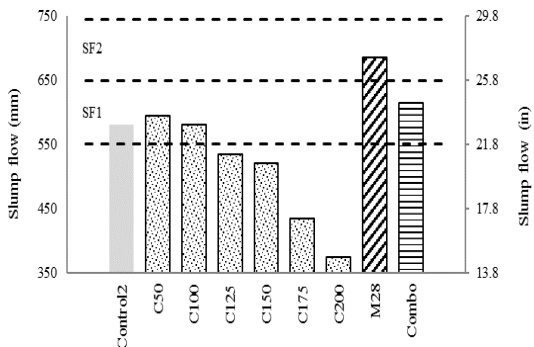


Figure 9. Results of J-ring test

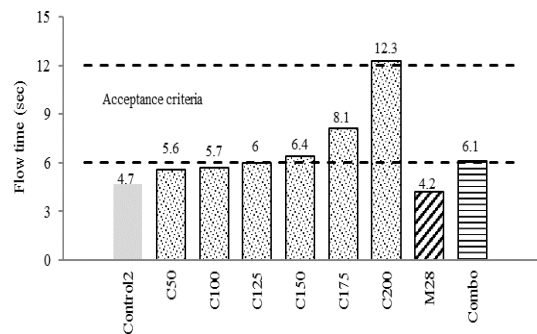


Figure 11. Results of V-funnel test

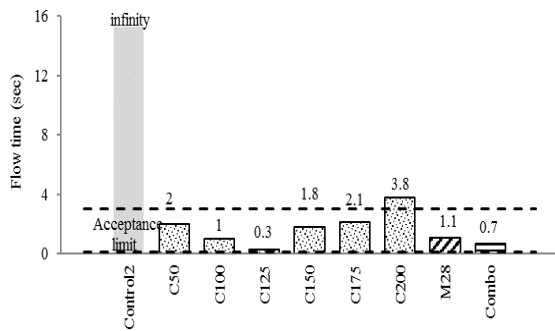


Figure 12. Results of V-funnel test at T₅minutes

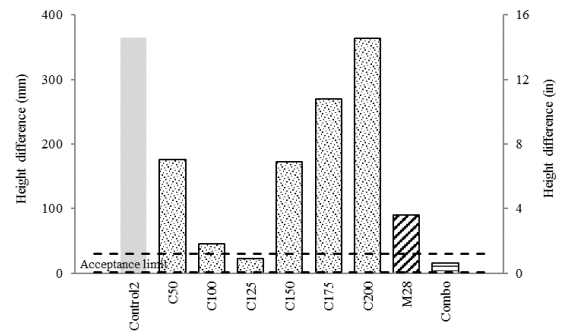


Figure 14. Results of U-Box test

3. 1. 4. L-box Test

The results of this test is demonstrated in Figure 13. The dashed lines in the figure, illustrate the range of acceptance limit complying with the requirements of EFNARK standard [16].

The figure illustrates that addition of CCP in the mixture up to 125 kg/m³, causes the rise in the concrete height ratio of the box defined as, concrete height at end of the box to the concrete height next to the rebar as shown in Figure 4d. The higher height ratio leads to the better passing ability of the concrete, however, the ratio will be out of allowable range if the dosage of CCP goes beyond the limit, and the reason for that is, occurrence of the dense viscosity in the mixtures. M28 sample shows a similar passing ability in comparison to C125 sample which shows MSG is more effective in flowability in mix design. The concrete height ratio is close to 1 when both admixtures are used at the same time, this means, the performance of the mixture is perfect, but it also shows that the concrete behavior is very similar to the condition when sample contains only MSG.

3. 1. 5. U-box Test

The data from this test are shown in Figure 14. The dashed lines represent the acceptance limit of EFNARK standard [16]. In this figure, it is not possible to illustrate the data for the control sample 1 since concrete is unable to flow through the rebars. The figure also, indicates that, there is a significant height difference of concrete flow in case of control sample 2 with SP, and that is because of

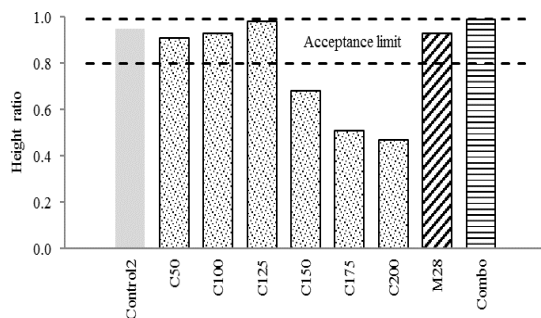


Figure 13. Results of L-Box test

segregation and blocking of components. Therefore, this shows that the height difference is not within the allowable limit, and as a result, SP is unable to guarantee the desirable characterization of SCC by itself. Once again, using 125 kg/m³ of CCP shows an observable increase in flowability and integrity of the concrete and of course, there is a decline in height difference, but the effect of CCP will be reversed if the dosage of CCP goes beyond the limit and, that is because of occurrence of high viscosity in the samples.

M28 sample shows poor passing ability due to the unsustainability of the mixture and stands out of acceptance standard range in comparison to sample containing 125 kg/m³ of CCP. CCP admixture is considered as a proper choice in this type of test, because it provides a sustainable mix design and preserves the integrity of concrete and furthermore, the role of CCP can be distinguished when using both admixtures in the sample, in which, sustainability returns to the concrete.

3. 2. Hardened Concrete

The followings are presentation of results and discussion on hardened concrete.

3. 2. 1. Compressive Strength Test

Figure 15 shows the results of compressive strength and Figure 16 demonstrates the percentages of the growth of the samples at different ages. The values on the top of the bars in this figure, indicate the growth at the age of 28

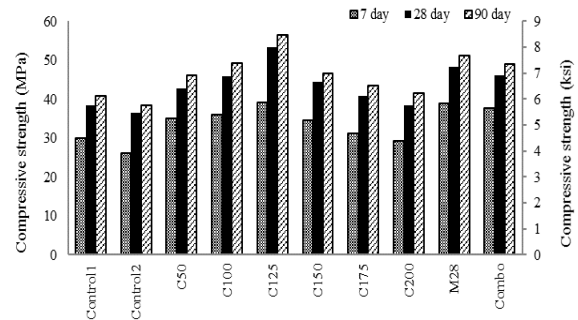


Figure 15. Results of compressive strength test

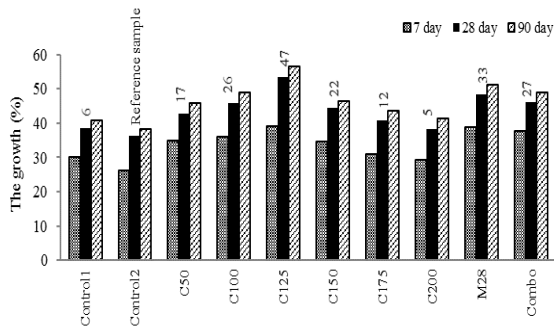


Figure 16. Compressive strength growth of samples at the different ages in comparison to control sample 2

days and they are compared to control sample 2. There are numerous points can be drawn from the data of Figure 16, one is using SP in control sample 2 reduces concrete strength by 6% in comparison to control sample 1. This can be attributed to unsustainability and loss of aggregate interlocking which may cause segregation of the components, the other one is, addition of CCP to the mix designs increases compressive strength of concrete in comparison to control sample 2. Figure 16 reveals the growth trend in compressive strength of mix designs with amount of 125 kg/m³ CCP, has raised by 47% but, strength starts to reduce if the amount goes beyond the limit and this is because of reduction of cohesion in cement paste due to the presence of unreacted CCP in the mixture. Also, according to Figure 16, the percentage of growth in compressive strength is 47% and 33% for C125 and M28, respectively in comparison to control sample 2. Finally, using CCP and MSG in mixture simultaneously, have no significant effects on concrete strength and illustrate the similar behavior as the sample with only MSG.

3. 2. 2. Water Absorption Test Figure 17 demonstrates that by increasing the amount of CCP to 125 kg/m³ in the mixture, percentage of water absorption has been reduced in comparison to control sample 2. The results are an indication of a desirable performance of CCP which lead to increase in consolidation and decrease

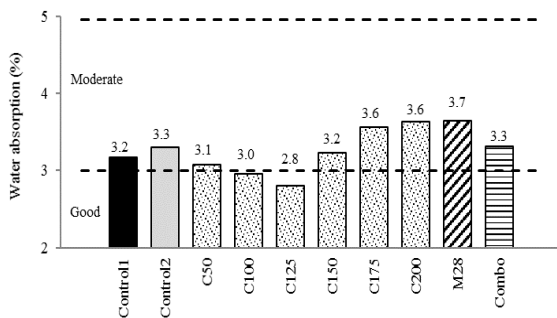


Figure 17. Results of water absorption test

in porosity of the mixtures, but percentage of water absorption starts to rise if the CCP amount goes beyond the defined limit, and that’s due to the presence of floating of unreacted CCP in the mix designs which has a tendency to absorb water.

Percentages of water absorption of the samples are categorized based on CEB-FIP standard [52]. Samples containing 125 kg/m³ CCP and MSG are in “good” and “moderate” categories, respectively. This shows a better performance of the sample containing 125 kg/m³ of CCP in comparison to MSG sample. Use of MSG may provide a condition for extra water absorption due to the unsustainability and discontinuity of mixture. Also, the data in Figure 17 show that application of using CCP and MSG, simultaneously in the mixture, have a relatively low effect on the reduction of percentage of water absorption in comparison to the sample with only MSG, and the category remains in the moderate region.

3. 2. 3. Electrical Resistivity Test Data of this test are shown in Figure 18 which indicates affirmative effect of CCP and MSG on increasing of electrical resistance. Figure demonstrates that by increasing the amount of CCP to 125 kg/m³ in mixture, specific electrical resistance rises, but resistance starts to reduce if the CCP amount goes beyond the limit, and this can be related to the role of free ions in atomic structure of material.

The categories on the figure, separated by the dashed lines, are the rate of corrosion in rebars in terms of electrical resistance. There are four levels of categories, low, low to moderate, high, and very high based on ACI 222R-01 [54] standard, and it can be seen that C125 and M28 samples have low and low to moderate corrosion rates, respectively.

Figure also shows, using CCP and MSG in mixture simultaneously, illustrate almost similar behavior as the sample with only MSG. It means that in this condition, the use of CCP illustrates no improvement in the mixture performance.

3. 3. The Statistical Variations The coefficient of variation (CV) Brown [55] is a measure for dispersion

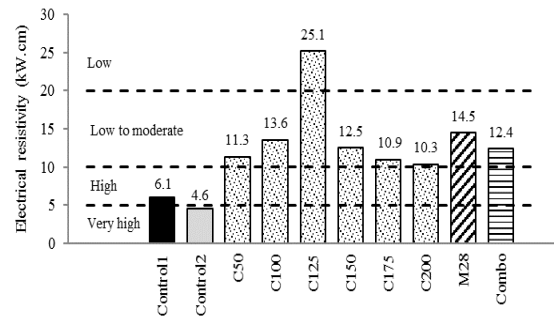


Figure 18. Results of electrical resistivity test

of probability distribution. It is often stated as a percentage, and is defined as the ratio of the standard deviation, σ to the mean value, μ .

Figure 19 shows the experimental data of variation coefficient for hardened concrete in comparison to fresh concrete regarding samples containing CCP. Observation of variation coefficients in Figure 19, indicates that there are more fluctuations in dispersion of probability distribution in fresh concrete in comparison to hardened concrete. This is indication of lower sensitivity in changing the dosage of CCP on hardened concrete with respect to fresh concrete tests. Figure 19 illustrates two distinguished results, the minimum effect of CCP on the properties of fresh concrete, is related to the slump flow and J-ring tests, whereas, this minimum effect on hardened concrete, is related to the compressive strength and water absorption tests. In contrast, the maximum effect of CCP on the properties of fresh and hardened concrete belongs to V-funnel $T_{5\text{minutes}}$ and electrical resistivity tests, respectively.

3. 4. Decision Making Method to Select the Optimal Mix Designs

In an overall approach, Table 9 is used to evaluate the effects of two applied admixtures on improving of fresh and hardened concrete properties. These properties were adopted from section 2.4. Mixture codes and concrete properties were tabulated in the table. The following steps in the table, explain the method of evaluation.

Step 1: Using the results from Figures 7 through 18, the evaluation was carried out to determine if any of the samples meets the requirements (i.e. falling within the acceptance criteria or having improvements in their properties relative to the control samples).

Step 2: For each property, samples meet the requirements are initially selected and listed.

Step 3: Frequency of selections for each mix design is counted.

Step 4: Finally, the samples are prioritized according to the frequency counted in step 3.

The results show that C125 (among the samples containing CCP) and Combo samples benefit from the

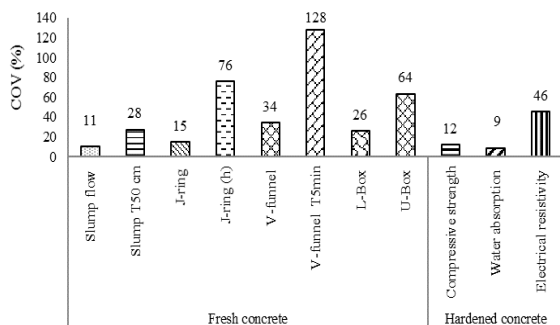


Figure 19. Variation coefficients of experimental data for samples containing CCP

highest improvement on concrete properties. M28 is next in the line.

CCP samples have higher mechanical property and durability in comparison to MSG sample. This is due to the stronger bond between aggregate and cement paste, as well as denser molecular structure in CCP. Appearance of superplasticizer in MSG sample, exhibits the improvement of the flowability in M28 sample, but on the other hand, superplasticizer can endanger the sustainability of the mixture. Whereas, CCP is able to eliminate this defect and sustains the mixture, since provides the sufficient viscosity for mixes. In the optimal dosage, C125 can be expected to have the best proportion in the components of the mixture. In the higher dosage, portion of CCP remains unreacted in the mixture and causes to reduce concrete characteristics.

In the Economic Analysis section, three selected samples, C125, Combo, and M28, are re-evaluated and finalized regarding cost- efficiency and practical engineering.

3. 5. Validation of Results

Figure 20 shares the values of optimal dosage of CCP (31.25%) and MSG consumption (7%), and compares them with the literature values from other researchers, introduced in section 1. The dashed lines on the figure illustrate the estimation of average values of CCP and MSG which were suggested in the literatures. These values are compared with the values obtained from the current research, and indicated as maximum off percentages of errors which are 23% and 26% for CCP and MSG, respectively. It should be noted that the chemical components in these two types of admixtures are not exactly identical in different regions which can be certainly influential on optimal dosages and, for this reasoning, the errors are normal and can be justified and neglected.

3. 6. Economic Analysis

Economic analysis is performed to figure out which admixture is more cost-effective to use. Table 10 is a summary of economic analysis for four mix designs, control sample 2, C125, M28, and combo. C125 were selected because of high performance among samples containing CCP (section 3.4). Cost estimation was performed on the basis of production of one cubic meter of concrete. In this research, the ratio of increase in strength to increase in cost relative to control sample 2 is referred as economic index for each mix design. This economic index is recognized as a factor for selection of the suitable economic condition among the mixtures. In calculating economic index, 28 days compressive strength was considered as a reference, since this is the most important property of concrete. The data in Figure 21 indicate that C125 sample with the value of 9.2, is more economical in comparison to other mixtures, because CCP is inexpensive and available in Iranian market.

TABLE 9. Comprehensive evaluation and prioritization of samples

Step	Mixture code	Properties											
		Fresh								Hardened			
		Slump flow	T _{50cm} Slump	J-ring	J-ring (h)	V-funnel	V-5min	L-box	U-box	Compressive strength	Water absorption	Electrical resistivity	
1	Control1	out*	out*	out*	out*	out*	out*	out*	out*	increase***	Moderate	High	
	Control2	within**	within**	within**	out*	out*	out*	within**	out*	Reference	Moderate	Very high	
	C50	within**	within**	within**	within**	out*	within**	within**	out*	increase***	Moderate	Low to moderate	
	C100	within**	within**	within**	within**	out*	within**	within**	out*	increase***	Good	Low to moderate	
	C125	within**	within**	out*	within**	within**	within**	within**	within**	increase***	Good	Low	
	C150	within**	within**	out*	out*	within**	within**	out*	out*	increase***	Moderate	Low to moderate	
	C175	out*	within**	out*	out*	within**	within**	out*	out*	increase***	Moderate	Low to moderate	
	C200	out*	out*	out*	out*	out*	out*	out*	out*	increase***	Moderate	Low to moderate	
	M28	within**	within**	within**	within**	out*	within**	within**	out*	increase***	Moderate	Low to moderate	
	Combo	within**	within**	within**	within**	within**	within**	within**	within**	increase***	Moderate	Low to moderate	
2	Initial selection	Control2	Control2							Control1			
		C50	C50				C50		C50				
		C100	C100	Control2	C50		C125	Control2		C100			
		C125	C125	C50	C100		C150	C100		C125			
		C150	C150	C100	C125		C175	C150		C175	C100		
		M28	C175	M28	M28		M28	M28		M28	C125		
		M28	M28	Combo	Combo		Combo	Combo		Combo	Combo		
		Combo	Combo										
3	Mixture code	Control1	Control2	C50	C100	C125	C150	C175	C200	M28	Combo		
	Frequency	1	4	7	8	9	5	4	1	7	9		
4	Prioritization	1. C125 and Combo C100 C50 and M28 C150 Control2 and C175											
		2. Control1 and C200											

* out of acceptance limits
 ** within acceptance limits
 *** increase in compressive strength

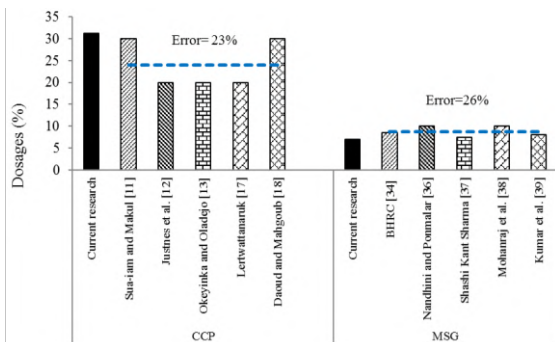


Figure 20. Verification of dosage of CCP and consumption of MSG via comparison with the literature values

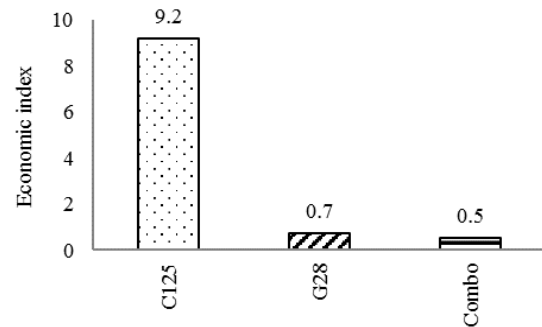


Figure 21. Estimated economic index based on compressive strength test

TABLE 10. Economic analysis for four mix designs

Mix design	Total Cost (\$)	Increase in cost relative to control sample 2 (%)	Compressive strength (MPa)	Increase in strength relative to control sample 2 (%)	Economic index
Control2	13.8	0.0	36.4	0.0	-
C125	14.5	5.1	53.4	46.7	9.2
M28	20.0	44.9	48.0	31.9	0.7
Combo	20.7	50.0	46.1	26.6	0.5

4. CONCLUSION

The followings are the most significant conclusions from the experimental work on fresh and hardened concrete samples:

1. The results show that, MSG has positive impacts on increasing of strength and durability of concrete. Also, it causes more flowability than CCP for the admixture. But, it cannot provide a sustainable concrete admixture and this is a kind of deficiency.
2. CCP can compensate the deficiency caused by MSG. CCP samples have higher mechanical property and durability in comparison to MSG sample. This is due to the denser molecular structure and stronger bond between aggregate and cement paste.
3. In a rational foresight, simultaneous application of admixtures, Combo, should be expected to have a proper mix design which benefits from MSG advantage, flowability and CCP advantages, sustainability, durability, and mechanical strength.
4. The variations in the CCP dosage often lead to higher coefficient of variations on fresh concrete rather than hardened concrete experiments. The V-funnel T5minutes test shows the maximum sensitivity to the amount of CCP, whereas the minimum sensitivity belongs to the water absorption test.
5. In an overall approach through the decision making method, the results show that Combo and C125 samples stand in the first priority among the entire samples. In this study, Code C125, refers to the sample containing the optimal dosage of CCP, 31.25%.
6. Regarding the economic analysis and practical engineering, the usage of CCP is more cost effective, because CCP is inexpensive and available in Iranian market.

5. ACKNOWLEDGMENTS

The authors would like to acknowledge the contribution of the following people, Dr. Naeini and his colleagues for providing us the mechanical testing facilities at Soil and Structural Laboratory.

6. REFERENCES

1. H., O. "Self Compacting High Performance Concrete." *Concrete International, Design and Construction*, Vol. 19, No. 7, (1997), 50–54. Retrieved from <https://www.sid.ir/en/Journal/ViewPaper.aspx?ID=134165>
2. Tregger, N., Gregori, A., Ferrara, L., and Shah, S. "Correlating dynamic segregation of self-consolidating concrete to the slump-flow test." *Construction and Building Materials*, Vol. 28, No. 1, (2012), 499–505. <https://doi.org/10.1016/j.conbuildmat.2011.08.052>
3. A.A., M., and F., A. D. "Application Of Nanotechnology In Self-Compacting Concrete Design." *International Journal of Engineering, Transaction B: Applications*, Vol. 22, No. 3, (2009), 229–244. Retrieved from <https://www.sid.ir/en/Journal/ViewPaper.aspx?ID=163471>
4. Abbas, S., Abbas, S., Ali, I., Ali, I., Abdulridha, A., and Abdulridha, A. "Behavior and Strength of Steel Fiber Reinforced Self-compacting Concrete Columns Wrapped by Carbon Fiber Reinforced Polymers Strips." *International Journal of Engineering, Transaction B: Applications*, Vol. 34, No. 2, (2020), 382–392. <https://doi.org/10.5829/IJE.2021.34.02B.10>
5. Kohnepooshi, O., Shadmand, M., and Hedayatnasab, A. "Strengthening of RC Beams using Steel Plate-fiber Concrete Composite Jackets: Finite Element Simulation and Experimental Investigation." *International Journal of Engineering, Transactions A: Basics*, Vol. 35, No. 1, (2022), 73–92. <https://doi.org/10.5829/ije.2022.35.01a.07>
6. Gibbs, J., Bartos, P. J. M., Zhu, W., Sonebi, M., and Tamimi, A. "Task 4—properties of hardened concrete." Final report of the European SCC project—Rational production and improved working environment through using self-compacting concrete, (1996).
7. Skarendahl, Å. "Market acceptance of self-compacting concrete, the Swedish experience." In Proceedings of the Second International Symposium on Self-Compacting Concrete Tokyo. 2001.
8. The European Guidelines for Self-Compacting Concrete (EFNARC), Specification, production and use, (2005).
9. Gao, C., Dong, Y., Zhang, H., and Zhang, J. "Utilization of distiller waste and residual mother liquor to prepare precipitated calcium carbonate." *Journal of Cleaner Production*, Vol. 15, No. 15, (2007), 1419–1425. <https://doi.org/10.1016/j.jclepro.2006.06.024>
10. Cao, M., Ming, X., He, K., Li, L., and Shen, S. "Effect of Macro-, Micro- and Nano-Calcium Carbonate on Properties of Cementitious Composites—A Review." *Materials*, Vol. 12, No. 5, (2019), 781. <https://doi.org/10.3390/ma12050781>
11. Sua-iam, G., and Makul, N. "Effect of limestone powder on the properties of self-consolidating concrete mixed with rice husk ash." *Engineering Journal of Research and Development*, Vol. 23, No. 4, (2012), 18–26.

12. Justnes, H., Østnor, T., De Weerd, K., and Vikan, H. "Calcedin marl and clay as mineral addition for more sustainable concrete structures." In Proceedings of the 36th International Conference on Our World in Concrete & Structures (pp. 14–16).
13. Okeyinka, O. M., and Oladejo, O. A. "The influence of calcium carbonate as an admixture on the properties of wood ash cement concrete." *International Journal of Emerging Technology and Advanced Engineering*, Vol. 4, No. 12, (2014), 432–437.
14. da Silva, P. R., and de Brito, J. "Durability performance of self-compacting concrete (SCC) with binary and ternary mixes of fly ash and limestone filler." *Materials and Structures*, Vol. 49, No. 7, (2016), 2749–2766. <https://doi.org/10.1617/s11527-015-0683-6>
15. Makul, N., and Sua-lam, G. "Properties of Self-Consolidating Concrete with Rice Husk Ash and Calcium Carbonate Powder." *ACI Materials Journal*, Vol. 115, No. 5, (2018), 675–684. <https://doi.org/10.14359/51702344>
16. EFNARC. Specification and guideline for self compacting concrete, (2002).
17. Lertwattanaruk, P., Sua-iam, G., and Makul, N. "Effects of calcium carbonate powder on the fresh and hardened properties of self-consolidating concrete incorporating untreated rice husk ash." *Journal of Cleaner Production*, Vol. 172, , (2018), 3265–3278. <https://doi.org/10.1016/j.jclepro.2017.10.336>
18. Daoud, O. M. A., and Mahgoub, O. S. "Effect of limestone powder on self-compacting concrete." *FES Journal of Engineering Sciences*, Vol. 9, No. 2, (2021), 71–78. <https://doi.org/10.52981/fjes.v9i2.680>
19. Cong, X., Gong, S., Darwin, D., and McCabe, S. L. "Role of Silica Fume in Compressive Strength of Cement Paste, Mortar, and Concrete." In *SL Report;90-2, University of Kansas Center for Research, Inc.* (pp. 1–37). University of Kansas Center for Research, Inc. Retrieved from <https://kuscholarworks.ku.edu/handle/1808/20405>
20. Nehdi, M., Pardhan, M., and Koshowski, S. "Durability of self-consolidating concrete incorporating high-volume replacement composite cements." *Cement and Concrete Research*, Vol. 34, No. 11, (2004), 2103–2112. <https://doi.org/10.1016/j.cemconres.2004.03.018>
21. Poon, C. S., Kou, S. C., and Lam, L. "Compressive strength, chloride diffusivity and pore structure of high performance metakaolin and silica fume concrete." *Construction and Building Materials*, Vol. 20, No. 10, (2006), 858–865. <https://doi.org/10.1016/j.conbuildmat.2005.07.001>
22. Duan, P., Shui, Z., Chen, W., and Shen, C. "Effects of metakaolin, silica fume and slag on pore structure, interfacial transition zone and compressive strength of concrete." *Construction and Building Materials*, Vol. 44, (2013), 1–6. <https://doi.org/10.1016/j.conbuildmat.2013.02.075>
23. Vikan, H., and Justnes, H. "Influence of silica fume on rheology of cement paste." In 3rd International Symposium on Self-Compacting Concrete (pp. 190–201). 2003.
24. Park, C. K., Noh, M. H., and Park, T. H. "Rheological properties of cementitious materials containing mineral admixtures." *Cement and Concrete Research*, Vol. 35, No. 5, (2005), 842–849. <https://doi.org/10.1016/j.cemconres.2004.11.002>
25. Elahi, A., Basheer, P. A. M., Nanukuttan, S. V., and Khan, Q. U. Z. "Mechanical and durability properties of high performance concretes containing supplementary cementitious materials." *Construction and Building Materials*, Vol. 24, No. 3, (2010), 292–299. <https://doi.org/10.1016/j.conbuildmat.2009.08.045>
26. Bouzoubaa, N., Bilodeau, A., Sivasundaram, V., Fournier, B., and Golden, D. M. "Development of ternary blends for high-performance concrete." *Materials Journal*, Vol. 101, No. 1, (2004), 19–29.
27. Gesoğlu, M., Güneş, E., and Özbay, E. "Properties of self-compacting concretes made with binary, ternary, and quaternary cementitious blends of fly ash, blast furnace slag, and silica fume." *Construction and Building Materials*, Vol. 23, No. 5, (2009), 1847–1854. <https://doi.org/10.1016/j.conbuildmat.2008.09.015>
28. Valipour, M., Pargar, F., Shekarchi, M., and Khani, S. "Comparing a natural pozzolan, zeolite, to metakaolin and silica fume in terms of their effect on the durability characteristics of concrete: A laboratory study." *Construction and Building Materials*, Vol. 41, (2013), 879–888. <https://doi.org/10.1016/j.conbuildmat.2012.11.054>
29. Shaikh, F., Kerai, S., and Kerai, S. "Effect of micro-silica on mechanical and durability properties of high volume fly ash recycled aggregate concretes (HVFA-RAC)." *Advances in concrete construction*, Vol. 3, No. 4, (2015), 317–331. <https://doi.org/10.12989/acc.2015.3.4.317>
30. Zhang, P., Gao, J.-X., Dai, X.-B., Zhang, T.-H., and Wang, J. "Fracture behavior of fly ash concrete containing silica fume." *Structural Engineering and Mechanics*, Vol. 59, No. 2, (2016), 261–275. <https://doi.org/10.12989/sem.2016.59.2.261>
31. Zhang, Z., Zhang, B., and Yan, P. "Comparative study of effect of raw and densified silica fume in the paste, mortar and concrete." *Construction and Building Materials*, Vol. 105, (2016), 82–93. <https://doi.org/10.1016/j.conbuildmat.2015.12.045>
32. Gupta, T., Chaudhary, S., and Sharma, R. K. "Mechanical and durability properties of waste rubber fiber concrete with and without silica fume." *Journal of Cleaner Production*, Vol. 112, (2016), 702–711. <https://doi.org/10.1016/j.jclepro.2015.07.081>
33. Barati, R., Ali Sahaf, S., Jamshidi, M., and Razazpor, A. "Examining the Impact of Micro Silica Gel Additive on the Compressive Strength and Water Absorption of Roller Compacted Concrete Pavement." *Modern Applied Science*, Vol. 10, No. 5, (2016). <https://doi.org/10.5539/mas.v10n5p194>
34. "Testing hardened concrete, British Standard." Compressive Strength of Test Specimens, BS EN, (2009), 12390–12393.
35. Joshi, R. C., Chatterji, S., Achari, G., and Mackie, P. "Reexamination of ASTM C 1202—Standard Test Method for Electrical Indication of Concrete's Ability to Resist Chloride Ion Penetration." *Journal of testing and evaluation*, Vol. 28, No. 1, (2000), 59–61.
36. Nandhini, K., and Ponmalar, V. "Microstructural behaviour and flowing ability of self-compacting concrete using micro- and nano-silica." *Micro & Nano Letters*, Vol. 13, No. 8, (2018), 1213–1218. <https://doi.org/10.1049/mnl.2018.0105>
37. Sharma, S. K. "Properties of SCC containing pozzolans, Wollastonite micro fiber, and recycled aggregates." *Heliyon*, Vol. 5, No. 8, (2019), e02081. <https://doi.org/10.1016/j.heliyon.2019.e02081>
38. Mohanraj, A., Senthilkumar, V., and Nandhini, K. "Effect of Micro-silica on the Fresh and Hardened Properties of Self-compacting Concrete Containing Pre-absorbed Superabsorbent Polymer." *Silicon*, Vol. 13, No. 10, (2021), 3569–3581. <https://doi.org/10.1007/s12633-020-00862-y>
39. Kumar, V., Imam, A., Srivastava, V., and Kushwaha, A. Y. "Effect of micro silica on the properties of hardened concrete." *International Journal of Engineering Research and Development*, Vol. 13, No. 11, (2017), 8–12.
40. ASTM C150, 'standard Specification for Portland Cement' American Society for Testing and Materials, (2005).
41. ASTM C33, 'Standard specification for concrete aggregates.' *Philadelphia, PA: American Society for Testing and Materials*, (2003).
42. Darvishvand, H. R., Taghia, S. A. H. S., and Ebrahimi, M. "The

- effect of size and shape of aggregate on compressive strength and ductility of concrete.” *Cement Wapno Beton*, Vol. 26, No. 1, (2021), 46–54.
<https://doi.org/https://doi.org/10.32047/CWB.2021.26.1.5>
43. Catalogue of silica gel, Sika company Pars Alborz structures (Parsyka), Retrieved from <http://parsica.co/index.php/features/header-styles/2018-11-16-09-57-27>
 44. Catalogue of Superplasticizer, Retrieved from <https://www.abadgarangroup.net/en-US/index>
 45. Catalogue of Air entrainment, Sika company Pars Alborz structures (Parsyka), Retrieved from <http://parsica.co/index.php/features/header-styles/2018-11-16-10-04-14>
 46. ACI 211.89. “Standard Practice for Selecting Proportions for Normal Heavyweight, and Mass Concrete.” American Concrete Institute Farmington Hills, MI, USA.
 47. ASTM C192. ‘Standard Practice for Making and Curing Concrete Test Specimens in the Laboratory,’ ASTM International: West Conshohocken, PA, USA, (2007).
 48. BS 1881. ‘Method of normal curing of test specimens (20 °C method).’ Testing concrete, Part 111, (1983).
 49. BS 1881. ‘Method for making test cubes from fresh concrete.’ Testing concrete, Part 108, (1983).
 50. Ganesh Babu, K., and Saradhi Babu, D. “Performance of fly ash concretes containing lightweight EPS aggregates.” *Cement and Concrete Composites*, Vol. 26, No. 6, (2004), 605–611.
[https://doi.org/10.1016/S0958-9465\(03\)00034-9](https://doi.org/10.1016/S0958-9465(03)00034-9)
 51. ASTM 642-97. ‘Standard Test Method for Density, Absorption, and Voids in Hardened Concrete.’ Annual book of ASTM standards. 4.01, (2000).
 52. International Federation for Structural Concrete, CEB-FIP, (1998).
 53. Ingason, H., Gustavsson, S., and Dahlberg, M. “Swedish National Testing and Research Institute;” Fire Experiments in a Two Dimensional Rack Storage: Brandforsk project, (1994), 701–917.
 54. ACI Committee 222. ‘Protection of metals in concrete against corrosion.’ ACI 222R-01, (2001).
 55. Brown, C. E. “Coefficient of Variation.” In Applied Multivariate Statistics in Geohydrology and Related Sciences (pp. 155–157). Berlin, Heidelberg: Springer Berlin Heidelberg.
https://doi.org/10.1007/978-3-642-80328-4_13

Persian Abstract

چکیده

اثرات دو افزودنی، پودر کربنات کلسیم (CCP) و ژل میکروسیلیکا (MSG) روی خواص بتن خود متراکم (SCC) مانند کارایی، مقاومت فشاری و دوام بررسی می‌شود. نتایج نشان می‌دهد که در برخی موارد، بتن با MSG قادر به ایجاد شرایط پایدار نیست، اگرچه روانی بالاتر است. نتایج آزمایشگاهی نشان می‌دهد که اثر CCP بر پایداری، مقاومت و دوام مخلوط قابل توجه است. طرح اختلاط Combo برای بهره‌مندی از ویژگی‌های مثبت دو افزودنی معرفی می‌شود. نتایج روش تصمیم‌گیری نشان می‌دهد که این مخلوط می‌تواند به عنوان یک نمونه مناسب همراه با نمونه حاوی دوز بهینه CCP در نظر گرفته شود. علاوه بر این، این روش نشان می‌دهد که دوز بهینه CCP 31/25٪ است که منجر به بهترین بهبود در خصوصیات بتن تازه و سخت شده می‌شود. در مهندسی کاربردی، تحلیل اقتصادی نشان می‌دهد که استفاده از CCP مقرون به صرفه‌تر است زیرا در بازار ایران در دسترس بوده و ارزان است.



Structural Behavior of Reinforced Concrete Horizontally Curved Box Beam with Opening

A. M. Hashim*, A. Y. Ali

Collage of Materials Engineering, University of Babylon, Hillah, Iraq

PAPER INFO

Paper history:

Received 16 September 2021

Received in revised form 26 November 2021

Accepted 02 December 2021

Keywords:

Circular Box Beam

Crack Pattern

Deformation Response

Ductility

Failure Mode

Opening

Stiffness

ABSTRACT

This work is dedicated to survey the structural reinforced concrete's behavior horizontally curved box beams with and without opening. Seven horizontally circular box beams were examined in the experimental work, one without opening, three with vertical opening and three with transverse opening. The test program includes the main variables; direction of opening, location of opening through profile of curved beams (effect of combination of internal forces). The beams were tested as a continuous beam with two spans, each span represents a quarter circle and under the action of two point loads each load located at top face of midspan of beam. The findings indicate that the ultimate load capacity was decreased for all specimens (CB2.V37, CB3.V60, CB4.V82, CB5.T37, CB6.T60 and CB7.T82) by about (5, 11.5, 1.5, 1.5, 46.4 and 18.66%) respectively, compared to the control CB1. When compared with the control specimen CB1, all specimens were indicating an increase in Service deformations in terms of deflection and twisting angle at midspan of the circular beams. The ductility was deteriorated for all specimens with opening (CB2.V37, CB3.V60, CB4.V82, CB5.T37, CB6.T60 and CB7.T82), as a percent was about (13.88, 15.3, 19.62, 0.5, 0.5 and 13.88%) respectively, compared with that of control specimen CB1. As a result, generally, a clear degradation with different percentages in overall structural behavior of box beams horizontally curved containing opening according to the location and direction of openings, in this study the transverse openings at 60°, where the opening under the combined maximum (shear and torsion) was led to a catastrophic decrease in the structural performance of horizontally curved box beam.

doi: 10.5829/ije.2022.35.04a.17

1. INTRODUCTION

Due to its structural efficiency, improved stability, serviceability, construction economy, and attractive aesthetics, box girders have achieved widespread popularity in highway and bridge systems [1]. These hollow sections are utilized to convey electrical and mechanical services while also lowering story height and construction costs. Many studies including experimental, theoretical and numerical investigations on the behavior of box beams have mainly concentrated on straight, single or multi-cell box girders, developing of numerical methods for analysis to evaluate the nonlinear response, collapse manner, and ultimate failure loads of multi-cell RC (reinforced concrete) box girder bridges under gradually rising static loads, a

comparison of experimental and computational analyses was carried out [2–6].

It is becoming more usual to use horizontally curved beams for urban interchanges or highway bridges, therefore it is required to build structures that are curved in plan. The curved beams shape can be circular, elliptical, or parabolic, and it's occasionally made up of circular arcs of various radii r and centers [7]. Many experimental investigations have looked into the structural behavior of curved beams that are loaded transversely to their plane and are exposed to torsion as well as bending and shear [8–15].

The most frequent shapes of openings in practice are circular and rectangular. Service pipes, such as plumbing, require circular apertures, but air-conditioning ducts, which are typically rectangular, require rectangular

*Corresponding Author Email: ameer.has81@yahoo.com
(A. M. Hashim)

openings. rectangular in shape. In regards to the presence of openings in the straight solid beams only, many researchers were concentrated on its structural behavior including deformations and stiffness, collapse mechanism, as well as classifying the size of openings as small or large openings, location of openings and its effect on the beam where subjected to flexural moment, shear and torsion either individually or in combination, also effect of shape of openings was studied [16–36]. Only one experimental study including horizontally curved solid beam with openings have been conducted [37]. It can be concluded from the above that there is no research on box beams with openings and horizontally curved.

Box beams may carry a variety of cables and ducts for services such as water supply, sewage, air conditioning, electricity, telephone, and computer network, may necessitate an opening in web or flange to reach and maintain those wires and ducts. Structural behavior of box beam curved in a plane with an opening in the transverse or vertical direction has not been thoroughly investigated, so the aim of this research is to:

1. Evaluate the structural response experimentally in terms of midspan deflection and midspan-twisting of horizontally curved box beams made of reinforced concrete with and without openings.
2. Examined experimentally variation in the mode of failure of reinforced concrete horizontally curved box beams with and without opening.
3. Investigate the influence of the presence of opening on ductility and stiffness criteria of reinforced concrete horizontally curved box beams.

2. EXPERIMENTAL PROGRAM

2.1. Material Properties

2.1.1. Concrete Self-Compacting concrete was selected for casting the samples due to narrow spaces and difficult geometry of box section. The mix proportions were designed by trial and error in accordance with the

European Guidelines for Self-Compacting Concrete (EFNARC) as proposed in literature [38] with a water/cement ratio of 0.43 by weight as shown in Table 1. Ordinary Portland cement (Type I) commercially available was utilized to cast all of the specimens throughout this research. Finely ground limestone powder, having calcium carbonate (CaCO_3) as its main component was utilized. The maximum size of rounded coarse aggregate and fine aggregate used in the current study were (12.5 and 4.75) mm respectively. A high range water reducing agent (HRWRA) superplasticizer made by sika company called **Sika ViscoCrete -5930-L** which meets **ASTM C-494** Types **A** and **F** used in this work. Following standard tests, the compressive and splitting tensile strengths of concrete were found as average 40 and 3.6 MPa, respectively.

2.1.2. Steel Reinforcement

Three different sizes of deformed bars ($\varnothing 12$, $\varnothing 10$ and $\varnothing 8$) were used, ($\varnothing 12\text{mm}$, $\varnothing 10\text{mm}$) for longitudinal reinforcement (circumference) and deformed bars of size ($\varnothing 8\text{mm}$) for closed stirrups. The steel reinforcement was assessed in accordance with to ASTM-A615/A-615M-05a. The yield stress of sizes ($\varnothing 12$, $\varnothing 10$ and $\varnothing 8$) were (560, 520 and 460 MPa) respectively.

2.2. Description of Specimens

Table 2, shows circular beam specimens CB1- CB7.T82 designation. Seven semi-circular continuous curved box beams were

TABLE 1. Mix proportion of self-compacting concrete (kg/m^3)

Materials	Proportions of mix
Cement	350
Limestone powder	100
Coarse aggregate	830
Fine aggregate	830
Water	150.5
Superplasticizer	8

TABLE 2. Designation and details of tested circular beam specimens

Specimen designation	Direction of opening	Location of opening	Effect of internal force at opening
CB1	---	---	---
CB2.V37	Vertical	37°	Moderate (shear, moment and torsion)
CB3.V60	Vertical	60°	Maximum (shear and torsion)
CB4.V82	Vertical	82°	Maximum (shear and moment)
CB5.T37	Transverse	37°	Moderate (shear, moment and torsion)
CB6.T60	Transverse	60°	Maximum (shear and torsion)
CB7.T82	Transverse	82°	Maximum (shear and moment)

designed in accordance with (ACI 318-19), (ACI 314R-16) and dimensions obeys AASHTO LRFD Bridge Design Specifications [39–41], consisting of two spans with hinged supports at both ends and a roller at the middle support, has a radius 1150 mm measured to the center line of cross section of the box beam as illustrated in Figure 1(a), and having cross section of dimensions 250 mm overall depth and 250 mm width with a top flange width 360mm, see Figure 1(b). The cross section of the beam includes hole with dimensions (130×130) mm to represent a box beam along the beam length, as shown in Figure 1(b). The ends of all beams extended 50 mm beyond the support’s centerlines. These beams were subjected to two-point loads at the middle of each span (angle 45°). Steel reinforcement (6Ø12) mm deformed bars were provided for top negative moment regions, (4Ø10) mm for bottom positive moment regions and (6Ø10+2 Ø8) mm as longitudinal torsion reinforcement with clear cover of 20 mm. The closed stirrups of Ø8 mm reinforcing bar were placed at 90mm center to center from angle (0) to angle (40°), and placed at 45mm center to center from angle (40°) to angle (90°) along the beam length for each span, noting that the angle measured from exterior support toward the interior support. Six beam specimens had openings with dimensions of (80*80 mm), Figures 1 and 2 show the details of cut of obstruction rebar at vertical opening of specimens (CB2.V37-CB4.V82) and details of cut of obstruction rebar at transverse opening of specimens (CB5.T37-CB7.T82), respectively, while the control beam was manufactured without opening. The location of opening through each span of beam was marked by angle measured from exterior support to the center of opening. The details of cut of obstruction rebar at opening of specimens are shown in Figure 3.

2. 3. Test Setup and Procedure Figure 4 shows the Test setup, including supporting, loading conditions and instruments. All specimens were setup inside testing machine which has a capacity of (2000 kN). The supporting system was hinged at exterior ends and roller

at the inner support. Four linear variable differential transformers (LVDTs) of (0.01mm precision, 100mm maximum capacity) to measure vertical deflection and twisting at midspan, two LVDTs one localized at exterior edge and the other at interior edge for each span of beam, see Figure 4 (a-c).

As load protocol, each specimen was subjected to monotonic load was applied gradually until failure, under two-point loading, each load applied at midspan of each panel of test specimen.

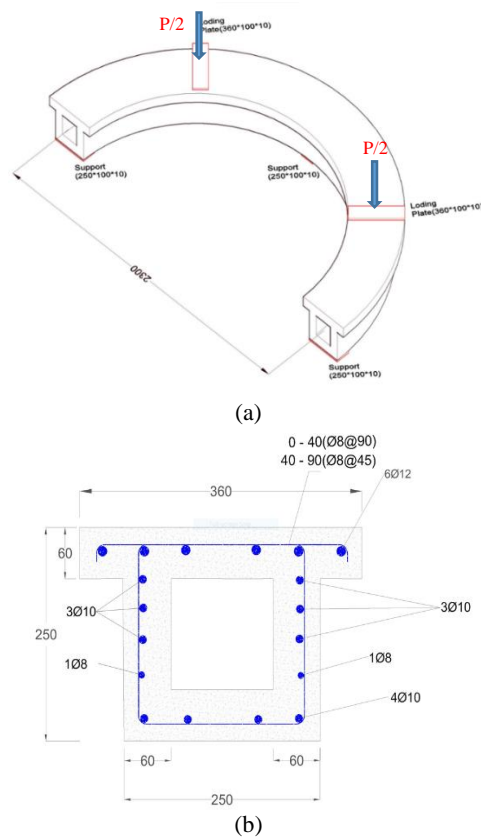


Figure 1. (a) Geometry and loading of all specimens (b) Cross section and reinforcement (all units in millimeters)

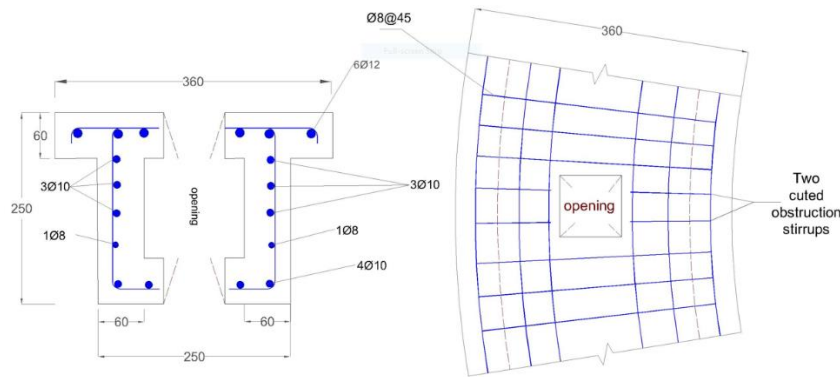


Figure 2. Details of cut of obstruction rebar at opening of specimens (CB2.V37- CB4.V82) (all units in millimeters)

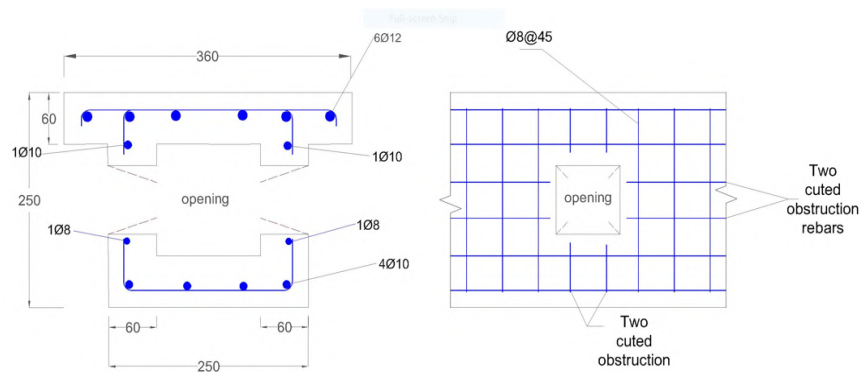


Figure 3. Details of cut of obstruction rebars at opening of specimens (CB5.T37- CB7.T82) (all units in millimeters)

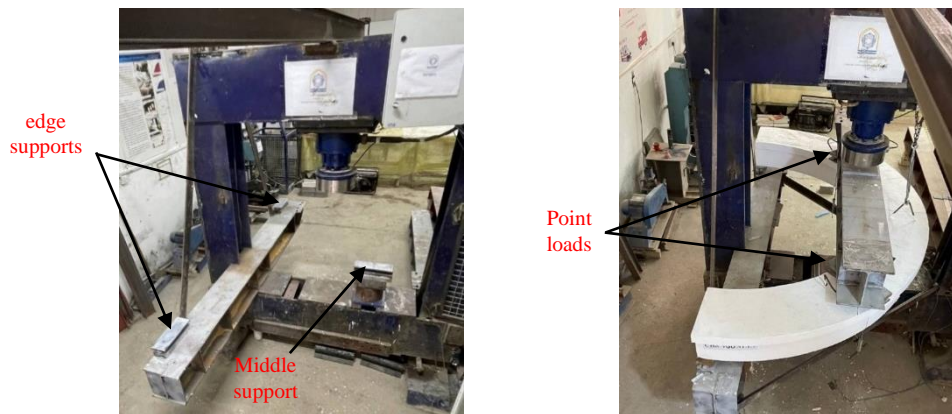
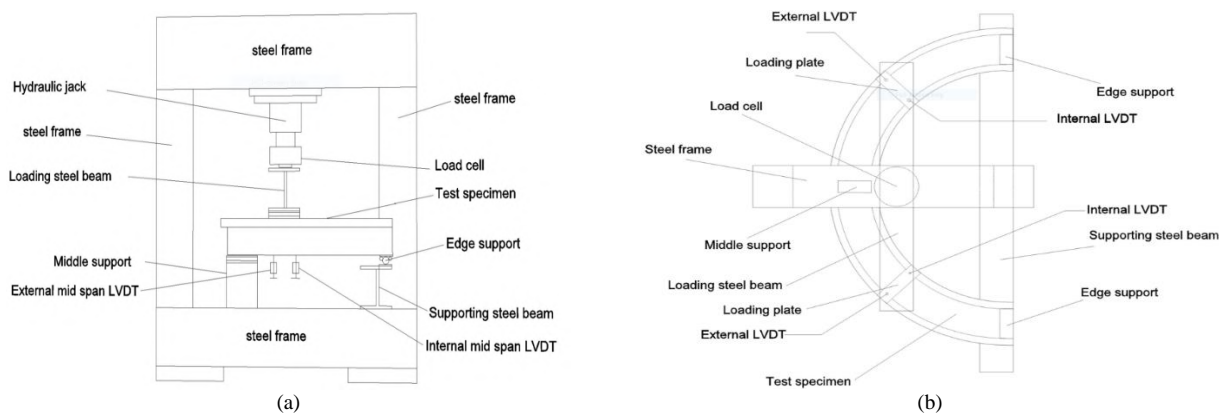


Figure 4. Test setup layout (a) Side view schematic drawing (b) Top view schematic drawing (c) photos

3. EXPERIMENTAL RESULTS AND DISCUSSION

3.1. Crack Pattern and Failure Modes The control specimen CB1 failed in a torsional-shear manner. At a load of around 50 kN, the first flexural crack was seen on the top face of highest negative moment (internal support). As the load was increased further, several flexural cracks observed at top face near internal support, at bottom face near midspan, and torsional-shear in the zones between the internal support and the loading

points, Figure 5(a) shows a photograph of the specimen after failure. The ultimate load of specimen CB1 was measured 407.25 kN.

Figure 5(b) represent the photograph of specimen CB2.V37 after failure. While, the diagonal crack was appeared in one corner of lower vertical opening at load of 50 kN, no considerable change in Crack pattern and failure modes of specimen CB2.V37, which includes vertical opening between the applied load and exterior support spaced at distance $d/2=125$ mm from the applied

load (37° measured from exterior support to the center of opening) by compare with control specimen CB1. It can be inferred that the existence of vertical openings at a 37° angle lowers the ultimate load capacity by roughly 5% (relative to the control beam), which was 385.74 kN.

Figure 5(c) represent the photograph of specimen CB3.V60 after failure, this specimen includes vertical opening positioned exactly at angle 60° measured from exterior support to the center of opening (in zone between the applied loads and internal support). Firstly, the flexural and diagonal cracks of specimen CB3.V60 were spread in a manner similar to control specimen CB1. The first visible inclined cracks at the corners of lower and upper vertical openings at load 90 kN were created. The increasing of applied load was accompanied by rapid propagation of diagonal cracks at the corners of lower vertical opening, causing frame type failure mode at vertical opening. It can be noted, that the presence of vertical openings at an angle (60°) diminish the ultimate load capacity by roughly 11.5% (when compared to control beam CB1) with maximum ultimate load capacity was about 360.3 kN.

Figure 5(d) shows the photograph of specimen CB4.V82 after failure, which includes vertical opening spaced at distance $d/2=125$ mm from face of internal support (82° measured from exterior support to the center of opening). The mode of failure of specimen CB4.V82 was torsional-shear, analogous to failure mode of control specimen CB1. Furthermore, all types of cracks were behaving in a mode similar to that of control specimen CB1. The ultimate load of beam CB4.V82 was measured 400.55 kN by forming large oblique torsional-shear cracks in zones between interior support and points of loading, caused very slit reduction in the ultimate load capacity (compared with control beam) was about 1.5%. Figure 5(e) shows the photograph of specimen CB5.T37 after failure. Specimen CB5.T37 includes transverse opening between the applied load and exterior support spaced at distance $d/2=125$ mm from the applied load (37° measured from exterior support to the center of opening). The diagonal crack was appeared in lower corner of transverse opening at load of 85 kN. Slight effect of presence of opening on the ultimate load capacity of Specimen CB5.T37 compared with control

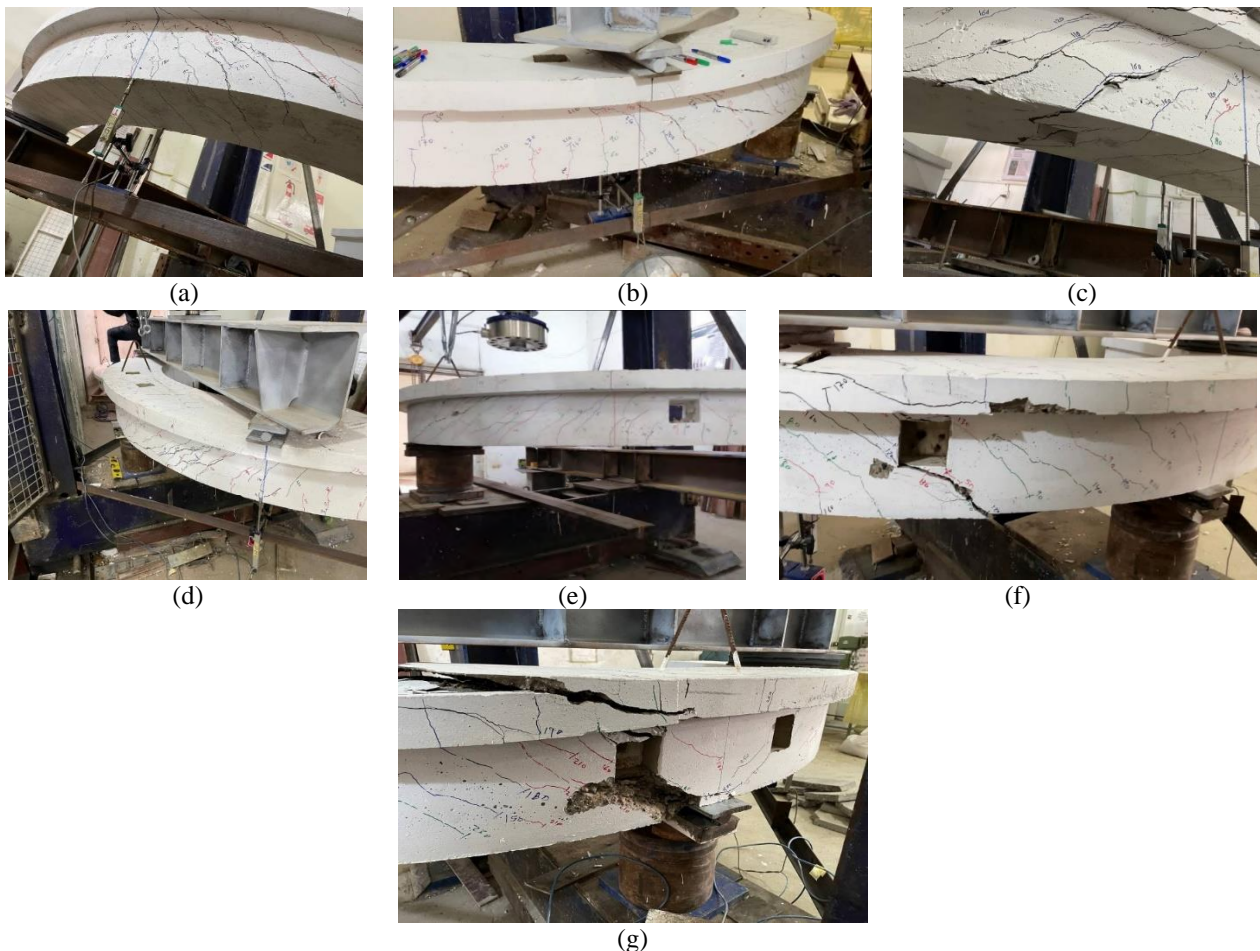


Figure 5. Specimens after failure: (a-g) specimens CB1- CB7.T82

beam CB1 was measured 401 kN, which was less than that for CB1 by about 1.5%. The mode of failure and behavior (shape and widen) of flexural, torsional and shear cracks were similar to that of control beam CB1.

Figure 5(f) presents the photograph of specimen CB6.T60 after failure. Specimen CB6.T60 includes transverse opening positioned exactly at angle 60° measured from exterior support to the center of opening (in zone between the applied loads and internal support). Firstly, the specimen CB6.T60 was loaded until the first crack appears at a load of 50 kN at the skew corners (beam type) of the transverse opening, also flexural torsional and shear cracks were observed, versus the increase in applied load in a pattern hassling to control specimen CB1. As load increased further, rapid widening of diagonal cracks at the corners of transverse opening led to a frame type failure mode at opening zone which occurred at ultimate load of 218 kN, indicating a large reduction by about 46.4% when compared with a control CB1.

Figure 5(g) illustrates the photograph of specimen CB7.T82 after failure. Specimen CB7.T82 includes transverse opening spaced at distance $d/2=125$ mm from face of internal support (82° measured from exterior support to the center of opening). At load about 80 kN, cracks were noticed in the top and bottom skew corners of the transverse openings as a result of the concentration of stresses at these regions. In general, behavior of flexural, torsional and shear cracks were identical to that of control beam CB1. The ultimate load of beam CB7.T82 was about 331.48 kN by forming sudden shear cracks at top and bottom cords of the opening (frame type failure mode) near internal support. When compared to control CB1, the presence of a transverse opening at an angle (82°) resulted in an 18.66 % reduction in ultimate load capacity.

3.2. Deformation Response

In this experimental work, deformations represent a deflection and twisting at midspan of the circular beams. Deformations response of circular beams could be described by the load-midspan deflection relationships as well as torsional moment-midspan twisting relationships at service loads (approximately 65% of maximum load) as proposed in [42]. Figures 6 and 7 represent the load-midspan deflection and torsional moment-midspan twisting response for specimens with vertical opening and transverse opening, respectively, compared to the control CB1. Furthermore, the service deflection, twisting and their contrast percentages compared with the control specimens were as shown in Table 3. The specimens (CB2.V37, CB3.V60 and CB4.V82) showed a clear increase in service midspan deflection and midspan twisting with a range (0-8.38%) and (21.6-103.3%), respectively, noticed that this increase corresponding to the reduction in ultimate load compared with the control

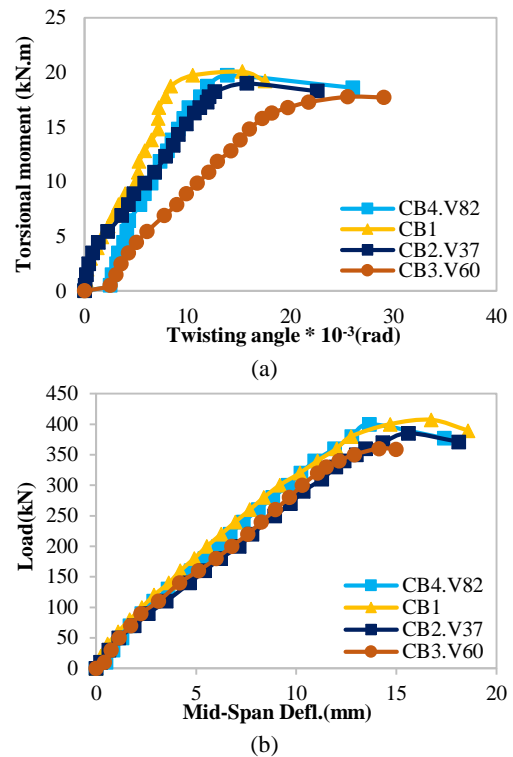


Figure 6. (a) Torsional moment-midspan twisting angle response for specimens with vertical opening (b) Load-midspan deflection response for specimens with vertical opening

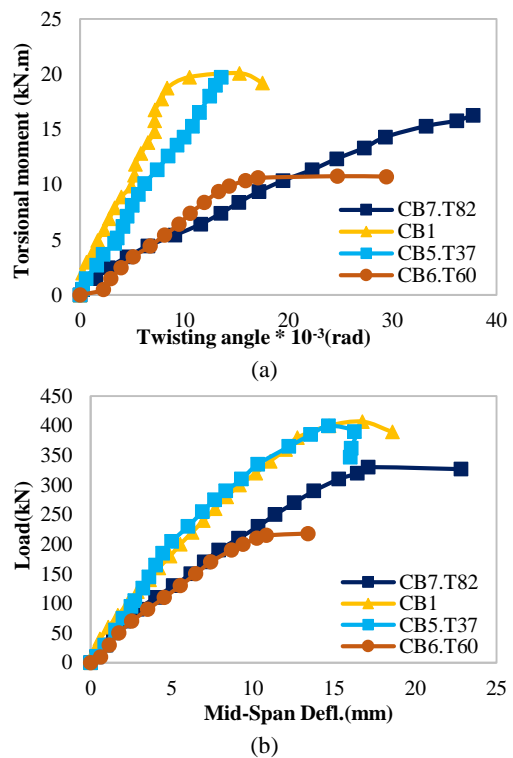


Figure 7. (a) Torsional moment-midspan twisting angle response for specimens with transverse opening (b) Load-midspan deflection response for specimens with transverse opening

TABLE 3. Service deformations of tested specimens

Specimen designation	Service deflection, Δs (mm)*	$\frac{\Delta s_i - \Delta s_r}{\Delta s_r} \times 100\%$ (**)	Service twisting, θs (Radian) $\times 10^{-3}$	$\frac{\theta s_i - \theta s_r}{\theta s_r} \times 100\%$ (**)
CB1.L1	8	---	6.15	---
CB2.V37.L1	8.66	8.38	7.48	21.6
CB3.V60.L1	8	0	12.5	103.3
CB4.V82.L1	8.11	1.37	8.05	30.9
CB5.T37.L1	7.06	-11.75	8.8	43
CB6.T60.L1	6.43	19.6	10.53	71.2
CB7.T82.L1	9.45	18.1	20.55	234.1

* (Pser.=0.65 Pult.) [42]

** Δs_r = Service deflection of the reference CB; Δs_i =Service deflection of the considered CB

CB1. The specimens (CB6.T60 and CB7.T82) showed a large increase in service midspan deflection and midspan twisting with a range (18.1-19.6)% and (71.2-234.1)% respectively, noticed that this increase were with the reduction in ultimate load compared with the control CB1, while the specimen CB5.T37 did not show an increase in the service midspan deflection, while an increase in service midspan twisting was about 43%.

3. 3. Ductility

Ductility can be defined as the ability to sustain inelastic deformations without lacking of the load carrying capacity prior to failure. The vertical displacement at maximum load Δu divided by vertical displacement at service load Δs is used to estimate ductility factors in the ongoing investigation (approximately 65 percent of maximum load) as proposed in [42]. Ductility factor μ was defined as $\mu = (\frac{\Delta u}{\Delta s})$, which proposed in [42]. As shown in Table 4, the presence of vertical openings was led to a reduction in the ductility of specimens (CB2.V37, CB3.V60 and CB4.V82) by (13.88%, 15.3%, 19.62%), respectively, compared to the control CB1. Furthermore, the reduction in the ductility of specimens with transverse opening

(CB5.T37, CB6.T60 and CB7.T82) was (0.5%, 0.5%, 13.88%), respectively, compared to the control CB1.

3. 4. Stiffness Criteria

Stiffness κ is defined as the amount of force necessary to cause unit deformation in a member. The slope of the secant drawn to each cycle in the hysterical curve at loading 0.75 times the maximum load of that cycle was measured as stiffness criteria as proposed in literature [43]. In this work Stiffness κ was defined as the ratio between the (0.75 of max applied load (P_{max})) and corresponding displacement, considering that each specimen subjecting to only one cycle of loading, Table 5 listed the variation in Stiffness κ compared to the control specimen CB1, where κ_i is stiffness of the considered beam and κ_r stiffness of the control beam. As a comparison with a control CB1, the stiffness of specimens with vertical opening showed stiffness degradation by about (14.11%, 10.2% and 3.98%) for (CB2.V37, CB3.V60 and CB4.V82), respectively. As specimens with transverse opening, a degradation was about (31.78% and 33%) for (CB6.T60 and CB7.T82), respectively, while the presence of opening at an angle (37°) for specimen CB5.T37 had no effect on its stiffness compared to the control CB1.

TABLE 4. Ductility factor of tested specimens

Specimen Designation	Service Deflection, Δs (mm)*	Ultimate Deflection, Δu (mm)	Ductility Factor, μ ($\frac{\Delta u}{\Delta s}$)	$\frac{\mu_i - \mu_r}{\mu_r} \times 100\%$ (**)
CB1.L1	8	16.75	2.09	---
CB2.V37.L1	8.66	15.6	1.8	-13.88
CB3.V60.L1	8	14.14	1.77	-15.3
CB4.V82.L1	8.11	13.65	1.68	-19.62
CB5.T37.L1	7.06	14.66	2.08	-0.5
CB6.T60.L1	6.43	13.4	2.08	-0.5
CB7.T82.L1	9.45	17.1	1.8	-13.88

* (Pser=0.65 Pult.) [42]

** μ_r = Ductility of the control CB; μ_i = Ductility of the considered CB

TABLE 5. Stiffness criteria of tested specimens

Specimen Designation	0.75 P _{max} * (kN)	Deflection at 0.75 P _{max} (mm)	Stiffness, κ (kN/mm)	$\frac{\kappa_i - \kappa_r}{\kappa_r} \times 100\%$ (**)
CB1	305.44	9.37	32.6	----
CB2.V37	289.3	10.35	28	-14.11
CB3.V60	270.22	9.23	29.27	-10.2
CB4.V82	300.4	9.6	31.3	-3.98
CB5.T37	300.75	9.03	33.3	2.14
CB6.T60	163.5	7.35	22.24	-31.78
CB7.T82	248.61	11.38	21.84	-33

* max applied load

** κ_i =Stiffness of the considered CB; κ_r = Stiffness of the control CB

4. CONCLUSIONS

The current researchers focused into how the inclusion of an opening affects the structural behavior of horizontally curved box beams. The following conclusions may be drawn from the experimental findings of this study.

1. The ultimate load capacity was decreased for specimens with vertical opening (CB2.V37, CB3.V60 and CB4.V82) by about (5%, 11.5% and 1.5%) respectively, while for specimens with transverse opening (CB5.T37, CB6.T60 and CB7.T82) were about (1.5%, 46.4% and 18.66%) respectively, as compared to the control CB1. It can be concluded that the presence of opening at an angle 60° where maximum shear and torsion in both directions, caused a largest lack in ultimate load capacity of the beam.
2. As mode of failure, no alteration was observed in specimens CB2.V37, CB4.V82 and CB5.T37, while for specimens CB3.V60, CB6.T60 and CB7.T82 was conversion from torsional-shear failure mode of control specimen CB1 to frame- type failure at opening zone.
3. Service response for all specimens with opening in terms of deflection and twisting angle at midspan of the circular beams were adversely affected (increased) when compared with the control specimen CB1.
4. The ductility was decreased for all specimens with opening (CB2.V37, CB3.V60, CB4.V82, CB5.T37, CB6.T60 and CB7.T82), as a percent was about (13.88%, 15.3%, 19.62%, 0.5%, 0.5% and 13.88%), respectively, compared with that of control specimen CB1.
5. The specimens containing opening were shown a clear degradation in its stiffness, except the stiffness of specimen CB5.T37 was not affected as a comparison with stiffness of control specimen CB1.

5. REFERENCES

1. Gupta, P. K., Singh, K. K., and Mishra, A. "parametric study on behaviour of box-girder bridges using finite element method." *Asian Journal of Civil Engineering (Building and Housing)*, Vol. 11, No. 1, (2010), 135–148.
2. Wasti, S. T., and Scordelis, A. C. "Comparative Structural Behavior of Straight, Curved and Skew Reinforced Concrete Box Girder Bridge Models." In *Analysis and Design of Bridges* (pp. 191–211). Dordrecht: Springer Netherlands. https://doi.org/10.1007/978-94-009-6122-7_7
3. Kurian, B., and Menon, D. "Estimation of Collapse Load of Single-Cell Concrete Box-Girder Bridges." *Journal of Bridge Engineering*, Vol. 12, No. 4, (2007), 518–526. [https://doi.org/10.1061/\(ASCE\)1084-0702\(2007\)12:4\(518\)](https://doi.org/10.1061/(ASCE)1084-0702(2007)12:4(518))
4. Arendts, J. G. Load distribution in simply supported concrete box girder highway bridges. Iowa State University, 1969.
5. Razaqpur, A. G., Nofal, M., and Mirza, M. S. "Nonlinear analysis of prestressed concrete box girder bridges under flexure." *Canadian Journal of Civil Engineering*, Vol. 16, No. 6, (1989), 845–853. <https://doi.org/10.1139/189-127>
6. Luo, Q. Z., Tang, J., and Li, Q. S. "Calculation of Moments on Top Slab in Single-Cell Box Girders." *Journal of Structural Engineering*, Vol. 129, No. 1, (2003), 130–134. [https://doi.org/10.1061/\(ASCE\)0733-9445\(2003\)129:1\(130\)](https://doi.org/10.1061/(ASCE)0733-9445(2003)129:1(130))
7. Subramani, T., Subramani, M., and Prasath, K. "Analysis of Three Dimensional Horizontal Reinforced Concrete Curved Beam Using Ansys." *International Journal of Engineering Research and Applications*, Vol. 4, No. 6, (2014), 156–161. Retrieved from www.ijera.com
8. Al-Tameemi, H. A., Ali, A., and Attiyah, A. N. "Three-dimensional nonlinear finite element analysis of reinforced concrete horizontally curved deep beams." *Journal of Babylon University/Engineering Sciences*, Vol. 18, No. 1, (2010), 1–18. Retrieved from https://www.researchgate.net/profile/Haider-Al-Tameemi/publication/332565074_Three-Dimensional_Nonlinear_Finite_Element_Analysis_of_Reinforced_Concrete_Horizontally_Curved_Deep_Beams/data/5cbde2e4a6fdcc1d49a85baf/3DNFEAHADB-H-A-J.pdf
9. Al-Mutairee, H. M. K. "Effect of Non-Uniform Distribution of Longitudinal Reinforcement on the Behavior of Reinforced Concrete Horizontally Curved Beams with Fixed-Ends." *Journal of University of Babylon*, Vol. 21, No. 3, (2013), 826–838. Retrieved from <https://www.iasj.net/iasj/article/78025>
10. Badawy, H. E. I., McMullen, A. E., and Jordaan, I. J. "Effect of Shear on Collapse of Curved Beams." *Journal of the Structural Division*, Vol. 103, No. 9, (1977), 1849–1866. <https://doi.org/10.1061/JSDEAG.0004725>
11. Chu, K.-H., and Thelen, A. "Plastic Analysis of Circular Balcony Girders." *Journal of the Structural Division*, Vol. 89, No. 6, (1963), 159–186. <https://doi.org/10.1061/JSDEAG.0000999>
12. Hsu, T. T. C., Inan, M., and Fonticciella, L. "Behavior of reinforced concrete horizontally curved beams." *Journal Proceedings*, Vol. 75, (1978), 112–123. Retrieved from

- <https://www.concrete.org/restrictedcountry.aspx>
13. Jordaen, I. J., Khalifa, M. M. A., and McMullen, A. E. "Collapse of Curved Reinforced Concrete Beams." *Journal of the Structural Division*, Vol. 100, No. 11, (1974), 2255–2269. <https://doi.org/10.1061/JSDEAG.0003931>
 14. Khalifa, M. M. A. "Collapse of reinforced concrete beams curved in plan." In Thesis presented to the University of Calgary, at Calgary, Alberta, Canada, in partial fulfillment of requirements for the degree of Master of Science, (1972).
 15. Mansur, M. A., and Rangan, B. V. "Study of design methods for reinforced concrete curved beams." *Journal Proceedings*, Vol. 78, (1981), 226–254. Retrieved from <https://www.concrete.org/restrictedcountry.aspx>
 16. Burton, K. T. "Influence of Embedded Service Ducts on the Strength of Continuous Reinforced Concrete T-Beams." *Journal Proceedings*, Vol. 62, (1965), 1327–1344. Retrieved from <https://www.concrete.org/publications/internationalconcreteabstractsportal.aspx?m=details&i=7748&m=details&i=7748>
 17. Dallal, M. S. "Behavior and design of reinforced concrete T-beams with large openings in the webs /," (1968). Retrieved from <https://hdl.handle.net/11244/2426>
 18. Mansur, M. A. "Deflections of reinforced concrete beams with web openings." *ACI Structural Journal*, (1992), 389. Retrieved from <http://citeseerx.ist.psu.edu/viewdoc/summary?doi=10.1.1.573.8180>
 19. Mansur, M. A. "Effect of openings on the behaviour and strength of R/C beams in shear." *Cement and Concrete Composites*, Vol. 20, No. 6, (1998), 477–486. [https://doi.org/10.1016/S0958-9465\(98\)00030-4](https://doi.org/10.1016/S0958-9465(98)00030-4)
 20. Mansur, M. A., and Tan, K.-H. Concrete beams with openings: analysis and design (Vol. 20). CRC Press, 1979.
 21. Mansur, M. A. "Design of reinforced concrete beams with web openings." In Proceedings of the 6th Asia-Pacific structural engineering and construction conference (ASPEC 2006) (pp. 5–6). Kuala Lumpur Malaysia, 2006. Retrieved from https://www.sefindia.org/forum/files/mamansur2006_designofreinforcedconcretebeams_with_openings_413.pdf
 22. Nasser, K. W., Acavalos, A., and Daniel, H. R. "Behavior and design of large openings in reinforced concrete beams." *Journal Proceedings*, Vol. 64, (1967), 25–33. Retrieved from <https://www.concrete.org/publications/internationalconcreteabstractsportal.aspx?m=details&ID=7540>
 23. Saksena, N. H., and Patel, P. "Experimental study of reinforced concrete beam with web openings." *International Journal of Advanced Engineering Research and Studies-India*, Vol. 2, No. 3, (2013), 66–68.
 24. Salam, S. A. "Beams with openings under different stress conditions." In Conference on Our World in Concrete and Structures, Singapore (pp. 25–26), 1985.
 25. Somes, N. F., and Corley, W. G. "Circular openings in webs of continuous beams." *Special Publication*, Vol. 42, (1974), 359–398. Retrieved from <https://www.concrete.org/publications/internationalconcreteabstractsportal/m/details/id/17293>
 26. Tan, K.-H., Mansur, M. A., and Huang, L.-M. "Reinforced concrete T-beams with large web openings in positive and negative moment regions." *Structural Journal*, Vol. 93, No. 3, (1996), 277–289. Retrieved from <https://www.concrete.org/publications/internationalconcreteabstractsportal/m/details/id/9687>
 27. Mansur, M. A., Tan, K.-H., and Wei, W. "Effects of creating an opening in existing beams." *Structural Journal*, Vol. 96, No. 6, (1999), 899–905. Retrieved from <https://www.concrete.org/publications/internationalconcreteabstractsportal/m/details/id/785>
 28. Hanson, J. M. "Square openings in webs of continuous joists." Portland Cement Assoc R & D Lab Bull, (1969).
 29. Chin, S. C., Shafiq, N., and Nuruddin, M. F. "FRP as strengthening material for Reinforced Concrete beams with openings — A review." *KSCE Journal of Civil Engineering*, Vol. 19, No. 1, (2015), 213–219. <https://doi.org/10.1007/s12205-011-0162-8>
 30. Ahmed, A., Fayyadh, M. M., Naganathan, S., and Nasharuddin, K. "Reinforced concrete beams with web openings: A state of the art review." *Materials & Design*, Vol. 40, (2012), 90–102. <https://doi.org/10.1016/j.matdes.2012.03.001>
 31. Mansur, M. A., and Hasnat, A. "Concrete Beams with Small Opening under Torsion." *Journal of the Structural Division*, Vol. 105, No. 11, (1979), 2433–2447. <https://doi.org/10.1061/JSDEAG.0005286>
 32. Mansur, M. A., and Alwis, W. A. M. "Reinforced fibre concrete deep beams with web openings." *International Journal of Cement Composites and Lightweight Concrete*, Vol. 6, No. 4, (1984), 263–271. [https://doi.org/10.1016/0262-5075\(84\)90021-6](https://doi.org/10.1016/0262-5075(84)90021-6)
 33. Mansur, M. A., Tan, K. H., and Lee, S. "Collapse Loads of R/C Beams with Large Openings." *Journal of Structural Engineering*, Vol. 110, No. 11, (1984), 2602–2618. [https://doi.org/10.1061/\(ASCE\)0733-9445\(1984\)110:11\(2602\)](https://doi.org/10.1061/(ASCE)0733-9445(1984)110:11(2602))
 34. Mansur, M. A., and Paramasivam, P. "Reinforced concrete beams with small opening in bending and torsion." *Journal Proceedings*, Vol. 81, (1984), 180–185. Retrieved from <https://www.concrete.org/publications/internationalconcreteabstractsportal/m/details/id/10677>
 35. Mansur, M. A., Tan, K. H., and Lee, S. L. "Design method for reinforced concrete beams with large openings." *Journal Proceedings*, Vol. 82, (1985), 517–524. Retrieved from <https://www.concrete.org/publications/internationalconcreteabstractsportal/m/details/id/10364>
 36. Mansur, M. A., Lee, Y. F., Tan, K. H., and Lee, S. L. "Tests on RC Continuous Beams with Openings." *Journal of Structural Engineering*, Vol. 117, No. 6, (1991), 1593–1606. [https://doi.org/10.1061/\(ASCE\)0733-9445\(1991\)117:6\(1593\)](https://doi.org/10.1061/(ASCE)0733-9445(1991)117:6(1593))
 37. Ali, A., and Hemzah, S. A. "Nonlinear analysis for behavior of RC horizontally semicircular curved beams with openings and strengthened by CFRP laminates." *International Journal of Scientific & Technology Research*, Vol. 3, No. 8, (2014), 136–145. Retrieved from <https://citeseerx.ist.psu.edu/viewdoc/download?doi=10.1.1.644.1460&rep=rep1&type=pdf>
 38. "The European Guidelines for Self- Compacting Concrete; Specification, Production and Use," (2005). Retrieved from <http://citeseerx.ist.psu.edu/viewdoc/download?doi=10.1.1.121.6496&rep=rep1&type=pdf>
 39. "ACI Committee 318, Building Code Requirements for Structural Concrete (ACI 318-19) and Commentary on Building Code Requirements for Structural Concrete (ACI 318R-19), Farmington Hills, Michigan," (2019).
 40. "ACI Committee 314 'Guide to Simplified Design for Reinforced Concrete Buildings' (ACI 314R-16), Farmington Hills, Michigan," (2016).
 41. "AASHTO LRFD Bridge Design Specifications 'American Association of State Highway and Transportation Officials' USA, Fifth Edition," (2010).
 42. Russell, J. S. "Prestrectives in Civil Engineering." Commemorating the 150th Anniversary of the American Society of Civil Engineering, ASCE Publications, (2003), 375.
 43. Ghobarah, A., and Said, A. "Seismic rehabilitation of beam-column joints using FRP laminates." *Journal of Earthquake Engineering*, Vol. 5, No. 1, (2001), 113–129. <https://doi.org/10.1142/S1363246901000297>

Persian Abstract

چکیده

این کار به بررسی رفتار بتن آرمه سازه‌های تیرهای جعبه منحنی افقی با و بدون باز شده اختصاص دارد. هفت تیر جعبه‌ای دایره‌ای افقی در کار آزمایشی مورد بررسی قرار گرفت، یکی بدون بازشو، سه تیر با بازشو عمودی و سه تیر با بازشو عرضی. برنامه آزمون شامل متغیرهای اصلی است. جهت بازشو، محل بازشو از طریق پروفیل تیرهای منحنی (اثر ترکیب نیروهای داخلی). تیرها به صورت یک تیر پیوسته با دو دهانه آزمایش شدند که هر دهانه یک چهارم دایره را نشان می‌دهد و تحت تأثیر دو بار نقطه‌ای هر بار در بالای وسط دهانه تیر قرار دارد. یافته‌ها نشان می‌دهد که ظرفیت بار نهایی برای همه نمونه‌ها (CB7.T82, CB6.T60, CB5.T37, CB4.V82, CB3.V60, CB2.V37) و (CB7.T82) و (CB6.T60, CB5.T37, CB4.V82) حدود (۵، ۱۱/۵، ۱/۵، ۱/۵، ۴۶/۴ و ۱۸/۶۶ درصد) به ترتیب در مقایسه با کنترل CB1 کاهش یافته است. و در مقایسه با نمونه کنترل CB1، همه نمونه‌ها نشان‌دهنده افزایش در تغییر شکل‌های سرویس از نظر انحراف و زاویه پیچش در وسط پرتوهای دایره‌ای بودند. شکل‌پذیری برای همه نمونه‌های دارای بازشدگی (CB3.V60, CB2.V37, CB4.V82, CB5.T37, CB6.T60, CB7.T82)، به عنوان درصدی در حدود (۱۳/۸۸، ۱۵/۳، ۱۹/۶۲، ۰/۵، ۰/۵ و ۱۳/۸۸) به ترتیب، در مقایسه با نمونه CB1 شاهد کاهش یافت. در نتیجه، به طور کلی، یک تخریب واضح با درصدهای مختلف در رفتار کلی سازه تیرهای جعبه‌ای منحنی افقی حاوی دهانه با توجه به موقعیت و جهت بازشوها، در این مطالعه بازشوه‌های عرضی در ۶۰ درجه، که در آن بازشو تحت حداکثر ترکیبی (برش و پیچش) منجر به کاهش فاجعه بار در عملکرد ساختاری تیر جعبه منحنی افقی شد.



Intelligent Controllers to Extract Maximum Power for 10 KW Photovoltaic System

M. Rupesh^{*a}, T. S. Vishwanath^b

^a BVRIT HYDERABAD College of Engineering for Women, Electrical & Electronics Engineering, Hyderabad, India

^b Electronics & Communication Engineering, Bheemanna Khandre Institute of Technology Bhalki, India

PAPER INFO

Paper history:

Received 26 October 2021

Received in revised form 21 December 2021

Accepted 23 December 2021

Keywords:

Intelligent Controller
Cascaded Feed Forward Neural Network
Particle Swarm Optimization
Genetic Algorithm
Maximum Power Point
Photovoltaic

ABSTRACT

This research looks at how photovoltaic (PV) cells generate energy in different weather conditions. Photovoltaic power today plays a key role in the production of energy and satisfying the needs of consumers all over the world. The PV cell's ability to generate electricity was entirely dependent on sunshine and temperature fluctuations in the environment. Several researchers are working on a variety of MPPT methods for a photovoltaic system. Outdated MPPT techniques are unable to withstand a dramatic change in weather conditions. The fundamental purpose of this study is to associate the numerous unadventurous and clever controllers for MPPT of the PV system, such as the PSO, GA, and CNFF. The MATLAB environment was used to create and simulate the recommended intelligent controller for MPPT in the PV system. Furthermore, the aforementioned findings like Voltage, Current and Power with respect to different irradiance and temperature are compared and evaluated. The performance of the above-mentioned topologies has been related to the optimum intelligent controller for the PV system and concluded that the CFFNN gives better efficiency with minimum time required to extract.

doi: 10.5829/ije.2022.35.04a.18

NOMENCLATURE

PV	Photovoltaic	f	Desired objective function
MPP	Maximum Power Point	X_i	Location of Particle
PSO	Particle Swarm Optimization	V_i	Speed of Particle
CFFNN	Cascaded Feed Forward Neural Network	w	Sluggishness weight
GA	Genetic Algorithm	r1, r2	Orbitory variables
N	Diode Constant	C1, C2	Reasoning and Common Coefficients
K	Blothzman Constant	P besti	Best location of particle of i
T	Temperatre in Kelvin	Gbest	Best global location of i
Q	Electricity Charge	MG	Micro Grid
I0	Maximum Diode Corrent	REG	Renewable Energy Generation
G	Irradiance	DG	Distribution Generation
Gref	Reference Irradiance	P & O	Perturb and Observation
Eg	Silicon diode Band Width	INC	Incremental Conductance
D	Duty Cycle		

1. INTRODUCTION

The growing pace of population expansion and levels of urbanization are to blame for the rapid rise in energy consumption, CO₂ emissions, and worldwide demand and supply insufficiency [1-2]. Under environmental concerns such as energy shortages and pollution,

renewable energy sources like solar and wind are the greatest ideal replacement energy sources, with solar and wind being the most prevalent energy in current power systems. Micro grid (MG) is a low-voltage distribution system that combines flexible DGs like wind, solar, and fuel cells with controllable storage and loads [3-6]. They increase network stability and offer long-lasting, high-

*Corresponding Author Email: m.rupesh1@gmail.com (M. Rupesh)

quality electricity. Managing an Micro Grid through a large number of Distributing Generations, variable loads, and ESA is challenging, especially given the high degree of renewable energy (REG) generating penetration. To highlight the high use of efficiency power, the REG is generally arranged using maximum power tracking (MPPT) algorithms [7-10]. As a result of the fluctuating and uncontrolled meteorological circumstances, it is classified as a generation that cannot be regulated [11-15]. Maximum power monitoring technology will be critical for getting the most energy out of a solar cell under a variety of weather situations. Regulating the solar powered non-linear current and voltage properties throughout times of low sunlight or incompletely covered conditions is a key issue. Researchers have proposed a number of MPPT techniques to obtain maximum energy output from a photovoltaic system.

P&O, Incremental Conductance and feedback power methods are among the numerous little MPPT approaches that are extremely common. Due to a lack of self-regulation capacity, the foregoing traditional approaches flop to reach the desired quickness of process and extreme power output. Various intelligent controllers based on MPPT methods are presented in this paper to attain peak power as well as operating speed (auto-adjustment). In the Matlab software, intelligence-based MPPT methods are modelled and assessed. The mathematical formulation for the solar system and the construction of the boost converter are described in section 2. Section 3 describes the different smart controllers. In section 4, the proposed smart regulators are designed and simulated in MATLAB, with the performance of the PV system evaluated under several climate situations. Section 5 concludes with the hardware and comparative investigation. The suggested research's conclusion is presented in section 6.

2. MODELING OF PV & BOOST CONVERTER

2.1. PV System Design The solar cell is shown as a dependent current source with extra series and parallel resistors connected to a diode in Figure 1. It's worth noting that when solar light is not there, the PV cell serves as a load and produces no power [16]. The actual current commencing the current source (PV cell) is determined by the amount of sunlight that shines on the PV cell (photo-current) (Figure 1). In an open circuit, the voltage is zero.

The Solar cell voltage generation will be affected by the voltage loss through the diode as given in Equation (1):

$$V = \left(\frac{NKT}{Q} \right) \ln \frac{I_L - I_0}{I_0} + 1 \tag{1}$$

where

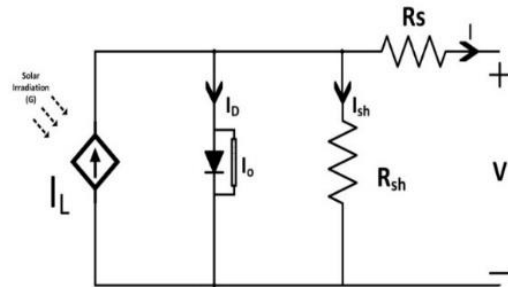


Figure 1. The Equivalent PV cell Circuit

PV Cell Open circuited Voltage = V

N stands for the diode constant 1.50

Boltz const K = (1.381x 10⁻²³ J.K⁻¹)

T = Temperature in Kelvin

Q stands for "elementary charge" (1.602 x 10⁻¹⁹ Coulomb)

I₀ is the Maximum current of a diode (A)

The Generated Current by light (Radiation) is given in Equation (2).

$$I_L = \left(\frac{G}{G_{ref}} \right) * (I_{L,ref} + \alpha_{Isc} (T_C - T_{C,ref})) \tag{2}$$

where

G = irradiation instantaneous (W/m²)

G_{ref} = standard Condition with reference irradiation 1000 Watts per square metre

I_{L,ref} denotes a reference. Under normal circumstances, photoelectric current 0.15 A

Instant temperature T_c.

T_{C,ref} stands Model temp at 298.0 K

α_{Isc} stands SC current temp co-effi (A/K)=0.0065 AK⁻¹

I_L = Current Generated by the Light = I_{ph} (A)

Output current and Reverse saturation current as Equations (3) and (4).

$$I_0 = I_{or} \left(\frac{T_c}{T_{ref}} \right)^3 e^{\frac{(Q+Eg)}{(K*N)*\left[\left(\frac{1}{T_{ref}}\right) - \left(\frac{1}{T_c}\right)\right]}} \tag{3}$$

$$I_{or} = \frac{I_{scn}}{e^{\left(\frac{V_{ocn}}{N*V_{tn}}\right)}} \tag{4}$$

where

I₀ = Current Capacity in Reverse

Current Capacity = I_{or}

E_g is the band gap of a silicon diode, which is 1.10 eV.

Current S C (I_{sh} = I_L)

Under SC circumstances, the maximum current generated by a cell: Volt = 0.00 V, which is shown in Equation (5).

$$I_{sh} = (I_L - I_0) * \left(e^{\frac{eV}{kT}} - 1 \right) A \tag{5}$$

2.2. Design of Boost Converter This converter is a DC-DC level up converter that transforms fluctuating

DC voltage caused by weather variations to a constant stepped up voltage that may be linked to an inverter for grid integration and residential use. This converter is made up of a diode, a MOSFET, and a load ingredient to obtain the output voltage. Depending on the triggering duty cycle, the output voltage varies. The fundamental construction of a boost converter is shown in Figure 2.

The duty cycle of MOSFET can be calculated as Equation (6).

$$D = \left[1 - \frac{V_{in(min)} * \eta}{V_{out}} \right] \tag{6}$$

Change in ripple current as Equation (7):

$$di = i_{ripple} * i_{out} * \frac{v_{out}}{v_{in}} \tag{7}$$

The output current of converter as Equation (8):

$$I_{out} = \frac{\text{Converter Power Rating}}{\text{Converter output voltage}} \tag{8}$$

Inductance of boost converter as Equation (9):

$$L = \frac{[v_{in}(v_{out}-v_{in})]}{di * f_s * v_{out}} \tag{9}$$

Acceptable change in voltage as in Equation (10)

$$Dv = \frac{v_{out}}{dv \text{ percent}/100} \tag{10}$$

Output capacitor to reduce the ripples as in Equation (11).

$$C = \frac{I_{out} * D}{f_s * dv} \tag{11}$$

Output Resistor as shown in Equation (12).

$$R = \frac{V_{out}}{I_{out}} \tag{12}$$

3. MPPT ALGORITHMS

3. 1. Particle Swarm Optimization

The movement of particles is influenced by two variables: the Pbest, which is used to save the best location of each particle as an individual best position, and the Gbest, which is discovered by comparing individual particle swarm positions [18] and saved as the best position of the

swarm. This method is used by the particle swarm to move towards the best place while continually revising its route and speed. As a result, each particle swiftly converges to an optimum or near-optimal global optimal. The equations that describe the conventional PSO technique are as follows in Equations (13) and (14).

$$V_i(k + 1) = wV_i(k) + C_1r_1(P_{best} - x_i(k)) + C_2r_2(g_{best} - x_i(k)) \tag{13}$$

$$x_i(k + 1) = x_i(k) + v_i(k + 1) \tag{14}$$

where i = 1, 2 3 N

where xi and vi are the speed and location of particle i; k is the repetition number; w is the sluggishness weight; r1 and r2 are arbitrary variables with ideals homogeneously spread between [0,1]; and c1 and c2 are the reasoning and common coefficients. The specific best location of particle I is pbest,i, while the swarm finest location of all particles is gbest. If the initialization requirement Equation (16) was met, the technique was modified as Equation (15):

$$P_{best} = x_{ik} \tag{15}$$

$$f(x_{ik}) > f(P_{best}) \tag{16}$$

where f is the desired objective function to be maximized. Step 1: Selection of Parameter:

For the suggested MPP procedure, the pulse width of the converter was outlined as the location of the particle, and the produced power was selected as the fitness value, assessment function. Each particle's location and preliminary speed were erratically adjusted in a identical spreading across the exploration space.

Step 2: Fitness Evaluation:

After the controller sends the duty cycle instruction, which indicates particle i's location, the fitness value of particle i is calculated.

Step 3: (Updating Distinct and Global Best Data):

By associating the afresh computed fitness values to the prior ones and substituting the pbest and gbest matching to their locations as needed, each particle's fitness values, separate best locations (Pbest), and global best fitness values (gbest) are informed.

Step 4 (Update Speed and Location of Each Particle): After analysing all particles, apprise the speeds and locations of each particle in the swarm using the PSO Equations (13) and (14).

Step 5 (Determination of Convergence): The converge criteria is either finding the best solution or completing the most iterations. The operation will end if the convergence condition is fulfilled; otherwise, repeat Steps 2 through 5.

Step 6. (Initialization):

The converge criteria in the conventional PSO technique is either finding the best solution or achieving the maximum number of repetitions. The fitness value of

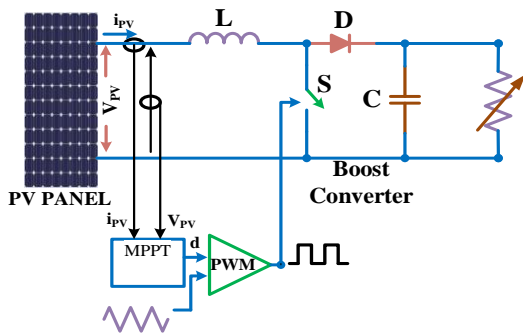


Figure 2. Boost Converter Circuit diagram

PV systems, on the other hand, is not constant since it varies depending on the weather and load.

When the PV module output changes, the PSO must be re-initialized and examine for a new MPP. When the following functions are met, the suggested PSO algorithm is reinitialized for this application using Equation (17):

$$\frac{P_i(k+1) - P_i(k)}{P_i(k)} > \Delta p \tag{17}$$

Particle swarm Optimization algorithm flowchart is shown in Figure 3.

3. 2. Genetic Algorithm The MPPT procedure, which is founded on the Genetic Algorithm (GA), is a natural genetics-inspired optimization method.

This approach, which is based on the notion of "endurance of the rightest," is used to identify an optimum set of parameters. In actuality, the search for a GA technique entails [17]. Selection, crossover, and mutation are the three basic operators. Selection is a method of choosing genetic material from the current generation's population for inclusion in the next generation's population depending on its fitness. The crossover operator connects two chromosomes to make new genetic material. The mutation operator tries to achieve some stochastic dissimilarity of GA in order to obtain quicker convergence by preserving genetic variety from one population generation to the next. To address this issue, the algorithm was tweaked to reset the initial

population whenever a change in irradiance or cell temperature is detected. As a result, if the following two requirements are fulfilled, the GA is reinitialized: Equations (18) and (19).

$$|V(k + 1) - V(k)| < \Delta V \tag{18}$$

$$\left| \frac{P_{pv}(k+1) - P_{pv}(k)}{P_{pv}(k)} \right| > \Delta P \tag{19}$$

At iteration, the intended output voltage matches to the chromosomal location (k). Four people are applied sequentially to the starting population, which is made up of chromosomal parents. Equation (20) gives the population's initial locations.

$$[P1, P2, P3, P4] = [0.8, 0.6, 0.4, 0.2]V_{oc} \tag{20}$$

The fitness is the produced power Ppv, which is ranked decreasingly and selected using elitism as a criteria.

To generate a kid, the crossover stage involves merging two chromosomal parents. In reality, Equations (21) and (22) are used in this phase.

$$child(k) = r P(r) - (1 - r)P(k + 1) \tag{21}$$

$$child(k + 1) = (r - 1) P(k) - (r)P(k + 1) \tag{22}$$

where r is an arbitrary integer. Equation (23). shows the relationship between the ISSBC's output voltage and duty cycle.

$$a(k) = child(k)/V \tag{23}$$

Genetic algorithm flowchart is shown in Figure 4.

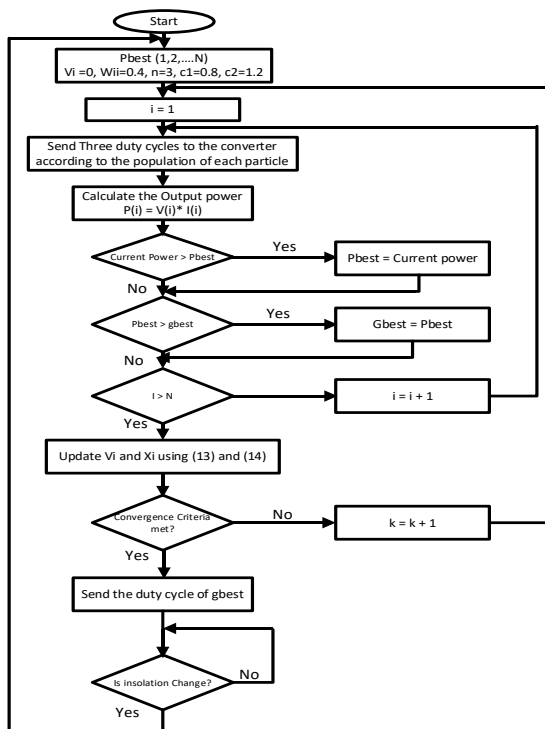


Figure 3. PSO Algorithm flowchart

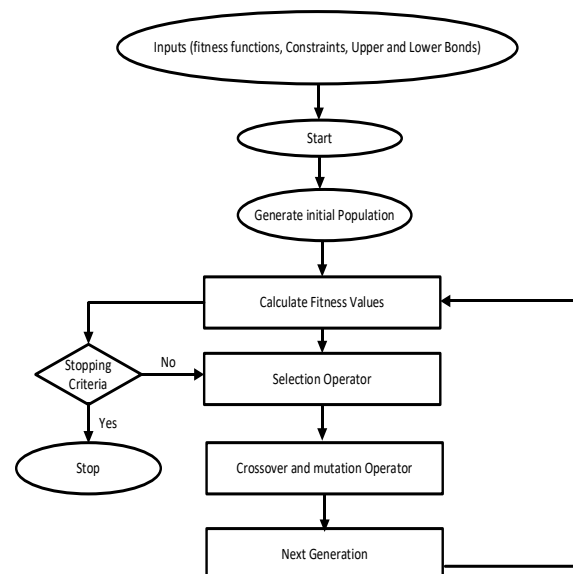


Figure 4. Genetic Algorithm Flowchart

3. 3. Cascaded Feed Forward Neural Network Method The CFNN is a feed-forward (FF) neural network with a connection from the influence layer and individually preceding layer to the subsequent layers.

The production layer is also publicly connected with the influence layer head-to-head to the hidden layer in a three-layer network. With enough hidden neurons, a cascading network with two or more layers, like FF networks, may learn any arbitrarily limited I-O connection [19-25]. The CFNN can be used for any kind of contribution to cartography creation.

The advantage of this method is that, it accounts for the non-linear relationship between entry and departure deprived of removing the linear association in the middle of the two.

The meeting created between the contribution and the production in a perceptron is a kind of unswerving connotation, however the meeting shaped in the middle of the influence and the invention in an FFNN is a subordinate connotation. An activation function in the hidden layer makes the connection non-linear. When the perceptron and multilayer grid connecting forms are merged, the grid is moulded through a straight link between the influence layer and the production layer, as well as the connection parenthetically. The CFNN is the network that results from this connecting model.

A cascading neural network is the network shaped by this linking paradigm (CFNN). The following are some examples of Equation (24):

$$y = \sum_{i=1}^n f^i w_i^i x_i + f^o (\sum_{j=1}^k w_j^o f_j^h (\sum_{i=1}^n w_{ji}^h x_i)) \quad (24)$$

where w_{ii} is the weight from the influence layer to the invention layer and f_i is the activation function. If a bias is applied to the influence layer, and each neuron in the hidden layer has an activation function of f_h , the equation becomes as Equation (25):

$$y = \sum_{i=1}^n f^i w_i^i x_i + f^o (w^b + \sum_{j=1}^k w_j^o f_j^h (w^b + \sum_{i=1}^n w_{ji}^h x_i)) \quad (25)$$

The CFNN model is used to analyse time series data in this study. Thus, the delays of time series data X_{t-1} , X_{t-2} , ..., X_{t-p} are represented by the neurons in the contribution layer, and the production is represented by the current data X_t .

As shown in Figure 5, the suggested multi-layered cataract neural network model was created for a procedure to trace extreme power spots for the PV arrangement. PV voltage and current are two of the contributions to this network. The gate pulse of the DC-DC converter is the source of this network's production. From the influence layer to the invention layer, there are four hidden layers. Each hidden layer uses a different number of neurons, for example, layer 1 uses 20 neurons, layer 2 uses 30 neurons, layer 3 uses 20 neurons, and layer 4 uses 5 neurons, as illustrated in Figure 5a. More than 10,000 data points, such as PV voltage, PV current, and gate pulse, were used to train the proposed network. The MPPT algorithm was created after more than 1000 epochs were completed, and the network was well-trained. As demonstrated in Figure 5b, the optimum

dynamic presentation of the suggested CNFF is 9.2922×10^{-17} . Figure 5c shows the pitch examination, μ , and authentication patterned for the planned CNFF. Finally, in Figure 5d, the planned system regression value is shown.

4. SIMULATION RESULTS

The discovery of the Maximum Power Point utilizing several methods has been implemented in this work, and the outcomes are presented in Figure 6.

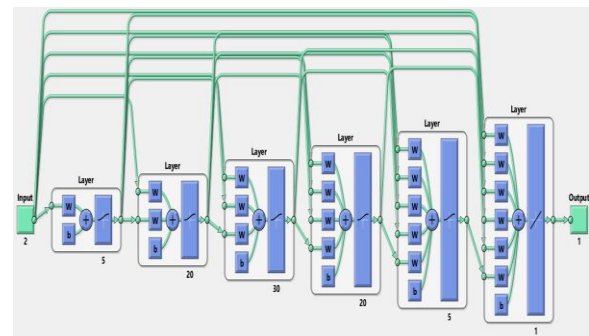


Figure 5a. CFFNN structure for MPPT Algorithm

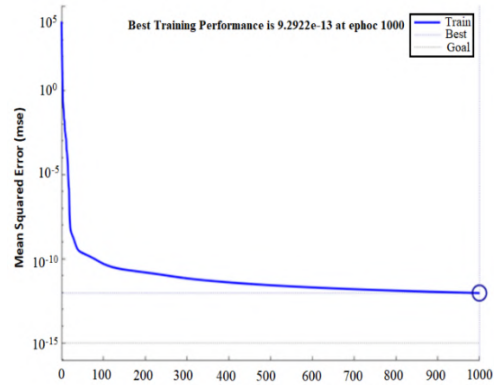


Figure 5b. Optimum dynamic presentation of CFFNN

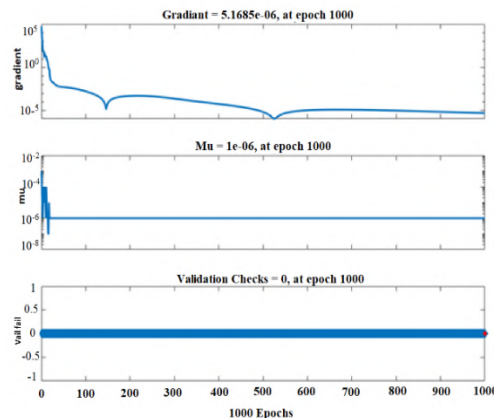


Figure 5c. Gradient, μ and Authentication check for anticipated CNFF

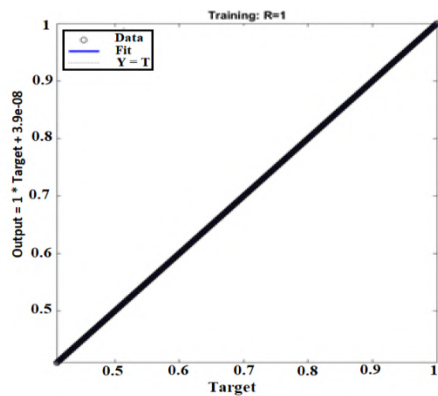


Figure 5d. Regression for suggested CNFF

4. 1. Particle Swarm Optimisation (PSO)

The proposed PSO technique was applied in a 10 kW PV system MATLAB/Simulink model. Under typical operating settings, this simulation model was examined. The simulation's outcomes are assessed. Adjustable irradiance has been added to the contribution of a PV model to assess the enactment of arrangement using the same simulation model. The PV produced power and MPPT power have been measured and displayed in Figure 7a under several weather conditions. Figure 7b shows the boost converter voltage and current waveforms under various climate circumstances, 494.5 V and 19.78 V, respectively. Figure 7c shows PV voltage 308 V and Boost converter voltage 494.4 V under varied irradiance conditions.

4. 2. Genetic Algorithm (GA)

As illustrated in Figure 6, the proposed GA Organizer was employed in a MATLAB/Simulink model for 10 kW rating. Under typical operating settings, this simulation model was examined. The simulation's outcomes are assessed. The changing irradiance input of the PV system has been used to the same simulation model, which analyses system performance. The PV power and MPPT power of 9743 W were measured and schemed in Figure 8a. under

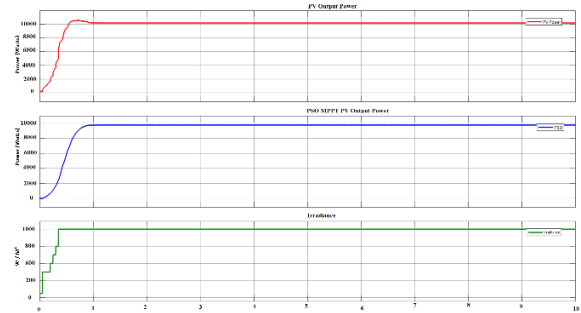


Figure 7a. PV power vs MPPT power under several irradiances

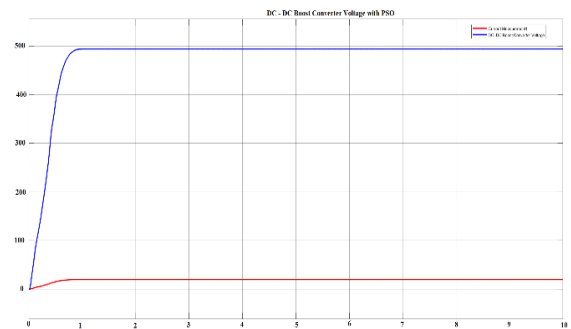


Figure 7b. Boost converter voltage and current

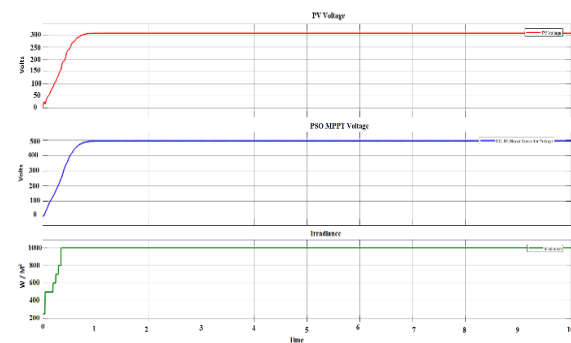


Figure 7c. PV Voltage vs Boost converter Voltage under several irradiance

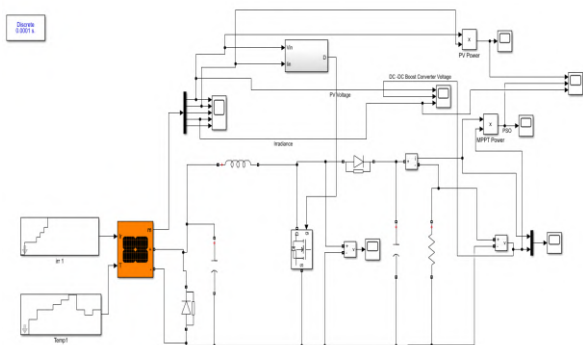


Figure 6. Simulation of 10 kW PV model for all MPPT Techniques

various weather conditions. Under various weather conditions, the boost converter voltage and current waveforms are shown. Figure 8b shows 491 V and 19.8 A correspondingly. Under different irradiance a, relate PV voltage 310 V and Boost converter voltage 491 V. are shown in Figure 8c.

4. 3. Cascaded Feed Forward Neural Network Method

As illustrated in Figure 6, the suggested CNFF Controller was executed in a MATLAB/Simulink model of a 10 KW rating. Under typical operating settings, this simulation model was examined. The simulation's outcomes are assessed. The changing irradiance input of the PV system has been used to the

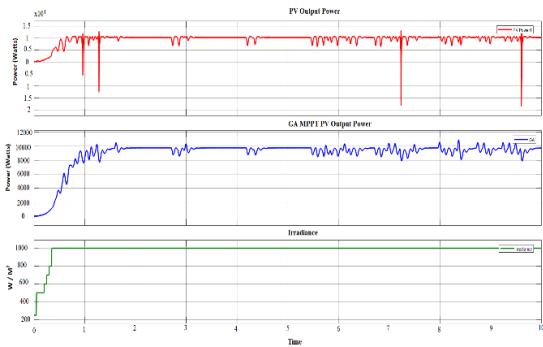


Figure 8a. PV power vs MPPT power under various irradiance

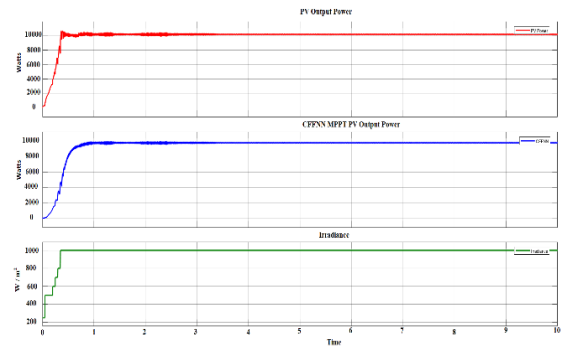


Figure 9a. PV power vs MPPT power under various irradiation

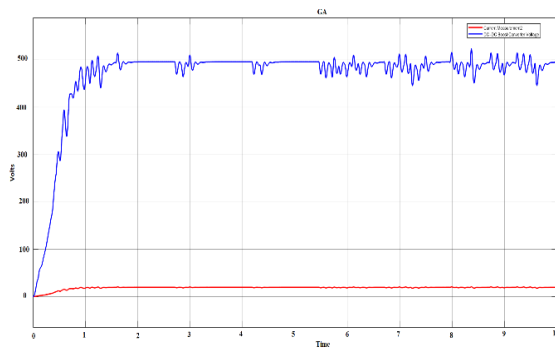


Figure 8b. Boost converter voltage and current

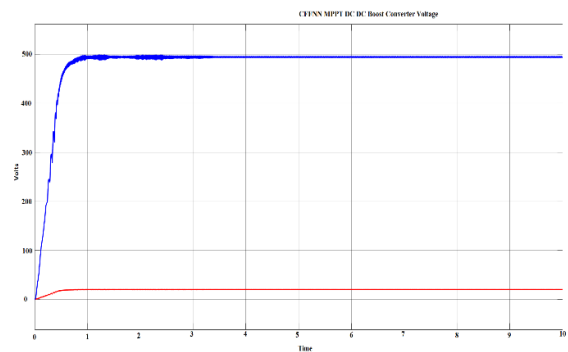


Figure 9b. Boost converter voltage and current

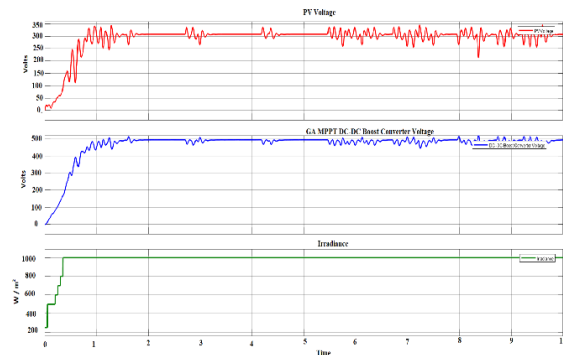


Figure 8c. PV Voltage vs Boost converter voltage under various irradiance

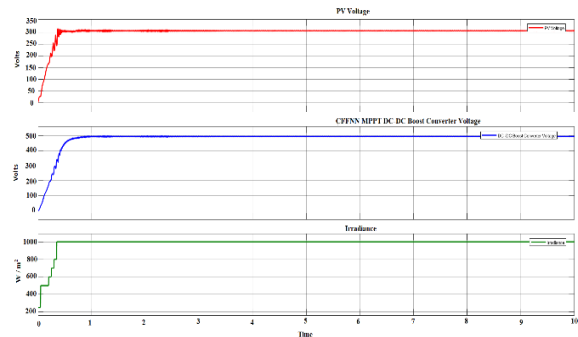


Figure 9c. PV Voltage vs Boost converter voltage under several irradiance

same simulation model, which analyses system performance. The PV power and MPPT power 9915 W have been measured and plotted in Figure 9a under various weather conditions. Figure 9b shows the boost converter voltage and current waveforms under several climate situations (422 V and 19.8, correspondingly).

5. HARDWARE IMPLEMENTATION

As illustrated in Figure 10a, the suggested scheme was constructed as a serviceable prototypical of a 10W PV

model and power converter. The suggested CNFF system has been connected to an Arduino Mega 2560, which allows duty cycle development based on input changes. Using a MATLAB simulation library, the Mega 2560 communicates directly with MATLAB. Table 2 contains design information. The suggested algorithm generates switching pulses, and its run cycle will alter when climate change occurs. Figure 10b shows how the suggested method generates half of the usage cycle. The suggested method generates a 90 percent operational cycle in Figure 10c. Figure 10e shows the suggested technique for the gate pulses under various climate circumstances in

MATLAB. Figure 10f shows a prototype model of a 28.20 V DC-DC converter with a 12 V input voltage.



Figure 10a. Working model of PV MPPT system

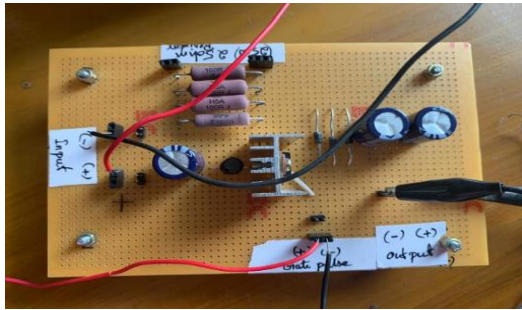


Figure 10b. DC-DC Converter Model

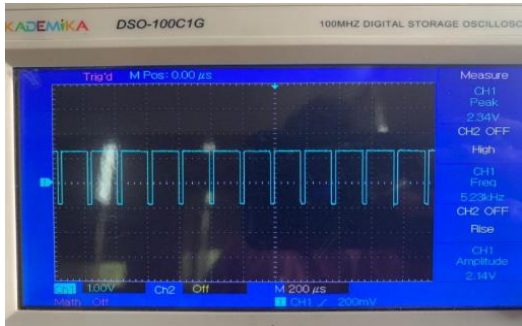


Figure 10c. Switching signal with 50 % duty cycle

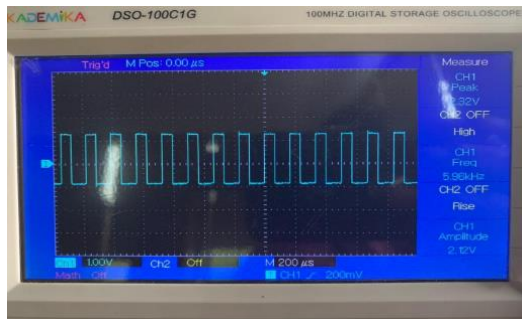


Figure 10d. Switching signal with 90 % duty cycle

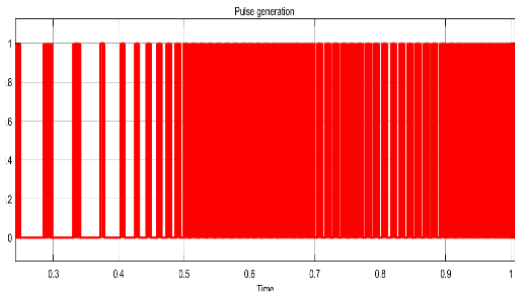


Figure 10e. Pulse generation by proposed CNFF algorithm

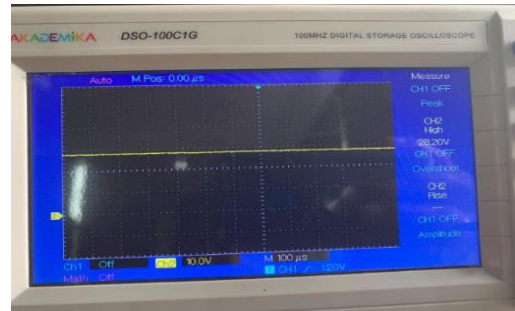


Figure 10f. DC-DC Converter Voltage 28.2 V for 12V of input

TABLE 1. Comparison table

S. No.	Name of algorithm	MPPT Power	Conversion Percentage
1	INC	8405	84.05%
2	P&O	9312	93.12%
3	Fuzzy	9773	97.73%
4	GA	9192	91.92%
5	PSO	9799	97.99%
6	CNFF	9915	99.15%

TABLE 2. Boost converter parameters

S. No.	Parameter	Value
1	Power	10W
2	Voc	21.20 V
3	Isc	0.66 A
4	Vmax	17.40 V
5	Imax	0.58 A
6	Capacitor C1	100 μf
7	Capacitor C2	4700 μf
8	Inductor	0.05 H
9	MOSFET	IRF540N
10	Resistance	33Ω

6. CONCLUSION

The maximum energy output of solar systems under a range of climatic circumstances was the focus of this study. The photovoltaic cell's mathematical model has been created, and its performance in various weather situations has been analyzed. As per the simulation findings, the MPPT process was required to produce the PV model maximum power. A number of MPPT processes were tried in this study under a range of climatological circumstances. The subsequent processes were analyzed, namely GA, PSO and CNFF. In comparison to other MPPT algorithms, The GA gives 91.92% of efficiency with 1.5s of time, The PSO MPPT gives maximum efficiency of 97.99% with 0.9s and finally the CFFNN delivers better outcomes like 99.15% of efficiency with 0.6 s of time according to simulation findings and comparative assessments. Finally, the suggested CFFNN MPPT algorithm was used to create and test prototype work model.

7. REFERENCES

1. M. Rupesh, T. S. Vishwanath "Comparative analysis of P & O and Incremental conductance methods for standalone PV system," *Internal Journal of Engineering and Technology*, Vol. 7, No. 3.29, (2018), 519-529. doi: 10.14419/ijet.v7i3.29.19303.
2. B. Hajipour, S.M Hasheminejad, H.R. Haghgou, "Extracting Technical Specifications of Solar Panel Type to design a 10 MW Hybrid Power Plant", *International Journal of Engineering, Transactions A: Basics*, Vol. 32, No. 4, April-2019, 562-568. doi: 10.5829/ije.2019.32.04a.14
3. M. Rupesh and T. V. Shivalingappa, "Evaluation of Optimum MPPT Technique for PV System using MATLAB/Simulink" *International Journal of Engineering and Advanced Technology*, No. 5, (2019), 1403-1408.
4. H. Rahimi Mirazizi, M. Agha Shafiyi, "Evaluating Technical Requirements to Achieve Maximum Power Point in PV Powered Z-Source Inverter", *International Journal of Engineering, Transactions C, Aspects*, Vol. 31, No. 6, (2018), 921-931. doi: 10.5829/ije.2018.31.06c.09
5. L. Yang and Z. Yunbo, "A Novel Improved Variable Step Size INC MPPT Method for PV Systems", Chinese Control and Decision Conference (CCDC), Nanchang, China. (2019), 5070-5073, doi: 10.1109/CCDC.2019.8832451
6. D. Singh and H. Singh "Technical Survey and Review on MPPT Techniques to attain Maxim Power of Photovoltaic System", 5th International Conference on Signal Processing Computing and Control (ISPCC), Solan, India, (2019), 265-268, doi: 10.1109/ISPCC48220.2019.8988382
7. M. L. Azad, P. K. Sadhu and S. Das, "Comparative Study between P & O and Incremental Conduction MPPT Techniqus - A Review", International Conference on Intelligent Engineering and Management (ICIEM), Landon, UK, (2020), 217-222, doi: 10.1109/ICIEM48762.2020.9160316
8. M. Sarvi, M. Derakhshan, M. Sedighizadeh, "A New Intelligent Controller for Parallel DC/DC Converters", *International Journal of Engineering, Transactions A: Basics*, Vol. 27, No. 1, (2014), 131-142. doi: 10.5829/idosi.ije.2014.27.01a.16
9. D. Haji and N. Genc "Fuzzy and P & O based MPPT Controllers under different Conditions" 7th International Conference on Renewable Energy Research and Applications (ICRERA) Paris, France, (2018), 649-655, doi: 10.1109/ICRERA.2018.8566943.
10. M. L. Shah, A. Dhaneria, P. S. Modi, H. Khambhadia and K K D, "Fuzzy Logic MPPT for Grid Tie Solar Inverter", IEEE International Conference for Innovation in Technology (INOCON), Bangalore, India, (2020), doi: 10.1109/INOCON50539.2020.9298323.
11. M. R. Javed, A. Waleed, U. S. Virk and S. Z. UI Hassan, "Comparison of the Adaptive Neural-Fuzzy Interface System (ANFIS) based Solar Maximum Power Point Tracking (MPPT) with other Solar MPPT Methods". IEEE 23rd International Multitopic Conference (INMIC) Bahawalpur, Pakistan, (2020), doi: 10.1109/INMIC50486.2020.9318178
12. T. Boutabba, S. Drid, L. Chrifi-Alaoui, M E Benbouzid, "A New Implementation of Maximum power Point Tracking based on Fuzzy Logic Algorithm for Solar Photovoltaic System", *International Journal of Engineering, Transactions A: Basics*, Vol. 31, No. 4, (2018), 580-587. doi: 10.58229/ije.2018.31.04a.09
13. H. Heidari, M Tarafdar Hagh, "Optimal Reconfiguration of Solar Photovoltaic Array using a Fast Parallelized Particle Swarm Optimization in Confront of Partial Shading", *International Journal of Engineering, Transaction B: Applications*, Vol. 32, No. 8, (2019), 1177-1185. doi: 10.5829/IJE.2019.32.08B.14
14. S Paul and J Thomas, "Comparison of MPPT using GA optimized ANN employing PI Controller for Solar PV system with MPPT using Incremental Conductance", International Conference on Power Signal Control and Computations (EPSCICON), Thrissur, India, (2014). doi: 10.1109/EPSCICON.2014.6887518
15. A Guediri, A. Guediri, S.Touil, "Optimization Using a Genetic algorithm based on DFIG Power Supply for the Electrical Grid", *International Journal of Engineering, Transaction A: Basics* Vol. 35, No. 1, (2022), 121-129. doi: 10.5829/IJE.2022.35.01A.11
16. L. Zaghba, M. Khennane, A. Borni, A. Fezzani, A.Bouchakour, Idriss Hadj Mahammed, Samir Hamid Oudjana "A Genetic Algorithm based improved P & O-PI MPPT Controller for stationery and Tracking Grid Connected Photovoltaic System", 7th International Renewable and Sustainable Energy Conference (IRSEC), Agadir, Morocco, (2019), 1-6. doi: 10.1109/IRSEC48032.2019.9078304
17. S. Paul, "Comparison of MPPT using GA Optimized ANN employed PI Controller with GA Optimized ANN employing fuzzy controller for PV System", IET 4th International Conference on Sustainable Energy and Intelligent Systems (SEISCON) Chennai, (2013), 266-271, doi: 10.1049/ic.2013.0324
18. R. Khanaki, M. A. M. Radzi, and M. H. Marhaban, "Comparison of ANN and P & O MPPT Methods for PV Applications under changing solar irradiance", IEEE Conference on Clean Energy and Technology (CEAT), Langkawi, Malasiya, (2013), 287-292, doi: 10.1109/CEAT.2013.6775642
19. H. Elaissauoui, M. Zerouali, A. E. Ougli and B. Thidaf, "MPPT Algorithm based on Fuzzy Logic and Artificial Neural Network (ANN) for a Hybrid Solar/Wind Power Generation System", 4th International Conference on Intelligent Computing in Data Sciences (ICDS), FEZ, Morocco, (2020), doi: 10.1109/ICDS50568.2020.9268747
20. M. S. Bouakkaz, A. Boukadoum, O. Boudebou, A. Bouraiou, N. boutasseta and I. Attoui, "ANN based MPPT Algorithm Design using Real Operating Climatic Condition", 2nd International Conference on Mathematics and Information Technology (ICMIT), Adrar, Algeria, (2020), 159-163, doi: 10.1109/ICMIT47780.2020.9046972

21. L. Bouselham, M. Hajji, B. Hajji and H Bouali, "A MPPT based ANN Controller applied to PV Pumping System", International Renewable and Sustainable Energy Conference (IRSEC), Marrakech, Morocco, (2016), 86-92, doi: 10.1109/IRSEC.2016.7983918
22. S. Messalti, A. G. Harrag and A E Loukriz, "A New Neural Networks MPPT Controller for PV Systems, IREC2015, the sixth" International Renewable Energy Congress, Sousse, Tunisia, (2015), doi: 10.1109/IREC.2015.7110907
23. Arulmozhiyal and K. R. Baskaran, "Implementation of a Fuzzy PI Controller for Speed Control of Induction Motors Using FPGA," *Journal of Power Electronics*, Vol. 10, (2010), 65-71, doi: 10.6113/JPE.2010.10.1.065
24. Sabir Messalti, D. Zhang, Abd Elhamid Loukriz., "Common Mode Circulating Current Control of Interleaved Three-Phase Two-Level Voltage-Source Converters with Discontinuous Space-Vector Modulation," IEEE Energy Conversion Congress and Exposition, Vol. 1-6, (2009), 3906-3912, doi: 10.1109/IREC.2015.7110907
25. Z. Yin Hai, Songsong Wang, Haixia Xia, Jinfa Ge., "A Novel SVPWM Modulation Scheme," in Applied Power Electronics Conference and Exposition. APEC 2009. Twenty-Fourth Annual IEEE, (2009), 128-131. doi: 10.1109/APEC.2009.4802644.

Persian Abstract

چکیده

این تحقیق به چگونگی تولید انرژی سلول های فتوولتائیک (PV) در شرایط آب و هوایی مختلف می پردازد. برق فتوولتائیک امروزه نقش کلیدی در تولید انرژی و رفع نیازهای مصرف کنندگان در سراسر جهان ایفا می کند. توانایی سلول PV برای تولید الکتریسیته کاملاً به نور خورشید و نوسانات دما در محیط بستگی دارد. چندین محقق بر روی انواع روش های MPPT برای یک سیستم فتوولتائیک کار می کنند. تکنیک های قدیمی MPPT قادر به مقاومت در برابر تغییرات چشمگیر در شرایط آب و هوایی نیستند. هدف اساسی این مطالعه، ارتباط کنترل کننده های متعدد غیرمراججویی و هوشمندانه برای MPPT سیستم PV، مانند GA، PSO، و CNFF است. محیط MATLAB برای ایجاد و شبیه سازی کنترل کننده هوشمند توصیه شده برای MPPT در سیستم PV استفاده شد. علاوه بر این، یافته های فوق الذکر مانند ولتاژ، جریان و توان با توجه به تابش و دمای مختلف مقایسه و ارزیابی می شوند. عملکرد توپولوژی های ذکر شده در بالا به کنترل کننده هوشمند بهینه برای سیستم PV مربوط می شود و نتیجه می گیرد که CFFNN با حداقل زمان لازم برای استخراج کارایی بهتری ارائه می دهد.



Mechanical Properties and Wear Behaviour of Stir Cast Aluminum Metal Matrix Composite: A Review

D. Kumar*, S. Angra, S. Singh

Mechanical Engineering Department, National Institute of Technology Kurukshetra, Haryana, India

PAPER INFO

Paper history:

Received 18 December 2021

Received in revised form 18 January 2021

Accepted 20 January 2022

Keywords:

Aluminum Metal Matrix Composites

Reinforcements

Stir Casting

Mechanical Properties

Wear

ABSTRACT

In this 21st century, various materials like metals, alloys, and composites are available for different industrial applications. Composite materials are gaining popularity due to their enhanced mechanical properties over other materials. However, for continuous improvement in the properties of these materials, different research groups are constantly involved in it. In this research paper, the focus is to review the mechanical properties like hardness, tensile strength, flexural strength, impact strength along with surface characteristics like wear resistance of AMMC's. As per the available literature, liquid state processing is more popular than solid-state processing due to the better dispersion of the reinforcement particles in the matrix materials. Stir casting is mostly used liquid state processing method because of its ease and the overall low cost of production. It has been noticed that the mechanical and surface characteristics of AMMC's can be improved by adding different reinforcement particles in small percentages (usually 0.5-20%). It has been observed that hardness, tensile strength, and flexural strength for mostly used AMMC's ranges from 38-99.6 HV, 100-478 MPa, and 199.52-430 MPa respectively. This research paper also included the influence of various working parameters on the wear rate of AMMC's. It is noticed that wear loss for AMMC's generally varies from 0.0050-0.004 g. The impact resistance is a crucial parameter in the study of AMMC's used for aerospace and automotive applications and it has been noticed that its value for popular AMMC's varies from 3.6-38 J.

doi: 10.5829/ije.2022.35.04a.19

NOMENCLATURE

Wt. %	Weight Percentage
MPa	Mega Pascal
B ₄ C	Boron Carbide

ZrO ₂	Zirconium Oxide
GNP	Graphene nanoplates
Al ₂ O ₃	Alumina
CNT	Carbon Nano Tubes

1. INTRODUCTION

The historical backdrop of the advanced composites began in the 1930s. In 1960, polymer-based composites' performance triggered numerous areas in research. The materials research leads to the development of intelligent materials such as alloys, ceramics and composites [1]. Due to matrix cracking, breakage, delamination and de-bonding of matrix [2], in 1970 aluminum-based metal matrix composites (AMMC's) using silicon carbide (SiC) whisker particles came into the picture as an alternative material for aerospace and automotive applications [3-7]. MMCs are the combination of two or more constituent materials

(where the matrix material consists of metal and reinforcement can be metal or non-metal) [8]. The addition of ceramic reinforcement to the matrix metal emerges a new version of the materials [9], which enhances the density, hardness, strength, wear-resistance and capability to endure environmental effects [6]. Stir casting method is found to be superior to other casting methods in terms of technical and economical aspects. The easiness, flexibility, bulk production and manufacturing of intricate components are the main advantages of the stir casting method for the production of AMMC's [7]. The composites are classified as mentioned in Figure 1.

*Corresponding Author Email: dimesh_61900120@nitkr.ac.in
(D. Kumar)

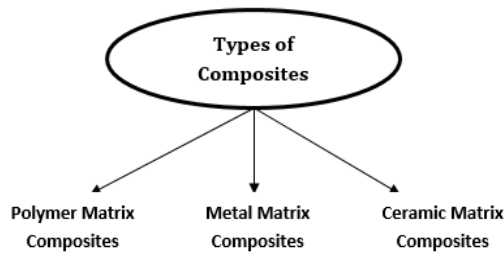


Figure 1. Classification of composites according to matrix metal

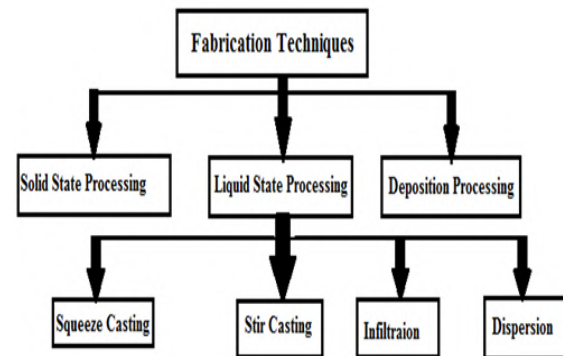


Figure 2. Classification of fabrication techniques

1. 1. Materials Used in MMCs

1. 1. 1. Matrix Material

The major portion of MMC's is the matrix material, as it gives shape to the composite and binds the reinforcement particles along with it. Aluminum, magnesium, copper, iron, and titanium are commonly used matrix for the fabrication of MMCs [10-14].

1. 1. 2. Reinforcement Materials

The reinforcement materials play important role in the fabrication of MMC's. These can be added in different percentages in the matrix materials to change their characteristics [15]. There are two types of reinforcements: organic and inorganic [16], which are further classified as shown in Table 1.

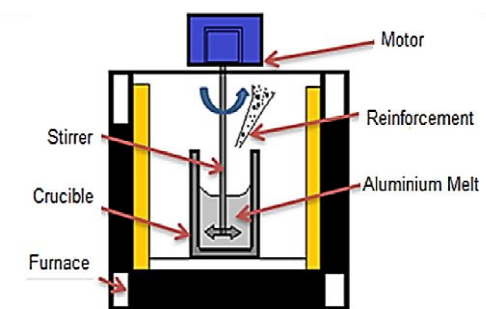


Figure 3. Setup for Stir Casting [38]

2. METHOD OF FABRICATION OF MMC

The literature review describes that there are various fabrication techniques which can be used to prepare MMC's. Figure 2 represents the types of fabrication techniques for MMC's. The main focus of the current study is on the stir casting method for MMC's fabrication and is also used for the formation of irregular and complex shapes [37].

TABLE 1. Types of Reinforcement

S. No.	Reinforcement Type	Reinforcement Name	Ref.	
1	Organic	Redmud	[5]	
		Flyash	[17]	
	Oxide	Al ₂ O ₃ , TiO ₂ , SiO ₂	[18-21]	
		Nitride	TiN, BN, Si ₃ N ₄	[22-24]
2	Inorganic	Carbide	TiC, SiC, CNT, B ₄ C	[25-29]
		Boride	TiB ₂ , ZrB ₂	[30-33]
		Others	Diamond	[34-36]

In this process, metal in powder, plate or ingot form is heated in the barometrical controlled heater and afterward permitted to arrive at the liquid state. When the base matrix metal is converted into a liquid state then the reinforcement such as ceramic metal or supplementary metals can be added either without preheating or in preheated form. The stirrer is used to mix the amalgamation formed due to addition of reinforcement in molten metal. The stirrer material should have melting characteristics like titanium carbide (TiC), silicon carbide (SiC), and graphite (Gr). After heating in the crucible, the molten metal is poured into the mould and allowed to solidify [39]. After solidification, the MMC's can be removed from the mould and processed further as per requirement. The setup for stir casting is shown in Figure 3.

3. REINFORCEMENTS EFFECTS ON MECHANICAL PROPERTIES

3. 1. Hardness

The hardness is an important property for MMC's as it is a measure of how much a material resists changes in its shape. Various researches show a comparative study of between the fabricated MMC's and their base metals. Bhubnaeswar [40] concluded that the 5, 10, 15, and 20 wt% SiC_p, when reinforced in the matrix of Al6061 using stir casting, the hardness of the fabricated composite increased. The 18%

increase in the hardness of fabricated composite has been recorded as compared to aluminum alloy. Reddy et al. [25] fabricated the Al6063-xTiC MMC using the stir casting fabrication technique. The MMC was fabricated as 5 /10 / 15 wt.% TiC along with Al6063 (see Figure 4). The 99.6 hardness value (HV) has been reported in the fabricated composite as compared to Al 6063 alloy, which has 59.6 HV [25].

The hardness value for the Al5083 matrix, when reinforced using SiC particles via stir casting method, increased to 85 BHN from 52 BHN, which principally increased the loads bearing capability due to SiC particles present in the composite. The hardness increment of 85% in developed material provides longer life and also enhances the wear resistance in fabricated material as reported by Chaubey et al. [28]. Yashpal et al. [41] performed hardness test on MMC produced by the combination of Al alloy and SiC reinforcement. It has been found that the mechanical properties such as yield strength, Young's modulus, and hardness are improved magnificently due to the homogeneous scattering of SiC particles in the matrix material. From the literature review, it has been noticed that hardness can be improved by using refined reinforced particles and by controlling the size of particulates present in the AMMC's.

3. 2. Tensile Strength

From the industry point of view, tensile testing has great importance before going to mass production stage of actual components that has to work under tensile loading. The testing also leads to cost reduction without compromising to the quality during production. The tensile testing concludes the functionality of the manufactured products [42].

Baradeswaran and Elaya Perumal [43] produced a MMC using Al7075, 5wt. % Gr and Al₂O₃ (2, 4, 6, and 8 Wt. %) via stir casting method. The tensile strength of 238 MPa had been achieved, which was 11% higher than pure Al alloy as shown in the Figure 5. Lata et al. [44] also opted stir casting route for the fabrication of Al7075-TiC (5, 10 and 15 wt. %) MMC and determined its tensile strength which had increased due to the uniform dispersion of TiC particles. A uniform trend was observed up to 10 wt. % of

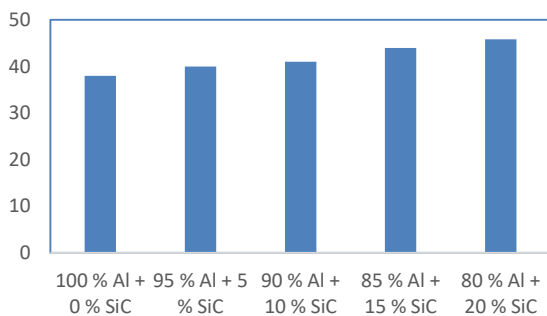


Figure 4. Hardness of various MMC's [40]

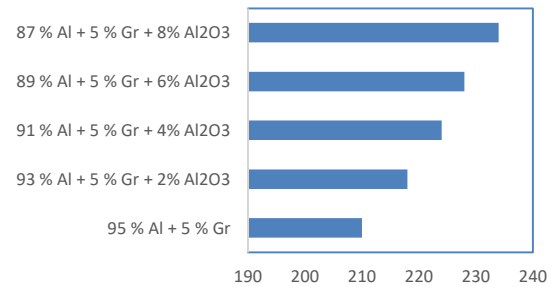


Figure 5. Tensile strength representation of AMMC's

TiC and beyond 10 wt. % of TiC the tensile strength has been increased [44]. Saravanan et al. [45] fabricated Al6061-5% Gr composite using stir casting route. An increment of 157 % in tensile strength as compared to Al6061 alloy (97 MPa to 249 MPa) has been observed.

Khanna et al. [46] fabricate Al6061-GO/CNT (0.5-2 Wt. % of GO/CNT) composite using stir casting method and concluded that the improvement in strength was due to constant dispersion and good cohesion characteristics of GO/CNT. It has been observed from the literature that the stirring operation is helpful in breaking agglomeration of different segregated reinforcement particles during fabrication of AMMC's. It has been also observed that the tensile strength can be improved via uniform mixing of reinforcements in the matrix material [43-47].

3. 3. Impact Testing

Impact testing has a crucial role in selecting the material for the particular application. The energy is required to cause the specimen to fail, relying on the material's application. Podder et al. [48] fabricated Al6063 and ZrO₂/TiO₂ (3:7, 1:1 and 7:3 Vol. %) composites by stir casting technique. The Charpy impact test machine (Aimil Co India Ltd.) has been utilized to measure impact energy. The higher impact energy has been found in the case of AMMC containing 7 Vol. % ZrO₂ and 3 Vol. % TiO₂ [48]. Al alloy LM25 was used as the matrix and boron carbide and alumina as reinforcement by Vijaya Ramnath et al. [49] for the production of MMC using stir casting technique. IS:1757 has been used to perform impact test. The highest impact energy of 2.42 J was observed for MMC with 95% LM25, 2% Al₂O₃, and 3% B₄C [49]. Kumar and Singh [50] tested Al4032-SiC (3-9 wt. %) composites for their impact strength. The MMC was prepared by stir casting technique. The uniform dispersion of reinforced particles enhances the impact energy of the fabricated material. The maximum impact energy of 42 J has been found for 6% SiC reinforced composite. It has been also observed that with increase of reinforcement percentage in MMC, its ductility decreases [50]. Ramnath et al. [51] reviewed the stir cast composite of Al6061/B₄C/Al₂O₃ and concluded that an increment of 21% in impact energy can be achieved by addition of 2 wt.

% Al₂O₃ and B₄C 3 wt. % reinforcement in the hybrid composite. Vijay Kashimatt and Hemanth Kymar [52] found that due to 3 wt. % particle addition of SiC in the Al alloy increases its impact energy from 0.075 J (pure Al alloy) to 0.0875 J (MMC). Gireesh et al. [53] developed a composite of Al6061/SiC/Al₂O₃ through stir casting process. The 17% increase in impact energy was achieved by addition of reinforcement in the hybrid composite [53]. Stir casting process was used to prepare composite of Al/SiC (0, 5, 10 and 20 wt. %) by Shukla et al. [54]. It has been observed that impact energy increases significantly up to 36% with increase in SiC reinforcement percentage. From the literature studied it has been found that resistance to dislocation of reinforced particles can be improved by increasing the reinforcement wt.% up to optimization level. By increasing the wt.% of reinforcement, interspacing in-between reinforced particles decreased, which results in the improvement of impact strength [52-55].

3. 4. Flexural Strength

The flexural test notifies about the maximum flexibility and bending of the material. The Volume/weight percentage of reinforcements has significant effect on the flexural strength of AMMC's. Other factors like the proportion of mixtures and grain size of reinforced particles also have crucial effects on the flexural behaviour of AMMC's. Vijaya Ramnath et al. [49] has fabricated the composite of aluminum alloy LM25 as base metal, boron carbide and alumina as reinforcement using stir casting method. ASTM: A-370 has been used to cut the specimen and tested on a three-point flexural test machine. The author has concluded that the flexural strength of fabricated AMMC decreases due to uneven dispersion and poor stirring of the reinforcement in AMMC. The maximum flexural strength (226.84 MPa) has been achieved in unreinforced Al alloy [49].

ASTM: B925-08 has been used to fabricate the specimen of AMMC reinforced with nano-alumina (1, 3, 5, and 7 Vol%). and tested on a three-point flexural test machine by Panda et al. [55]. The author has concluded that due to fine grain size and accurate dispersion of added reinforcement increases the flexural strength. The maximum flexural strength has been achieved with reinforcement of 7 Vol.% [56]. Surya and Prasanthi [57] reported that increment in the flexural strength has been observed in MMC of Al7075/SiC (5,10, and 15 Wt. %). The composite with 15 wt. % SiC particles contribute higher flexural strength of 320 N/mm² as compared to aluminum alloy 7075 (175 N/mm²). Baradeswaran and Elaya Perumal [43] concluded that the increment in the weight percentage of the reinforcement increases the mechanical, physical, and metallurgical properties of the composite. The authors concluded that the flexural strength of Al 7075 with reinforcements of alumina 8wt.% and graphene 5wt.% was increased from 185 N/mm² to 430 N/mm² as shown in Figure 6 [43]. The literature also reported that the homogenous mixing and binding action

of reinforcements enhances the flexural strength of the AMMC's [43, 56, 57].

4. EFFECT OF PROCESS PARAMETERS ON WEAR

In this era, the advancement of tribological properties is the key development for the materials and the enhancement of wear resistance is also the main concern in the existing metals. This material phenomenon gives us an idea about the deformation of the metal and loss in functionality of the material. Table 2 shows the wear of different MMC's.

Stir casting method was adopted by Thiraviam et al. [24] to fabricate MMC with steel and alumina chips (5, 7.5, and 10 wt. %) reinforcement. The wear rate has been improved due to presence of the steel chips in fabricated AMMC [24]. Patil et al. has fabricated Al7075-TiC/Gr (4, 8, and 12 Vol. % of TiC and Gr) MMC. It has been observed that the interfacial bonding of Al alloy and reinforcement particles to be essential factor for improving wear resistance [10]. Figure 7 shows the wear comparison under different loads [61].

The liquid state processing was used to fabricate Al6061-SiC (2, 4, 6 wt.% of SiC) composite by Veeresh Kumar et al. [58]. The wear resistance has been significantly increased with increase in wt.% of SiC

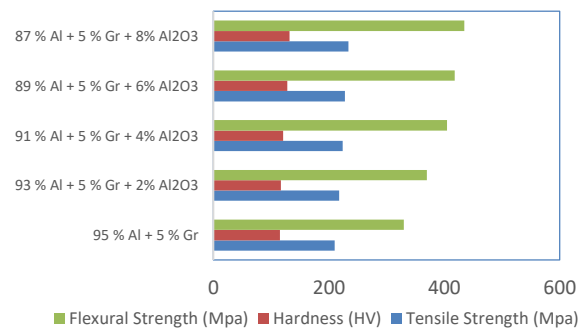


Figure 6. Effect of composition on mechanical properties

TABLE 2. Wear data for various AMMC

S No	Reinforcement	Wear		Ref.
		Al Alloy	AMMC	
1	6% SiC	130 x 10 ⁻³ mg/m	88 x 10 ⁻³ mg/m	[58]
2	1% Al ₂ O ₃ + 8% SiC	0.0050 g	0.0015 g	[21]
3	0.5% CNT + 2% TiC	0.0039g	0.0020 g	[59]
4	8% Al ₂ O ₃ + 5% Gr	0.0029 mm ³ /m	0.0015 mm ³ /m	[43]
5	1% Al ₂ O ₃ + 8% SiC	0.485 g	0.150 g	[60]
6	4% Al ₂ O ₃	0.017 g	0.004 g	[24]

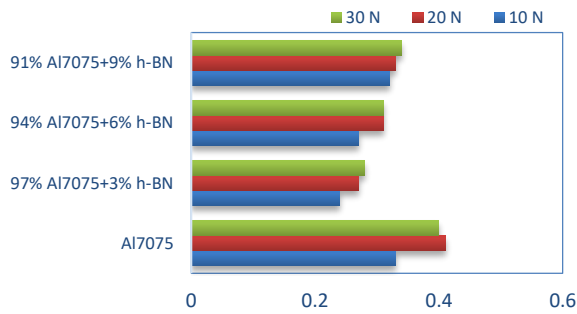


Figure 7. Wear rate under different loads

particles. So, It was concluded that superior wear resistance has been achieved with 6wt.% of SiC along with Al6061 alloy. Kuldeep et al. [62] fabricated stir cast MMC of Al7075 and hexagonal-boron nitride (h-BN) with 3, 6, and 9 wt. %. The study described that reinforcement with 3 wt. % h-BN produced the best result for wear rate. The decrement of 24.5% in wear loss was found in AMMC as compared to base alloy.

4. 1. Wear Affected By Average Load

Wear predominantly dependent on average load during testing of MMC's. The outcomes indicate that wear rate increases as the average load was increased during analysis on pin and disc apparatus. This can be the resultant of abrasion and delamination on MMC surface due to the increment of load [63-65].

4. 2. Wear Affected By Slid Velocity

The wear behaviour is also affected by slid velocity in composite material. The literature outcomes indicates that decrement in the wear rate was observed for slid velocity up to 5 m/s. After 5 m/s of slid velocity, the oxidation, abrasion and melting of the MMC surface starts which increases the material loss [66-68].

4. 3. Wear Affected By Slid Distance

Slid distance is another important factor in wear analysis of metal matrix composite. From the literature studied, it has been concluded that during wear test, the wear largely depends on slid distance as well as on slid time, which are proportional to each other. Wear rate increases with the enhancement of both the parameters. This is because of melting and formation of hardened layer on the contact surfaces of AMMC's and wear testing tool [69-71].

4. 4. Wear Affected by Weight Percent of Reinforcement

The percentage of reinforcement weight affects the physical and mechanical characteristics of the composite. However, the reinforcement's weight proportion also influences the surface properties. The decrement in the wear rate has been observed as percentage of reinforcement increases in the fabricated composite. The

coarse particles and excessive addition of reinforcement proportions leads to porosity which causes increment in material loss [71-73].

5. CONCLUSIONS

This review paper discusses about Aluminum based metal matrix composites with diverse reinforcements. The tribo-mechanical properties are discussed and based on the current review following conclusions can be drawn:

- 1) The Aluminum metal matrix composites has wide applications in aerospace, automotive and defence industries.
- 2) The stir casting is the most reliable technique to fabricate aluminum metal matrix composites due to its technical and economic aspects.
- 3) The working parameters like stirring speed, stirring time, melting temperature and impeller size have significant effect on the composite quality. The reinforcement weight / Volume percentage, shape and size have crucial relation to the performance of fabricated composite.
- 4) The hardness, tensile strength and flexural strength for mostly used AMMC's ranges from 38-99.6 HV, 100-478 MPa and 199.52-430 MPa respectively. Also, the impact energy for AMMC's varies from 3.6-38 J. The enhancement in these mechanical properties largely depends upon grain refinement, uniform dispersion, and interspacing of reinforcement particles in the fabricated composite material.
- 5) The wear behaviour of the fabricated composite significantly affected by the average load, slid distance, slid velocity, and reinforcement weight percentage during the wear test. The material loss generally observed in the range of 0.0050-0.004 g. The abrasion, oxidation, melting and delamination of the surface are the main reason observed as wear loss.

6. REFERENCES

1. S. M. Alloys, "Theoretical Analysis on the Behavior of Reinforced Industrial Shed Structures with Shape Memory Alloys," Vol. 35, No. 01, (2022), 228-236.
2. P. Gholami, M. A. Kouchakzadeh, and M. A. Farsi, "A continuum damage mechanics-based piecewise fatigue damage model for fatigue life prediction of fiber-reinforced laminated composites," *International Journal of Engineering, Transactions C: Aspects.*, Vol. 34, No. 6, (2021), 1512-1522, doi: 10.5829/ije.2021.34.06c.15.
3. A. K. Sharma, R. Bhandari, A. Aherwar, and R. Rimašauskiene, "Matrix materials used in composites: A comprehensive study," *Materials Today Proceeding.*, Vol. 21, (2020), 1559-1562, doi: 10.1016/j.matpr.2019.11.086.
4. M. Patel, B. Pardhi, D. Prasad Sahu, and S. K. Sahu, "Different Techniques Used for Fabrication of Aluminium Metal Matrix Composites," *International Journal of Engineering &*

- Technology*, Vol. 7, No. 1, (2021), doi: 10.29126/23951303/ijet-v7i1p1.
5. C. Kar and B. Surekha, "Characterisation of aluminium metal matrix composites reinforced with titanium carbide and red mud," *Material Research Innovation*, Vol. 25, No. 2, (2021), 67-75, doi: 10.1080/14328917.2020.1735683.
 6. S. Wakeel and A. A. Khan, "Review article a review on the mechanical properties of aluminium based metal matrix * Saif Wakeel and Ateeb Ahmad Khan," Vol. 6, (2017), 1096-1100.
 7. M. A. Aswad, S. H. Awad, and A. H. Kaayem, "Study on Iraqi Bauxite Ceramic Reinforced Aluminum Metal Matrix Composite Synthesized by Stir Casting," Vol. 33, No. 7, (2020), 1331-1339.
 8. S. Singh and S. Angra, "Experimental evaluation of hydrothermal degradation of stainless steel fibre metal laminate," *Engineering Science & Technology an International Journal*, Vol. 21, No. 1, (2018), 170-179, doi: 10.1016/j.jestch.2018.01.002.
 9. Z. Hosseini, S. M. Beidokhti, J. V. Khaki, and M. Pourabdoli, "Preparation of Porous Alumina / Nano-Nickel Composite by Gel Casting and Carbothermic Reduction," Vol. 35, No. 01, (2022), 220-227.
 10. N. A. Patil, S. R. Pedapati, O. Mamat, and A. M. H. S. Lubis, "Morphological characterization, statistical modeling and wear behavior of AA7075-Titanium Carbide-Graphite surface composites via Friction stir processing," *Journal of Material Research Technology*, Vol. 11, (2021), 2160-2180, doi: 10.1016/j.jmrt.2021.02.054.
 11. P. Kumar, K. Skotnicova, A. Mallick, M. Gupta, T. Cegan, and J. Jurica, "Mechanical characterization of graphene nanoplatelets reinforced mg-3sn alloy synthesized by powder metallurgy," *Metals (Basel)*, Vol. 11, No. 1, (2021), 1-14, doi: 10.3390/met11010062.
 12. G. Singh, R. Gaddam, V. Petley, R. Datta, R. Pederson, and U. Ramamurty, "strain-controlled fatigue in B-modified Ti-6Al-4V alloys," *Scripta Materialia*, Vol. 69, No. 9, (2013), 698-701, doi: 10.1016/j.scriptamat.2013.08.008.
 13. K. Sandesh, S. S. Sunder, and N. Radhika, "Effect of reinforcement content on the adhesive wear behavior of Cu10Sn5Ni/Si3N4 composites produced by stir casting," Vol. 24, No. 9, (2017), 1052-1060, doi: 10.1007/s12613-017-1495-1.
 14. B. Radovan, F. Mária, K. Peter, and J. Fűzer, "Preparation and properties of Fe-based composite materials," *Proceeding World Powder Metallurgy Congress Exhibition World, PM 2010*, Vol. 5, No. August 2017, 2010.
 15. M. Golestanipour, H. K. Ayask, N. Sasani, and M. H. Sadeghian, "A Novel, Simple and Cost-Effective Al A356/Al2O3 Nano-composite Manufacturing Route with Uniform Distribution of Nanoparticles," Vol. 28, No. 9, (2015), 1320-1327.
 16. A. AKPINAR BORAZAN and D. GOKDAI, "Effect of Organic Reinforcement Usage on Mica/Polyester Composite Material," *Cumhuriyet Science Journal*, Vol. 38, No. 4, (2017), doi: 10.17776/csj.348276.
 17. H. Kala, K. K. S. Mer, and S. Kumar, "A Review on Mechanical and Tribological Behaviors of Stir Cast Aluminum Matrix Composites.," *Procedia Materials Science*, Vol. 6, (2014), 1951-1960, doi: 10.1016/j.mspro.2014.07.229.
 18. J. Bhatt, N. Balachander, S. Shekher, R. Karthikeyan, D. R. Peshwe, and B. S. Murty, "Synthesis of nanostructured Al-Mg-SiO₂ metal matrix composites using high-energy ball milling and spark plasma sintering," *Journal of Alloys & Compound*, Vol. 536, No. SUPPL.1, (2012), S35-S40, doi: 10.1016/j.jallcom.2011.12.062.
 19. R. Casati, A. Fabrizi, A. Tuissi, K. Xia, and M. Vedani, "ECAP consolidation of Al matrix composites reinforced with in-situ γ -Al₂O₃ nanoparticles," *Material Science Engineering A*, Vol. 648, (2015), 113-122, doi: 10.1016/j.msea.2015.09.025.
 20. A. M. Sadoun, A. Fathy, A. Abu-oqail, H. T. Elmetwaly, and A. Wagih, "Structural , mechanical and tribological properties of Cu - ZrO₂/GNPs hybrid nanocomposites," *Ceramics International*, (2019), doi: 10.1016/j.ceramint.2019.11.258.
 21. S. Hossain, Rahman, M. M., Chawla, D., Kumar, A., Seth, P. P., Gupta, P., ... & Jamwal, A., "Materials Today : Proceedings Fabrication , microstructural and mechanical behavior of Al-Al₂O₃ -SiC hybrid metal matrix composites," *Material Today Proceeding*, (2019), 3-6, doi: 10.1016/j.matpr.2019.10.089.
 22. N. Gangil, H. Nagar, R. Kumar, and D. Singh, "Shape memory alloy reinforced magnesium matrix composite fabricated via friction stir processing," *Material Today Proceeding*, Vol. 33, (2020), 378-381, doi: 10.1016/j.matpr.2020.04.172.
 23. Falodun, O.E., Obadele, B.A., Oke, S.R., Ige, O.O. and Olubambi, P.A., "Effect of TiN and TiCN additions on spark plasma sintered Ti - 6Al - 4V," *Particulate Science & Technology*, Vol. 38, No. 2, (2020), 156-165, doi: 10.1080/02726351.2018.1515798.
 24. T. R. Thiraviam, R. V. Ravisankar, P. K. Pradeep Kumar, T. R. Thanigaivelan, and A. R. Arunachalam, "A novel approach for the production and characterization of aluminium-alumina hybrid metal matrix composites," *Material Research Express*, Vol. 7, No. 4, (2020), doi: 10.1088/2053-1591/ab8657.
 25. P. V. Reddy, P. Ramanjaneyulu, B. V. Reddy, and P. S. Rao, "Simultaneous optimization of drilling responses using GRA on Al-6063/TiC composite," *SN Applied Science*, Vol. 2, No. 3, (2020), 1-10, doi: 10.1007/s42452-020-2214-5.
 26. P. Malhotra, R. K. Tyagi, N. K. Singh, and B. Singh, "Materials Today : Proceedings Experimental investigation and effects of process parameters on EDM of Al7075/SiC composite reinforced with magnesium particles," *Material Today Proceeding*, (2019), doi: 10.1016/j.matpr.2019.11.069.
 27. E. Ghasali, R. Yazdani-rad, K. Asadian, and T. Ebadzadeh, "Production of Al-SiC-TiC hybrid composites using pure and 1056 aluminum powders prepared through microwave and conventional heating methods," *Journal of Alloys & Compound*, Vol. 690, (2017), 512-518, doi: 10.1016/j.jallcom.2016.08.145.
 28. A. Chaubey, R. Dwivedi, R. Purohit, R. S. Rana, and K. Choudhary, "Experimental inspection of aluminium matrix composites reinforced with SiC particles fabricated through ultrasonic assisted stir casting process," *Material Today Proceeding*, Vol. 26, (2019), 3054-3057, doi: 10.1016/j.matpr.2020.02.634.
 29. Adil Nazaruiddin and T. S. Krishnakumar, "Effect of Addition of Nanoparticles on the Mechanical Properties of Aluminium," *International Journal of Engineering & Research*, Vol. V4, No. 08, (2015), 268-272, doi: 10.17577/ijertv4is080371.
 30. M. A. Shaik and B. R. Golla, "Two body abrasion wear behaviour of Cu-ZrB₂ composites against SiC emery paper," *Wear*, Vol. 450-451, 203260, (2020), doi: 10.1016/j.wear.2020.203260.
 31. V. Mohanavel, M. Ravichandran, and S. S. Kumar, "Materials Today : Proceedings Tribological and mechanical properties of Zirconium Di-boride (ZrB₂) particles reinforced aluminium matrix composites," *Material Today Proceeding*, (2019), 7-9, doi: 10.1016/j.matpr.2019.07.603.
 32. P. Lakshmanan, "Turning experiments on Al/B4C metal matrix nanocomposites," *Material Science Forum*, Vol. 979 MSF, (2020), 16-21, doi: 10.4028/www.scientific.net/MSF.979.16.
 33. A. Nirala, S. Soren, N. Kumar, and D. R. Kaushal, "Materials Today : Proceedings A comprehensive review on mechanical properties of Al-B₄C stir casting fabricated composite," *Material Today Proceeding*, (2019), 10-13, doi: 10.1016/j.matpr.2019.09.172.
 34. J. L. Amorós, E. Blasco, A. Moreno, and C. Feliu, "Mechanical properties obtained by nanoindentation of sintered zircon - glass matrix composites," *Ceramic International*, Vol. 46, No. 8, (2020), 10691-10695, doi: 10.1016/j.ceramint.2020.01.075.
 35. C. B. Abraham, V. B. Nathan, S. R. Jaipaul, D. Nijesh, M. Manoj, and S. Navaneeth, "Materials Today : Proceedings Basalt fibre

- reinforced aluminium matrix composites - A review," *Material Today Proceeding*, (2019), doi: 10.1016/j.matpr.2019.06.135.
36. V. Srinivas, A. Jayaraj, V. S. N. Venkataramana, T. Avinash, and P. Dhanyakanth, "Effect of Ultrasonic Stir Casting Technique on Mechanical and Tribological Properties of Aluminium-Multi-walled Carbon Nanotube Nanocomposites," *Journal Bio and Tribo Corrosion*, Vol. 6, No. 2, (2020), 1-10, doi: 10.1007/s40735-020-0331-8.
 37. N. Munasir, Triwikantoro, M. Zainuri, R. Bäbler, and Darminto, "Corrosion polarization behavior of Al-SiO₂ composites in 1M and related microstructural analysis," *International Journal of Engineering Transaction A Basics*, Vol. 32, No. 7, (2019), 982-990, doi: 10.5829/ije.2019.32.07a.11.
 38. S. Liu, Y. Wang, T. Muthuramalingam, and G. Anbuechhiyan, "Effect of B₄C and MOS₂ reinforcement on micro structure and wear properties of aluminum hybrid composite for automotive applications," *Composites Part B Engineering*, Vol. 176, (2019), 107329, doi: 10.1016/j.compositesb.2019.107329.
 39. V. K. Sharma, R. C. Singh, and R. Chaudhary, "Effect of flyash particles with aluminium melt on the wear of aluminium metal matrix composites," *Engineering Science and Technology an International Journal*, Vol. 20, No. 4, (2017), 1318-1323, doi: 10.1016/j.jestch.2017.08.004.
 40. T. Bhubnaeswar, "Investigation of Mechanical Properties of Aluminium Silicon Carbide Hybride Metal Matrix Composite (Mmcs) Bhagwat T. Dhekwar , Aliva Mohanty , Jagdish Pradhan , Saswati Nayak," Vol. 5, No. 4, (2017), 88-105.
 41. Yashpal, Sumankant, C. S. Jawalkar, A. S. Verma, and N. M. Suri, "Fabrication of Aluminium Metal Matrix Composites with Particulate Reinforcement: A Review," *Material Today Proceeding*, Vol. 4, No. 2, (2017), 2927-2936, doi: 10.1016/j.matpr.2017.02.174.
 42. M. Aktar Zahid Sohag, P. Gupta, N. Kondal, D. Kumar, N. Singh, and A. Jamwal, "Effect of ceramic reinforcement on the microstructural, mechanical and tribological behavior of Al-Cu alloy metal matrix composite," *Material Today Proceeding*, Vol. 21, 1407-1411, (2020), doi: 10.1016/j.matpr.2019.08.179.
 43. A. Baradeswaran and A. Elaya Perumal, "Study on mechanical and wear properties of Al 7075/Al₂O₃/graphite hybrid composites," *Composites Part B Engineering*, Vol. 56, (2014), 464-471, doi: 10.1016/j.compositesb.2013.08.013.
 44. S. Lata, Pandey, A., Sharma, A., Meena, K., Rana, R., & Lal, R. "An Experimental Study and Analysis of the Mechanical Properties of Titanium Dioxide Reinforced Aluminum (AA 5051) Composite," *Material Today Proceeding*, Vol. 5, No. 2, (2018), 6090-6097, doi: 10.1016/j.matpr.2017.12.214.
 45. M. Saravanan, R. M. Pillai, K. R. Ravi, B. C. Pai, and M. Brahmakumar, "Development of ultrafine grain aluminium-graphite metal matrix composite by equal channel angular pressing," *Composite Science Technology*, Vol. 67, No. 6, (2007), 1275-1279, doi: 10.1016/j.compscitech.2006.10.003.
 46. V. Khanna, V. Kumar, and S. Anil, "Mechanical properties of aluminium-graphene/ carbon nanotubes (CNTs) metal matrix composites: Advancement, opportunities and perspective," *Material Research Bulletin*, Vol. 138, (2021), p. 111224, doi: 10.1016/j.materresbull.2021.111224.
 47. D. H. Xiao, J. N. Wang, D. Y. Ding, and H. L. Yang, "E ffect of rare earth Ce addition on the microstructure and mechanical properties of an Al-Cu-Mg-Ag alloy," Vol. 352, (2003), 84-88, doi: 10.1016/S0925-8388(02)01162-3.
 48. D. Podder, S. Chakraborty, and U. K. Mandal, "RSM analysis of impact property and characterization of Al6063-Cu-TiO₂-ZrO₂ composites fabricated by stir casting process," *Sādhanā*, Vol. 46, No. 2, (2021), doi: 10.1007/s12046-021-01583-7.
 49. B. Vijaya Ramnath, C. Elanchezhian, M. Jaivignesh, S. Rajesh, C. Parswajinan, and A. Siddique Ahmed Ghias, "Evaluation of mechanical properties of aluminium alloy-alumina-boron carbide metal matrix composites," *Materials and Design*, Vol. 58, (2014), 332-338, doi: 10.1016/j.matdes.2014.01.068.
 50. D. Kumar and P. K. Singh, "ScienceDirect Microstructural and Mechanical Characterization of Al-4032 based Metal Matrix Composites," *Material Today Proceeding*, Vol. 18, (2019), 2563-2572, doi: 10.1016/j.matpr.2019.07.114.
 51. B. V. Ramnath, Vijaya, C. Elanchezhian, R. M. Annamalai, S. Aravind, T. Sri Ananda Atreya, V. Vignesh, and C. Subramanian "Aluminium metal matrix composites - A review," *Reviews on Advanced Materials Science*, Vol. 38, No. 1, (2014), 55-60,.
 52. Vijay Kashimatt, M. G., & Hemanth Kymar, C., "Characterization and Mechanical Properties of LM25-SiC Composites," (2021).
 53. C. Hima Gireesh, K. Durga Prasad, and K. Ramji, "Experimental Investigation on Mechanical Properties of an Al6061 Hybrid Metal Matrix Composite," *Journal of Composite Science*, Vol. 2, No. 3, (2018), doi: 10.3390/jcs2030049.
 54. M. Shukla, S. K. Dhakad, P. Agarwal, and M. K. Pradhan, "ScienceDirect Characteristic Behaviour of Aluminium Metal Matrix Composites : A Review," *Material Today Proceeding*, Vol. 5, No. 2, (2018), 5830-5836, doi: 10.1016/j.matpr.2017.12.180.
 55. S. Panda, K. Dash, and B. C. Ray, "Processing and properties of Cu based micro- and nano-composites," Vol. 37, No. 2, (2014), 227-238.
 56. S. Singh and S. Angra, "Flexural and Impact Properties of Stainless Steel based Glass Fibre Reinforced Fibre Metal Laminate under Hygrothermal Conditioning," Vol. 31, No. 1, (2018), 164-172.
 57. M. S. Surya and G. Prasanthi, "Manufacturing, microstructural and mechanical characterization of powder metallurgy processed Al7075/SiC metal matrix composite," *Material Today Proceeding*, (2020), doi: 10.1016/j.matpr.2020.03.315.
 58. G. B. Veeresh Kumar, C. S. P. Rao, and N. Selvaraj, "Studies on mechanical and dry sliding wear of Al6061-SiC composites," *Composites Part B Engineering*, Vol. 43, No. 3, (2012), 1185-1191, doi: 10.1016/j.compositesb.2011.08.046.
 59. B. M. Girish, B. P. Shivakumar, M. B. Hanamantraygouda, and B. M. Satish, "Wear behaviour of hot forged SiC reinforced aluminium 6061 Composite materials," *Australian Journal of Mechanical Engineering*, (2020), 1-8, doi: 10.1080/14484846.2020.1714353.
 60. Nayim, S. T. I., Hasan, M. Z., Seth, P. P., Gupta, P., Thakur, S., Kumar, D., & Jamwal, A., "Materials Today : Proceedings Effect of CNT and TiC hybrid reinforcement on the micro-mechano-tribo behaviour of aluminum matrix composites," *Material Today Proceeding*, (2019), 8-11, doi: 10.1016/j.matpr.2019.08.203.
 61. M. P. Reddy, Himyan, M. A., Ubaid, F., Shakoore, R. A., Vyasraj, M., Gururaj, P., ... & Gupta, M. "Enhancing thermal and mechanical response of aluminum using nanolength scale TiC ceramic reinforcement," *Ceramic International*, (2018), doi: 10.1016/j.ceramint.2018.02.135.
 62. B. Kuldeep, K. P. Ravikumar, and S. Pradeep, "Effect of Hexagonal Boron Nitrate on Microstructure and Mechanical Behavior of Al7075 Metal Matrix Composite Producing by Stir
 63. R. Prathipa, C. Sivakumar, and B. Shanmugasundaram, "Experimental Investigation of Aluminium (Al6061) Alloy with Fly Ash Metal Matrix Composite Material," Vol. 25, No. 5, (2021), 270-288.
 64. M. Jagannatham, M. S. S. Saravanan, K. Sivaprasad, and S. P. K. Babu, "Mechanical and Tribological Behavior of Multiwalled Carbon Nanotubes-Reinforced AA7075 Composites Prepared by Powder Metallurgy and Hot Extrusion," *Journal of Materials Engineering and Performance*, Vol. 27, No. 11, (2018), 5675-5688, doi: 10.1007/s11665-018-3681-3.
 65. R. Arunbharathi, R. Rathish, R. S. Vignesh, P. S. Seelan, and R. V. Prasanth, "Mechanical and Tribological Characteristics of Particulates Embedded Aluminium Based Composites - A Review,"

- Vol. XIV, No. 3, (2021), 12-16.
66. J. J. Rino, D. Chandramohan, and K. S. Sucitharan, "An Overview on Development of Aluminium Metal Matrix Composites with Hybrid Reinforcement," Vol. 1, No. 3, (2012), 196-203.
 67. N. Radhika, R. Reghunath, and M. Sam, "Improvement of mechanical and tribological properties of centrifugally cast functionally graded copper for bearing applications," Vol. 233, No. 9, (2019), 3208-3219, doi: 10.1177/0954406218805508.
 68. G. B. Rao Bannaravuri, P. K., Raja, R., Apparao, K. C., Rao, P. S., Rao, T. S., ... & Prince, R. M. R., "Impact on the microstructure and mechanical properties of Al-4.5Cu alloy by the addition of MoS₂," *International Journal of Lightweight Materials and Manufacture*, Vol. 4, No. 3, (2021), 281-289, doi: 10.1016/j.ijlmm.2021.01.001.
 69. G. Królczyk, E. Feldshtein, L. Dyachkova, M. Michalski, T. Baranowski, and R. Chudy, "On the microstructure, strength, fracture, and tribological properties of iron-based MMCs with addition of mixed carbide nanoparticulates," *Materials (Basel)*, Vol. 13, No. 13, (2020), doi: 10.3390/ma13132892.
 70. N. Subramani, R. Haridass, S. Pramodh, A. Prem Anand, and N. Manikandan, "Mechanical strength analysis of Al6061&Al2024 based metal matrix composite prepared through stir casting method," *Material Today Proceeding*, Vol. 47, (2021), 4513-4517, doi: 10.1016/j.matpr.2021.05.417.
 71. K. V. Mahendra and K. Radhakrishna, "Characterization of stir cast Al-Cu-(fly ash + SiC) hybrid metal matrix Composites," *Journal of Composite Materials*, Vol. 44, No. 8, (2010), 989-1005, doi: 10.1177/0021998309346386.
 72. H. Garg, Sehgal, K., Lamba, R., & Kajal, G. *A Systematic Review: Effect of TIG and A-TIG Welding on Austenitic Stainless Steel BT - Advances in Industrial and Production Engineering*, No. September. Springer Singapore, (2019).
 73. S. Murugan, S. Jegan, and V. Velmurugan, "Tribological Wear Behaviour and Hardness Measurement of SiC, Al₂O₃ Reinforced Al Matrix Hybrid Composite," *Journal of The Institution of Engineers (India): Series D*, Vol. 98, No. 2, (2017), 291-296, doi: 10.1007/s40033-016-0134-8.

Persian Abstract

چکیده

در قرن بیست و یکم، مواد مختلفی مانند فلزات، آلیاژها و کامپوزیت ها برای کاربردهای مختلف صنعتی در دسترس هستند. مواد کامپوزیت به دلیل خواص مکانیکی افزایش یافته نسبت به مواد دیگر محبوبیت پیدا می کنند. با این حال، برای بهبود مستمر در خواص این مواد، گروه های مختلف تحقیقاتی به طور مداوم درگیر آن هستند. در این مقاله تحقیقاتی، تمرکز بر بررسی خواص مکانیکی مانند سختی، استحکام کششی، مقاومت خمشی، مقاومت ضربه ای به همراه ویژگی های سطحی مانند مقاومت به سایش AMMC است. طبق ادبیات موجود، پردازش حالت مایع به دلیل پراکندگی بهتر ذرات تقویت کننده در مواد ماتریس، محبوب تر از پردازش حالت جامد است. ریخته گری همزن به دلیل سهولت و هزینه کم تولید بیشتر از روش پردازش حالت مایع استفاده می شود. مشخص شده است که ویژگی های مکانیکی و سطحی AMMC ها را می توان با افزودن ذرات تقویت کننده مختلف در درصد های کوچک (معمولاً ۰.۵-۲٪) بهبود بخشید. مشاهده شده است که سختی، استحکام کششی و استحکام خمشی برای AMMC های بیشتر مورد استفاده به ترتیب بین HV ۳۸-۹۹/۶، ۱۰۰-۴۷۸ MPa و ۱۹۹/۵۲-۴۳۰ MPa است. مقاله تحقیقاتی همچنین شامل تأثیر پارامترهای مختلف کاری بر نرخ سایش AMMC می شود. توجه شده است که کاهش سایش برای AMMC به طور کلی از ۰/۰۰۴-۰/۰۰۵ گرم متغیر است. مقاومت در برابر ضربه یک پارامتر حیاتی در مطالعه AMMC های مورد استفاده برای کاربردهای هوا فضا و خودرو است و توجه شده است که مقدار آن برای AMMC های محبوب بین ۳،۶-۳۸ J متفاوت است.



A Method for Automatic Lane Detection using a Deep Network

A. A. Fallah*, A. Soleymani, H. Khosravi

Department of Electronics, Faculty of Electrical Engineering, Shahrood University of Technology, Shahrood, Iran

PAPER INFO

Paper history:

Received 15 December 2021

Received in revised form 21 January 2022

Accepted 22 January 2022

Keywords:

Lane Detection

Deep Learning

Generative Adversarial Networks

Semi-supervised Learning

ABSTRACT

Lane detection is amongst the most important operations during the automatic driving process. This process aims to detect lane lines to control the vehicle's direction in a specific lane on the road and it can be effective in preventing accidents. Besides being online, the most requirement for lane detection methods in automatic driving is their high accuracy. The use of deep learning to create fully automated systems in lane detection has been done extensively. Automated learning-based methods used for road lane detection are often of supervised type. One of the disadvantages of these methods, despite their excellent accuracy, is that they need a set of labeled data, which limits the development procedure of the lane detection system, and most importantly establishing a standard set of labeled data is very time-demanding. The recommended solution is to use appropriate learning approaches that can be used to achieve the relative accuracy of the supervised approaches and to improve their speed. It also enables us to use different datasets without a constraint label that the tagged dataset would create in the algorithm development relative to the new dataset. In this research, we present an automatic semi-supervised learning method using deep neural networks to extract the data of lane lines, using labeled (mask for detected lines) and unlabeled datasets. The results demonstrate the suitable accuracy of the adopted method according to the proposed approach and also improves its computational complexity due to the significant reduction in the number of teachable network parameters.

doi: 10.5829/ije.2022.35.04a.20

1. INTRODUCTION

Road lane detection is one of the most important processes in automatic driving [1-6]. With road lane detection systems, we can analyze the video images of violations such as lane deviation. One of the most important remarks for lane detection is the comprehensiveness of the proposed method to be applied to all types of roads. In other words, when an algorithm or a method is designed for lane detection based on a dataset, the capability of applying it to another dataset is of high importance. In most learning-based methods for road lane detection, the executive method learning paradigm usually uses the supervised type to obtain appropriate accuracy. Such a paradigm limits the used algorithms. For example, an algorithm would work on a specific dataset because it is trained solely with unique data. Also, such an approach requires the use of labeled data, which has its own limitations. To overcome these

limitations, methods with a different paradigm from the supervised method can be used, such as Semi-Supervised methods that are presented as the solution in this study. In this method, the authors attempt to provide a model that is independent of the time resulting from dataset labeling. Since labeling the dataset is time-consuming, we try to perform the lane detection process on a dataset in which only a few of the data have labels. In the remainder of the paper, section 2 describes the background research in this area. Then, section 3 details the proposed method. The experimental results of implementing the suggested method are presented in section 4. Finally, section 5 provides the conclusion.

2. LITERATURE REVIEW

In addition to the extensive researches that are conducted in engineering sciences in order to improve the traffic

*Corresponding Author Institutional Email:
Aliasghar.fallah@Shahroodut.ac.ir (A. A. Fallah)

conditions, including improving the mechanical and electrical conditions of the the vehicles [7-8], road identification and detection of lanes on them is a critical task for automatic control in self-driving vehicles. The following provides some of the research in this field.

In general, road identification and detection of its lanes have two paradigms [9]. One is the use of classic methods in machine vision, and another is the adoption of deep learning methods. Many pieces of research have already been conducted on comparison review and stating the advantages and disadvantages of the proposed methods for road data extraction and lane detection [10-14]. Here we also deal with some methods that employ deep learning for road and its lanes detection. In terms of application, road and lane detection can be stated in three different scenarios [14]. The first is the detection of only the motion boundary of the driver itself (one direction of the considered road) [15-17]. The second is the detection of the number of available motion directions on a road [18-19]. Finally, the third is the detection of all roads present in the image [20-21] (which may include two different motion lanes) and the last one poses more challenges than the previous two cases. Mostly, learning-based approaches are exploited to implement each of the aforementioned approaches. Considering the proposed method in this paper, we focus on the literature that used learning algorithms for lane detection. For instance, Satti et al. [22] adopted a convolutional neural network and a Sobel edge detection algorithm using Huff transform for lanes detection in different situations, such as daytime, low-lit environments, and night. The authors used a supervised approach with a set of 4000 labeled data and employed data augmentation operations to increase the sample count and thus improve the training process. The results indicate the high accuracy of the method in both cases of using data augmentation and discarding it in all test situations. Another research was carried out by Lee and Liu [9], in which a method named 3TCNN was introduced. In this method, first, a convolutional network with five convolutional layers is used. Then, at the end of the fifth layer, a triple branch is used for lanes detection, road identification, and route prediction using a regression process. The regression operation in this task is for the estimation of routes lanes in the cases the road lanes in the image are covered due to vehicles' motion. Among the notable remarks in this research is the accuracy of 94% in the suggested method. Another study done by Wang et al. [23] utilizes a convolutional network to form a double-level set segmentation model. Another idea is to exploit cloud computing techniques for the segmentation and identification of edges to reduce the computational burden of the training process. Using a deep convolutional network and two given segmentation methods used in the following operations, the lanes are detected in the last stage of the lane detection task by using a transfer matrix formed in the previous stage. One

of the notable points to mention regarding this study is the diversity of tests on samples under different conditions. Moreover, the accuracy of higher than 97% in the lane detection method in the case of images with an ideal environment, and high accuracy in the challenging test cases are worth mentioning. Zou et al. [24] used a deep network shaped by combining convolutional and recurrent neural network (RNN) [25] networks for road lane detection. They employed a convolutional network to obtain the features available in the image. Then, using an LSTM network, which is a type of RNN network, and utilizing the extracted features sent by the convolutional network, the system is trained and road lanes are detected. The remark that is worth noting here is that the authors used two datasets with large scale and high volume, and the designed system was tested under challenging conditions. The obtained results highlighted the high accuracy of the suggested algorithm. Generally, when using deep networks for lane detection, a deep convolutional neural network is used as the base method in adaptation for specific operations. Convolutional neural networks are very popular because of their compatibility with a variety of feature extraction methods in signals, including various machine learning models or even group models of conflict algorithms such as q_{xy} [26], which determine and extract two-dimensional features. However, the research works mentioned so far all are supervised types. The main issue with such methods is their high accuracy thanks to adopting a large set of data for classification and lane detection operations, and most importantly the time consumption of lanes labeling (determination), i.e., making a mask as the desired output of the problem. On the other hand, the lane detection process by using unsupervised learning methods lacks sufficient detection accuracy compared to supervised methods, in addition to independence on the time-demanding labeling process. Therefore, the application of semi-supervised methods is of special importance because it reduces the time required for labeling all the data, as well as providing a specific dataset as the main training part besides the unlabeled auxiliary dataset. In these present methods, the unlabeled data play the role of auxiliary data for training purposes. Nonetheless, this type of data needs a large amount of data compared to the labeled data during the training process.

3. PROPOSED METHOD

3. 1. Generative Adversarial Network (GAN)

Generative Adversarial Network (GAN) is a type of deep network that was introduced by Goodfellow et al. [27]. This network consists of one main generative and one discriminator part. The training process of each network is performed using the two-person game theory idea [27].

Training of each of the mentioned networks should have the higher accuracy possible. This approach means that each network enjoys optimal performance in its structure. Thereby, it can be said that the adversarial performance of the whole network is similar to a game with zero-sum optimal if each of the present networks has an optimal performance. In this type of network, the training process is usually in an unsupervised manner; however, the network can be used for supervised processes as well. Amongst the simplest deep adversarial networks is the auto-encoder deep network. As stated previously, GANs are normally trained in an unsupervised manner, although supervised and semi-supervised types are also applicable [28]. Semi-supervised GAN is a type of GANs that can be adopted for classification processes. This is described in the following subsection.

3. 2. Semi-Supervised GAN

3. 2. 1. Semi-supervised Learning Paradigm In learning paradigms, a specific learning policy for the system to be implemented is adopted according to the type and nature of the data. Based on whether the data is labeled or unlabeled the supervised or unsupervised learning is employed. Basically, for a system trained with supervised learning, the accuracy and performance of the system will be much better. Additionally, more comprehensive criteria can be presented for evaluating the system's performance. Nevertheless, it has the problem of a costly and time-demanding labeling process. Hence, the idea of using a semi-supervised paradigm is proposed in which the dataset is composed of both labeled and unlabeled data. The way of integrating these datasets in the training process depends on the adopted algorithm for the problem under study. Even though the obtained results from applying these semi-supervised methods are not very satisfying, they are widely used. Thanks to their fast speed compared to fully-supervised methods and their relative accuracy in comparison to the implemented paradigm [29].

3. 2. 2. Semi-supervised GAN This network as shown in Figure 1 is composed of two main parts, namely, the discriminator and the generative, which are artificial networks used based on the nature of the problem and its application. The major difference between the semi-supervised network and standard GAN is the presence of a labeled dataset in the former.

As it is observed in the network structure, in a problem with n classes, the final output will be $n + 1$ classes; one of them is the false (counterfeit) data class, represented by false. This network is often used for classification processes. However, the feedforward network can also be adopted for image segmentation by applying a specific approach. To this end, a deep network with a base convolutional structure is used in the

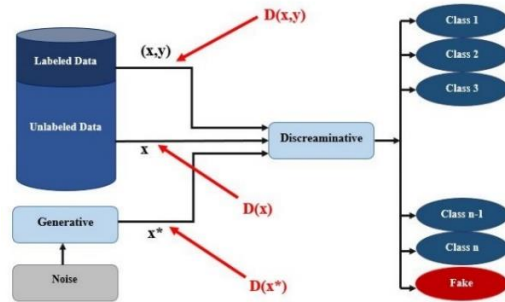


Figure 1. Semi-supervised generative adversarial network

discriminator network for image segmentation, with the only exception that an inverse convolution process (several inverse convolution processes based on the conditions) substitutes the fully-connected layer that is used at the end of the network for classification. The generative part of the network generates the false dataset. This network uses a random noise vector to produce images with the same dimensions as the original images. In general, based on the nature of the implementation operations, both parts of the network can be determined from a structural viewpoint. The final output of the network, as per its design structure, is the segmented image of the original image.

3. 3. Implementation Details Our goal of using semi-supervised GANs is to perform the image segmentation process. The overall layout and procedure are illustrated in Figure 2. To this aim, a dataset including 1210 labeled samples, and 5800 unlabeled samples, that the dimensions of each of the input images are $3 * 320 * 480$, are used for the lane detection process. This is carried out in the form of a semi-supervised GAN with two main parts. In the following, each of these parts (the discriminator network and the generative network) is described in more detail.

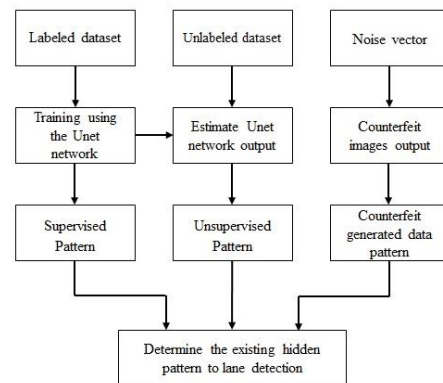


Figure 2. Semi-Supervised Generative Adversarial Network

3.3.1. Discriminator Network This network, as is shown in Figure 1, has 3 inputs. Two inputs are for the training data, which perform the training process of both supervised and unsupervised parts of the discriminator. The third input is for the generative network. The supervised training process is carried out using the labeled dataset. This part of the network trains the main parameters of the image segmentation process. A UNet model (Figure 3) is used here for the segmentation process. The second part of the dataset is unlabeled. This part of the dataset is used for the unsupervised training of the whole system based on a cost function specified for the dataset. The cost function is usually similar to the supervised section because the parameters trained in the supervised section must be used to perform the segmentation process. The third input to the discriminator model is the output of the generative part.

3.3.2. Generative Network This part uses a random noise vector to produce counterfeit images. The point that is worth mentioning is that the results obtained from the generative network for the training do not affect training the discriminator section. This means that, in training the whole system, the weights of the discriminator do not change during training the generative part. However, it does not mean that the generative part has no impact on the whole network training process. Conversely, the optimality of performance of this section significantly affects the overall results of the network with the given objective. We adopt a decoder with inverse convolutional layers in the generative section of the network to build counterfeit images, the layer-like arrangement of which is presented in Table 1.

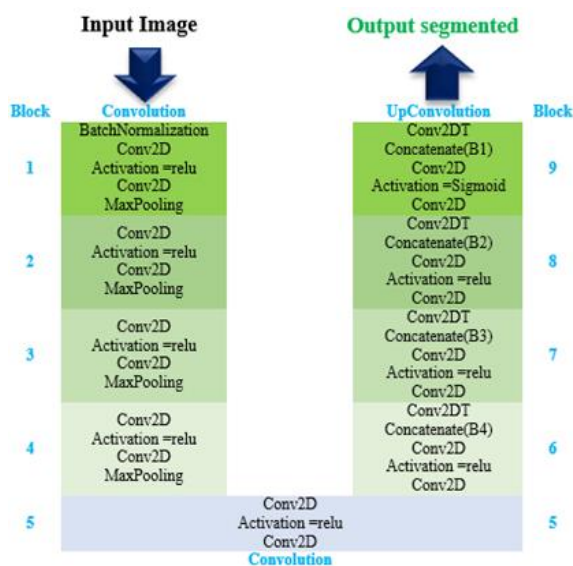


Figure 3. Unet model used in discriminator network

TABLE 1. The layer structure of the generating network

Layer	Filter Kernel Size	Stride	Padding	BN*	AF*
Dense	512 -	-	-	-	-
Conv2DT	256 3	2	Same	+	Relu
Conv2DT	128 3	2	Same	+	Relu
Conv2DT	64 3	2	Same	+	Relu
Conv2DT	1 3	2	Same	-	Sigm oid

* AF(Activation Function) * BN(Batch Normalization)

In sections 3.3 and 3.4, the general implementation was stated. As more details that can be mentioned, the value of the learning coefficient of the model is initialized with a value of 0.01 and changes dynamically. In all available models, we used Adam optimizer to run. The important point that can be made is the optimal number of training parameters, which is less computationally complex compared to the input dimensions and the number of data used than other Unet networks with the models used in training. We will refer to it in the results. Also, the number of repetitions of the training phase is equal to 500. To run the proposed method, we have used Python 3.2 as well as Google Colab using the GPU environment.

4. EMPIRICAL RESULTS

Based on what we stated about the overall procedure of the road lane detection process, the item that can show us the overall quality of performance of the semi-supervised GAN with more clarity is the output of the two main parts of the network, i.e., the generative and discriminator parts. This section presents the results obtained by applying the proposed method to the two main parts of the network.

4.1. The Output of the Generative Network By producing the dataset and participating in the main part of network training with the unsupervised part of the discriminator section, the generative part of the semi-supervised GAN plays a key role in the convergence of the network to a stable value. Figure 4 shows several images produced by the generative network during the training process. Images a, b, c, g, h, and i have been produced by the generative network. For images a, b, and c, the performance of the network in terms of image generation is satisfactory. Images d, e, and f verify this

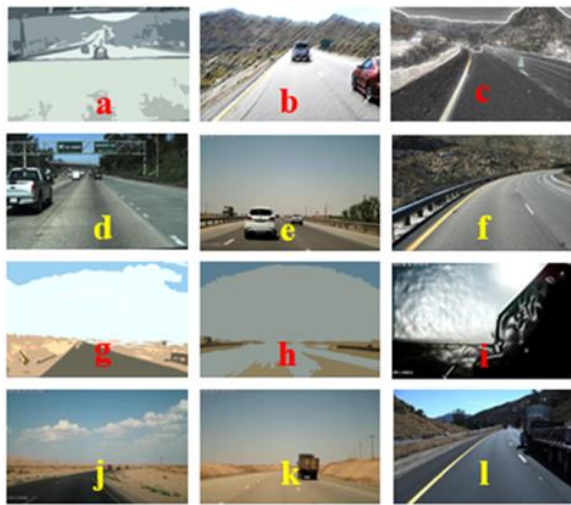


Figure 4. several images produced by the generative network and similar images corresponding to them in the main dataset

claim. These images are available in the used dataset. On the other side, generated images g, h, and i which are somehow similar to images j, k, and l, suffer from relatively low quality. However, the overall performance of the generative network is desirable in proportion to the problem objective.

4. 2. Lane Detection Using The Discriminator

Road lanes detection that is the main objective of this research study is the output of the main part in the supervised section. To evaluate the performed task, the Intersection Over Union (IoU) criterion is utilized. IoU is one of the most common criteria used in machine vision processing operations, including segmentation and object recognition. Figure 5 illustrates the conceptual generality of this criterion. The mathematical nature of this criterion is defined in Equations (1) and (2).

$$IoU = \frac{GroundTruth \cap Predicted}{GroundTruth \cup Predicted} = \frac{TP}{FP+TP+FN} \quad (1)$$

$$ACC = \frac{N_{GroundTruth \cap Predicted}}{N_{GroundTruth}} = \frac{N_{TP}}{N_{TP+FN}} \quad (2)$$

In Equation (2), the variables N_TP and N_(TP+FN) are the number of points (pixels) predicted as lines and pixels of lines in GroundTruth, respectively. Figure 6 shows several outputs related to the lane detection process. As

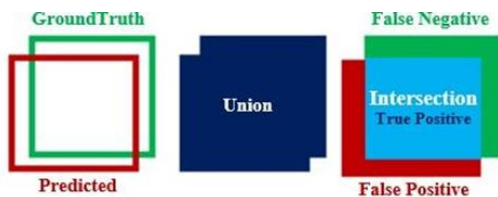


Figure 5. Conceptual generality of the IoU criterion

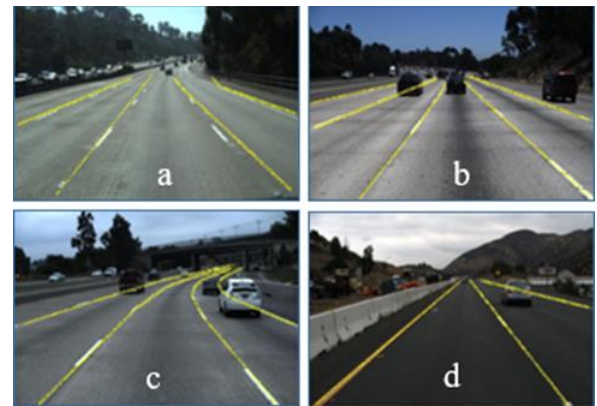


Figure 6. Several outputs related to the lane detection process

is observed, images a, b, c, and d are the final outputs of the road lane detection system. For all cases in Figure 6, the detection process is almost clear. One of the major adverse features of these images is the detection of parts of the image in addition to the lanes. Nonetheless, in the case of outputs shown in Figure 7, the detection operation is incorrect and undesirable.

As stated previously, detection of images in Figure 6 for all lanes is rather suitable but its drawback is the determination of parts of the image as the lanes. Yet, in Figure 8 that is ideal for lane detection, detection of additional parts is the minimum besides detecting all lanes. According to Figures 6-8, the process of identifying road lines has visually yielded good results compared to an example of the output of road line identification using the ResNet50 network shown in Figure 9. In terms of criterion evaluation, the results of method used are lower than the methods in which identification operations are fully supervised and based on deep networks with complex criteria. The reason for this is the data used. In our research process, we have used less labeled educational data than other researches. We have also used networks with a much simpler and faster architecture in terms of computational complexity than other methods. Therefore, according to the stated reasons, the results obtained using the semi-supervised method implemented are completely justifiable. The values of the Accuracy and IoU criteria for the implemented system and a number of other methods is summarized in Table 2.



Figure 7. (a) Incorrect lane detection, (b) failure to accurately identify lane



Figure 8. Optimal lane detection with minimal additional detection error



Figure 9. Sample output of lane detection using ResNet50

The results obtained in Table 2 are output of the observed part of the network for test data, which has a corresponding label (mask), in which the values of ACC pixel accuracy and the average IoU in the network training for these two parts are calculated. Pixel accuracy here refers to the class that pixels will take based on the probability of output of the sigmoid function. The pixel resolution specified by Accuracy is, as stated, the ratio of the number of correctly defined points (pixels) to the total number of pixels of the lines in the corresponding mask image (GroundTruth). According to Table 2, the difference between the pixel accuracy percentage of the proposed method compared to the other methods is a small difference, as can be seen in Figures 8-9 the proposed method output are compared to the method presented in the ResNet50 network. But, the amount of IoU criterion compared to the supervised methods has relatively significant difference. On the other hand, the

TABLE 2. Pixel-based identification accuracy and IOU criterion values

Method	Paradigm	Labeled training images dataset	ACC	IOU	Trainable Parameters Complexity
AlexNet	sup	TuSample 3636	96.11	0.84	60 milion
VGG16	sup	TuSample 3636	96.33	0.85	138 Million
LaneNet	sup	TuSample 3636	95.38	0.81	100 milion
ResNet50	sup	TuSample 3636	96.39	0.86	~46 milion
S-GAN	Semi sup	TuSample 1210	90.73	0.67	21 milion

amount of computational complexity of the proposed method has been significantly reduced according to the parameters of the whole network.

5. CONCLUSION

In most learning-based methods for road lane detection, the executive method learning paradigm usually uses the supervised type to obtain appropriate accuracy. These methods usually have limitations such as the need for the type of labeled data, which is a costly operation. On the other hand, in methods with unsupervised paradigm, despite the fact that most of the existing methods are real-time, there are several challenges in the process of lane detection such as relatively low accuracy of lane detection, and the inability to apply performance evaluation criteria parametrically. Given the challenges posed by the methods outlined above, it makes sense to pursue methods that can alleviate some of these limitations. One of the ideas is to use semi-supervised methods.

In this research, we presented a method in which we proceeded to the process of identifying road lines by changing the semi-supervised generative adversarial

deep Network in terms of operational purpose. The advantage of this method, despite its relatively lower percentage of accuracy compared to supervised methods, is its higher speed. It is mainly because the number of parameters required to train the semi-supervised method compared to deep networks with much more complex structures that operate with a supervised paradigm, is lower. Another very important advantage of this method is that it requires less labeled datasets than the supervised methods. The ability of the proposed method to use several different types of datasets in terms of labeled and unlabeled in the discriminator, is another important advantage by which the algorithm can be trained for different types of roads with different structures and used for the intended purpose. Given these advantages, it is possible to provide a comprehensive algorithm and even a suitable business system for different types of datasets in terms of performance by providing appropriate and logical solutions.

6. APPENDIX

The mathematical nature of the employed algorithm for semi-supervised GAN is based on the base methods of

these networks. The following presents the general mathematical concept of the implemented method.

As stated previously, GANs include two main sections. One is the generative network that establishes a dataset adaptive to the original data by using a random noise vector, and the other is a discriminator network that is responsible for discriminating the real data from the counterfeit data. The operational procedure of this network is based on the min-max algorithm and is specified according to a game theory as given in Equation (3).

$$\min_{(G)} \max_{(D)} V(D, G) = E_{x \sim p_{data}(x)} [\log(D(x))] + E_{z \sim p_z(z)} [\log(G(z))] \quad (3)$$

Equation (1) is the main base for all GANs. It is constant and, based on various networks of this type, the other equations differ. In fact, this equation is a fixed generality for all networks.

For a semi-supervised GAN, to minimize the error of the discriminator section as per the available algorithm structure, we need to minimize the error of three sections of its inputs. One of the errors is associated with the generative section, the second is related to the unlabeled dataset, and finally is the error of the dataset associated with the supervised section of the discriminator network. Equation (4) shows the overall form of the error in the discriminator section of the semi-supervised GAN.

$$L_D = -E_{x \sim p_{data}(x)} [\log(D(x))] - E_{z \sim p_z(z)} [\log(1 - D(G(z)))] + \gamma E_{x, y \sim p(x, y)} [\log(y, P(y|x, D))] \quad (4)$$

where, function D represents the discriminator function of the supervised section present in the segmentation process. This function is given by Equation (5).

$$D(x) = [1 - P(y = \text{fake}|x)] \quad (5)$$

And finally, the error of the generative section of the network is calculated by Equation (6) [30].

$$L_G = E_{z \sim p_z(z)} [\log(1 - D(G(z)))] \quad (6)$$

7. REFERENCES

- Garnett, N., Cohen, R., Pe'er, T., Lahav, R., Levi, D., "3d-lanenet: end-to-end 3d multiple lane detection", In Proceedings of the IEEE/CVF International Conference on Computer Vision, (2019), 2921-2930.
- Cudrano, P., Mentasti, S., Matteucci, M., Bersani, M., Arrigoni, S., Cheli, F., "Advances in centerline estimation for autonomous lateral control", In 2020 IEEE Intelligent Vehicles Symposium (IV), (2020), 1415-1422, doi: 10.1109/IV47402.2020.9304729.
- Huval, B., Wang, T., Tandon, S., Kiske, J., Song, W., Pazhayampallil, J., Andriluka, M., Rajpurkar, P., Migimatsu, T., Cheng-Yue, R., Mujica, F., "An empirical evaluation of deep learning on highway driving", arXiv preprint arXiv, (2015).
- Lee, S., Kim, J., Shin Yoon, J., Shin, S., Bailo, O., Kim, N., Lee, T.H., Seok Hong, H., Han, S.H., So Kweon, I., "Vpnet: Vanishing point guided network for lane and road marking detection and recognition", In Proceedings of the IEEE International Conference on Computer Vision, (2017), 1947-1955.
- Pourasad, Y., "Optimal Control of the Vehicle Path Following by Using Image Processing Approach", *International Journal of Engineering, Transactions C: Aspects*, Vol. 31, No. 9, (2018), 1559-1567, doi: 10.5829/ije.2018.31.09c.12.
- Feizi, A., "Convolutional gating network for object tracking", *International Journal of Engineering, Transactions A: Basics*, Vol. 32, No. 7, (2019), 931-939, doi: 10.5829/ije.2019.32.07a.05.
- Righettini, P., Roberto S., "Driving Technologies for the Design of Additive Manufacturing Systems", *HighTech and Innovation Journal*, Vol. 2, No.1, (2021), 20-28, doi: 10.28991/HIJ-2021-02-01-03.
- Kapeller, H., Dominik D., Dragan S., "Improvement and Investigation of the Requirements for Electric Vehicles by the use of HVAC Modeling", *HighTech and Innovation Journal*, Vol. 2, No. 1, (2021), 67-76, doi: 10.28991/HIJ-2021-02-01-07.
- Lee, D.H., Liu, J.L., "End-to-End Deep Learning of Lane Detection and Path Prediction for Real-Time Autonomous Driving", arXiv preprint arXiv, (2021).
- Yenikaya, S., Yenikaya, G., Düven, E., "Keeping the vehicle on the road: A survey on on-road lane detection systems", *ACM Computing Surveys (CSUR)*, (2013), 1-43, doi: 10.1145/2522968.2522970.
- Zhang, Y., Lu, Z., Zhang, X., Xue, J.H., Liao, Q., "Deep Learning in Lane Marking Detection: A Survey", *IEEE Transactions on Intelligent Transportation Systems*, (2021), doi: 10.1109/TITS.2021.3070111.
- Feniche, M., Mazri, T., "Lane detection and tracking for intelligent vehicles: A survey", In 2019 International Conference of Computer Science and Renewable Energies (ICCSRE), (2019), 1-4, doi: 10.1109/ICCSRE.2019.8807727.
- Hillel, A.B., Lerner, R., Levi, D., Raz, G., "Recent progress in road and lane detection: a survey", *Machine Vision and Applications*, (2014), 727-745, doi: 10.1007/s00138-011-0404-2.
- Liang, D., Guo, Y.C., Zhang, S.K., Mu, T.J., Huang, X., "Lane detection: a survey with new results", *Journal of Computer Science and Technology*, (2020), 493-505, doi: 10.1007/s11390-020-0476-4.
- Oliveira, G.L., Burgard, W., Brox, T., "Efficient deep models for monocular road segmentation", In 2016 IEEE/RSJ International Conference on Intelligent Robots and Systems (IROS), (2016), 4885-4891, doi: 10.1109/IROS.2016.7759717.
- Liu, X., Deng, Z., Yang, G., "Drivable road detection based on dilated FPN with feature aggregation." In 2017 IEEE 29th International Conference on Tools with Artificial Intelligence (ICTAI), (2017), 1128-1134, doi: 10.1109/ICTAI.2017.00172.
- Mamidala, R.S., Uthkota, U., Shankar, M.B., Antony, A.J., Narasimhadhan, A.V., "Dynamic approach for lane detection using Google Street view and CNN", 2019 IEEE Region 10 Conference (TENCON), (2019), 2454-2459, doi: 10.1109/TENCON.2019.8929655.
- Li, J., Mei, X., Prokhorov, D., Tao, D., "Deep neural network for structural prediction and lane detection in traffic scene", *IEEE Transactions on Neural Networks and Learning Systems*, (2016), 690-703, doi: 10.1109/TNNLS.2016.2522428.
- Hou, Y., Ma, Z., Liu, C., Loy, C.C., "Learning lightweight lane detection cnns by self attention distillation", In Proceedings of the IEEE/CVF International Conference on Computer Vision, (2019), 1013-1021.
- He, B., Ai, R., Yan, Y., Lang, X., "Accurate and robust lane detection based on dual-view convolutional neural network", In 2016 IEEE Intelligent Vehicles Symposium (IV), (2016), 1041-1046, doi: 10.1109/IVS.2016.7535517.

21. Bai, M., Mattyus, G., Homayounfar, N., Wang, S., Lakshmikanth, S.K., Urtasun, R., "Deep multi-sensor lane detection", In 2018 IEEE/RSJ International Conference on Intelligent Robots and Systems (IROS), (2018), 3102-3109, doi: 10.1109/IROS.2018.8594388
22. Satti, S.K., Devi, K.S., Dhar, P., Srinivasan, P., "A machine learning approach for detecting and tracking road boundary lanes", *ICT Express*, Vol. 7, No. 1, (2021), 99-103, doi: 10.1016/j.icte.2020.07.007.
23. Wang, W., Lin, H., Wang, J., "CNN based lane detection with instance segmentation in edge-cloud computing", *Journal of Cloud Computing*, (2020), 1-10, doi: 10.1186/s13677-020-00172-z.
24. Zou, Q., Jiang, H., Dai, Q., Yue, Y., Chen, L., Wang, Q., "Robust lane detection from continuous driving scenes using deep neural networks", *IEEE Transactions on Vehicular Technology*, (2019), 41-54, doi: 10.1109/TVT.2019.2949603.
25. Khosravi, E., Maghsoudi, H., "Design of an Intelligent Controller for Station Keeping, Attitude Control, and Path Tracking of a Quadrotor Using Recursive Neural Networks", *International Journal of Engineering, Transactions B: Applications*, Vol. 32, No. 5, (2019), 747-758, doi: 10.5829/ije.2019.32.05b.17.
26. Prenga, D., "General features of the q-XY opinion model" *Journal of Human, Earth, and Future*, Vol. 1, No. 2, (2020), 87-96, doi: 10.28991/HEF-2020-01-02-05.
27. Goodfellow, I., Pouget-Abadie, J., Mirza, M., Xu, B., Warde-Farley, D., Ozair, S., Courville, A., Bengio, Y., "Generative adversarial nets", *Advances in Neural Information Processing Systems*, (2014).
28. Odena, A., "Semi-supervised learning with generative adversarial networks", arXiv preprint arXiv, (2016).
29. Namjoy, A., Bosaghzadeh, A., "A Sample Dependent Decision Fusion Algorithm for Graph-based Semi-supervised Learning" *International Journal of Engineering, Transactions B: Applications*, Vol. 33, No. 5 (2020), 1010-1019, doi: 10.5829/ije.2020.33.05b.35.
30. Souly, N., Spampinato, C., Shah, M., "Semi supervised semantic segmentation using generative adversarial network", In *Proceedings of the IEEE International Conference on Computer Vision*, (2017), 5688-5696.

Persian Abstract

چکیده

شناسایی خطوط جاده‌ای یکی از مهم‌ترین عملیات‌هایی است که در فرایند رانندگی خودکار مطرح می‌شود. این فرایند به منظور مشخص‌سازی خطوط جاده جهت کنترل حرکت ماشین در یک خط مشخص در جاده صورت می‌گیرد و می‌تواند برای جلوگیری از تصادفات مؤثر باشد. مهم‌ترین لازمه‌ای که در تعیین خطوط جاده برای فرایند رانندگی خودکار خودروها در کنار برخط بودن روش‌های پیشنهادی مطرح می‌شود، دقت بالایی است که باید روش‌های ارائه‌شده آن را تضمین کنند. استفاده از یادگیری عمیق برای ایجاد سیستم‌های تماماً خودکار در شناسایی خطوط بسیار انجام شده است. روش‌های خودکار مبتنی بر یادگیری که برای شناسایی خطوط جاده استفاده شده‌اند، اغلب از نوع نظارت‌شده هستند. از معایب این روش‌ها علیرغم دقت بسیار خوبی که دارند، نیازمند بودن آنها به یک مجموعه داده برچسب‌گذاری می‌باشد که خود هم باعث محدودیت در روند توسعه سیستم شناسایی خطوط می‌شود و نکته مهم‌تر اینکه تهیه یک مجموعه داده استاندارد دارای برچسب، بسیار زمان‌بر است. راهکاری که بدین منظور توصیه می‌شود، استفاده از رویکردهای مناسب یادگیری است که بتوان با استفاده از آنها هم دقت نسبی موجود در رویکردهای نظارت‌شده را بدست آورد، هم سرعت آنها را بهبود بخشید و هم اینکه بتوان با استفاده از مجموعه داده‌گان متفاوت بدون برچسب محدودیتی که مجموعه داده برچسب‌دار در توسعه الگوریتم نسبت به مجموعه داده‌گان جدید ایجاد می‌کند، در آینده برطرف ساخت. در این فرایند پژوهشی ما اقدام به ارائه یک روش خودکار، و مبتنی بر یادگیری نیمه‌نظارتی با استفاده از شبکه‌های عصبی عمیق جهت استخراج خطوط جاده نموده‌ایم، که در آن از دو مجموعه داده متفاوت دارای برچسب (ماسک خطوط شناسایی شده) و بدون برچسب استفاده شده‌است. نتایج حاصل از روش انجام شده نشان از دقت مناسب روش بکارگرفته شده با توجه به رویکرد پیشنهادی و همچنین بهبود پیچیدگی محاسباتی آن با توجه به کاهش قابل توجه تعداد پارامترهای قابل آموزش شبکه دارد.



Refractive Index Perception and Prediction of Radio wave through Recursive Neural Networks using Meteorological Data Parameters

S. Adebayo^a, F. O. Aweda^{*b}, I. A. Ojedokun^c, O. T. Olapade^b

^a *Mechatronics Engineering Programme, College of Agriculture, Engineering, and Science, Bowen University, Iwo, Osun State, Nigeria*

^b *Physics and Solar Energy Programme, College of Agriculture, Engineering, and Science, Bowen University, Iwo, Osun State, Nigeria*

^c *Electrical and Electronics Department, Federal University, Otuoke, Nigeria*

P A P E R I N F O

Paper history:

Received 26 August 2021

Received in revised form 02 November 2021

Accepted 23 December 2021

Keywords:

Radio Refractivity

Meteorological Data

International Telecommunication Union

Long-Short Term Memory

Wireless Communication

A B S T R A C T

Radio refractivity is very crucial in the optimal performance of radio systems and is one of the attributes that affect electromagnetic waves in the troposphere. This study presented a comparison of different variants of recurrent neural networks to predict radio refractivity index. The radio refractivity index is predicted based on forty-one years (1980 to 2020) metrological data obtained from the MERRA-2 data re-analysis database. The refractivity index was computed using International Telecommunication Union (ITU) standard. The correlation refractivity index was categorized into strong, weak and no correlation. Rainfall, relative humidity, and air pressure fall in the first category, the temperature falls in the second category while wind speed falls in the last one. The true future and predicted values of the radio refractivity index are close with GRU performing better than the other two models (LSTM and BiLSTM) which proves the accuracy of the proposed model. In conclusion, the proposed model can establish a radio refractivity status of locations at different times of the season, which is of great importance in the effective design, development, and deployment of radio communication systems.

doi: 10.5829/ije.2022.35.04a.21

1. INTRODUCTION

Wireless communication (WC) is the transmission of information from the source to the destination without a physical connection. The channel of propagation of signals is the atmosphere which consist of three layers: troposphere, stratosphere, and ionosphere. The troposphere and ionospheric possess challenges ranging from scattering, absorption, obstruction and so on which cause severe impairment on the received signal. In the troposphere, there is the presence of some meteorological parameters such as temperature, relative humidity and pressure which varies in quantity per time and are responsible for radio signal disorientation and consequently, corruption of the transmitted signals. Radiowave [1] is one of the components of the electromagnetic spectrum and a means of signal propagation in the WC channel. It was first discovered by

a Scottish Mathematician James Clerk Maxwell in the mid- 1860. The prediction of Maxwell was verified in the laboratory by Marconi in 1899 [2]. Radio waves are electromagnetic radiation with a wavelength falling between 3cm and 30km and frequency is between 3kHz and 3GH. Radio waves travel at the speed of light and thus enhances the speed at which information is received. Waves are characterized by reflection, interference, diffraction, absorption, scattering, and refraction. The heterogeneous nature of the tropospheric layers, due to the presence of meteorological parameters enhances large scale variation in the signal strength and direction [3]. Consequently, rapid fluctuation of the signal over some time and distance occurs. Other physical impairments suffered by WC in a refracted channel include sub-refraction, super refraction and ducting and these impairments cause performance degradation and drop calls at the receiving end [4]. Several researchers have

*Corresponding Author Institutional Email:
aweda.francis@bowen.edu.ng (F. O. Aweda)

resulted in taking measurements of metrological data in the troposphere during wet and dry seasons within a certain period. These measurements were taken to study the trend of the effect of these parameters on the received signal. Consequently, the refractive nature of the WC channel can be observed and necessary action by network designers and operators could be taken to ameliorate the effect of the refractive nature of the troposphere. To overcome the challenges in measurement taken for estimating the radio refractivity and refractivity gradient, which could be because of human and equipment error, this research, therefore, focuses on developing a model using a machine learning approach. Machine Learning (ML) is a process of developing a machine that will enable it to learn without programming the machine explicitly [5]. ML process includes data collection of historical meteorological data, data preprocessing the data, features extraction, algorithm training, model evaluation, and model deployment. The focus of this work is to create a reliable platform on metrological data perception as well as predicting radio refractivity index for the communication design process. Due to the challenges faced by engineers, researchers and designers of wireless communication systems, this work presents a suitable recurrent neural network model for predicting radio refractivity index using different meteorological parameters. This model will help during the condition of the ducts by hidden from sight in residential and commercial buildings, and performance issues that may stay undetected. Thus, for effective propagation of radio waves through the atmosphere, there is a need to continuously understudy the variation of these parameters over some time and the result thoroughly analyzed to aid the planning of network providers in rendering quality services to their customers [6]. Gao et al. [7] examined the effect of moisture and temperature on radio refractivity and its influence on radar ray path. Analysis of the different radio refractivity concerning atmospheric temperature and moisture was done. The results showed that moisture gradient is a significant contributor to radio refractivity gradient at the lower troposphere. Hence, moisture has a more significant influence on the radar ray path calculations than temperature. Adediji et al. [8] looked at the radio refractivity gradient and its effect on the earth radius factor (k factor) over Akure, Southwestern Nigeria. Okoro and Agbo [9], Oluwole [10] worked on Meteorological Parameters and the effect on tropospheric radio refractivity for Akure South –West, and in Minna north central Nigeria. Oluwole [10] reported that the variation in radio wave propagation in Akure is because of changes in temperature, pressure, and humidity. However, Data for the daily intervals of these parameters in the troposphere for Akure were obtained from Nigeria Meteorological Agency (NIMET) for the year 2013. The result revealed that Akure has the lowest radio refractivity in January (dry season) the highest radio

refractivity in August (wet season) due to an increase in the humidity and temperature in the troposphere. The model used is not a predictive one and it was used to capture only Akure. Study by Amajama [11] established a mathematical relationship between radio refractivity and its meteorological components with a new mathematical equation to determine radio refractivity. The study revealed the correlations between radio refractivity and metrological parameters which was given as atmospheric temperature: 0.99; atmospheric pressure: 0.91; and relative humidity: 0.99. Zhang et al. [12] evaluate the performance of different machine-learning-based models in comparison to the empirical model for the prediction of radio signal path loss. It was concluded that machine-learning-based models perform better in terms of prediction accuracy and computational efficiency than the empirical model. However, the research is not in any way related to the propagation condition of radio signals in southwestern Nigeria. Neural Networks had been used in predicting metrological parameters for certain regions such as Pakistan [13] and West Java [14]. Applying neural networks to metrological data in Nigeria will help in gaining useful insight. Thus, this research aims to bridge the gaps in knowledge by developing a radio refractivity predictive model using long-short term memory (LSTM), Bi long-short term memory (BiLSTM) and Gated Recurrent Unit (GRU) neural network.

2. ARTIFICIAL NEURAL NETWORK

An artificial neural network is a machine learning process that uses a similar principle of operation to the working operation of a human brain. The neural networks used in deep learning consists of several layers connected. The network learns from a massive volume of data and uses algorithms to train a neural network. There are several popular neural networks which include a feed-forward neural network [15] which is used in general regression and classification problems. Convolutional neural network (CNN) is generally used for image recognition [16], deep neural network (DNN) is for acoustic modelling [17]. A deep belief network (DBN) has been used for cancerous cell detection [18] while a recurrent neural network (RNN) is generally used in speech recognition [19].

2. 1. Recurrent Neural Network (RNN) In feed-forward network, information flow in the forward direction from the input nodes without loops or cycle in the network. Decisions are based on the current input without memory of the past and future. FFN is greatly impaired by the inability to handle sequence data because; it does not have a scope of memory or time.

RNN is an improved feed-forward network that allows previous outputs to be used as inputs. The internal state (memory) in RNN is used to process sequences of inputs. This network architecture has been applied in natural language processing problems [20] such as text mining, sentiment analysis and machine translation. The network can be represented mathematically as:

For the given hidden layers, the new state is given as:

$$h_{(t)} = f_c(h_{(t-1)}, x_{(t)}) \quad (1)$$

where f_c is the function with c parameter, $h(t - 1)$ is the previous state and $x(t)$ is the input vector at time step t . Applying activation function gives:

$$h_{(t)} = \tanh(W_{hh}h_{(t-1)} + W_{hx}x_{(t)}) \quad (2)$$

and the output state is given as:

$$y_{(t)} = W_{hy}h_{(t)} \quad (3)$$

W is the input weight, h is the hidden vector for a single neuron, W_{hh} is the previous weight, W_{hx} is the weight at the current input state, and \tanh is the activation function. RNN structure can be classified into four categories: multiple-input, multiple-output (MIMO), single-input, single-output (SISO), single-input, multiple-outputs (SIMO) and multiple-input, single-output (MISO). RNN is greatly affected by the problems of vanishing and exploding gradient. This makes RNN training a very difficult task. There is also a limitation on the length of sequence data it can process when using hyperbolic tangent function (\tanh) or Rectified Linear Unit (ReLU) activation function. Thus, the need for better variants of this network architecture.

2. 2. Long-Short Time Memory (LSTM) Network Architecture

Long Short-Term Memory (LSTM) network was developed to address the problem of the RNN which is the vanishing gradient problem. LSTM is capable of processing and predicts time series data. This is achieved using the back-propagation method. The architecture of the LSTM network consists of three gates:

1. Input gate. This gate determines the values to go through using a sigmoid function while the tanh function determines the level of importance of the value through weights. This weight ranges from -1 to 1 as represented in equation:

$$i_t = \sigma(W_i[h_{t-1}, x_t] + b_i) \quad (4)$$

$$c_t = \tanh(W_c[h_{t-1}, x_t] + b_c) \quad (5)$$

2. Forget gate decide, using the sigmoid function, input values to be discarded from the network. This is done by examining the values of the previous state (h_{t-1}), the input (x_t) and outputs for each number in the cell state (C_{t-1}). When the value is 0, the value is omitted while the value 1 is kept. The forget gate is represented in Equation (6):

$$f_t = \sigma(W_f[h_{t-1}, x_t] + b_f) \quad (6)$$

3. The gate in this architecture is the output gate. This gate has a sigmoid function which decides the values to let through either 0 or 1. The tanh function in this gate gives weights to the values which reflect the level of importance. The final out is further multiplied with the output of a sigmoid function.

$$o_t = \sigma(W_o[h_{t-1}, x_t] + b_o) \quad (7)$$

$$h_t = o_t * \tanh(c_t) \quad (8)$$

Gated Recurrent Unit (GRU)

GRU is another variant of Recurrent Neural networks with similar architecture as LSTM. The cell state is replaced with a hidden state in the transfer of information. Furthermore, unlike the LSTM with three gates, GRU has two gates: a reset gate and an update gate. The update gate is like the forget and input gate in an LSTM. This gate determines the type of information to discard or accept. The reset gate is used to decide the level of past information to forget. It has been shown that due to fewer operations in GRU, the training time is shorter than LSTM.

The reset gate is given as:

$$r_t = \sigma(W^{(ir)}\bar{x}_t + W^{(hr)}h_{t-1}) \quad (9)$$

The updated gate is given as:

$$z_t = \sigma(W^{(iz)}\bar{x}_t + W^{(hz)}h_{t-1}) \quad (10)$$

The process input is given as:

$$\tilde{h}_t = \tanh(W^{(i\tilde{h})}\bar{x}_t + W^{(h\tilde{h})}h_{t-1}) \quad (11)$$

The hidden state update is given as:

$$h_t = (1 - z_t) * h_{t-1} + z_t * \tilde{h}_t \quad (12)$$

And the output is given as:

$$y_t = h_t \quad (13)$$

3. METHODOLOGY

3. 1. Proposed Model

The research work involves the collection of data from meteorological database parameters. The dataset was analyzed by clustering to gain insight into data and to help data simplification which may be needed before further processing. Neural networks extract relevant features from the dataset for training to predict the radio refractivity index of an environment. The model was compared with other statistical developed models for evaluation and validation. The performance of the proposed model was further evaluated on some selected metrics such as Mean Average Error (MAE), Root Mean Square Error (RMSE) and R square.

3. 2. Study Area The stations used for this research consists of the following Abuja, Awka, Calabar, Enugu, Ibadan, Ikeja, Ilorin, Kaduna, Maiduguri, Port Harcourt, Sokoto and Yola. These stations were selected across the entire country (see Table 1).

These stations are divided into different climatic areas to show the effect of radio transmission across the entire country. Figure 1 shows the station presents in Nigeria.

3. 4. Data Collection The data used in this study consists of monthly rainfall, air temperature, water

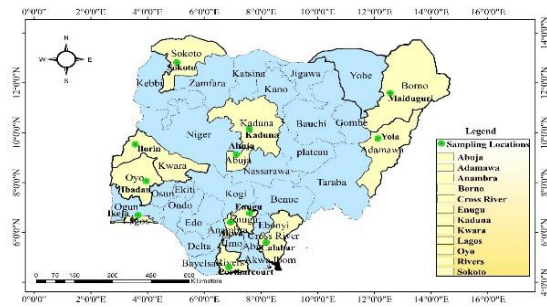


Figure 1. Map showing selected stations across Nigeria

TABLE 1. The coordinate of the stations used

Stations	Longitude °N	Latitude °E
Abuja	9.0723	7.4913
Awka	6.2105	7.0722
Calabar	4.9828	8.3345
Enugu	6.4599	7.5489
Ibadan	7.4020	3.9173
Ikeja	6.6059	3.3491
Ilorin	8.5000	4.5500
Kaduna	10.6093	7.4295
Maiduguri	11.8333	13.1500
Port Harcourt	4.7774	17.0134
Sokoto	13.0058	5.2475
Yola	9.2035	12.1495

vapour, pressure, relative humidity, wind speed and direction for twelve stations which were obtained from the archive of the HelioClim website of soda (<http://www.soda-pro.com>) of MERRA-2 meteorological re-analysis data as recommended by Gelaro et al. [21]. The assessment of the data was on 22nd August 2020. The data of forty-one years spanning from 1980 to 2020 were obtained as a monthly average for January to December of every year in comma-separated value (CSV) data format.

3. 3. Dataset Preprocessing Radio refractivity and radio refractive index data were computed using the formula provided by the Radio communication sector of the International Telecommunication Union (ITU-R). ITU-R is saddle with the responsibility of ensuring efficient and economical use of the radiofrequency spectrum by all radio communication services. This is

TABLE 2. Selected Metrological Dataset for Ibadan Station

Date	Station	Temp. (K)	RH (%)	Pressure (hPa)	Rainfall (kg/m ²)	Wind Speed (m/s)	Wind direction (deg)	Refractivity Index
1980-01-31	Ibadan	298.56	78.48	990.22	43.64	1.33	219.77	2576.23
1980-02-28	Ibadan	299.05	78.77	988.83	68.55	1.71	219.13	2576.34
1980-03-31	Ibadan	299.27	81.01	989.22	105.14	2.35	213.82	2645.25
1980-04-30	Ibadan	299.09	83.47	989.43	90.25	2.48	214.60	2729.19
1980-05-31	Ibadan	298.40	86.54	991.07	151.17	2.19	220.69	2844.09

done by the provision of radio refractive index, n , and is computed by Equation (14):

$$n = 1 + N \times 10^{-6} \quad (14)$$

The radio refractivity, N , is given as:

$$N = 77.6 \frac{P_d}{T} + 72 \frac{e}{T} + 3.75 \times 10^5 \frac{e}{T^2} \quad (15)$$

where the dry component of the radio refractivity, N_{dry} is given as:

$$N_{dry} = 77.6 \frac{P_d}{T} \quad (16)$$

and the wet component, N_{wet} is:

$$N_{wet} = 72 \frac{e}{T} + 3.75 \times 10^5 \frac{e}{T^2} \quad (17)$$

P_d and P is the dry and total atmospheric pressure respectively, while e is the water vapour pressure all in (hPa). T is the absolute temperature given in Kelvin.

Since $P_d = P - e$, Equation (1) can be rewritten as:

$$N = 77.6 \frac{P}{T} + 72 \frac{e}{T} + 3.75 \times 10^5 \frac{e}{T^2} \quad (18)$$

The relationship between water vapour pressure e and relative humidity is given as follows:

$$e = \frac{H.e_s}{100} \tag{19}$$

$$e_s = EF.a.exp\left[\frac{(b-\frac{t}{d}).t}{t+c}\right] \tag{20}$$

$$EF_{water} = 1 + 10^{-4}[7.2 + P.(0.00320 + 5.9 \times 10^{-7}.t^2)] \tag{21}$$

$$EF_{ice} = 1 + 10^{-4}[2.2 + P.(0.00382 + 6.4 \times 10^{-7}.t^2)] \tag{22}$$

where t: temperature (°C), P: pressure (hPa), H: relative humidity (%), e_s : saturation vapour pressure (hPa) at the temperature t (°C) and the coefficients a, b, c, and d are: for water: a = 6.1121, b = 18.678, c = 257.14, d = 234.5. This is valid between -40 and +50° for ice: a = 6.1115, b = 23.036, c = 279.82, d = 333.7. This is valid between -80° and 0° [6].

3. 5. Evaluation Metrics The developed model was evaluated using the following statistical methods:

1. Mean Average Error (MAE): this is given in equation:

$$MAE = \frac{\sum_{i=1}^n |m_i - p_i|}{n} \tag{23}$$

2. Root mean square error which is given in the equation

$$RMSE = \sqrt{\frac{\sum_{i=1}^n (m_i - p_i)^2}{n}} \tag{24}$$

R squared is given as:

$$R^2 = \frac{(\sum_{i=1}^n (P_i - \bar{P})(P'_i - \bar{P}'))^2}{\sum_{i=1}^n (P_i - \bar{P})^2 \sum_{i=1}^n (P'_i - \bar{P}')^2} \tag{25}$$

where P_i is the observed data, P'_i is the simulated data, \bar{P} is the mean of the observed data, \bar{P}' is the mean of the simulated data and e is the model error. Where m_i is the prediction data while p_i pi is the observed data, n is the number of errors

3. 6. Open-source Tools The research relied heavily on open-source software. Python 3.8 was the chosen programming language that has the capability of importing libraries such as Numpy, Pandas, and Scikit-Learn for data preprocessing and data management. TensorFlow [22] and Keras [23] provided the framework for training the algorithms. Matplotlib [24] library helped in creating figures and graphs.

4. RESULTS AND DISCUSSION

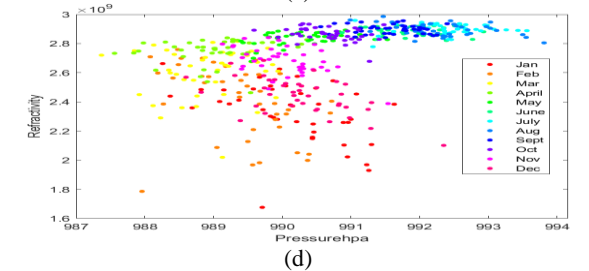
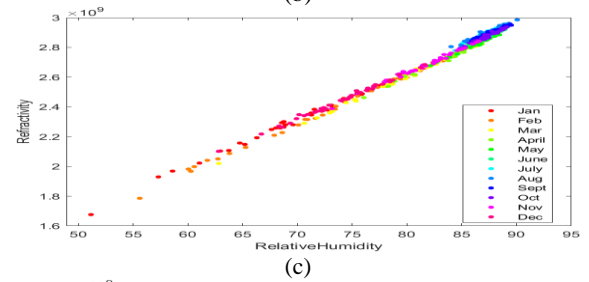
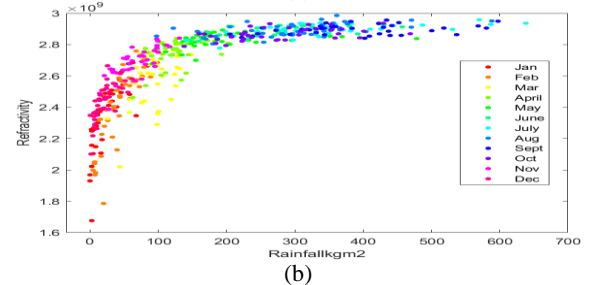
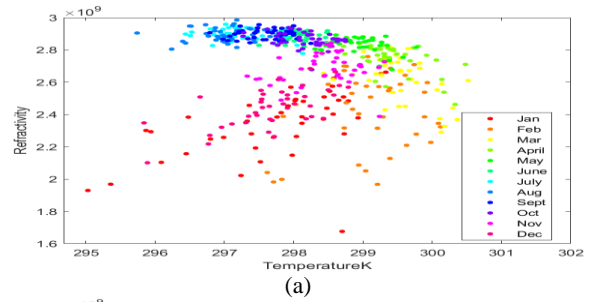
4. 1. Data Visualization The effect of environmental parameters on the refractivity of a radio waves can be grouped into three categories from Figure 2(a) to 2(f). This is categorized as follows:

1. Weak Correlation: Figure 2(a) shows the correlation between refractivity and temperature. The effect of the

increase in temperature on radio refractivity is not apparent, although the temperature was at its highest in February before it started falling to rise again in November. It can be deduced that the effect of temperature contributes little to variation of radio refractivity index in this region as proven by [25].

2. Strong Correlation: Figures 2(b), 2(c) and 2(d) are plots of refractivity against rainfall, relative humidity, and pressure respectively. The result revealed a strong correlation between each of these features and radio refractivity. It can be seen, from Figure 2(b), that as the rainfall increases, the radio waves refractivity increases as well for the number of years considered. The Result from Figures 2(b), 2(c) and 2(d) agree with several studies [25, 26].

3. No Correlation: The relationship between wind speed, wind direction and refractivity does not show any correlation as shown in Figures 2(e) and 2(f).



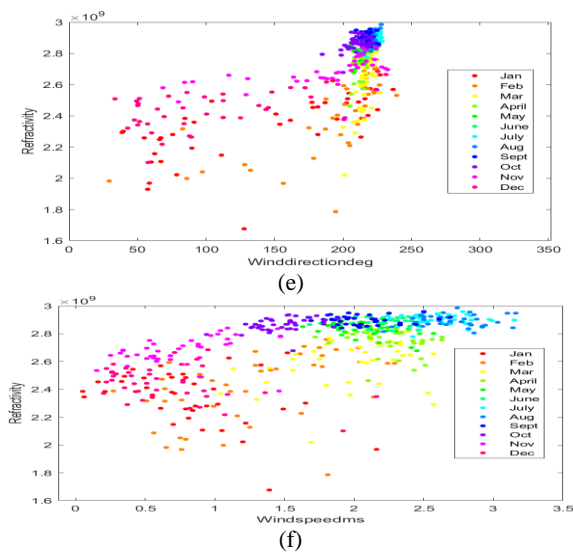


Figure 2. Explanatory Data Analysis of the refractivity against various metrological parameters

4. 2. Dataset Distribution Pattern

The metrological dataset for the considered location is presented in Table 3. The 491-dataset span over 41 years. The minimum and maximum temperatures are 295.03K and 301.39K respectively. The relative humidity, within these years, ranges between 51.13 and 90.06 while the atmospheric pressure is between 987.37 and 993.81. The rainfall is at its lowest mostly in December or January, while it is at its highest in July. The rainfall minimum and maximum datasets are between 0.01 and 638.32. The radio refractivity index values fall between 1677.02 and 2986.68.

4. 3. Training and Test Dataset

Figure 3 shows the split ratio of the dataset into train and test sets. 80% of the dataset was set for the training set while the remaining 20% was used for the test set. The training dataset span from 1980 to 2012 while the test dataset is from 2013 to 2020.

TABLE 3. Descriptive statistics of the measured meteorological data for input to RNN

Statistical Parameter	T (K)	RH (%)	P (hPa)	RF (mm)	Refractivity Index
Count	491.000000	491.000000	491.000000	491.000000	491.000000
Mean	298.260061	82.325336	990.575112	178.840035	2708.644544
Std	0.974740	7.045053	1.311667	141.762511	234.514598
Min	295.030000	51.130000	987.370000	0.010744	1677.023932
25%	297.590000	78.725000	989.600000	57.609324	2578.606102
50%	298.200000	85.710000	990.470000	141.306552	2809.317710
75%	298.995000	87.370000	991.620000	285.793902	2882.642596
Max	301.390000	90.060000	993.810000	638.320680	2986.682195

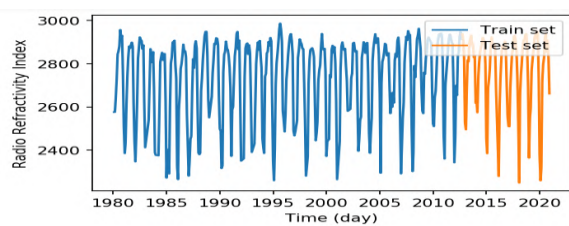


Figure 3. Train and test set split ratio of 4 to 1

4. 4. Performance of the Training Algorithm

Table 4. Shows the performance of LSTM, BiLSTM and GRU models based on three evaluation metrics: R2, MAE and RMSE. The architecture of the models is greatly determined by the neurons in the hidden layers as well as the hyper-parameter turning. To obtain the optimal architecture, the hidden layers were varied from two to five, with each layer containing thirty neurons. The coefficient of determination (R²) for LSTM, BiLSTM and GRU with 2 layers is 0.84, 0.79, 0.87. This shows that the

GRU model performs better. Furthermore, the performance of the model reduces as the complexity of the model increases. R² value reduces from 0.87 to 0.71 when the layers of the network were increased from 2 to 5. The MAE and RMSE values reveal that with an increase in neurons, GRU and BiLSTM tend to marginally minimize prediction errors in comparison with the LSTM neural network model. GRU outperformed both the BiLSTM and LSTM with just a marginal gap. Table 4 also shows that the MAE and RMSE in radio refractivity index prediction using GRU with one hidden layer has the lowest error.

Furthermore, the difference in the performance of LSTM, BiLSTM and GRU in radio refractivity index prediction in terms of training and validation loss is presented in Figure 3. The minimum training and validation cost (loss) functions are 0.0105 and 0.0145 at epoch 87th for BiLSTM, 0.0156 and 0.0160 at 73rd for LSTM and 0.0153 and 0.0112 at epoch 67th for GRU. This shows that the GRU model has a faster convergence

time, although BiLSTM has the lowest cost function. The training process was stopped when the validation error trend changes from descending to ascending to avoid model overfitting.

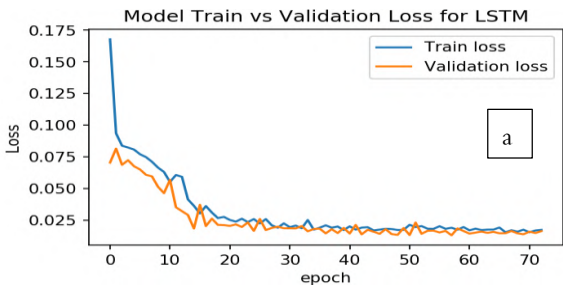
Figure 4 shows the radio refractivity index predictions for the 3 trained models using 20% of the dataset (test set). All the models performed well because

the predicted values are very close to the true future values (see Figure 5).

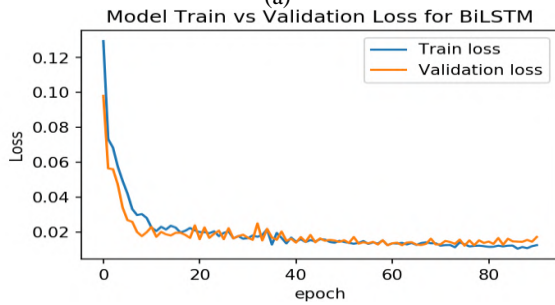
Bazoobandi [27] stated that a wavelet neural network has two types of parameters, namely wavelet function parameters (translation, dilation) and the weights between the hidden layer and output layer.

TABLE 4. Performance of radio refractivity index prediction for different RNN variants using statistical metrics

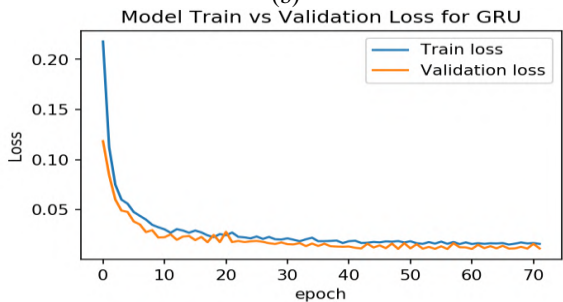
Hidden Layer	LSTM			BiLSTM			GRU		
	MAE (unit)	RMSE	R ²	MAE (unit)	RMSE	R ²	MAE (unit)	RMSE	R ²
2	57.08	74.75	0.84	53.07	86.12	0.79	51.10	67.78	0.87
3	60.25	78.45	0.83	53.11	86.34	0.79	52.68	67.85	0.87
4	59.17	97.74	0.73	54.02	87.37	0.79	71.03	85.83	0.79
5	60.93	85.98	0.79	67.92	92.29	0.76	80.54	100.77	0.71



(a)

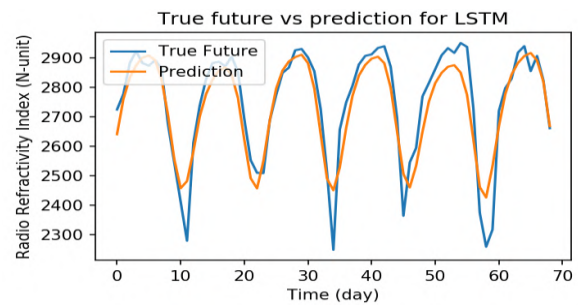


(b)

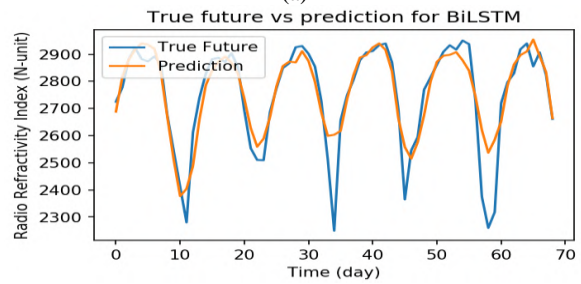


(c)

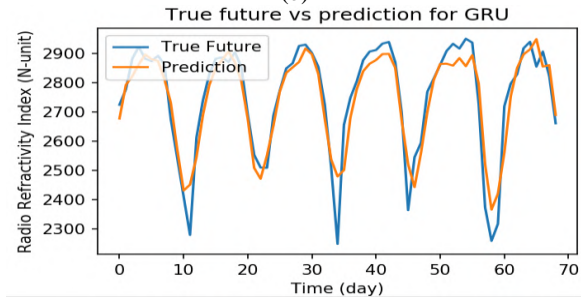
Figure 4. Performance of Model Training against validation Loss



(a)



(b)



(c)

Figure 5. Prediction Performance of LSTM, BiLSTM & GRU

5. CONCLUSION

Radio refractivity is an important feature in the behavioral patterns of electromagnetic waves, which translate to the performance of the communication systems. The focus of this study is to present a comparison of different variants of recurrent neural networks to predict radio refractivity index. The radio refractivity index was predicted based on forty-one years (1980-2020) metrological data. These data are categorized as temperature, pressure relative humidity and rainfall, and they were obtained from the website of Solar Radiation Data (SoDa) database. The refractivity index was computed using International Telecommunication Union (ITU) standard. The data were analyzed through the explanatory data analysis (EDA) method for better perception. Long- and short-term memory (LSTM), Bi-Long- and short-term Memory (BiLSTM) and Gated Recurrent Unit (GRU) neural networks were trained to learn features from the dataset. The refractivity index for the year 2021 was predicted based on the knowledge learned from the previous forty-one years. The trained model's predictions and estimation were validated against each other. The correlation of the features considered concerning the radio refractivity index was categorized into strong, weak and no correlation. Rainfall, relative humidity, and pressure fall in the first category, the temperature falls in the second category while wind speed falls in the last. The true future and predicted values of the radio refractivity index are close with GRU performing better than the other two models (LSTM and BiLSTM) which proves the accuracy of the proposed model. The proposed model can establish a radio refractivity status of locations at different times of the season, which is of great importance in the effective design, development, and deployment of radio communication systems. Therefore, this research recommends to the government of the Federal Republic of Nigeria, to create research centres for data collection and analysis.

6. REFERENCES

- Sizun, H. and de Fornel, P., "Radio wave propagation for telecommunication applications, Springer, (2005). http://www.eletrica.ufpr.br/armando/index_arquivos/Radio%20Wave%20Propagation.pdf
- Erceg, V., Greenstein, L.J., Tjandra, S.Y., Parkoff, S.R., Gupta, A., Kulic, B., Julius, A.A. and Bianchi, R.J.J.o.s.a.i.c., "An empirically based path loss model for wireless channels in suburban environments", Vol. 17, No. 7, (1999), 1205-1211, doi: 10.1109/49.778178.
- Seybold, J.J.I., Hoboken, New Jersey, "Introduction to rf propagation. John wiley & sons", (2005), doi: 10.1002/0471743690.
- Dinc, E. and Akan, O.B.J.I.c.m., "Beyond-line-of-sight communications with ducting layer", Vol. 52, No. 10, (2014), 37-43.
- Mohammed, M., Khan, M.B. and Bashier, E.B.M., "Machine learning: Algorithms and applications, Crc Press, (2016). <https://doi.org/10.1201/9781315371658>
- Boano, C.A., Tsiftes, N., Voigt, T., Brown, J. and Roedig, U.J.I.T.o.I.I., "The impact of temperature on outdoor industrial sensor applications", Vol. 6, No. 3, (2009), 451-459, doi: 10.1109/TII.2009.2035111.
- Gao, J., Brewster, K. and Xue, M., "Variation of radio refractivity with respect to moisture and temperature and influence on radar ray path", *Advances in Atmospheric Sciences*, Vol. 25, No. 6, (2008), 1098-1106.
- Adediji, A., Ajewole, M. and Falodun, S., "Distribution of radio refractivity gradient and effective earth radius factor (k-factor) over akure, south western nigeria", *Journal of Atmospheric and solar-Terrestrial Physics*, Vol. 73, No. 16, (2011), 2300-2304.
- Okoro, O. and Agbo, G.J.G.J.o.s.F.r., "The effect of variation of meteorological parameters on the tropospheric radio refractivity for minna", Vol. 12, (2012), 37-41.
- Oluwole, F.J., "Variation of metrological parameters as they affect the tropospheric radio refractivity for akure south-west nigeria", *International Journal of Environment*, Vol. 7, No. 10, (2013), 458-460.
- Amajama, J., "Mathematical relationships between radio refractivity and its meteorological components with a new linear mathematical equation to determine radio refractivity", *International Journal of Innovative Science, Engineering & Technology*, Vol. 2, No. 12, (2015), 953-957.
- Zhang, Y., Wen, J., Yang, G., He, Z. and Wang, J., "Path loss prediction based on machine learning: Principle, method, and data expansion", *Applied Sciences*, Vol. 9, No. 9, (2019), 1908.
- Javeed, S., Alimgeer, K.S., Javed, W., Atif, M. and Uddin, M., "A modified artificial neural network based prediction technique for tropospheric radio refractivity", *Plos One*, Vol. 13, No. 3, (2018), e0192069.
- Priatna, M.A. and Djamal, E.C., "Precipitation prediction using recurrent neural networks and long short-term memory", *Telkomnika*, Vol. 18, No. 5, (2020), 2525-2532.
- Fine, T.L., "Feedforward neural network methodology, Springer Science & Business Media, (2006).
- Albawi, S., Mohammed, T.A. and Al-Zawi, S., "Understanding of a convolutional neural network", in 2017 international conference on engineering and technology (ICET), IEEE. (2017), 1-6.
- Yangzhou, J., Ma, Z. and Huang, X., "A deep neural network approach to acoustic source localization in a shallow water tank experiment", *The Journal of the Acoustical Society of America*, Vol. 146, No. 6, (2019), 4802-4811.
- Ronoud, S. and Asadi, S., "An evolutionary deep belief network extreme learning-based for breast cancer diagnosis", *Soft Computing*, Vol. 23, No. 24, (2019), 13139-13159.
- Amberkar, A., Awasarmol, P., Deshmukh, G. and Dave, P., "Speech recognition using recurrent neural networks", in 2018 international conference on current trends towards converging technologies (ICCTCT), IEEE. (2018), 1-4. <https://doi.org/10.1007/s10772-021-09808-0>
- Yin, W., Kann, K., Yu, M. and Schütze, H., "Comparative study of cnn and rnn for natural language processing", arXiv preprint arXiv:1702.01923, (2017).
- Gelaro, R., McCarty, W., Suárez, M.J., Todling, R., Molod, A., Takacs, L., Randles, C.A., Darmenov, A., Bosilovich, M.G. and Reichle, R.J.J.o.c., "The modern-era retrospective analysis for research and applications, version 2 (merra-2)", Vol. 30, No. 14, (2017), 5419-5454.
- Abadi, M., Agarwal, A., Barham, P., Brevdo, E., Chen, Z., Citro, C., Corrado, G.S., Davis, A., Dean, J. and Devin, M., "Tensorflow:

- Large-scale machine learning on heterogeneous distributed systems. Arxiv 2016", arXiv preprint arXiv:1603.04467, (2019).
23. Gulli, A. and Pal, S., "Deep learning with keras, Packt Publishing Ltd, (2017). <https://www.packtpub.com/product/deep-learning-with-keras/9781787128422>
 24. Bisong, E., Matplotlib and seaborn, in Building machine learning and deep learning models on google cloud platform. 2019, Springer.151-165.
 25. Agbo, E., Ettah, E. and Eno, E., "The impacts of meteorological parameters on the seasonal, monthly, and annual variation of radio refractivity", *Indian Journal of Physics*, (2020), 1-13.
 26. Aweda, F., Adebayo, S., Samson, T. and Ojedokun, I., "Modelling net radiative measurement of meteorological parameters using merra-2 data in sub-sahara african town", *Iranian (Iranica) Journal of Energy & Environment*, Vol. 12, No. 2, (2021), 173-180.
 27. Bazoobandi, H.J.I.J.o.E., "Wavelet neural network with random wavelet function parameters", *International Journal of Engineering, Transactions A: Basics*, Vol. 30, No. 10, (2017), 1510-1516, doi: 10.5829/ije.2017.30.10a.12.

Persian Abstract

چکیده

فرکانس رادیویی در عملکرد بهینه سیستم های رادیویی بسیار حیاتی است و یکی از ویژگی هایی است که بر امواج الکترومغناطیسی در تروپوسفر تأثیر می گذارد. این مطالعه مقایسه ای از انواع مختلف شبکه های عصبی بازگشتی را برای پیش بینی ضریب شکست رادیویی ارائه کرد. ضریب شکست رادیویی بر اساس داده های اندازه شناسختی چهل و یک ساله (۱۹۸۰ تا ۲۰۲۰) به دست آمده از پایگاه داده تحلیل مجدد داده های MERRA-2 پیش بینی می شود. ضریب شکست با استفاده از استاندارد اتحادیه بین المللی مخابرات (ITU) محاسبه شد. ضریب شکست همبستگی به دو دسته قوی، ضعیف و بدون همبستگی طبقه بندی شد. بارندگی، رطوبت نسبی و فشار هوا در دسته اول قرار می گیرند، دما در دسته دوم و سرعت باد در دسته آخر کاهش می یابد. آینده واقعی و مقادیر پیش بینی شده ضریب شکست رادیویی نزدیک به GRU هستند که بهتر از دو مدل دیگر (LSTM) و (BiLSTM) عمل می کنند که دقت مدل پیشنهادی را ثابت می کند. در نتیجه، مدل پیشنهادی می تواند وضعیت فرکانس رادیویی مکان ها را در زمان های مختلف فصل ایجاد کند که در طراحی، توسعه و استقرار مؤثر سیستم های ارتباط رادیویی از اهمیت بالایی برخوردار است.



Experimental Study on Compressive Behavior of Concrete-filled Double-skin Circular Tubes with Active Confinement

S. T. Nemati Aghamaleki^a, M. Naghipour^{*a}, J. Vaseghi Amiri^a, M. Nematzadeh^b

^a Department of Civil Engineering, Babol University of Technology, Babol, Iran

^b Department of Civil Engineering, Faculty of Engineering and Technology, University of Mazandaran, Babolsar, Iran

PAPER INFO

Paper history:

Received 10 November 2020

Received in revised form 23 December 2020

Accepted 04 January 2021

Keywords:

Concrete-filled Double-skin Tubes

Diameter-to-thickness Ratio

Active Confinement

Regression-based Design Formula

ABSTRACT

A convenient family member of composite columns is concrete filled double skin tube (CFDST); it contains two tubes of concentric steel and also shell concrete that there is between them. The superior or equal potential offering characteristics of CFDST columns are more than counterparts of filled steel tubes of classical concrete (CFST). The purposes of the present study are to provide experimental investigation results into the prestressed load-carrying capacity of CFDST columns. Here, an innovative technique is used to confined concrete prestressing, in which the fresh concrete is compressed for a short-run duration. Sixty-four total specimens were tested with various outer thickness and diameter, inner thickness and diameter, and also CFDST columns of concrete strength that resist axial compression. The experimental results support that the present technique prestressed confined concrete, and it demonstrates that CFDST specimens' load-carrying capacity enhanced significantly.

doi: 10.5829/ije.2022.35.04a.22

1. INTRODUCTION

Provided confining pressure to the concrete core leads to deformability performance, ductility, and strength of reinforced concrete (RC) columns significant improvement; it can be done through the critical region and potential hinge of plastic. Most recently, transverse reinforcement of closely spaced installation is the most commonly adopted method to columns confining pressure improvement, which has been adopted in low-strength concrete columns made popularly [1, 2]. Therefore, confining steel content required for strength of higher concrete RC columns will dramatically enhance if the same ductility and strength level provided to the strength of lower concrete are constant [3, 4].

The design of columns can be as a member of composite to confining action efficiency improvement, in which confined of the concrete can be through FRP wraps [5, 6], steel plates [7, 8], and tubes of hollow steel [9-11]. The steel tube of concrete-filled (CFST) columns has

become popular in constructing tall buildings amongst these measures recently. One of the reasons is that CFST columns performance is superior to columns of ordinary RC under torsion [12, 13], under uni-axial load [14-18], and under flexure [19-21], based on experimental and theoretical research. Several examples of composite structures with CFST columns in circular or square forms, as external or internal structural members, are built. A good example in China is the Canton Tower in Guangzhou [1], comprising twenty-four inclined circular CFST members with a maximum diameter of 2000 mm and wall thickness of 50 mm. Another example is for Northern America. In the Museum of Flight at King County Airport (Seattle, Washington, USA) bar-reinforced concrete filled hollow sections are used for the columns supporting the roof of the exhibit hall, allowing to fulfil the required fire resistance without the need of sprayed fire protection [10]. Nevertheless, some disadvantages of CFST columns are as follows: (1) Under compression of uni-axial, steel can share the larger

*Corresponding Author Institutional Email: m-naghi@nit.ac.ir
(M. Naghipour)

external load part's comparison concrete at the same area of cross-section because its stiffness is higher under the action of composite. (2) Under flexure, the contribution of central concrete, which is near the axis of neutral, to the strength of flexural is insignificant. (3) under torsion, the contribution of central concrete to the strength of torsion is insignificant. (4) the initial concrete elastic dilation under compression is fractional [22]. Therefore, the steel tube confining pressure to concrete during the stage of elastic is relatively low. The development of which can be more rapid until the formation of concrete micro-cracking at the immense strain [23]. The improvement on the CFST columns ratio of strength-to-weight is limited due to the infilled concrete heavy self-weight. The above discussions reveal that the in-filled concrete central part can replace another smaller tube of hollow steel with a similar strength of torsion, uni-axial, and flexure. This construction form of the column is known as the double skin tabular of concrete-filled (CFDST) columns [24].

Furthermore, Yagishita et al. [25] concluded that the absorption of energy, strength, and ductility of CFDST columns than CFT columns enhanced when they were subjected to axial loading and cyclic loading. Rahmani et al. [19] examined CFTs and CFDSTs cyclically and reached identical conclusions. Hence, the role of CFDSTs in the earthquake-affected becomes essential. The resistance of CFDSTs against fire is better than empty tubes and CFTs. Li et al. [26] deduced the existence of composite action among steel and concrete over fire exposure, and its fire performance is favorable.

Therefore, the deficiency of campaigns dealing with CFDST columns characterization and active confinement application study is prominent in the literature in this regard. Also, most of the tested CFDST columns had investigated the stiffness, ductility, and stiffness of SFDST with the pressure of passive confining. Active confinement is an innovative and novel avenue of studies and researches in this regard. The effectiveness of active confinement has increased by applying prestressing to material, where passive confinement depends on dilating concrete overloading to begin the confining pressures generation [27-29].

Typically, the confinement effect is expressed via the ratio of volumetric, which is the relation of reinforcement to the core of concrete. Thus, experimental program results evaluation is the main purpose of this study, where active confinement effects were compared and tested on tubes of double-skin circular concrete-filled in compression. The primary parameters of the ratio of diameter-to-thickness of the inner and outer tube, active confinement, and concrete compressive strength on load-carrying capacity were investigated to their effect on the general ductility and strength establishment. Finally, for the design purpose, a model of regression-base is proposed for the CFDST columns loading-carrying

capacity evaluation. The predicted strength of the results obtained by the authors and other researchers comparison regarding CFDST columns, validity of the proposed model was evaluated.

2. MATERIAL PROPERTIES

2.1. Steel Coupon Tests

With the aims of tensile coupons in order to grip were flattened through the test machine. The alignments of the coupons were carefully performed and accurately gripped. The incorrect alignment can cause the failure of premature due to the stresses of undesirable bending. The preparation and testing of the coupons were in the machine of displacement-controlled of 250 KN capacity (Figure 1). The test of the tensile coupon was conducted under the ASTM A370 [30] standard test with a 2 mm/min loading rate. The stress and strain were the computer's output data. These were plotted to establish the strength of ultimate, elasticity modulus, and yield strength. Table 1 demonstrates the summary of averaged material and individual properties. Where f_y indicates the strength of yield and f_u shows the strength of ultimate. Moreover, the averaged elastic modulus (E_s) is reported as 200 GPa.



Figure 1. Shape of coupons for tensile tests

TABLE 1. Results of coupon test of circular hollow sections

Steel Coupon	f_y (MPa)	f_u (MPa)	E_s (MPa)
SC1	345	410	2.01×10^5
SC2	340	405	2×10^5
SC3	350	420	2.01×10^5
Average	345	411	2×10^5

2. 2. Concrete Cylinder Tests As the final considered step in fabricating the experimental archetypes, the gap among the skins of hollow steel was suffused by Ordinary Portland Concrete (OPC). Two OPC grades (i.e., C10 and C20) were prepared in this study as the most commonly used mix is water, cement, and aggregates. Concrete specimens compressive strength were cast in the cylinder specimen of 150 (mm) × 300 (mm) and compacted based on ACI 211.1. Then, the cylinders were cured at the temperature of ambient. The results of the cylinder are summarized in Table 2.

3. TEST SPECIMENS

3. 1. Specimen Preparation Eight specimens' groups were tested with various values of D_i/t_i , D_o / t_o , and f_c in this study. For each group, eight specimens were created, divided into the following categories containing two specimens: (1) prestressed compressed concrete of double-skin tube-confined; (2) non-prestresses concrete of double-skin tube-confined. Based on the definitions mentioned above, the confinement of prestressed compressed concrete of double-skin tube-confined is active. In contrast, the confinement of non-prestresses concrete of double-skin tube-confined is passive. Moreover, for only 15 to 30 min, the short-term pressure is applied to fresh concrete, that a stable pressure should be established during the process (Figure 2).

TABLE 2. Cylinder specimen for the properties of concrete

Concrete cylinders	Mass (g)	(MPa) f_{cu}	E_c (MPa)
C10	2450	10	1.48×10^5
C20	2450	20	4.2×10^5



Figure 2. Applying preloading process on the fresh concrete

$$\sigma = E \times \varepsilon \quad (1)$$

where σ indicates stress, E represents elasticity modulus, and ε shows the strain.

$$\varepsilon = \frac{(0.5 \times 345)}{2 \times 10^5} = 860 \mu\varepsilon \quad (2)$$

So, it was decided to create two internal steel tubes types with diameters of 39mm and 1 mm thickness (t_i) and 41mm with 2 mm thickness (t_i). The selection of outer steel tubes was 114 mm ($t_o = 2.5$ mm), 111.6 mm ($t_o = 1.3$ mm), 8 mm 8 ($t_o = 2$ mm), 86 mm ($t_o = 1$ mm). The length of all columns was prepared at 250 mm. For fabricating sixty-four columns, 128 steel tubes were totally used to confirm the test results validity. The outer tube surface was shaved with the metal lathe to obtain various values for the thickness of the steel tube, while the steel tubes' inner diameter remained constant. Furthermore, metal lathes were cut off the specimens exceeded length after the active confinement to attain the genuine flat surface (see Figure 3).

The tubes tested dimensions are shown in Table 3, in which L_a indicates the column's actual length, D_o demonstrate the diameter of the outer tube, D_i shows the diameter of the inner tube. Besides, t_o and t_i represent the thickness of the outer and inner tubes. Figure 4 illustrates the composite columns' cross-section.

3. 2. Concrete Cylinder Tests Using the correlation of digital image (DIC), the CFDST columns' force-displacement values were recorded under the active or passive confinement. In order to obtain the displacement for the force applied per second, two points were signed at the end and top of the specimens based on this procedure (see Figure 5).

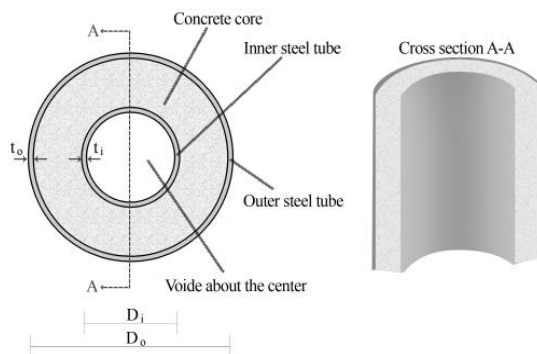
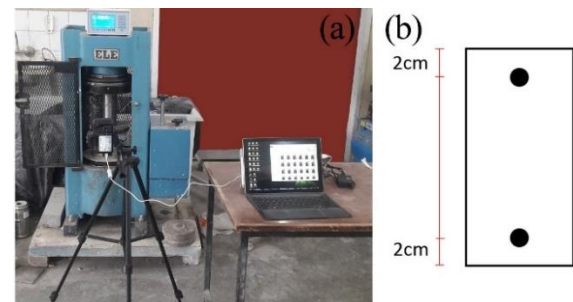
Using the testing machine of ELE with the capacity of 2000 kN after at least 28 days of curing time of the concreting date, these tests were accomplished. The amplification of load was based on the strategy of load-controlled until occurring the specimen failure. A load of



Figure 3. Before and after cutting off the process of a sample specimen

TABLE 3. columns' dimensional properties

Tag	P_o	L_a/D_o	D_o/t_o	D_i/t_i	f'_c (MPa)
SN1-P	0	2.71	86	39	19.51
SN1-A	0.5 f_y	2.41	86	39	19.51
SN2-P	0	2.70	86	39	10.35
SN2-A	0.5 f_y	2.45	86	39	10.35
SN3-P	0	2.72	86	20.5	20.92
SN3-A	0.5 f_y	2.38	86	20.5	20.92
SN4-P	0	2.72	86	20.5	9.84
SN4-A	0.5 f_y	2.44	86	20.5	9.84
SN5-P	0	2.65	44	39	20.18
SN5-A	0.5 f_y	2.30	44	39	20.18
SN6-P	0	2.65	44	39	9.84
SN6-A	0.5 f_y	2.30	44	39	9.84
SN7-P	0	2.65	44	20.5	21.85
SN7-A	0.5 f_y	2.36	44	20.5	21.85
SN8-P	0	2.66	44	20.5	11.01
SN8-A	0.5 f_y	2.33	44	20.5	11.01
SN9-P	0	2.10	85.84	39	19.51
SN9-A	0.5 f_y	1.85	85.84	39	19.51
SN10-P	0	2.08	85.84	39	10.35
SN10-A	0.5 f_y	1.85	85.84	39	10.35
SN11-P	0	2.10	85.84	20.5	20.92
SN11-A	0.5 f_y	1.88	85.84	20.5	20.92
SN12-P	0	2.11	85.84	20.5	9.84
SN12-A	0.5 f_y	1.86	85.84	20.5	9.84
SN13-P	0	2.09	45.6	39	20.18
SN13-A	0.5 f_y	1.80	45.6	39	20.18
SN14-P	0	2.01	45.6	39	9.84
SN14-A	0.5 f_y	1.75	45.6	39	9.84
SN15-P	0	2.07	45.6	20.5	21.85
SN15-A	0.5 f_y	1.82	45.6	20.5	21.85
SN16-P	0	2.06	45.6	20.5	11.62
SN16-A	0.5 f_y	1.80	45.6	20.5	11.62

**Figure 4.** Composite column's cross-section**Figure 5.** a) DIC monitoring system; b) Schematic marking of the two points for force-displacement recoding of the specimens

axial with the average rate of a load equal to 42 kN/min was enhanced to 0.29 Mpa/s monotonically, which decreases within the 0.15 to 0.35 Mpa/s range that complies with the recommendations of ASTM C39 (ASTM C39/ C39M) [31] for concrete specimens.

4. RESULTS AND DISCUSSION

4. 1. Failure Modes

Since the ratios of diameter-to-thickness (D_o/t_o and D_i/t_i), ratios of length-to-diameter (L_a/D_o and L_a/D_i), and forces of active confinement were different, the steel hollow section's failure modes were different slightly under the axial compression. The local buckling by the portion of top to middle causes all of the CFDST specimens' failure modes observed to be under passive confinement. Nevertheless, local buckling was on the top specimens and specimens' end if the concrete was actively confined.

The attained CFDST specimen's failure modes were considered into the following groups: (1) the local buckling mode of the outer tube is subordinated with in-filled concrete shear failure. It is worth noting that which is similar to the CFDST columns' obtained results under passive confinement. (2) CFDST columns' local buckling mode under active confinement. Using filled concrete of C10 and C20, the investigation on one specimen failure mode was for outer tube diameter for 86 and 114 mm under the passive and active confinement (see Table 4). Figure 6 indicates the SN15 specimen's progressive failure under the active and passive confinement. The evident buckling of apparent steel was not observed in the points of (a) and (b) until attaining the first point of the peak. Nevertheless, point (c) deformation can be observed at the specimen's end with the axial load enhancement. Finally, in point (d), the buckling of outwards becomes apparent at the specimen's middle. All specimen of active confined processes (for instance, the points of (e), (f), and (g)) was identical to the passive. Point (h) was the exception of the local bulking area that experienced the buckling of outwards at the end and top specimen.

TABLE 4. CFDST columns' failure modes with the filled concrete of C10 and C20 under passive or active confinement

Type	Passive		Active	
	D _o =86	D _o =114	D _o =86	D _o =114
C10				
C20				

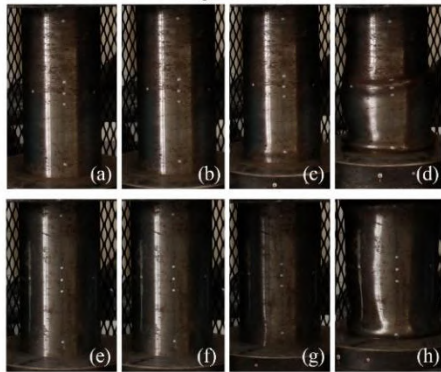
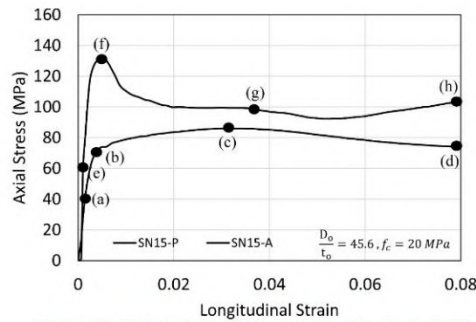


Figure 6. Failure modes of SN15 specimen under passive and active confinement

4. 2. Specimens' Comparison under Active/Passive Confinements

Figures 7 and 8 illustrate the stress of axial is plotted toward the strain that obtained for tubular columns of concrete-filled of double-skin (CDFST) without and with the active confinement ($0.5f_y$), also with different $D_i(39t_i, 20.5t_i)$, and $D_o(86t_o, 84t_o, 45.6t_o, 44t_o)$. The curves of the present study represent axial deformation with the strain of nominal axial that measured as the deformation of general axial ratio to the initial length of the column. CFDST columns' steel skin in the condition of passive buckled severely, and deformations of the plastic enhanced rapidly at the

specimens' middle by achieving the strength of the ultimate specimen. Nevertheless, occurring the ultimate

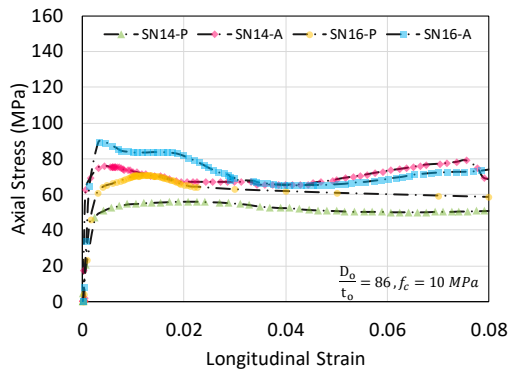
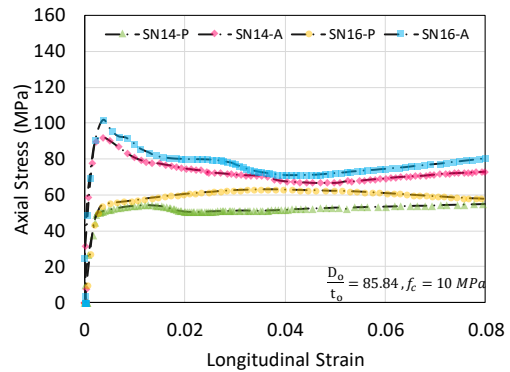
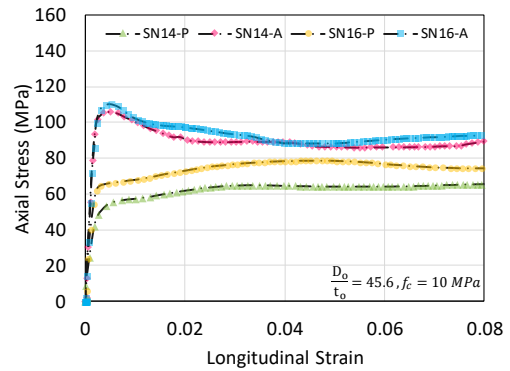
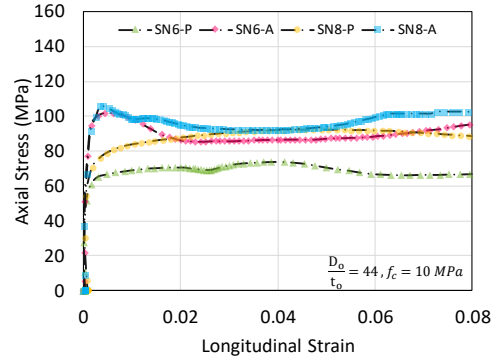


Figure 7. Strain-stress curve under active confinement against passive confinement for C10 filled concret

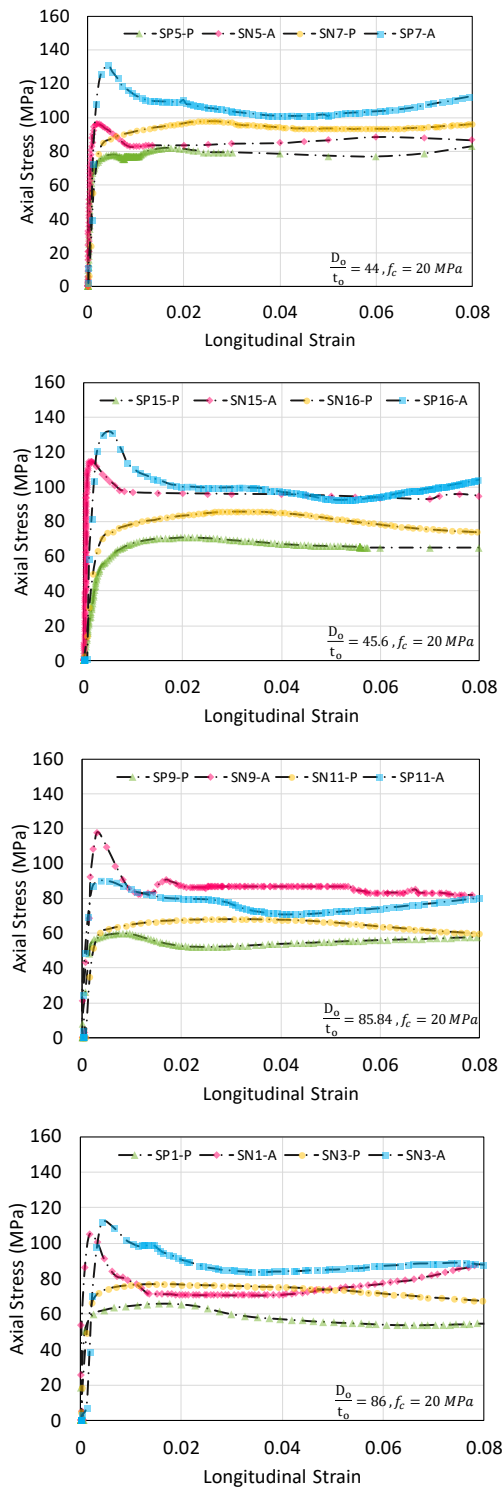


Figure 8. Strain-stress curve under active confinement against passive confinement for C20 filled concrete

strength, deformations at the specimens' end and top increase under the active preloading. This phenomenon causes a drop of abrupt in the curve of stress-strain

simultaneous to infill concrete crushing. The loading procedure was concluded since the experiment's progress became very slow after the peak load by dropping specimen capacity for filled concrete of C10 and C20 under the active confinement.

Figures 7 and 8 noticed that the drop of axial stress after the terminal load under the passive confining was not abruptly against the longitudinal strain curves. Instead, it was processed by the long ductility stage. The good performance of ductility exhibits by the results of the tested specimens. Moreover, the CFDST stress axial compressive for columns of filled concrete of C10 and C20 under the condition active preloading decreased as the ratio of D_o/t_o was enhanced, as indicated in the figures. For instance, the CFDST specimens' ultimate strength with filled concrete of C10 decreased to 15% approximately when the ratio of D_o/t_o amplify from 44 to 86. For the filled concrete of C20, increasing the D_o/t_o ratio from 44 to 86 experienced a 12% reduction.

Degradation in the specimens' ductility and compression capacity could be imputed to the inner or outer tubes' characteristics according to the curves of stress-strain for filled concrete of C10 and C20. The external tube's ratio of D_o/t_o is higher ($D_o/t_o = 86$). So, due to the early buckling of local outward, it suffers, and outer steel section compression capacity cannot efficiently be exploited. The thicker external steel tube of CFDST specimens (SN7-A and SN8-A) development has a greater compression capacity over the SN4-A and SN3-A specimens. Results confirm the effect of active confinement on the circular tube of a double skin. Filled concrete of C20 has better performance than its load of crushing since the standard strength concrete of C10 in the specimens of CFDST is appropriately confined. Moreover, the outcomes of this study imply that the D_i/D_o affects the strength of ultimate axial of short circular columns of CFDST roughly subject to the condition of preloading. The strength of axial compressive columns for the circular columns of CFDST that are short with D_i/t_i equivalent to 20.5 (the range of D_i/D_o was from 0.36-0.48) enhanced by decreasing D_i/D_o .

4. 3. Different Inner Diameter's Effect on the Ratios of Thickness under the Active/Passive Confinements

Figures 9 and 10 were depicted based on the characteristics of the internal tube effect subject to active or passive confinement for the filled concrete of C10 and C20 in columns of CFDST, respectively. As results show, axial loading capacity is enhanced gradually by D_i/t_i reduction for filled concrete of C10 and C20 subject to active or passive confinement. For example, since the ratio of internal diameter to thickness for $D_o/t_o = 86$ enhanced from 25.5 till 39, axial loading capacity for C20 and C10 subject to active confinement reduced by 26% and 14.28%, respectively. It is noteworthy that for $D_o/t_o = 44$, this decreased for

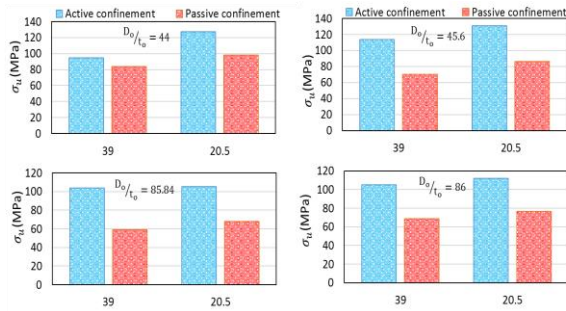


Figure 9. Compressive stress of CFDST specimens under passive and active confinements for C10 concrete

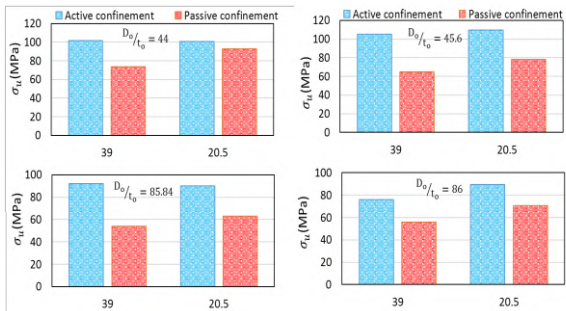


Figure 10. Compressive stress of CFDST specimens under passive and active confinements for C20 concrete

active confinement was approximately 2.19%. Additionally, when using filled concrete of C10, it was reported that passive confinement reduced axial loading capacity by around 22% compared with active confinement. Furthermore, if the D_o/t_o was constant, the axial loading capacity associated with reducing the thickness tube or internal diameter could not increase specifically. Therefore, the lower D_i/t_i for columns of CFDST can be used subject to the condition of active preloading.

Improving the strength of CFDST specimens axial compressive can be occurred by the outer steel tube's strength of concrete and ratio of diameter to thickness subject to active confinement. Consequently, the effect of active confinement on CFDST specimens, in addition to inner and outer steel tubes' contribution to columns' ultimate compression load in such significant enhancement, is essential.

4. 4. Prediction Of CFDST Column Strength

In order to predict the capacities of members bearing, structural design is highly essential. A consistent sensitivity and reliability framework must spread realistic and accurate approaches of prediction if failure is avoided. Thus, the design of the specifications step is done with the aim of standard methods, and the prediction of offer capacity is formulated based on various theories' backgrounds. The most prominent

design specifications of composite members are the ACI code [33] associated with some tentative equations provided by Hassanein et al. [34] and Uenaka et al., [35] which are widely used for research aims. Today, the technology of composite members is constantly evolving, and compression's new form is created sections arise. Hence, the development of other technical approaches is compulsory to satisfy composite construction's needs. In this line, considering the active preloading to prediction capabilities assessment, this section of the study suggested a novel formulation for columns of a double skin. A fundamental understanding of methods and also underlying theories is essential before comparing results .

1) By the equation obtained using the ACI code [32], the strength of the ultimate axial of composite columns of single skin containing the bar of reinforcing can be determined. Nevertheless, with the ACI code [32], the effect of concrete confinement on the proposed formula is ignored. The following modified equation that obtained from the ACI code [32] is for the strength of the CFDST stub column ultimate axial involving internal steel tube contribution is declared as follows:

$$(P_u)_{ACI} = f_{yo}A_o + 0.85f_cA_c + f_{yi}A_i \tag{3}$$

Where f_{yo} and f_{yi} indicate the strength of yield of outer and internal steel tubes, respectively. Besides, f_c demonstrate the strength of compressive of annulus concrete. A_o and A_i show the area of cross-sectional of the outer and internal steel tubes, respectively. Finally, A_c represents the area of cross-sectional of annulus concrete.

2) Additionally, some researchers suggested equations for the strength of the CFDST columns ultimate axial's calculation in order to modify the ACI code recommended formula. Uenaka et al. [33] obtained the determining equation of strength of CFDST columns ultimate axial from the proposed equation of Architectural Institute of Japan (AIJ) [34] for the columns of CFST stub. The strength of sandwiched concrete and inner and outer steel tubes is superimposed elementally by Uenaka et al. [33]. Next, the effect of confinement of the inner tube on the strength of CFDST columns ultimate axial is not as practical as the outer one [1]. Uenaka et al. [33] followed modified expression of ultimate axial strength estimation is obtained from AIJ [34]:

$$(P_u)_{Uenaka\ et\ al.} = (2.86 - 2.59(\frac{D_i}{D_o}))f_{yo}A_o + 0.85f_cA_c + f_{yi}A_i, \text{ for } 0.2 < (\frac{D_i}{D_o}) < 0.7 \tag{4}$$

where the internal steel tubes diameter is shown by D_i .

3) the proposed model of Hassanein et al. [35] could be used to strengthen the ultimate axial of circular stub columns of CFDST, and that estimates the strength of the ultimate axial of circular stub columns of CFST. It is

noteworthy that it is based on the design model, and Liang and Fragomeni's [36] developed it regarding the previous model proposed by Hassanein et al. [35]. It aims to predict the strength of the ultimate axial of stub columns of CFDST involving carbon steels and stainless. The following model of novel design is extended by Hassanein et al. [35]:

$$(P_u)_{Hassanein et al.} = \gamma_o f_{yo} A_o + (\gamma_c f_c + 4.1 f'_{rp,o}) A_c + \gamma_i f_{yi} A_i \tag{5}$$

where the coefficient of γ_o can be used for the effect of strain hardening explanation on the external steel, and it can obtain as follows:

$$\gamma_o = 1.458 \left(\frac{D_o}{t_o}\right)^{-0.1}, \quad 0.9 < \gamma_o < 1.1 \tag{6}$$

γ_c shows the recommended strength attenuation coefficient of Liang [37], and also can obtain as follows (D_c means $D_o - 2t_o$):

$$\gamma_c = 1.85 D_c^{-0.135}, \quad 0.85 < \gamma_c < 1.0 \tag{7}$$

The pressure of lateral confining of $f'_{rp,o}$ for $47 < \frac{D_o}{t_o} < 150$ expressed as follows:

$$f'_{rp,o} = (0.006241 - 0.0000357 \frac{D_o}{t_o}) f_{yo} \tag{8}$$

The coefficient of γ_i can explain the effect of strain hardening on the internal steel and can be obtained as follows:

$$\gamma_i = 1.458 \left(\frac{D_i}{t_i}\right)^{-0.1}, \quad 0.9 < \gamma_i < 1.1 \tag{9}$$

Based on the study's results, the main parameter that affects the final stress in the tubes of a double skin of filled concrete is the factor of active confinement. In the present study, the analysis of multi-expression linear regression was applied to present a comprehensive and novel relationship that can use for the active and passive confinement in the columns of CFDST. The following formula is extracted from the linear regression of multi-expression:

$$(P_u)_{Present study} = 303.54A - 147.81 \frac{L_a}{D_o} + 3.934 \frac{D_o}{t_o} - 3.1 \frac{D_i}{t_i} + 8.163 f_c + 0.762 A_{so} + 12082.82 \left((0.006241 - 0.0000357 \frac{D_o}{t_o}) f_{yo} \right) - 25266.9 \tag{10}$$

The effective coefficient is shown by A subject to active confinement and considered 0 and 0.5 for passive and active confinement.

Figure 11 indicates the test results of CFDST specimens' predicted scatter plots and values of observed P_u . The data reported by others as shown in Figure 11 are scattered with low R^2 . However, our data are close to the linear model with high R^2 value of 0.89. In Figure 11, almost all values of predicted P_u from Hassanein et al. [35] and ACI code [32] were underestimated. Nevertheless, the present study and Uenaka et al. [33] predicted P_u are closer to an ideal line ($y=x$). The $R^2 =$

0.61 obtained from the Uenaka et al. [33] proposed method is better among the three empirical methods.

It is worth noting that none of the three methods consider the effect of active confinement. It is possible to adapt a novel method to composite the processes of column design with high-fidelity and accurate modifications that include active confinement. Figure 12 exhibits the relevance presented equation and traditional methods error to implement the prediction error outcomes visually.

Table 5 shows the empirical equation comparison and the proposed equation of regression-baes according to the strength values of normalized ultimate axial. The predicted capacities of axial load-carrying for the columns of CFDST are not accurate almost because the tentative equations do not consider the active confinement effect. The performance of the Uenaka et al. [33] proposed method with the average ratio 1.02 and 0.23 standard deviation is better among the three

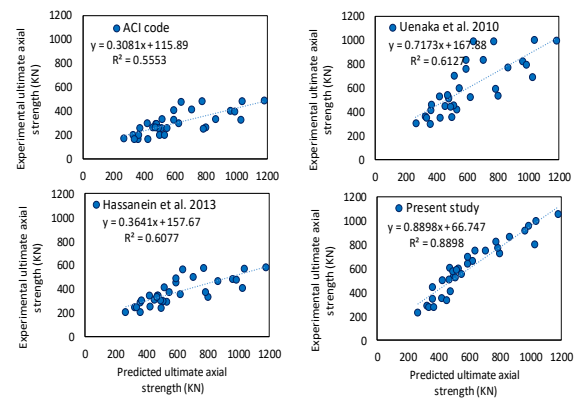


Figure 11. Scatter plots between the observed and the predicted value of P_u for the proposed and existing equations

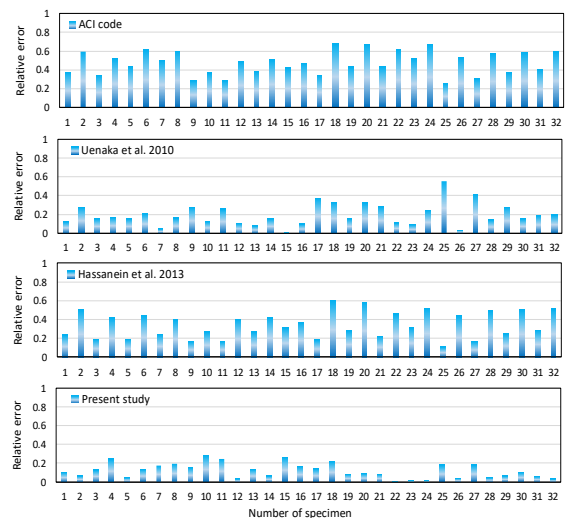


Figure 12. Relative error plots of the proposed and existing equations for the ultimate axial strength of CFDST columns

TABLE 5. Comparison of the experimental ultimate axial strength of CFDST columns with and without active confinement for the proposed and existing equations

N_u (KN)	N_u/N_{u-ACI}	$N_u/N_{u-Uenaka}$	$N_u/N_{u-Hassanein}$	N_u/N_{u-MLR}
324.74	1.60	0.89	1.31	2.10
497	2.47	1.38	2.03	1.27
263.99	1.52	0.87	1.24	2.87
358.99	2.10	1.20	1.72	1.16
361.07	1.79	0.87	1.23	1.73
530.34	2.60	1.26	1.79	1.14
334.39	2.01	0.95	1.33	2.58
422.62	2.51	1.19	1.66	1.15
418.78	1.40	0.78	1.20	1.89
473.98	1.59	0.89	1.36	1.00
367.99	1.40	0.79	1.20	2.57
508.96	1.95	1.11	1.67	1.30
478	1.61	0.93	1.36	1.72
620.98	2.05	1.18	1.74	1.18
453.96	1.72	1.01	1.46	2.27
491.97	1.89	1.11	1.60	1.12
514.98	1.53	0.73	1.23	1.07
1025.97	3.11	1.48	2.50	1.47
470	1.77	0.87	1.40	1.16
799.97	3.03	1.48	2.39	1.28
591.13	1.79	0.78	1.28	1.10
863.85	2.57	1.12	1.85	1.14
547.53	2.11	0.92	1.45	1.22
784.75	3.05	1.32	2.09	1.17
637.98	1.34	0.64	1.12	0.98
1036.92	2.14	1.03	1.80	1.16
590.97	1.44	0.71	1.20	1.00
960.98	2.37	1.16	1.98	1.18
773.97	1.60	0.78	1.33	1.07
1180	2.41	1.18	2.02	1.24
705.07	1.69	0.84	1.40	1.10
986.99	2.47	1.24	2.05	1.16
Avg	2.02	1.62	1.59	1.15
Std	0.50	0.43	0.36	0.21

empirical methods (see Table 5). The best performance by values of N_u in columns of CFDST in this study is shown by average value 1.01 and 0.15 standard deviation of $N_{u,Exp}/N_{u,Present\ study}$. Overall, the results illustrated that the proposed MLR model in simulation and prediction of ultimate axial strength of CFDST columns

with active confinement is most reliable compared with those empirical equations.

5. CONCLUSION

The construction and design of formidable and massive engineering structures has been increasing in recent decades. These sturdy structures are designed for various aims, have a longer service life, and are needed for worldwide sustainable solutions. Thus, the cost optimization could be done through composite structures, and also the concerns mitigate because they couple the materials favorable engineering properties. In this line, CFDST members can enhance composite construction efficiency potentially. Nevertheless, delving these members into the main aspects is through the compression characteristics assessment of each cross-section element to provide reliable design guidelines. The test program in this study has sixty-four composite columns. In order to anticipate the performance of variables and characterize the internal and external steel tubes in the columns of CFDST, four various ratios of D_o/t_o , two ratios of D_i/t_i , and two distinct grades of strength were used. In this regard, the stress against the curves of strain and modes of failure subject to passive and active confinement were examined. Moreover, the application of the proposed design CFDST columns formula in the present study was evaluated through three prediction procedures of design capacity compared to the experimental results. The following conclusions can be considered in the scope of this study:

- The capacity of the load-carrying of specimens of CFDST can be noticeably enhanced by converting the type of confinement to active using this technique. The improvement ratio between the actively-confined and passively-confined CFDST differs from 1.25 to 1.75.

- The capacity of the circular columns load-carrying can improve effectively by the increase and decrease of concrete strength and steel tube D_o/t_o , respectively .

- Since the ratio of tube D_i/t_i enhances, the capacity of the CFDST loading capacity for the values of permanent D_o/t_o in the active confinement could not increase specifically when the tube thickness or inner diameter decrease .

- The provided capacity method of Uenaka in double skin columns capacity prediction performs very well. However, it is noteworthy that the formulation of this method is for CFDST columns of non-prestressed and does not consider the condition of active confinement .

- The predictions of the proposed formula are in line with the empirical results compared to the current formulas of strength prediction. They can predict the strength of the circular short CFDST columns compressive reasonably in the existence of active and passive confinement.

6. REFERENCES

- Han, L.-H., Li, W. and Bjorhovde, R., "Developments and advanced applications of concrete-filled steel tubular (cfst) structures: Members", *Journal of constructional steel research*, Vol. 100, (2014), 211-228, doi: 10.1016/j.jcsr.2014.04.016.
- Essopjee, Y. and Dundu, M., "Performance of concrete-filled double-skin circular tubes in compression", *Composite Structures*, Vol. 133, (2015), 1276-1283, doi: 10.1016/j.compstruct.2015.08.033.
- Borzouyi Kutenayi, S., Kiahosseini, S. and Talebpour, M., "The effect of caspian sea water on corrosion resistance and compressive strength of reinforced concrete containing different sio2 pozzolan", *International Journal of Engineering, Transactions A: Basics*, Vol. 30, No. 10, (2017), 1464-1470, doi: 10.5829/ije.2017.30.10a.06.
- Wang, Y., Chen, G., Wan, B., Han, B. and Ran, J., "Axial compressive behavior and confinement mechanism of circular frp-steel tubed concrete stub columns", *Composite Structures*, Vol. 256, (2021), 113082, doi: 10.1016/j.compstruct.2020.113082.
- Hemmati, A. and Mojaddad, S., "Effect of steel confinement on behavior of reinforced concrete frame", *Journal of Rehabilitation in Civil Engineering*, Vol. 7, No. 3, (2019), 1-14, doi: 10.22075/jrce.2018.13791.1252.
- Seyed Razzaghi, M., Esfandyari, R. and Nateghi, F., "The effects of internal and external stiffeners on hysteretic behavior of steel beam to cft column connections", *International Journal of Engineering, Transactions A: Basics*, Vol. 27, No. 7, (2014), 1005-1014, doi: 10.5829/idosi.ije.2014.27.07a.01.
- Cheng, B. and Su, R., "Numerical studies of deep concrete coupling beams retrofitted with a laterally restrained steel plate", *Advances in Structural Engineering*, Vol. 14, No. 5, (2011), 903-915, doi: 10.1260/1369-4332.14.5.903.
- Zhao, X.-L., Tong, L.-W. and Wang, X.-Y., "Cfdst stub columns subjected to large deformation axial loading", *Engineering Structures*, Vol. 32, No. 3, (2010), 692-703, doi: 10.1016/j.engstruct.2009.11.015.
- Young, B. and Ellobody, E., "Experimental investigation of concrete-filled cold-formed high strength stainless steel tube columns", *Journal of Constructional Steel Research*, Vol. 62, No. 5, (2006), 484-492, doi: 10.1016/j.jcsr.2005.08.004.
- Kodur, V. and MacKinnon, D., "Simplified design of concrete-filled hollow structural steel columns for fire endurance", *Journal of Constructional Steel Research*, Vol. 1, No. 46, (1998), 298, doi: 10.1016/s0143-974x(98)80034-5.
- Zhu, A.-Z., Xu, W., Gao, K., Ge, H.-B. and Zhu, J.-H., "Lateral impact response of rectangular hollow and partially concrete-filled steel tubular columns", *Thin-Walled Structures*, Vol. 130, (2018), 114-131, doi: 10.1016/j.tws.2018.05.009.
- Mohammed, A.H., Mohammedali, T.K. and Hussin, A.K., "Experimental study on performance of fiber concrete-filled tube columns under axial loading", *International Journal of Engineering, Transactions C: Aspects*, Vol. 32, No. 12, (2019), 1726-1732, doi: 10.5829/ije.2019.32.12c.05.
- Wang, W.-D., Jia, Z.-L., Shi, Y.-L. and Tan, E.L., "Performance of steel-reinforced circular concrete-filled steel tubular members under combined compression and torsion", *Journal of Constructional Steel Research*, Vol. 173, (2020), 106271, doi: 10.1016/j.jcsr.2020.106271.
- Thai, S., Thai, H.-T., Uy, B. and Ngo, T., "Concrete-filled steel tubular columns: Test database, design and calibration", *Journal of Constructional Steel Research*, Vol. 157, (2019), 161-181, doi: 10.1016/j.jcsr.2019.02.024.
- Wei, Y., Jiang, C. and Wu, Y.-F., "Confinement effectiveness of circular concrete-filled steel tubular columns under axial compression", *Journal of Constructional Steel Research*, Vol. 158, (2019), 15-27, doi: 10.1016/j.jcsr.2019.03.012.
- Liu, X., Xu, C., Liu, J. and Yang, Y., "Research on special-shaped concrete-filled steel tubular columns under axial compression", *Journal of Constructional Steel Research*, Vol. 147, (2018), 203-223, doi: 10.1016/j.jcsr.2018.04.014.
- Jin, L., Fan, L., Li, P. and Du, X., "Size effect of axial-loaded concrete-filled steel tubular columns with different confinement coefficients", *Engineering Structures*, Vol. 198, (2019), 109503, doi: 10.1016/j.engstruct.2019.109503.
- Yuan, F., Huang, H. and Chen, M., "Effect of stiffeners on the eccentric compression behaviour of square concrete-filled steel tubular columns", *Thin-Walled Structures*, Vol. 135, (2019), 196-209, doi: 10.1016/j.tws.2018.11.015.
- Rahmani, Z., Naghipour, M. and Nematzadeh, M., "Flexural performance of high-strength prestressed concrete-encased concrete-filled steel tube sections", *International Journal of Engineering, Transactions C: Aspects*, Vol. 32, No. 9, (2019), 1238-1247, doi: 10.5829/ije.2019.32.09c.03.
- Jiang, Y., Silva, A., Macedo, L., Castro, J.M., Monteiro, R. and Chan, T.-M., "Concentrated-plasticity modelling of circular concrete-filled steel tubular members under flexure", in *Structures*, Elsevier. Vol. 21, (2019), 156-166.
- Al Zand, A.W., Badaruzzaman, W.H.W., Mutalib, A.A. and Hilo, S.J., "Flexural behavior of cfst beams partially strengthened with unidirectional cfrp sheets: Experimental and theoretical study", *Journal of Composites for Construction*, Vol. 22, No. 4, (2018), 04018018, doi: 10.1061/(asce)cc.1943-5614.0000852.
- Ho, J. and Dong, C., "Improving strength, stiffness and ductility of cfdst columns by external confinement", *Thin-Walled Structures*, Vol. 75, (2014), 18-29, doi: 10.1016/j.tws.2013.10.009.
- Wei, S., Mau, S., Vipulanandan, C. and Mantrala, S., "Performance of new sandwich tube under axial loading: Experiment", *Journal of Structural Engineering*, Vol. 121, No. 12, (1995), 1806-1814, doi: 10.1061/(asce)0733-9445(1995)121:12(1806).
- Han, L.-H., Huang, H., Tao, Z. and Zhao, X.-L., "Concrete-filled double skin steel tubular (CFDST) beam-columns subjected to cyclic bending", *Engineering Structures*, Vol. 28, No. 12, (2006), 1698-1714, doi: 10.1016/j.engstruct.2006.03.004.
- Yagishita, F., Kitoh, H., Sugimoto, M., Tanihira, T. and Sonoda, K., "Double skin composite tubular columns subjected to cyclic horizontal force and constant axial force", in *Proc., 6th ASCCS Int. Conf. on Steel-Concrete Composite Structures*, Univ. of Southern California Los Angeles. (2000), 497-503.
- Li, W., Ren, Q.-X., Han, L.-H. and Zhao, X.-L., "Behaviour of tapered concrete-filled double skin steel tubular (CFDST) stub columns", *Thin-Walled Structures*, Vol. 57, (2012), 37-48, doi: 10.1016/j.tws.2012.03.019.
- Nematzadeh, M., Hajirasouliha, I., Haghinejad, A. and Naghipour, M., "Compressive behaviour of circular steel tube-confined concrete stub columns with active and passive confinement", *Steel Composite Structures, An International Journal*, Vol. 24, No. 3, (2017), 323-337, doi: 10.1016/j.engstruct.2016.10.008.
- Nematzadeh, M., Naghipour, M., Jalali, J. and Salari, A., "Experimental study and calculation of confinement relationships for prestressed steel tube-confined compressed concrete stub columns", *Journal of Civil Engineering Management*, Vol. 23, No. 6, (2017), 699-711, doi: 10.3846/13923730.2017.1281837.
- Nematzadeh, M., Fazli, S., Naghipour, M. and Jalali, J., "Experimental study on modulus of elasticity of steel tube-confined concrete stub columns with active and passive

- confinement", *Engineering Structures*, Vol. 130, (2017), 142-153, doi: 10.1016/j.engstruct.2016.10.008.
30. Testing, A.S.f., Materials. Committee A-01 on Steel, S.S. and Alloys, R., "Standard test methods and definitions for mechanical testing of steel products, ASTM International, (2017).
 31. Concrete, A.I.C.C.o. and Aggregates, C., "Standard test method for compressive strength of cylindrical concrete specimens, ASTM international, (2014).
 32. Committee, A., "Building code requirements for structural concrete: (aci 318-02) and commentary (aci 318r-02), American Concrete Institute. (2002).
 33. Uenaka, K., Kitoh, H. and Sonoda, K., "Concrete filled double skin circular stub columns under compression", *Thin-Walled Structures*, Vol. 48, No. 1, (2010), 19-24, doi: 10.1016/j.tws.2009.08.001.
 34. AII, *Standard for structural calculation of steel reinforced concrete structures*. 2001.
 35. Hassanein, M., Kharoob, O. and Liang, Q., "Circular concrete-filled double skin tubular short columns with external stainless steel tubes under axial compression", *Thin-Walled Structures*, Vol. 73, (2013), 252-263, doi: 10.1016/j.tws.2013.08.017.
 36. Liang, Q.Q. and Fragomeni, S., "Nonlinear analysis of circular concrete-filled steel tubular short columns under axial loading", *Journal of Constructional Steel Research*, Vol. 65, No. 12, (2009), 2186-2196, doi: 10.1016/j.jcsr.2009.06.015.
 37. Liang, Q.Q., "Performance-based analysis of concrete-filled steel tubular beam-columns, part i: Theory and algorithms", *Journal of Constructional Steel Research*, Vol. 65, No. 2, (2009), 363-372, doi: 10.1016/j.jcsr.2008.03.007.

Persian Abstract

چکیده

یکی از عضوهای رایج و در دسترس ستون‌های کامپوزیتی، لوله دو جداره پر شده از بتن (CFDST) است. این ستونها شامل دو لوله از فولاد متحدالمرکز و همچنین بتنی است که بین آنها وجود دارد. مشخصه‌های مکانیکی ستون‌های CFDST بیشتر از نمونه‌های مشابه با لوله‌های یک جداره فولادی پر شده از بتن (CFST) است. هدف از مطالعه حاضر ارائه نتایج تحقیقات آزمایشگاهی در مورد ظرفیت باربری ستون‌های CFDST با پیش‌تندگی فعال است. در اینجا، یک تکنیک ابتکاری برای پیش‌تندگی بتن محصور شده استفاده می‌شود که در آن بتن تازه برای مدت کوتاهی فشرده می‌شود. در مجموع شصت و چهار نمونه با ضخامت‌ها و قطرهای بیرونی و داخلی مختلف و همچنین ستون‌های CFDST با مشخصه‌های مختلف بتن، آزمایش شدند. نتایج آزمایشگاهی نشان می‌دهد که روش به کارگرفته شده برای بتن محصور شده ظرفیت باربری نمونه‌های CFDST را به طور قابل توجهی افزایش می‌دهد.



Applications of Modified Simple Additive Weighting Method in Manufacturing Environment

T. K. Biswas, S. Chaki*

Automobile Engineering Department, MCKV Institute of Engineering, Liluah, Howrah, West Bengal, India

PAPER INFO

Paper history:

Received 16 August 2021

Received in revised form 24 January 2022

Accepted 27 January 2022

Keywords:

Modified Simple Additive Method

Multiple-criteria Decision Making

Non-traditional Machining

Flexible Manufacturing System

Industrial Robot

ABSTRACT

Multiple criteria decisions making (MCDM) techniques are employed widely by decision-makers for ranking the potential alternatives under conflicting environments to select the best one for different industrial problems. Present work employed a modified Simple Additive Weighting (SAW) method to solve different decision-making problems in the manufacturing industry such as industrial robot selection, flexible manufacturing systems selection and, non-traditional machining processes selection respectively. The proposed methodology is simple and involves lesser mathematical complexity. The ranking obtained by the proposed modified SAW method corroborates well with other popular MCDM methods like MOORA, MABAC, TOPSIS and AHP for solving similar problems. It indicates the robustness of the proposed method. However, the proposed method is better compared to those methods through its simplicity, lesser computational complexity, and lesser computational time. Further, sensitivity analysis indicates the stability of the method. Being generic the method can be applied for solving problems related to ranking and selection in any societal segment.

doi: 10.5829/ije.2022.35.04a.23

1. INTRODUCTION

Multi-criteria decisions making (MCDM) is a popular method for making decision in daily lives or complex engineering problems under multiple conflicting criteria. It helps in evaluating and determining the best possible alternative and precise ranking preorders of the considered alternatives. Such approaches are useful for an organization in reduction of the product cost, enhancement of productivity, up-gradation of product quality, and improvement of sales volume in the market. Since the inception of the concept, several popular MCDM methods are evolved and been employed in almost every domain of engineering and management [1-4].

The recent trend towards increased productivity and maintaining uniform quality has incorporated computer-based automation within the manufacturing domain. To cater to that need large applications are being observed on non-traditional machining (NTM) processes,

industrial robots, additive manufacturing along flexible manufacturing systems (FMS) etc. However, those processes or equipment are generally dependent on several variables or attributes that bear complex relationships among themselves, and selecting an appropriate process or equipment from available alternatives always processes a challenge to the practicing engineers. The industrial robot selection problem has been investigated in the recent past through various MCDM approaches like MOORA [5], COPRAS [6], Fuzzy Delphi method, TOPSIS [7], VIKOR [8], Best-worst method [9], etc. Along with, the development of robot prototype [10], controller [11], and optimization of motors in powertrain [12] has been also studied by the researchers.

The FMS selection is another prominent MCDM problem, where methods like MOORA [5], fuzzy AHP, PROMETHEE [13], AHP-TOPSIS [14], TOPSIS [15] have been incorporated by researchers. Determining a suitable nontraditional machining (NTM) process from

*Corresponding Author Institutional Email: chaki.s@mckvie.edu.in
(S. Chaki)

several alternatives has been also evaluated by researchers through TOPSIS-AHP [16], MOORA [7], fuzzy AHP [17] methods.

Literature indicates the application of a number of MCDM techniques for the selection of robots, FMS, and NTM processes. But those methods bear complex mathematical steps and are computationally expensive. However, robustness and stability are found adequate for almost all the above-mentioned processes. The simple Additive Weighting (SAW) method, a comparatively simple and computationally inexpensive method has been already used in different application domains [18,19]. The present work proposed and envisaged working of a less critical approach of MCDM i.e. modified Simple Additive Weighting (SAW) method that incorporates a simple process of scaling during computation of normalized decision matrix. It simplifies the further computation. In this process, a negative performance score never appears during computation and it always remains greater than one during ranking evaluation, which is advantageous.

The present work has investigated the efficacy of the modified SAW method through three different modern-day manufacturing problems that include selecting industrial robots, FMS, and NTM processes. A comparative study of the ranking by proposed modified SAW method and other popular techniques like MOORA (Multi-objective optimization by ratio analysis) and MABAC (Multi-Attribute Border Approximation Area Comparison) method is determined and presented for each of the problems. Finally, the stability of the proposed method is investigated through sensitivity analysis.

2. MODIFIED SAW METHOD:

Modification of conventional Simple additive weighting (SAW) method [19] has been detailed as follows:

Step 1. Establishment of the initial decision matrix

$$X = [x_{ij}]_{m \times n} \tag{1}$$

Step 2. The decision matrix is normalized as

$$N = [r_{ij}]_{m \times n} \tag{2}$$

In this step, dimensions of criteria are converted into non-dimensional forms.

For Benefit type criteria, r_{ij} ,

$$r_{ij} = \frac{x_{ij} - x_i^-}{x_i^+ - x_i^-} \tag{3}$$

For non-beneficial type criteria, r_{ij} ,

$$r_{ij} = \frac{x_i^+ - x_{ij}}{x_i^+ - x_i^-} \tag{4}$$

Here, x_{ij} , x_i^+ and x_i^- are the elements from the initial decision matrix (X), where $x_i^+ = \max(x_1, x_2, \dots, x_m)$ and $x_i^- = \min(x_1, x_2, \dots, x_m)$.

Step 3. For sets of beneficial and non-beneficial criteria, each normalized criterion r_{ij} is computed on a scale of 0-1 where 0 corresponds to the minimum and 1 to the maximum assigned value for the corresponding indicator. Now, r_{ij} is classified into five scale values ranging from 1-5 where 5 is the extreme importance, 4 is very strong importance, 3 is strong importance, 2 is moderate importance and 1 is the equal importance. During computation, when the normalized value of criteria are in the interval of ($>0.80, 1.00$), then the scale value is taken as $g=5$, If the criteria value lies in the interval of ($>0.60, 0.80$), then $g=4$, if the normalized value of all criteria lies in the interval of ($>0.40, 0.60$) then $g=3$, ($>0.20, 0.40$) then $g=2$ and ($>0.00, 0.20$) and finally $g=1$. This scaled normalized decision matrix is identified by (V_{ij}).

Step 4. The elements of the weighted scale value (Q) are calculated based on the expression:

$$Q_{ij} = w_i \cdot v_{ij} \tag{5}$$

Step 5. Finally, the overall score (S_i) of the alternatives is computed using Equation (6), and rank the alternatives are determined based on the descending value of S_i .

$$S_i = \sum_{j=1}^n q_{ij} \tag{6}$$

3. PERFORMANCE EVALUATION OF MODIFIED SAW METHOD:

To show the applicability and efficacy of the modified SAW method in solving MCDM problems following examples are considered in the manufacturing environment.

3. 1. Case Study1: Industrial Robot Selection In this example, seven different industrial robots are analyzed based on five different criteria such as load capacity (LC), repeatability (RE), maximum tip speed (MTS), memory capacity (MC), and manipulator reach (MR) to find out the best robot among them. Here, except repeatability other criteria are of beneficial types. The decision matrix and criteria weights determined by Bhangale et al. [20] have been used and given in Table 1.

The normalized decision matrix has been determined using Equations (2)- (4). Scaling of normalized decision matrix has been done using step 3 explained in section 2 (Table 2). Table 3 indicates weighted scaled values (Q) computed using Equation (4).

Finally, the overall score S_i of alternatives has been computed using Equation (6) and subsequent ranking is determined (Table 3).

TABLE 1. Decision matrix of industrial robot selection [20]

Sl. No	Alternatives	Criteria				
		LC	RE	MTS	MC	MR
1	ASEA-IRB 60/2	60	0.4	2540	500	990
2	Cincinnati Milacrone T3-726	6.35	0.15	1016	3000	1041
3	Cybotech V15 Electric Robot	6.8	0.1	1727.2	1500	1676
4	Hitachi America Process Robot	10	0.2	1000	2000	965
5	Unimation PUMA 500/600	2.5	0.1	560	500	915
6	United States Robots Maker 110	4.5	0.08	1016	350	508
7	Yaskawa Electric Motoman L3C	3	0.1	177	1000	920
Weight considered (Wi)		0.1574	0.1825	0.2385	0.2172	0.2043

TABLE 2. Scaled Normalized decision matrix, V

Sl. No.	Alternatives	Criteria				
		LC	RE	MTS	MC	MR
1	ASEA-IRB 60/2	5	1	5	1	3
2	Cincinnati Milacrone T3-726	1	4	2	5	3
3	Cybotech V15 Electric Robot	1	5	4	3	5
4	Hitachi America Process Robot	1	4	2	4	2
5	Unimation PUMA 500/600	1	5	1	1	2
6	United States Robots Maker 110	1	5	2	1	1
7	Yaskawa Electric Motoman L3C	1	5	1	2	2

TABLE 3. Weighted scale value matrix, Q, Overall score Si and corresponding rank

Sl. No	Alternatives	Criteria					Si	Rank
		LC	RE	MTS	MC	MR		
1	ASEA-IRB 60/2	0.787	0.183	1.193	0.217	0.613	2.992	3
2	Cincinnati Milacrone T3-726	0.157	0.730	0.477	1.086	0.613	3.063	2
3	Cybotech V15 Electric Robot	0.157	0.913	0.954	0.652	1.022	3.697	1
4	Hitachi America Process Robot	0.157	0.730	0.477	0.869	0.409	2.642	4
5	Unimation PUMA 500/600	0.157	0.913	0.239	0.217	0.409	1.934	7
6	United States Robots Maker 110	0.157	0.913	0.477	0.217	0.204	1.968	6
7	Yaskawa Electric Motoman L3C	0.157	0.913	0.239	0.434	0.409	2.151	5

3. 2. Case Study2: FMS Selection In this example the decision matrix developed by Karsak and Kuzgunkaya [21] on Flexible Manufacturing Systems (FMS) selection is given in Table 6 and has been solved using the modified SAW method. The chosen problem has eight alternatives and seven criteria. Out of these, all the five criteria such as reduction in labor cost (LC), reduction in WIP (RWIP), reduction in setup cost (RSC), increase in market response (IMR), improvement in quality (IQ) are beneficial attributes and others two i.e. capital and maintenance cost (CMC), and floor space

used (FSU) are non-beneficial attributes. The criteria weights determined through AHP method for the same problem by Rao and Parnichkun [22] have been employed here for analysis (Table 4).

The normalized decision matrix, weighted scale value matrix, and the overall score are determined through stepwise computation by using Equations (2)-(5) of the modified SAW method. Table 5 indicates the final rank of alternatives obtained through the modified SAW method.

TABLE 4. Decision matrix for FMS selection [21,22]

Alternative FMS	Criteria						
	RLC (%)	RWIP (%)	RSC (%)	IMR	IQ	CMC (\$ 000)	FSU (ft ²)
1	30	23	5	0.745	0.745	1500	5000
2	18	13	15	0.745	0.745	1300	6000
3	15	12	10	0.5	0.5	950	7000
4	25	20	13	0.745	0.745	1200	4000
5	14	18	14	0.255	0.745	950	3500
6	17	15	9	0.745	0.5	1250	5250
7	23	18	20	0.5	0.745	1100	3000
8	16	8	14	0.255	0.5	1500	3000
Weight considered (Wi)	0.1129	0.1129	0.0445	0.1129	0.2861	0.2861	0.0445

3. 3. Case Study3: Non-traditional Machining (NTM) Process Selection

In this example, the best NTM process is selected from nine different unconventional machining processes with ten important criteria for each of the processes. Among ten criteria, material removal rate (MR1), efficiency (η), safety (S), work material (WM), and shape feature (SF) are considered as the beneficial criteria and surface finish (TSF), power requirement (PR), cost (C), tooling and fixtures (TF), tool consumption (TC), are the non-beneficial criteria. The decision matrix and corresponding criteria weights computed using the AHP method by Chakladar and Chakraborty [16] are used in the present computation (Table 6).

The overall score (S_i) for different processes is computed by the modified SAW method through Equations (2)-(6). Ranking obtained by modified SAW method for alternatives is given in Table 7.

TABLE 5. Comparative study of ranking for FMS selection

FMS Alternative	1	2	3	4	5	6	7	8
S_i	3.59	3.29	2.53	4.07	3.89	2.38	4.15	1.27
Rank	4	5	6	2	3	7	1	8

TABLE 6. Decision matrix for NTM process selection [16]

Alternatives	Criteria									
	TSF	PR	MR ₁	C	η	TF	TC	S	WM	SF
Ultrasonic machining (USM)	1	10	500	2	4	2	3	1	5	5
Water jet machining (WJM)	2.5	0.22	0.8	1	4	2	2	3	5	4
Abrasive jet machining (AJM)	2.5	0.24	0.5	1	4	2	2	3	5	4
Electrochemical machining (ECM)	3	100	400	5	2	3	1	3	1	1
Chemical machining (CHM)	3	0.4	15	3	3	2	1	3	3	1
Electric discharge machining (EDM)	3.5	2.7	800	3	4	4	4	3	1	5
Wire electrical discharge machining (WEDM)	3.5	2.5	600	3	4	4	4	3	1	5
Electron beam machining (EBM)	2.5	0.2	1.6	4	5	2	1	3	5	5
Laser beam machining (LBM)	2	1.4	0.1	3	5	2	1	3	5	5
Weight considered (Wi)	0.0783	0.0611	0.1535	0.1073	0.0383	0.0271	0.0195	0.0146	0.2766	0.2237

TABLE 7. Comparative study of ranking for NTM process selection

Alternatives	USM	WJM	AJM	ECM	CHM	EDM	WEDM	EBM	LBM
S_i	4.584	3.871	3.87	1.498	2.295	3.141	2.988	3.829	4.015
Rank	1	3	4	9	8	6	7	5	2

4. RESULTS AND DISCUSSION

It has been observed from Table 3 that, Cybotech V15 electric robot is considered as the best alternative according to the Modified SAW method for the robot selection problem. That robot is specifically suitable for multiple purposes including welding, drilling, routing, assembly, and many other operations.

While solving the FMS selection problem, Table 5 indicates FMS7 as the best alternative with a considerably high percentage reduction of labor cost, work in process, and set up costs along with high improvement in quality and considerable improvement in market response. It has been observed to be achieved at considerably low capital and maintenance costs which is beneficial from a managerial point of view.

During NTM process selection, Ultrasonic Machining (USM) has been determined as the best alternative based on the criteria chosen for analysis and given in Table 7. The USM process is particularly useful for machining high precision parts from hard and brittle difficult-to-machine materials.

Further, the sensitivity of the solution to a change in the criteria weight obtained through the modified SAW method was evaluated to estimate the stability of the method. This analysis has been conducted with case study 1 for industrial robot selection. There are five criteria (C1-C5) and the possible interchanges are ten ($5C_2$) as shown in Figure 1. During analysis, weights of a pair of criteria are interchanged for all alternatives, i.e., all industrial robots under study. But from the sensitivity plot given in Figure 1, the ranking of the robots does not observe to vary to a great extent even after interchanging the criteria weights. Moreover, in all the cases, the Cybotech V15 Electric robot always outperforms others. It indicates the high stability of the modified SAW method.

The study of sensitivity for the modified SAW method has been further extended by comparing the ranking of industrial robot selection problems with four other popular MCDM methods such as MABAC, MOORA, TOPSIS, and AHP. It can be observed from

Figure 2 that, the Cybotech V15 Electric robot is ranked as the best alternative for all methods under study while other alternatives have placed in different positions. It establishes the robustness of the proposed method. Similar results have been obtained with the other two case studies.

A comparative study between the proposed modified SAW method with other MCDM methods, like MABAC, AHP, TOPSIS, COPRAS, ELECTRE, PROMETHEE, etc in terms of computational time, simplicity, mathematical calculations involved, stability, robustness, and type of information obtained has been shown in Table 8. The simplicity of the modified SAW method is high and it is easy to implement. The computational time is very less. The involvement of very less mathematical calculation causes ease in implementation. The superiority of the proposed method compared to other MCDM methods will surely encourage decision-makers to employ it in practical applications. Comparison of modified SAW method with other MCDM methods for Industrial Robot Selection problem is shown in Figure 2.

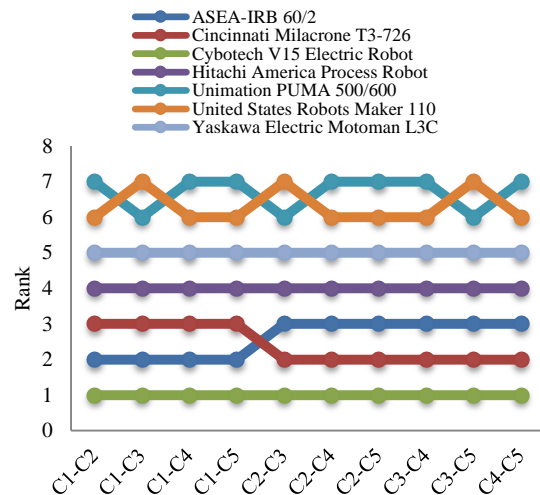


Figure 1. Sensitivity analysis of modified SAW method for Industrial Robot Selection problem

TABLE 8. Comparative performance of some popular MCDM method

MCDM method	Computational time	Simplicity	Mathematical calculation involved	Stability	Robustness	Information type
MODIFIED SAW	Very less	Very simple	Minimum	Good	High	Quantitative
MABAC	less	Simple	Moderate	Good	High	Quantitative
AHP	Very high	Very critical	Maximum	Poor	Less	Mixed
TOPSIS	Moderate	Moderately critical	Moderate	Medium	Moderate	Quantitative
COPRAS	Moderate	Moderately critical	Moderate	Medium	Moderate	Quantitative
ELECTRE	High	Moderately critical	Moderate	Medium	Moderate	Mixed
PROMETHEE	High	Moderately critical	Moderate	Medium	Moderate	Mixed

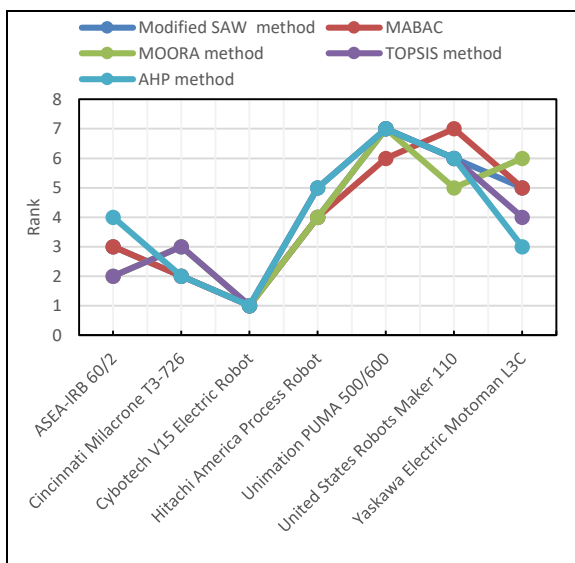


Figure 2. Comparison of modified SAW method with other MCDM methods for Industrial Robot Selection problem

5. CONCLUSION

Present work proposed a modified SAW method for decision making under conflicting environments from a significant number of available alternatives for a complex engineering problem. The efficacy of the proposed method was tested for three case studies based on robot selection, FMS selection, and non-traditional machining process selection, respectively.

- For the robot selection problem, Cybotech V15 electric robot is considered as the best alternative which is specifically suitable for multiple purposes including welding, drilling, routing, assembly, and many other operations
- For FMS selection problem, FMS7 is selected as the best alternative with a considerably high percentage reduction of labor cost, work in process, and set up costs along with improvement in quality and market response while capital and maintenance costs remained quite low.
- For the NTM process selection problem, Ultrasonic Machining has been determined as the best alternative which is useful for providing high precision parts from hard and brittle difficult-to-machine materials.
- The proposed method employed a concept of forming a scaled normalized decision matrix that simplified further computation resulting in non-occurrence of negative performance score during the evaluation of ranking.
- The method is stable during sensitivity analysis, as ranks obtained for the alternatives remained almost unchanged even with interchanging the criteria weights.

- The method is robust as the best ranking obtained through the modified SAW method is found to corroborate well with that has been obtained by other popular MCDM methods.
- Compared to other available methods, the proposed method is simple, easy to understand, involves minimum mathematical calculation with low computation time, and is quantitative in nature.
- With such advantages, the modified SAW method may be effectively employed for solving ranking and selection problems in any sector of society.

6. REFERENCES

1. Mardani, A., Jusoh, A., Nor, K. MD., Khalifah, Z., Zakwan, N., Valipour, A., "Multiple criteria decision-making techniques and their applications – a review of the literature from 2000 to 2014", *Economic Research-Ekonomska Istraživanja*, Vol. 28, No. 1, (2015), 516-571. DOI: 10.1080/1331677X.2015.1075139
2. Phan Nguyen, H., Vu Ngo, N., Tam Nguyen, C., "Study on Multi-objects Optimization in EDM with Nickel Coated Electrode using Taguchi-AHP-Topsis", *International Journal of Engineering, Transactions B: Applications*, Vol. 35, No. 02, (2022), 276-282, DOI: 10.5829/ije.2022.35.02b.02
3. Tabasi, S., Kakha, G. H., "An Application of Fuzzy-VIKOR Method in Environmental Impact Assessment of the Boog Mine Southeast of Iran", *International Journal of Engineering, Transactions C: Aspects* Vol. 34, No. 6, (2021), 1548-1559. DOI: 10.5829/ije.2021.34.06c.19
4. Dadashpour, I., Bozorgi-Amiri, A., "Evaluation and Ranking of Sustainable Third-party Logistics Providers using the D-Analytic Hierarchy Process", *International Journal of Engineering, Transactions B: Applications*, Vol. 33, No. 11, (2020), 2233-2244. DOI: 10.5829/IJE.2020.33.11B.15
5. Chakraborty, S., "Applications of the MOORA method for decision making in manufacturing environment", *International Journal of Advanced Manufacturing Technology*, Vol. 54, No. 9, (2010), 1155-1166. DOI: 10.1007/s00170-010-2972-0
6. Vahdani, B., Mousavi, S.M., Tavakkoli-Moghaddam, R., Ghodrathnama, A., Mohammadi, M., "Robot selection by multiple criteria complex proportional assessment method under an interval-valued fuzzy environment", *International Journal of Advanced Manufacturing Technology*, Vol. 73, (2014), 687-697, DOI: 10.1007/s00170-014-5849-9
7. Parameshwaran, R., Praveen Kumar, S., Saravanakumar, K., "An integrated fuzzy MCDM based approach for robot selection considering objective and subjective criteria", *Applied Soft Computing*, Vol. 26, (2015), 31-41, DOI: 10.1016/j.asoc.2014.09.025
8. Ghorabae, M.K., "Developing an MCDM method for robot selection with interval type-2 fuzzy sets", *Robotics and Computer-Integrated Manufacturing*, Vol. 37, (2016), 221-232. DOI: 10.1016/j.rcim.2015.04.007
9. Rashid, T., Ali, A., Chu, Y-M., "Hybrid BW-EDAS MCDM methodology for optimal industrial robot selection", *PLoS ONE*, Vol. 16, No. 2, (2021), e0246738. DOI: 10.1371/journal.pone.02467
10. Garduño-Aparicio, M., Rodríguez-Reséndiz, J., Macias-Bobadilla, G., and Thenozhi, S., "A Multidisciplinary Industrial Robot Approach for Teaching Mechatronics-Related Courses," *IEEE Transactions on Education*, Vol. 61, No. 1, (2018), 55-62, DOI: 10.1109/TE.2017.2741446.

11. Martínez-Prado, M., Rodríguez-Reséndiz, J., Gómez-Loenzo, R., Herrera-Ruiz, G., Franco-Gasca, L., "An FPGA-Based Open Architecture Industrial Robot Controller," *IEEE Access*, Vol. 6, (2018), 13407-13417, DOI: 10.1109/ACCESS.2018.2797803.
12. Padilla-Garcia, E. A., Rodriguez-Angeles, A., Reséndiz, J. R., Cruz-Villar, C. A., "Concurrent Optimization for Selection and Control of AC Servomotors on the Powertrain of Industrial Robots," *IEEE Access*, Vol. 6, (2018), 27923-27938, DOI: 10.1109/ACCESS.2018.2840537.
13. Taha, Z., Rostam, S., "A hybrid fuzzy AHP-PROMETHEE decision support system for machine tool selection in flexible manufacturing cell", *Journal of Intelligent Manufacturing*, Vol. 23, (2012), 2137-2149. DOI: 10.1007/s10845-011-0560-2
14. Mishra, R., Pundir, A.K., Ganapathy, L., "Evaluation and prioritisation of manufacturing flexibility alternatives using integrated AHP and TOPSIS method: Evidence from a fashion apparel firm", *Benchmarking: An International Journal*, Vol. 24, No. 5, (2017), 1437-1465. DOI: 10.1108/BIJ-07-2015-0077
15. Mathew, M., Thomas, J., "Interval valued multi-criteria decision making methods for the selection of flexible manufacturing system", *International Journal of Data and Network Science*, Vol. 3, No. 4, (2019), 349-358. DOI: 10.5267/j.ijdns.2019.4.001
16. Chakladar, N.D., Chakraborty, S., "A combined TOPSIS-AHP method based approach for non-traditional machining processes selection". *Proceedings of the Institution of Mechanical Engineers Part B, Journal of Engineering Manufacture*, Vol. 222, No. 12, (2008) 1613-1623. DOI: 10.1243/09544054JEM1238
17. Roy, M.K., Ray, A., Pradhan, B.B., "Non-traditional machining process selection using integrated fuzzy AHP and QFD techniques: a customer perspective", *Production & Manufacturing Research*, Vol. 2, No. 1, (2014), 530-549, DOI: 10.1080/21693277.2014.938276
18. Afshari, A., Mojahed, M., Yusuff, R. M., "Simple Additive Weighting approach to Personnel Selection problem", *International Journal of Innovation, Management and Technology*, Vol. 1, No. 5, (2010), 311-315. DOI: 10.7763/IJIMT.2010.V1.89
19. Biswas, T., Saha, P., "Selection of commercially available scooters by new MCDM method", *International of Data and Network Science*, Vol. 3, No. 2, (2019), 137-144. DOI: 10.5267/j.ijdns.2018.12.002
20. Bhangale, P.P., Agrawal, V.P., Saha, S.K., "Attribute based specification, comparison and selection of a robot", *Mechanism and Machine Theory*, Vol. 39, (2004), 1345-1366. DOI: 10.1016/j.mechmachtheory.2004.05.020
21. Karsak, E.E., Kuzgunkaya, O., "A fuzzy multiple objective programming approach for the selection of a flexible manufacturing system", *International Journal of Production Economics*, Vol. 79, (2002), 101-111. DOI: 10.1016/S0925-5273(00)00157-2
22. Rao, R.V., Pamichkun, M., "Flexible manufacturing system selection using a combinatorial mathematics-based decision-making method". *International Journal of Production Research*, Vol. 47, (2008), 6981-6998. DOI: 10.1080/00207540802389227

Persian Abstract

چکیده

تکنیک‌های تصمیم‌گیری چند معیاره (MCDM) به طور گسترده توسط تصمیم‌گیرندگان برای رتبه‌بندی گزینه‌های بالقوه در محیط‌های متضاد به کار گرفته می‌شوند تا بهترین گزینه برای مشکلات صنعتی مختلف انتخاب شود. کار حاضر از روش وزن‌دهی افزودنی ساده (SAW) برای حل مشکلات مختلف تصمیم‌گیری در صنعت تولید مانند انتخاب ربات صنعتی، انتخاب سیستم‌های تولید انعطاف‌پذیر و انتخاب فرآیندهای ماشین‌کاری غیر سنتی استفاده می‌کند. روش پیشنهادی ساده است و شامل پیچیدگی ریاضی کمتری است. رتبه‌بندی به دست آمده با روش پیشنهادی اصلاح شده SAW به خوبی با روش‌های رایج MCDM مانند MOORA، MABAC، TOPSIS و AHP برای حل مسائل مشابه تأیید می‌شود. این نشان دهنده اعتبار و پایدارای روش پیشنهادی است. با این حال، روش پیشنهادی به دلیل سادگی، پیچیدگی محاسباتی کمتر و زمان محاسباتی کمتر در مقایسه با آن روش‌ها بهتر است. علاوه بر این، تجزیه و تحلیل حساسیت نشان دهنده پایدارای روش است. از آنجایی که روش عمومی است، می‌توان برای حل مسائل مربوط به رتبه‌بندی و انتخاب در هر بخش اجتماعی استفاده کرد.



Probabilistic Assessment of Bending Strength of Statically Indeterminate Reinforced Concrete Beams

H. A. T. Nguyen*

Faculty of Civil Engineering, University of Architecture Ho Chi Minh City, HCMC, Vietnam

PAPER INFO

Paper history:

Received 27 November 2021

Received in revised form 11 January 2022

Accepted 13 January 2022

Keywords:

Reinforced Concrete Beam

Moment Redistribution

Reliability Index

Failure Probability

Monte Carlo Simulation

ABSTRACT

This paper presents a reliability analysis of a two-span reinforced concrete beam, taking into account of random variations in cross-sectional dimensions, area and position of reinforcement for sagging and hogging bending moments, material strengths, loads and model uncertainties. In addition, the limit state functions for the statically indeterminate beam were derived; considering the static equilibrium requirement after the moments were redistributed as well as the codified allowable limit for the adjusted moment at each beam section. A large number of Monte Carlo simulations were performed in which the basic variables were modeled with normal, lognormal and Gumbel distributions. When the elastic moment distribution was used in evaluating the beam reliability, the two-span beam behaved as a series system with three critical nodes located at the interior support and midspan sections. The probability that the system had at least one overloaded node was greater than the failure probability of an individual node. However, considering moment redistribution made it possible to reduce the amount of reinforcement whilst maintaining the reliability of the beam. When the reinforcement area was reduced by 26% at the support section or 14% at the midspan sections, the failure probability was predicted to be 6.90×10^{-5} , which is deemed acceptable for a 50 year reference period.

doi: 10.5829/ije.2022.35.04a.24

1. INTRODUCTION

Building structures are to satisfy requirements including safety of the structures against collapse, limitations on damage, deflection, vibration or other criteria. According to current structural codes, the design of reinforced concrete beams as well as other structural members is normally based on partial safety factors and characteristic values of action and resistance effects [1]. The code-based method is a refined version of the deterministic approach and can be classified as semi-probabilistic. On the other hand, a full probabilistic approach would not use partial factors of safety but directly consider inherent uncertainties in the loading, material properties and other random variables relevant to the structure behavior and safety.

Reliability is the ability of a structure to satisfy the specified requirements at any time during its design life

[2]. Each requirement can be considered as a limit state. Let R and E be the resistance and load effect respectively. The failure probability P_f of a structure can be written as $P_f = P(R < E)$ or $P_f = P(R/E < 1)$ or in general:

$$P_f = P(Z(R, E) < 0) \quad (1)$$

where Z is the limit state function and P_f is the probability of limit state violation [3]. The measurement of reliability can be identified with the survival probability $P_s = (1 - P_f)$ or the reliability index β which is the ratio of the mean value of Z to its standard deviation if Z is normally distributed. For other distribution of Z , β is just a conventional measure of the reliability and using P_f or P_s would be more meaningful. For structural members of residential and office buildings assessed at the ultimate limit state, the recommended target reliability index is 3.8 corresponding to a target failure probability of 7.23×10^{-5} for a reference period of 50 years [4]. Examples of

*Corresponding Author Institutional Email:
uan.nguyenuanh@uah.edu.vn (H. A. T. Nguyen)

application of reliability analysis in building structures include prediction of flexural behavior of beams subjected to pitting corrosion [5], evaluation of shear strength of deep beams with and without web reinforcement [6], torsional design of reinforced concrete beams strengthened with CFRP laminate [7]. The list also includes assessment of existing reinforced concrete beams when strengthened with additional reinforcing bars [8], evaluation of bearing capacity of slabs considering compressive membrane action [9], structural fire safety assessment of slabs exposed to fire [10], reliability analysis of seismic hazard [11], seismic assessment of buildings with soft-story and torsional irregularities [12]. As a contribution to the trend of reliability-based design, the present paper discusses a probabilistic procedure for evaluation of flexural strength of a statically indeterminate reinforced concrete beam considering the effect of moment redistribution.

Whilst a beam is normally designed based on its elastic moment envelope, moment redistribution allows the transfer of moments from critical sections where plastic hinges have formed to underutilized sections. Experimental studies showed that moment redistribution in reinforced concrete beams could occur not only at the ultimate limit state but also at the serviceability limit state [13]. A good capacity for plastic rotation and moment redistribution was also observed in high-strength concrete beams with low tensile reinforcement ratios [14]. The neutral axis depth of the beam was found to effect the redistribution ratio [15]. The plastic zones in the beam after yielding could behave like rotational springs [16]. The practical approach to allow for moment redistribution is using codified moment redistribution factor to adjust the bending moment diagram obtained from a linear elastic analysis without explicit verification of the rotation capacity. Alternatively, a plastic analysis is performed to determine the rotational demand and capacity of the hinges from first principles [17]. Some nonlinear failure analysis models have been proposed such as a stress resultant beam element with embedded discontinuity in rotations [18], a damaged-plasticity model for the concrete [19], and a fictitious crack model based on nonlinear fracture mechanics [20]. To ensure rotation capacity at the section of plastic hinges, contemporary design codes specify the allowable redistribution ratio as a function of the ratio of neutral axis depth to the section effective depth [21, 22]. The redistribution limit can also be based on the net tensile strain of the reinforcement [23].

In this paper, a two-span concrete beam is first reinforced in accordance with Eurocode 2. The limit state functions for flexural strength of the beam are then developed considering the codified limits for the redistribution ratio as well as the requirement for static equilibrium after the moments were redistributed, following the lower bound approach of plastic theory [1].

The effectiveness of moment redistribution in maintaining the beam reliability when the provided steel areas are less than the elastic-moment-based steel areas is examined via a large number of Monte Carlo simulations.

2. METHODS

2. 1. Ultimate Bending Strength and Moment Redistribution to Eurocode 2

The design moment capacity at the ultimate limit state of a singly reinforced rectangular beam, M_{Rd} , assuming that the reinforcement has yielded, can be obtained from the following expressions:

$$M_{Rd} = A_s f_{yd} (d - 0.5x) \quad (2)$$

$$x b f_{cd} = A_s f_{yd} \quad (3)$$

where A_s and f_{yd} are the area and design yield strength of the tension reinforcement, d and b are the effective depth and width of the section respectively; f_{cd} is the design compressive strength of concrete and x corresponds to the depth of the equivalent rectangular concrete stress block. The design strengths are taken as $f_{cd} = 0.85 f_{ck} / \gamma_c$ and $f_{yd} = f_{yk} / \gamma_s$ in which f_{ck} and f_{yk} are the characteristic compressive strength of concrete and yield strength of reinforcement, $\gamma_c = 1.5$ and $\gamma_s = 1.15$ are the partial factors of safety for the concrete and reinforcement, respectively [1].

In case moment redistribution is implemented, the redistribution ratio δ , which is the ratio of the modified moment to elastic moment at a section, for concrete with f_{ck} less than or equal to 50 MPa, should satisfy:

$$\delta \geq 0.44 + 1.25c/d \quad (4)$$

where $c = x/0.8$ is the depth of the neutral axis of the section. It is also recommended that the bending moment capacity at any section should not be less than 70% of the elastic moment, i.e. $\delta \geq 0.7$. Static equilibrium must be maintained after redistribution of moments. Do Carmo and Lopes tested 10 two-span beams up to failure [14]. The recommendations of Eurocode 2 were found to be within safety limits and very similar to the experimental results for both normal-strength and high-strength concrete beams. The test also showed that the recommendations of ACI 318 were conservative for high-strength concrete beams whilst the Canadian code prediction for high values of c/d might be unsafe.

2. 2. Case Study Beam and Random Variables for Reliability Analysis

Figure 1 depicts a two-span beam subjected to the concentrated permanent loads G_1 , G_2 with the same characteristic value of G_k and imposed load Q_1 , Q_2 with the same characteristic value of Q_k . The beam self-weight was already included in the permanent load. The beam has a span length of 8 meters and is part of a floor system for general office use. The characteristic

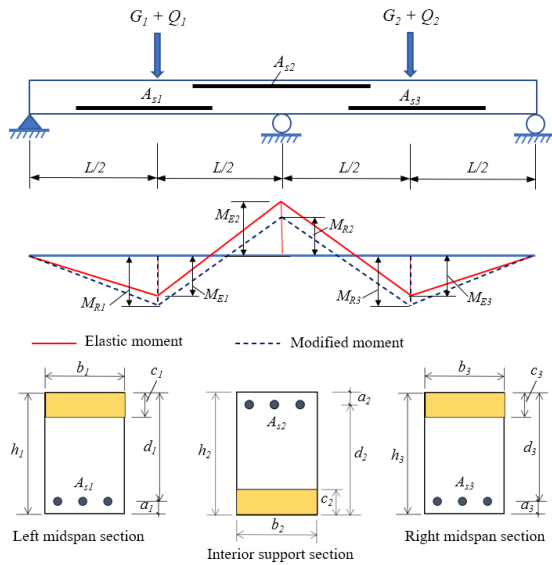


Figure 1. Bending moment diagram and cross sections details of investigated beam

compression strength of the concrete is $f_{ck} = 25$ MPa and yield strength of the steel reinforcement is $f_{yk} = 500$ MPa. The cross sections have a nominal overall depth of $h = 600$ mm, width $b = 300$ mm and reinforcement axis distance of $a = 60$ mm. The maximum moments derived from an elastic analysis are M_{E1} , M_{E2} and M_{E3} . The areas of tension reinforcement provided at the critical sections with maximum moments are A_{s1} and A_{s3} at midspans and A_{s2} over the interior support of the beam. The moments of resistance of the sections associated with the steel areas A_{s1} , A_{s2} and A_{s3} are M_{R1} , M_{R2} and M_{R3} , respectively.

Table 1 presents the statistical properties of basic random variables X adopted by the reliability analysis, which include dimensions of cross sections, areas and positions of reinforcements, strengths of materials, loads and model uncertainties. The statistical data of the variables are obtained from real buildings in European countries and reported in the European publication EUR 29410 [24]. The normal distribution is suitable for symmetric random variables with low variation (coefficient of variation less than 0.3) such as the dead load and geometrical dimensions of cross-sections. The lognormal distribution with lower limit at zero is recommended for representation of mechanical properties of materials whose logarithms are normally distributed. The Gumbel distribution, which has a simple exponential shape, can be used to represent the distribution of extreme values of random variables such as the live load and wind pressure. In Table 1, the subscripts 1, 2, 3 included in the parameters h , b , A_s , a , f_s , f_c correspond to the midspan section of the left span, the interior support section, and the midspan section of the right span, respectively. The live loads Q_1 , Q_2 were modeled by a Gumbel distribution with an average of

TABLE 1. Statistical properties of random variables

Symbol, X	Mean, μ_X	Standard deviation, σ_X	Distribution
b_1, b_2, b_3	b	10 mm	Normal
A_{s1}, A_{s2}, A_{s3}	A_{s1}, A_{s2}, A_{s3}	$0.02\mu_X$	Normal
a_1, a_2, a_3	a	10 mm	Normal
f_{y1}, f_{y2}, f_{y3}	$f_{yk} + 2\sigma_X$	$0.053\mu_X$	Lognormal
f_{c1}, f_{c2}, f_{c3}	$f_{ck} + 2\sigma_X$	$0.121\mu_X$	Lognormal
G_1, G_2	G_k	$0.1\mu_X$	Normal
Q_1, Q_2	$0.6Q_k$	$0.35\mu_X$	Gumbel
θ_R	1	0.1	Normal
θ_E	1	0.1	Normal

$0.6Q_k$ and coefficient of variation of 0.35 as recommended by the EUR 29410 for general offices with a 50 year reference period. The model uncertainties factors θ_E and θ_R take account of imprecision and incompleteness of the relevant theoretical models for load and resistance effects [24].

2. 3. Limit State Functions

2. 3. 1. Without Moment Redistribution Since redistribution of moment is not considered, the bending capacity of each critical section of the beam must be checked against the elastic moment at that section. The limit state functions $Z_1(X)$, $Z_2(X)$ and $Z_3(X)$ for flexural strength of individual cross sections (left midspan, interior support, right midspan) are given by Equations (5)-(7) where the expressions for moment capacity M_{R1} , M_{R2} and M_{R3} were derived from Equations (2)-(3). The expressions of maximum moments M_{E1} , M_{E2} and M_{E3} at the midspan and support sections were obtained from a conventional elastic structural analysis of the two-span beam [25].

$$Z_1(X) = M_{R1} - M_{E1} = \theta_R A_{s1} f_{y1} \left(d_1 - \frac{0.5 A_{s1} f_{y1}}{0.85 b_1 f_{c1}} \right) - \theta_E \{0.2031(G_1 + Q_1) - 0.0469(G_2 + Q_2)\} L \quad (5)$$

$$Z_2(X) = M_{R2} - M_{E2} = \theta_R A_{s2} f_{y2} \left(d_2 - \frac{0.5 A_{s2} f_{y2}}{0.85 b_2 f_{c2}} \right) - \theta_E (G_1 + Q_1 + G_2 + Q_2) 0.09375 L \quad (6)$$

$$Z_3(X) = M_{R3} - M_{E3} = \theta_R A_{s3} f_{y3} \left(d_3 - \frac{0.5 A_{s3} f_{y3}}{0.85 b_3 f_{c3}} \right) - \theta_E \{0.2031(G_2 + Q_2) - 0.0469(G_1 + Q_1)\} L \quad (7)$$

2. 3. 2. With Moment Redistribution

When moment redistribution is considered, it is not compulsory to reinforce each beam section based on the elastic moment. The beam can be designed on the basis of the lower bound approach (or “safe” or “static” method) which is allowed by Eurocode 2. The modified moments can now be taken as the moments of resistance M_{R1} , M_{R2}

and M_{R3} of the sections as shown in Figure 1. The yield condition is hence not violated anywhere. In order to maintain static equilibrium after the moments were redistributed as required by the lower bound method [1], the limit state functions $Z_4(X)$ and $Z_5(X)$ are written as Equations (8) and (9) for the left and right spans. The total bending resistance is $(M_{R1} + 0.5M_{R2})$ for the whole left span and $(M_{R3} + 0.5M_{R2})$ for the whole right span. The total static applied moment of the left and right spans are $(G_1 + Q_1)L/4$ and $(G_2 + Q_2)L/4$ respectively when the concentrated loads are applied at midspan of the beam.

$$Z_4(X) = \theta_R \left\{ A_{s1} f_{y1} \left(d_1 - \frac{0.5A_{s1} f_{y1}}{0.85b_1 f_{c1}} \right) + 0.5A_{s2} f_{y2} \left(d_2 - \frac{0.5A_{s2} f_{y2}}{0.85b_2 f_{c2}} \right) \right\} - \theta_E (G_1 + Q_1)L/4 \quad (8)$$

$$Z_5(X) = \theta_R \left\{ A_{s3} f_{y3} \left(d_3 - \frac{0.5A_{s3} f_{y3}}{0.85b_3 f_{c3}} \right) + 0.5A_{s2} f_{y2} \left(d_2 - \frac{0.5A_{s2} f_{y2}}{0.85b_2 f_{c2}} \right) \right\} - \theta_E (G_2 + Q_2)L/4 \quad (9)$$

In addition, the limit state functions $Z_6(X)$, $Z_7(X)$ and $Z_8(X)$ of Equations (10)-(12) are derived to reflect the allowable limits for the redistribution ratio given by Equation (4). These functions relate the adjusted moment ratios M_{R1}/M_{E1} , M_{R2}/M_{E2} and M_{R3}/M_{E3} to the ratio of the depth of the compression zone to the effective depth of the sections c_1/d_1 , c_2/d_2 and c_3/d_3 . Eurocode 2 suggests that using the codified redistribution ratios with linear elastic analysis is possible without explicit verification of the rotation capacity in continuous beams [1].

$$Z_6(X) = \frac{M_{R1}}{M_{E1}} - \max \left\{ \left(0.44 + \frac{1.25f_{y1}A_{s1}}{0.68f_{c1}b_1d_1} \right); 0.7 \right\} \quad (10)$$

$$Z_7(X) = \frac{M_{R2}}{M_{E2}} - \max \left\{ \left(0.44 + \frac{1.25f_{y2}A_{s2}}{0.68f_{c2}b_2d_2} \right); 0.7 \right\} \quad (11)$$

$$Z_8(X) = \frac{M_{R3}}{M_{E3}} - \max \left\{ \left(0.44 + \frac{1.25f_{y3}A_{s3}}{0.68f_{c3}b_3d_3} \right); 0.7 \right\} \quad (12)$$

2. 3. 3. Monte Carlo Simulation and Strength Evaluation

A large number of Monte Carlo simulations were performed to evaluate the ultimate flexural strength of individual cross sections as well as the whole beam. Firstly, independent random values of the variables with statistical properties given by Table 1 were generated using MATLAB built-in random number generators [26]. The limit state functions, or safety margins, of individual cross sections, Equations (5)-(7), and the whole beam, Equations (8)-(12), were then calculated. The random simulation process was repeated for 10 million times during which the number of failure events with negative safety margins were counted. Table 2 presents the criteria for a failure event relating to the strengths of an individual cross section and of the whole beam. The ratio of the number of failure events to the total number of trials defines the failure probability P_f .

TABLE 2. Failure criteria for individual cross sections and whole beam

Checked item	Failure criteria
Left midspan section, without moment redistribution	$Z_1(X) < 0$
Interior support section, without moment redistribution	$Z_2(X) < 0$
Right midspan section, without moment redistribution	$Z_3(X) < 0$
Whole beam, without moment redistribution	$(Z_1(X) < 0)$ or $(Z_2(X) < 0)$ or $(Z_3(X) < 0)$
Whole beam, with moment redistribution	$(Z_4(X) < 0)$ or $(Z_5(X) < 0)$ or $(Z_6(X) < 0)$ or $(Z_7(X) < 0)$ or $(Z_8(X) < 0)$

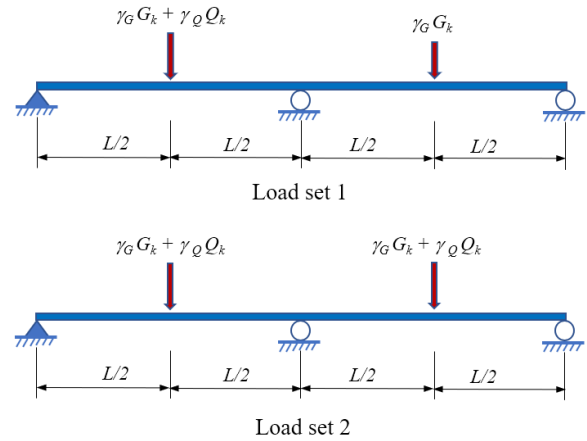


Figure 2. Load arrangements for design bending moment

3. RESULTS AND DISCUSSIONS

3. 1. Design Reinforcement to Eurocode 2 The required reinforcement areas were first determined using the Eurocode 2 conventional approach. For this symmetric beam, the elastic moment envelope can be obtained by considering the load arrangements shown in Figure 2; with the load set 1 aiming at getting the maximum sagging moment at the left midspan section and the load set 2 aiming at finding the maximum hogging moment at the interior support section.

At the ultimate limit state, the partial safety factors are $\gamma_G = 1.35$ and $\gamma_Q = 1.5$ for the permanent and imposed loads respectively. The maximum design moments were $M_{Ed2} = 317$ kNm at the interior support and $M_{Ed1} = 298$ kNm at the midspan section. The corresponding reinforcement areas computed using Equations (2)-(3) were $A_{s2} = 1591$ mm² at the interior support and $A_{s1} = A_{s3} = 1476$ mm² at the midspan sections.

3. 2. Reliability of Individual Cross Sections versus Whole Beam

The reinforcement areas based on the

elastic moment envelope were considered as the mean values of the reinforcement areas used in the Monte Carlo simulations. Table 3 presents the failure probability P_f and reliability index β for individual sections and the whole beams with and without moment redistribution (MR), obtained from 10^7 simulations.

The β values of both the midspan and support sections were higher than the recommended target value of 3.8. The P_f values for the individual sections and the whole beam either with or without moment redistribution were all well below the target failure probability of 7.23×10^{-5} , indicating that the traditional design approach was conservative. Without moment redistribution, the probability that the beam had at least one overloaded section was higher than the failure probability of any individual cross section. By contrast, considering moment redistribution resulted in the failure probability of the beam being significantly lower than the elastic-moment-based failure probability (Table 3).

Further Monte Carlo simulations were performed in which the mean reinforcement areas were reduced. Figure 3 shows the probability density functions (PDFs) of the elastic-based-moment and safety margin for the interior support section when its steel reinforcement area

TABLE 3. Reliability of beam with Eurocode-2-based reinforcement areas

Individual cross sections				Whole beam	
Midspan		Interior support		Without MR	With MR
P_f	β	P_f	β	P_f	P_f
2.39×10^{-5}	4.401	0.46×10^{-5}	4.320	5.02×10^{-5}	1.20×10^{-5}

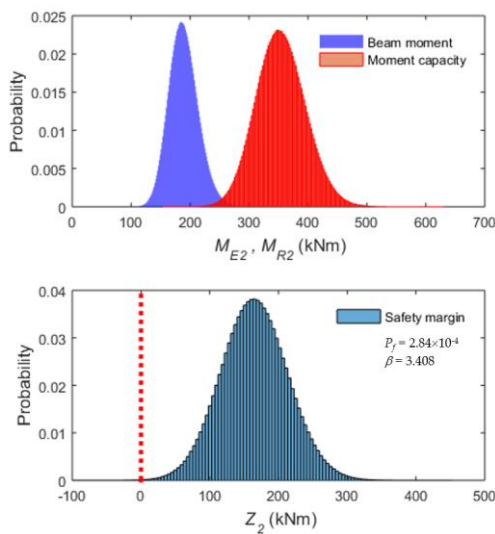


Figure 3. PDF of moment capacity of cross section at support with 20% reduction in A_{s2}

was reduced by 20%. The elastic-moment-based P_f of the interior support section was found to be 2.84×10^{-4} which is nearly four times higher the recommended target failure probability. However, the redistributed-moment-based P_f of the corresponding beam was 4.76×10^{-5} which is below the target failure probability (Figure 4). In the event that the reinforcement amount of each midspan section was reduced by 10%, the elastic-moment-based P_f of the midspan sections was 1.12×10^{-4} (Figure 5) whilst the beam with moment redistribution was still robust with a P_f value of 4.16×10^{-5} (Figure 6).

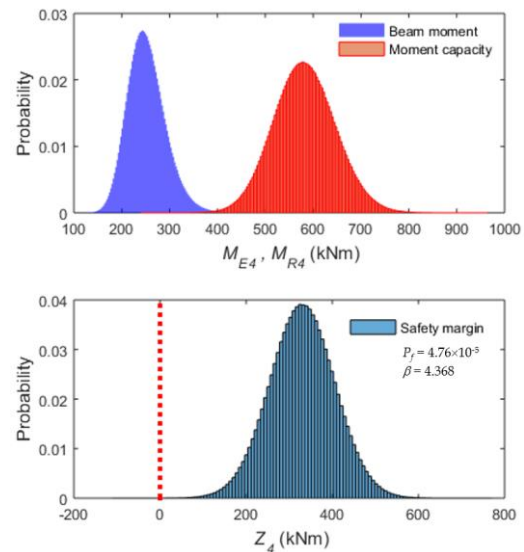


Figure 4. PDF of moment capacity of whole beam with 20% reduction in A_{s2}

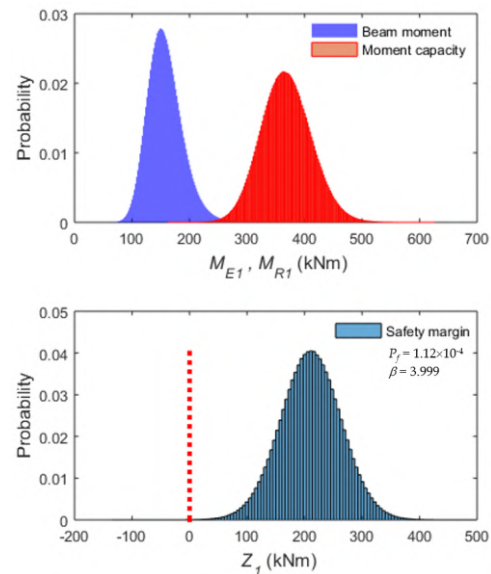


Figure 5. PDF of moment capacity of cross section at midspan with 10% reduction in A_{s1} and A_{s3}

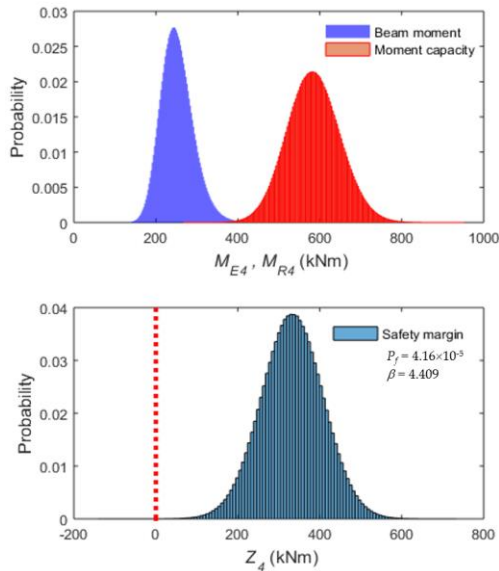


Figure 6. PDF of moment capacity of whole beam with 10% reduction in A_{s1} and A_{s3}

Let $A_{s,prov}$ be the steel areas provided for the beam sections and A_s be the steel areas resulted from the elastic moment envelope. Considering the $A_{s,prov}$ to A_s ratio varying from 0.7 to 1, the random simulations were performed again with $A_{s,prov}$ assigned to the mean values of the reinforcement areas. Figures 7 and 8 compare the elastic-moment-based P_f and β values of the sections with the modified-moment-based P_f and β values of the beam, for various $A_{s,prov}/A_s$ values.

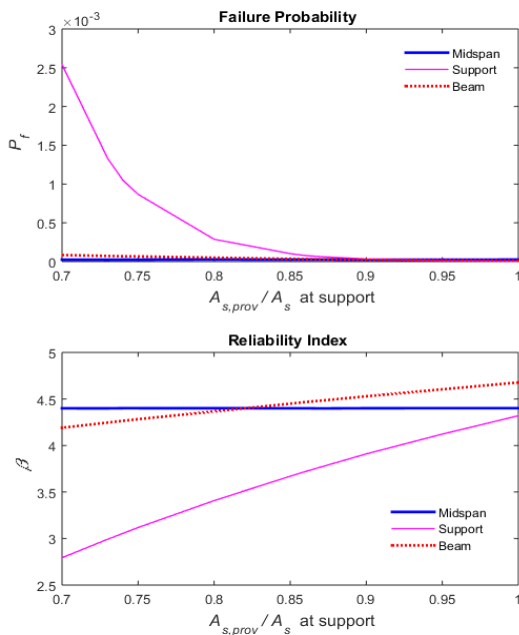


Figure 7. Reliability of individual cross sections and whole beam with reduction in A_{s2}

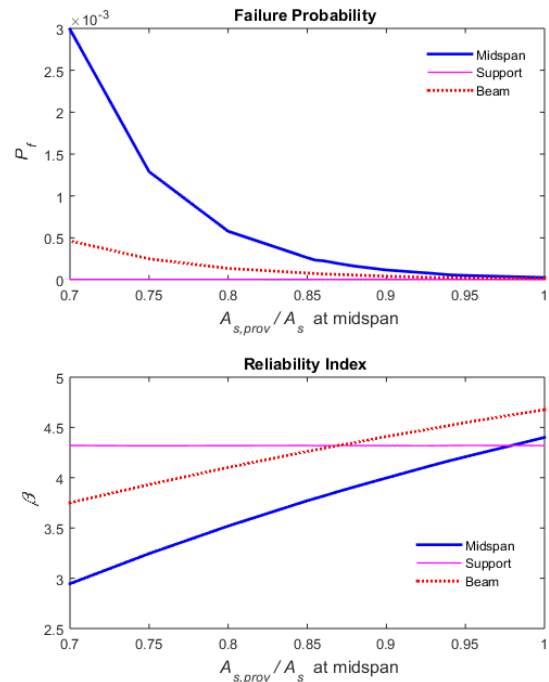


Figure 8. Reliability of individual cross sections and whole beam with reduction in A_{s1} and A_{s3}

3. 3. Reinforcement Modification and Beam Performance

Figure 9 allows identification of the failure probability and reliability index of the beam with moment redistribution considered when the

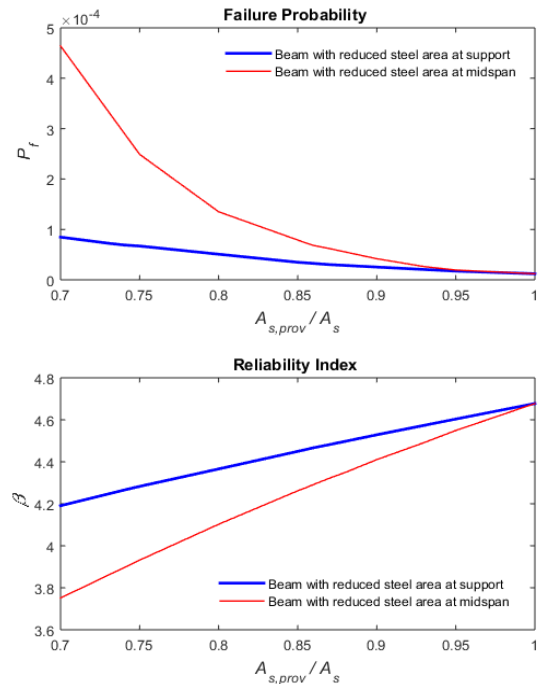


Figure 9. Performance of beam with reduced reinforcement areas

reinforcement areas at either the support or midspan sections were modified. For instance, using $A_{s,pro}/A_s = 0.9$ at the interior support section would provide $P_f = 2.53 \times 10^{-5}$ and $\beta = 4.529$ for the beam. Alternatively, taking $A_{s,pro}/A_s = 0.9$ at the midspan sections would result in $P_f = 4.18 \times 10^{-5}$ and $\beta = 4.410$ for the beam. For a further steel reduction with $A_{s,pro}/A_s$ equal to 0.74 at the support section or 0.86 at the midspan sections, the beam would still be acceptable with $P_f = 6.90 \times 10^{-5}$ and $\beta = 4.280$. The advantage of moment redistribution in statically indeterminate reinforced concrete beams was also confirmed by experimental data presented in the relevant literature. Testing 33 two-span beams, Scott and Whittle [13] observed that 23 specimens which failed in flexure essentially all achieved the designed 30% moment modification by the end of the test. The redistribution ratio limit of 0.7 specified by Eurocode 2 was hence guaranteed. The formation of plastic hinges was well recognized by the test. Another experimental work on two-span beams performed by Ehsani et al. [27] revealed a reduction of 18.5% in the measured moment compared with the elastic moment at the ultimate load, indicating a redistribution ratio of 0.815.

Moreover, the desired reliability of the beam could still be maintained when the reinforcement areas at all three critical sections (midspan sections 1, 3 and support section 2) were reduced properly. For instance, Table 4 presents the failure probability P_f , survival probability P_s and reliability index β of the beam in response to some reinforcement modification scenarios. As can be seen, all the obtained P_f values were lower than the target failure probability of 7.23×10^{-5} and the predicted β values were higher than the target reliability index of 3.80 for a reference period of 50 years.

TABLE 4. Examples of successful reinforcement modifications options

$A_{s,pro}/A_s$ at section			Beam performance		
1	2	3	P_f	P_f	β
0.89	0.94	0.89	6.74×10^{-5}	0.999933	4.283
0.91	0.90	0.91	6.66×10^{-5}	0.999933	4.290
0.93	0.87	0.93	6.68×10^{-5}	0.999933	4.284
0.95	0.83	0.95	6.97×10^{-5}	0.999930	4.275
0.97	0.80	0.97	6.90×10^{-5}	0.999931	4.282

4. CONCLUSIONS

From the research that has been carried out, the effect of moment redistribution on the flexural strength reliability of the statically indeterminate reinforced concrete beam can be seen.

- When the elastic moment distribution was used, the two-span beam behaved as a series system with three critical nodes located at the interior support and midspan sections. The probability that the system had at least one overloaded node was proved to be greater than the failure probability of each node.
- Without using moment redistribution, a 9% reduction in the support reinforcement area or a 2% reduction in the midspans reinforcement area was found to place the elastic-based beam in a vulnerable state with a P_f of 7.50×10^{-5} which exceeded the target value.
- When moment redistribution was considered, it was possible to reduce the amount of reinforcement whilst maintaining the reliability of the beam. The beam can still be deemed acceptable with a P_f of 6.90×10^{-5} when the reinforcement area was reduced by 26% at the support section or 14% at the midspan sections.
- Reasonable adjustments of the reinforcements of the support section simultaneous with the midspan sections were also found to ensure the beam reliability yet save the steel reinforcement amount.

5. REFERENCES

1. EN 1992-1-1:2004, "Eurocode 2 - Design of Concrete Structures, Part 1-1: General Rules and Rules for Buildings", Brussels, European Committee for Standardization, (2004).
2. ISO 2394:2015, "General principles on reliability for structures", Geneva, International Standards Organization, (2015).
3. Melchers, R.E. and Beck, A.T., "Structural reliability analysis and prediction", New Jersey, John Wiley & Sons, (2018).
4. EN 1990:2002, "Eurocode - Basis of structural design", Brussels, European Committee for Standardization, (2005).
5. Ghanooni-Bagha, M., Shayanfar, M.A., Reza-Zadeh, O. and Zabih-Samani, M., "The effect of materials on the reliability of reinforced concrete beams in normal and intense corrosions", *Maintenance and Reliability*, Vol. 19, No. 3, (2017), 393-402, doi: 10.17531/ein.2017.3.10.
6. Shahnewaz, M., Rteil, A. and Alam, M.S., "Shear strength of reinforced concrete deep beams—a review with improved model by genetic algorithm and reliability analysis", *Structures*, Vol. 23, (2020), 494-508, doi: 10.1016/j.istruc.2019.09.006.
7. Fadaee, M.J. and Dehghani, H., "Reliability-based torsional design of reinforced concrete beams strengthened with CFRP laminate", *International Journal of Engineering, Transactions A: Basics*, Vol. 26, No. 10, (2013), 1103-1110, doi: 10.5829/idosi.ije.2013.26.10a.01.
8. Khmil, R., Tytarenko, R., Blicharsky, Y. and Vegera, P., "Development of the procedure for the estimation of reliability of reinforced concrete beams, strengthened by building up the stretched reinforcing bars under load", *Eastern-European Journal of Enterprise Technologies*, Vol. 5, No. 7, (2018), 32-42, doi: 10.15587/1729-4061.2018.142750.
9. Arshian, A.H. and Morgenthal, G., "Probabilistic assessment of the ultimate load-bearing capacity in laterally restrained two-way reinforced concrete slabs", *Engineering Structures*, Vol. 150, (2017), 52-63, doi: 10.1016/j.engstruct.2017.07.035.
10. Heidari, M., Robert, F., Lange, D. and Rein, G., "Probabilistic study of the resistance of a simply-supported reinforced concrete

- slab according to Eurocode parametric fire", *Fire Technology*, Vol. 55, No. 4, (2019), 1377-1404, doi: 10.1007/s10694-018-0704-4.
11. Shahpari, A. and Yazdani, A., "The use of monte-carlo simulations in seismic hazard analysis in Tehran and surrounding areas", *International Journal of Engineering, Transactions C: Aspects*, Vol. 25, No. 2, (2012), 159-166, doi: 10.5829/idosi.ije.2012.25.02c.9.
 12. Razmkhah, M.H., Kouhestanian, H., Shafaei, J., Pahlavan, H. and Shamekhi Amiri, M., "Probabilistic seismic assessment of moment resisting steel buildings considering soft-story and torsional irregularities", *International Journal of Engineering, Transactions B: Applications*, Vol. 34, No. 11, (2021), 2476-2493, doi: 10.5829/IJE.2021.34.11B.11.
 13. Scott, R. and Whittle, R., "Moment redistribution effects in beams", *Magazine of Concrete Research*, Vol. 57, No. 1, (2005), 9-20, doi: 10.1680/macr.2005.57.1.9.
 14. Do Carmo, R.N. and Lopes, S.M., "Ductility and linear analysis with moment redistribution in reinforced high-strength concrete beams", *Canadian Journal of Civil Engineering*, Vol. 32, No. 1, (2005), 194-203, doi: 10.1139/04-080.
 15. Lou, T., Peng, C., Karavasilis, T.L., Min, D. and Sun, W., "Moment redistribution versus neutral axis depth in continuous PSC beams with external CFRP tendons", *Engineering Structures*, Vol. 209, (2020), 109927, doi: 10.1016/j.engstruct.2019.109927.
 16. Farouk, M.A. and Khalil, K.F., "New analytical method for computing moment redistribution in RC beams under concentrated load", *Australian Journal of Structural Engineering*, Vol. 22, No. 2, (2021), 120-139, doi: 10.1080/13287982.2021.1912518.
 17. Sturm, A.B., Visintin, P. and Oehlers, D.J., "Closed-form expressions for predicting moment redistribution in reinforced concrete beams with application to conventional concrete and ultrahigh performance fiber reinforced concrete", *Structural Concrete*, Vol. 21, No. 4, (2020), 1577-1596, doi: 10.1002/suco.201900498.
 18. Jukić, M., Brank, B. and Ibrahimbegović, A., "Embedded discontinuity finite element formulation for failure analysis of planar reinforced concrete beams and frames", *Engineering Structures*, Vol. 50, (2013), 115-125, doi: 10.1016/j.engstruct.2012.07.028.
 19. Earij, A., Alfano, G., Cashell, K. and Zhou, X., "Nonlinear three-dimensional finite-element modelling of reinforced-concrete beams: Computational challenges and experimental validation", *Engineering Failure Analysis*, Vol. 82, (2017), 92-115, doi: 10.1016/j.engfailanal.2017.08.025.
 20. Słowik, M., 2019. The analysis of failure in concrete and reinforced concrete beams with different reinforcement ratio. *Archive of Applied Mechanics*, Vol. 89, No. 5, (2019), 885-895. doi: 10.1007/s00419-018-1476-5.
 21. AS 3600:2018, "Concrete Structures", Sydney, Standards Australia Limited, (2018).
 22. CSA A23.3:2019, "Design of Concrete Structures", Rexdale, Canadian Standards Association, (2019).
 23. ACI 318-19, "Building Code Requirements for Structural Concrete and Commentary", Michigan, American Concrete Institute, (2019).
 24. Markova, J., Sousa, M., Dimova, S., Athanasopoulou, A., Iannaccone, S. and Pinto, A., "Reliability of structural members designed with the Eurocodes NDPs selected by EU and EFTA member states", EUR 29410 EN Publication by European commission and joint research centre, (2018).
 25. Hibbeler, R.C., "Structural analysis", 10th ed, Upper Saddle River, Pearson Prentice Hall, (2017).
 26. MathWorks, "MATLAB R2015a", Massachusetts, The MathWorks Inc., (2015).
 27. Ehsani, R., Sharbatdar, M.K. and Kheyroddin, A., "Ductility and moment redistribution capacity of two-span RC beams", *Magazine of Civil Engineering*, Vol. 90, No. 6, (2019), 104-118. doi: 10.18720/MCE.90.10.

Persian Abstract

چکیده

این مقاله یک تحلیل قابلیت اطمینان یک تیر بتن مسلح دو دهانه را ارائه می‌کند، که تغییرات تصادفی در ابعاد مقطع، مساحت و موقعیت آرمانور برای ممان‌های خمشی فرورفتگی و گریز، مقاومت مواد، بارها و عدم قطعیت‌های مدل را در نظر می‌گیرد. علاوه بر این، توابع حالت حدی برای تیر از نظر استاتیکی نامعین، با در نظر گرفتن نیاز تعادل ایستایی پس از توزیع مجدد ممان‌ها و همچنین حد مجاز مدون برای گشتاور تنظیم شده در هر مقطع پرتو، استخراج شد. تعداد زیادی شبیه‌سازی مونت کارلو انجام شد که در آن متغیرهای پایه با توزیع‌های نرمال، لگ نرمال و گامبل مدل‌سازی شدند. هنگامی که توزیع گشتاور الاستیک در ارزیابی قابلیت اطمینان تیر مورد استفاده قرار گرفت، تیر دو دهانه به عنوان یک سیستم سری با سه گره بحرانی واقع در بخش پشتیبانی داخلی و بخش میانی رفتار کرد. احتمال اینکه سیستم حداقل یک گره اضافه بار داشته باشد بیشتر از احتمال شکست یک گره منفرد بود. با این حال، در نظر گرفتن توزیع مجدد لنگر، کاهش میزان آرمانور را در عین حفظ قابلیت اطمینان تیر ممکن کرد. زمانی که ناحیه آرمانور ۲۶ درصد در بخش پشتیبانی یا ۱۴ درصد در بخش‌های میانی کاهش یافت، احتمال شکست ۰/۰۰۰۰۶۹ پیش‌بینی شد که برای یک دوره مرجع ۵۰ ساله قابل قبول تلقی می‌شود.

AIMS AND SCOPE

The objective of the International Journal of Engineering is to provide a forum for communication of information among the world's scientific and technological community and Iranian scientists and engineers. This journal intends to be of interest and utility to researchers and practitioners in the academic, industrial and governmental sectors. All original research contributions of significant value focused on basics, applications and aspects areas of engineering discipline are welcome.

This journal is published in three quarterly transactions: Transactions A (Basics) deal with the engineering fundamentals, Transactions B (Applications) are concerned with the application of the engineering knowledge in the daily life of the human being and Transactions C (Aspects) - starting from January 2012 - emphasize on the main engineering aspects whose elaboration can yield knowledge and expertise that can equally serve all branches of engineering discipline.

This journal will publish authoritative papers on theoretical and experimental researches and advanced applications embodying the results of extensive field, plant, laboratory or theoretical investigation or new interpretations of existing problems. It may also feature - when appropriate - research notes, technical notes, state-of-the-art survey type papers, short communications, letters to the editor, meeting schedules and conference announcements. The language of publication is English. Each paper should contain an abstract both in English and in Persian. However, for the authors who are not familiar with Persian, the publisher will prepare the latter. The abstracts should not exceed 250 words.

All manuscripts will be peer-reviewed by qualified reviewers. The material should be presented clearly and concisely:

- *Full papers* must be based on completed original works of significant novelty. The papers are not strictly limited in length. However, lengthy contributions may be delayed due to limited space. It is advised to keep papers limited to 7500 words.
- *Research notes* are considered as short items that include theoretical or experimental results of immediate current interest.
- *Technical notes* are also considered as short items of enough technical acceptability with more rapid publication appeal. The length of a research or technical note is recommended not to exceed 2500 words or 4 journal pages (including figures and tables).

Review papers are only considered from highly qualified well-known authors generally assigned by the editorial board or editor in chief. Short communications and letters to the editor should contain a text of about 1000 words and whatever figures and tables that may be required to support the text. They include discussion of full papers and short items and should contribute to the original article by providing confirmation or additional interpretation. Discussion of papers will be referred to author(s) for reply and will concurrently be published with reply of author(s).

INSTRUCTIONS FOR AUTHORS

Submission of a manuscript represents that it has neither been published nor submitted for publication elsewhere and is result of research carried out by author(s). Presentation in a conference and appearance in a symposium proceeding is not considered prior publication.

Authors are required to include a list describing all the symbols and abbreviations in the paper. Use of the international system of measurement units is mandatory.

- On-line submission of manuscripts results in faster publication process and is recommended. Instructions are given in the IJE web sites: www.ije.ir-www.ijeir.info
- Hardcopy submissions must include MS Word and jpg files.
- Manuscripts should be typewritten on one side of A4 paper, double-spaced, with adequate margins.
- References should be numbered in brackets and appear in sequence through the text. List of references should be given at the end of the paper.
- Figure captions are to be indicated under the illustrations. They should sufficiently explain the figures.
- Illustrations should appear in their appropriate places in the text.
- Tables and diagrams should be submitted in a form suitable for reproduction.
- Photographs should be of high quality saved as jpg files.
- Tables, Illustrations, Figures and Diagrams will be normally printed in single column width (8cm). Exceptionally large ones may be printed across two columns (17cm).

PAGE CHARGES AND REPRINTS

The papers are strictly limited in length, maximum 6 journal pages (including figures and tables). For the additional to 6 journal pages, there will be page charges. It is advised to keep papers limited to 3500 words.

Page Charges for Papers More Than 6 Pages (Including Abstract)

For International Author ***	\$55 / per page
For Local Author	100,000 Toman / per page

AUTHOR CHECKLIST

- Author(s), bio-data including affiliation(s) and mail and e-mail addresses).
- Manuscript including abstracts, key words, illustrations, tables, figures with figure captions and list of references.
- MS Word files of the paper.



THOMSON REUTERS

WEB OF SCIENCE



Scopus®



CAS®

A DIVISION OF THE
AMERICAN CHEMICAL SOCIETY



Scientific Indexing Services

Google
Scholar